Two-photon water splitting and related work for a green hydrogen economy

Dissertation

in kumulativer Form

zur Erlangung des akademischen Grades

Doctor rerum naturalium (Dr. rer. nat.)

der Mathematisch-Naturwissenschaftlichen Fakultät

der Universität Rostock

vorgelegt von

Jacob Schneidewind

Rostock, 2021

https://doi.org/10.18453/rosdok_id00002965

Die vorliegende Arbeit entstand in der Zeit von Oktober 2017 bis Oktober 2020 am Leibniz-Institut für Katalyse unter der Betreuung von Prof. Matthias Beller.

Gutachter:

Prof. Dr. Matthias Beller, Leibniz-Institut für Katalyse/Universität Rostock

Prof. Dr. Stefanie Tschierlei, Technische Universität Braunschweig

Prof. Dr. Burkhard König, Universität Regensburg

Jahr der Einreichung: 2020

Jahr der Verteidigung: 2021

Erklärung

Ich gebe folgende Erklärung ab:

1. Die Gelegenheit zum vorliegenden Promotionsvorhaben ist mir nicht kommerziell vermittelt worden. Insbesondere habe ich keine Organisation eingeschaltet, die gegen Entgelt Betreuerinnen/Betreuer für die Anfertigung von Dissertationen sucht oder die mir obliegenden Pflichten hinsichtlich der Prüfungsleistungen für mich ganz oder teilweise erledigt.
2. Ich versichere hiermit an Eides statt, dass ich die vorliegende Arbeit selbstständig angefertigt und ohne fremde Hilfe verfasst habe. Dazu habe ich keine außer den von mir angegebenen Hilfsmitteln und Quellen verwendet und die den benutzten Werken inhaltlich und wörtlich entnommenen Stellen habe ich als solche kenntlich gemacht.
3. Ich habe mich bisher weder an der Universität Rostock noch an einer anderen Hochschule um den Doktorgrad beworben.

Acknowledgments

I would like to wholeheartedly thank Prof. Matthias Beller for the trust and opportunities that he has gifted me over the last six and a half years. Starting with agreeing to a meeting and offering a research internship in 2014 despite me having no practical experience and then welcoming me back into his group in 2015, he has always provided a *Vertrauensvorschuss* beyond what could have been asked for. This was then followed by incredible support for completing my Bachelor and Master education. Over the last three years he has given me the amazing opportunity to pursue research in an independent and open fashion while also lending his ongoing support and encouragement. These experiences have had a profoundly positive impact on my personal and professional development and I could not have asked for a better mentor. He is showing the kind of leadership and support that inspires other minds and gives me something to aspire to in the future.

I would like to thank Dr. Henrik Junge for his outstanding support, which has enabled most of the research presented herein. By providing space, both literally and figuratively, resources and scientific insight he was instrumental to the success of this work.

Furthermore, I want to thank Dr. Ralf Jackstell, who has been an unwavering source of support during my time at LIKAT. By taking hours out of each day for five weeks during my first stay at the institute, he taught me a lot of the skills that were essential for this work. He has continued to be a great teacher while being part of his group and beyond. In this context I also want to thank Dr. Rosa Adam-Ortiz, Dr. Maximilian Hertrich and Dr. Anahit Pews-Davtyan, from whom I learned various valuable scientific skills.

I also want to thank Hrishi Olickel, who was a crucial part of both the water splitting and baseline correction work and who has always been a great friend and source of meaningful discussions. Also I want to thank Hebe Hilhorst, who provided very valuable feedback.

I would like to thank those with whom I collaborated to perform the research presented herein: Dr. Wolfgang Baumann for various cooperations on NMR spectroscopy and valuable discussions. Prof. Stefan Lochbrunner and Miguel A. Argüello Cordero for their work in spectroscopy and insightful scientific discussions, Dr. Stefanie Kreft, Dr. Roland Schoch and Dr. Jabor Rabeah for great scientific work and exchange, Dr. Jagadeesh Rajenahally, who has also been a great colleague in our office, and Dr. Kathiravan Murugesan as well as Thirusangumurugan Senthamarai. Also I want to thank Prof. Frank Glorius, Dr. Mario Wiesenfeldt and Daniel Moock for a very fruitful cooperation on the hydrogenation projects.

Also, I want to thank Prof. David Milstein and Dr. Stephan Kohl, who helped advance the water splitting project through insightful discussions and by providing their original data. I would like to thank Prof. Robert H. Morris for enabling early work on the water splitting project.

Most of the work presented here has only been possible due to the amazing technical, analytical and administrative support by the staff of LIKAT, especially Susann Buchholz, Andreas Hutter, Astrid Lehmann, Matthias Auer, Anja Kammer, Petra Bartels, Dr. Torsten Dwars, Torsten Weiss, Anne Tonn and Nicole Aulerich.

I also want to thank the entire Beller Group and other members of LIKAT for providing such a great working environment of friends and colleagues, especially Moritz Horstmann, Maximilian Marx, Dr. Helge Lange, Dr. Alexander Léval, Dr. Patrick Piehl, Dr. Rui Sang, Dr. Wei Zhou, Hilario Huerta, Dr. Anastasiya Agapova, Dr. Pavel Ryabchuk, Peter Kucmierczyk, Dr. Sören Hancker, Dr. Marcel Garbe, Dr. Florian Scharnagl, Ricarda Dühren, Gordon Neitzel, Dr. Elisabetta Alberico, Dr. Annette-Enrica Surkus, Dr. Nils Rockstroh, and Dr. Fabrizio Monda.

I want to extend a special thank you to Tobias Täufer and Alexander Wotzka for a great, shared time as PhD & PostDoc Representatives of LIKAT.

Lastly, I want to thank my family and friends for their great and unconditional support in everything I pursue.

Abstract

Photocatalytic water splitting is a promising approach for low-cost production of green hydrogen. So far, developed photocatalysts have largely been inspired by the reaction blueprint of photosynthesis, but have struggled to accommodate the kinetically complex absorption of four photons. Furthermore, lack of broad visible light utilization has hampered their efficiency.

In this work, discovery of a new mechanism for light-driven water splitting is described. In this mechanism, only two photons are required to complete the reaction, significantly reducing kinetic complexity. Furthermore, the two absorbed photons have different wavelengths, spanning a large part of the visible spectrum up to red light. The mechanism was discovered through a combined kinetic, spectroscopic and computational study of a previously reported reaction using a molecular ruthenium complex. We show that absorption of the first, shorter wavelength photon produces an intermediate capable of absorbing the second, longer wavelength photon. Second photon absorption directly induces O-O bond formation, enabling subsequent O_2 and H_2 release. This two-photon mechanism can therefore address both kinetic complexity and visible light utilization by moving beyond the reaction blueprint of photosynthesis. We hope that this can inspire the development of a new class of water splitting catalysts capable of economic green hydrogen production.

In work related to water splitting, the oxidation half-reaction for a photochemical CO_2 reduction system was elucidated and a new baseline correction for improved data analysis in chemistry and biology was developed. Furthermore, in research related to hydrogen valorization, catalysts speciation and side product formation for ruthenium catalyzed reductive amination was illuminated and the active catalyst for a rhodium catalyzed arene hydrogenation reaction was identified.

Zusammenfassung

Photokatalytische Wasserspaltung ist ein attraktiver Weg für die kostengünstige Produktion von grünem Wasserstoff. Bisher entwickelte Photokatalysatoren wurden überwiegend durch den Mechanismus der natürlichen Photosynthese inspiriert, wobei sich jedoch Probleme ergaben, die kinetisch komplexe Absorption von vier Photonen zu bewältigen. Darüber hinaus ist die mangelnde Nutzung von einem Großteil des sichtbaren Lichts noch immer ein Problem für viele Katalysatoren.

In dieser Arbeit wird die Entdeckung eines neuen Mechanismus für lichtgetriebene Wasserspaltung beschrieben. In diesem Mechanismus sind lediglich zwei Photonen für die gesamte Reaktion erforderlich, was die kinetische Komplexität erheblich reduziert. Des Weiteren haben die beiden Photonen unterschiedliche Wellenlängen, welche einen großen Teil des Spektrums sichtbaren Lichts bis in den roten Bereich abdecken. Der Mechanismus wurde durch eine kombinierte kinetische, spektroskopische und computerchemische Untersuchung einer zuvor berichteten Reaktion entdeckt, welche auf einem molekularen Rutheniumkomplex basiert. Wir zeigen, dass die Absorption des ersten, kurzwelligeren Photons ein Zwischenprodukt generiert, welches in der Lage ist, das zweite, langwelligere Photon zu absorbieren. Die Absorption des zweiten Photons induziert direkt die Bildung der O-O Bindung und ermöglicht die anschließende Freisetzung von O_2 und H_2. Dieser Zwei-Photonen Mechanismus kann daher sowohl die kinetische Komplexität verringern als auch die Nutzung von sichtbarem Licht verbessern. Wir hoffen, dass dies die Entwicklung einer neuen Klasse von Photokatalysatoren inspiriert, welche über den Mechanismus der Photosynthese hinausgehen und die wirtschaftliche Produktion von grünem Wasserstoff ermöglichen.

Weitere Arbeiten, welche im Zusammenhang mit der Wasserspaltung durchgeführt wurden, führten zudem zur Aufklärung der Oxidations-Halbreaktion in einem photokatalytischen System zur CO_2-Reduktion sowie zur Entwicklung eines neuen Algorithmus für Basislinienkorrektur, welcher die Datenanalyse für chemische und biologische Analysemethoden verbessern kann. Darüber hinaus wurden in Forschungsarbeiten im Zusammenhang mit Wasserstoffvalorisierung der Mechanismus von Katalysatordesaktivierung und Nebenproduktbildung in der Ruthenium-katalysierten reduktiven Aminierung aufgeklärt und die aktive Katalysatorspezies für eine Rhodium-katalysierte Aren-Hydrierungsreaktion identifiziert.

Table of Contents

Table of Figures

Table of Tables

List of Abbreviations

Abbreviation	Full description
AG	Aerogel
bpy	Bipyridine
CAAC	Cyclic(alkyl)(amino)carbene
CASSCF	Complete active space self-consistent field
CDot	Carbon dot
CI	Conical intersection
DFT	Density functional theory
DOI	Digital object identifier
EPR	Electron paramagnetic resonance
EU	European Union
IPCC	Intergovernmental Panel on Climate Change
IR	Infrared
LBC	Logistic Baseline Correction
MECI	Minimum energy conical intersection
MJ	Megajoule
MLCT	Metal-to-ligand charge-transfer
NHE	Normal hydrogen electrode
NMR	Nuclear magnetic resonance
PCET	Proton-coupled electron transfer
qPCR	Quantitative polymerase chain reaction
PEC	Photoelectrochemical (water splitting)
PNN	2-((Di-tert-butylphosphinomethyl)-6-diethylaminomethyl)pyridine
PV	Photovoltaic
QTH	Quartz tungsten halogen
SARS	Severe acute respiratory syndrome
SI	Supporting information
SOE	Solid oxide electrolysis
TD	Time-dependent
THF	Tetrahydrofuran
TS	Transition state
TW	Terawatt
UV	Ultraviolet
XAS	X-ray absorption spectroscopy

1 Introduction

In its report on limiting global warming to 1.5 °C, the Intergovernmental Panel on Climate Change has clearly outlined the importance of green hydrogen in attaining this goal.[1] Green hydrogen is produced using renewable energy, and will play a pivotal role in the global transition towards carbon neutrality.[2] This has also been recognized by the German federal government, which introduced its new national hydrogen strategy in 2020, aiming to advance hydrogen technologies to commercial maturity.[2] The future importance of green hydrogen, a chemical vector for renewable energy, is clearly evident when looking at the currently consumed energy mix in the European Union (see Figure 1): fossil fuel derived energy vectors, such as petroleum product and natural gas, makeup more than 60% of final energy consumption, while electricity only accounts for 20.9%.

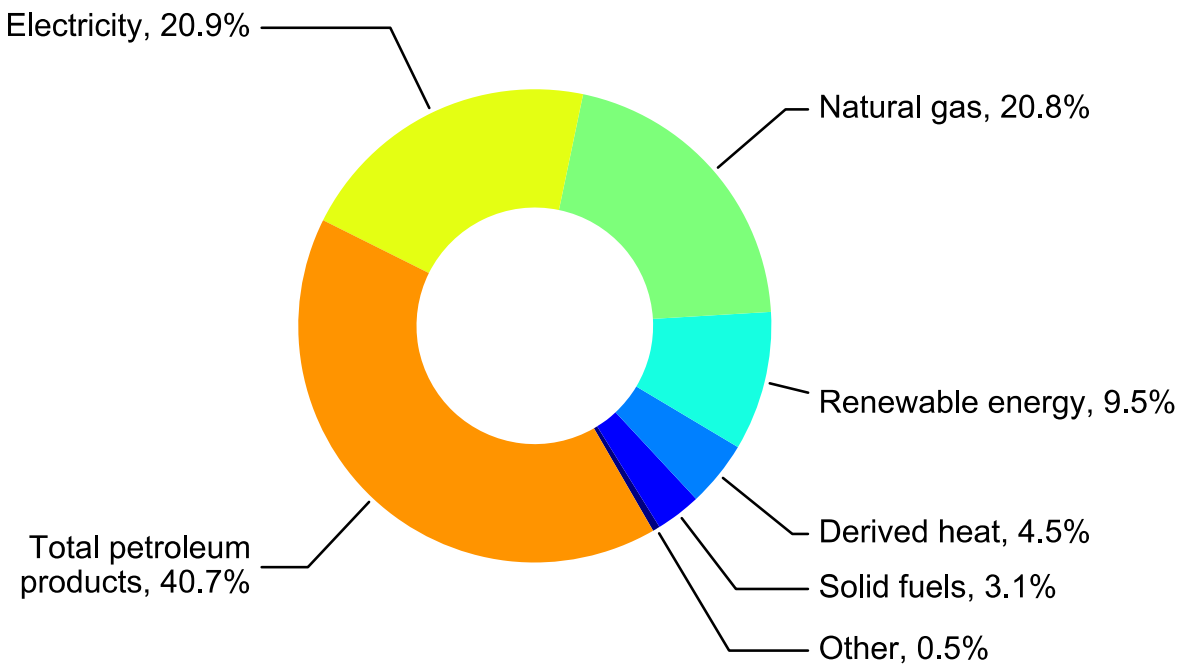

Figure 1 Share of energy products in total final energy consumption in the European Union (2018)
Total petroleum products contain all petroleum products, which are not converted to electricity (heating oil, petrol etc.). Electricity contains electricity derived from all sources (including renewables). Renewable energy contains all forms of renewable energy, which are not converted to electricity (wood, solar thermal etc.). Solid fuels mostly refer to coal, which is not used for electricity production. Data source: [3]

This shows that in its current form, our energy economy and its infrastructure are mostly designed for chemical energy vectors. In the future, some sectors such as mobility might be partially electrified (especially using renewable electricity), increasing the share of electricity in the final energy consumption. There are, however, limits to these renewable electrification efforts due to issues such as

grid stability[4] or energy density (i.e. in the context of aviation). Instead, the use of renewable chemical energy vectors can allow for the continued utilization of existing chemical energy vector infrastructure. This will ease the replacement of fossil fuels by renewable energy. Green hydrogen is an ideal replacement for fossil fuels in this context: On the one hand, it can be used directly as a cleanly combustible fuel.[5] On the other hand, together with CO_2, it can be converted to a range of carbon based energy vectors (such as diesel,[6] methane[7] or methanol[8]), which are currently in use. This means infrastructure pieces such as combustion engines can continue to be used but being powered by renewable energy instead of fossil fuels. Effectively, replacing fossil fuels with green hydrogen can be seen as switching our chemical energy vector supply chain to renewable energy at its earliest point.

1.1 The Hydrogen Production Problem

In contrast to these promises of green hydrogen stands the fact that currently, more than 96% of globally available hydrogen is derived from fossil sources instead of renewable energy.[9] This shows that presently, green hydrogen is not competitive from an economical perspective. Political interventions such as subsidies or carbon taxation can alter this balance and are changing over time, but have not yet lead to a situation in which green hydrogen is economically feasible on a large scale.

The overarching question to realize the promises of green hydrogen is therefore: *How can we produce green hydrogen in an economically competitive way?* Only once this question has been answered can we expect to see an adoption of green hydrogen on a global scale.

1.1.1 Water Splitting – Overview

To enable the use of green hydrogen globally, it has to be produced by splitting water into H_2 and O_2 using renewable energy. This necessity arises from the extraordinary scale at which hydrogen will have to be produced in the future: assuming that hydrogen is used to provide 1.7×10^{20} J annually (30% of current global energy demand of 18 TW-year) and using a heating value of 120 MJ/kg, around 1.4 Gt (1.4×10^{12} kg) of hydrogen will have to be produced annually. Other approaches that have been proposed for green hydrogen production (e.g. biomass,[10] splitting of mineral acids[11] or oxidation of other organic matter[12]) might be used in smaller scale applications but can likely not be used to match this demand. Water splitting, however, combines an abundantly available starting material with a well tolerable side product (O_2). Ideally, seawater should be used as a starting material to avoid competitive use of fresh water and/or energy intensive desalination.

From a chemical perspective, water splitting is the combination of two redox half-reactions, water oxidation and water reduction (see Figure 2).

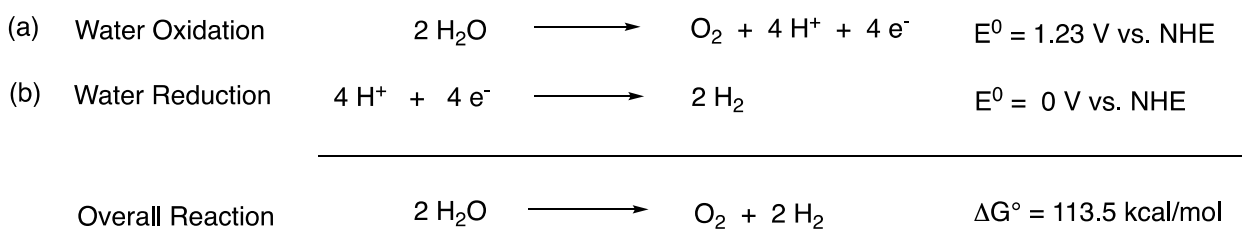

Figure 2 Overview of redox half reactions, potentials and Gibbs free energy for water splitting

Water oxidation is a four-electron oxidation reaction (1.23 V vs. NHE) in which two H_2O molecules are combined to form O_2. Water reduction is a two-electron reduction (0 V vs. NHE), combining two protons and two electrons to form H_2. The overall reaction to form one equivalent of O_2 and two equivalents of H_2 has a Gibbs free energy of 113.5 kcal/mol, making it highly endergonic.

Due to its endergonic nature, energy must be invested to produce H_2 and O_2 from H_2O, explaining why this reaction can be used to convert the invested energy into chemical energy. Hence, we can also classify approaches to water splitting by the form of input energy.

1.2 Water Electrolysis

Water electrolysis, referring to the use of electrical energy to drive water splitting, is currently the most established approach for green hydrogen production. For this approach, any renewable electricity source (solar, wind, geothermal etc.) can be used to drive an electrolyzer, producing H_2 and O_2. The main factors determining hydrogen cost are therefore electricity price as well as investment and operating costs for the electrolyzer.[13] Recent techno-economic analyses show that water electrolysis is, in fact, economical for certain niche applications with very low (or free) electricity prices.[13] This can apply to power-to-gas applications, where free surplus renewable electricity (such as solar or wind) is converted to hydrogen.[14] Water electrolysis can therefore be used for grid balancing, wherein hydrogen is produced during peak availability of solar or wind and converted back to electricity during peak demand.

Production of green hydrogen using surplus electricity, however, cannot be expected to lead to large-scale availability, as hydrogen production capacity in this case is bound by the degree of electrification (currently ca. 20% in the EU, see Figure 1). Instead, new renewable energy capacity dedicated to green hydrogen production will have to be built. Techno-economic analyses show that this is not

currently economically feasible: in case of photovoltaic/electrolyzer systems, hydrogen would be produced at a cost of ca. $5.4 - 6/kg, which is contrasted by the current price of fossil fuel derived hydrogen of $1.4/kg (see Figure 3).[6] This cost arises from the construction and maintenance cost of new photovoltaic (PV) capacity combined with investment and operating costs for electrolyzers.
Over time, one can expect that the cost of both PV capacity and electrolyzers will further decrease. In fact, this cost reduction over time can be modeled using learning curves, which account for technological improvements as well as cost savings due to economies of scale. Det*z et al*. have shown that based on learning curve models, the largest cost reductions can be expected for PV/solid oxide electrolysis (SOE).[6] For this approach, green hydrogen production cost could become competitive with fossil fuel derived hydrogen between 2040 and 2050 (see Figure 3).

Given the pressing nature of climate change, green hydrogen technologies will have to be deployed as soon as possible and by the middle of the century we need to already have achieved wide spread carbon neutrality.[15] Hence, two conclusions can be drawn from this assessment of green hydrogen production using water electrolysis: Either, future work should focus on improving both photovoltaic and electrolyzer technologies to significantly accelerate cost reduction. Or, alternative technologies for green hydrogen production should be explored which might lead to a more rapid attainment of cost competitiveness. Ultimately, both conclusions are likely valid and both approaches should be followed, also in the interest of hedging risks. This work will focus on the exploration of alternative technologies for green hydrogen production, which could significantly decrease its cost.

1.3 Photoelectrochemical, Solar Thermal and Biocatalytic Water Splitting

Among alternative approaches for green hydrogen production are photoelectrochemical (PEC), solar thermal and biocatalytic water splitting. While these are interesting approaches to water splitting, they are beyond the focus of this work and will only be briefly summarized below.
PEC water splitting refers to the use of photoelectrodes to generate an electrical potential by sun light absorption, which is used to drive water splitting catalyzed by materials deposited on the electrodes.[16] Hence, it is closely related to PV/electrolysis, although being a more integrated system. It has been argued that due to this similarity to PV/electrolysis, PEC cannot be expected to significantly outperform PV/electrolysis in terms of future cost reductions.[16]
Solar thermal water splitting refers to using concentrated solar power to drive a thermal water splitting cycle.[17] Since it relies on high-temperature thermal reactions (ca. 800 – 1500 °C), relatively complex solar concentrator plants are required for its operation. Furthermore, these high temperatures pose significant challenges for the design of appropriate water splitting materials.[17]

Biocatalytic water splitting refers to the use of entire organisms or parts of enzymatic machinery to perform a modified version of photosynthesis.[18] Hence, sun light energy is directly utilized to drive the water splitting reaction. This approach benefits from already existing machinery for photosynthesis but faces the challenges of dealing with its relatively low efficiency and the need to modify it to produce H_2 instead of biological energy carriers.[18]

1.4 Photocatalytic Water Splitting

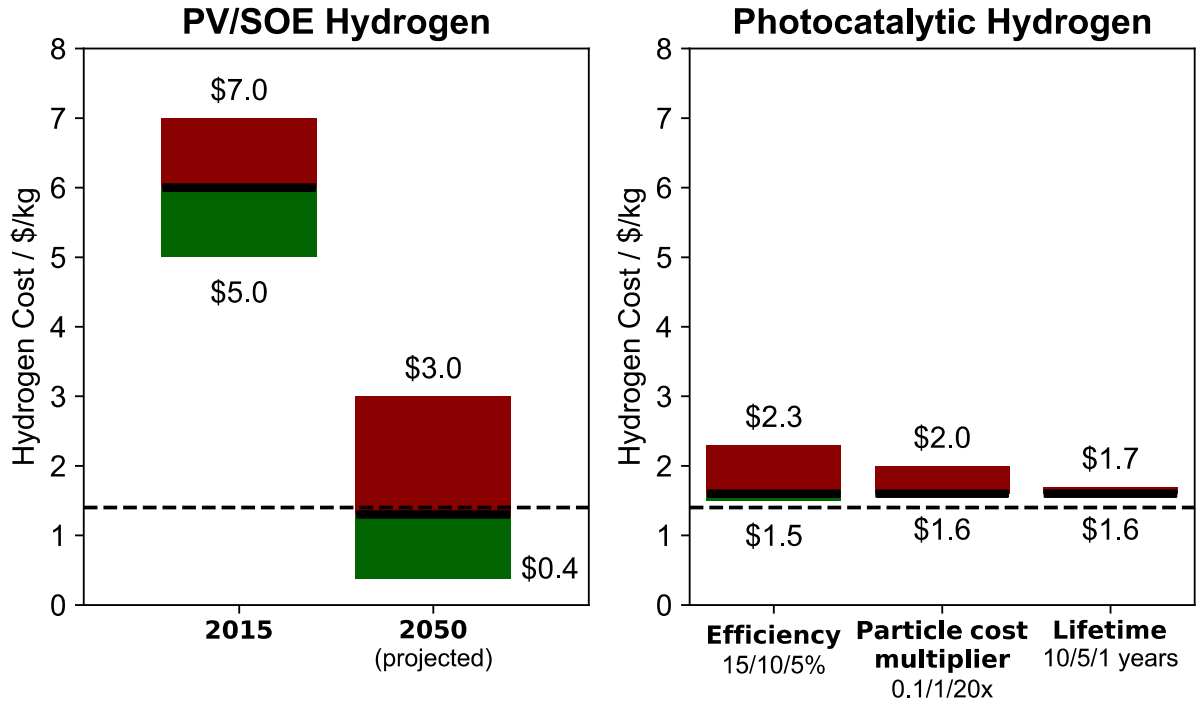

Figure 3 Cost of green hydrogen production using either PV/electrolysis or photocatalysis
Left: cost range of green hydrogen produced using PV/solid oxide electrolysis (SOE), upper and lower bounds of confidence intervals are shown above and below bars, respectively. Values for 2015 estimate (average cost ca. $6/kg) and 2050 projection (average cost ca. $1.3/kg) are shown. Dotted line shows current price of fossil fuel derived hydrogen ($1.4/kg). Data source: [6]
Right: estimate of green hydrogen cost produced using photocatalysis in single bed, suspended particle reactor (see Figure 4). Average cost (solar-to-hydrogen efficiency: 10%, particle cost multiplier: 1x, lifetime: 5 years) is $1.6/kg. Sensitivity of estimated price to variation of efficiency, particle cost multiplier and lifetime is shown, with upper and lower bounds of confidence intervals shown above and below bars, respectively. Dotted line shows current price of fossil fuel derived hydrogen ($1.4/kg). Data source: [19]

In photocatalytic water splitting, a photocatalyst is employed to split water directly using photon energy (sun light). Hence, it is akin to photosynthesis, but only utilizes artificial components. A crucial aspect of photocatalytic water splitting is that it can be carried out in very simple devices, such as plastic baggie reactors (see Figure 4): for these devices, a photocatalyst is dissolved or suspended in water and placed in a transparent plastic baggie. Irradiation of the baggie leads to evolution of H_2 and O_2, which are collected and then separated to yield pure H_2.[19]

Techno-economic analysis by Pinaud *et al.* has shown that due to this simple device construction, photocatalytic water splitting could be used to produce hydrogen at a cost competitive with fossil fuel derived hydrogen ($1.6, see Figure 3).[19] This cost estimate showed relatively low sensitivity to photocatalyst cost and lifetime, while variations in efficiency affected hydrogen cost by up to $0.7/kg. Even when taking this sensitivity analysis into account, hydrogen production costs for photocatalytic water splitting would be significantly lower compared to PV/electrolysis (see Figure 3). This makes it a highly interesting avenue to explore, with the potential to achieve the desired rapid attainment of cost competitiveness.

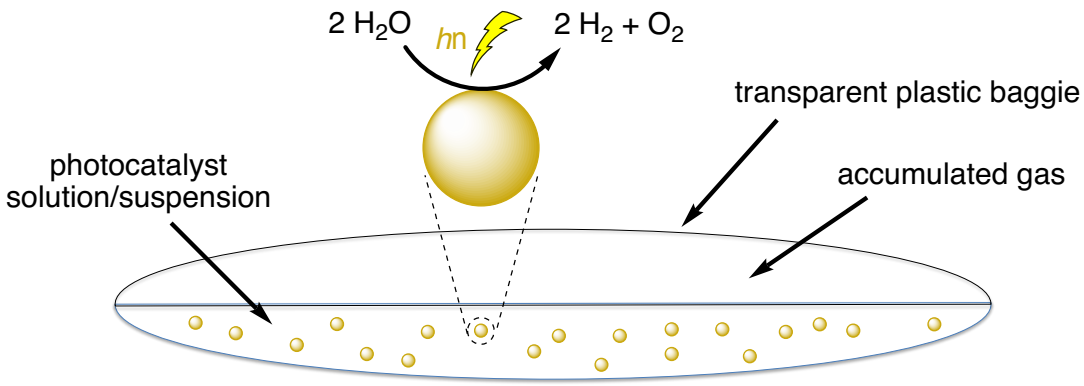

Figure 4 Illustration of single bed plastic baggie reactor for photocatalytic water splitting
Adapted from [19].

The key technological challenge for photocatalytic water splitting is the development of commercially viable photocatalysts to accomplish this reaction. Lack of such catalysts is the reason why we are currently limited to hypothetical techno-economic analyses instead of actual data from deployment of this technology. But given its highly promising nature, development of photocatalyst for water splitting has attracted significant academic attention in the last decades.[20] In the following we want to briefly summarize different approaches, which have been used in this development.

1.4.1 Photosynthesis Inspired Systems

In photosynthesis, water splitting occurs via four consecutive photon absorptions in photosystem II.[21] Each photon is absorbed by the light-harvesting complex, generating a pair of redox equivalents (one hole and one electron).[21] Each hole is utilized for a one-electron oxidation of the oxygen-evolving complex, and since water oxidation is a four-electron oxidation, four of these absorption events are necessary to complete the reaction (see Figure 5). In the process, the oxygen evolving complex cycles through four different oxidation levels, known as Kok's cycle.[22]

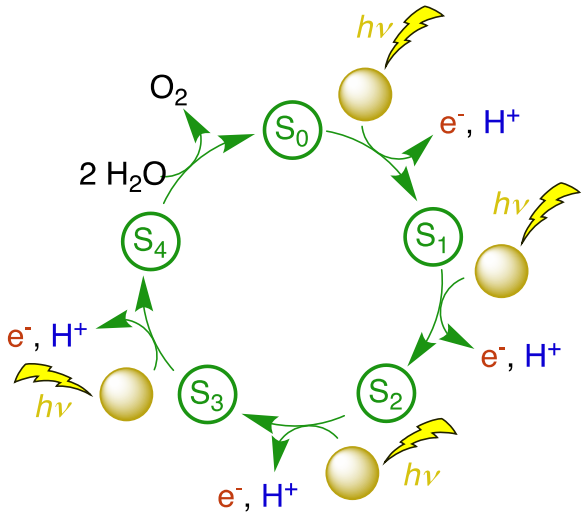

Figure 5 Generic reaction cycle for photosynthesis inspired systems for water splitting
S_0 – S_4 refers to different states/oxidation levels of water oxidation catalyst. Yellow circle represents photoactive component (semiconductor, photosensitizer, light harvesting complex) responsible for light absorption and generation of redox equivalents. Reaction cycle shows a generic sequence of four proton-coupled electron transfers, although the order of electron and proton transfers as well as H_2O coordination varies between Kok's cycle and different waver splitting catalysts.

A large part of the literature on photocatalytic water splitting has been inspired by this reaction sequence.[23] In the most general sense, these systems can be thus be characterized in a very similar way: the photoactive component, typically a semiconductor or photosensitizer, absorbs a photon to generate an electron-hole pair. The hole then travels to the active site for water oxidation, which, in most cases, is a dedicated water oxidation catalyst.[20] This leads to one-electron oxidation of the water oxidation catalyst. After four of these absorption-oxidation events, O_2 is released.[24] In the process, protons are also released, which combine with electrons to form hydrogen at the active site for water reduction, which is often also a dedicated catalyst.[20] Overall, this approach can be seen as a 4-photon-4-electron sequence.

Semiconductors which have been used as the photoactive components include TiO_2,[25] $SrTiO_3$,[26] $BiVO_4$,[27] and Ta_3N_5,[28] among others.[29] Molecular photosensitizers, such as $[Ru(bpy)_3]^{2+}$ and its derivatives, have also been used as the photoactive component, often in the form of dye-sensitized materials.[30] A wide range of heterogeneous[31] as well as homogeneous[32] water oxidation catalysts have been developed, along with a variety of water reduction catalysts.[33] Photocatalysts capable of performing water splitting without the addition of any sacrificial reagents, also referred to as overall water splitting, mostly combine a semiconductor with other heterogeneous catalysts.[20] Homogeneous water oxidation and reduction catalysts have mostly served to provide mechanistic insights instead,[34] as there has been no reproducible, homogeneous photocatalyst system for overall water splitting reported to date.

Among others, two major challenges have become apparent for this approach:

1. *High kinetic complexity due to the need to orchestrate consecutive absorption of four photons.* Since each photon absorption only generates one electron-hole pair, four photon absorptions are necessary to complete the reaction. With each one-electron oxidation, an increasingly reactive intermediate of the water oxidation catalyst is formed, which might decay or decompose before the next photon absorption.[35] This lowers productivity and efficiency of these systems, contributing to them not yet being suitable for commercial application.

2. *Lack of broad wavelength utilization.*
   To achieve high solar-to-hydrogen efficiency, a large fraction of the solar spectrum must be utilized for water splitting. This means that photocatalysts should utilize the visible light range effectively, since it constitutes the majority of sunlight suitable for water splitting (the lower energy bound is 1.23 eV or 1010 nm for this approach). Most semiconductors which have been used, however, only absorb UV and/or blue light,[20] severely limiting the maximum attainable solar-to-hydrogen efficiency. The reason for this problem is that all electron-hole pairs are generated by the same photoactive component with the same mechanism, hence all have the same redox potential. This redox potential has to match or exceed the highest redox potential encountered during water splitting, which is at least 1.23 V vs. NHE, but is almost always higher due to overpotential. At this point it should be noted that the four redox steps usually have different potentials, with some being considerably lower.[24] However, since all redox equivalents are generated in the same way, the step with the highest redox potential determines the required potential of electron-hole pairs. In case of semiconductors, this determines the required band gap and the minimum energy of photons, which will be absorbed. Due to overpotentials and energy losses, mostly semiconductors with band gaps exceeding 2.5 eV have been used, which leads to systems with poor absorbance of most visible light.[23]

A considerable amount of effort has been made to address the utilization of visible light by water splitting photocatalysts.[36,37] From a formal perspective, the most straight forward approach is to lower overpotentials and energy losses, enabling the use of smaller band gap semiconductors.[28,37] Another approach is to mimic the Z scheme found in photosynthesis: in this approach, electrons from O_2 generation are transferred to a redox mediator before H_2 evolution. Through a second photon absorption for each transferred electron, the redox potential of these electrons can be altered to match the required maximum potential.[36] This allows for the use of two different photoactive components, which independently might not match the required maximum potential, but do when operated in series. Therefore, the range of usable wavelengths can be broadened,[38] but at the cost of further increasing kinetic complexity (eight photon absorptions in total), which can lower productivity and efficiency.[39]

Another approach to improve utilization of longer wavelengths is photon upconversion, in which two longer wavelength photons are converted to one shorter wavelength photon, which can be absorbed by the photoactive component.[40,41] Similar to the Z scheme approach this increases the number of required photons, further increasing kinetic complexity.

Compared to improving utilization of visible light, less work has been dedicated to addressing the problem of kinetic complexity in the context of photosynthesis inspired systems. In principle, one could imagine to utilize phenomena such as singlet fission[42] to generate multiple electron-hole pairs for each photon absorption. This would lower the number of required photons, thus decreasing kinetic complexity. However, since each triplet state produced during singlet fission has less than half the potential of the excited singlet state, shorter wavelengths of light would be required, making use of visible light even more challenging.[43] While use of singlet fission for water splitting has been explored theoretically,[43] we are not aware of any experimental work which has implemented singlet fission, or other multiple exciton generation approaches, for overall water splitting.

1.4.2 H_2O_2 Pathway for Water Splitting

Instead of altering the photophysical processes, the problem of kinetic complexity can also be addressed by moving away from the photosynthesis inspired 4-photon-4-electron sequence. One alternative reaction pathway proceeds via H_2O_2; since H_2O_2 is the product of two-electron oxidation of H_2O, its formation requires only two electron-hole pairs, and hence only two photon absorptions. Two separately formed H_2O_2 molecules can then react in a catalytic disproportionation to form O_2 and H_2O, while liberated electrons and protons are combined to form H_2. Overall, this pathway can therefore be seen as a 2x 2-photon-2-electron sequence (see Figure 6)

Such a reaction pathway has been realized using a C_3N_4/CDot photocatalyst.[44] In this system, semiconductor C_3N_4 is the photoactive component while CDots catalyze H_2O_2 disproportionation.

The fact that two 2-photon-2-electron sequences can operate independently, instead of one 4-photon-4-electron sequence, does indeed lower kinetic complexity and makes the C_3N_4/CDot system comparatively productive.[44] However, a major challenge of this approach is that H_2O_2 formation is more endergonic than O_2 formation, requiring a higher redox potential (1.78 V vs. NHE instead of 1.23 V vs. NHE for O_2). This means that only larger band gap semiconductors can be used, which exacerbates the challenge of utilizing visible light. In fact, for the C_3N_4/CDot system, only light with wavelengths < 450 nm can be used to drive the reaction, severely limiting the theoretical maximum solar-to-hydrogen efficiency. Furthermore, the additional energy, which has to be invested for H_2O_2 formation compared to O_2 formation is lost again during H_2O_2 disproportionation, also limiting thermodynamic efficiency.

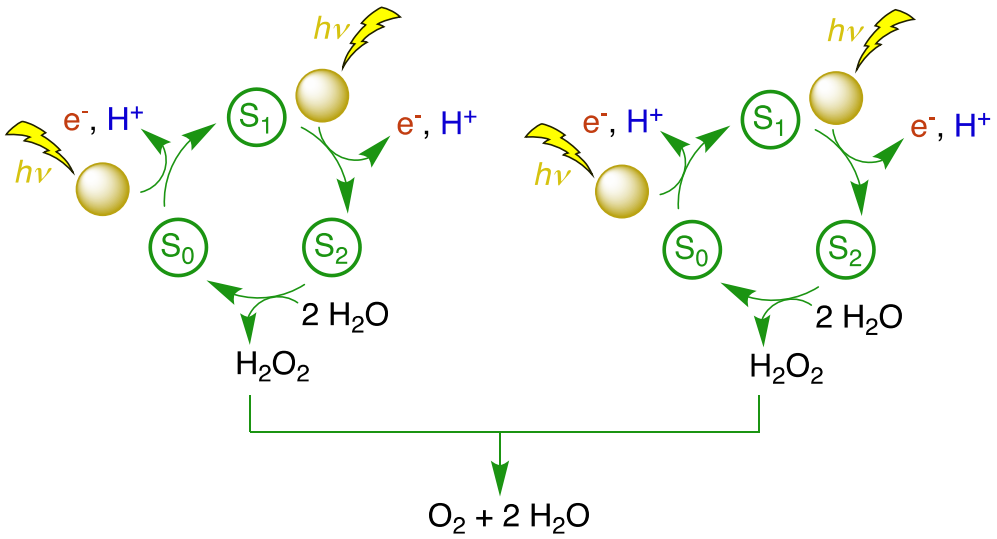

Figure 6 Generic reaction cycle for H_2O_2 pathway for water splitting
S_0 – S_2 refers to different states/oxidation levels of active site for H_2O_2 generation. Yellow circle represents photoactive component (semiconductor, photosensitizer) responsible for light absorption and generation of redox equivalents. Reaction cycle shows a generic sequence of two proton-coupled electron transfers, although the order of electron and proton transfers as well as H_2O coordination can vary between different systems.

1.4.3 A Bottom-Up Approach to Address Fundamental Challenges

The above assessment shows that progress has been made to address both the challenges of utilizing visible light as well kinetic complexity. These approaches, however, have only been able to address one challenge at a time, while sometimes exacerbating the other. Overall, this has not yet resulted in photocatalysts suitable for commercial application. Hence, the question arises: *How can we identify new approaches to simultaneously tackle these fundamental challenges in photocatalytic water splitting?*

One answer to this question might be to adopt a bottom-up approach: by studying untypical but well-defined molecular water splitting reactions, we might be able to identify new mechanisms for light-driven water splitting. These new mechanisms could open up reaction pathways beyond those inspired by photosynthesis or based on H_2O_2 and could allow tackling the fundamental challenges in a new way. Ultimately, obtained mechanistic insight could then be used to design new systems or modify existing ones, leading on a path to commercially viable photocatalysts.
Of crucial importance for this approach is to select appropriate molecular water splitting systems to study, which should ideally fulfill the following criteria:

1. An untypical mode of water splitting, which should hint at an underlying mechanism that is distinct from typical 4-photon-4-electron or 2x 2-photon-2-electron reaction sequences.

2. Well-defined reactions and products that account for the whole reaction sequence of overall water splitting. Hence, no sacrificial reagents should be used.
3. A cyclic reaction, which would in principle enable a photocatalytic cycle.
4. Formation of H_2 and O_2 (instead of H_2O_2) to avoid energetic issues arising from formation of thermodynamically less favorable products.

To identify potential candidates, the literature on such untypical water splitting reactions was surveyed, with the results shown in Table 1. In the following, these reactions will be briefly summarized.

Godemann *et al.* reported a titanocene system capable of H· radical release, followed by light-induced HO· formation (see Table 1, entry I).[45] While the reaction cycle is closed, formation of unstable radical species instead of H_2 and O_2 makes this system less promising compared to others. A version of this system capable of H_2 formation has been reported,[46] although not in combination with HO· formation.

Goez *et al.* have reported a similar kind of reaction using $[Ru(bpy)_3]^{2+}$ (see Table 1, entry II).[47,48] Photoionization of excited state $*[Ru(bpy)_3]^{2+}$ was reported to produce solvated electrons, and irradiation of resulting $[Ru(bpy)_3]^{3+}$ was found to produce HO· radicals. While this is also a closed reaction cycle, formation of electrons and HO· radicals makes it less suitable for further studies.

McGrail *et al.* found that irradiation of an uranyl aqua complex can produce H_2 and a peroxo-bridged product complex upon irradiation (see Table 1, entry III).[49] Due to the relatively stable peroxo complex this reaction is not cyclic.

Kee *et al.* described that irradiation of a manganese half-sandwich complex leads to formation of H_2, H_2O_2 as well as decomposition products of the complex (see Table 1, entry IV).[50] Formation of H_2O_2 instead of O_2 and irreversible decomposition of the complex render this system less promising.

Kunkely *et al.* identified a copper complex capable of reducing carbonates to CO in presence of water, generating a dimeric hydroxo complex. Irradiation of this hydroxo complex was found to produce O_2 as well as H_2O_2 and led to partial decomposition of the complex (see Table 1, entry V).[51] In this system, carbonates instead of protons are reduced, but the source of electrons is still water splitting. While this reaction is interesting, only a minimal amount of analytical data supporting these results was reported, which also leads to ambiguity as to whether O_2 or H_2O_2 is formed initially.

Table 1 Overview of molecular water splitting systems

Entry	Reaction	Fulfillment of criteria	Ref.
I	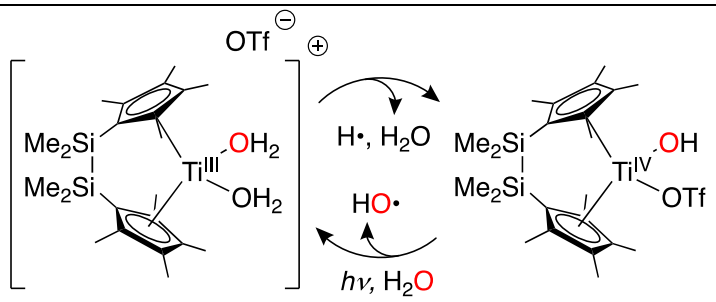	⊕ Closed cycle ⊖ Formation of H· and HO· radicals instead of H_2 and O_2	45, 46
II	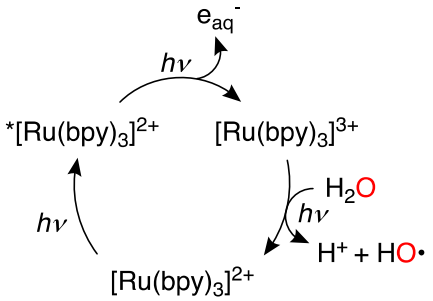	⊕ Closed cycle ⊖ Formation of e_{aq}^- and HO· radicals instead of H_2 and O_2	47, 48
III	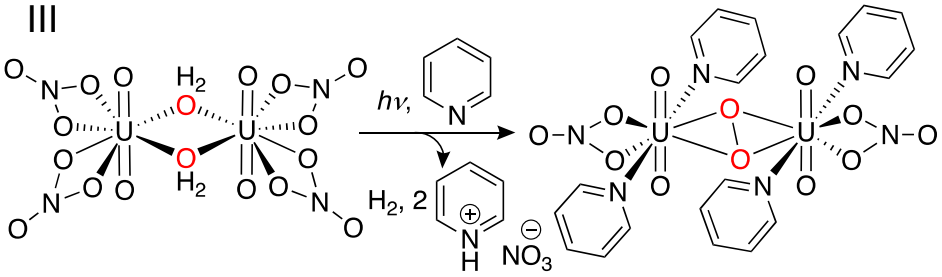	⊕ Formation of H_2 ⊖ Formation of stable peroxo complex (not cyclic)	49
IV	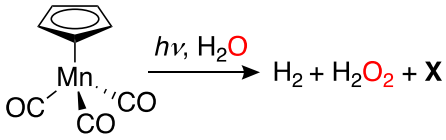	⊕ Formation of H_2 ⊖ Formation of H_2O_2 and decomposition products (not cyclic)	50

Entry	Reaction	Fulfillment of criteria	Ref.
V	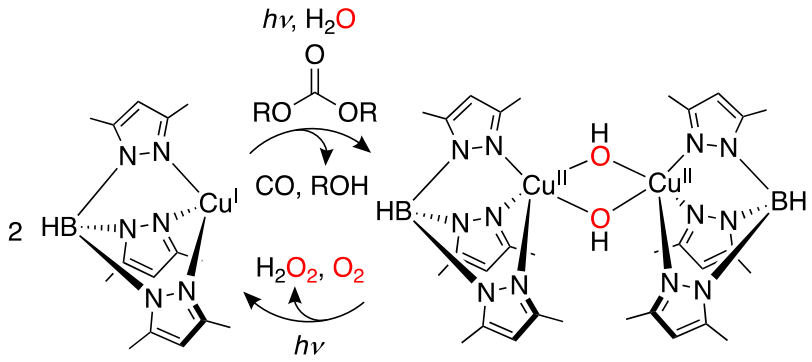	⊕ Closed cycle ⊖ Formation of H_2O_2, partial decomposition of complex	51
VI	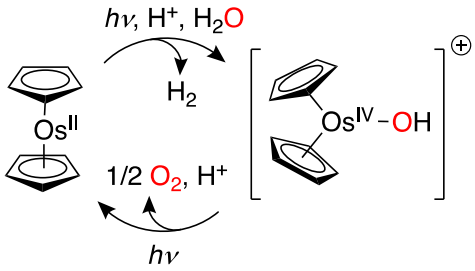	⊕ Formation of H_2 and O_2 ⊖ Two steps require incompatible reaction conditions (not truly cyclic)	52, 53
VII	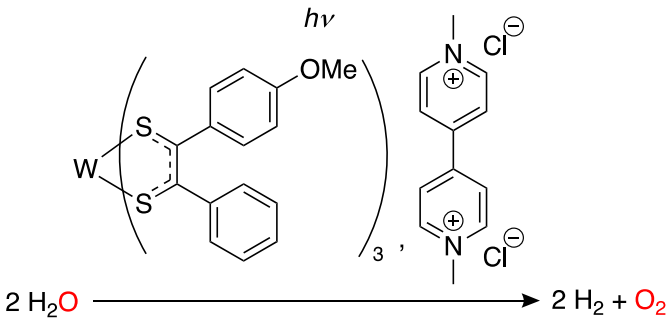	⊖ Not reproducible	54, 55
VIII	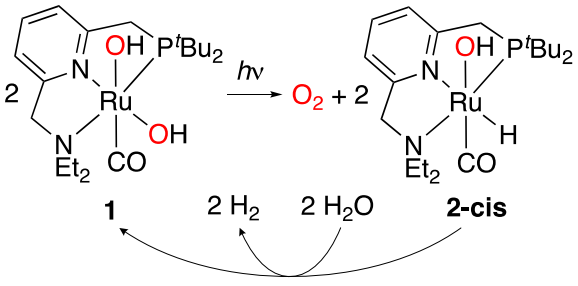	⊕ Closed cycle ⊕ Formation of H_2 and O_2 ⊖ Different reaction conditions for two steps, but in principle compatible	56

In another report by Kunkely *et al*. it was found that irradiation of osmocene in the presence of protons and water leads to evolution of H_2 along with formation of an Os(IV) aqua complex, which can be deprotonated to form a hydroxo complex (see Table 1, entry VI).[52] Irradiation of the hydroxo complex leads to evolution of O_2 and regeneration of osmocene. This reaction is interesting due to formation of both H_2 and O_2, but the two reaction steps require incompatible reaction conditions (H_2 formation requires a strongly acidic environment, which is not compatible with the Os(IV) hydroxo complex). In a later report, Ge *et al*. also studied this reaction, in which case no O_2 formation could be detected.[53]
Katakis *et al.* reported that a tungsten dithiolene complex in combination with methyl viologen could act as photocatalyst for overall water splitting (see Table 1, entry VII).[54] This would be the first and, to the best of our knowledge, only homogeneous photocatalyst for water splitting. Multiple research groups, however, have subsequently failed to reproduce these results.[55]

Lastly, Kohl *et al*. reported that broadband irradiation of ruthenium pincer (PNN) dihydroxo complex **1** in water at room temperature leads to evolution of O_2 combined with formation of ruthenium hydride complex **2** (see Table 1, entry VIII).[56] Heating **2** in water then leads to liberation of H_2 and regeneration of **1**. Hence, this reaction constitutes a closed cycle for formation of both H_2 and O_2. While the two reaction steps require different temperatures, they are in principle compatible. It can therefore be argued that this reaction sequence contains the untypical but complete water splitting reactivity that we seek for our study. In the following, we will therefore focus on this reaction.

1.4.4 Water Splitting using Ruthenium Dihydroxo Complex

Starting with the second step of the reaction sequence, liberation of H_2 from hydride complex **2** has already been studied computationally,[57–60] and similar reactions have been investigated experimentally.[61] From these results it can be concluded that this redox neutral process proceeds via protonation of the hydride ligand, leading to H_2 formation and subsequent hydroxo coordination. Therefore, the light-driven, first reaction step contains all redox steps and constitutes the core water splitting reactivity of this system.
In their original report, Kohl *et al*. performed initial mechanistic studies for the light-driven step and reported the following findings:

1. Through isotope labeling it was found that O-O bond formation occurs intramolecularly without significant solvent involvement.
2. $^3O_2$ is formed by the reaction, as confirmed by trapping experiments.
3. Small amounts of HO· radicals could be detected, but it was ruled out that these were part of the reaction sequence, since addition of radical scavengers did not inhibit the reaction.

4. Addition of catalase leads to disappearance of HO· radicals, indicating that they result from a Fenton type reaction of H_2O_2, which might be present under reaction conditions.

Based on these observations, Kohl *et al*. proposed that the reaction proceeds via light-induced reductive elimination of H_2O_2 from **1**, which subsequently disproportionates to form $^3O_2$. Subsequent theoretical studies have shown, however, that reductive elimination of H_2O_2 from **1** is not energetically feasible, with barrier heights exceeding 100 kcal/mol.[57,62] Therefore, H_2O_2 might only be formed as a side product of the actual water splitting mechanism.

Chen *et al*.[62] attempted to elucidate the mechanism theoretically, but could not identify a feasible pathway: in their mechanism, the reaction starts from a hydrogen-bonded dimer of **1**, which undergoes intersystem crossing and intermolecular proton transfer after excitation. However, the resulting triplet species has a thermal barrier of 50 kcal/mol for O-O bond formation, which cannot be overcome for a reaction conducted at room temperature. Aside from this study, no further theoretical or experimental work has been reported to elucidate this reaction.

We can conclude that the reaction reported by Kohl *et al*. fulfills our criteria for an untypical water splitting system. It might therefore provide us with mechanistic insight into a new approach for water splitting that could be used to address some of the fundamental challenges that have been identified. The core reactivity of this system, however, has so far not been understood.

2 Motivation, Goals and Methods

2.1 Primary Objective

In light of the arguments outlined above, the primary objective of this work is to establish a mechanistic understanding for the untypical water splitting reaction reported by Kohl *et al*. This might lead us to the discovery of a fundamentally new mechanism for water splitting, beyond either the reaction blueprints of photosynthesis or H_2O_2 pathways. A new mechanism could open different perspectives to address challenges such as high kinetic complexity and insufficient visible light utilization. Ultimately, overcoming these challenges could enable a path to commercially viable photocatalysts for water splitting, which may be used for large-scale production of green hydrogen.

To tackle this objective, we employed a symbiotic combination of different experimental and theoretical methods: Experimental kinetic studies were enabled by the construction of highly sensitive *in situ* oxygen detection set-ups. Ultrafast-pump probe spectroscopy was used to study photophysical properties, supported by computational kinetic modeling. To connect experimental insights and develop a holistic mechanistic understanding, density functional theory (DFT) as well as complete active space self-consistent field (CASSCF) computations were used.

2.2 Secondary Objectives

Aside from this primary objective, a number of secondary objectives are addressed in this work.

2.2.1 Mechanistic Elucidation of Oxidation Half-Reaction in Photocatalytic CO_2 Reduction

Photocatalytic CO_2 reduction is a technology for solar energy utilization that is closely related to photocatalytic water splitting.[63] In fact, when the reaction is performed without sacrificial reagents, water oxidation should provide the necessary electrons for CO_2 reduction.

Part of this work is dedicated to the mechanistic elucidation of the oxidation half-reaction in a novel heterogeneous photocatalyst for CO_2 reduction. Just like in water splitting, gaining this understanding is motivated by the possibility to use the respective knowledge to overcome kinetic bottlenecks and fundamental challenges of this reaction.

Since the oxidation half-reaction was studied, the developed *in situ* methods for O_2 detection were used for kinetic experiments, along with a range of analytical and spectroscopic methods to characterize material changes during the reaction.

2.2.2 Novel Algorithm for Improved Data Analysis in Chemistry and Biology

While analyzing *in situ* kinetic O_2 data for water splitting as well as CO_2 reduction, it became apparent that there were no suitable algorithms for baseline correction of this type of data. Closer inspection of the problem revealed that the produced data type is part of an entire class of datasets, spanning chemistry and biology, for which no general baseline correction method exists.

To improve data analysis for this class of datasets, part of this work is dedicated to the development of a novel, generally applicable baseline correction algorithm. It also aims to thoroughly evaluate this algorithm through synthetic benchmarking and application of the algorithm to experimental data from chemistry, biology and spectroscopy. The final aim is to make the algorithm publicly accessible so that other scientists can use it to improve their data analysis.

2.2.3 Catalyst Speciation and Mechanism for Ruthenium Catalyzed Reductive Amination

Valorization of hydrogen is an important part of establishing a firm role for hydrogen in the global economy. Such a central role of hydrogen is crucial to aid adoption of green hydrogen technologies. In this context, reductive amination offers a convenient way to use hydrogen for the production of high value amines from readily available carbonyl compounds.[64]

Part of this work is dedicated to investigating catalyst speciation as well as the reaction mechanism in a novel ruthenium catalyst system for reductive amination. Understanding of catalyst deactivation can help to improve productivity and efficiency of the system, while an understanding of the reaction mechanism helps to avoid side product formation. For these studies, *in situ* nuclear magnetic resonance spectroscopy (NMR) was used as the primary method. Given that the studied catalyst is based on ruthenium, skills and knowledge obtained by studying the ruthenium-based water splitting system could be used to enrich this work.

2.2.4 Identification of Active Catalyst in Rhodium Catalyzed Arene Hydrogenation

Another approach to hydrogen valorization is arene hydrogenation, which can convert readily available aromatic feedstock into valuable, saturated carbo- and heterocycles using hydrogen.[65]

The main objective for this part of the work is to identify the active catalyst species for a novel rhodium arene hydrogenation catalyst, which has shown unprecedented reactivity and selectivity.[66] Identification of the active species is a cornerstone for mechanistic studies, which can illuminate how this catalyst attains its unusual reactivity and selectivity.

Methodologically, this study is based on kinetic *in situ* NMR spectroscopy and can therefore draw from skills obtained during kinetic studies of water splitting and CO_2 reduction, as well as from previous insights into *in situ* NMR spectroscopy used for studying reductive amination.

3 Results and Discussion

This chapter is structured based on the five publications included in this work, with each subsection corresponding to one publication. Within each subsection, references to the manuscript or supporting information (SI) are referring to the manuscript or supporting information (SI) of the respective publication. Appendix is abbreviated as "Ap.". In some sections, parts of the corresponding manuscript are paraphrased or adapted.

3.1 Two-Photon Water Splitting at Molecular Ruthenium Complex

Publication Title: "Two-photon water splitting at a molecular ruthenium complex", *submitted*
Supporting Information: Available in Ap. 8.1.

3.1.1 Synthesis, Properties and Reactivity of 1

Starting point for the mechanistic elucidation of water splitting using complex **1** was a reproduction of the results reported by Kohl *et al.*[56] While **1** can be synthesized by heating **2** in H_2O, a number of side products are also formed, complicating access to pure **1** (see Ap. 8.1 SI Section 3.1.4). Kohl *et al.* reported that reaction of **2** with N_2O yields pure **1** and is the preferred route to access the complex.[56] In this reaction, the hydride ligand of **2** is formally oxidized to a second hydroxo ligand. This synthesis route proved challenging at first, but ultimately we found that it is crucial for the reaction to be conducted in the presence of a precise amount of water: reaction of a THF solution of **2** containing 9 equivalents of water with N_2O reliably yields pure samples of **1** (see Ap. 8.1 SI Section 3.1.1). This finding was inspired by theoretical studies that have highlighted the crucial role of hydrogen bonding in the reaction of N_2O with ruthenium hydride complexes.[67,68] Furthermore, we also developed a new synthesis route to access **1** via reaction of [(PNN)$RuCl_2$(CO)] with Ag_2O (see Ap. 8.1 SI Section 3.1.3). This double halide abstraction reaction yields **1** in just one synthesis step from easily accessible [(PNN)$RuCl_2$(CO)] (see Ap. 8.1 SI Section 3.4). Hence, this reaction might be used to easily synthesize derivatives of **1** to explore structure-reactivity relationships in the future. However, the new synthesis procedure is not fully optimized yet and does not yield product of the same purity as the N_2O synthesis route.

With pure **1** in hand, we characterized its physicochemical properties. Regarding its optical properties, the lowest energy absorption feature is a metal-to-ligand charge-transfer band from 350 – 400 nm in H_2O (see Chapter 6.1 Manuscript Figure 2), which was also confirmed by TD-DFT calculations (see Ap. 8.1 SI Sections 11.2.2 and 11.2.3). This is in contrast to findings by Kohl *et al.*, who reported absorption features at energies lower than the MLCT transition.[56] The authors reported, however, that their product was green and we found that a green discoloration of **1** (which is a yellow solid) can result from impurities formed during the N_2O reaction (see Ap. 8.1 SI Section 3.1.1). We therefore attribute these

additional absorption features found by Kohl *et al.* to impurities in the final product. **1** also shows weak fluorescence at λ_{em} = 500 nm when excited at λ_{ex} = 370 nm.

Irradiation of **1** for two days in water using a broadband quartz tungsten halogen (QTH) light source (320 – 1000 nm) leads to formation of **2-cis** in ca. 20% yield. Using NMR spectroscopy (see Ap. 8.1 SI Section 4.1.2) as well as DFT calculations (Ap. 8.1 SI Section 11.2.9) we confirmed the cis arrangement of hydride and hydroxo ligands as shown in Table 1, entry VIII. **2-cis** is an isomer of the more stable **2-trans**, in which hydride and hydroxo ligand are in a trans arrangement, and **2-cis** slowly converts to **2-trans** after irradiation is stopped (see Ap. 8.1 SI Section 4.1.2). Aside from **2-cis**, another product is formed, which we tentatively assign to an oxo-bridged dimer of **1** (**Oxo dimer**) resulting from formal dehydration (see Ap. 8.1 SI Section 4.1.2). We recorded a concentration-time profile for the irradiation of **1** and developed a kinetic model to describe the resulting data (see Ap. 8.1 SI Figure 4.1-1). From this modeling it became clear that **Oxo Dimer** is an off-cycle species and not an intermediate en route to formation of **2-cis** (see Ap. 8.1 SI Section 4.1.3).

For the detection of oxygen evolution, we developed a highly sensitive *in situ* set-up based on fluorescence quenching optical oxygen sensors (see Ap. 8.1 SI Section 4.2.1), which allowed for sub-µmol/l O_2 detection (see Ap. 8.1 SI Figure 4.2-1). Using *in situ* O_2 detection, O_2 formation could be detected in both the liquid and gas phase (see Ap. 8.1 SI Section 4.2 and 4.3). Comparing the rate of **2-cis** formation from our concentration-time profile/kinetic model with the initial rate of O_2 formation in the liquid phase, we confirmed that both products are formed in the same reaction (see Ap. 8.1 SI Section 4.4). Formed O_2 appears to be consumed again during the reaction, possibly due to photochemical oxidation of **1** (see Ap. 8.1 SI Section 4.3.2). A lower yield of **2** (45% vs. 20%), formation of **Oxo Dimer** and consumption of O_2 slightly differ from the original results of Kohl *et al.* (in their report, accumulation of O_2 in the gas phase was reported). Despite these differences, the core water splitting reactivity is identical and these differences do not impact the following mechanistic investigation. In future work, however, improving the yield of **2** and suppressing O_2 consumption should be addressed.

3.1.2 Kinetic Studies

With the core water splitting reactivity in hand, we proceeded to investigate the mechanism of the reaction. The first striking observation revealed by kinetic studies was that the water splitting reaction rate shows a square dependence on irradiation intensity (see Chapter 6.1 Manuscript Figure 3). This indicates that two photons are absorbed during the reaction in a non-linear fashion.[69] There are two mechanisms, which could explain this behavior:

1. Two equivalents of **1** separately absorb one photon each, generating two equivalents of a transient intermediate, which then react in a bimolecular reaction. This would be akin to the mechanism of triplet-triplet annihilation.[40]

2. **1** absorbs one photon, generating a transient intermediate, which subsequently absorbs the second photon.[69,70]

It should be noted that if the intermediate was not transient, no square intensity dependence could be observed (see Ap. 8.1 SI Section 10.2). To differentiate these scenarios, we studied how different wavelengths for irradiation affect the rate of water splitting. A transient intermediate responsible for absorption of the second photon would likely have a different absorption behavior compared to **1**. This would imply that the response of water splitting to different wavelengths would be different from what would be expected if only **1** was responsible for photon absorption.

First, we studied the effect of different irradiation wavelengths on formation of **2-cis** (see Figure 7A). Irradiation using a 320 – 400 nm filtered light source resulted in formation of **2-cis** in 6% yield after 17 h. Expectedly, when using a 495 – 1000 nm filtered light source, no **2-cis** was formed, since **1** does not significantly absorb this wavelength range. Strikingly, using both the 320 – 400 nm and 495 – 1000 nm light sources simultaneously, the yield of **2-cis** increased to 10%.

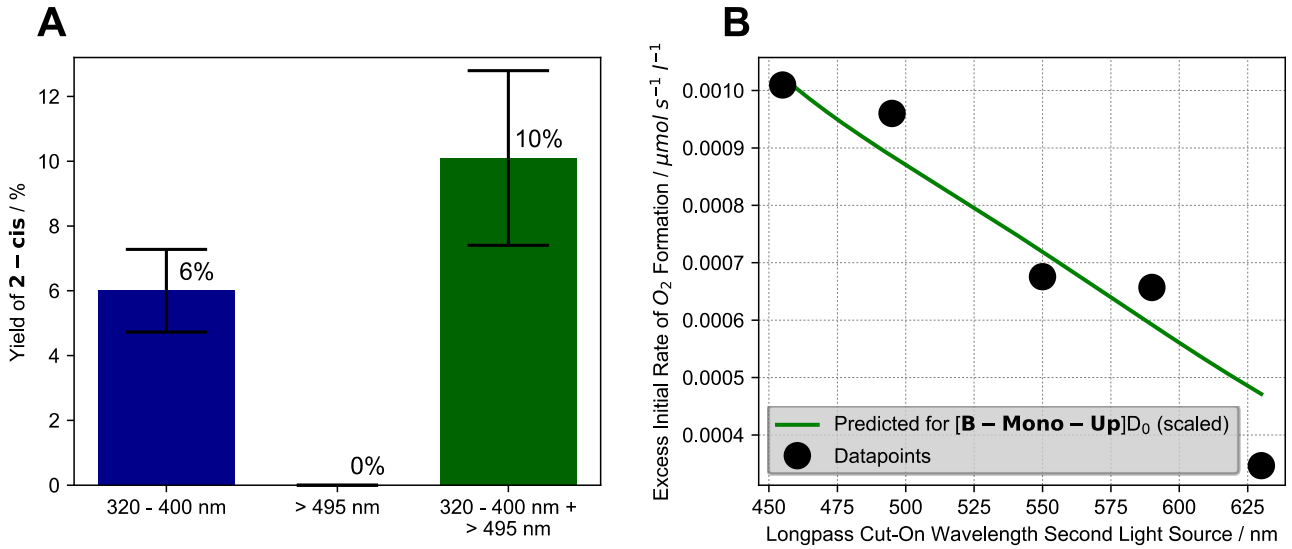

Figure 7 Effects of different wavelengths on water splitting reaction
A Dependence of **2-cis** yield on irradiation using either 320 – 400 nm, > 495 nm irradiation or both simultaneously for 17 h. Colored bars and text indicate average values while black error bars indicate range of experimental values.
B Dependence of excess initial rate of O_2 formation on longpass filter cut-on wavelength of second light source (first light source: 320 – 400 nm), along with scaled, predicted behavior for [**B-Mono-Up**]D_0.
Source: Publication I

These results show that using light, which is not significantly absorbed by **1**, can synergistically enhance the water splitting reaction. This observation suggests that excitation of **1** by a 320 – 400 nm photon leads to formation of a transient intermediate, which absorbs a second, longer wavelength photon to complete the reaction.

To investigate the effect more closely, a series of dual irradiation experiments were performed: a solution of **1** was simultaneously irradiated using a 320 – 400 nm filtered light source as well as a second light source with different longpass filters. This results in X – 1000 nm intervals (455 – 1000 nm, 495 – 1000 nm etc.) for the second light source. For each longpass filter, the excess initial rate of O_2 formation was determined, which was calculated by subtracting the initial rates of single light source irradiation (320 – 400 nm or X – 1000 nm) from the dual irradiation rate (see Ap. 8.1 SI Section 4.2.5).
In this experiment, 320 – 400 nm irradiation excites **1** to form the transient intermediate while the effect of longpass filters on excess initial rate effectively probes the intermediate's absorption behavior. As can be seen in Figure 7B, already starting at 630 nm an excess initial rate can be observed, which increases roughly linearly all the way to 455 nm. We can thus conclude that absorption of a 455 – 630 nm photon by the transient intermediate is the second photon absorption to complete the water splitting reaction. The experimental longpass filter/excess rate relationship is in good agreement with the predicted behavior for the computationally identified intermediate ([**B-Mono-Up**]D_0, see Figure 7B green line, below and Ap. 8.1 SI Section 11.4.1).

3.1.3 Ultra-Fast Spectroscopy and Kinetic Modeling

The dynamics of **1** were investigated using ultrafast pump-probe spectroscopy (see Ap. 8.1 SI Section 9). Two transient species could be identified, with lifetimes of τ = 6 ps and τ = 150 ps, respectively (see Ap. 8.1 SI Figure 9.2-1). Based on its decay associated spectrum, the τ = 6 ps species could be assigned to an emissive singlet state of **1**. For the τ = 150 ps species the decay associated spectrum shows good agreement with computationally identified species [**B-Trans**]T_0 (see Ap. 8.1 SI Figure 9.2-1). [**B-Trans**]T_0 is an isomer of the computationally identified intermediate [**B**]T_0 (see below).
To gain a better understanding of the relationship between kinetic and spectroscopic results, a simple kinetic model for the consecutive two-photon process was developed (see Ap. 8.1 SI Section 10). In this model, a system of differential equations describes the consecutive absorption of two photons to form O_2 as well as a third step in which O_2 is consumed again. It also takes into account the experimentally determined photon flux values. By numerically solving the system of differential equations in combination with an optimization algorithm, the kinetic model was fitted to experimental irradiation intensity/rate data. Optimization parameters are the transient intermediate lifetime and quantum efficiencies for each step. Since the optimization problem is underdetermined, only a range of optimal parameters can be defined. Yet, we can conclude that to explain the experimentally observed rates, the lower bound for transient intermediate lifetime is 10 ns. Hence, the τ = 150 ps species is likely not the corresponding intermediate. Given that this species could be assigned to isomer [**B-Trans**]T_0, we propose that it might partially isomerize to form [**B**]T_0 below the detection limit (as [**B**]T_0 absorbs 400 – 700 nm light more weakly compared to [**B-Trans**]T_0, see Ap. 8.1 SI Section 9.2). Future work should aim to directly detect [**B**]T_0 through higher sensitivity measurements.

3.1.4 Computational Studies

To tie together experimental insights and develop a holistic mechanistic understanding, we performed DFT as well as CASSCF computations, with the results shown in Figure 8. DFT was used for ground state calculations as well as vertical excitations (time dependent formalism), while CASSCF was used to described multi-configurational systems such as conical intersections.

While a detailed description of the mechanism is to be found in the manuscript, it can be summarized as follows (spin states of species are indicated behind square brackets): a hydrogen-bonded dimer of **1**, named [**A**]S_0, is excited by a 320 – 400 nm photon to form [**A**]S_n (observed in pump-probe spectroscopy), which then undergoes intersystem crossing and an intermolecular proton-coupled electron transfer (PCET) to form [**B**]T_0. In [**B**]T_0, the left hydroxo-oxo ruthenium complex has been formally oxidized to Ru(III), while the right ruthenium hydroxo complex has been reduced to Ru(I), hence this species can be seen as a charge-transfer state.

Since O-O bond formation occurs intramolecularly,[56] we can conclude that the second photon is absorbed by the left ruthenium complex, [**B-Mono**]D_0. Indeed, the time dependent (TD)-DFT UV/Vis spectrum of [**B-Mono-Up**]D_0 (conformational isomer of [**B-Mono**]D_0) agrees well with the dual irradiation data (see Figure 7, Ap. 8.1 SI Section 11.4.1). Excitation of [**B-Mono**]D_0 by a 455 – 630 nm photon leads to population of the D_2 state, which converts to hydroperoxo complex [**C-Mono**]D_0 via two conical intersections (see Figure 8B) without significant barriers. Hence, photon absorption directly induces a highly endothermic O-O bond formation, during which two electrons are transferred to the left ruthenium center, reducing it formally to Ru(I).

In the full dimeric model, [**C**]T_0, a second PCET takes place from the hydroperoxo ligand to the right Ru(I) center, forming a superoxo complex on the left ([**D**]T_0) as well the first hydrido hydroxo product complex [**F**]S_0 on the right. This step has a modest barrier of 13.7 kcal/mol, which can likely be overcome with residual vibrational energy from the second photo absorption. In a small fraction of all reactions, hydrolysis of [**C**]T_0 might occur instead, which could explain the formation of H_2O_2 as a side product, as observed by Kohl *et al.* [56]

The superoxo ligand in [**D**]T_0 is then displaced by water, releasing $^3O_2$ and forming complex [**E**]S_0. [**E**]S_0 can react with water in a formal oxidative addition, forming the second hydrido hydroxo complex [**F**]S_0.[57,59]

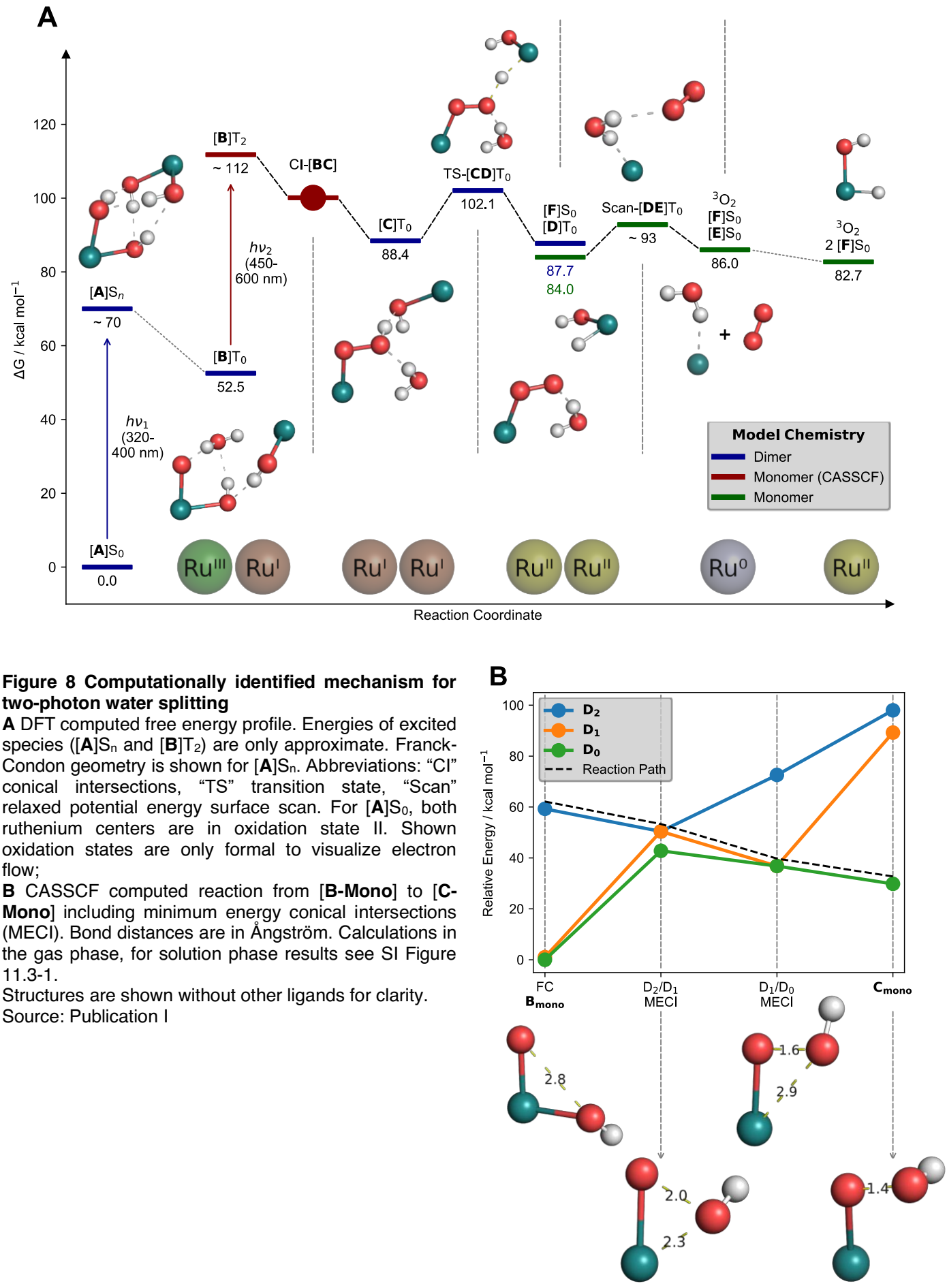

Figure 8 Computationally identified mechanism for two-photon water splitting

A DFT computed free energy profile. Energies of excited species ([**A**]S_n and [**B**]T_2) are only approximate. Franck-Condon geometry is shown for [**A**]S_n. Abbreviations: "CI" conical intersections, "TS" transition state, "Scan" relaxed potential energy surface scan. For [**A**]S_0, both ruthenium centers are in oxidation state II. Shown oxidation states are only formal to visualize electron flow;

B CASSCF computed reaction from [**B-Mono**] to [**C-Mono**] including minimum energy conical intersections (MECI). Bond distances are in Ångström. Calculations in the gas phase, for solution phase results see SI Figure 11.3-1.

Structures are shown without other ligands for clarity.

Source: Publication I

To close the water splitting cycle, both equivalents of [**F**]S_0 can react with one equivalent of water each to release two equivalents of H_2 in total and regenerate [**A**]S_0. For each equivalent of [**F**]S_0, this reaction is endothermic by 13.2 kcal/mol, accounting for the entire thermodynamic energy change of water splitting (see Ap. 8.1 SI Table 11.2-7).

3.1.5 Discussion

Overall, kinetic results have shown that the water splitting reaction occurs via consecutive, non-linear absorption of a 320 – 400 nm photon followed by a 455 – 630 nm photon. These two photons are absorbed by two different reaction species. Computational studies, supported by ultra-fast spectroscopy, then revealed a holistic mechanistic picture: in its most minimal form (see Figure 9A), absorption of the first photon by **A** generates charge-transfer intermediate **B**, which absorbs the second photon to generate hydroperoxo intermediate **C**. **C** can then liberate O_2 as well as H_2 without additional photon absorptions to regenerate **A**.

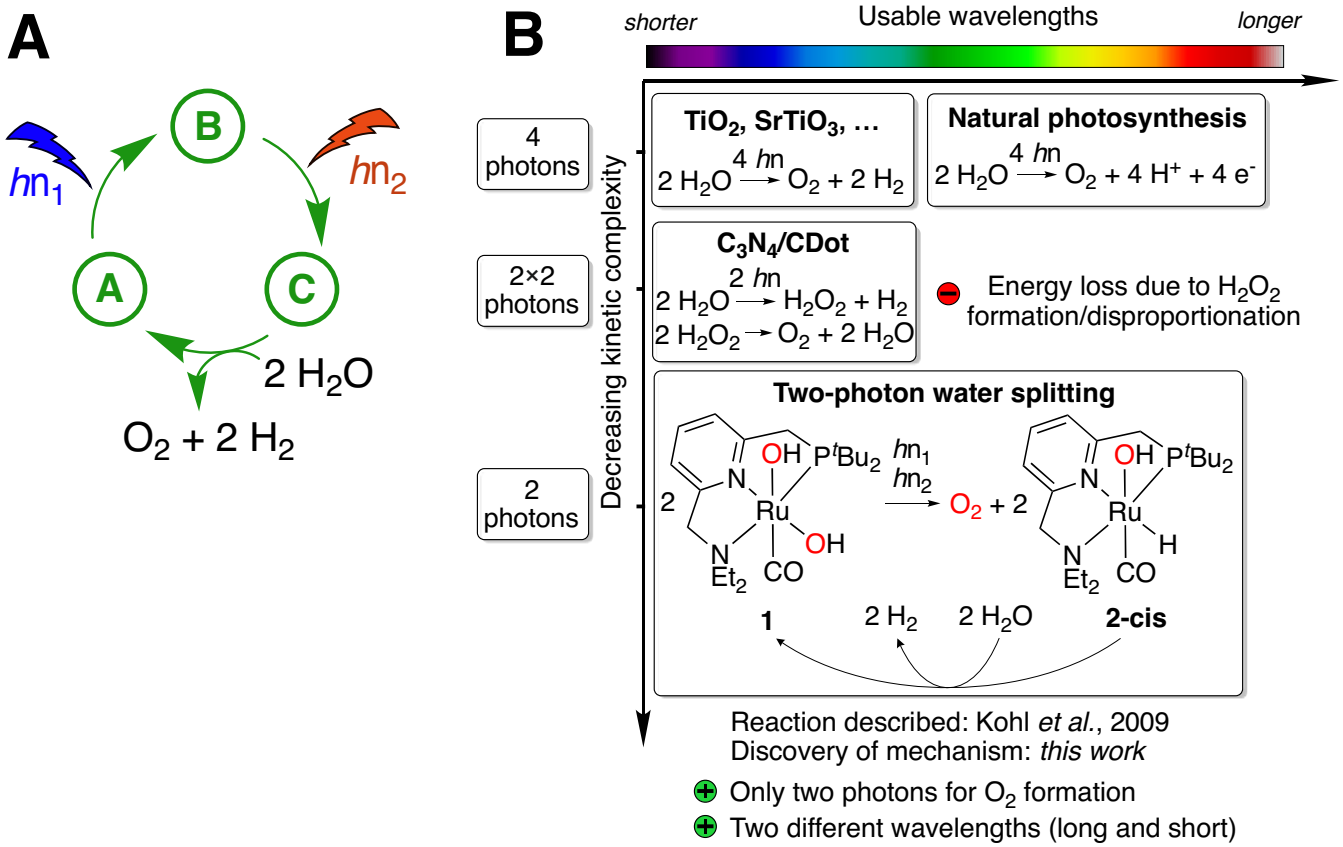

Figure 9 Summary of two-photon water splitting mechanism and relation to previous work
A Minimal schematic mechanism for two-photon water splitting in the style of Figure 5 and Figure 6.
B Overview of approaches to light-driven water splitting, arranged by usable wavelength range (top scale) and kinetic complexity (side scale). Note that wavelength ranges are only approximate.
Source: Publication I (**B**)

When we put these results into the context of previous mechanisms for water splitting (see Figure 9B), we can see that it presents a completely new paradigm, which addresses the two fundamental challenges that were identified in Section 1.4.1: kinetic complexity is significantly reduced by requiring only two instead of 4 or 2×2 photons. Effectively, a 2-photon-4-electron sequence is operative in this system. Furthermore, instead of relying on only one mechanism for photon absorption, each absorption step is specific for the respective redox step. Tailoring photon absorptions to redox events in this way allows for the utilization of different wavelengths, ultimately spanning a large section of the visible spectrum up to red light.

In its current form, however, this water splitting reaction does not proceed with high yield or efficiency. The relatively poor utilization of photons (see SI section 10.4) is likely due to a short lifetime of [**B**]T_0, which makes absorption of the second photon difficult. To some extent, this was expected, since the molecular structure of **1** was in no way been optimized for photochemical reactions or the stabilization of charge transfer states. It might therefore be reasonable to propose that structural changes can be made to **1,** which would significantly enhance its photochemical performance, while also addressing the problem of O_2 consumption. To aid also other researchers in advancing this field, all original data of the project has been made publicly available at: https://github.com/jschneidewind/Water-Splitting.

In conclusion, we successfully identified the mechanism of this untypical water splitting reaction. As we had hoped, this has presented us with a fundamentally new approach to water splitting, which can tackle some of the fundamental challenges in this field. These insights might therefore be used in the future for either the bottom-up construction of new water splitting systems or for the modification of existing approaches. By taking advantage of lower kinetic complexity and broad visible light utilization, this could lead us to economically viable water splitting systems for green hydrogen production.

Disclaimer: Parts of chapter 3.1 were paraphrased, adapted or taken from the manuscript of publication I. This manuscript was completely written by me and has not been published yet.

3.2 Oxidation Half-Reaction in Photochemical CO_2 Reduction using Cu/TiO_2

Publication title: "Improving Selectivity and Activity of CO_2 Reduction Photocatalysts with Oxygen", DOI: 10.1016/j.chempr.2019.04.006

Supporting Information: Available at https://www.sciencedirect.com/science/article/pii/S2451929419301640

Photochemical CO_2 reduction can be seen as an extension of photocatalytic water splitting: electrons are ideally provided by water oxidation, but instead of combining them with protons to produce H_2, they are used to reduce CO_2 to various carbon based energy carriers.[63] Direct access to these carbon based energy carriers is the attractive feature of photochemical CO_2 reduction, but it comes at the cost of having to mediate are more complex reduction half-reaction compared to water reduction.[63]
Various photocatalysts for CO_2 reduction have been developed, with Cu/TiO_2 systems being especially prominent.[71,72] For these systems, CO is typically formed as the primary product of CO_2 reduction, with H_2 being formed as a side product due to water reduction. In our group, a particularly active Cu/TiO_2 photocatalyst for CO_2 reduction in water was developed using an unusual TiO_2 aerogel component, designated as Cu/TiO_2(AG). Use of this aerogel component was found to significantly increase surface area.[73] For this system, however, no formation of O_2 could be observed during photochemical CO_2 reduction. Lack of O_2 formation has been a common problem in Cu/TiO_2 catalyzed CO_2 reduction, as indicated in multiple previous reports.[74,75] Not detecting O_2 formation raises the question what oxidation half-reaction provides the necessary electrons for CO_2 reduction? Answering this question is crucial to understand the entire electron flow of the reaction, which in turn provides the foundation for targeted improvements.

This question concerning the oxidation half-reaction was further compounded by an observation that addition of O_2 actually increases formation of CO. Through detailed *in situ* spectroscopic and kinetic experiments (see Chapter 6.2 Manuscript), it was shown that this is due the presence of O_2 controlling speciation of the copper catalyst: initially, the Cu(II) precursor is reduced to a catalytically active Cu(I) species under photochemical reaction conditions. Over the course of the reaction, however, active Cu(I) species are further reduced to inactive Cu(0) species. Presence of O_2 enables a reactivation of Cu(0) species by oxidation to Cu(I), which prolongs catalytic activity (see Figure 10). To investigate this effect, O_2 levels during photochemical reactions were monitored using the developed *in situ* O_2 detection set-up. Surprisingly, O_2 consumption far exceeded the amount, which would be expected if O_2 would only be consumed by copper oxidation (see Chapter 6.2 Manuscript Figure 2A). In fact, the amounts of O_2 consumption could only be explained by reductive chemisorption (photoadsorption) of O_2 on the TiO_2(AG) surface.[76] Photoadsorption of O_2 could also be observed for TiO_2(AG) not

containing any copper. Three distinct reduction processes were therefore identified during the photochemical reaction: CO_2 reduction, Cu reduction and reductive chemisorption of O_2. Yet, the electron source for these reduction processes was still unknown.

When comparing O_2 photoadsorption by different TiO_2 materials, the rate and amount of photoadsorption correlated with the number of surface hydroxyl groups (see Chapter 6.2 Manuscript Figure 2A),[77] hinting at their involvement in the reaction. TiO_2(AG) showed the highest number of surface hydroxyl groups as well as the highest degree of O_2 photoadsorption. For Cu/TiO_2(AG), the number of surface hydroxyl groups was reduced by roughly half after the reaction, showing that they are a reaction component which is consumed. Consistent with this picture of surface hydroxyl groups being a consumable part of the reaction is that in a long term experiment, It was found that both O_2 photoadsorption and CO_2 reduction ceased once ca. 10 mol% of O_2 (with respect to TiO_2(AG)) were consumed.

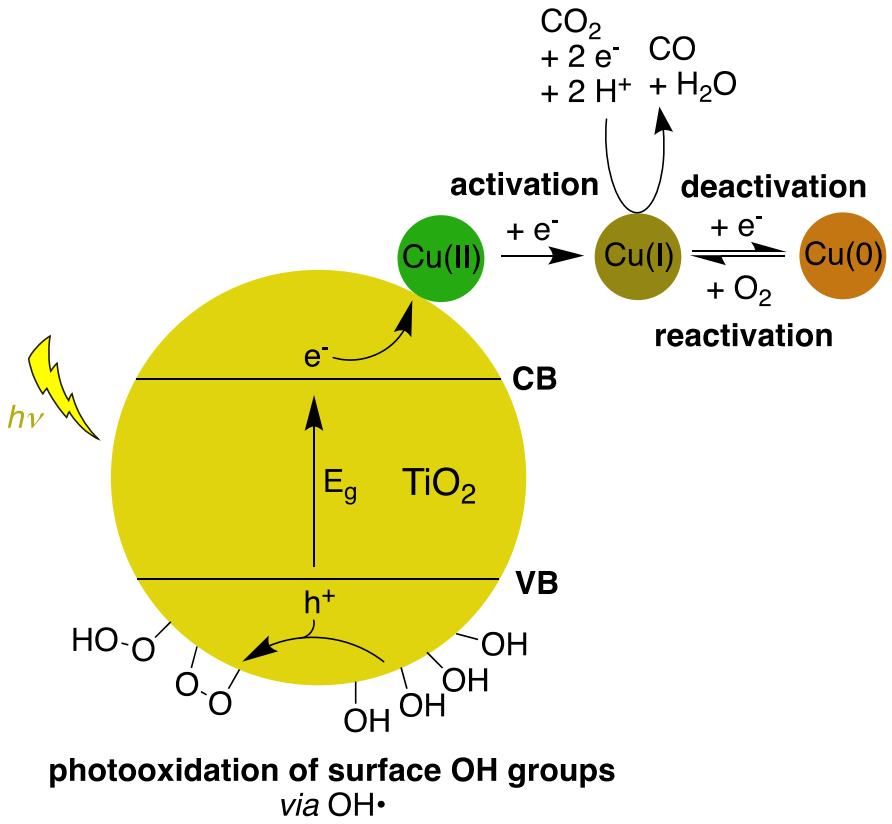

Figure 10 Schematic overview of mechanism for photochemical CO_2 reduction at Cu/TiO_2(AG) including surface oxidation
E_g is the band gap energy, h^+ represents electron holes. Adapted from Publication II.

Grätzel and co-workers have described that under irradiation, TiO_2 surface hydroxyl groups can be oxidized to form surface peroxo and superoxo species, via the intermediacy of HO· radicals.[78] This oxidation reaction could be a candidate for the missing oxidation half-reaction in this system. Using

electron paramagnetic resonance (EPR) spectroscopy, HO· radicals formed during irradiation of Cu/TiO_2(AG) could be trapped and detected (see Chapter 6.2 Manuscript Figure 3). Furthermore, using a chemical detection assay, surface bound peroxo species formed after a photochemical reaction in the presence of O_2 were identified (see Chapter 6.2 Manuscript Figure 2B). These results indicate that photooxidation of surface hydroxyl groups is the oxidation process responsible for reductive chemisorption of O_2. To investigate whether the same photooxidation process also provides electrons for CO_2 reduction, a photochemical reaction in the absence of O_2 was conduced followed by the same peroxo assay. In this case, surface bound peroxo species could also be identified (see Chapter 6.2 Manuscript Figure 2B).

Based on the consumption of surface hydroxyl groups, detection of HO· radicals and formation of surface bound peroxo species, we can conclude that photooxidation of surface hydroxyl groups is the oxidation half reaction in this photochemical CO_2 reduction system (see Figure 10). This insight also explains the superior activity of Cu/TiO_2(AG) compared to previous Cu/TiO_2 systems: due to the high surface area, a large number of surface hydroxyl groups are present, which can provide electrons for CO_2 reduction. However, this oxidation half-reaction also implies that TiO_2(AG) does not act as a catalyst but rather as a substrate in this reaction. Future work should therefore focus on exploring ways to remove surface bound peroxo species and regenerate hydroxyl groups, enabling a catalytic cycle.

3.3 Improving Data Analysis Through Versatile Baseline Correction

Publication title: "Improving Data Analysis in Chemistry and Biology Through Versatile Baseline Correction", *accepted*

Supporting Information: Available in Ap. 8.2.

For both water splitting and CO_2 reduction, *in situ* O_2 measurements were crucial. In these measurements, data of the type shown in Figure 11B is produced: before the start of the reaction, there is a baseline O_2 value, which significantly increases (as in Figure 11) or decreases once the reaction is started. At the end of the reaction, a new baseline O_2 value is reached due to the formation or consumption of O_2 in the reaction. The reaction, or in more general terms the "feature", permanently alters the baseline value and therefore introduces a signal offset, O_s, between pre- and post-feature datapoints. This class of features is therefore referred to as "baseline-altering features" herein.

Such a behavior is distinct from the kind of features observed in NMR or IR spectroscopy, for example (see Figure 11A): these peak shaped feature start at the baseline and return back to it, without significant alteration. Hence, this class of features is referred to as "non-baseline-altering features".

Distinction of these two feature classes is important when baseline correction is performed. For non-baseline varying features encountered in NMR,[79] infrared (IR)[80] or Raman spectroscopy,[81] chromatography,[82] mass spectrometry[83] or calorimetry,[84] classical baseline correction is typically applied during data analysis. In classical baseline correction, measurement M(x) is seen as the sum of a signal f(x) and baseline g(x). The aim is to recover g(x) from M(x), so that it can be subtracted from M(x), obtaining pure and unbiased f(x). This is typically done in two steps:

1. g(x) is recovered by selecting pre- and post-feature baseline datapoints and fitting them with some approximate function g*(x) (see Figure 11A, top).
2. With approximate function g*(x) in hand, baseline values in the feature region are interpolated, which allows for subtraction of g*(x) from the entirety of M(x), obtaining approximate signal f*(x) (see Figure 11A, bottom).

Classical baseline correction does not generalize to baseline-altering features because any attempt of fitting g*(x) to pre- and post-feature baseline datapoints would be heavily distorted by unknown signal offset O_s (see Figure 11A, top). Due to this problem, state-of-the-art baseline correction for baseline-altering features is often performed by using only pre-feature datapoints for fitting of g*(x).[85,86] For this approach, referred to as pre-feature fitting, extrapolation of the feature region is required, which sacrifices accuracy and reliability compared to classical baseline correction's interpolation.

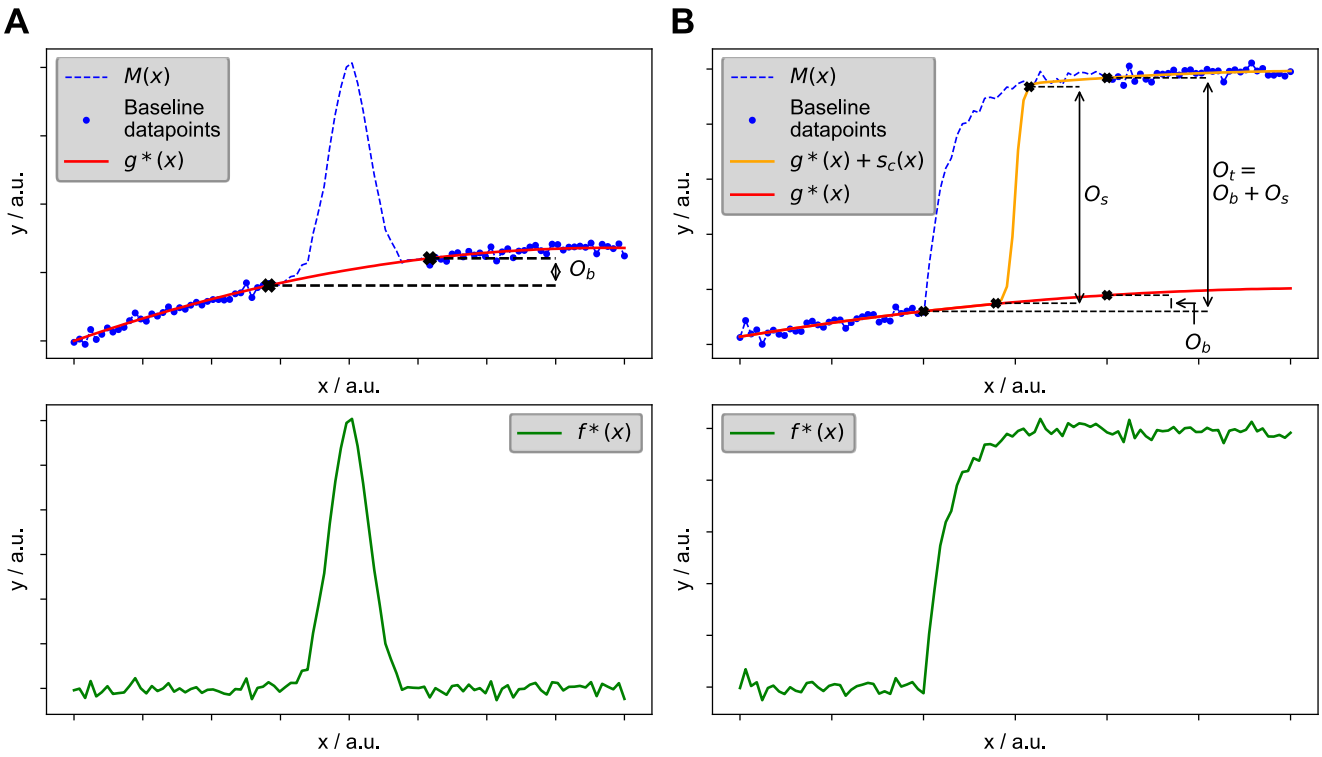

Figure 11 Examples of non-baseline-altering and baseline-altering features with corresponding baseline corrections
In both cases, the synthetic baseline consists of a second-order polynomial and Gaussian noise was added to the simulated measurement (a.u. = arbitrary unit).
A Top: Measurement of non-baseline-altering feature (M(x), dashed line) with datapoints considered for baseline fitting highlighted. Baseline approximation g*(x) (red) and corresponding baseline offset (O_b) are shown. Bottom: Baseline corrected signal f*(x) obtained by subtraction of g*(x) from M(x).
B Top: Baseline-altering feature with total offset (O_t) between the two baseline intervals highlighted along with signal offset O_s and baseline offset O_b. Logistic Baseline Correction (LBC) fit is shown in orange (showing that it captures O_s) and thus obtained baseline approximation g*(x) is shown in red. Bottom: f*(x) obtained by subtraction of g*(x) (obtained via LBC) from M(x).
Source: Publication III.

The absence of an adequate method for baseline correction of baseline-altering features is a serious concern, since this feature class is commonly encountered in chemistry and biology: whenever there is chemical reaction, a saturation or accumulation process, or edge behavior, baseline-altering features result. This kind of baseline correction problem is for example encountered when analyzing chemical reaction,[87] X-ray absorption spectroscopy (XAS),[86] or quantitative polymerase chain reaction data[85] (qPCR, the main method for detection of SARS-CoV-2 virus[88]).

Inspired by having encountered this problem our self while analyzing *in situ* O_2 data, we set out to develop a generally applicable method for baseline correction of baseline-altering features.

They key challenge is that signal offset O_s is unknown beforehand. Knowing O_s would allow for shifting of post-feature datapoints by this magnitude on the y-axis, restoring a classical baseline correction problem. However, the observed total offset between pre- and post-feature datapoints, O_t, is the sum of

signal offset O_s and baseline offset O_b (see Figure 11B, top). Since O_s is unknown, the baseline, and hence O_b, cannot be determined, which in turn prevents determination of O_s, because baseline and signal cannot be separated.

This recursive problem is resolved by introducing a new algorithm: Logistic Baseline Correction (LBC). In LBC, instead of fitting only $g^*(x)$ to baseline datapoints, a function of the form $g^*(x) + s_c(x)$ is fitted (see Figure 11B, top). $s_c(x)$ is logistic step function of the form:

$$s_c(x) = \frac{c}{1 + e^{r(x - x_0)}} \qquad \text{Equation (1)}$$

c refers to step magnitude, while r describes logistic growth rate and x_0 is the logistic midpoint. For LBC, r and x_0 are automatically determined in each situation and fixed, with c and the parameters of $g^*(x)$ being optimized during fitting. For this formalism, $s_c(x)$ introduces a step of magnitude c between pre- and post-feature datapoints while $g^*(x)$ describes the baseline. Since step magnitude c is optimized iteratively along with the parameters of $g^*(x)$, we hypothesized that c would approach O_s, allowing $g^*(x)$ to become a good description of the baseline without influence of the signal offset. This was verified using synthetic data experiments (see Ap. 8.2 SI Figure 2), which showed that c and $g^*(x)$ reliably describe O_s and baseline, respectively, for various baseline shapes, levels of noise, number of available datapoints and baseline intervals. Using synthetic data it was also shown that LBC significantly improved subsequent data analysis for the baseline corrected signal $f^*(x)$ obtained by subtraction of $g^*(x)$ from $M(x)$, as compared to pre-feature fitting (see Chapter 6.3 Manuscript Figure 2).

To demonstrate the utility of LBC for experimental data analysis, it was applied to chemical reaction, qPCR and XAS data.

As an example for chemical reaction data, *in situ* O_2 measurement of potassium iodide catalyzed H_2O_2 disproportionation was chosen (see Figure 12). In this case, LBC provides an excellent fit of baseline datapoints (see Figure 12A), which results in a baseline corrected signal that starts at 0 vol% O_2 and has the expected flat pre- and post-feature regions (see Figure 12B). Due to these characteristics, the signal can be analyzed by fitting an integrated rate law, obtaining information on the rate constant and final amount of O_2 (see Figure 12B). This analysis cannot be properly performed when pre-feature fitting is used instead of LBC (see Chapter 6.3 Manuscript Figure 3A).

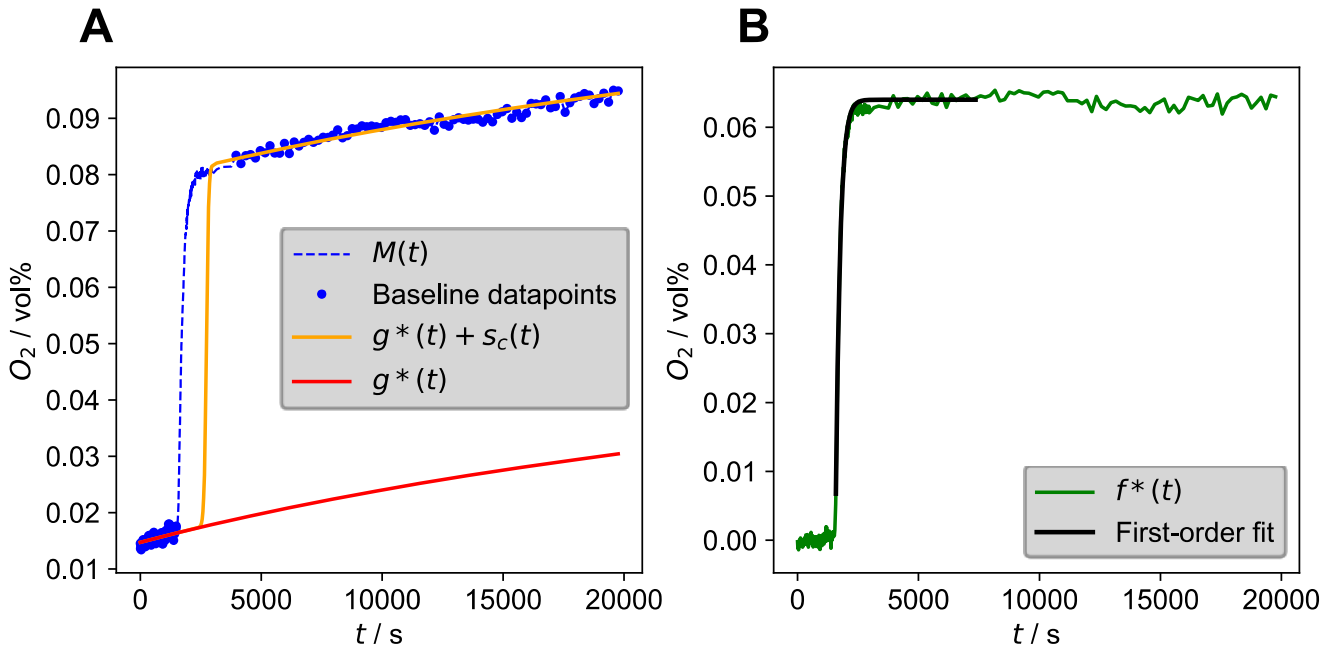

Figure 12 Analysis of O_2 evolution signal obtained *in situ* for potassium iodide catalyzed H_2O_2 disproportionation
A LBC using a fourth-order polynomial for g*(t).
B LBC corrected signal showing stationary post-feature phase and good fit of integrated first-order rate law (see Ap. 8.2 SI Section 2).
Note: For visualization purposes, the measurement is only shown up to 20000 s, but the entire measurement lasts 60000 s (see Ap. 8.2 SI Figure 4B). The integrated first-order rate law is only fitted starting at 1589 s due to an apparent induction period caused by diffusion.
Source: Publication III.

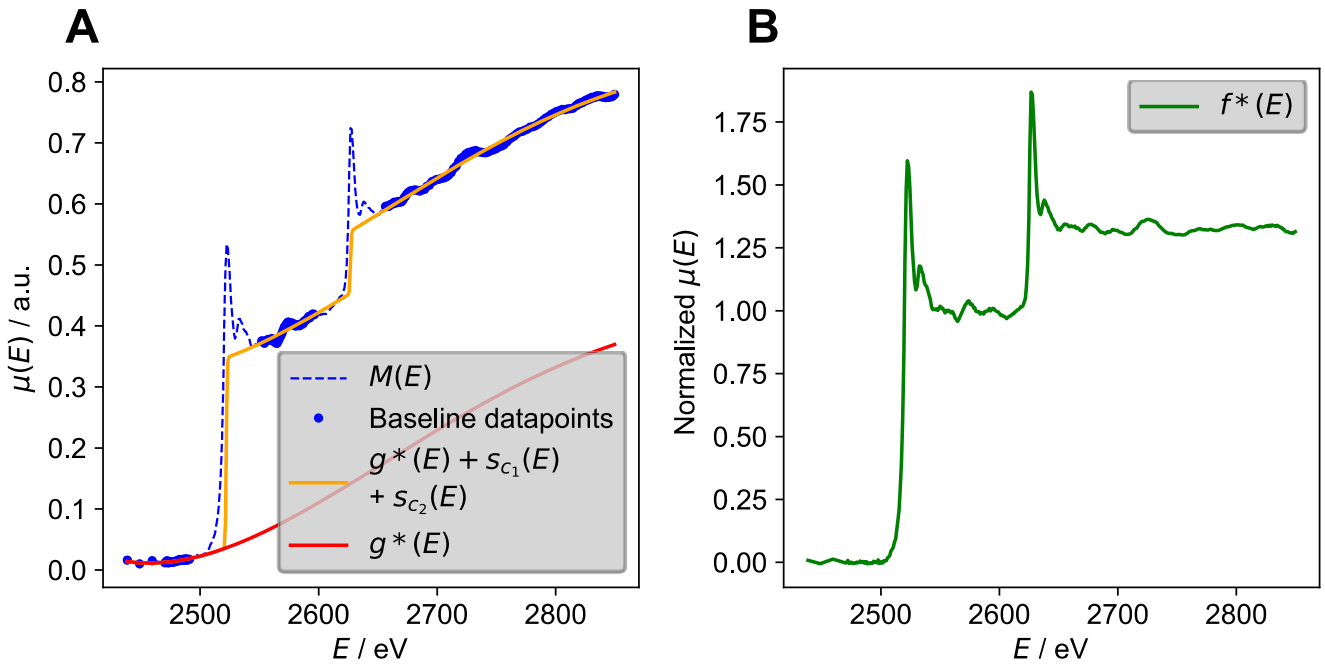

Figure 13 Application of LBC to X-ray absorption spectrum of molybdenum foil
A LBC applied to molybdenum L_{23}-edge region of the spectrum using a fourth-order polynomial for g*(E) and two logistic functions to account for both steps.
B Baseline corrected, normalized L_{23}-edge region of spectrum obtained using LBC.
Source: Publication III.

For qPCR data analysis, LBC was benchmarked against state-of-the-art algorithms by using a literature known reference dataset.[85] It outperformed most previously reported methods (see Ap. 8.2 SI Figure 8), with especially low bias in the analysis (see Chapter 6.3 Manuscript Figure 4).
For the last example, LBC was applied to X-ray absorption spectroscopy (XAS) data (see Figure 13). To illustrate that LBC can also handle multiple features, the L_{23}-edge region of a molybdenum foil spectrum was chosen. In this case, two $s_c(E)$ functions are used during fitting to account for both absorption edges (see Figure 13A). This results in an excellent description of the baseline while also determining edge step magnitude $\Delta\mu_e$ (identical to c), which is needed for normalization in XAS analysis. Simultaneous determination of baseline and $\Delta\mu_e$, also for multiple features, is a significant simplification of state-of-the-art XAS data analysis workflows, which typically require multiple separate steps.[86]

We can conclude that LBC is the first generally applicable method for baseline correction of baseline-altering features. Given the ubiquitous nature of this feature class in chemistry and biology, it is a valuable tool to improve data analysis for a range of analysis techniques. This has been exemplified by applying LBC to chemical reaction, qPCR and XAS data. To aid other scientists in adopting this new method, all code related to LBC is open source (https://github.com/jschneidewind/LBC) and an easy-to-use web interface has been created (https://lbc.olickel.com) that allows for application of LBC even without coding experience.

Disclaimer: Parts of chapter 3.3 were paraphrased, adapted or taken from the manuscript of publication III. This manuscript was completely written by me and is licensed under a CC-BY license, allowing for copying, redistributing and adapting.

3.4 Catalyst Speciation and Reaction Mechanism for Ruthenium Catalyzed Reductive Amination

Publication title: "Simple ruthenium-catalyzed reductive amination enables the synthesis of a broad range of primary amines", DOI: 10.1038/s41467-018-06416-6

Supporting Information: Available at https://www.nature.com/articles/s41467-018-06416-6

Reductive amination is a highly useful method for hydrogen valorization, as it allows for the conversion of readily available carbonyl compounds into valuable amines.[64] Thus obtained amines can be building blocks for various pharmaceutical, agricultural and material applications.[64] While a handful of homogeneous reductive amination catalysts have previously been reported,[89,90] a particularly simple and versatile ruthenium catalyst was identified in our group. Based on $[RuCl_2(PPh_3)_3]$, this catalyst allows for the conversion of aldehydes and ketones into primary amines using H_2 and NH_3 (see Figure 14A). A broad substrate scope spanning nearly 100 different carbonyl compounds was demonstrated (see Chapter 6.4 Manuscript).

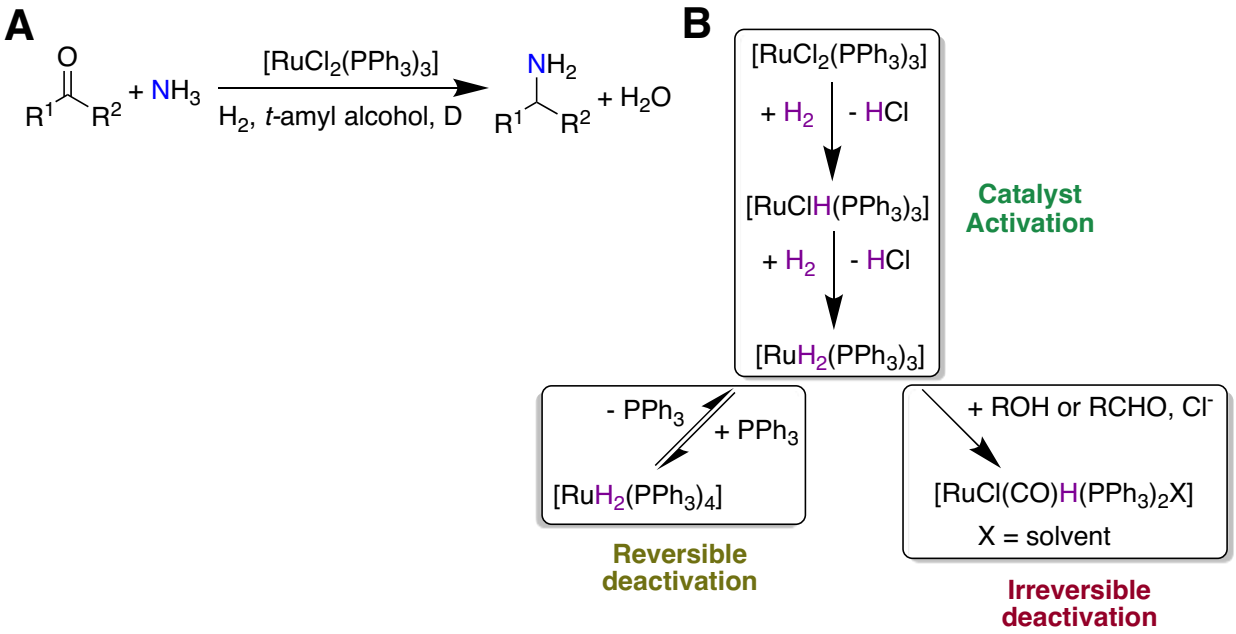

Figure 14 Reductive amination reaction and catalyst speciation
A General reaction equation for $[RuCl_2(PPh_3)_3]$ catalyzed reductive amination using H_2 and NH_3.
B Catalyst speciation elucidated via *in situ* NMR spectroscopy and catalytic experiments.
Adapted from Publication IV.

We were interested in investigating the reaction mechanism, which could hopefully provide useful insights for further improvements in the future. To this end, catalyst speciation starting from $[RuCl_2(PPh_3)_3]$ and H_2 was studied via *in situ* NMR spectroscopy. Using ^{31}P, ^{1}H and 2D NMR techniques, it was found that $[RuCl_2(PPh_3)_3]$ initially converts to monohydride species $[RuClH(PPh_3)_3]$, which can further react with H_2 to form $[RuH_2(PPh_3)_3]$ (see Figure 14B). In separate catalytic

experiments, it was confirmed that [$RuClH(PPh_3)_3$] (and likely [$RuH_2(PPh_3)_3$]) can act as a catalyst for reductive amination. [$RuH_2(PPh_3)_3$] is in an equilibrium with [$RuH_2(PPh_3)_4$] via association of PPh_3. Due to the lack of vacant coordination sites in [$RuH_2(PPh_3)_4$], association of PPh_3 can be seen as a pathway for reversible catalyst deactivation. Importantly, under reaction conditions, decarbonylation of either the solvent (when methanol is used) or substrate can occur, leading to formation of stable carbonyl complexes such as [$RuCl(CO)H(PPh_3)_2X$] (X being a solvent molecule). Experimentally, it was found that [$RuCl(CO)H(PPh_3)_3$] was a less active and selective catalyst for reductive amination compared to [$RuClH(PPh_3)_3$], suggesting that formation of carbonyl complexes is a pathway for irreversible catalyst deactivation (see Figure 14B).

We also investigated the formation of different intermediates and side products during reductive amination. Condensation of carbonyl compounds with ammonia leads to formation of primary imines, while condensation with product primary amines can lead to formation of secondary imines. Only the hydrogenation of primary imines yields the desired primary amine product, as hydrogenation of secondary imines produces secondary amines. Since the condensation reactions are equilibria, addition of excess NH_3 can favor formation of primary imines and ultimately primary amines. Under some reaction conditions, an imidazoline side product was observed. This is formed due to thermal cyclization of three primary imine molecules.[91] Its formation can therefore be suppressed by employing a highly active catalyst that quickly hydrogenates primary imine, keeping its stationary concentration low.

In conclusion, *in situ* NMR studies and catalytic experiments provided valuable insights into catalyst speciation and deactivation pathways as well as the mechanisms of side product formation. This knowledge can be used for future development of more active and selective reductive amination catalysts, thus advancing hydrogen valorization technologies.

3.5 Identification of Active Catalyst in Rhodium Catalyzed Arene Hydrogenation

Publication title: "Mechanistic Understanding of the Heterogeneous, Rhodium-Cyclic(Alkyl)(Amino)Carbene-Catalyzed (Fluoro-)Arene Hydrogenation", DOI: 10.1021/acscatal.0c01074

Supporting Information: Available at https://pubs.acs.org/doi/abs/10.1021/acscatal.0c01074

Arene hydrogenation is another interesting reaction for hydrogen valorization, converting arene feedstock into useful saturated carbo- and heterocycles. In 2017, Wiesenfeldt *et al.* reported a highly active rhodium catalyst for the challenging hydrogenation of (fluoro)-arenes with excellent cis-selectivity (see Figure 15).[66]

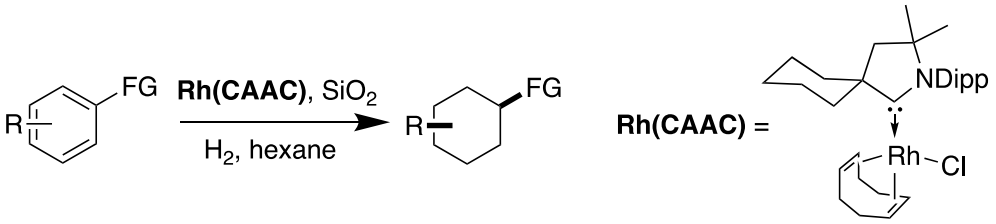

Figure 15 General reaction scheme for rhodium catalyzed arene hydrogenation

Homogeneous complex **Rh(CAAC)** was employed as a catalyst, although the reaction was found to require a heterogeneous additive, such as SiO_2. This suggests that, potentially, the heterogeneous additive acts as a support for a heterogeneous catalyst formed under reaction conditions. In a later experiment without substrate, **Rh(CAAC)** was indeed shown to decompose under reaction conditions, leading to formation of a rhodium containing SiO_2 material designated as **Rh/SiO$_2$**. **Rh/SiO$_2$** displayed effectively the same catalytic activity as the combination of **Rh(CAAC)** + SiO_2, although this could also be due to leaching of deposited rhodium. To facilitate further mechanistic studies, the nature of the active species had to be clarified.

We therefore turned to *in situ* NMR experiments to perform kinetic experiments, monitoring substrate consumption and product formation over time. The hypothesis was that if **Rh(CAAC)** is only a precursor of the active species, there should be an induction period for the reaction. In turn, if **Rh/SiO$_2$** is the active species, no such induction period should be observed when it is used as the catalyst. These kinetic *in situ* NMR experiments were complicated by the fact, however, that this is a three-phasic, high-pressure (20 bar) reaction: hydrogen, being a gas, has to diffuse into the liquid solvent to react with **Sub-1**, potentially mediated by a solid state catalyst. To enable H_2 diffusion as well as liquid/solid phase mixing, the entire reaction system had to be mixed inside the high-pressure NMR tube while being measured. We therefore turned to an experimental set-up developed by Baumann and Selent,[92] which enables high-pressure gas injection and circulation through a reaction solution.

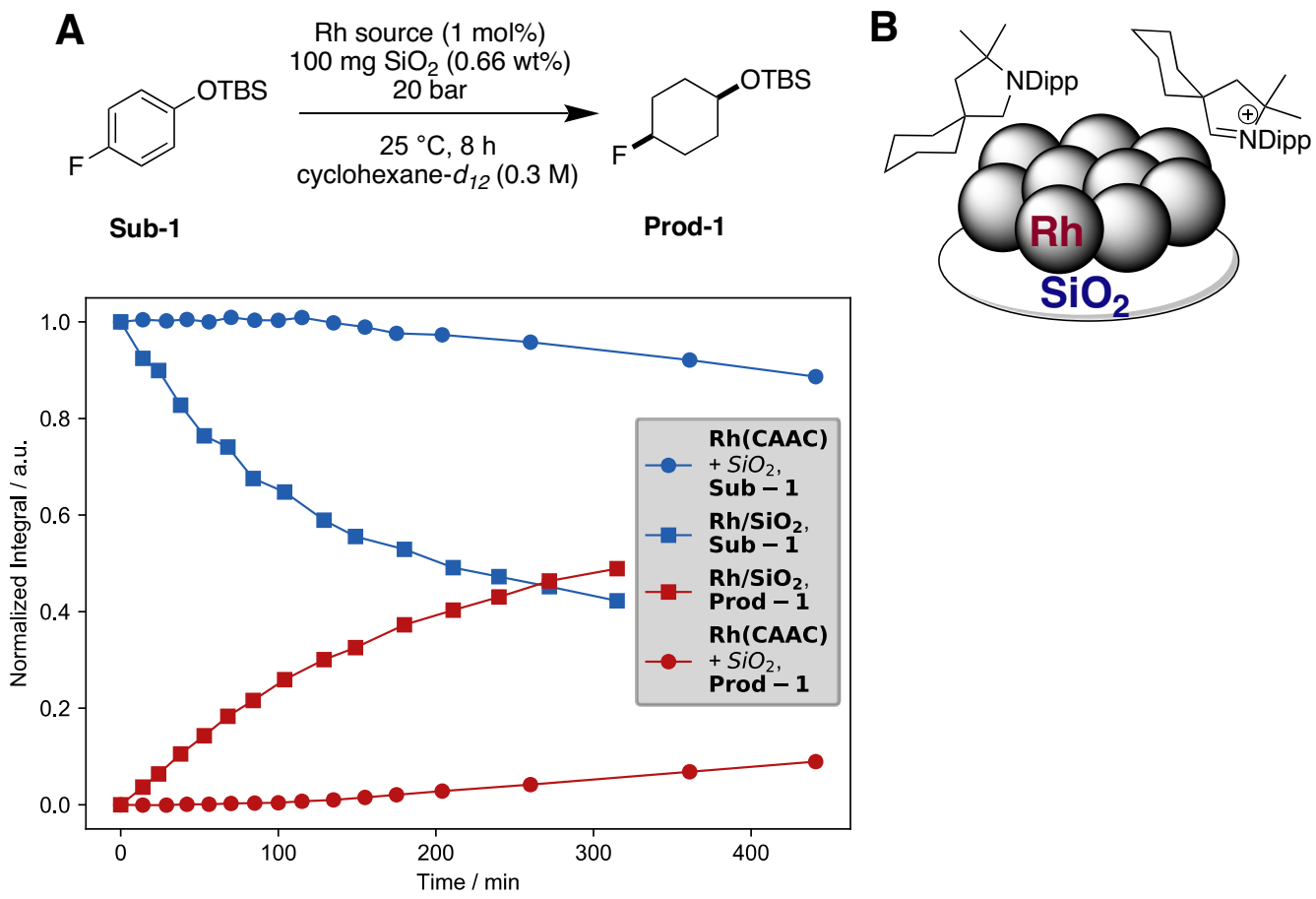

Figure 16 *In situ* NMR results and proposed active catalyst species
A Reaction equation and results of *in situ* NMR spectroscopy monitoring concentrations of **Sub-1** and **Prod-1**.
B Proposed active catalyst species composed of metallic Rh nanoparticles with surface bound CAAC-derived modifiers on SiO_2.
Adapted from Publication V.

Using this set-up, hydrogen can be bubbled through the reaction solution while it is inside the spectrometer. Bubbling of H_2 facilitates diffusion into the liquid phase. Furthermore, we hoped that it would also agitate the solution sufficiently to allow for mixing of solid and liquid phase, although no such three-phasic reactions had previously been performed using the set-up. To our delight, arene hydrogenation could be observed with this experimental set-up using both **Rh(CAAC)** + SiO_2 as well as **Rh/SiO₂** as catalysts (see Figure 16A). Signal quality, however, was sub-par, requiring a special computational workflow for quantification (see Publication V SI Section F). In case of **Rh(CAAC)** + SiO_2 a pronounced induction period was observed, which was completely absent in case of **Rh/SiO₂** (see Figure 16). These observations show that **Rh(CAAC)** is indeed only a precursor, which is converted to the active catalyst **Rh/SiO₂**.

With this knowledge of the active catalyst species, characterization of **Rh/SiO₂** was performed using X-ray photoelectron spectroscopy, transmission electron spectroscopy, X-ray absorption spectroscopy and solid-state NMR. Using these techniques, it was found that **Rh/SiO₂** consists of SiO_2-supported, metallic rhodium nanoparticles with surface-bound pyrrolidine and pyrrolidinium species. These species

are derived from the cyclic(alkyl)(amino)carbene ligand of **Rh(CAAC)** and act as reactivity modifiers, giving **Rh/SiO_2** its unusual reactivity and selectivity (see Chapter 6.5 Manuscript).

We can conclude that kinetic experiments using a special high-pressure *in situ* NMR set-up provided information on the active catalyst species for rhodium catalyzed arene hydrogenation. Identification of the active species enabled detailed characterization studies, ultimately identifying the important role of surface-bound organic species in modulating catalyst activity. This insight can pave the way for future design of highly active and selective heterogeneous catalysts through targeted surface modification.

4 Conclusion

While the important role of green hydrogen for a global transition to carbon neutrality has been recognized, its economical production remains challenging. Water electrolysis powered by renewable electricity is a promising and maturing pathway, although it could take several decades until it becomes fully competitive with fossil hydrogen sources. We therefore turned our attention to photocatalytic water splitting, which might promise drastically lower production costs due to simple water splitting devices. The current technological challenge of this approach is development of suitable photocatalysts, hampered by two fundamental challenges: high kinetic complexity and lack of broad visible light utilization.

To open up new ways for addressing these challenges, this work set out to discover a new mechanism for light-driven water splitting by studying a previously reported, untypical water splitting reaction. Through combined kinetic, spectroscopic and computational studies, the first mechanism for water splitting that only requires two photons was identified. In comparison with the reaction blueprint of photosynthesis, this significantly lowers kinetic complexity. Furthermore, in the newly discovered mechanism, the two photons are absorbed by different species and can have different wavelengths, spanning a large part of the visible spectrum. Due to these attractive features, this mechanism could inspire the development of a new class of water splitting systems, which address the fundamental challenges by going beyond the reaction blueprint of photosynthesis.

Regarding the secondary objectives of this work, the oxidation half-reaction for a photocatalytic CO_2 reduction system was elucidated, revealing oxidation of TiO_2 surface hydroxyl groups to be the electron source. A new and generally applicable algorithm for baseline correction was developed, which can be used to improve data analysis for various techniques in chemistry and biology. For ruthenium catalyzed reductive amination, catalyst speciation and deactivation as well as side product formation pathways were illuminated. Lastly, the active catalyst in a rhodium catalyzed arene hydrogenation reaction was identified through *in situ* spectroscopy.

5 Outlook

Short-term goals for further work on two-photon water splitting might include:

1. Direct detection of second photon absorbing intermediate [**B**]T_0 using ultra-fast spectroscopy.
2. Addressing the issue of O_2 consumption, which appears to not be an intrinsic problem for water splitting using complex **1**, since it was not observed by Kohl *et al.*[56]
3. Exploring the reactivity of structural derivatives of **1**, especially including modification of the pincer ligand. This might pave the way for an understanding of structure/reactivity relationships, which could be used to increase the lifetime of the second photon absorbing intermediate, improving reaction yields and rates.

To also aid other researchers in advancing these goals, all original data of our study has been made publicly available at https://github.com/jschneidewind/Water-Splitting. The repository includes original data files as well as analysis code with detailed documentation. In combination with information on the used techniques in the supporting information, this will hopefully help other researchers to also explore this exciting field, accelerating progress.

In the long-term, two approaches for utilizing the two-photon mechanism can be envisioned:

1. Development of completely new water splitting catalysts. Such systems would likely be homogeneous in nature, given that molecular complex **1** already provides a closed reaction cycle, which could in principle be used to construct a catalyst. This raises the fundamental question whether it is feasible to construct a useful homogeneous water splitting photocatalyst, also in light of issues such as ligand oxidation and complex decomposition?
2. Integration of two-photon water splitting into existing catalyst platforms. In this approach, attractive features of the newly discovered mechanism, such as broad utilization of visible light through different absorbing intermediates or demand for less than four photons, would be used to improve existing systems. It might be to conceivable, for example, to incorporate photon induced O-O bond formation by oxo-hydroxo coupling into defined heterogeneous systems, such as metal-organic frameworks. The fundamental scientific question here is how targeted integration of mechanistic features into existing systems can be achieved?

Ultimately, the goal of this field is to create photocatalysts that can realize the promises of low-cost green hydrogen production via photocatalytic water splitting. Once green hydrogen can be produced economically, there would be an incentive to expand renewable energy capacity, replacing fossil chemical energy carriers with renewable ones. These renewable chemical energy carriers could then be traded globally using existing infrastructure, improving accessibility to renewable energy and accelerating the global transition to carbon neutrality.

6 Publications

Nr.	Publication	Contribution	Notes
I	**J. Schneidewind*,** M. A. Argüello-Cordero, H. Junge, S. Lochbrunner, M. Beller; ***submitted***; Two-photon water splitting at a molecular ruthenium complex	Full paper, 85%	Lone corresponding and first author
II	S. Kreft, R. Schoch, **J. Schneidewind,** J. Rabeah, E. V. Kondratenko, V. A. Kondratenko, H. Junge, M. Bauer, S. Wohlrab, M. Beller*, *Chem* **2019**, *5*, 1818–1833; Improving Selectivity and Activity of CO_2 Reduction Photocatalysts with Oxygen	Full paper, 20%	/
III	**J. Schneidewind*,** Hrishi Olickel, *Chemistry – Methods* **2020**, *accepted*; Improving Data Analysis in Chemistry and Biology Through Versatile Baseline Correction	Full paper, 90%	Lone corresponding and first author, selected as front cover
IV	T. Senthamarai, K. Murugesan, **J. Schneidewind,** N. V. Kalevaru, W. Baumann, H. Neumann, P. C. J. Kamer, M. Beller*, R. V. Jagadeesh*, *Nature Communications* **2018**, *9*, 1–12; Simple ruthenium-catalyzed reductive amination enables the synthesis of a broad range of primary amines	Article, 15%	/
V	D. Moock, M. P. Wiesenfeldt, M. Freitag, S. Muratsugu, S. Ikemoto, R. Knitsch, **J. Schneidewind,** W. Baumann, A. H. Schäfer, A. Timmer, M. Tada, M. R. Hansen, F. Glorius*, *ACS Catalysis* **2020**, *10, 11,* 6309-6317; Mechanistic Understanding of the Heterogeneous, Rhodium-Cyclic(Alkyl)(Amino)Carbene-Catalyzed (Fluoro-)Arene Hydrogenation	Full paper, 5%	/

6.1 Two-photon water splitting at a molecular ruthenium complex

J. Schneidewind*, M. A. Argüello-Cordero, H. Junge, S. Lochbrunner, M. Beller, ***submitted***

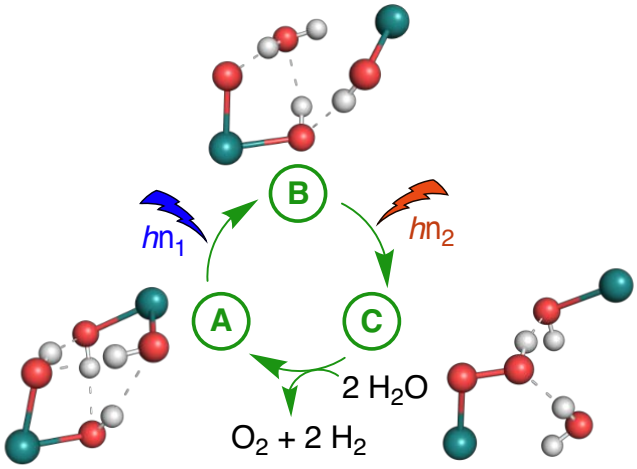

Contributions: I conceived and coordinated the project, performed all experimental (except ultrafast pump-probe spectroscopy) and computational work, wrote analysis software, performed data analysis, curated data for supporting information and public repository, and wrote the complete manuscript. Overall, my contribution amounts to ca. 85%.

Abstract: Water splitting to give molecular oxygen and hydrogen or the corresponding protons and electrons is a fundamental four-electron redox process, which forms the basis of photosynthesis and is a promising approach to convert solar into chemical energy. Inspired by photosynthesis, artificial water splitting systems largely rely on the absorption of four photons to complete the reaction, with each photon transferring one of the electrons. Correctly orchestrating these four absorptions creates a high degree of kinetic complexity, which has thus far hindered systems from becoming competitive with other approaches to solar energy conversion. Another challenge faced by artificial water splitting systems has been the utilization of visible light, with most systems being limited to shorter wavelengths. Here, we show for the first time a mechanism for overall water splitting that only requires two photons. Furthermore, the two absorbed photons have different wavelengths, spanning a large part of the visible spectrum. This mechanism was discovered through detailed kinetic, spectroscopic and computational studies of a previously reported reaction involving Milstein's ruthenium complex. We show that two-photon water splitting is enabled by absorption of the first, shorter wavelength photon, which produces an intermediate capable of absorbing the second, longer wavelength photon. The second absorption then causes O-O bond formation and liberation of O_2. Due to the lower kinetic complexity and intrinsic utilization of a wide wavelength range, we believe that this mechanism will inspire the development of a new class of water splitting systems that go beyond the reaction blueprint of photosynthesis.

Two-photon water splitting at a molecular ruthenium complex

Jacob Schneidewind[1,*], Miguel A. Argüello Cordero[2], Henrik Junge[1], Stefan Lochbrunner[2], Matthias Beller[1]

Affiliations

1 Leibniz-Institut für Katalyse e.V., Albert-Einstein-Str. 29a, Rostock 18059, Germany.

2 Institute for Physics and Department of Life, Light and Matter, University of Rostock, 18051 Rostock, Germany

*Corresponding author, e-mail: Jacob.Schneidewind@catalysis.de

Jacob Schneidewind ORCID	0000-0002-5328-6626
Stefan Lochbrunner ORCID	0000-0001-9729-8277
Henrik Junge ORCID	0000-0002-7603-1984
Matthias Beller ORCID	0000-0001-5709-0965

This file includes:

Summary

Water splitting to give molecular oxygen and hydrogen or the corresponding protons and electrons is a fundamental four-electron redox process, which forms the basis of photosynthesis[1] and is a promising approach to convert solar into chemical energy.[2] Inspired by photosynthesis, artificial water splitting systems largely rely on the absorption of four photons to complete the reaction, with each photon transferring one of the electrons.[3] Correctly orchestrating these four absorptions creates a high degree of kinetic complexity, which has thus far hindered systems from becoming competitive with other approaches to solar energy conversion.[2] Another challenge faced by artificial water splitting systems has been the utilization of visible light, with most systems being limited to shorter wavelengths.[4] Here, we show for the first time a mechanism for overall water splitting that only requires two photons. Furthermore, the two absorbed photons have different wavelengths, spanning a large part of the visible spectrum. This mechanism was discovered through detailed kinetic, spectroscopic and computational studies of a previously reported reaction involving Milstein's ruthenium complex.[5] We show that two-photon water splitting is enabled by absorption of the first, shorter wavelength photon, which produces an intermediate capable of absorbing the second, longer wavelength photon. The second absorption then causes O-O bond formation and liberation of O_2. Due to the lower kinetic complexity and intrinsic utilization of a wide wavelength range, we believe that this mechanism will inspire the development of a new class of water splitting systems that go beyond the reaction blueprint of photosynthesis.

Introduction

Water splitting is a four-electron redox process, which is accomplished in natural photosynthesis by consecutive absorption of four photons in photosystem II (Kok's cycle).[1,6] The kinetic complexity of orchestrating these four photon absorption and redox events is solved in nature through the so-called Z scheme, a complex chain of light-driven redox reactions enabling an efficient flow of electrons through the responsible enzymes.[7] Artificial water splitting systems are attractive means of converting solar into chemical energy and could play a pivotal role in a global transition towards the use of renewable energy.[2] Photocatalysts for water splitting have largely adopted a similar approach to natural photosynthesis, relying on absorption of four photons to accomplish water splitting.[3] This is because most systems are based on semiconductors, for which absorption of a photon produces one electron/hole pair (except for processes like singlet fission[8,9]) and thus, four of these events are required to complete the reaction.[3] Due to the absence of an equally elegant electron transfer system like the Z scheme, however, artificial systems have struggled to deal with this kinetic complexity, resulting in systems, which are not yet productive enough to compete with other approaches for solar energy conversion.[2] Progress has been made to address this challenge by using alternative reaction pathways,[10,11] although these can present other hurdles (see Figure 1).

Another longstanding challenge for artificial water splitting systems has been the efficient utilization of visible light, with most systems being limited to UV and blue light.[4] While in nature this is also addressed using the Z scheme, advances for artificial systems include the combination of smaller band gap semiconductors with low overpotential catalysts,[12,13] artificial Z schemes,[7] photon upconversion,[14,15] and the combination of different photoanodes and cathodes.[16] A challenge shared by these approaches is that electrons and holes are generated with the same mechanism for each of the four redox steps. While each step might have a different redox potential,[17] the respective mechanism thus has to match the largest of all potentials, therefore setting the minimum energy requirement for all photon absorptions.

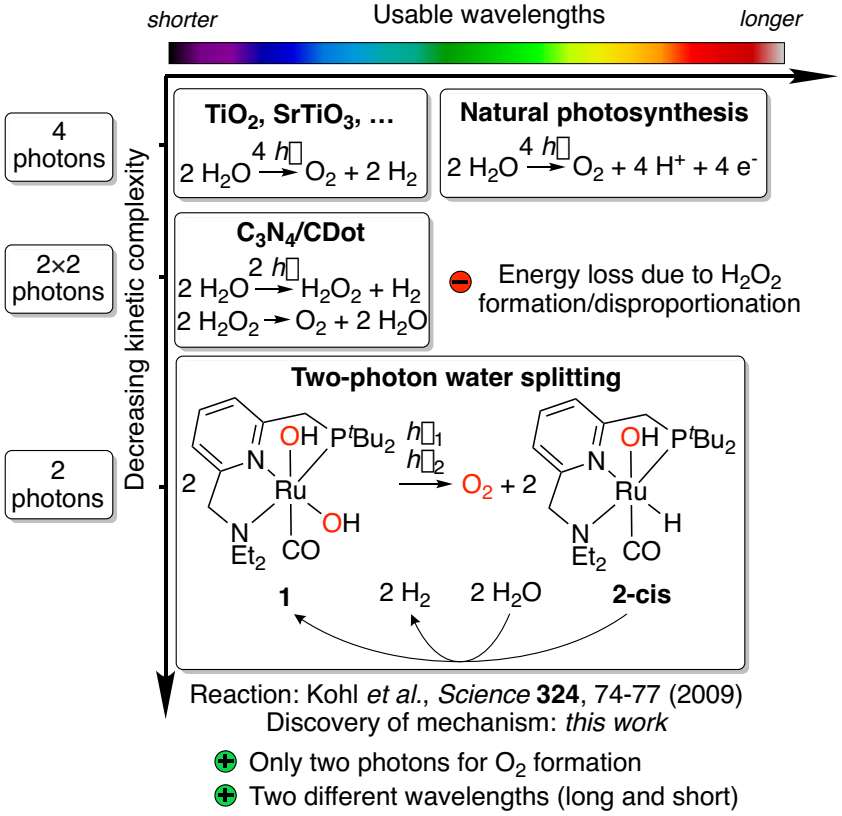

Figure 1 Overview of approaches to light-driven water splitting, arranged by usable wavelength range (top scale) and kinetic complexity (side scale). Note that wavelength ranges are only approximate.

Results

Here, we report a new mechanism for overall water splitting which potentially addresses both of these challenges by requiring only two photons (instead of four) to complete the reaction, drastically reducing kinetic complexity and simplifying the reaction blueprint of natural photosynthesis. Furthermore, the photons are absorbed sequentially by different reaction species at two different wavelengths up to the red part of the spectrum, allowing broader utilization of visible light by tailoring photon absorption for each redox event. Related two-photon mechanisms have been reported in the context of photochromism,[18,19] organic photoredox reactions,[20,21] and OH· generation.[22–24] To the best of our knowledge, an overall water splitting mechanism that only requires two photons has not been described before. Furthermore, it is also the first water splitting mechanism in which photons are absorbed sequentially by different reaction species.

In their seminal study in 2009, Milstein and coworkers reported that broadband irradiation of ruthenium dihydroxo complex **1** lead to evolution of O_2 and concomitant formation of hydrido hydroxo complex **2** (see Figure 1).[5] Heating **2** in water led to evolution of H_2 and regeneration of **1**, closing the quasi-catalytic cycle. Due to the different reaction conditions for both steps and moderate yields, the reaction is not catalytic, but it contains the core reactivity of an overall water splitting process. Since the second step is redox neutral, all electron transfer events for water splitting occur during irradiation of **1,** the reaction that is subject of this study.

Through elegant isotope labeling and trapping experiments, Milstein and coworkers showed that O-O bond formation occurs intramolecularly and that O_2 is formed in its triplet ground state.[5] While originally it was proposed that irradiation of **1** produces H_2O_2, which then disproportionates to form O_2 and water,[5] subsequent theoretical studies have shown this pathway to be unlikely.[25,26] Our experimental results also indicate that H_2O_2 disproportionation catalyzed by **1** is too slow to explain the observed O_2 formation rate (see SI Section 5) and our theoretical results agree with previous findings that H_2O_2 formation from **1** is not energetically feasible (see SI Section 11.2.8).

We therefore set out to elucidate the mechanism by first studying the physico-chemical behavior of **1**. Synthesis and characterization of **1** gave results consistent with Milstein and coworkers' structural assignment of **1** being a cis-dihydroxo complex (see SI Section 3.1.1). The lowest energy absorption feature is a metal-to-ligand charge-transfer (MLCT) band from 350 – 400 nm (see Figure 2 and SI Section 11.2.3) and weak fluorescence in water can be observed at 500 nm when **1** is irradiated at 370 nm (see Figure 2). Irradiation of **1** for two days in water using a broadband quartz-tungsten-halogen light source (320 – 1000 nm) leads to formation of **2-cis** in ca. 20% yield (concentration-time profile see SI Figure 4.1-1 and Section 4.1.2 for structural assignment). **2-cis** refers to the isomer of **2** in which hydrido and hydroxo ligands are in a cis configuration. Reversible formation of a side product, named **Oxo Dimer**, is also observed, which is tentatively assigned to an oxo-bridged dimer that slowly hydrolyses back to **1** (see SI Section 4.1.2). Using in situ O_2 detection, formation of O_2 can be unambiguously detected in both the liquid and the gas phase (see SI Sections 4.2 and

4.3). Kinetic modeling of the concentration-time profile for the formation of **2-cis** and the initial rate of O_2 formation in the liquid phase show that both occur at a comparable rate, indicating that they are part of the same reaction (see SI Section 4.4). Notably, the formed O_2 appears to be consumed again during irradiation, likely due to photochemical oxidation of **1** (see SI Section 4.3.2). A lower yield of **2** (45% vs. 20%), formation of the **Oxo Dimer** side product and consumption of O_2 slightly differ from the original results.[5] Nevertheless, the core water splitting reactivity is identical and these differences do not impact the water splitting mechanistic investigation herein.

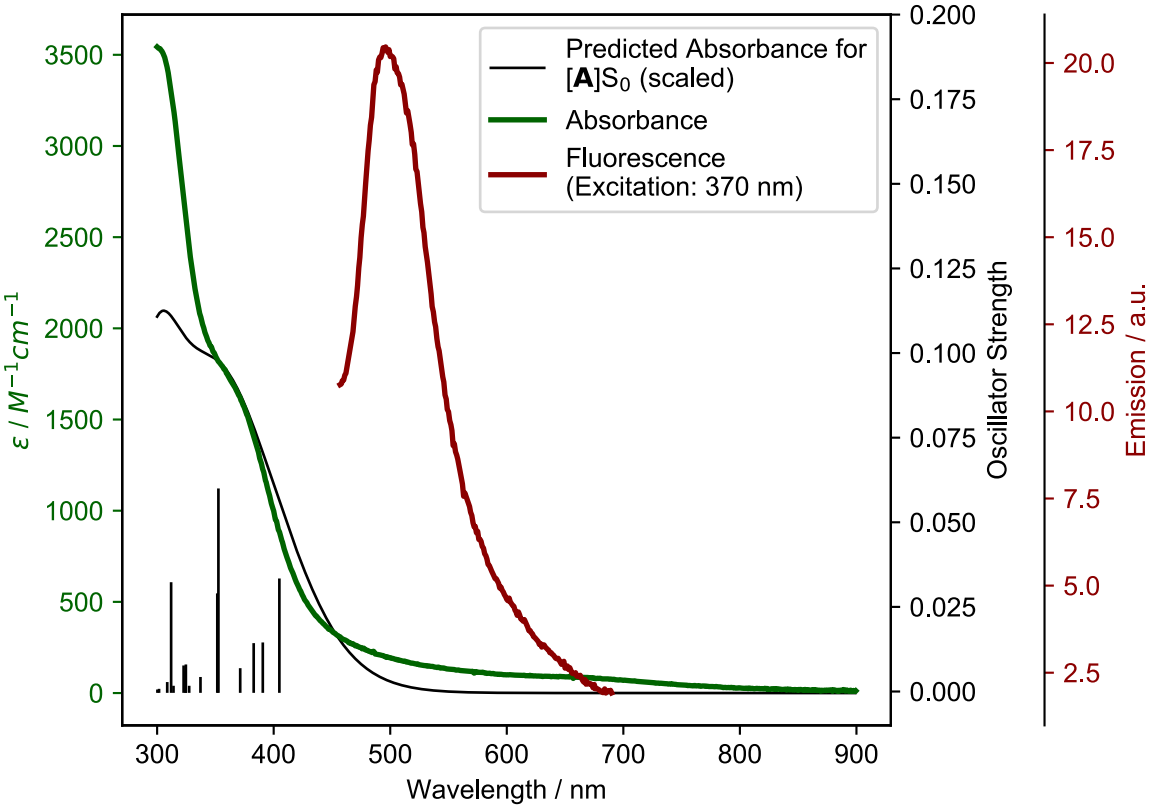

Figure 2 Experimental (green) and theoretical (black) absorbance of **1** (theoretical model [**A**]S_0, see below) as well experimental fluorescence (red). Individual theoretical transitions are shown as vertical lines.

Kinetic studies

Next, we performed kinetic studies based on initial rates of O_2 formation in the liquid phase as well as NMR measurements of **2-cis** formation. Running the reaction in D_2O instead of H_2O shows that there is only a small H/D kinetic isotope effect (1.18, see SI Section 4.2.4). Furthermore, the reaction rate does not increase with increasing temperature (see SI section 4.2.4). We then studied how the initial rate of O_2 formation varies with photon flux density: for these experiments, irradiation was performed using a 320 – 500 nm filtered light source and we found that the rate increases non-linearly with increasing photon flux densities. In fact, the relationship can be described well using a square dependence (see Figure 3), indicating that two photons are absorbed during the reaction.[18]

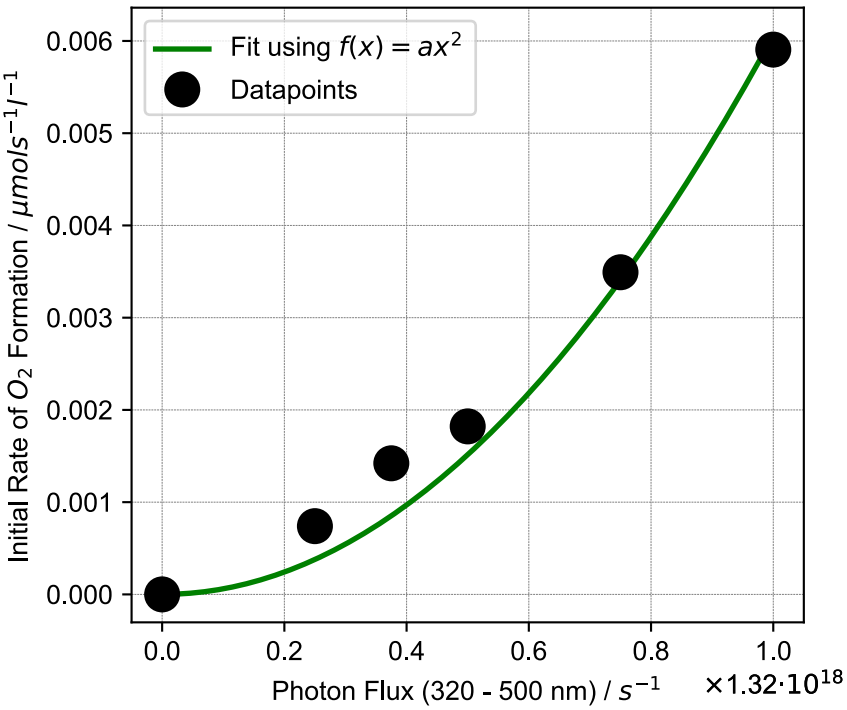

Figure 3 Dependence of initial rate of O_2 formation on photon flux (black dots) along with square fit (green).

Based on this observation, there are two feasible reaction pathways:

1. Two equivalents of **1** separately absorb one photon each, generating two equivalents of an intermediate, which then react in a bimolecular reaction (akin to triplet-triplet annihilation[14]) or

2. **1** absorbs a photon, generating an intermediate, which then absorbs a second photon. Simultaneous two-photon excitation can be excluded as the photon flux densities used in our experiments are too low to observe this effect.[27]

To determine the operative pathway we studied the effects of using different wavelengths for irradiation by using either one or two different light sources simultaneously. When **1** is irradiated using a 320 – 400 nm filtered light source, **2-cis** is formed in 6% yield after 17 h. Expectedly, when irradiation is performed using a 495 – 1000 nm filtered light source, no **2-cis** is formed (as **1** does not significantly absorb > 495 nm light). Remarkably, when both the 320 – 400 nm and 495 – 1000 nm light source are used simultaneously, **2-cis** yield increases to 10% (see Figure 4A).

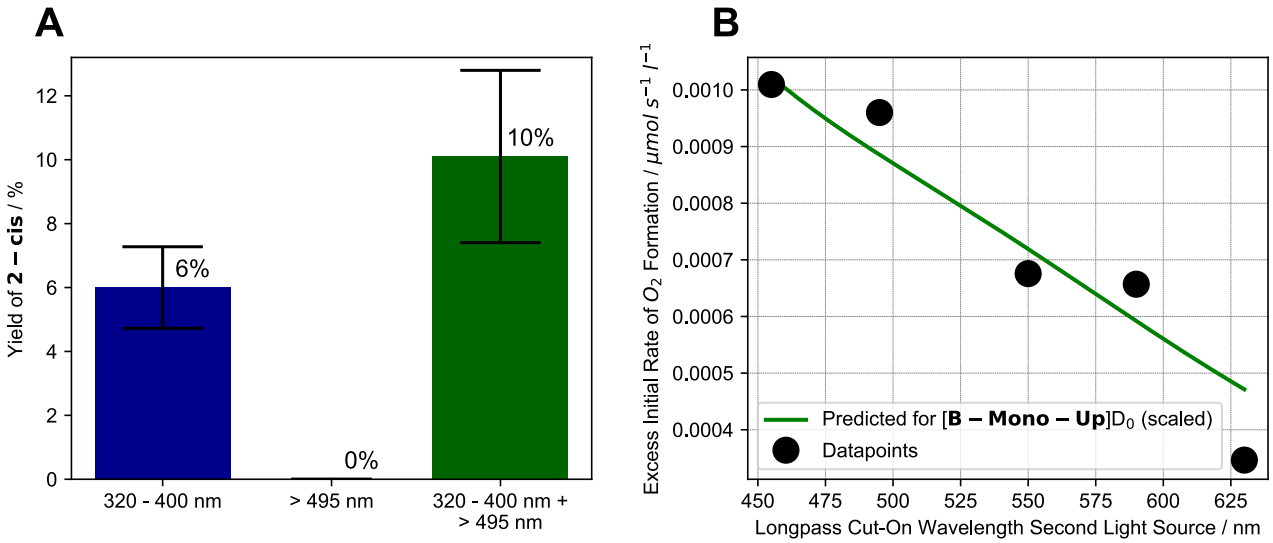

Figure 4 **A** Effect of different irradiation wavelengths and dual irradiation on formation of **2-cis** after 17 h of irradiation. Colored bars and text indicate average values while black error bars indicate upper and lower limit of experimental values; **B** Dependence of excess initial rate of O_2 formation on longpass cut-on wavelength of second light source (first light source: 320 – 400 nm) along with scaled, predicted behavior for [**B-Mono-Up**]D (see below)$_0$.

These results show that using light, which is not significantly absorbed by the starting complex **1**, can enhance the water splitting reaction in a synergistic way**.** In turn, this suggests that excitation of **1** by a 320 – 400 nm photon leads to formation of an intermediate, which absorbs a second, longer wavelength photon to complete the water splitting reaction.

To investigate this effect more closely we performed the following series of dual irradiation experiments: a solution of **1** was simultaneously irradiated with a 320 – 400 nm filtered light source

as well as a second light source with different longpass filters, resulting in X – 1000 nm wavelength intervals (455 – 1000 nm, 495 – 1000 nm etc.) for the second light source. For each longpass filter, the excess initial rate of O_2 formation was determined, which was calculated by subtracting the initial rates of single light source irradiation (320 – 400 nm or X – 1000 nm) from the dual irradiation rate (details see SI Section 4.2.5).

In this experiment, 320 – 400 nm irradiation excites **1** and generates the intermediate, while the effect of longpass filters on excess initial rate effectively probes the absorption behavior of the intermediate for water splitting. Figure 4B shows that already starting at 630 nm, an excess initial rate can be observed, which increases roughly linearly all the way to 455 nm. This indicates that an intermediate, which can absorb 455 – 630 nm photons, is responsible for the second photon absorption during water splitting. The experimental longpass filter/excess rate relationship is in good agreement with a theoretical prediction for the computationally identified intermediate ([**B-Mono-Up**]D_0, see Figure 4B green line, below, and SI section 11.4.1).

Ultrafast pump-probe spectroscopy and kinetic modeling

To investigate the dynamics of **1** after excitation, we performed ultrafast pump-probe spectroscopy, exciting **1** with 400 nm laser pulses (details see SI section 9). In fact, two transient species could be detected, having lifetimes of τ = 6 ps and τ = 150 ps, respectively. Decay associated spectra (DAS) indicate that the τ = 6 ps species corresponds to an emissive singlet state of **1**, explaining the complex's weak fluorescence. DAS for the τ = 150 ps species agree well with the predicted DAS for an isomer of the computationally identified intermediate, [**B-Trans**]T_0 (see SI Figure 9.2-1). To gain a better understanding of the relationship between kinetic and spectroscopic results we developed a simple kinetic model for the consecutive two-photon process (see SI section 10). This model shows good agreement with photon flux density dependence (see SI Figure 10.3-1) as well as dual irradiation data (see SI Section 10.4). Based on this model, the lifetime of the second photon

absorbing intermediate has to be at least 10 ns to explain the observed rates. Therefore, the τ = 150 ps species is likely not the corresponding intermediate, although it might partially isomerize to it below the detection limit (see SI section 9.2). Direct detection of the intermediate might thus require higher sensitivity measurements, which should be the goal for future studies of this system.

Computational studies

To connect the described experimental insights and develop a holistic mechanistic understanding, we performed single- (density functional theory, DFT) as well as multi-configurational (complete active space self-consistent field, CASSCF) computations. Regarding previous theoretical studies, only Chen and Fang investigated a mechanism for O_2 formation that does not proceed via H_2O_2 disproportionation.[26] The authors proposed a hydrogen-bonded dimer of **1**, which upon excitation undergoes intermolecular proton transfer followed by O-O bond formation. While the O-O bond formation step is energetically infeasible in this mechanism (barrier of almost 50 kcal/mol), the first reaction step offers an interesting starting point for our study. In the following, the electronic state (spin and energy level) is indicated for each intermediate behind square brackets.

Start for our mechanism (see Figure 5A) is also a hydrogen-bonded dimer of **1**, named [**A**]S_0, for which time-dependent (TD)-DFT calculations reproduce the experimental UV/Vis spectrum well (see Figure 2). Excitation of the MLCT band at 350 – 400 nm (see SI Section 11.2.3 for natural transition orbitals) leads to population of an excited singlet state, [**A**]S_n, with an energy of 57 – 70 kcal/mol (relative to [**A**]S_0) based on absorption and florescence (500 nm) wavelengths. This species was also observed in pump-probe spectroscopy. Intersystem crossing combined with a proton-coupled electron transfer (PCET) leads to formation of [**B**]T_0 (52.5 kcal/mol relative to [**A**]S_0). PCET of excited metal complexes has ample precedent.[28] In [**B**]T_0, the left ruthenium center has been formally oxidized to Ru(III) (although spin density is largely on oxo ligand), while the right one has

been reduced to Ru(I), leading to a charge-transfer state (see SI Figure 11.2-12 for spin density). This means that the first photon absorption has transferred the first of four electrons.

[**B**]T_0 subsequently absorbs the second photon. Since O-O bond formation occurs intramolecularly,[5] one can expect that the second photon absorption is centered on the left part of the dimer, [**B-Mono**]D_0, containing a hydroxo and oxo ligand. Indeed, the TD-DFT UV/Vis spectrum for [**B-Mono-Up**]D_0 (conformational isomer of [**B-Mono**]D_0, see SI section 11.4.1) agrees well with the dual irradiation data (see Figure 4, details see SI Section 11.4.1). Hence, photon absorption by [**B-Mono**]D_0 was studied using CASSCF (see Figure 5B). Absorption of a 455 – 630 nm photon (transition wavelength CASSCF: 482 nm, [**B**]T_0 TD-DFT: 539 nm, see SI Section 11.3.1) leads to population of the D_2 state (59 kcal/mol in energy relative to [**B-Mono**]D_0, see Figure 5B). For this transition, electron density is transferred from the hydroxo ligand and ruthenium center to the oxo ligand (see SI Figure 11.3-4). Energetically downhill, at 50 kcal/mol relative energy, the D_2/D_1 minimum energy conical intersection (MECI) was located (peaked, bifurcating[29]). At this point, the O-O distance has shortened from 2.8 to 2.0 Å and depopulation of the O-O σ* orbital occurs for the D_1 state (see SI Figure 11.3-5), instead populating a Ru-CO π* orbital, which leads to a bent CO coordination. Further downhill at 37 kcal/mol, the D_1/D_0 MECI was located (sloped, single path[29]), for which the O-O bond is almost completely formed (1.6 Å). Here, depopulation of the Ru-CO π* orbital occurs for D_0, instead populating the Ru(dz^2) orbital (see SI Figure 11.3-6). Finally, at 30 kcal/mol relative energy, the O-O bond is fully formed in hydroperoxo complex [**C-Mono**]D_0 Overall, this reaction can be seen as a photoinduced reductive elimination to enable a highly endothermic O-O bond formation. Formally, two electrons are transferred to the left ruthenium center in the process, reducing it from Ru(III) to Ru(I). Hence, the second photon absorption transfers the second and third out of four electrons.

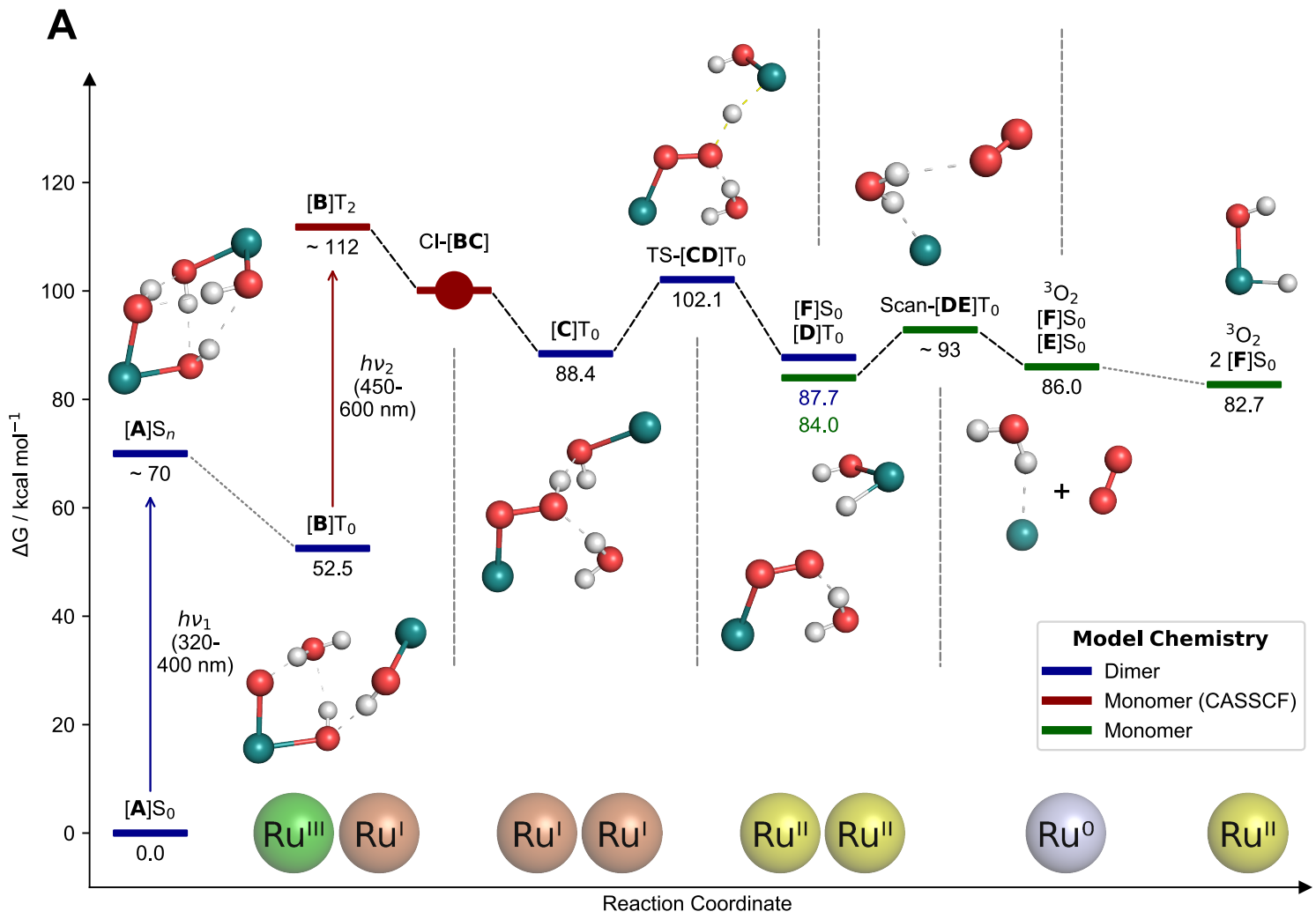
A
ΔG / kcal mol⁻¹
120
100
80
60
40
20
0
[A]Sn
~ 70
[A]S0
0.0
hν1
(320-
400 nm)
[B]T2
~ 112
hν2
(450-
600 nm)
[B]T0
52.5
CI-[BC]
[C]T0
88.4
TS-[CD]T0
102.1
[F]S0
[D]T0
87.7
84.0
Scan-[DE]T0
~ 93
3O2
[F]S0
[E]S0
86.0
3O2
2 [F]S0
82.7
+
Model Chemistry
Dimer
Monomer (CASSCF)
Monomer
RuIII
RuI
RuI
RuI
RuII
RuII
Ru0
RuII
Reaction Coordinate

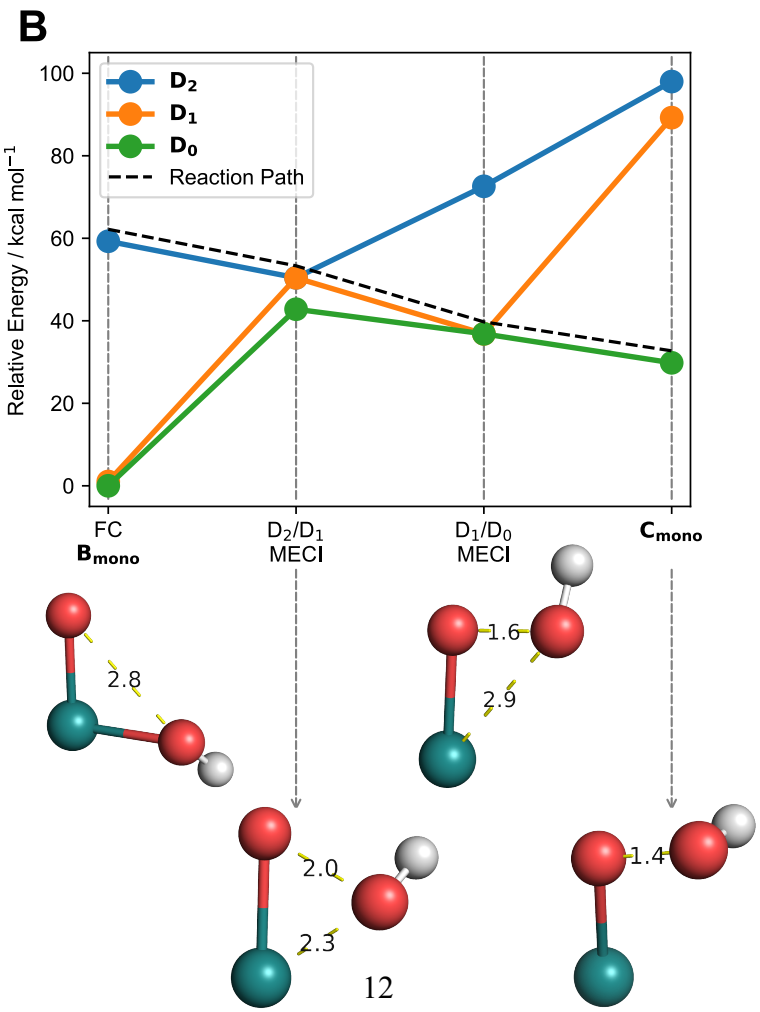
B
Relative Energy / kcal mol⁻¹
100
80
60
40
20
0
D2
D1
D0
Reaction Path
FC
Bmono
D2/D1
MECI
D1/D0
MECI
Cmono
2.8
1.6
2.9
2.0
2.3
1.4

Figure 5 **A** DFT computed free energy profile. Energies of excited species ([**A**]S_n and [**B**]T_2) are only approximate. Franck-Condon geometry is shown for [**A**]S_n. Abbreviations: "CI" conical intersections, "TS" transition state, "Scan" relaxed potential energy surface scan. For [**A**]S_0, both ruthenium centers are in oxidation state II. Shown oxidation states are only formal to visualize electron flow; **B** CASSCF computed reaction from [**B-Mono**] to [**C-Mono**] including minimum energy conical intersections (MECI). Bond distances are in Ångström. Calculations in the gas phase, for solution phase results see SI Figure 11.3-1. Structures are shown without other ligands for clarity.

The remaining reaction steps were calculated using DFT in the triplet ground state. In the dimeric model [**C**]T_0 (spin density see SI Figure 11.2-13), the fourth and final electron transfer can take place via a PCET from the hydroperoxo ligand to the right Ru(I) center. This forms a superoxo ligand (bond distance of 1.3 Å) on the left ruthenium ([**D**]T_0, spin density see SI Figure 11.2-14), while generating the first hydrido hydroxo product complex [**F**]S_0 on the right. This step has a modest barrier of 13.7 kcal/mol. Likely this barrier can be overcome with residual vibrational energy from the second photon absorption. Furthermore, it can likely explain the small amount of H_2O_2 formation observed by Milstein and co-workers: in a small fraction of all reactions, hydrolysis of [**C**]T_0 might occur, liberating H_2O_2 instead of directly forming the superoxo ligand.

At this point the hydrogen-bonded dimer [**D**]T_0 [**F**]S_0 likely dissociates, as the monomer parts are 3.7 kcal/mol more stable than the dimeric structure. The superoxo ligand in [**D**]T_0 is then displaced by water, leading to liberation of $^3O_2$ and formation of Ru(0) complex [**E**]S_0 (oxidation states of superoxo complexes are ill defined, so the conversion of Ru(II) to Ru(0) during superoxo dissociation is just a formal reduction). Finally, in a formal oxidative addition of water, [**E**]S_0 can be converted to a second equivalent of [**F**]S_0.[25,30,31] The ligand configuration in [**F**]S_0 is different from **2-cis**. However, experimentally it was found that independent of water splitting, complex **2** isomerizes during irradiation to form **2-cis** (see SI section 4.1.2). To close the reaction sequence for overall water splitting, redox neutral protonation of the hydride ligands in two [**F**]S_0 equivalents leads to liberation of two H_2 molecules and regeneration of [**A**]S_0,[25,30–32] which is endothermic by 13.2 kcal/mol per [**F**]S_0 (see SI Table 11.2-7).

Conclusion

In summary, we describe a mechanism for overall water splitting, which requires absorption of only two photons. Kinetic results show that a consecutive, non-linear absorption of a 320 – 400 nm photon followed by a 455 – 630 nm photon occurs. These are absorbed by two different species. Computational investigations, supported by ultra-fast spectroscopy, revealed that the first photon absorption causes a spin-flip and the first proton-coupled electron transfer, resulting in a charge-transfer state, which is capable of absorbing the second photon. The second photon absorption enables a highly endothermic O-O bond forming reaction by transferring the second and third electrons. This results in a reaction product that can undergo the fourth and final electron transfer without additional energy input, completing the water splitting reaction. For this particular model reaction system, the reaction does not proceed with high yield or efficiency, as **1**'s structure has in no way been optimized for photochemical reactions. We hope, however, that the detailed mechanistic insight laid out herein can inspire a new class of artificial water splitting systems which take advantage of: 1. the low kinetic complexity of requiring only two photons and 2. the intrinsic ability of this mechanism to utilize a wide wavelength range. Ultimately, this could give rise to efficient and economical water splitting systems that go beyond the reaction blueprint of natural photosynthesis.

Acknowledgments: Hrishi Olickel is gratefully acknowledged for providing computational resources and valuable discussions. Maximilian Marx (LIKAT) is acknowledged for crystallization attempts of **1**, IR measurements and valuable discussions. Prof. David Milstein (Weizmann Institute of Science) and Dr. Stephan Kohl (TU Berlin) are acknowledged for valuable disucssions and providing original analysis data. Dr. Wolfgang Baumann and Susann Buchholz (both LIKAT) are acknowledged for performing NMR measurements. Dr. Jabor Rabeah (LIKAT) is acknowledged for performing EPR measurements. Peter Kucmierczyk (Evonik), Dr. Nils Rockstroh, Astrid Lehmann, Andreas Hutter, Matthias Auer and Anja Kammer (all LIKAT) are acknowledged for technical support. Prof. Robert H. Morris (Univeristy of Toronto) is acknowledged for enabling early experimental work. Financial support by Fonds der Chemischen Industrie (Kekulé-Stipendium n. 102151 for J.S.) is gratefully acknowledged.

Author contributions: J. S. conceived and coordinated the project, performed all experimental (except ultrafast pump-probe spectroscopy) and computational work, wrote analysis software, performed data analysis, curated data for supporting information and public repository, and wrote the manuscript. M. A. A. C. and S. L. planned ultrafast pump-probe spectroscopy experiments, M. A. A. C. performed pump-probe spectroscopy experiments and analyzed resulting data. H. J. and M. B. provided experimental infrastructure and resources as well as funding. All authors discussed the results and revised the manuscript.

Data availability: Original data supporintg the results of this study is available at: https://github.com/jschneidewind/Water-Splitting (including for Figures 2 - 5)

Code availabbility: Code developed for this study is availale at: https://github.com/jschneidewind/Water-Splitting

Competing interests: The authors have no competing interests.

Correspondence and requests for materials should be adressed to J. S. (Jacob.Schneidewind@catalysis.de).

References

1. Kern, J. *et al.* Structures of the intermediates of Kok's photosynthetic water oxidation clock. *Nature* **563**, 421–425 (2018).
2. J. Detz, R., H. Reek, J. N. & Zwaan, B. C. C. van der. The future of solar fuels: when could they become competitive? *Energy Environ. Sci.* **11**, 1653–1669 (2018).
3. Hisatomi, T. & Domen, K. Reaction systems for solar hydrogen production via water splitting with particulate semiconductor photocatalysts. *Nat. Catal.* 1 (2019) doi:10.1038/s41929-019-0242-6.
4. Takata, T. & Domen, K. Particulate Photocatalysts for Water Splitting: Recent Advances and Future Prospects. *ACS Energy Lett.* **4**, 542–549 (2019).
5. Kohl, S. W. *et al.* Consecutive Thermal H2 and Light-Induced O2 Evolution from Water Promoted by a Metal Complex. *Science* **324**, 74–77 (2009).
6. Kok, B., Forbush, B. & McGLOIN, M. Cooperation of charges in photosynthetic o2 evolution–i. a linear four step mechanism. *Photochem. Photobiol.* **11**, 457–475 (1970).
7. Wang, Y. *et al.* Mimicking Natural Photosynthesis: Solar to Renewable H2 Fuel Synthesis by Z-Scheme Water Splitting Systems. *Chem. Rev.* **118**, 5201–5241 (2018).
8. Einzinger, M. *et al.* Sensitization of silicon by singlet exciton fission in tetracene. *Nature* **571**, 90–94 (2019).
9. Martinez, M. S., Nozik, A. J. & Beard, M. C. Theoretical limits of multiple exciton generation and singlet fission tandem devices for solar water splitting. *J. Chem. Phys.* **151**, 114111 (2019).
10. Liu, J. *et al.* Metal-free efficient photocatalyst for stable visible water splitting via a two-electron pathway. *Science* **347**, 970–974 (2015).
11. Kuttassery, F. *et al.* One Electron-Initiated Two-Electron Oxidation of Water by Aluminum Porphyrins with Earth's Most Abundant Metal. *ChemSusChem* **10**, 1909–1915 (2017).

12. Wang, Q. *et al.* Oxysulfide photocatalyst for visible-light-driven overall water splitting. *Nat. Mater.* **18**, 827–832 (2019).
13. Wang, Z. *et al.* Overall water splitting by Ta 3 N 5 nanorod single crystals grown on the edges of KTaO 3 particles. *Nat. Catal.* **1**, 756 (2018).
14. Yu, T. *et al.* Triplet–Triplet Annihilation Upconversion for Photocatalytic Hydrogen Evolution. *Chem. – Eur. J.* **25**, 16270–16276 (2019).
15. Zhang, M. *et al.* Improving Hematite's Solar Water Splitting Efficiency by Incorporating Rare-Earth Upconversion Nanomaterials. *J. Phys. Chem. Lett.* **3**, 3188–3192 (2012).
16. Seger, B. *et al.* 2-Photon tandem device for water splitting: comparing photocathode first versus photoanode first designs. *Energy Environ. Sci.* **7**, 2397–2413 (2014).
17. Wang, L.-P. & Van Voorhis, T. Direct-Coupling O2 Bond Forming a Pathway in Cobalt Oxide Water Oxidation Catalysts. *J. Phys. Chem. Lett.* **2**, 2200–2204 (2011).
18. Mutoh, K., Nakagawa, Y., Sakamoto, A., Kobayashi, Y. & Abe, J. Stepwise Two-Photon-Gated Photochemical Reaction in Photochromic [2.2]Paracyclophane-Bridged Bis(imidazole dimer). *J. Am. Chem. Soc.* **137**, 5674–5677 (2015).
19. Kobayashi, Y., Mutoh, K. & Abe, J. Stepwise two-photon absorption processes utilizing photochromic reactions. *J. Photochem. Photobiol. C Photochem. Rev.* **34**, 2–28 (2018).
20. Ghosh, I., Ghosh, T., Bardagi, J. I. & König, B. Reduction of aryl halides by consecutive visible light-induced electron transfer processes. *Science* **346**, 725–728 (2014).
21. Glaser, F., Kerzig, C. & Wenger, O. S. Multi-Photon Excitation in Photoredox Catalysis: Concepts, Applications, Methods. *Angew. Chem. Int. Ed.* **59**, 10266–10284 (2020).
22. Goez, M., Schiewek, M. & Musa, M. H. O. Near-UV Photoionization of [Ru(bpy)3]2+: A Catalytic Cycle with an Excited Species as Catalyst. *Angew. Chem. Int. Ed.* **41**, 1535–1538 (2002).

354 23. Goez, M., von Ramin-Marro, D., Othman Musa, M. H. & Schiewek, M. Photoionization of
355 [Ru(bpy)3]2+: A Catalytic Cycle with Water as Sacrificial Donor. *J. Phys. Chem. A* **108**, 1090–
356 1100 (2004).
357 24. Domcke, W., Ehrmaier, J. & Sobolewski, A. L. Solar Energy Harvesting with Carbon Nitrides
358 and N-Heterocyclic Frameworks: Do We Understand the Mechanism? *ChemPhotoChem* **3**, 10–
359 23 (2019).
360 25. Yang, X. & Hall, M. B. Mechanism of Water Splitting and Oxygen−Oxygen Bond Formation by
361 a Mononuclear Ruthenium Complex. *J. Am. Chem. Soc.* **132**, 120–130 (2010).
362 26. Chen, Y. & Fang, W.-H. Mechanism for the Light-Induced O2 Evolution from H2O Promoted
363 by Ru(II) PNN Complex: A DFT Study. *J. Phys. Chem. A* **114**, 10334–10338 (2010).
364 27. Li, R.-Q. *et al.* A two-photon excited O2-evolving nanocomposite for efficient photodynamic
365 therapy against hypoxic tumor. *Biomaterials* **194**, 84–93 (2019).
366 28. Wenger, O. S. Proton-Coupled Electron Transfer with Photoexcited Metal Complexes. *Acc.*
367 *Chem. Res.* **46**, 1517–1526 (2013).
368 29. Fdez. Galván, I., Delcey, M. G., Pedersen, T. B., Aquilante, F. & Lindh, R. Analytical State-
369 Average Complete-Active-Space Self-Consistent Field Nonadiabatic Coupling Vectors:
370 Implementation with Density-Fitted Two-Electron Integrals and Application to Conical
371 Intersections. *J. Chem. Theory Comput.* **12**, 3636–3653 (2016).
372 30. Sandhya, K. S. & Suresh, C. H. Water Splitting Promoted by a Ruthenium(II) PNN Complex:
373 An Alternate Pathway through a Dihydrogen Complex for Hydrogen Production.
374 *Organometallics* **30**, 3888–3891 (2011).
375 31. Ma, C., Piccinin, S. & Fabris, S. Reaction Mechanisms of Water Splitting and H2 Evolution by a
376 Ru(II)-Pincer Complex Identified with Ab Initio Metadynamics Simulations. *ACS Catal.* **2**,
377 1500–1506 (2012).

32. Li, H. & Hall, M. B. Computational Mechanistic Studies on Reactions of Transition Metal Complexes with Noninnocent Pincer Ligands: Aromatization–Dearomatization or Not. *ACS Catal.* **5**, 1895–1913 (2015).

6.2 Improving Selectivity and Activity of CO_2 Reduction Photocatalysts with Oxygen

S. Kreft, R. Schoch, J. Schneidewind, J. Rabeah, E. V. Kondratenko, V. A. Kondratenko, H. Junge, M. Bauer, S. Wohlrab, M. Beller*, *Chem* **2019**, *5*, 1818–1833

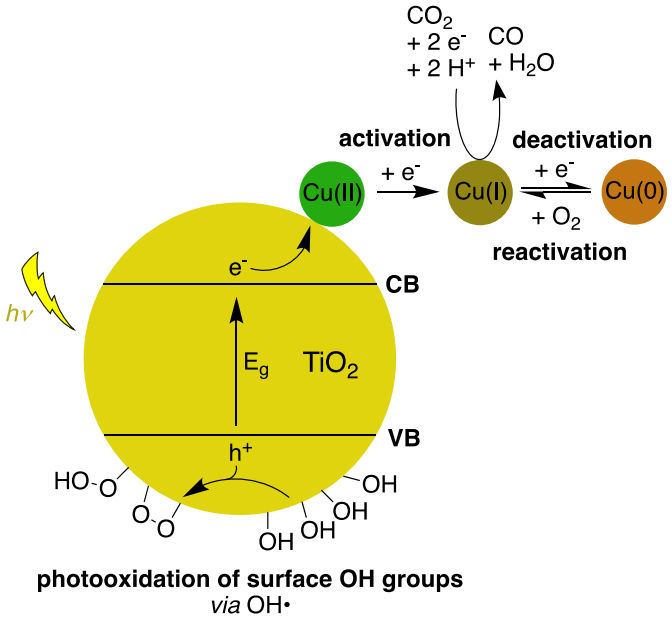

Contributions: I carried out experiments with the optical oxygen meter set-up for O_2 detection and performed data analysis and interpretation, designed the experiments for the oxidation half-reaction section together with S.K. and wrote the oxidation half-reaction section, which accounts for ca. 20% of the manuscript. Furthermore, I revised the entire manuscript. Overall, my contribution amounts to ca. 20%.

Abstract: A highly porous photocatalyst (copper on TiO_2 aerogel) was synthesized and applied in aqueous CO_2 reduction without using external sacrificial electron donors. For the first time, complete selectivity toward CO and improved catalyst productivity are observed in the presence of oxygen. The optimal activity is achieved in a feed containing 0.5 vol% O_2 in CO_2. In situ XAS, EPR, and UV-Vis measurements suggest, among different Cu oxidation states, Cu(I) to be the most active species in photocatalytic CO_2 reduction. Oxygen sensing of the catalyst in the presence of O_2/CO_2 mixtures indicated an unexpected photoadsorption of oxygen on the titania surface. We propose photooxidation of surface hydroxyl groups to be the electron source for CO_2 reduction, which is supported by hydroxyl group consumption, detection of hydroxyl radicals using in situ EPR, and detection of surface peroxide species after the reaction.

Chem

CellPress

Article

Improving Selectivity and Activity of CO_2 Reduction Photocatalysts with Oxygen

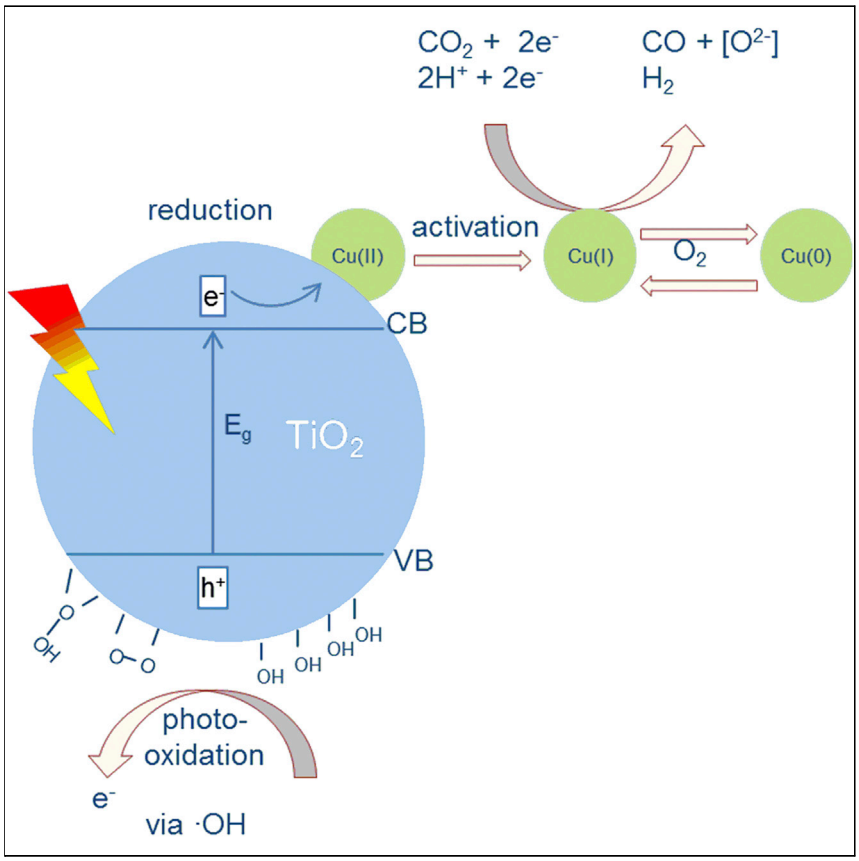

A highly porous copper-loaded titanium dioxide material has been developed to catalyze reduction of CO_2 to CO using light as the energy source. In this system, activity for CO production could be enhanced by addition of oxygen, which stabilizes the catalytically active Cu(I) oxidation state. The oxidation half-reaction has also been investigated, and the titanium dioxide itself was found to be the electron source.

Stefanie Kreft, Roland Schoch, Jacob Schneidewind, ..., Matthias Bauer, Sebastian Wohlrab, Matthias Beller

evgenii.kondratenko@catalysis.de (E.V.K.)
matthias.beller@catalysis.de (M.B.)

HIGHLIGHTS

Synthesized Cu/TiO_2 aerogel is active in CO_2 reduction compared to commonly used P25

Enhanced activity in the presence of small amounts of O_2

Photooxidation of surface hydroxyl groups provides electrons for CO_2 reduction

Various *in situ* investigations provide evidence of mechanism (e.g., EPR, XAS, UV-vis)

Kreft et al., Chem 5, 1818–1833
July 11, 2019
https://doi.org/10.1016/j.chempr.2019.04.006

Chem

CellPress

Article

Improving Selectivity and Activity of CO_2 Reduction Photocatalysts with Oxygen

Stefanie Kreft,[1] Roland Schoch,[2,3] Jacob Schneidewind,[1,3] Jabor Rabeah,[1] Evgenii V. Kondratenko,[1,*] Vita A. Kondratenko,[1] Henrik Junge,[1] Matthias Bauer,[2] Sebastian Wohlrab,[1] and Matthias Beller[1,4,*]

SUMMARY

A highly porous photocatalyst (copper on TiO_2 aerogel) was synthesized and applied in aqueous CO_2 reduction without using external sacrificial electron donors. For the first time, complete selectivity toward CO and improved catalyst productivity are observed in the presence of oxygen. The optimal activity is achieved in a feed containing 0.5 vol% O_2 in CO_2. *In situ* XAS, EPR, and UV-vis measurements suggest, among different Cu oxidation states, Cu(I) to be the most active species in photocatalytic CO_2 reduction. Oxygen sensing of the catalyst in the presence of O_2/CO_2 mixtures indicated an unexpected photoadsorption of oxygen on the titania surface. We propose photooxidation of surface hydroxyl groups to be the electron source for CO_2 reduction, which is supported by hydroxyl group consumption, detection of hydroxyl radicals using *in situ* EPR, and detection of surface peroxide species after the reaction.

INTRODUCTION

Usage of carbon dioxide (CO_2) under ambient conditions for the formation of organic matter is of fundamental importance in biology[1,2] and is considered to be a key step for future artificial photosynthesis[3,4] to convert this inexpensive and non-toxic C_1 building block into more valuable products.[5,6] Since the beginning of the 20th century, CO_2 has been used on a large-scale in industry, particularly for the production of urea.[7,8] More recently, the synthesis of various carbonates was also commercialized.[9–11] In all these examples, the oxidation state of CO_2 remains unchanged. When CO_2 is involved in reduction reactions, the spectrum of the products generated can be significantly extended. For this purpose, hydrogen-rich chemicals such as CH_4 and lower alkanes are typically applied to convert CO_2 into syngas (a mixture of H_2 and CO).[12] In addition, direct hydrogenation to methanol or hydrocarbons[13,14] continues to attract attention as alternative CO_2 valorizations. Recently, electrochemical,[15,16] photochemical reductions,[17,18] and combined approaches[19] also became attractive from both fundamental and applied viewpoints. Undoubtedly, the direct photocatalytic conversion of CO_2 into methanol[20] or formic acid[21] without additional reductants constitutes a benign and straightforward way to access these important building blocks. The selective deoxygenation of CO_2 to CO is also important because of the industrial use of the latter in large-scale Fischer-Tropsch synthesis, methanol synthesis, olefin hydroformylation, etc. Compared to the photocatalytic water-splitting process, fewer homogenous and heterogeneous systems are known for direct CO_2 conversion into CO without formation of other carbon-containing products. For example, molecular-defined systems consisting of a photosensitizer (PS) and a CO_2 reduction catalyst, e.g., Fe–[22,23], Ni–[24], Cu–,[25] Re–,[26] or Ru–[27] complexes, have been reported. Notably, in all these studies, external

The Bigger Picture

The consumption of fossil fuels for energy generation results in harmful CO_2 emissions, necessitating carbon-neutral energy sources for global environmental sustainability. Instead of releasing CO_2 into the atmosphere, using it as a renewable carbon feedstock for the synthesis of valuable chemicals and/or fuels is highly desirable. Photocatalytic CO_2 reduction to C_1 compounds combines the use of solar energy with CO_2 valorization and is of great interest in basic research. Semiconductors, especially TiO_2, are commonly used as photocatalysts. In this work, a highly porous TiO_2 aerogel was synthesized and applied in aqueous CO_2 reduction to CO. Thereby, improved catalyst productivity was observed in the presence of oxygen. Furthermore, progress in understanding the lesser known and challenging oxidation process has been achieved.

sacrificial reducing agents such as amines or alcohols are required, thus hampering potential applications. Complementary to the use of these molecular-defined systems, heterogeneous catalysts based on semiconductors like CdS,[28,29] ZrO_2,[30] Ga_2O_3,[31] graphene,[32] and especially TiO_2[14,17] were described for photocatalytic reduction of CO_2. In these materials, a photon with energy equal or higher than the band gap (E_g) of the semiconductor is absorbed and leads to the excitation of an electron from the valence band (VB) to the conduction band (CB). Thereby an electron-hole pair is generated. In order to make this process more efficient and to prevent a recombination of these charge carriers, co-catalysts that reduce CO_2 are deposited on the surface.[17,33] However, such studies were mainly performed in the presence of sacrificial reductants such as alcohols[34,35] or hole scavengers.[36–38] In fact, only a small number of materials, such as TiO_2, Ga_2O_3,[39] N-doped ZnO,[40] and $MTaO_3$ (M = K, Na, Li),[41,42] promote CO_2 conversion into CO without additional reagents.

Since the pioneering work of Honda and Fujishima in the early 70's,[43] TiO_2 has been among the best known semiconductors for photocatalysis owing to its abundance, semiconducting properties, low costs, and chemical stability.[17,44,45] The primary crystal structures of titania are anatase and rutile, while the electrons of the former structure have a much longer lifetime (1 ms) of the excited state resulting in improved photocatalytic CO_2 reduction.[46] So far, titania-based catalysts with supported Pt,[47] Ag,[48] Au,[49,50] Pd,[51] Cu,[52–65] Fe,[66] or Ni[67] species have been applied for photocatalytic CO_2 reduction. Among the known copper/titanium dioxide (Cu/TiO_2) materials (Table S1), active catalysts in batch or continuous-flow reactors required the presence of Cu(I) species.[52,54,57,62–64] Thereby, the presence of Cu(0) decreased the activity.[58,62,63] In gas-phase reactions, primarily, CH_4 and CO were generated upon light-driven CO_2 reduction.[52,54,57–59,64,65] In contrast, CO_2 reduction in aqueous solutions toward oxygenates[55,56,60–63] or methane[53,55] competes with water reduction to form H_2 preferentially.

In addition to the supported co-catalyst, the crystallite size and specific surface area of TiO_2 are key parameters affecting overall performance of the material. For example, usage of TiO_2 crystallites larger than 20 nm led to a substantial decrease in photocatalytic activity.[68] On the basis of significantly smaller particles and mainly because of their high specific surface area, we speculated that metal-supported anatase aerogels may constitute promising catalytic materials.[69–71] Surprisingly, apart from aerogels with supported platinum species,[72,73] their counterparts with other supported metals have been scarcely investigated for the target reaction.

In this work, we describe the synthesis of composite materials like Cu/TiO_2-AG (AG: aerogel) possessing Cu(II)-nanoparticles on the surface of a highly porous TiO_2 aerogel (TiO_2-AG) and their application for room-temperature photocatalytic CO_2 reduction without any external sacrificial reagents. Remarkably, the presence of oxygen (O_2) improved the CO productivity and practically suppressed H_2 generation.

RESULTS AND DISCUSSION

Preparation and Characterization of Catalytic Materials

TiO_2-AG and Cu/TiO_2-AG were synthesized as previously described (Section S2).[73–75] N_2-physisorption measurements revealed that these samples possess a specific surface area of 480 m^2/g (Section S6). This value is almost 10 times higher than the specific surface area of commercially available TiO_2 (P25). The reasons for this difference are the larger particles and the random aggregation of the P25 powder in contrast to the defined wire-like structure[74] of the TiO_2-AG. The content of

[1]Leibniz-Institut für Katalyse, an der Universität Rostock e.V., Albert-Einstein-Straße 29a, Rostock 18059, Germany

[2]Universität Paderborn, Department Chemie, Warburger Str. 100, Paderborn 33098, Germany

[3]These authors contributed equally

[4]Lead Contact

*Correspondence: evgenii.kondratenko@catalysis.de (E.V.K.), matthias.beller@catalysis.de (M.B.)

https://doi.org/10.1016/j.chempr.2019.04.006

copper (Cu) determined by inductively coupled plasma atomic emission spectroscopy (ICP-AES) is used in the abbreviations of the catalysts (see also Section S5).

Powder X-ray diffraction (XRD) analysis proved that the TiO_2-AG samples are composed of the anatase phase with nanosized crystallites as determined from the XRD reflection (101) (Figure S7). Transmission electron microscopy and high-angle annular dark field (TEM-HAADF) images revealed the preservation of the wire-like structure of the TiO_2-AG after addition of Cu-nanoparticles (Figures S8 and S9). Because of the low difference in molecular weights between Cu and titanium, it is difficult to distinguish between them in the TEM image. However, the three spectra recorded by energy dispersive x-ray spectroscopy (EDX) at different positions showed the same intensive Cu signal concluding a homogeneous dispersion of Cu. The calculated Ti:Cu ratio was about 9:1 in all three considered areas (Figure S9B EDX data), which corroborates the Cu/Ti ratio in 6.3_Cu/TiO_2-AG. Thereby, the Cu species seem to be finely dispersed on the surface of the support (Figure S9), which correlates with the XRD pattern without significant Cu reflections (Figure S7). As determined by x-ray photoelectron spectroscopy (XPS) (Figure S10A), the only weak Cu 2p3/2 peak was observed at 933.1 eV, which is characteristic for Cu(II) species.[76] The typical satellite peak in the area of around 941 eV can only be presumed because of the low signal intensity. This low-intensity signal at rather high Cu loading (6.3 wt %) supports the high Cu dispersion on the surface of the aerogel.

Reduction Half-Reaction

All catalytic experiments were performed in a batch reactor using a CO_2-saturated-catalyst dispersion in water at room temperature under UV-A/Vis (320–500 nm) irradiation (Section S4). In general, besides H_2 and CO, no CH_4 or any other gaseous or liquid products (formic acid, methanol) could be detected by gas chromatography equiped with a thermal conductivity detector (GC/TCD), gas chromatography/mass spectrometry (GC-MS), and capillary electrophoresis. Selected catalytic results are summarized in Table 1. While common commercial TiO_2 samples showed neither CO nor H_2 production within the detection limit (Table 1, entries 1 and 2), the synthesized TiO_2-AG displayed some activity, albeit mainly for water reduction (Table 1, entry 3). Testing 6.3_Cu/TiO_2-AG, CO generation was 3 times higher than that with pristine TiO_2-AG; however, hydrogen evolution still dominated (Table 1, entry 4). Unfortunately, the activity of Cu/TiO_2-AG decreased significantly over time (Table 1, entries 4–7), which suggests a rapid catalyst deactivation (see "Improving Catalyst Activity and Selectivity" and "The Nature of Active Cu Species"). When Cu loading was reduced to 0.3 wt %, the activity toward CO increased strongly, while H_2 generation was slightly affected (Table 1, entry 8). In agreement with previous observations, we believe that less Cu on the surface leads to higher dispersion and smaller particles, which prevents charge recombination and thereby promotes CO_2 photo reduction.[59,63,65] Lowering the amount of the catalyst further increased catalytic activity (Table 1, entry 9), apparently because of improved light absorption by the catalyst.

Although the highest activity was achieved with 0.3_Cu/TiO_2-AG, most of the analytical investigations were performed on the 6.3_Cu/TiO_2-AG because of clearer and easier interpretation of the recorded data. Regarding the analysis of the copper species (e.g. oxidation state), *in situ* measurements of 0.3_Cu/TiO_2-AG would not have been possible in an aqueous solution.

To demonstrate the importance of the aerogel support for CO_2 reduction, a reference Cu-containing catalyst on the basis of the TiO_2-P25 support was prepared

Table 1. Photocatalytic Reduction of CO_2 in H_2O with Various TiO_2 and Cu/TiO_2 Catalysts

Entry	Catalyst	Reaction Time (h)	$Amount_{H2}$ (μl) (Activity [$\mu mol \cdot g_{cat}^{-1} \cdot h^{-1}$])	$Amount_{CO}$ (μl) (Activity [$\mu mol \cdot g_{cat}^{-1} \cdot h^{-1}$])
1	TiO_2-P25	4	n.d.	n.d.
2	TiO_2 Anatase	4	n.d.	n.d.
3	TiO_2-AG	4	240 (200)	1.8 (1.5)
4	6.3_Cu/TiO_2_AG	4	530 (430)	6.2 (5.1)
5	6.3_Cu/TiO_2_AG	6	580 (320)	6.6 (3.6)
6	6.3_Cu/TiO_2_AG	20	750 (120)	7.5 (1.2)
7	6.3_Cu/TiO_2_AG	0.5	41 (290)	4.3 (28)
8	0.3_Cu/TiO_2_AG	4	600 (490)	13.2 (10.9)
9	0.3_Cu/TiO_2_AG[a]	4	80 (610)	3 (26)
10	0.5_Cu/TiO_2_P25[b]	4	n.d.	n.d.
11	CuO NP	4	n.d.	n.d.
12	-	4	n.d.	n.d.
13	6.3_Cu/TiO_2_AG[c]	4	n.d.	n.d.
14	6.3_Cu/TiO_2_AG[d]	4	550 (450)	n.d.

All experiments have been performed at least twice and the averages are shown. Differences between the measurements are between 1% and 14%.
Experimental conditions: 12.6 mg catalyst, 7.5 mL H_2O, 60 min flushing with CO_2, 20°C, 4 h irradiation, Lumatec lamp: 2.5 W output, Filter 320–500 nm, gases analyzed by GC, Activity = n (gas)/(m(catalyst)*t).
n.d., not detectable; detection limit see Supplemental Information.
[a]Catalyst amount: 1.2 mg.
[b]Preparation method in Procedure S3.
[c]without irradiation.
[d]without CO_2.

(see Section S3). When this material was applied, no photochemical reduction was observed under standard reaction conditions (Table 1, entry 10). This demonstrates that the application of the TiO_2-AG is an important prerequisite for successful CO_2 reduction. Similarly, commercially available CuO NP showed no formation of CO and H_2 (Table 1, entry 11). Moreover, as expected, no conversion was detected without catalyst or light (Table 1, entries 12–13). When the tests were performed in the absence of CO_2 with 6.3_Cu/TiO_2-AG, hydrogen was the only product (Table 1, entry 14). Thus, CO_2 is the only carbon source for CO.

Furthermore, the influence of different salts in aqueous media was investigated using 1.3 mg of the 0.3_Cu/TiO_2-AG catalyst (Figure S11). Notably, generation of CO occurred in 1 M $NaHCO_3$ solution also, although the reduction of CO_2 under basic conditions is more difficult, which is also shown by our investigations. In CO_2-saturated 1 M $NaHCO_3$ and H_2O, respectively, nearly the same CO and H_2 evolution was observed. Also, using an $NaHCO_3$ solution resulted in nearly the same productivity. A severe deviation of the pH value above phosphate buffer, 0.1 M NaOH) led to decreased CO generation, and in the case of the phosphate buffer, the hydrogen generation also diminished significantly. Of course, by addition of

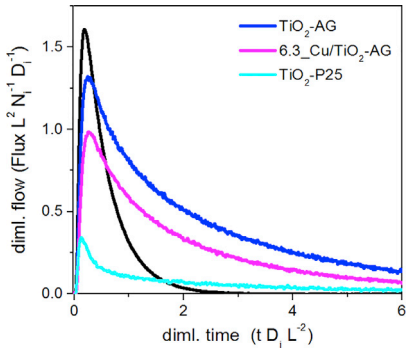

Figure 1. Dimensionless Responses of $^{13}CO_2$ (Colored Curves) and Ar (Black Line) after Pulsing of a $^{13}CO_2$:Ar = 1:1 Mixture over Different Catalysts at Room Temperature

L, N_i, and D_i stand for reactor length, number of molecules (Ar or $^{13}CO_2$), and diffusion coefficient of Ar or $^{13}CO_2$, respectively. See also Figure S12.

CO_2 to 0.1 M NaOH, the pH value is comparable to that of an $NaHCO_3$ solution (after establishment of equilibrium). This is the reason why the NaOH-CO_2 system shows higher activity compared to the phosphate buffer-CO_2 system, which stabilizes a more acidic pH.

CO_2 Adsorption and CO Formation – Why Cu and TiO_2 Are Essential

In order to understand the general mechanism of the aqueous CO_2 reduction and to get insights into the specific roles of Cu and the kind of TiO_2 support (TiO_2-P25 versus TiO_2-AG), we performed $^{13}CO_2$ ($^{13}CO_2$:Ar=1:1) pulse experiments in a temporal analysis of products (TAP) reactor operating with about 10 μs time resolution in the absence of light. This technique enables near-to-molecular understanding of heterogeneously catalyzed reactions.[77–79] The use of $^{13}CO_2$ unambiguously determines formation of CO from CO_2 by means of mass spectrometry. Before the pulse experiments, all materials were treated in high vacuum (about 10^{-5} Pa) at 80°C to remove water and CO_2 adsorbed from air while exposing the catalytic materials to ambient conditions. According to the profound mathematical procedure developed by Gleaves et al.,[80] the obtained transient responses of $^{13}CO_2$ and Ar were transformed into a dimensionless form. As seen in Figure 1, the response of $^{13}CO_2$ is situated under the Ar signal (black line) and crosses the latter. This is a "fingerprint"[80] for reversible adsorption of CO_2. Moreover, the position of the crossing point between the $^{13}CO_2$ and Ar responses is an indicator for the strength of CO_2 adsorption; the closer this point is to the x axis, the higher the ratio of the constant of adsorption to the constant of desorption is. On this basis, it can be concluded that TiO_2-P25 adsorbs CO_2 stronger than TiO_2-AG although the latter material has higher surface area (480 versus 56 $m^2 \cdot g^{-1}$). Such difference may be related to the phase compositions of TiO_2-P25 and TiO_2-AG, being composed of rutile and anatase and pure anatase phases, respectively. An activity-improving factor is the presence of Cu species. Indeed, ^{13}CO is detected as a product of $^{13}CO_2$ reduction only over 6.3_Cu/TiO_2-AG (Figure S12). EPR measurements also demonstrate the significance of Cu for the CO_2 reduction. *In situ* experiments in the presence of 5,5-dimethyl-1-pyrroline N-oxide (DMPO) as a spin trap showed that an organic radical intermediate ($\cdot CO_2^-$) was formed over 6.3_Cu/TiO_2-AG (Figure S13B), while only traces were observed over bare TiO_2-AG (Figure S13A). All these results together with the TAP data (Figure 1) support the importance of an active Cu species for CO_2 activation.

Oxidation Half-Reaction

Given that no external sacrificial oxidant is added to the system, one expects that water oxidation (forming O_2 or H_2O_2) provides the necessary electrons for CO_2 and/or proton reduction. Similar to other previous reports in TiO_2

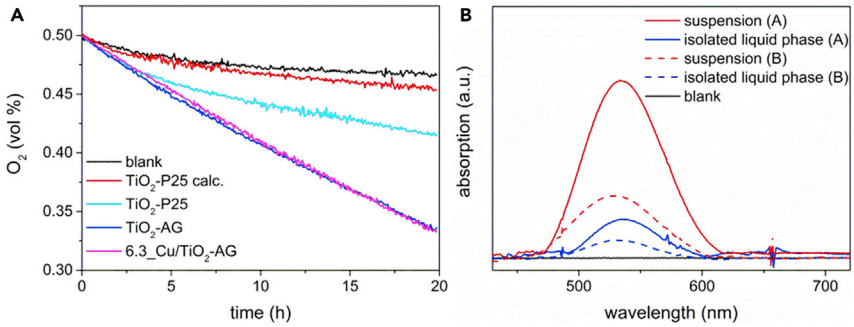

Figure 2. Photoadsorption of O_2 and Formation of Peroxo Species

(A) Following the O_2 concentration during the photocatalytic reduction of 0.5 vol % O_2/CO_2 mixture with Cu/TiO_2-AG and TiO_2-AG.

(B) Colorimetric detection of peroxide after long-term photoreaction under 0.5 vol % O_2/CO_2 (A) and after 20 h photoreaction under pure CO_2 (B). See also Figures S16 and S17.

photocatalysis,[59,60] we were unable to detect O_2 formation in the gas phase using GC/TCD or an optical O_2 detection set-up (see Section S16). Furthermore, in TAP experiments where ^{13}CO formation occurred, no O_2 was detected (Figure S12). As an alternative oxidation product, H_2O_2 could also not be identified by a typical H_2O_2 detection test (conversion of yellow chromate into dark blue chromium(VI) peroxide).[81] Therefore, we concluded the TiO_2-AG material must be involved in the oxidation reaction(s). Notably, the involvement of Cu in a stoichiometric fashion can be excluded because of the small overall amount.

Interestingly, during optical O_2 detection studies in photoreactions with a 0.5 vol % O_2/CO_2 atmosphere, we observed light-induced O_2 uptake instead of evolution (Figure 2A). Studying photoadsorption of O_2 under CO_2 reduction conditions with different TiO_2 materials (Figure 2), we found that TiO_2-P25 (calcined at 500 °C) had the lowest uptake, while regular TiO_2-P25 showed a higher consumption. TiO_2-AG and 6.3_Cu/TiO_2-AG photoadsorbed the largest amount of O_2 and did not show significantly different behavior. It appears that the amount of O_2 consumed during Cu re-oxidation (vide infra) is too small to be detected in this configuration.

This observed trend of O_2 photoadsorption correlated with the number of surface hydroxyl groups on the different materials.[82] Calcination of TiO_2 lowers the number of surface hydroxyl groups,[83] explaining the difference between calcinated and non-calcinated TiO_2-P25. Our TiO_2-AG was synthesized at low temperature (<100°C), so a larger degree of surface hydroxylation is to be expected. The high surface area obtained should further enhance the total number of surface hydroxyl groups.

Indeed, when analyzing TiO_2-AG and TiO_2-P25 by FTIR spectroscopy (Figure S14), a significantly stronger absorption at 3,300 cm^{-1} (stretching vibration of OH groups attached to titania)[84] was observed for TiO_2-AG, indicating a higher number of surface hydroxyl groups. This result was corroborated by XPS analysis: here the O1s peak at around 531.3 eV is assigned to OH groups on the TiO_2 surface.[85] Comparing TiO_2-AG and TiO_2-P25, it was found that the number of OH groups on the aerogel was around six times higher (rel. area 50% versus rel. area 8.1%, see Figure S15B).

It has been described that reductive photoadsorption of O_2 on TiO_2 can proceed to form (surface-bound) superoxo and peroxo species. Electrons for this process are provided by photooxidation of surface hydroxyl groups.[82,86–89] Via

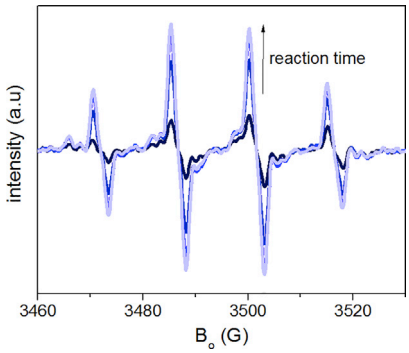

Figure 3. EPR Spectra of TiO_2-AG in CO_2-Saturated H_2O during the Photocatalytic CO_2 Reduction in the Presence of DMPO
See also Figure S13.

intermediate ·OH radicals, this photooxidation has been reported to also result in surface-bound superoxo and peroxo species.[88,90–92]

To investigate this possibility in our system, we have conducted a long-term photoreaction (5 d reaction time, 6.3_Cu/TiO_2-AG, 0.5 vol % O_2/CO_2 atmosphere) and compared the number of surface hydroxyl groups before and after via titration (Section S15C).[93] Indeed, the number of surface hydroxyl groups was reduced by roughly one-half. Using *in situ* EPR spectroscopy and DMPO as a spin trap,[94] we detected ·OH radicals during the irradiation of TiO_2-AG, as identified by the characteristic four-line signal at g = 2.007 (aN ≈ aH = 15.1 G) due to the DMPO-OH spin adduct formation (Figure 3).[95] ·OH radicals are presumed to be an intermediate in surface hydroxyl group photooxidation. Finally, analyzing the suspension after the long-term reaction, we detected peroxide via a coloring enzymatic reaction[91,96] in the suspension, and, to a lesser degree, in the isolated liquid phase (Figures 2B and S17). This difference between the suspension and liquid phase shows that most peroxide species are bound to the TiO_2 surface.

Hence, the consumption of surface hydroxyl groups, detection of ·OH radical intermediates by EPR, and formation of peroxide species after the reaction provide conclusive evidence for reductive O_2 photoadsorption via photooxidation of surface hydroxyl groups. The superior O_2 photoadsorption capability of TiO_2-AG can thus be explained by the higher number of surface hydroxyl groups in this material.

These observations led us to hypothesize that photooxidation of surface hydroxyl groups also provides the electrons for CO_2 and/or proton reduction. After a standard photoreaction with 6.3_Cu/TiO_2-AG under a pure CO_2 atmosphere, we thus applied the same coloring enzymatic reaction for peroxide detection. Indeed, peroxide species were detected in the suspension and to a lesser degree in the isolated liquid phase, again showing that most peroxide species are bound to the TiO_2 surface (Figure 2B). This demonstrates that surface hydroxyl group photooxidation is likely the oxidative process providing electrons for CO_2 and/or proton reduction.

We further investigated this theory via a final long-term experiment with 6.3_Cu/TiO_2-AG using a feed with 0.5 vol % O_2 in CO_2. If surface hydroxyl group photooxidation is indeed responsible for O_2 adsorption and CO_2 and/or proton reduction, O_2 adsorption should level off at some point and the material should lose its ability to reduce CO_2 and/or protons. O_2 adsorption does indeed level off after ca. 5 d (Figure S16), having consumed 0.33 vol % O_2, which corresponds to roughly 10 mol % O_2 with respect to TiO_2-AG. We conclude that O_2 consumption is stoichiometric with respect to the OH-groups of the TiO_2 surface and also that O-vacancies and/or

Ti^{3+} defects are not responsible for the photoadsorption since Ti^{3+} was not detectable using EPR. After the long-term reaction, the material was regenerated with air (vide infra) and again exposed to standard reaction conditions in a 0.5 vol % O_2/CO_2 atmosphere for 20 h. In this case, no CO or H_2 formation was observed; and the O_2 photoadsorption was significantly reduced (Figure S16B). These observations indicate that the material has been stripped of its ability to donate electrons because of the consumption of surface hydroxyl groups via surface oxidation (the fact that some O_2 photoadsorption was still observed can be attributed to a certain degree of reversibility).[97]

Overall, we can conclude that electrons for CO_2 and/or proton reduction, photoadsorption of O_2, and likely also Cu(II) reduction (vide infra) result from photooxidation of surface hydroxyl groups. This oxidation process proceeds via ·OH radical intermediates and results in strongly surface-bound peroxide species, which have been detected colorimetrically. The high activity of TiO_2-AG supported materials in CO_2 and/or proton reduction can be explained by a high number of available surface hydroxyl groups. It is necessary to identify ways to release surface bound peroxides and to regenerate surface hydroxyl group to enable a truly catalytic process with respect to the TiO_2.

Improving Catalyst Activity and Selectivity

In order to check potential leaching of the metal, the 6.3_Cu/TiO_2-AG catalyst and the reaction solution were investigated after 4 h of reaction time. ICP analysis of the filtrate showed no detectable Cu in this phase. Remarkably, the spent Cu catalyst showed a change in color from pale blue to dark gray, although no color change was observed during the investigation of TiO_2-AG without Cu. If Ti^{3+} would have been formed, a light purple dispersion would have appeared. As indicated by *in situ* EPR, XAS, and UV-vis measurements the color change is due to reaction-induced reduction of the Cu(II) species (Figures S18, S20, and S21, section "The Nature of Active Cu Species"). To analyze if these reduced species can be reoxidized, the dark-colored catalyst suspension obtained after 4 h of photoreaction was flushed with air for 30 min. To our delight this treatment led to the original pale blue suspension. Moreover, the catalyst became active again and could be easily re-activated four times (Figure S19A). It is important to note that this oxidation led to a highly selective CO_2 reduction. After the first two runs, only CO was produced through CO_2 reduction and no H_2 was generated despite the aqueous media (Figure S19B). To address the question of the selectivity change and to characterize the Cu species before, during, and after each irradiation (hv) and reoxidation (redox) step, *in situ* XAS measurements were performed (Section S20). The results, shown below, clearly demonstrate that catalyst reoxidation affects its activity in CO formation; a certain degree of oxidation of the Cu species seems to be important for the target reaction. To verify this hypothesis, we performed CO_2 photoreduction tests in the presence of various amounts of O_2 added to the CO_2-containing reaction mixture (Figure 4). Clearly, CO_2 reduction in the presence of O_2 looks irrational at first site because the latter gas is far more easily reduced than the former one (E^0 CO_2/CO = −0.53 V versus O_2/H_2O = 1.23 V).[98,99] Moreover, it was shown by Strunk and coworkers that the presence of O_2 inhibits product formation of photocatalytic CO_2 reduction in the presence of TiO_2 (P25).[100] Nevertheless, adding 0.5 vol % O_2 to CO_2 in the presence of our Cu/TiO_2-AG catalyst improved CO formation after 20 h by nearly one order of magnitude. To the best of our knowledge this is the first time that such behavior has been observed. In the presence of O_2, we presume an *in situ* re-oxidation of less reactive Cu(0) species to Cu(II). Interestingly, hydrogen was also formed in this experiment but the ratio of CO/H_2 strongly increased in

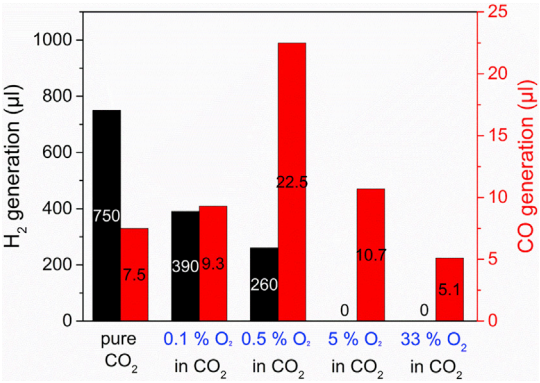

Figure 4. Photocatalytic CO_2 Reduction with 6.3_Cu/TiO_2-AG Catalyst by Using Different CO_2/O_2 Mixtures

Conditions: catalyst: 12.6 mg 6.3_Cu/TiO_2-AG, medium 7.5 mL H_2O, 20°C, 20 h, Lumatec lamp: 2.5 W output, Filter 320–500 nm. See also Table S22.

comparison to the corresponding O_2-free test. Consequently, applying 5 vol % of O_2 led to an excellent CO:H_2 ratio because even traces of hydrogen were not observed. The reason for the change in selectivity might be the re-oxidation of H_2 to H_2O by the addition of O_2. Further increasing the concentration of O_2 led to deactivation of the catalyst. To provide fundamental insights into the effect of O_2 on photocatalytic CO_2 reduction, *in situ* XAS and *operando* UV-vis measurements were performed (vide infra).

In order to show the influence of O_2 on the Cu sites during the reaction and the importance of the TiO_2-AG support, we performed the CO_2 reduction in 0.5 % O_2/CO_2 mixture also with TiO_2-AG and TiO_2-P25 (Table S22). As expected, TiO_2-P25 was also not active in this atmosphere (Table S22, entry 5). In comparison to 6.3_Cu/TiO_2-AG, the material TiO_2-AG was also less active with regard to H_2 and CO generation (Table S22, entry 3). Interestingly, the addition of O_2 not only led to a decrease in H_2_ but also in CO generation (Table S22, entries 3 and 4), which is in contrast to the tests with 6.3_Cu/TiO_2-AG (Table S22, entries 1 and 2). This also shows the importance of the Cu co-catalyst and its reactivation for the CO_2 reduction by O_2.

The Nature of Active Cu Species

Operando UV-vis spectroscopy was applied to monitor changes in the oxidation state of Cu after different irradiation times upon CO_2 reduction in the presence and the absence of O_2. Figure 5 shows the UV-vis spectra expressed as the relative Kubelka-Munk function $F_{rel}(R)$ calculated according to Equation 1, while the absorption spectra are given in Figure S21. R_0 and R_i represent the reflectance of the catalyst before irradiation and after certain times of irradiation, respectively.

$$F_{rel}(R) = \frac{\left(1 - \frac{R_i}{R_0}\right)^2}{2\frac{R_i}{R_0}} \qquad \text{(Equation 1)}$$

The absorption spectrum of fresh Cu/TiO_2-AG before irradiation (Figure S21A) is characterized by a strong band below 350 nm and by several less defined broad bands between 400 and 900 nm. According to the literature, absorption bands between 600 and 900 nm can be ascribed to transitions between d-d orbitals of Cu(II),[85,91,96,101] while the bands below 450 nm are ascribed to charge transfer transitions in TiO_2[93] and CuO.[91] Thus, Cu(II) is the main species in fresh Cu/TiO_2-AG. This

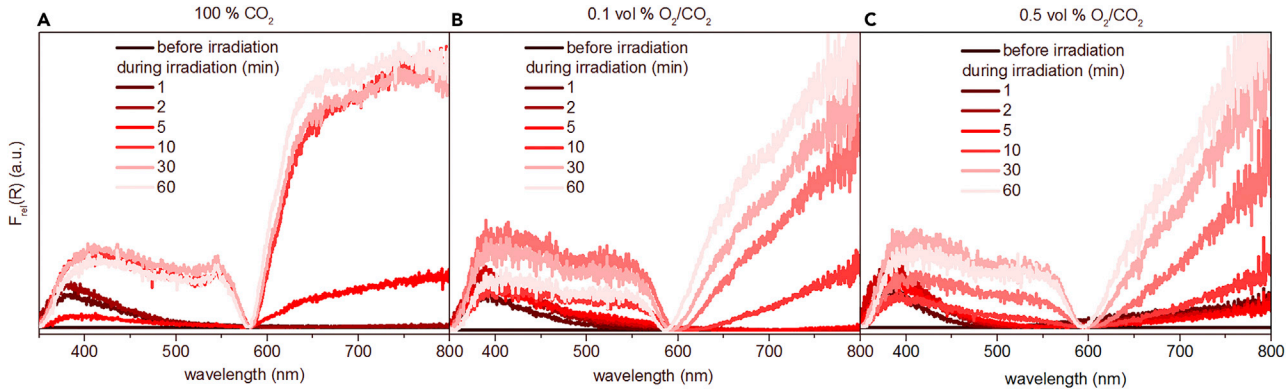

Figure 5. UV-vis Spectra (Relative Kubelka-Munk Calculated According to Equation 1) of Fresh Cu/TiO_2-AG and after Different Irradiation Times in Various Feeds of O_2/CO_2 Mixtures

(A–C) 100% CO_2 (A), 0.1 vol % O_2/CO_2 (B), and 0.5 vol % O_2/CO_2 (C) mixtures. See also Figure S21.

conclusion is in agreement with the results of EPR (Figure S18) and XAS analysis (Figure 6).

For deriving insights into reaction-induced changes of the oxidation state of Cu, we analyzed the UV-vis spectra expressed as $F_{rel}(R)$. Such presentation directly illustrates how the spectrum of fresh Cu/TiO_2-AG changes. As seen in Figure 5A, a band with a maximum of 380 nm appeared after catalyst exposure to light for 1 min in the presence of CO_2 and in the absence of O_2 (Figure 5A). This band can be tentatively assigned to the presence of Cu(I) as concluded from the reference UV-vis spectrum of Cu_2O (Figure S21F).[101] Its intensity increased within the first 2 min of irradiation, but decreased after 3 min of irradiation. This band was not apparent after longer catalyst exposure to light, while the intensity of $F_{rel}(R)$ between 350 and 580 nm continuously increased. Moreover, the intensity of $F_{rel}(R)$ above 580 nm also grew. Appearance of a sharp minimum in $F_{rel}(R)$ at around 580 nm can caused by the formation of metallic Cu. The UV-vis spectrum of metallic Cu is characterized by the absorption edge at 580 nm,[84,101] which is clearly seen in Figure S21.

When using a feed with a CO_2/O_2 ratio of 1, the absorption edge at 580 nm could hardly be observed, (Figure S21E) thus indicating that Cu(0) was not formed. Cu(I) species were also not identified under these reaction conditions. Thus, Cu(II) was the main oxidation state of copper in Cu/TiO_2-AG upon CO_2 irradiation in the presence of large amounts (33 vol %) of O_2. Importantly, both Cu(0) and Cu(I) species were formed during irradiation when O_2 concentration was lowered to 0.1 or 0.5 vol %. However, the kinetics of Cu(II) reduction and accordingly the fraction of different Cu species are affected by O_2 concentration. From a qualitative point of view, higher O_2 content leads to slower reduction of Cu(II) to Cu(I) and Cu(0) and to a lower Cu(0) fraction. Temporal changes in the UV-vis spectra in Figures 5A–5C suggest Cu(0) species dominate after 10 or 30 min of exposure to light in the absence of O_2 or in the presence of low (0.1 and 0.5 vol %) amounts of O_2.

Furthermore, the oxidation state of Cu was investigated by *in situ* X-ray absorption spectroscopy before, during, and after the reaction. Thereby, the measurements were carried out using a dedicated cell described in detail in the Supplemental Information (Section S20). XANES (X-ray absorption near edge structure) analysis enables

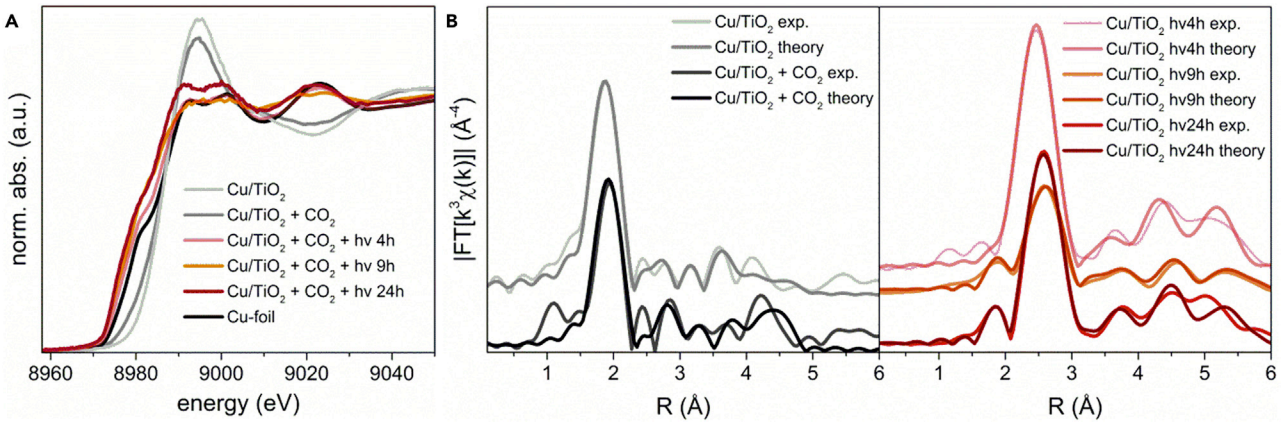

Figure 6. XAS Analysis before and after Various Reaction Times

(A and B) X-ray absorption spectra (A) and Fourier transformed EXAFS spectra (B) of the initial catalyst (6.3_Cu/TiO_2-AG) in a CO_2-saturated aqueous dispersion during illumination after 4 h, 9 h, and 24 h and of a Cu foil as reference. See also Procedure S20.

beside the assignment of the oxidation state also the determination of a reference proportion to a certain sample spectrum.[102,103] Therefore, the spectra of the initial catalyst (6.3_Cu/TiO_2-AG) and of a Cu-foil were applied as references to facilitate an investigation of the reduction degree during the reaction. Analysis of the EXAFS (extended X-ray absorption fine structure) part of an X-ray absorption spectrum allows the identification of neighboring atoms, their number, and their distance to the absorbing atom.[104] With this, the local structure of a Cu atom was determined. XANES analysis showed unambiguously a Cu(II) species with an absorption edge at 8,987.5 eV in the initial substance (Figure 6A). No changes are observed when the suspension is subjected to CO_2 atmosphere. Irradiation caused a reduction of Cu(II) and a Cu(0) species as concluded from the appearance of a signal with an edge energy of 8,979.5 eV. Comparison with a Cu-foil spectrum revealed a similar edge position and white line shape. The spectra of the reaction mixture illuminated for 4 h, 9 h, and 24 h uninterruptedly revealed a similar trend.

To obtain a more detailed insight into the local geometric structure around the Cu centers, thorough analysis of the EXAFS spectra was carried out.[105] The structural parameters obtained are shown in the supplementary information (Table S20B), while the corresponding spectra are given in Figure 6B. In the case of the initial 6.3_Cu/TiO_2-AG catalyst, the typical backscattering and distances of CuO were adjusted.[106] To optimize the fitting error, a Ti shell in a characteristic distance of a Cu-Ti mixed oxide ($Cu_{0.25}Ti_{0.75}O_2$) was added to the model.[107] Because of the small number of Cu backscatterer and the significant contribution of Ti neighboring atoms, very small Cu oxide particles finely distributed on the titanium oxide support can be deduced, which is in perfect agreement with the results of XRD and TEM analysis.

For the analysis of the spectra measured during the photoinduced reaction, exclusively Cu backscatter in distances similar to metallic Cu were adjusted, since through the LC-XANES fits (Table S20A), metallic Cu was identified as the major component. The high amount of Cu backscatterers and the absence of Ti contributions led to the conclusion that larger metallic Cu-domains are formed during the reaction in comparison to the initial catalyst. Illumination of the sample for 9 h and 24 h led to the formation of even smaller metallic Cu domains, since the number of backscatterers became significantly smaller.

Table 2. Results of CO Formation after 10 min, 30 min, and 20 h in Various O_2/CO_2 Mixtures

Amount of O_2 in CO_2 Atmosphere	$Amount_{10min}$ [$\mu mol_{CO}/g_{cat}$]	$Amount_{30min}$ [$\mu mol_{CO}/g_{cat}$]	$Amount_{20h}$ [$\mu mol_{CO}/g_{cat}$]
0 vol %	11.4	14.1	24.7
0.1 vol %	13.8	16.9	30.5
0.5 vol %	8.9	15.5	74.2

Summarizing the results of UV-vis and XAS tests of CO_2 photoreduction in the absence of added O_2, it can be concluded that during photocatalytic CO_2 reduction over Cu/TiO_2-AG, Cu(II) is initially reduced to Cu(I) followed by further reduction to Cu(0).

Finally, the below discussion is aimed at identifying factors affecting catalyst activity for CO_2 reduction to CO. Table 2 shows the amount of CO formed after 10 min, 30 min, and 20 h using feeds with different O_2/CO_2 ratios. After 10 min of reaction, the highest amount of CO was obtained in the presence of 0.1 vol % O_2, while operating with 0.5 vol% O_2 resulted in the lowest amount. The difference between the feeds became significantly smaller after 30 min of reaction. When irradiating for 20 h, the amount of CO strongly increased in the presence of 0.5 vol % O_2, while the increase in the absence of O_2 or in the presence of 0.1 vol % was significantly lower and only marginally compared to the CO generation after 30 min. These results reveal that the duration of efficient CO_2 reduction to CO depends on the O_2 content. This effect can be explained by considering the changes in the oxidation state of Cu under reaction conditions. Cu(0) is the main species after 30 min of CO_2 reduction without added O_2. In the absence of O_2, as well as in the presence of just 0.1 vol % O_2, the amount of CO formed between 30 min and 20 h is lower than the amount of CO formed between 0 and 30 min. Thus, we conclude that metallic Cu(0) species have low intrinsic activity for the target reaction. Regardless of O_2 content, the highest rate of CO formation was achieved at the beginning of the photocatalytic process, i.e., within the first 30 min. On the basis of the UV-vis spectra, Cu(I) is present during this time and thus can be assigned as an active species for CO_2 photoreduction. This statement is supported by the fact that the rate of Cu(I) reduction to Cu(0) is suppressed in the presence of O_2 thus resulting in stabilization of Cu(I) for longer reaction time. The amount of CO initially increased with rising O_2 content and passed a maximum at 0.5 vol % (Figure 4). According to UV-vis analysis (Figure S21), Cu(II) is not reduced in large amounts to Cu(I) or Cu(0) at higher O_2 concentration. Thus, Cu(I) is proposed to be the active species for CO_2 photoreduction to CO.

In conclusion, the first highly selective photocatalytic reduction of CO_2 to CO in aqueous solution is described. Key to success was the use of a specific Cu(II)-supported TiO_2-AG catalyst system, which shows high activity for CO generation (28.2 $\mu mol \cdot g_{cat}^{-1} \cdot h^{-1}$) in UV-A/Vis light (320–500 nm). The rate for CO_2 reduction decreases with time but can be improved when performing the reaction in the presence of O_2. To the best of our knowledge such behavior is observed for the first time and may lead to completely new CO_2 reduction catalysts. UV-vis measurements in the presence of O_2 suggest photogenerated Cu(I) as the active species. Regarding the mechanism, we found that the electrons for CO_2/proton reduction in the active catalyst can be provided by photooxidation of the TiO_2 surface hydroxyl groups. The regeneration of these surface hydroxyl groups has to be solved in the future to develop truly catalytic reductions. This opens up a new research field for photocatalysis without sacrificial electron donors, which should be addressed in upcoming studies.

SUPPLEMENTAL INFORMATION

Supplemental Information can be found online at https://doi.org/10.1016/j.chempr.2019.04.006.

ACKNOWLEDGMENTS

This work has been supported by the BMBF within the project "Kopernikus projects for the Energiewende: P2X concepts" (03SFK2B) and the Danish National Research Foundation within the project "CADIAC." Financial support by Fonds der Chemischen Industrie (Kekulé-Stipendium n. 102151 for J.S.) is gratefully acknowledged. The authors thank Dr. Rafael daSilva for his contribution in material synthesis and also Dr. S. Bartling, Dr. H. Lund, Dr. C. Kreyenschulte, Dr. J. Radnik, and A. Simmula for their analytical support.

AUTHOR CONTRIBUTIONS

S.K. performed the catalyst synthesis, the analysis of the standard material characteristic data, the experiments for analyzing the surface species, the photocatalytic experiments and the *operando* UV-vis measurements. R.S. and S.K. planned and carried out the XAS experiments. R.S. and M. Bauer designed the used liquid cell and analyzed the related data. J.S. carried out the experiments with the optical oxygen meter set-up for the O_2 detection and performed data analysis and interpretation; designed the experiments for the oxidation half-reaction section together with S.K. and wrote the oxidation half-reaction section. J.R. and S.K. prepared the *in situ* EPR measurements and J.R. evaluated the obtained results. V.A.K. performed the $^{13}CO_2$ pulse experiments in the temporal analysis of products (TAP) reactor and analyzed together with E.V.K. the experimental data. E.V.K. and S.K. planned UV-vis tests and analyzed the UV-vis data. S.W. was involved in the material development and the interpretation of the analytical results. S.K., S.W., E.V.K., H.J., and M. Beller developed the concept and arranged the whole data for the publication. All authors were involved in the discussion of the results and commented on the manuscript.

DECLARATION OF INTERESTS

The authors declare no competing interests.

Received: August 22, 2018
Revised: September 25, 2018
Accepted: April 12, 2019
Published: May 6, 2019; corrected online: July 23, 2019

REFERENCES AND NOTES

1. Asmatulu, E. (2016). Biological Systems for Carbon Dioxide Reductions and Biofuel Production (The Royal Society of Chemistry), pp. 274–293.

2. Becklin, K.M., Walker, S.M., Way, D.A., and Ward, J.K. (2017). CO_2 studies remain key to understanding a future world. New Phytol. *214*, 34–40.

3. Tu, W., Zhou, Y., and Zou, Z. (2014). Photocatalytic conversion of CO_2 into renewable hydrocarbon fuels: state-of-the-art accomplishment, challenges, and prospects. Adv. Mater. *26*, 4607–4626.

4. Zhou, H., Yan, R., Zhang, D., and Fan, T. (2016). Challenges and perspectives in designing artificial photosynthetic systems. Chemistry *22*, 9870–9885.

5. Mikkelsen, M., Jørgensen, M., and Krebs, F.C. (2010). The teraton challenge. A review of fixation and transformation of carbon dioxide. Energy Environ. Sci. *3*, 43–81.

6. Yuan, L., and Xu, Y.-J. (2015). Photocatalytic conversion of CO_2 into value-added and renewable fuels. Appl. Surf. Sci. *342*, 154–167.

7. Bosch, C., and Meiser, W. (1922). Process of manufacturing urea. US patent US1429483 A.

8. Glibert, P.M., Harrison, J., Heil, C., and Seitzinger, S. (2006). Escalating worldwide use of urea – a global change contributing to coastal eutrophication. Biogeochemistry *77*, 441–463.

9. Büttner, H., Longwitz, L., Steinbauer, J., Wulf, C., and Werner, T. (2017). Recent developments in the synthesis of cyclic carbonates from epoxides and CO_2. Top. Curr. Chem. *375*, 50.

10. Sakakura, T., and Kohno, K. (2009). The synthesis of organic carbonates from carbon dioxide. Chem. Commun. 1312–1330.

11. Pescarmona, P.P., and Taherimehr, M. (2012). Challenges in the catalytic synthesis of cyclic and polymeric carbonates from epoxides and CO_2. Catal. Sci. Technol. *2*, 2169–2187.

12. Mette, K., Kühl, S., Düdder, H., Kähler, K., Tarasov, A., Muhler, M., and Behrens, M. (2014). Stable performance of Ni catalysts in the dry reforming of methane at high temperatures for the efficient conversion of CO_2 into syngas. ChemCatChem *6*, 100–104.

13. Moret, S., Dyson, P.J., and Laurenczy, G. (2014). Direct synthesis of formic acid from carbon dioxide by hydrogenation in acidic media. Nat. Commun. *5*.

14. Kondratenko, E.V., Mul, G., Baltrusaitis, J., Larrazábal, G.O., and Pérez-Ramírez, J. (2013). Status and perspectives of CO_2 conversion into fuels and chemicals by catalytic, photocatalytic and electrocatalytic processes. Energy Environ. Sci. *6*, 3112–3135.

15. Jones, J.-P., Prakash, G.K.S., and Olah, G.A. (2014). Electrochemical CO_2 reduction: recent advances and current trends. Isr. J. Chem. *54*, 1451–1466.

16. Zhang, L., Zhao, Z.J., and Gong, J. (2017). Nanostructured materials for heterogeneous electrocatalytic CO_2 reduction and their related reaction mechanisms. Angew. Chem. Int. Ed. *56*, 11326–11353.

17. Habisreutinger, S.N., Schmidt-Mende, L., and Stolarczyk, J.K. (2013). Photocatalytic reduction of CO_2 on TiO_2 and other semiconductors. Angew. Chem. Int. Ed. *52*, 7372–7408.

18. Nikokavoura, A., and Trapalis, C. (2017). Alternative photocatalysts to TiO_2 for the photocatalytic reduction of CO_2. Appl. Surf. Sci. *391*, 149–174.

19. León, A., Reuquen, P., Garín, C., Segura, R., vargas, P., Zapata, P.A., and Orihuela, P. (2017). FTIR and Raman characterization of TiO_2 nanoparticles coated with polyethylene glycol as carrier for 2-methoxyestradiol. Appl. Sci. *7*, 49.

20. Hou, J., Cheng, H., Takeda, O., and Zhu, H. (2015). Three-dimensional bimetal-graphene-semiconductor coaxial nanowire arrays to harness charge flow for the photochemical reduction of carbon dioxide. Angew. Chem. Int. Ed. *54*, 8480–8484.

21. Stock, M., and Dunn, S. (2011). $LiNbO_3$ - A polar material for solid-gas artificial photosynthesis. Ferroelectrics *419*, 9–13.

22. Rosas-Hernández, A., Alsabeh, P.G., Barsch, E., Junge, H., Ludwig, R., and Beller, M. (2016). Highly active and selective photochemical reduction of CO_2 to CO using molecular-defined cyclopentadienone iron complexes. Chem. Commun. *52*, 8393–8396.

23. Takeda, H., Ohashi, K., Sekine, A., and Ishitani, O. (2016). Photocatalytic CO_2 reduction using Cu(I) photosensitizers with a Fe(II) catalyst. J. Am. Chem. Soc. *138*, 4354–4357.

24. Thoi, V.S., Kornienko, N., Margarit, C.G., Yang, P., and Chang, C.J. (2013). Visible-light photoredox catalysis: selective reduction of carbon dioxide to carbon monoxide by a nickel N-heterocyclic carbene–isoquinoline complex. J. Am. Chem. Soc. *135*, 14413–14424.

25. Guo, Z., Yu, F., Yang, Y., Leung, C.F., Ng, S.M., Ko, C.C., Cometto, C., Lau, T.C., and Robert, M. (2017). Photocatalytic conversion of CO_2 to CO by a copper(II) Quaterpyridine complex. ChemSusChem *10*, 4009–4013.

26. Takeda, H., Koike, K., Inoue, H., and Ishitani, O. (2008). Development of an efficient photocatalytic system for CO_2 reduction using rhenium(I) Complexes based on mechanistic studies. J. Am. Chem. Soc. *130*, 2023–2031.

27. Rosas-Hernández, A., Junge, H., and Beller, M. (2015). Photochemical reduction of carbon dioxide to formic acid using ruthenium(II)-based catalysts and visible light. ChemCatChem *7*, 3316–3321.

28. Liu, B.-J., Torimoto, T., and Yoneyama, H. (1998). Photocatalytic reduction of CO_2 using surface-modified CdS photocatalysts in organic solvents. J. Photochem. Photobiol. A *113*, 93–97.

29. Kanemoto, M., Ishihara, K., Wada, Y., Sakata, T., Mori, H., and Yanagida, S. (1992). Visible-light induced effective photoreduction of CO_2 to CO catalyzed by colloidal CdS microcrystallites. Chem. Lett. *21*, 835–836.

30. Sayama, K., and Arakawa, H. (1993). Photocatalytic decomposition of water and photocatalytic reduction of carbon dioxide over zirconia catalyst. J. Phys. Chem. *97*, 531–533.

31. Park, H.-A., Choi, J.H., Choi, K.M., Lee, D.K., and Kang, J.K. (2012). Highly porous gallium oxide with a high CO_2 affinity for the photocatalytic conversion of carbon dioxide into methane. J. Mater. Chem. *22*, 5304–5307.

32. Yang, M.-Q., and Xu, Y.-J. (2016). Photocatalytic conversion of CO_2 over graphene-based composites: current status and future perspective. Nanoscale Horiz. *1*, 185–200.

33. Li, K., Peng, B., and Peng, T. (2016). Recent advances in heterogeneous photocatalytic CO_2 conversion to solar fuels. ACS Catal. *6*, 7485–7527.

34. Ulagappan, N., and Frei, H. (2000). Mechanistic study of CO_2 photoreduction in Ti silicalite molecular sieve by FT-IR spectroscopy. J. Phys. Chem. A *104*, 7834–7839.

35. Bahnemann, D.W., Hilgendorff, M., and Memming, R. (1997). Charge carrier dynamics at TiO_2 particles: reactivity of free and trapped holes. J. Phys. Chem. B *101*, 4265–4275.

36. Liu, S., Zhao, Z., and Wang, Z. (2007). Photocatalytic reduction of carbon dioxide using sol-gel derived titania-supported CoPc catalysts. Photochem. Photobiol. Sci. *6*, 695–700.

37. Handoko, A.D., and Tang, J. (2013). Controllable proton and CO_2 photoreduction over Cu_2O with various morphologies. Int. J. Hydr. Energ. *38*, 13017–13022.

38. Sasirekha, N., Basha, S.J.S., and Shanthi, K. (2006). Photocatalytic performance of Ru doped anatase mounted on silica for reduction of carbon dioxide. Appl. Catal. B *62*, 169–180.

39. Yamamoto, M., Yoshida, T., Yamamoto, N., Nomoto, T., Yamamoto, Y., Yagi, S., and Yoshida, H. (2015). Photocatalytic reduction of CO_2 with water promoted by Ag clusters in Ag/Ga_2O_3 photocatalysts. J. Mater. Chem. A *3*, 16810–16816.

40. Núñez, J., de la Peña O'Shea, V.A., Jana, P., Coronado, J.M., and Serrano, D.P. (2013). Effect of copper on the performance of ZnO and $ZnO_{1-x}N_x$ oxides as CO_2 photoreduction catalysts. Catal. Today *209*, 21–27.

41. Zhou, H., Li, P., Guo, J., Yan, R., Fan, T., Zhang, D., and Ye, J. (2015). Artificial photosynthesis on tree trunk derived alkaline tantalates with hierarchical anatomy: towards CO_2 photo-fixation into CO and CH_4. Nanoscale *7*, 113–120.

42. Li, K., Handoko, A.D., Khraisheh, M., and Tang, J. (2014). Photocatalytic reduction of CO_2 and protons using water as an electron donor over potassium tantalate nanoflakes. Nanoscale *6*, 9767–9773.

43. Fujishima, A., and Honda, K. (1972). Electrochemical photolysis of water at a semiconductor electrode. Nature *238*, 37–38.

44. Schneider, J., Matsuoka, M., Takeuchi, M., Zhang, J., Horiuchi, Y., Anpo, M., and Bahnemann, D.W. (2014). Understanding TiO_2 photocatalysis: mechanisms and materials. Chem. Rev. *114*, 9919–9986.

45. Li, X., Yu, J., and Jaroniec, M. (2016). Hierarchical photocatalysts. Chem. Soc. Rev. *45*, 2603–2636.

46. Yamakata, A., Vequizo, J.J.M., and Matsunaga, H. (2015). Distinctive behavior of photogenerated electrons and holes in anatase and rutile TiO_2 powders. J. Phys. Chem. C *119*, 24538–24545.

47. Xiong, Z., Wang, H., Xu, N., Li, H., Fang, B., Zhao, Y., Zhang, J., and Zheng, C. (2015). Photocatalytic reduction of CO_2 on Pt^{2+}–Pt^0/TiO_2 nanoparticles under UV/vis light irradiation: a combination of Pt^{2+} doping and Pt nanoparticles deposition. Int. J. Hydr. Energ. *40*, 10049–10062.

48. Li, K., Peng, T., Ying, Z., Song, S., and Zhang, J. (2016). Ag-loading on brookite TiO_2 quasi nanocubes with exposed {210} and {001} facets: activity and selectivity of CO_2 photoreduction to CO/CH_4. Appl. Catal. B *180*, 130–138.

49. Rossetti, I., Villa, A., Compagnoni, M., Prati, L., Ramis, G., Pirola, C., Bianchi, C.L., Wang, W., and Wang, D. (2015). CO_2 photoconversion to fuels under high pressure: effect of TiO_2 phase and of unconventional reaction conditions. Catal. Sci. Technol. *5*, 4481–4487.

50. Collado, L., Reynal, A., Coronado, J.M., Serrano, D.P., Durrant, J.R., and de la Peña O'Shea, V.A. (2015). Effect of Au surface plasmon nanoparticles on the selective CO_2 photoreduction to CH4. Appl. Catal. B *178*, 177–185.

51. Vaiano, V., Sannino, D., and Ciambelli, P. (2015). Steam reduction of CO_2 on Pd/TiO_2 catalysts: a comparison between thermal and

photocatalytic reactions. Photochem. Photobiol. Sci. *14*, 550–555.

52. Aguirre, M.E., Zhou, R., Eugene, A.J., Guzman, M.I., and Grela, M.A. (2017). Cu_2O/TiO_2 heterostructures for CO_2 reduction through a direct Z-scheme: Protecting Cu_2O from photocorrosion. Appl. Catal. B *217*, 485–493.

53. Zhang, T., Low, J., Huang, X., Al-Sharab, J.F., Yu, J., and Asefa, T. (2017). Copper-decorated microsized nanoporous titanium dioxide photocatalysts for carbon dioxide reduction by water. ChemCatChem *9*, 3054–3062.

54. Liu, L., Zhao, C., Miller, J.T., and Li, Y. (2017). Mechanistic study of CO_2 photoreduction with H_2O on Cu/TiO_2 nanocomposites by in situ X-ray absorption and infrared spectroscopies. J. Phys. Chem. C *121*, 490–499.

55. Fang, B., Xing, Y., Bonakdarpour, A., Zhang, S., and Wilkinson, D.P. (2015). Hierarchical $CuO–TiO_2$ hollow microspheres for highly efficient photodriven reduction of CO_2 to CH4. ACS Sustain. Chem. Eng. *3*, 2381–2388.

56. Gonell, F., Puga, A.V., Julián-López, B., García, H., and Corma, A. (2016). Copper-doped titania photocatalysts for simultaneous reduction of CO_2 and production of H_2 from aqueous sulfide. Appl. Catal. B *180*, 263–270.

57. Jeong, S., Kim, W.D., Lee, S., Lee, K., Lee, S., Lee, D., and Lee, D.C. (2016). Bi_2O_3 as a promoter for Cu/TiO_2 photocatalysts for the selective conversion of carbon dioxide into methane. ChemCatChem *8*, 1641–1645.

58. Li, Y., Wang, W.-N., Zhan, Z., Woo, M.-H., Wu, C.-Y., and Biswas, P. (2010). Photocatalytic reduction of CO_2 with H_2O on mesoporous silica supported Cu/TiO_2 catalysts. Appl. Catal. B *100*, 386–392.

59. Liu, L., Gao, F., Zhao, H., and Li, Y. (2013). Tailoring Cu valence and oxygen vacancy in Cu/TiO_2 catalysts for enhanced CO_2 photoreduction efficiency. Appl. Catal. B *134–135*, 349–358.

60. Slamet, Nasution, H., Purnama, E., Riyani, K., and Gunlazuardi, J. (2009). Effect of copper species in a photocatalytic synthesis of methanol from carbon dioxide over copper-doped titania catalysts world appl. Sci. J. *6*, 112–122.

61. Nasution, H., Purnama, E., Kosela, S., and Gunlazuardi, J. (2005). Photocatalytic reduction of CO_2 on copper-doped Titania catalysts prepared by improved-impregnation method. Catal. Commun. *6*, 313–319.

62. Tseng, I.H., and Wu, J.C.-S. (2004). Chemical states of metal-loaded titania in the photoreduction of CO_2. Catal. Today *97*, 113–119.

63. Tseng, I.H., Wu, J.C.S., and Chou, H.-Y. (2004). Effects of sol–gel procedures on the photocatalysis of Cu/TiO_2 in CO_2 photoreduction. J. Catal. *221*, 432–440.

64. Zhang, Q., Gao, T., Andino, J.M., and Li, Y. (2012). Copper and iodine co-modified TiO_2 nanoparticles for improved activity of CO_2 photoreduction with water vapor. Appl. Catal. B *123–124*, 257–264.

65. Singhal, N., Ali, A., Vorontsov, A., Pendem, C., and Kumar, U. (2016). Efficient approach for simultaneous CO and H_2 production via photoreduction of CO_2 with water over copper nanoparticles loaded TiO_2. Appl. Catal. A *523*, 107–117.

66. Do, J.Y., Im, Y., Kwak, B.S., Kim, J.-Y., and Kang, M. (2015). Dramatic CO_2 photoreduction with H_2O vapors for CH_4 production using the $TiO_2/Fe–TiO_2$ double-layered films. Chem. Eng. J. *275*, 288–297.

67. Kwak, B.S., Vignesh, K., Park, N.-K., Ryu, H.-J., Baek, J.-I., and Kang, M. (2015). Methane formation from photoreduction of CO_2 with water using TiO_2 including Ni ingredient. Fuel *143*, 570–576.

68. Zhygotsky, A., Rynda, E., Kochkodan, V., Zagorny, M., Lobunets, T., Kuzmenko, L., and Ragulya, A. (2013). Effect of dispersity and porous structure of TiO_2 nanopowders on photocatalytic destruction of azodyes in aqueous solutions. J. Chem. Chem. Eng. *7*, 949–957.

69. Gesser, H.D., and Goswami, P.C. (1989). Aerogels and related porous materials. Chem. Rev. *89*, 765–788.

70. Pajonk, G.M. (1991). Aerogel catalysts. Appl. Catal. *72*, 217–266.

71. Pietron, J.J., Stroud, R.M., and Rolison, D.R. (2002). Using three dimensions in catalytic mesoporous nanoarchitectures. Nano Lett. *2*, 545–549.

72. Puskelova, J., Baia, L., Vulpoi, A., Baia, M., Antoniadou, M., Dracopoulos, V., Stathatos, E., Gabor, K., Pap, Z., Danciu, V., et al. (2014). Photocatalytic hydrogen production using $TiO_2–Pt$ aerogels. Chem. Eng. J. *242*, 96–101.

73. da Silva, R.O., Heiligtag, F.J., Karnahl, M., Junge, H., Niederberger, M., and Wohlrab, S. (2015). Design of multicomponent aerogels and their performance in photocatalytic hydrogen production. Catal. Today *246*, 101–107.

74. Heiligtag, F.J., Rossell, M.D., Süess, M.J., and Niederberger, M. (2011). Template-free co-assembly of preformed Au and TiO_2 nanoparticles into multicomponent 3D aerogels. J. Mater. Chem. *21*, 16893–16899.

75. Heiligtag, F.J., Kränzlin, N., Süess, M.J., and Niederberger, M. (2014). Anatase–silica composite aerogels: a nanoparticle-based approach. J. Solgel Sci. Technol. *70*, 300–306.

76. Ghijsen, J., Tjeng, L.H., van Elp, J., Eskes, H., Westerink, J., Sawatzky, G.A., and Czyzyk, M.T. (1988). Electronic structure of Cu_2O and CuO. Phys. Rev. B *38*, 11322–11330.

77. Perez-Ramirez, J., and Kondratenko, E.V. (2007). Evolution, achievements, and perspectives of the TAP technique. Catal. Today *121*, 160–169.

78. Morgan, K., Maguire, N., Fushimi, R., Gleaves, J.T., Goguet, A., Harold, M.P., Kondratenko, E.V., Menon, U., Schuurman, Y., and Yablonsky, G.S. (2017). Forty years of temporal analysis of products. Catal. Sci. Technol. *7*, 2416–2439.

79. Gleaves, J.T., Yablonsky, G., Zheng, X., Fushimi, R., and Mills, P.L. (2010). Temporal analysis of products (TAP)—recent advances in technology for kinetic analysis of multi-component catalysts. J. Mol. Catal. A *315*, 108–134.

80. Gleaves, J.T., Yablonskii, G.S., Phanawadee, P., and Schuurman, Y. (1997). TAP-2: an interrogative kinetics approach. Appl. Catal. A *160*, 55–88.

81. Buchera, G., Kampe, M., and Roelcke, J.F. (2005). Peroxides and chromium compounds - The ether test for identity. Z. Naturforsch. B. *60*, 1–6.

82. Boonstra, A.H., and Mutsaers, C.A.H.A. (1975). Relation between the photoadsorption of oxygen and the number of hydroxyl groups on a titanium dioxide surface. J. Phys. Chem. *79*, 1694–1698.

83. Yu, J.C., Lin, J., Lo, D., and Lam, S.K. (2000). Influence of thermal treatment on the adsorption of oxygen and photocatalytic activity of TiO_2. Langmuir *16*, 7304–7308.

84. Lv, K., Zuo, H., Sun, J., Deng, K., Liu, S., Li, X., and Wang, D. (2009). (Bi, C and N) codoped TiO2 nanoparticles. J. Hazard. Mater. *161*, 396–401.

85. Bharti, B., Kumar, S., Lee, H.N., and Kumar, R. (2016). Formation of oxygen vacancies and Ti^{3+} state in TiO_2 thin film and enhanced optical properties by air plasma treatment. Sci. Rep. *6*, 32355.

86. Harbour, J.R., Tromp, J., and Hair, M.L. (1985). Photogeneration hydrogen peroxide aqueous TiO_2 dispersions. Can. J. Chem. *63*, 204–208.

87. González-Elipe, A.R., Soria, J., and Munuera, G. (1978). EPR study of oxygen adsorption on X-ray irradiated anatase. Chem. Phys. Lett. *57*, 265–268.

88. Munuera, G., Gonzalez-Elipe, A.R., Soria, J., and Sanz, J. (1980). Photo-adsorption and photo-desorption of oxygen on highly hydroxylated TiO_2 surfaces. part 3. Role of H_2O_2 in photo-desorption of O_2. J. Chem. Soc. Farad. Trans. 1 *76*, 1535–1546.

89. Berger, T., Sterrer, M., Diwald, O., and Knözinger, E. (2005). Charge trapping and photoadsorption of O_2 on dehydroxylated TiO_2 nanocrystals—An electron paramagnetic resonance study. ChemPhysChem *6*, 2104–2112.

90. Jaeger, C.D., and Bard, A.J. (1979). Spin trapping and electron spin resonance detection of radical intermediates in the photodecomposition of water at titanium dioxide particulate systems. J. Phys. Chem. *83*, 3146–3152.

91. Daskalaki, V.M., Panagiotopoulou, P., and Kondarides, D.I. (2011). Production of peroxide species in Pt/TiO_2 suspensions under conditions of photocatalytic water splitting and glycerol photoreforming. Chem. Eng. J. *170*, 433–439.

92. Kiwi, J., and Graetzel, M. (1987). Specific analysis of surface-bound peroxides formed during photoinduced water cleavage in titanium dioxide-based microheterogeneous systems. J. Mol. Catal. *39*, 63–70.

93. Oosawa, Y., and Grätzel, M. (1988). Effect of surface hydroxyl density on photocatalytic oxygen generation in aqueous TiO_2 suspensions. J. Chem. Soc. Faraday Trans. 1 *84*, 197–205.

94. Rosen, G.M., and Rauckman, E.J. (1984). Spin trapping of superoxide and hydroxyl radicals. Methods Enzymol. *105*, 198–209.

95. Makino, K., Hagiwara, T., and Murakami, A. (1991). A mini review: fundamental aspects of spin trapping with DMPO. Radiat. Phys. Chem. *37*, 657–665.

96. Shiraishi, F., Nakasako, T., and Hua, Z. (2003). Formation of hydrogen peroxide in photocatalytic reactions. J. Phys. Chem. A *107*, 11072–11081.

97. Stradella, L. (1984). Energetics of the adsorption-desorption cycles of oxygen on a titania-based catalyst. J. Mol. Catal. *26*, 105–115.

98. Bratsch, S.G. (1989). Standard electrode potentials and temperature coefficients in water at 298.15 K. J. Phys. Chem. Ref. Data *18*, 1–21.

99. Jitaru, M. (2007). Electrochemical carbon dioxide reduction - Fundamental and applied topics. J. Univ. Chem. Technol. Metall. *42*, 333–344.

100. Dilla, M., Schlögl, R., and Strunk, J. (2017). Photocatalytic CO_2 reduction under continuous flow high-purity conditions: quantitative evaluation of CH_4 formation in the steady-state. ChemCatChem *9*, 696–704.

101. Praliaud, H., Mikhailenko, S., Chajar, Z., and Primet, M. (1998). Surface and bulk properties of Cu–ZSM-5 and Cu/Al2O3 solids during redox treatments. Correlation with the selective reduction of nitric oxide by hydrocarbons. Appl. Catal. B *16*, 359–374.

102. Gotthardt, M.A., Schoch, R., Wolf, S., Bauer, M., and Kleist, W. (2015). Synthesis and characterization of bimetallic metal–organic framework Cu–Ru-BTC with HKUST-1 structure. Dalton Trans. *44*, 2052–2056.

103. Kau, L.S., Hodgson, K.O., and Solomon, E.I. (1989). X-ray absorption edge and EXAFS study of the copper sites in zinc oxide methanol synthesis catalysts. J. Am. Chem. Soc. *111*, 7103–7109.

104. Ene, A.B., Bauer, M., Archipov, T., and Roduner, E. (2010). Adsorption of oxygen on copper in Cu/HZSM5 zeolites. Phys. Chem. Chem. Phys. *12*, 6520–6531.

105. Okemoto, A., Ueyama, K., Taniya, K., Ichihashi, Y., and Nishiyama, S. (2017). Direct oxidation of benzene with molecular oxygen in liquid phase catalysed by heterogeneous copper complexes encapsulated in Y-Type zeolite. Catal. Commun. *100*, 29–32.

106. Yamada, H., Soejima, Y., Zheng, X.G., and Kawaminami, M. (2000). Structural study of CuO at low temperatures. Trans. Mat. Res. Soc. Japan *25*, 1199–1202.

107. Xueping, H., Zhanchang, P., Xiao, Z., Chumin, X., Shirong, C., Yu, X., and Zhigang, W. (2009). First-principles studies of Cu(II) doped anatase titanium dioxide. J. Mater. Sci. Eng. *27*, 613–616.

6.3 Improving Data Analysis in Chemistry and Biology Through Versatile Baseline Correction

J. Schneidewind*, Hrishi Olickel, *Chemistry – Methods* **2020**, *accepted*

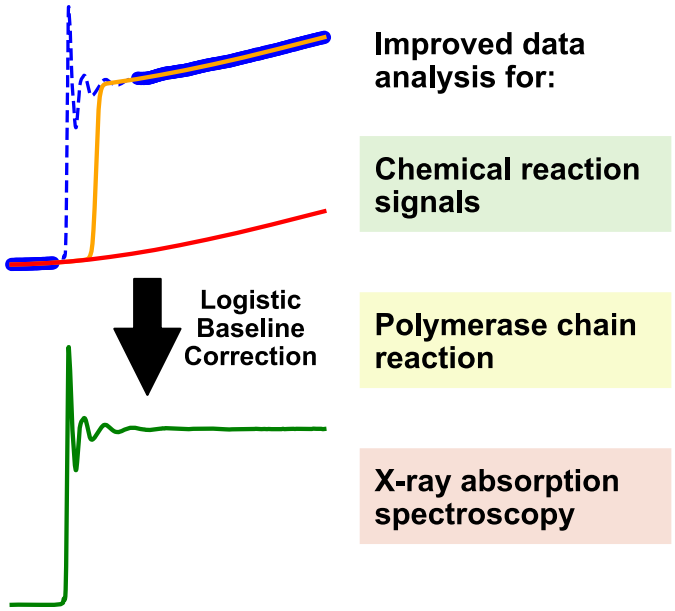

Contributions: I conceived and coordinated the project, performed all research work and code development (except for web tool), analyzed the data, curated information for supporting information and public repository and wrote the complete manuscript. Overall, my contribution amounts to ca. 90%.

Abstract: Accurate data analysis is a cornerstone for the meaningful interpretation of measurements in chemistry and biology. To enable accurate analysis, it is often necessary to remove the background from a measurement via baseline correction, as is commonly done for spectroscopy or chromatography. However, no equivalent methods for baseline correction exist for an entire group of measurements, which includes chemical reaction measurements, quantitative polymerase chain reaction and X-ray absorption spectroscopy. This is because these measurements give rise to a different class of features in their signals, which prevent the application of classical baseline correction methods. In this work, a general method for baseline correction of these features is developed, which is shown to simplify and improve data analysis for these measurements. Through publicly accessible and easy to use software we expect this method to be broadly useful to improve and simplify data analysis for chemists and biologists.

Chemistry Methods

New Approaches to Solving Problems in Chemistry

Chemistry Europe
European Chemical Societies Publishing

Reprint

WILEY-VCH

Improving Data Analysis in Chemistry and Biology Through Versatile Baseline Correction

Jacob Schneidewind*[a] and Hrishi Olickel[b]

Accurate data analysis is a cornerstone for the meaningful interpretation of measurements in chemistry and biology. To enable accurate analysis, it is often necessary to remove the background from a measurement via baseline correction, as is commonly done for spectroscopy or chromatography. However, no equivalent methods for baseline correction exist for an entire group of measurements, which includes chemical reaction measurements, quantitative polymerase chain reaction and X-ray absorption spectroscopy. This is because these measurements give rise to a different class of features in their signals, which prevent the application of classical baseline correction methods. In this work, a general method for baseline correction of these features is developed, which is shown to simplify and improve data analysis for these measurements. Through publicly accessible and easy to use software we expect this method to be broadly useful to improve and simplify data analysis for chemists and biologists.

1. Introduction

Interpretation of measurements in chemistry and biology relies on accurate processing and analysis of the acquired data. During data analysis it is often found that the features of interest are superimposed on a (possibly varying) background. This background then has to be accounted for accurately analyzing the features.[1] When a mathematical model is available that can accurately describe the entire feature, it is best to include a function to describe the baseline in the model and to fit this combination of feature and baseline model to all datapoints (an approach herein referred to as combined fitting).[2] In cases where no model for the entire feature is available, or where combined fitting proves challenging, the baseline might be modeled separately and can then be subtracted from the data to obtain a baseline corrected signal. This corrected signal then forms the basis for subsequent analyses. While this approach is statistically inferior to combined fitting, since it does not utilize all available information to approximate the baseline, it is often necessary due to the lack of accurate feature models. Furthermore, it can also serve as a preparatory step for improved combined fitting models. This kind of separate baseline estimation is for example encountered when processing nuclear magnetic resonance (NMR),[3] infrared (IR)[4,5] or Raman[6] spectroscopy, chromatography,[7] mass spectrometry[8] or calorimetry[9] data.

In contrast, analysis of chemical reaction measurements, quantitative polymerase chain reaction (qPCR)[10] or X-ray absorption spectroscopy (XAS)[11] data (and others[12]) would also benefit from such baseline correction, but there are no equivalent baseline correction methods available for these measurements compared to the ones mentioned above. This is a serious shortcoming, as these measurements are crucial to understand the mechanisms of chemical reactions,[13] analyze DNA/RNA in medicinally relevant samples (such as detection of the SARS-CoV-2 virus[14]) or to elucidate the structure and properties of materials,[15] respectively.

The reason for the lack of equivalent baseline correction methods for these measurements (chemical reaction measurements, qPCR, XAS and others[12]) compared to the measurements mentioned above (NMR, IR spectroscopy etc.) is that these two groups of measurements give rise to two different classes of features: NMR, IR spectroscopy and others produce peak shaped features, meaning that the feature starts and ends at baseline value (see Figure 1A). This means that the baseline is unaffected by the feature and hence this class of features is herein referred to as non-baseline-altering features. In contrast, chemical reactions, qPCR or XAS produce features that do not return to baseline value because the state of the system is changed by the feature (e.g. accumulation of a chemical species or occurrence of an absorption edge, see Figure 1B). Hence, the feature introduces a vertical offset in the signal (signal offset O_s, see Figure 1B) between datapoints preceding and succeeding the feature. Due to this effect of the feature on the baseline, this class of features is herein referred to as baseline-altering features.

To understand why there are no equivalent baseline correction methods for baseline-altering features we first want to look at how classical baseline correction methods for non-baseline-altering features (e.g. NMR, IR spectroscopy) proceed (see Figure 1A): Seeing the measurement M(x) as the sum of a

[a] J. Schneidewind
Leibniz-Institut für Katalyse e.V.
Albert-Einstein-Str. 29a
Rostock 18059 (Germany)
E-mail: Jacob.Schneidewind@catalysis.de
[b] H. Olickel
Yale-NUS College
16 College Avenue West
Singapore 138527 (Singapore)

Supporting information for this article is available on the WWW under https://doi.org/10.1002/cmtd.202000027

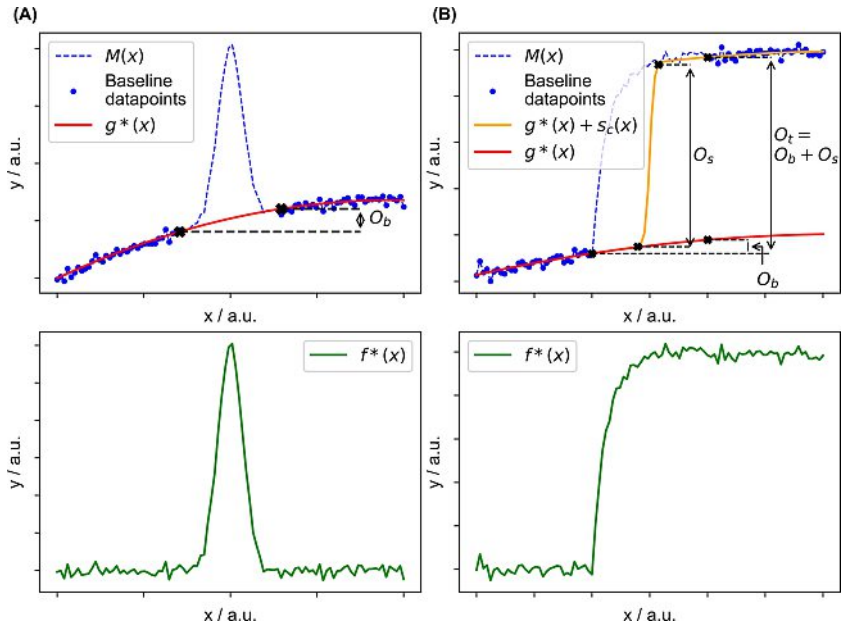

Figure 1. Examples of non-baseline-altering and baseline-altering features with the corresponding baseline corrections. In both cases, the synthetic baseline consists of a second-order polynomial and Gaussian noise was added to the simulated measurement (a.u. = arbitrary unit). (A) Top: Measurement of non-baseline-altering feature (M(x), dashed line) with datapoints considered for baseline fitting highlighted. Baseline approximation g*(x) (red) and corresponding baseline offset (O_b) are shown. Bottom: Baseline corrected signal f*(x) obtained by subtraction of g*(x) from M(x). (B) Top: Baseline-altering feature with total offset (O_t) between the two baseline intervals highlighted along with signal offset O_s and baseline offset O_b. Logistic Baseline Correction (LBC) fit is shown in orange (showing that it captures O_s) and thus obtained baseline approximation g*(x) is shown in red. Bottom: f*(x) obtained by subtraction of g*(x) (obtained via LBC) from M(x).

signal f(x) and baseline g(x), baseline correction aims to recover g(x) from M(x), so that it can be subtracted from M(x), obtaining f(x).

1. Recovery of g(x) is done by selecting baseline data points which precede and succeed the feature (herein referred to as pre- and post-feature, even where the measurement is not necessarily time-dependent), and fitting them with some approximate function g*(x) (see Figure 1A, top).
2. With the approximate function g*(x) in hand, baseline values in the feature region can be interpolated, allowing for subtraction of g*(x) from the entire range of interest of M(x), obtaining an approximate signal f*(x) (see Figure 1A, bottom).

This approach to baseline correction does not generalize to baseline-altering features because the feature introduces an unknown signal offset (O_s) between pre- and post-feature baseline data points. Any attempted fit to these baseline data points would be heavily distorted by this offset, explaining why there are no equivalent baseline correction methods for this class of features (found in chemical reaction measurements, qPCR, XAS etc.). To circumvent this problem, state-of-the-art baseline correction methods for qPCR[10] or XAS[11] mostly estimate g*(x) by only fitting pre-feature baseline data points. This one-sided approach, however, relies on an extrapolation of g*(x) into the feature region (instead of an interpolation as described above for classical baseline correction). Extrapolation instead of interpolation compromises accuracy and reliability (see below) and such approaches are therefore not equivalent – in design or accuracy – to classical baseline correction.

In this work, a new and general method for baseline correction of baseline-altering features is developed, resulting in a generally applicable tool to improve data analysis for various measurements in chemistry and biology. It is shown that using this method, analysis of chemical reaction measurements, qPCR and XAS data is simplified with improved accuracy and reliability. Furthermore, a public web interface (https://lbc.olickel.com) has been created to allow a broad group of scientists to ease transition to the new method and improve their data analysis using this new tool.

2. Results and Discussion

2.1. Problem Statement

The fundamental problem in baseline correction of baseline-altering features is that the signal offset O_s is unknown beforehand. Knowing O_s would allow the shifting of post-feature data points by this magnitude on the y-axis, restoring a classical (non-baseline-altering feature) baseline correction problem. The observed total vertical offset, O_t, between pre- and post-feature data points, however, is the sum of O_s and baseline offset O_b (see Figure 1B, top). Since O_s is unknown, the baseline and thus O_b, cannot be determined. Not knowing O_b in return prevents the determination of O_s, as the signal (and therefore its offset) cannot be separated from the baseline.

2.2. Logistic Baseline Correction Algorithm

To resolve this problem, the following solution is proposed: Instead of solely fitting a function g*(*x*) to pre- and post-feature data points, a function of the form $g^*(x)+s_c(x)$ is fitted, wherein $s_c(x)$ is a one-parameter function that introduces a step of magnitude *c* between pre- and post-feature data points. Step magnitude *c* is included as an additional optimization parameter in the fitting procedure and is therefore iteratively optimized along with the parameters of g*(*x*). For a conservatively chosen g*(*x*), which does not overfit the baseline data points, it is hypothesized that *c* approaches O_s in the optimization, yielding the best fit. If *c* approximates O_s the classical baseline correction problem is restored and we expect g*(*x*) to be an accurate description of the baseline. This hypothesis is based on the consideration that a conservatively chosen g*(*x*) only has sufficient degrees of freedom to describe the baseline, not the signal offset. Conversely, $s_c(x)$ only has one degree of freedom, being able to solely describe the signal offset. An optimal solution to the fitting optimization problem is therefore for $s_c(x)$ to approach O_s and for g*(*x*) to approach g(*x*). In addition, restoring the problem to classical baseline correction also allows for this class of problems to benefit from advances in classical baseline correction methodology.

To implement the proposed solution the following algorithm has been devised:

1. Selection of function g*(*x*) to describe the baseline and selection of feature start point x_s and feature end point x_e. These points are used to define the baseline intervals: all points preceding the feature start point are considered the pre-feature baseline interval and all points succeeding the feature end point are considered the post-feature baseline interval (unless there are multiple features, see XAS section). The g*(*x*) function has to be chosen by the user and feature start and end points are either chosen by the user or defined automatically (see qPCR section).

2. Calculation of the midpoint x_0 between x_s and x_e, followed by calculation of the 75th percentile point (x_{75}) between feature start and end point: $x_{75} = \frac{x_e - x_0}{2}$.

3. Defining $s_c(x)$ to be a logistic function of the form:

$$s_c(x) = \frac{c}{1 + e^{r(x-x_0)}} \tag{1a}$$

With *r* being the logistic growth rate which is defined as $r = \frac{\ln\left(\frac{1}{v_{75}}\right)}{x_{75}}$. v_{75} is a parameter that determines the value of $s_c(x)$ at the 75th percentile point x_{75}. Using for example $v_{75} = 9.9 \cdot 10^5$ ensures that $s_c(x)$ reaches 99.9999% of its maximum value at x_{75}, preventing $s_c(x)$ from altering the shape of g*(*x*) (as long the value of v_{75} is sufficiently high is does not have an influence on the result of the algorithm).

4. Fitting of $g^*(x)+s_c(x)$ to the selected baseline intervals by optimizing the parameters of g*(*x*) as well as step magnitude *c* using the least squares method with the following definition for the residual:

$$\overrightarrow{res} = \vec{w}(\vec{y} - s_c(\vec{x}) - g^*(\vec{x})) \tag{1b}$$

with $\overrightarrow{res}$ being a vector of the residuals, $\vec{y}$ being the vector of baseline datapoint y values, $\vec{x}$ being the vector of baseline datapoint x values and *w* being a vector of weights for each residual value. For unweighted fitting (used in most cases presented herein), all entries of *w* are equal to one. The weight vector can be used to weigh pre- and post-feature datapoints differently (see qPCR section) or to account for heteroscedasticity by weighing according to data variance.[16] After optimization, g*(*x*) is an approximation of the baseline and parameter *c* has approached signal offset O_s.

5. Subtraction of optimized g*(*x*) from M(*x*) to yield the baseline corrected signal f*(*x*):

$$f^*(x) = M(x) - g^*(x) \tag{1c}$$

Using a continuously differentiable logistic function (as compared to a step function) allows for easy application of gradient based optimization algorithms in the fitting procedure,[17] and affords a smooth function to continuously describe the background. In contrast to a step function, however, the curvature of a logistic function could alter the shape of optimized g*(*x*). Therefore, v_{75} is set so that the curvature is completely confined to the interval between pre- and post-feature datapoints (e.g. by having $s_c(x)$ reach 99.9999% of its maximum value at the 75th percentile point for $v_{75} = 9.9 \cdot 10^5$). This ensures that $s_c(x)$ only accounts for compensating O_s. Ultimately, both a step function or a logistic function can be used for $s_c(x)$, but in the following examples a logistic function will be used.

In optimization step 4, only parameter *c* is optimized along with the parameters of g*(*x*). Since $s_c(x)$ is linear in *c* and this term is simply subtracted from g*(*x*) (see equation (1b)), this method has the same computational complexity as classical baseline correction. Thus, when g*(*x*) is a linear predictor function (such as a polynomial), fitting can still be performed using linear least squares (a weighted least squares implementation of LBC is also available at https://github.com/jschneidewind/LBC). Furthermore, using such a general description of the step yields a baseline correction method which is agnostic to feature and baseline shape, as $s_c(x)$ can describe the offset of any baseline-altering feature and can be combined with any (conservative) g*(*x*) to describe the baseline. The required user input for this algorithm is only the selection of feature start and end point (which can be automated if desired, see qPCR section) and the choice of g*(*x*) (see below for details on user input).

Due to the choice of $s_c(x)$, this approach is herein referred to as "Logistic Baseline Correction" (LBC). In the following we will refer to the use and results of LBC in the following ways: use of

LBC is specified by the choice for g*(*x*) and feature start and end values (e.g. "LBC was performed using a third-order polynomial for g*(*x*) and feature start and end points were set at 0 and 2, respectively"). *LBC fit* refers to optimized $g^*(x)+s_c(x)$, *LBC baseline* refers to optimized g*(*x*) obtained via LBC and *c* refers to optimized step magnitude. Finally, *LBC corrected signal* refers to f*(*x*) obtained after subtraction of the LBC baseline from M(*x*).

2.3. Pre- and Post-Feature and Combined Fitting

As baseline correction utilizing only pre-feature baseline datapoints (herein referred to as pre-feature fitting) is currently in common use for baseline-altering features,[10,11] we briefly want to outline this method as well to facilitate comparison.

Pre-feature fitting comprises three steps:

1. Selection of function g*(*x*) to describe the baseline and selection of feature start point x_s. All points preceding x_s are considered the pre-feature baseline interval.

2. Fitting of g*(*x*) to the pre-feature baseline interval by optimizing the parameters of g*(*x*) using the least squares method with the following definition for the residual:

$$\overrightarrow{res} = \vec{y} - g^*(\vec{x}) \tag{1d}$$

3. Subtraction of optimized g*(*x*) from M(*x*) to yield the baseline corrected signal f*(*x*) (see equation (1c)).

Analogously, one can select a feature end point and fit g*(*x*) to the post-feature baseline interval instead. This method is herein referred to as post-feature fitting. User input for both methods is the selection of g*(*x*) and a feature start (pre-feature fitting) or end (post-feature fitting) point. In analogy to the LBC terminology, use of either method is specified by these inputs (e.g. "pre-feature fitting was performed using a second-order polynomial for g*(*x*) and 0 as the feature start point"). *Pre- (or post-)feature baseline* refers to optimized g*(*x*) obtained using either method and *pre- (or post-)feature corrected signal* refers to f*(*x*) obtained after subtraction of the pre- (or post-)feature baseline from M(*x*).

Aside from the above described methods, when a model for the entire feature is available, one can also attempt to model baseline and feature simultaneously (combined fitting). For this approach, a function g*(*x*) to describe the baseline and a function h*(*x*) to describe the feature are selected. The sum of both functions is then fitted to the entire measurement by optimizing the parameters of g*(*x*) and h*(*x*) (residual definition: $\overrightarrow{res} = M(\vec{x}) - g^*(\vec{x}) - h^*(\vec{x})$).

2.4. Assumptions

There are two main assumptions underlying all methods (including LBC) described above. The first assumption is that baseline g(*x*) and signal f(*x*) are simply additive and therefore M(*x*) can be decomposed into $g(x)+f(x)$. This assumption is justified in cases where the processes giving rise to the baseline are independent from those giving rise to the feature. It breaks down, however, when there is a correlation between baseline and feature, such as Mie scattering in IR spectroscopy.[18] More elaborate combined fitting approaches may possibly account for such correlation but are not explored herein. For the examples considered, baseline and feature processes can be considered to be reasonably independent, allowing this assumption to hold.

The second assumption is that pre- and post-post feature baseline intervals can both be described by the same baseline approximating function g*(*x*). This assumption holds when the process giving rise to the baseline is unaffected by both the feature as well as the passage of time (in case of time dependent measurements) or changes in energy (in case of spectroscopy). In case of XAS, this assumption might be violated because the background X-ray attenuation coefficient varies strongly with energy.[19] Such changes in baseline behavior might be modeled by using a function for g*(*x*) with more degrees of freedom (e.g. a higher-order polynomial, see XAS section below).

2.5. User Input

LBC (as well as pre- and post-feature fitting) requires the user to select a function for g*(*x*) and to select feature start and end points (or to select hyperparameters for an algorithm to make the selection, see qPCR section).

Regarding g*(*x*) selection, on the one hand, the selected function should have sufficient degrees of freedom to account for the complexity of a given baseline (see Evaluation using Synthetic Data section). On the other hand, if g*(*x*) has too many degrees of freedom it could lead to overfitting, meaning that g*(*x*) would attempt to account for even minute variations in the baseline intervals. Overfitting can make baseline correction less reliable and could also remove useful information from the measurement. In case of XAS, for example, fine-structure information could be lost if the baseline is over fitted. To strike the correct balance, it was found that for the examples considered herein, polynomial functions of various orders are a suitable choice for g*(*x*). While LBC can be used with essentially any function for g*(*x*), polynomials were found to be able to describe a wide range of baseline shapes while giving fine control over their degrees of freedom by changing their order. Therefore, the provided web interface for LBC provides the possibility to choose various polynomials for g*(*x*) and the interactive graphing aids in identifying an appropriate fit.

Regarding the choice of feature start and end points, the resulting baseline intervals should not contain parts of the feature, as this would distort the resulting fit for g*(*x*). Again, the interactive graphing of the web interface aids in identifying appropriate start and end points as well as saving these parameters into a library for future use.

In the following we will analyze the performance of LBC, including assessing its robustness to different data properties

and user inputs and applying it to experimental data from chemical reaction measurements, qPCR and XAS measurements. In the process, LBC will be compared to state-of-the-art baseline correction methods.

2.6. Evaluation Using Synthetic Data

To evaluate the performance of LBC it was tested on synthetic data of the form shown in Figure 1B. The synthetic measurement is the sum of a polynomial baseline representing g(x), an exponential signal representing f(x), as it can be found in first order chemical reactions,[20] and Gaussian noise (for more examples of synthetic data, see SI Figure 1). LBC was performed using a polynomial of the same order as g(x) for g*(x) and feature start and end points were set at 0 and 2, respectively (baseline intervals [−2, 0] and [2, 4]). As it can be seen in Figure 1B, LBC does indeed yield a fit to the baseline data points by introducing a step of magnitude $\sim O_s$ halfway between the two intervals and produces a baseline estimate g*(x) which is unaffected by the feature.

Performance analysis on this synthetic data set shows that after optimization, c does indeed accurately describe O_s for various baseline shapes, which were obtained by random variation of the polynomial function's parameters and by varying the polynomial order (see SI Figure 2A). Furthermore, g*(x) shows a low root-mean-square deviation (RMSD) from g(x) under these alterations. Both the accuracy of c and the RMSD of g*(x) show a well behaved response to increasing amounts of noise as well as reduced numbers of data points to be fitted (see SI Figure 2B and C). Furthermore, the method is robust to changes of the feature start and end points, tolerating symmetric and asymmetric pre- and post feature intervals of various sizes (see SI Figure 2D). It is noteworthy that LBC is significantly more robust to these changes than pre-feature fitting (see SI Figure 2F). Regarding the choice of g*(x), the accuracy of c shows a robust response even when the order of the polynomial chosen for g*(x) is significantly higher than the order of the actual baseline polynomial (see SI Figure 2E), showing that overfitting is not especially problematic in this situation. When the order of g*(x) is lower than the actual baseline polynomial, however, the error in c sharply increases (see SI Figure 2E), as g*(x) does not have sufficient degrees of freedom to describe g(x).

Based on these results, we can conclude that for this synthetic dataset with various baseline shapes, levels of noise, number of data points, baseline intervals, and choices for g*(x), LBC can accurately recover both signal offset O_s and a good approximation of the baseline g(x). Synthetic data generation is also enabled on the web interface, allowing for further examination of LBC behavior.

Since baseline correction is usually not an end in itself but rather a preprocessing step to enable accurate analysis of the feature of interest, we want to evaluate and compare the effect of LBC on the feature analysis results. For this, we are using the same form of synthetic data as above. Our signal shows product formation for a first-order chemical reaction. For such a reaction, integrated rate law (2) describes the time-dependent product concentration *[B]:*

$$[B] = [A_0] - [A_0]e^{-kt} \tag{2}$$

Here, aim of feature analysis is to obtain k, which is the rate constant of the reaction and an important component of chemical kinetic analysis.[21] To obtain k, equation (2) is fitted to the baseline corrected signal with initial reactant concentration $[A_0]$ being set to 1 and k being the only parameter to be optimized (see Figure 2A). The test data set for this analysis consists of a second-order polynomial baseline with fixed parameters, a fixed level of random Gaussian noise and the first-order chemical reaction signal (for which k is set to 4). Analysis is performed in four ways:

1) LBC with a second-order polynomial for g*(x), feature start and end points set at 0 and 2, respectively, and fitting of equation (2) to LBC corrected signal.

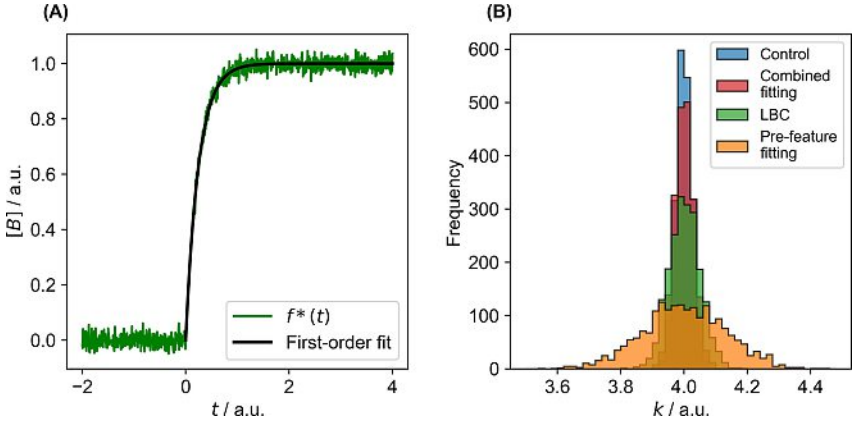

Figure 2. (A) LBC corrected, synthetic first-order chemical reaction signal (green) along with fit of integrated rate law (2) (black). (B) Histogram of k obtained via fitting of integrated rate law (2) to signals obtained using different baseline correction methods. Pre-feature fitting is shown in orange, LBC in green and the control (fitting of (2) to signal containing noise but no baseline) in blue. Furthermore, combined fitting of baseline and feature is shown in red. Analyses were performed 2000 times with randomly varying Gaussian noise in measurement.

2) Pre-feature fitting with a second-order polynomial for g*(x) and feature start point set at 0 and fitting of equation (2) to the pre-feature corrected signal.
3) Combined fitting using the sum of equation (2) and a second-order polynomial for g*(x).
4) As a control, the chemical reaction signal without baseline (only containing Gaussian noise) is analyzed by fitting equation (2).

All analyses were performed 2000 times with randomly varying Gaussian noise to obtain accurate mean and standard deviation values for k.

A histogram showing the distribution of k for each approach is shown in Figure 2B. While the mean value of k for all approaches is close to 4, pre-feature fitting shows the highest standard deviation (4.0 ± 0.13), which is almost three times higher than the standard deviation for LBC (4.0 ± 0.049). LBC approaches the standard deviation of the control (4.0 ± 0.025). Combined fitting (4.0 ± 0.030) gives an even lower standard deviation than LBC. The same trends are also maintained when rate law (2) is fitted as a two-parameter function (optimizing both $[A_0]$ and k, see SI Figure 3C and D).

While pre-feature fitting yields the correct mean, its standard deviation is higher because it utilizes fewer data points over a more narrow range compared to LBC. It therefore requires extrapolation into the feature region, which is comparatively less precise. These characteristics also result in a less reliable procedure, as can be seen for test data sets with more noise or fewer data points (SI Figure 3A and 3B), where the precision of pre-feature fitting can become too low to allow for feature analysis. LBC, however, utilizes more data points over a significantly wider range (pre- and post-feature), enabling interpolation in the feature region. This allows capturing the shape of the baseline over the entire measurement range more precisely and reliably. Combined fitting further improves on these advantages by additionally utilizing data points in the feature region. Based on these synthetic data experiments, using LBC allows for a systematically precise baseline estimate, which yields precise feature analysis results.

We now want to apply LBC to experimental data to see if these conclusions generalize. Again we will focus on the effect of the baseline correction procedure on feature analysis results. Use cases are chemical reaction measurements (reaction kinetics), quantitative polymerase chain reaction and X-ray absorption spectroscopy. These examples can also be found in the library of https://lbc.olickel.com to allow users to perform their own experimentation.

2.7. Chemical Reaction Measurement

The chemical application example is similar to the synthetic data used above: a chemical reaction is monitored *in situ* for one of its products and addition of the reactant produces a chemical reaction signal. In this case, hydrogen peroxide (H_2O_2) disproportionation catalyzed by potassium iodide (KI) was studied by the authors through measurement of the evolved oxygen:

$$2\,H_2O_2 \xrightarrow[H_2O]{KI} O_2 + 2\,H_2O \qquad \text{(reaction 1)}$$

Aim of the analysis in this case is to obtain the total amount of evolved oxygen and the rate constant, both of which require baseline correction to be determined. *In situ* oxygen measurement was achieved using optical oxygen detection, which, in this case, shows a non-linear baseline due to slow, underlying equilibration processes (see Figure 3, top). Addition of hydrogen peroxide at $t = 1500$ s produces the oxygen reaction signal of interest, which is expected to be stationary in the post-feature phase. For analysis, feature start and end point were set at $t = 1500$ s and $t = 4000$ s, respectively.

Pre-feature fitting is used as a reference baseline correction approach (Figure 3A). For pre-feature fitting, however, only a first-order polynomial for g*(t) gave a reasonable result as higher-order polynomials failed to converge on a reasonable baseline (see SI Figure 4A). This baseline description falls short of describing the post-feature baseline region accurately and hence, no stationary phase is obtained for the pre-feature corrected signal (Figure 3A, bottom). Thus it is not possible to accurately determine the total amount of evolved oxygen.

In contrast, using LBC allows for utilization of pre- and post-feature data points, enabling an approximation of the non-linear baseline with a fourth-order polynomial for g*(t) (Figure 3B). This results in the expected stationary phase after the reaction once the baseline has been subtracted (Figure 3B, bottom). The total amount of evolved oxygen can now be obtained from the average value of the stationary phase or directly from parameter c of $s_c(t)$, which has approached signal offset O_s. Both values are identical within four significant figures, giving 0.064 vol% O_2.

After baseline correction it is also possible to analyze the reaction signal to obtain k. Since potassium iodide catalyzed hydrogen peroxide disproportionation can be described reasonably well as being first-order in hydrogen peroxide, equation (2) can again be used for analysis (as we work with normalized data in the following, a normalized version of equation (2), equation (2a), see SI section 2, was used). Fitting equation (2a) with two parameters, $[A_0]$ and k, to the normalized pre-feature corrected signal results in only an acceptable fit, since the post-feature region is not stationary (see Figure 3A, bottom). In case of the normalized LBC corrected signal, however, a good fit is obtained (Figure 3B, bottom). Parameter of interest k differs by roughly 6.5% between the two approaches, being $5.24 \times 10^{-3}\ s^{-1}$ in case of pre-feature fitting and $5.58 \times 10^{-3}\ s^{-1}$ for LBC. In addition to LBC and pre-feature fitting, it was also attempted to model baseline and feature together by using combined fitting with a second-order polynomial function for g*(t) and equation (2b) (see SI section 2) for h*(t). With this method, a reasonable fit over the entire measurement range is obtained, which also accurately describes the feature (see SI Figure 4E and 4F). Using a higher-order polynomial, reasonable fits can be obtained (see SI Figure 4G and 4H), but the reliability of the fit depends strongly on the quality of the initial guess for the

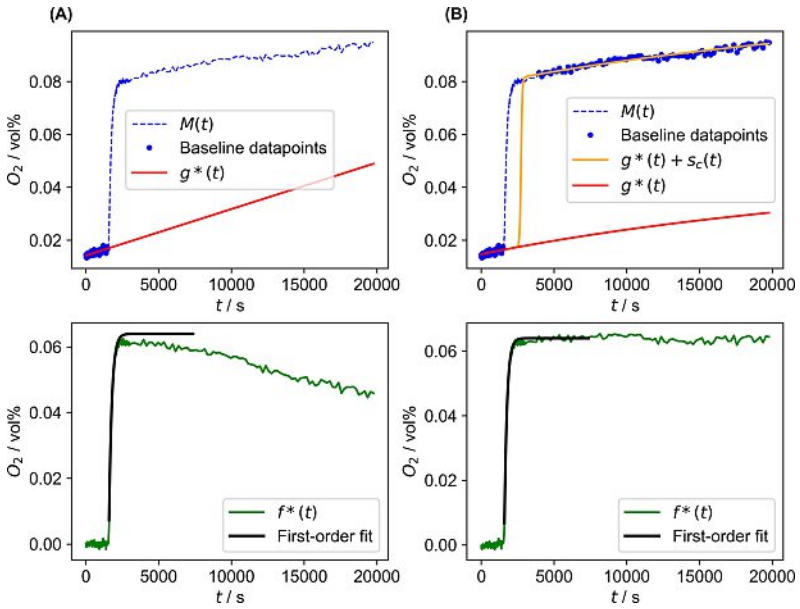

Figure 3. Analysis of oxygen evolution signal obtained *in situ* from KI catalyzed H_2O_2 disproportionation. (A) Top: Linear baseline fit obtained using pre-feature fitting. Bottom: Pre-feature corrected signal f*(*t*) showing non-stationary post-feature phase. Fit of integrated rate law (2a) shown in black (see SI section 2). (B) Top: LBC using a fourth-order polynomial for g*(*t*). Bottom: LBC corrected signal showing stationary post-feature phase and good fit of integrated rate law (2a) (see SI section 2). Note: For visualization purposes, the measurement is only shown up to 20000 s, but the entire measurement lasts 60000 s (see SI Figure 4B). The integrated rate law (2a) is only fitted starting at 1589 s due to an apparent induction period caused by diffusion.

optimization parameters (see SI Figure 12 and SI section 5). A high quality initial guess can in fact be generated using LBC (see SI section 5).

For this chemical application example we can conclude that LBC allows capturing the non-linear nature of the observed baseline, which is a prerequisite to accurately determine the total amount of evolved oxygen (something pre-feature fitting falls short of). Furthermore, the choice of baseline correction method has a substantial effect on the quantification of *k*.

2.8. Quantitative Polymerase Chain Reaction (qPCR)

Quantitative polymerase chain reaction (qPCR) is a method to quantify DNA or RNA in a sample and is widely used in different life science disciplines,[22–24] and is currently one of the main methods to detect the SARS-CoV-2 virus.[14] Quantification is achieved by amplifying fluorescence-marked DNA or RNA using polymerase chain reaction in stepwise amplification cycles (amplification cycle number is denoted as *n*). The increase in fluorescence produces fluorescence amplification curves (see Figure 4A), displaying a baseline-altering feature, which can be analyzed to obtain the initial amount of DNA or RNA present in the sample. Baseline fluorescence/absorption, however, has to be removed to enable this analysis.[10,25]

State-of-the-art qPCR curve analysis tools mostly utilize pre-feature fitting for baseline correction, usually based on the first 6–8 viable cycles (of the nine methods cited in [10], five use pre-feature fitting).[10,26] Some methods, such as 5PSM[27] and a recent improvement on this method,[2] have been proposed which use combined fitting. To compare the effect of pre-feature fitting versus LBC in qPCR analysis, a curve analysis algorithm was devised which is compatible with both baseline correction approaches. The algorithm comprises three steps:

1. Determination of feature start and end points by fitting a linear regression to the first and last *m* data points, each. The first data point, whose fluorescence value exceeds that of the start linear regression model by more than *i* standard deviations and is only followed by data points also exceeding this threshold is considered the feature beginning. In return, the last data point which has a lower fluorescence than the end linear regression model by more than *i* standard deviations and is only preceded by data points which are also below this threshold, marks the feature's end (see SI Figure 5).
2. Baseline correction is performed in two ways: 1. Pre-feature fitting using a first-order polynomial for g*(*n*) (this provides superior performance compared to pre-feature fitting with a second-order polynomial). 2. LBC using a second order polynomial for g*(*n*). LBC is performed with a weight-factor for pre-feature data points to give them a higher weight in the fitting procedure (details see SI Section 3.2).
3. The exponential amplification phase of a given baseline corrected signal is extracted by selecting the interval from feature start to the point preceding the second derivative maximum (SDM). In this phase, exponential amplification occurs and can be described by equation (3):

$$F_n = F_0 E_{amp}{}^n \tag{3}$$

With F_n being the fluorescence at amplification cycle *n*, F_0 being the fluorescence of the initial DNA amount (hence F_0 is

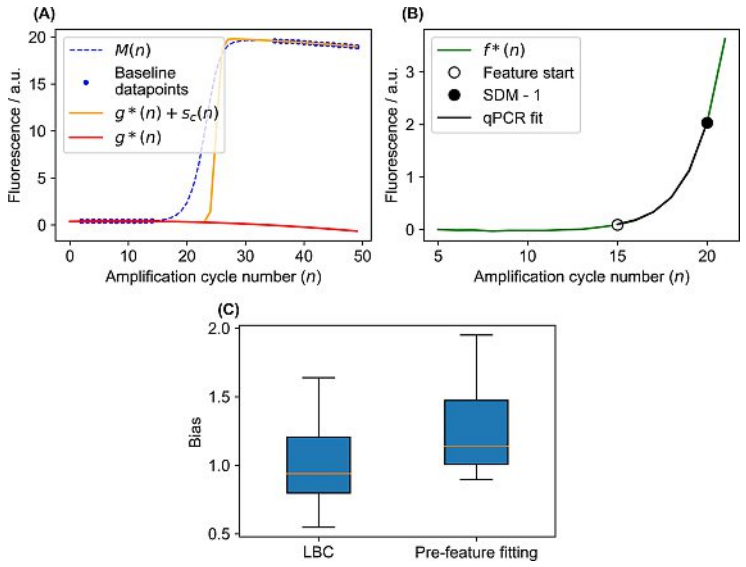

Figure 4. Analysis of qPCR data using the algorithm outlined above. (A) Visualization of LBC applied to a single amplification curve from the reference dataset, using a second-order polynomial for g*(*n*). (B) Fit of equation (3) to exponential amplification phase of baseline-corrected signal from (A). (C) Comparison of analysis bias for all 63 genes from reference dataset analyzed using either LBC or pre-feature fitting for baseline correction ($m=3$, $i=5$). Bias is defined to be the normalized ratio of observed target quantities for the most and least concentrated sample. In case of no bias it is expected to be one. Median is shown as orange line, boxes extend from lower to upper quartile values and whiskers show 5th and 95th percentile, respectively.

the quantity of interest) and E_{amp} being amplification efficiency.[10] For a given gene, E_{amp} is determined by fitting equation (3) as a two-parameter (F_0 and E_{amp}) function to the exponential phase of a random subsample (size N) of reactions. The obtained mean value of E_{amp} is then used to fit equation (3) as a one-parameter function (F_0 being the only parameter) to the exponential phase of all reactions for a given gene (see Figure 4B). Thus obtained F_0 values are linearly related to initial DNA quantities and were used for performance evaluation. It has been noted that the use of equation (3) can introduce quantification bias, as it assumes a constant amplification efficiency, although E_{amp} significantly decreases over the course of amplification.[28] We have therefore used a small fitting window (only up to $n=$SDM − 1) and found low bias in comparison with other methods for the used reference dataset (see below).

Analysis performance of the above described algorithm was assessed by analyzing the triplicate, 63 gene, five-fold dilution reference dataset published by Vermeulen et al.[29] The obtained F_0 values were used for performance evaluation, assessed with the indicators developed by Ruijter et al.[10] Based on this methodology, the algorithm was found to perform on par (for both pre-feature fitting and LBC) with most state-of-the-art qPCR curve analysis tools and performed superior to combined fitting methods such as 5PSM (see SI Figure 8). Here it should be noted, however, that an improved combined fitting method has recently been described.[2]

Pre-feature fitting and LBC were first compared in a regime with a comparatively high number of considered baseline data points. This regime is defined by a larger number of data points considered in the linear regression of step 1 ($m=5$) and a higher cut-off threshold ($i=7$). In this regime, both approaches perform similar in terms of accuracy and precision indicators (see SI Figure 7). In case of lower sample/data quality (as compared to the reference data set) and/or larger initial DNA amounts, early amplification can reduce the number of available baseline data points. Pre-feature fitting and LBC were therefore also compared in a lower data point number regime ($m=3$, $i=5$). Comparison in this regime shows that while precision indicators are still comparable (see SI Figure 6), LBC outperforms pre-feature fitting for accuracy indicators, such as bias and linearity.

Regarding bias, Figure 4C shows boxplots for bias values of LBC and pre-feature fitting for all 63 genes, with a value of one indicating no bias. Bias values obtained using LBC differ significantly ($p=0.001$, two-sided T-test, details see SI Section 3.3) from those obtained using pre-feature fitting in this lower baseline data point number regime, with LBC bias values being closer to one (LBC mean bias: 1.03, pre-feature fitting mean bias: 1.26, see Figure 4C). This result is in line with previous arguments and observations outlined in this paper, as LBC enables the consideration of more baseline data points over a wider range, thus being able to perform better when fewer total baseline data points are available.

We can therefore conclude that for qPCR curve analysis, LBC performs similarly to pre-feature fitting when a higher number of baseline data points are available, but enables more accurate (less biased) analysis in a lower baseline data point number regime. Improvements in accuracy/bias are especially significant, since these improvements cannot be obtained by simply measuring more replicates.[10]

2.9. X-Ray Absorption Spectroscopy (XAS)

X-ray absorption spectroscopy (XAS) is a widely used analytical tool to elucidate structural and electronic features of a material.[30–32] Usually, absorption edges are studied, which are element-specific energy thresholds, where X-ray energy surpasses the required amount of energy to excite particular core electrons.[33] This process gives rise to a baseline-altering edge feature (see Figure 5A). Depending on the measurement mode (transmission or fluorescence), there is either a continuously decreasing (background absorption) or increasing (background fluorescence) baseline. This baseline has to be corrected to enable subsequent analyses such white line analysis,[34] pre-edge peak analysis,[35,36] X-ray absorption near edge structure (XANES) and extended X-ray absorption fine structure (EXAFS).[15] Aside from baseline correction, further analysis usually requires normalization based on the edge step magnitude $\triangle\mu_e$.[37] State-of-the-art baseline correction is typically done by pre-feature fitting using a first-order polynomial for g*(*E*).[37] The edge step magnitude $\triangle\mu_e$ is subsequently determined by additionally performing post-feature fitting using a polynomial for g*(*E*) and then calculating the difference of the pre- and post-feature g*(*E*) at edge step energy E_0. With $\triangle\mu_e$ in hand the spectrum can be normalized (this process will be abbreviated as conventional baseline correction/normalization, CBCN).[37] Other methods, such as the MBACK algorithm have also been proposed, where data is matched to tabulated, element specific values to account for the absorption edge.[19]

In contrast to the conventional approach, applying LBC to X-ray absorption spectra enables baseline correction utilizing both pre- and post-feature data points. Furthermore, $\triangle\mu_e$ is simultaneously determined since *c* approaches it in the optimization (*vide supra*). To demonstrate this, LBC has been applied to X-ray absorption spectra of molybdenum foil (see Figure 5A, from Farrel Lytle Database[38]) as well as Fe_3C (Larch database[37]), $FeCl_3$ (Farrel Lytle Database[38]) and copper foil (Larch database[37], see SI Figures 9A, 9B and 11, respectively). For the molybdenum foil spectrum there are actually two absorption edges (L3 at 2520 eV and L2 at 2625 eV, see Figure 5A) in close vicinity. Therefore, LBC was performed with two logistic functions (each having its own step magnitude value) to account for both edges. A fourth-order polynomial was used for g*(*E*) and the two sets of feature start and end points were set at $-/+30$ eV from the L3 and L2 absorption peaks. These four points produce three baseline intervals to be fitted (all points preceding the L3 feature start point, the interval from the L3 feature end point to the L2 feature start point and all points succeeding the L2 feature end point). Normalization was done using the *c* value for the L3 edge. As can be seen in Figure 5B, using LBC yields a normalized spectrum with the expected flat pre- and post-feature regions.

To evaluate and compare the effect of LBC on subsequent analysis, pre-edge peak analysis was performed for the copper foil spectrum and white line analysis for the molybdenum foil spectrum. Pre-edge peaks are lower-energy electronic transitions, which can be observed for first-row transition metals ~10 eV below the absorption edge.[35,39,40] These peaks contain information on coordination number, ligand types as well as spin and oxidation state, which is encoded in pre-edge peak position, multiplicity and intensity.[35] Pre-edge peak intensity in the copper foil spectrum differed by ~6% between the LBC corrected/normalized signal and the signal obtained by conventional baseline correction/normalization (details see SI section 4 and SI Figure 11). When analyzing different materials, pre-edge intensity can vary quite subtly depending on the ligand type. For example, in case of iron halide complexes, intensity was found to differ in the single digit percent region depending on the nature of the halide.[35] Hence, the choice of baseline correction/normalization method might play an appreciable role for certain pre-edge peak analysis problems, where subtle differences in pre-edge peak intensity have to be resolved.

White lines are the main peaks observed at the onset of transition metal *L*-edges.[41] They result from 2*p* electron excitation to unoccupied *d* states and their intensity has been found to contain information about a metal's electron configuration.[41] This information can for example be used to study the properties of metal alloys.[34] To determine white line intensities the spectrum's background has to be determined, which is the sum of the baseline and an approximation of the absorption edge(s). Using LBC, the background of the molybde-

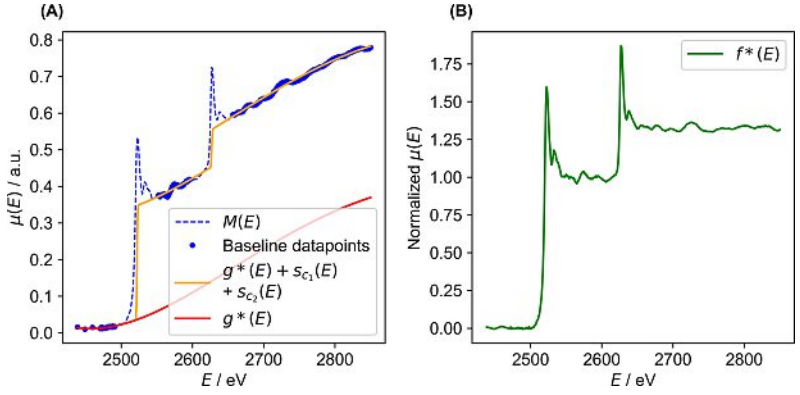

Figure 5. Application of LBC to X-ray absorption spectrum of molybdenum foil. (A) LBC applied to molybdenum L_{23}-edge region of the spectrum using a fourth-order polynomial for g*(*E*) and two logistic functions to account for both steps. (B) Baseline corrected, normalized L_{23}-edge region of spectrum obtained using LBC.

num foil spectrum is conveniently described by $g^*(E) + s_{c_1}(E) + s_{c_2}(E)$ (see Figure 5A), as the logistic functions serve as an approximation of the absorption edges. The state-of-the-art method for determining the background, as described by Pearson,[34,41] uses post-feature fitting with a first-order polynomial for g*(*E*) applied to baseline datapoints succeeding each edge ($g^*_1(E)$ for the L3 and $g^*_2(E)$ for the L2 edge of the molybdenum spectrum). This is followed by extrapolation of each g*(*E*) into the respective edge region. To account for the absorption edges, the value of $g_1^*(E)$ is set to zero for all energies preceding the L3 absorption edge and the value of $g^*_2(E)$ is set equal to $g^*_1(E)$ for all energies preceding the L2 absorption edge (see SI Figure 10A). Comparing LBC and the Pearson method, we can see that LBC describes baseline datapoints (which also represent the background) more accurately by a factor of more than two, with a RMSD of $4.4 \cdot 10^{-3}$ (LBC) versus $9.0 \cdot 10^{-3}$ (Pearson, see SI Figure 10B). White line intensities differ by ca. 10% between the two methods (LBC: 0.2188, Pearson: 0.2446). While a more thorough comparison would have to be carried out to assess the accuracy of both methods, the lower RMSD of LBC gives reason to hypothesize that LBC does improve accuracy for white line analysis.

Regarding analysis of XAS data, we can conclude that LBC enables baseline correction that utilizes pre- and post-edge data points while simultaneously determining the edge step magnitude. This can be considered a simplification of the conventional approach to baseline correction and normalization while also utilizing more data points for baseline correction. Analysis of pre-edge peaks and white lines shows that using LBC provides analysis results that differ from those obtained using state-of-the-art methods. The superior description of baseline datapoints when using LBC gives reason to hypothesize that LBC enables more accurate analysis, but more thorough investigations will have to be carried out to confirm this.

3. Conclusions

Herein we have developed, to the best of our knowledge, the first general method for baseline correction of baseline-altering features, validated it using synthetic and experimental data and have made it publicly available through open-source code and a web interface.

By combining a baseline-describing function with a highly constrained logistic function, LBC allows baseline correction to be performed utilizing both pre- and post-feature baseline data points. This enables interpolation of the feature region. Comparing LBC to the commonly used, state-of-the-art method pre-feature fitting shows that this interpolation enables significantly improved precision and reliability when analyzing synthetic data.

The applicability of LBC was then studied by applying it to relevant, real-life examples from various fields. For a chemical reaction measurement, use of LBC was crucial to recover a physically meaningful signal with a stationary post-feature phase while also providing a baseline corrected signal, which could be accurately analyzed. For qPCR, use of LBC compared to pre-feature fitting yielded a statistically significant improvement of analysis bias for a well-established reference dataset. Lastly, for X-ray absorption spectroscopy, LBC simplified data analysis by simultaneously providing a baseline estimate and a value for the edge step magnitude, which would otherwise take multiple, independent fitting steps. It was also shown that LBC could handle analysis of data containing multiple features. For subsequent analysis, such as pre-edge peak and white line analysis, it has been shown that LBC does yield results that differ from those obtained using state-of-the-art methods. Given a superior description of baseline data points by LBC, it can be hypothesized that these results are more accurate.

LBC is conceptually related to combined fitting (which is used in the 5PSM[27] method for qPCR and the MBACK[19] method for XAS), in that both methods utilize pre- and post-feature data points to estimate the baseline (with combined fitting simultaneously using feature data points). We would therefore like to make some comparative remarks. When analyzing synthetic features, combined fitting shows superior performance compared to LBC (see SI Figure 3), as it utilizes feature data points (in addition to baseline data points) for baseline fitting. For the reaction kinetics example, combined fitting was also successfully applied to accurately describe both the feature and baseline. However, the convergence of combined fitting became significantly less reliable for initial optimization parameter guesses, which were further from the optimal solution (see SI Figure 12A). This can likely be explained be explained by the fact that combined fitting introduces more degrees of freedom during the fitting step, which can lead to interference between baseline and feature fitting. These convergence problems however, can be solved by using the optimized LBC baseline and feature magnitude parameters as an initial guess for combined fitting, yielding excellent convergence (see SI Figure 12B). LBC has also proven to be successful in cases where combined fitting cannot be used, since no model is available to describe the entire feature. This is for example the case for XAS data due to the complex shape of the absorption edge. For reaction kinetics data, the rate law to describe a complex kinetic profile is often not known, in which case the profile is analyzed using approaches other than rate law fitting (such as the initial rate method,[42] reaction progress kinetic analysis[20] or variable time normalization analysis[43]). In all these cases, baseline correction is still needed for accurate analysis, and LBC, which does not require any knowledge about the feature, can be used. We can therefore see that LBC and combined fitting are complementary approaches: on the one hand, when there is adequate knowledge about the feature, combined fitting can be used, along with optimized LBC parameters as an initial guess to improve convergence. On the other hand, when no feature description is available, LBC can still provide a good baseline description. Due to the improved precision of combined fitting, however, it is worthwhile to pursue more functions that can also describe features well, as has been recently demonstrated for qPCR.[2]

Through these examples, it has been established that LBC is widely applicable to measurements from various fields. In fact,

LBC can be applied to any measurement containing a baseline-altering feature. It is only constrained by the two main assumptions underlying it: an additive relationship between feature and baseline and the possibility to describe pre- and post-feature datapoints by the same function. Further research should therefore focus on exploring modifications to LBC that can account for more complex correlations between feature and baseline as well as different descriptions for pre- and post-feature datapoints. Automated parameter estimation is also a possible avenue of exploration, enabled by the simplicity and low CPU cost of the underlying algorithm.

Overall, LBC can be regarded as a significant improvement over the state-of-the-art for baseline correction of baseline-altering features. Importantly, the simplicity of LBC should enable it to be used by researchers from various backgrounds, further aided by publicly available code (https://github.com/jschneidewind/LBC and https://github.com/hrishioa/lbc) and a web interface (https://lbc.olickel.com). With the improvements, simplicity and accessibility offered by LBC, we expect it to be widely used to advance data analysis in chemistry and biology.

Materials and Methods

All computational analyses were performed using Python with the NumPy library.[44] Graphics were generated using Matplotlib.[45] The least squares method implemented in SciPy[46] was used for optimization.

Details regarding the synthetic data experiments can be found in SI Section 1. The oxygen measurement of KI catalyzed H_2O_2 disproportionation was obtained *in situ* using an optical oxygen detector. Experimental details can be found in SI Section 2.1. For qPCR analysis, the technical reference dataset from ref. [10] was used. Although the original dataset consists of 64 genes, one gene was omitted from analysis to enable comparison with the results of ref. [10], where this gene was also not considered. A detailed description of the developed qPCR algorithm and the performance evaluation workflow can be found in SI Section 3. X-ray absorption spectra of copper foil and Fe_3C were taken from the Larch library.[37] The X-ray absorption spectra of molybdenum foil and $FeCl_3$ were taken from the Farrel Lytle Database, found at ref. [38]. Larch's "pre_edge()" function was used for reference conventional baseline correction/normalization. For application of LBC to the molybdenum foil spectrum, the following definition of the residual was used: $\overrightarrow{res} = \vec{y} - s_{c_1}(\vec{x}) - s_{c_2}(\vec{x}) - g^*(\vec{x})$. Further details regarding XAS analysis can be found in SI Section 4.

Author Contributions: J.S. has designed and performed the research, analyzed the data and has written the paper. H.O. developed the web interface and revised the paper.

Data and Code Availability: Used datasets are publicly available at the cited references and are also uploaded at https://github.com/jschneidewind/LBC. Python code for the implementation of LBC and application to the different use cases presented herein is available at https://github.com/jschneidewind/LBC. Source code for the web interface can be found at https://github.com/hrishioa/lbc.

Acknowledgments

Prof. Dr. Matthias Beller and Dr. Henrik Junge (both Leibniz-Institute for Catalysis) are gratefully acknowledged for providing experimental infrastructure and helpful discussions. Hebe Hilhorst, Dr. Roland Schoch (University Paderborn) and Aaron Pang are acknowledged for helpful discussions. Financial support by Fonds der Chemischen Industrie (Kekulé-Stipendium n. 102151) is gratefully acknowledged.

Conflict of Interest

The authors declare no conflict of interest.

Keywords: baseline correction · data analysis · reaction kinetics · polymerase chain reaction · spectroscopy

[1] Z.-M. Zhang, S. Chen, Y.-Z. Liang, *Analyst* **2010**, *135*, 1138–1146.
[2] J. Tellinghuisen, A.-N. Spiess, *Biomol. Detect. Quantif.* **2019**, *17*, 100084.
[3] J. H. Ardenkjær-Larsen, B. Fridlund, A. Gram, G. Hansson, L. Hansson, M. H. Lerche, R. Servin, M. Thaning, K. Golman, *Proc. Mont. Acad. Sci.* **2003**, *100*, 10158–10163.
[4] K. H. Liland, T. Almøy, B.-H. Mevik, *Appl. Spectrosc.* **2010**, *64*, 1007–1016.
[5] H. Martens, E. Stark, *J. Pharm. Biomed. Anal.* **1991**, *9*, 625–635.
[6] J. Zhao, H. Lui, D. I. McLean, H. Zeng, *Appl. Spectrosc.* **2007**, *61*, 1225–1232.
[7] Z. Xu, X. Sun, P. de B. Harrington, *Anal. Chem.* **2011**, *83*, 7464–7471.
[8] H. Shin, M. P. Sampat, J. M. Koomen, M. K. Markey, *OMICS J. Integr. Biol.* **2010**, *14*, 283–295.
[9] R. Svoboda, *Thermochim. Acta* **2017**, *658*, 55–62.
[10] J. M. Ruijter, M. W. Pfaffl, S. Zhao, A. N. Spiess, G. Boggy, J. Blom, R. G. Rutledge, D. Sisti, A. Lievens, K. De Preter, S. Derveaux, J. Hellemans, J. Vandesompele, *Methods* **2013**, *59*, 32–46.
[11] K. V. Klementev, *J. Phys. Appl. Phys.* **2000**, *34*, 209–217.
[12] F. J. Roughton, J. W. Severinghaus, *J. Appl. Physiol.* **1973**, *35*, 861–869.
[13] T. Beweries, J. Thomas, M. Klahn, A. Schulz, D. Heller, U. Rosenthal, *ChemCatChem* **2011**, *3*, 1865–1868.
[14] L. Zou, F. Ruan, M. Huang, L. Liang, H. Huang, Z. Hong, J. Yu, M. Kang, Y. Song, J. Xia, Q. Guo, T. Song, J. He, H.-L. Yen, M. Peiris, J. Wu, *N. Engl. J. Med.* **2020**, DOI: 10.1056/NEJMc2001737.
[15] D. C. Koningsberger, R. Prins, *X-ray absorption: principles, applications, techniques of EXAFS, SEXAFS, and XANES*, John Wiley & Sons, New York, **1988**.
[16] J. Tellinghuisen, *Analyst* **2007**, *132*, 536–543.
[17] J. J. Moré, *Numer. Anal.* **1978**, 105–116.
[18] P. Bassan, A. Kohler, H. Martens, J. Lee, H. J. Byrne, P. Dumas, E. Gazi, M. Brown, N. Clarke, P. Gardner, *Analyst* **2010**, *135*, 268–277.
[19] T.-C. Weng, G. S. Waldo, J. E. Penner-Hahn, *J. Synchrotron Radiat.* **2005**, *12*, 506–510.
[20] D. G. Blackmond, *Angew. Chem. Int. Ed.* **2005**, *44*, 4302–4320; *Angew. Chem.* **2005**, *117*, 4374–4393.
[21] D. T. Gillespie, *Annu. Rev. Phys. Chem.* **2007**, *58*, 35–55.
[22] C. Lee, J. Kim, S. G. Shin, S. Hwang, *J. Biotechnol.* **2006**, *123*, 273–280.
[23] H. Hagège, P. Klous, C. Braem, E. Splinter, J. Dekker, G. Cathala, W. de Laat, T. Forné, *Nat. Protoc.* **2007**, *2*, 1722–1733.
[24] A.-B. Nygard, C. B. Jørgensen, S. Cirera, M. Fredholm, *BMC Mol. Biol.* **2007**, *8*, 67.
[25] J. M. Ruijter, C. Ramakers, W. M. H. Hoogaars, Y. Karlen, O. Bakker, M. J. B. van den Hoff, A. F. M. Moorman, *Nucleic Acids Res.* **2009**, *37*, e45–e45.
[26] S. Pabinger, S. Rödiger, A. Kriegner, K. Vierlinger, A. Weinhäusel, *Biomol. Detect. Quantif.* **2014**, *1*, 23–33.
[27] A.-N. Spiess, C. Feig, C. Ritz, *BMC Bioinf.* **2008**, *9*, 221.
[28] J. Tellinghuisen, A.-N. Spiess, *Anal. Chem.* **2015**, *87*, 8925–8931.
[29] J. Vermeulen, K. De Preter, A. Naranjo, L. Vercruysse, N. Van Roy, J. Hellemans, K. Swerts, S. Bravo, P. Scaruffi, G. P. Tonini, B. De Bernardi, R. Noguera, M. Piqueras, A. Cañete, V. Castel, I. Janoueix-Lerosey, O.

Delattre, G. Schleiermacher, J. Michon, V. Combaret, M. Fischer, A. Oberthuer, P. F. Ambros, K. Beiske, J. Bénard, B. Marques, H. Rubie, J. Kohler, U. Pötschger, R. Ladenstein, M. D. Hogarty, P. McGrady, W. B. London, G. Laureys, F. Speleman, J. Vandesompele, *Lancet Oncol.* **2009**, *10*, 663–671.
[30] K. L. Stone, R. K. Behan, M. T. Green, *Proc. Mont. Acad. Sci.* **2005**, *102*, 16563–16565.
[31] P. U. P. A. Gilbert, A. Young, S. N. Coppersmith, *Proc. Mont. Acad. Sci.* **2011**, *108*, 11350–11355.
[32] A. L. Roe, D. J. Schneider, R. J. Mayer, J. W. Pyrz, J. Widom, L. Que, *J. Am. Chem. Soc.* **1984**, *106*, 1676–1681.
[33] G. N. George, B. Hedman, K. O. Hodgson, *Nat. Struct. Biol.* **1998**, *5 Suppl*, 645–647.
[34] J. K. Okamoto, D. H. Pearson, A. Hightower, C. C. Ahn, B. Fultz, in *Transm. Electron Energy Loss Spectrom. Mater. Sci. EELS Atlas*, John Wiley & Sons, Ltd, **2005**, pp. 317–352.
[35] T. E. Westre, P. Kennepohl, J. G. DeWitt, B. Hedman, K. O. Hodgson, E. I. Solomon, *J. Am. Chem. Soc.* **1997**, *119*, 6297–6314.
[36] P. Chandrasekaran, S. C. E. Stieber, T. J. Collins, J. Lawrence Que, F. Neese, S. DeBeer, *Dalton Trans.* **2011**, *40*, 11070–11079.
[37] M. Newville, *J. Phys. Conf. Ser.* **2013**, *430*, 012007.
[38] "Farrel Lytle Database," can be found under http://ixs.csrri.iit.edu/data/Farrel_Lytle_data/RAW/, accessed **2020**.
[39] F. de Groot, G. Vankó, P. Glatzel, *J. Phys. Condens. Matter* **2009**, *21*, 104207.
[40] T. Yamamoto, *X-Ray Spectrom.* **2008**, *37*, 572–584.
[41] D. H. Pearson, C. C. Ahn, B. Fultz, *Phys. Rev. B* **1993**, *47*, 8471–8478.
[42] J. Casado, M. A. Lopez-Quintela, F. M. Lorenzo-Barral, *J. Chem. Educ.* **1986**, *63*, 450.
[43] J. Burés, *Angew. Chem. Int. Ed.* **2016**, *55*, 16084–16087; *Angew. Chem.* **2016**, *128*, 16318–16321.
[44] S. van der Walt, S. C. Colbert, G. Varoquaux, *Comput. Sci. Eng.* **2011**, *13*, 22–30.
[45] J. D. Hunter, *Comput. Sci. Eng.* **2007**, *9*, 90–95.
[46] E. Jones, T. Oliphant, P. Peterson, others, *SciPy: Open Source Scientific Tools for Python*, **2001**.

Manuscript received: June 11, 2020
Version of record online: October 13, 2020

6.4 Simple ruthenium-catalyzed reductive amination enables the synthesis of a broad range of primary amines

T. Senthamarai, K. Murugesan, J. Schneidewind, N. V. Kalevaru, W. Baumann, H. Neumann, P. C. J. Kamer, M. Beller*, R. V. Jagadeesh*, *Nature Communications* **2018**, *9*, 1–12

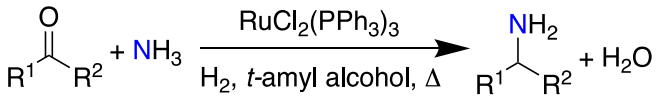

Contributions: I designed mechanistic catalytic experiments, analyzed the data of *in situ* NMR experiments and wrote the discussion section of the manuscript, which accounts for ca. 20% of the manuscript. Furthermore, I revised the entire manuscript. Overall, my contribution amounts to ca. 15%.

Abstract: The production of primary benzylic and aliphatic amines, which represent essential feedstocks and key intermediates for valuable chemicals, life science molecules and materials, is of central importance. Here, we report the synthesis of this class of amines starting from carbonyl compounds and ammonia by Ru-catalyzed reductive amination using H_2. Key to success for this synthesis is the use of a simple $RuCl_2(PPh_3)_3$ catalyst that empowers the synthesis of >90 various linear and branched benzylic, heterocyclic, and aliphatic amines under industrially viable and scalable conditions. Applying this catalyst, $-NH_2$ moiety has been introduced in functionalized and structurally diverse compounds, steroid derivatives and pharmaceuticals. Noteworthy, the synthetic utility of this Ru-catalyzed amination protocol has been demonstrated by upscaling the reactions up to 10 gram-scale syntheses. Furthermore, in situ NMR studies were performed for the identification of active catalytic species. Based on these studies a mechanism for Ru-catalyzed reductive amination is proposed.

nature COMMUNICATIONS

ARTICLE

DOI: 10.1038/s41467-018-06416-6 OPEN

Simple ruthenium-catalyzed reductive amination enables the synthesis of a broad range of primary amines

Thirusangumurugan Senthamarai[1], Kathiravan Murugesan[1], Jacob Schneidewind[1], Narayana V. Kalevaru[1], Wolfgang Baumann[1], Helfried Neumann[1], Paul C.J. Kamer[1], Matthias Beller[1] & Rajenahally V. Jagadeesh[1]

The production of primary benzylic and aliphatic amines, which represent essential feedstocks and key intermediates for valuable chemicals, life science molecules and materials, is of central importance. Here, we report the synthesis of this class of amines starting from carbonyl compounds and ammonia by Ru-catalyzed reductive amination using H_2. Key to success for this synthesis is the use of a simple $RuCl_2(PPh_3)_3$ catalyst that empowers the synthesis of >90 various linear and branched benzylic, heterocyclic, and aliphatic amines under industrially viable and scalable conditions. Applying this catalyst, $-NH_2$ moiety has been introduced in functionalized and structurally diverse compounds, steroid derivatives and pharmaceuticals. Noteworthy, the synthetic utility of this Ru-catalyzed amination protocol has been demonstrated by upscaling the reactions up to 10 gram-scale syntheses. Furthermore, in situ NMR studies were performed for the identification of active catalytic species. Based on these studies a mechanism for Ru-catalyzed reductive amination is proposed.

[1] Leibniz-Institut für Katalyse e. V. an der Universität Rostock, Albert-Einstein-Str. 29a, 18059 Rostock, Germany. Correspondence and requests for materials should be addressed to M.B. (email: Matthias.Beller@catalysis.de) or to R.V.J. (email: Jagadeesh.Rajenahally@catalysis.de)

The development of efficient catalytic reactions for the selective and sustainable synthesis of amines from readily available and inexpensive starting materials by utilizing abundant and green reagents continues to be an important goal of chemical research[1–6]. In particular, the development of simple and easily accessible catalysts for reductive aminations is highly important because these reactions allow for the cost-efficient production of different kinds of amines[7–30]. Among reductive aminations, the reaction of carbonyl compounds with ammonia in presence of molecular hydrogen to produce primary amines is of central importance and continues to be a major challenge[17–30]. In general, amines are essential chemicals used widely in many research areas and industrial productions related to chemistry, medicine, biology, and material science[1–6]. The majority of existing pharmaceuticals, agrochemicals, biomolecules, and natural products contain amine functionalities, which constitute key structural motifs and play vital roles in their functions[1–6]. Among different kinds of amines, primary benzylic and aliphatic amines constitute valuable fine and bulk chemicals, that serve as versatile feedstocks and key intermediates for advanced chemicals, life science molecules and polymers[1–34]. Regarding their synthesis, catalytic reductive amination of carbonyl compounds (aldehydes and ketones) with ammonia in presence of molecular hydrogen represents a waste-free process to access various linear and branched benzylic and aliphatic amines[17–27]. In addition, catalytic amination of alcohols with ammonia also constitutes a sustainable methodology to produce primary amines[35–38]. Apart from transition metal-catalyzed aminations, the Leuckart-Wallach reaction[39–41] and reduction of oxime ethers with borane[42–44] have also been applied. Noteworthy, selective introduction of primary amine moieties in functionalized compounds by utilizing ammonia constitutes a benign and economic methodology[17–27]. Ammonia, which is produced in >175 million tons per year scale, is considered to be an abundant and green chemical used enormously for the large scale production of urea and other fertilizers as well as various basic chemicals[45–50]. Although ammonia is used extensively for the production of simple molecules, its reactions still encounter common problems such as the requirement of high temperatures or pressures and low selectivity towards the formation of a single desired product[45–50]. Hence, the development of more active and selective catalysts for an effective utilization of ammonia, especially for its insertion in advanced and complex molecules, is highly demanded and challenging.

Reductive amination for the preparation of primary amines, especially in industry, is mainly carried out using heterogeneous catalysts[17–23]. Compared to heterogeneous catalysts, homogeneous catalysis for amination of structurally diverse molecules is less studied and remains challenging[24–27]. Transition metal-catalyzed reactions involving ammonia are often difficult to perform or do not even occur. This problem is mainly due to the deactivation of homogeneous catalysts by the formation of stable Werner-type ammine complexes as well as due to the harsh conditions required for the activation of ammonia. In addition, common problems in reductive aminations, such as over alkylation and reduction to the corresponding alcohols, also affect catalyst viability. In order to utilize ammonia successfully and to overcome these problems, there is a need to develop highly efficient homogeneous catalysts, which is the prime task of this investigation. To date, a few catalysts based on Rh-[24,25], Ir-[25] and Ru-[26,27] complexes were reported for the preparation of primary amines from carbonyl compounds and ammonia using hydrogen. Initially, Beller and co-workers[24] have reported a $[Rh(COD)Cl]_2$-TPPTS catalyst system for the synthesis of simple primary amines from aldehydes and aqueous ammonia using NH_4OAc as additive. Following this work, $Rh[(dppb)(COD)]BF_4$ and $[Rh(COD)Cl]_2$-BINAS catalysts were also applied[25]. Next, $[Ir(COD)Cl]_2$-BINAS was found to be able to catalyze the amination of a few simple ketones with ammonia[25]. Regarding Ru-catalysts, $RuHCl(CO)(PPh_3)_3$-xantphos/-dppe in presence of $Al(OTf)_3$ is known to catalyze the preparation of simple primary amines from ketones[26]. Recently, $RuHCl(CO)(PPh_3)_3$-(S,S)-f-binaphane[27] in presence of $NaPF_6$ or NH_4I using NH_3, as well as $Ru(OAc)_2$-C_3-TunePhos[30] using NH_4OAc have been used for enantioselective reductive amination of ketones to obtain chiral primary amines. These homogeneous catalysts, however, have only been applied in (enantioselective) reductive aminations of simple substrates and have not been used for the preparation of functionalized amines. Despite these advances, the design of simpler yet efficient homogeneous catalysts for the preparation of a broad range of structurally diverse primary amines is highly desired and continues to be an important task from both a research and an industry perspective.

In a lot of cases, homogeneous catalysts applied for challenging reactions and advanced organic synthesis operations are based on sophisticated or synthetically demanding metal complexes and ligands. However, a fundamental and economically important principle is that to achieve a convenient and practical chemical synthesis, the catalyst must be simple, effective and commercially available and/or easily accessible. In this regard, triphenylphosphine (PPh_3)-based metal complexes are found to be expedient and advantageous for catalysis applications, since PPh_3 is a stable and comparatively cheap ligand[51–55]. Among PPh_3-based Ru-complexes, $RuCl_2(PPh_3)_3$ is considered to be the simplest and least expensive one and is also commercially available. Interestingly, $RuCl_2(PPh_3)_3$ is known to catalyze a number of organic reactions[56–62]. Herein we demonstrate that $RuCl_2(PPh_3)_3$ is an efficient and highly selective homogeneous precatalyst for reductive amination, allowing the preparation of a variety of primary amines of industrial importance. By applying this Ru-precatalyst and starting from inexpensive and readily available carbonyl compounds (aldehydes, ketones), ammonia and molecular hydrogen, we undertook the synthesis of functionalized and structurally diverse linear and branched benzylic, heterocyclic, and aliphatic amines including drugs and steroid derivatives. Another objective is to demonstrate up-scaling of the homogeneous amination protocol to gram-scale syntheses. Furthermore, efforts were also made to identify catalytically active species and reaction intermediates by performing kinetic and in situ NMR investigations. Based on these studies, a plausible reaction mechanism is proposed.

Results

Selection of catalyst and reaction conditions. Reductive amination of benzaldehyde (1) to benzylamine (2) with ammonia using molecular hydrogen was chosen as a benchmark reaction. At first, in presence of PPh_3 different metal precursors were tested. As shown in Table 1, the in situ generated Fe-, Co-, Mn-, Ni- and Cu-PPh_3 complexes were not active for the formation of benzylamine (Table 1 entries 1–5). However, in situ generated Ru(II)-PPh_3 complexes showed some activity and produced benzylamine in up to 40% yield (Table 1, entries 6 and 7). After observing this reactivity, we next tested in situ generated Ru-complexes with differently substituted PPh_3-type ligands as well as simple nitrogen ligands (L1–L10). Among these, Ru-catalysts containing either PPh_3 or derivatives with electron donating groups in *para* position showed the highest activity (Table 2; entries 1,4,5). However, none of the tested nitrogen ligands (L7–L10) produced the desired product (Table 2, entries 7–10). Unfortunately, using in situ generated Ru-complexes the yield of benzylamine did not improve beyond 53% (Table 2).

Table 1 Reductive amination of benzaldehyde: activity of different catalysts

Entry	Metal precursor	L	Yield of benzylamine [%]
1	$FeCl_2$	PPh_3	nd
2	$CoCl_2.6H_2O$	PPh_3	nd
3	$MnCl_2$	PPh_3	nd
4	$NiCl_2.6H_2O$	PPh_3	nd
5	$CuCl_2$	PPh_3	nd
6	$[RuCl_2(p\text{-cymene})]_2$	PPh_3	40
7	$[RuCl_2(benzene)]_2$	PPh_3	35
8	$[RuCl_2(p\text{-cymene})]_2$	-	nd
9	-	PPh_3	nd

Reaction conditions: 0.5 mmol benzaldehyde, 2 mol% metal precursor, 6 mol% PPh_3, 5–7 bar NH_3, 40 bar H_2 1.5 mL *t*-amyl alcohol, 130 °C, 24 h, GC yields using n-hexadecane as standard
L Ligand, *nd* not detected

Next we turned our interest to molecularly defined Ru-complexes. To our delight, the commercially available complexes $RuCl_2(PPh_3)_3$ and $RuCl_2(PPh_3)_4$ showed excellent activity and selectivity for the formation of benzylamine in 92–95% yields (Table 2, entries 11–12). Further, Ru(tris(4-methoxyphenyl)phosphine)$_3Cl_2$ and Ru(tris(4-chlorophenyl) phosphine)$_3Cl_2$ were also prepared and tested for their reactivity (Table 2; entries 13 and 14). The former displays similar activity compared to $RuCl_2(PPh_3)_3$ (Table 2, entry 13), while the latter was less active (Table 2, entry 14), reflecting the same ligand trend observed in case of in situ generated complexes. In presence of highly active catalysts, we observed 4–7 % of benzyl alcohol (**3**) as the side-product (Table 2, entries 11–13). In case of less-active and or non-active catalysts, undesired side products such as N-benzylidenebenzylamine (**4**) and 2,4,5-triphenyl-2-imidazoline (**5**) were formed (Table 2, entries 1–10). Dibenzylamine (**6**) was not observed under any of these conditions.

Kinetic investigations. After having identified $RuCl_2(PPh_3)_3$ as one of the most active precatalysts, we performed kinetic investigations on this system and examined the effect of (a) reaction time, (b) catalyst concentration, (c) hydrogen pressure, (d) reaction temperature, (e) ammonia pressure, and (f) substrate (benzaldehyde) concentration on activity and product distribution (Fig. 1). For reaction time, in Fig. 1a it can be seen that after 5 h, secondary imine **4** is predominantly present (ca. 60%), with only 30% of target product **2**. Over the course of the reaction, **4**, which appears to be an intermediate, is consumed to yield up to 95% **2** after 24 h (for the mechanism of this transformation vide infra). During the reaction, an increasing amount (up to 4%) of benzyl alcohol is also formed. The cyclic side product **5** can be observed at various reaction times and its amount appears to decrease. This trend, however, is presumably an artifact of the kinetic measurements (see SI). From Fig. 1a it can be concluded that 24 h is an ideal reaction time to obtain maximum yield of **2**. Fig. 1b shows how catalyst loading affects the product distribution. At lower (<2 mol%) loadings, increased amounts of intermediate **4** and side product **5** are obtained, while beyond 2 mol% almost no **4** or **5** along with maximum yield of **2** and some benzyl alcohol **3** were observed. A catalyst loading of 2 mol% is therefore necessary to achieve excellent yield of benzylamine. Similar trends in the product distribution are observed for varied H_2 pressure (Fig. 1c) and reaction temperature (Fig. 1d). Thus 40 bar H_2 pressure and 130 °C reaction temperature are found to be optimum to suppress the formation of intermediates/side products (**4**/**5**) and to yield maximum amounts of the target product benzylamine. When investigating the effect of ammonia pressure, we found that at less than 5 bar side product **6** (dibenzylamine) is formed in up to 20% (Fig. 1e) yield with a concomitant decrease in the yield of **2**. Hence, a minimum NH_3 pressure of 5 bar is required to selectively form the desired product **2** (for mechanistic details vide infra). Further, on increasing the concentration of benzaldehyde (>0.5 mmol) the amount of **5** gradually increases, leading to formation of **5** in up to 80% yield (for 2 mmol benzaldehyde) (Fig. 1e).

Synthesis of linear primary amines from aldehydes. Under optimized reaction conditions, we explored the scope of $RuCl_2(PPh_3)_3$-catalyzed reductive amination for the synthesis of

Table 2 Reductive amination of benzaldehyde using ruthenium catalysts

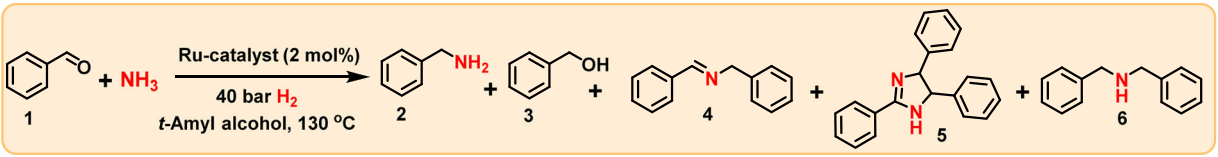

Entry	Ru-precursor/ Defined Ru-catalyst	L	Yield (%)				
			2	3	4	5	6
1 [a]	$[RuCl_2(p\text{-cymene})]_2$	L1	40	2	40	17	-
2 [a]	$[RuCl_2(p\text{-cymene})]_2$	L2	5	-	60	33	-
3 [a]	$[RuCl_2(p\text{-cymene})]_2$	L3	2	-	25	70	-
4 [a]	$[RuCl_2(p\text{-cymene})]_2$	L4	50	5	20	24	-
5 [a]	$[RuCl_2(p\text{-cymene})]_2$	L5	53	4	16	25	-
6 [a]	$[RuCl_2(p\text{-cymene})]_2$	L6	10	2	42	44	-
7 [a]	$[RuCl_2(p\text{-cymene})]_2$	L7	-	-	20	76	-
8 [a]	$[RuCl_2(p\text{-cymene})]_2$	L8	-	-	18	79	-
9 [a]	$[RuCl_2(p\text{-cymene})]_2$	L9	-	-	25	74	-
10 [a]	$[RuCl_2(p\text{-cymene})]_2$	L10	-	-	30	68	-
11 [b]	$RuCl_2(PPh_3)_3$	-	95	4	-	-	-
12 [b]	$RuCl_2(PPh_3)_4$	-	92	7	-	-	-
13 [b]	$RuCl_2$(tris(4-methoxyphenyl)phosphine)$_3$	-	95	4	-	-	-
14 [b]	$RuCl_2$(tris(4-chlorophenyl)phosphine)$_3$	-	50	-	49	-	-

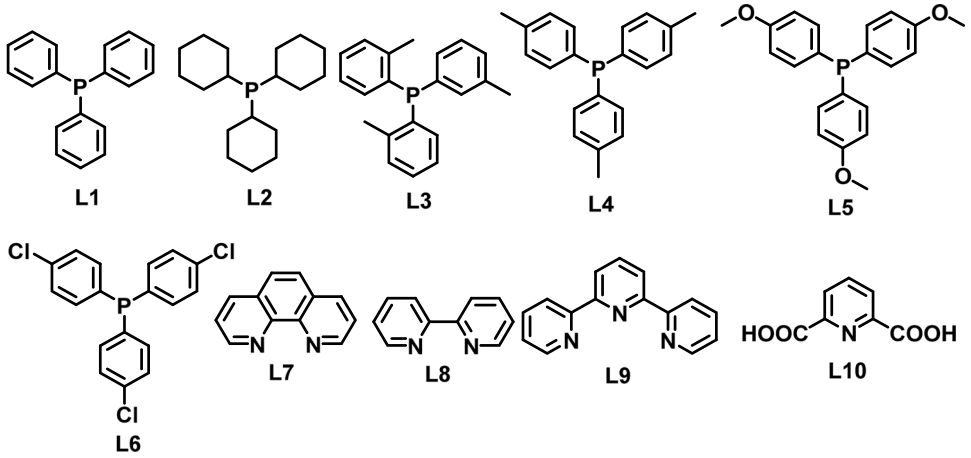

Reaction conditions: [a]0.5 mmol benzaldehyde, 1 mol% $[RuCl_2(p\text{-cymene})]_2$ (2 mol% with respect to the monomer), 6 mol% ligand, 5-7 bar NH_3, 40 bar H_2 1.5 mL *t*-amyl alcohol, 130 °C, 24 h, GC yields using n-hexadecane as standard. [b]Same as 'a' but using 2 mol% defined catalyst.

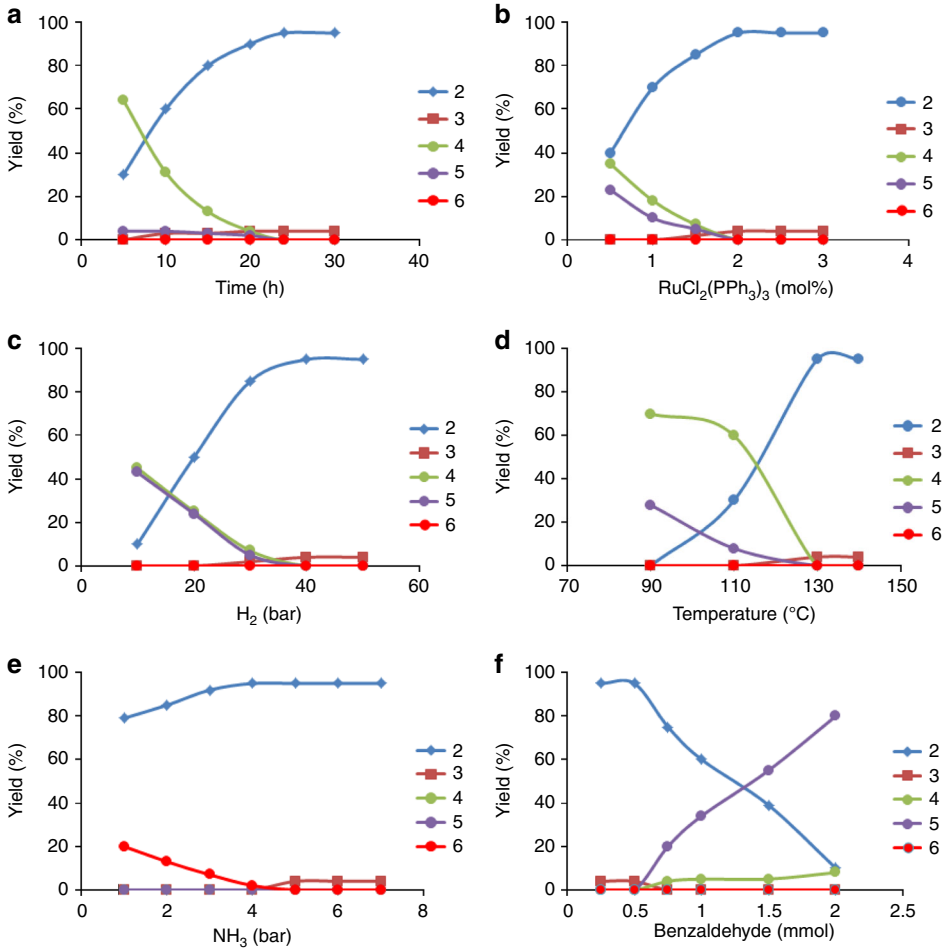

Fig. 1 Kinetic investigations on the Ru-catalyzed reductive amination of benzaldehyde. **a** Yield vs reaction time, **b** yield vs concentration of $RuCl_2(PPh_3)_3$, **c** yield vs pressure of H_2, **d** yield vs temperature, **e** yield vs pressure of NH_3, **f** yield vs concentration of benzaldehyde. 2 = Yield of benzylamine; 3 = yield of benzyl alcohol; 4 = yield of *N*-benzylidenebenzylamine; 5 = yield of 2,4,5-triphenyl-4,5-dihydro-1H-imidazole, 6 = yield of dibenzylamine. Reaction conditions: For Fig. 1a: 0.5 mmol benzaldehyde, 2 mol% $RuCl_2(PPh_3)_3$, 5–7 bar NH_3, 40 bar H_2, 1.5 mL t-amyl alcohol, 130 °C, 5–30 h; for Fig. 1b: 0.5 mmol benzaldehyde, 0.5–3 mol% $RuCl_2(PPh_3)_3$, 5–7 bar NH_3, 40 bar H_2, 1.5 mL t-amyl alcohol, 130 °C, 24 h; for Fig. 1c: 0.5 mmol benzaldehyde, 2 mol% $RuCl_2(PPh_3)_3$, 5–7 bar NH_3, 10–50 bar H_2, 1.5 mL t-amyl alcohol, 130 °C, 24 h; for Fig. 1d: 0.5 mmol benzaldehyde, 2 mol% $RuCl_2(PPh_3)_3$, 5–7 bar NH_3, 40 bar H_2, 1.5 mL t-amyl alcohol, 90–140 °C, 24 h. for Fig. 1e: 0.5 mmol benzaldehyde, 2 mol% $RuCl_2(PPh_3)_3$, 1–7 bar NH_3, 40 bar H_2, 1.5 mL t-amyl alcohol, 130 °C, 24 h; for Fig. 1f: 0.25–2 mmol benzaldehyde, 2 mol% $RuCl_2(PPh_3)_3$, 5–7 bar NH_3, 40 bar H_2, 1.5 mL t-amyl alcohol, 130 °C, 24 h. Yields were determined by GC using n-hexadecane as standard

various primary amines. As shown in Fig. 2, industrially relevant and structurally diverse benzylic, heterocyclic, and aliphatic aldehydes underwent reductive amination and offered linear primary amines in good to excellent yields. Simple as well as sterically hindered benzaldehydes were selectively converted to their corresponding benzyl amines in up to 95% yield (Fig. 2; products **2** and **7**–**13**). In order to apply this amination methodology for organic synthesis and drug discovery, achieving a high degree of chemoselectivity is important. In this regard, we conducted the reaction of sensitive halogenated and functionalized benzaldehydes. Delightfully, halogen-substituted benzaldehydes, including more sensitive iodo-substituted compounds, selectively underwent reductive amination without any significant dehalogenation (Fig. 2; products **14**–**21**). Gratifyingly, various functional groups such as ethers, thio-ethers, carboxylic acid-esters and boronic acid-esters, amides and challenging C–C triple bonds were all well-tolerated without being reduced (Fig. 2; products **22**–**40**). In all these cases, the aldehyde group was selectively aminated to produce functionalized amines in up to 88% yield.

Heterocycles are regarded as highly valuable compounds and these motifs serve as integral parts of a large number of life science molecules and natural products. Thus, the preparation of heterocyclic primary amines is routinely needed en route to the production of pharmaceutically and agriculturally valuable products. Consequently, a series of different heterocyclic amines were synthesized (Fig. 2; products **41**–**49**). The primary amines of pyridine, methylenedioxybenzene and benzodioxane, furan and thiophene were obtained in 87–92% yields.

Success in the amination of aromatic and heterocyclic aldehydes prompted us to validate this catalyst also for aliphatic substrates. Commonly, amination of aliphatic aldehydes is more challenging and most reported catalysts exhibit lower reactivity towards these substrates. In addition, the reaction of aliphatic aldehydes is often troubled by the formation of unwanted aldol reaction products. In spite of these problems, the $RuCl_2(PPh_3)_3$ precatalyst is found to be highly active and selective for the preparation of aliphatic primary linear amines too (Fig. 2). Accordingly, various primary araliphatic and aliphatic linear amines including allylic ones (products **56** and **57**) were obtained in up to 92% yield. Importantly, phenylethylamines (products **50** and **51**), which function as monoaminergic neuromodulators and neurotransmitters in the human CNS, have been prepared in up to 90% yield.

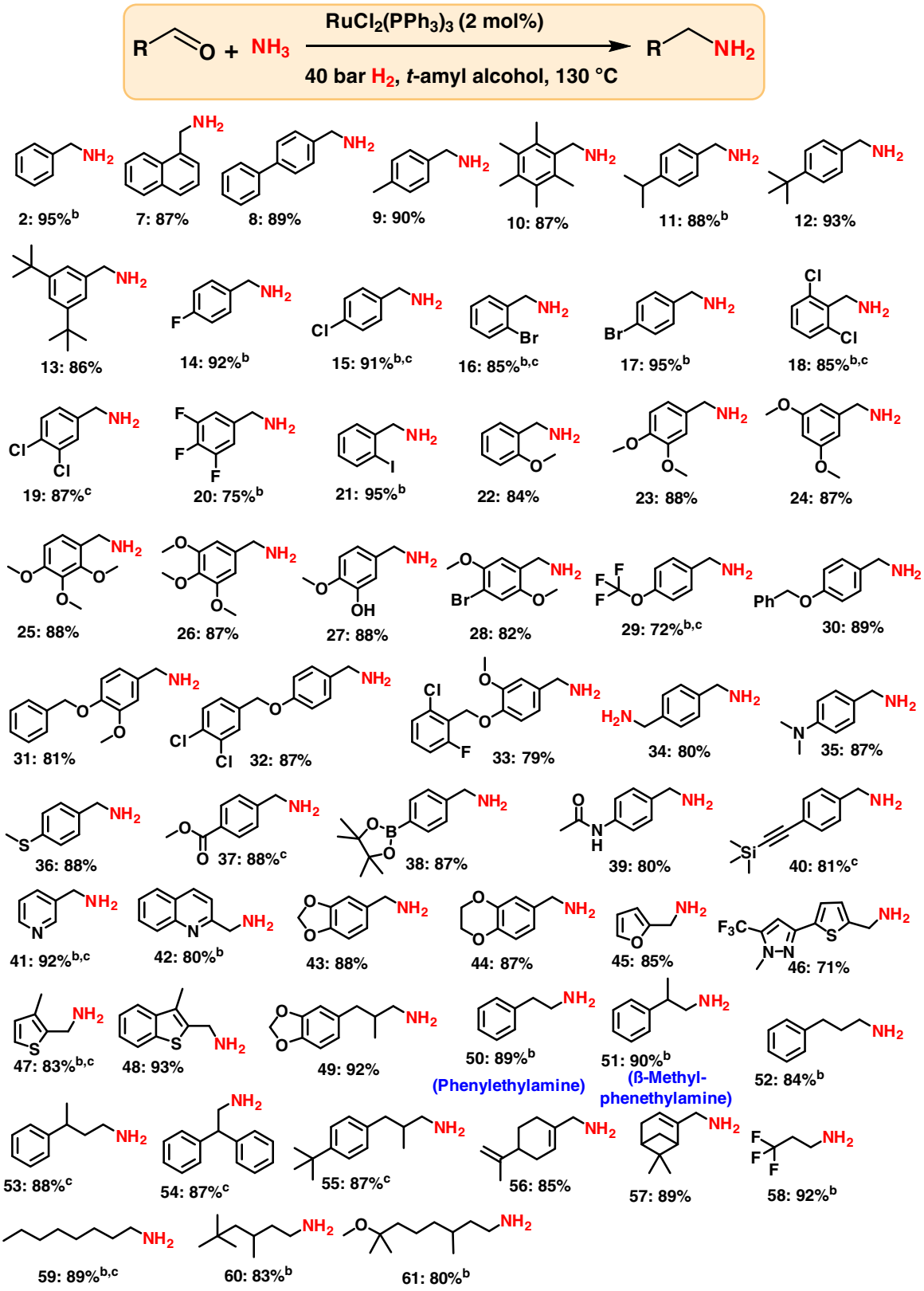

Fig. 2 Ru-catalyzed synthesis of linear primary benzylic, heterocyclic, and aliphatic amines. [a]Reaction conditions: [a]0.5 mmol aldehyde, 2 mol% $RuCl_2(PPh_3)_3$, 5–7 bar NH_3, 40 bar H_2 1.5 mL *t*-amyl alcohol, 130 °C, 24 h, isolated yields. [b]GC yields using n-hexadecane as standard. [c]same as 'a' for 30 h. Isolated as free amines and converted to hydrochloride salts. Corresponding hydrochloride salts were subjected to NMR analysis

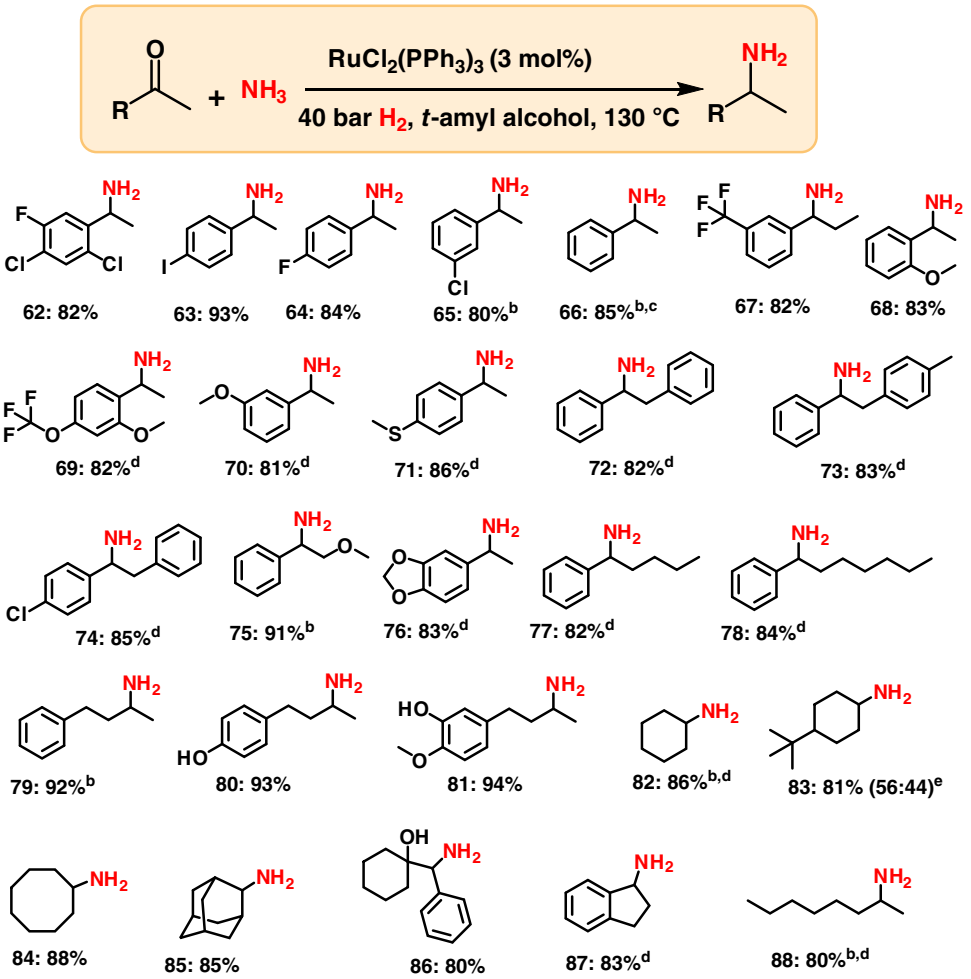

Fig. 3 $RuCl_2(PPh_3)_3$-catalyzed synthesis of branched primary amines from ketones. [a]Reaction conditions: 0.5 mmol ketone, 3 mol% $RuCl_2(PPh_3)_3$, 5–7 bar NH_3, 40 bar H_2 1.5 mL *t*-amyl alcohol, 130 °C, 24 h, isolated yields. [b]GC yields using n-hexadecane as standard. [c]Same as 'a' with 1 mol% catalyst. [d]Same as 'a' for 30 h. [e]Diastereomeric ratio. Isolated as free amines and converted to hydrochloride salts. Corresponding hydrochloride salts were subjected to NMR analysis

Synthesis of branched primary amines from ketones. After having successfully performed the reductive amination of aldehydes, we were interested in the general applicability of this ruthenium precatalyst for the synthesis of branched primary amines starting from different ketones (Fig. 3). Compared to aldehydes, the reaction of ketones with ammonia to form primary amines is more difficult. Remarkably, the $RuCl_2(PPh_3)_3$ precatalyst is also active towards aromatic ketones (Fig. 3). Further, the applicability of this catalyst system was also explored for aliphatic ketones. Here, the aliphatic branched primary amines were obtained in up to 94% yield (Fig. 3).

Applications to life science molecules. To showcase the valuable applications of this amination protocol, we carried out the preparation of existing drugs as well as the introduction of $-NH_2$ moieties into drugs and complex molecules. The amination of important drugs such as Nabumetone, Pentoxifylline, and Azaperone (Fig. 4; products **92–94**) as well as steroid derivatives has been demonstrated (Fig. 4; products **95–97**). Such an insertion of amino groups into life science molecules represents a resourceful technique for further functionalization and modulation of their activities, which is highly useful in drug discovery.

Upscaling for the preparation of amines on gram-scale. In order to show practical utility and to demonstrate potential for implementation in industrial production, the upscaling of synthetic methodologies is very important. Especially in homogeneous catalysis upscaling is a challenging task. Therefore, to demonstrate the applicability of this homogeneous catalytic amination protocol, we performed gram-scale synthesis of six selected amines. As shown in (see Supplementary Figure 1), 2–10 g of four aldehydes and two ketones were successfully aminated to yield their corresponding primary amines in more or less similar yields to those of 50–100 mg scale reactions.

We were interested to compare our methodology to an established amination protocol. The Leuckart-Wallach reaction is a prime example, finding application also on an industrial scale[39–41]. We therefore subjected 15 aldehydes and ketones, which have been studied in this work, to Leuckart-Wallach reaction conditions[39–41] to prepare the corresponding primary amines. As shown in Supplementary Table 1, the reaction worked well for simple aldehydes/ketones and gave 53–75% of corresponding primary amines (Supplementary Table 1; entries 1–3). For a majority of substituted and structurally diverse as well as heterocyclic aldehydes and ketones it gave poor yields (5–15%) (Supplementary Table 1; entries 4–9). The Leuckart-Wallach reaction failed to yield the desired primary amine for sensitive substrates (e.g., TMS or halogen containing) as well as some (hetero)cyclic and steroid derivatives (Supplementary Table 1; entries 10–15). A majority of the sensitive functional groups were

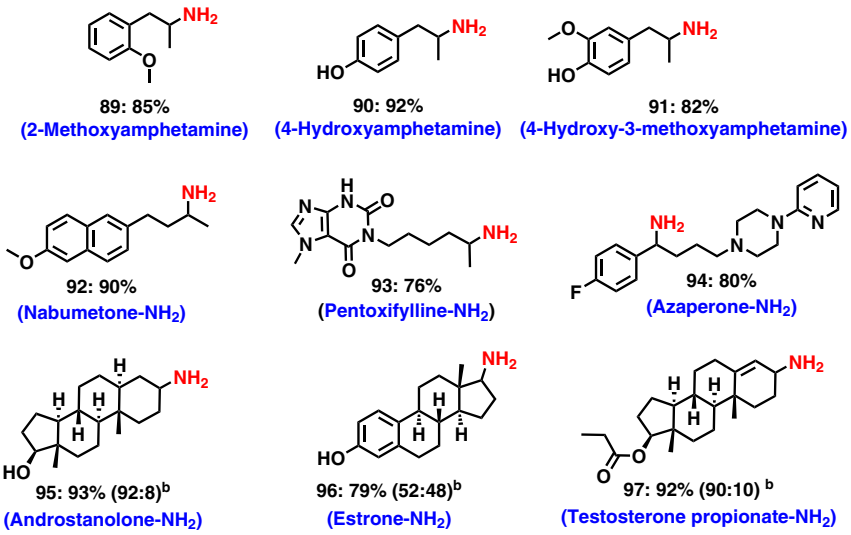

Fig. 4 Synthesis of drugs and amination of complex molecules. [a]Reaction conditions: 0.5 mmol ketone, 3 mol% $RuCl_2(PPh_3)_3$, 5–7 bar NH_3, 40 bar H_2 1.5 mL t-amyl alcohol, 130 °C, 24 h, isolated yields. Isolated as free amines and converted to hydrochloride salts. Corresponding hydrochloride salts were subjected to NMR analysis. [b]Diastereomeric ratio

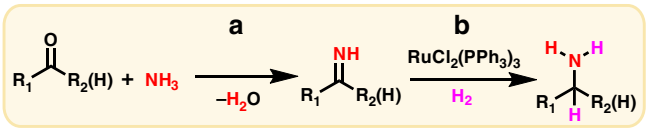

Fig. 5 Ru-catalyzed reductive amination of carbonyl compounds with NH_3 using H_2. **a** Noncatalytic condensation reaction; **b** catalytic hydrogenation reaction

not tolerated. Gratifyingly, for all these substrates, the $RuCl_2(PPh_3)_3$ precatalyst using ammonia and hydrogen worked well and produced the corresponding primary amines in 72–93% yields. These results clearly reveal that catalytic reductive amination using $RuCl_2(PPh_3)_3$ is more generally applicable for the preparation of primary amines compared to the traditional Leuckart-Wallach reaction.

Discussion

A general reaction pathway for the catalytic reductive amination of carbonyl compounds is shown in Fig. 5. Initially, the carbonyl compound undergoes condensation with ammonia to form the corresponding primary imine. Subsequently, the intermediate imine is hydrogenated to give the primary amine. The hydrogenation step is catalyzed by a catalytic species derived from the precatalyst, $RuCl_2(PPh_3)_3$.

We were interested to gain mechanistic insight into the hydrogenation step and to determine the nature of the active catalyst species. For this purpose, we studied the interaction of $RuCl_2(PPh_3)_3$ with hydrogen using in situ NMR in a model system consisting solely of the ruthenium precatalyst, methanol and C_6D_6. Figure 6 depicts the hydride region of the obtained ^1H NMR spectra. Initially, even in the absence of H_2, a quartet at $\delta_H = -17.6$ ppm is observed along with a broad singlet at $\delta_P = 55$ ppm in the $^{31}P\{^1H\}$ NMR spectrum (see SI). We assign these signals to $[RuHCl(PPh_3)_3]$[63], which is likely formed in small amounts via methanol oxidation. In presence of H_2 (1.5 bar) at room temperature, the quartet corresponding to $[RuHCl(PPh_3)_3]$ broadens[63] and two new hydride signals appear: a broad singlet at $\delta_H = -12.5$ ppm and a triplet of triplets at $\delta_H = -10.9$ ppm. Using ^1H-^{31}P HMBC NMR (see Supplementary Figures 6–13) we were able to assign the hydride triplet of triplets to two multiplets in the $^{31}P\{^1H\}$ NMR spectrum (at $\delta_P = 34.8$ ppm and $\delta_P = 58.4$ ppm; see SI), which is consistent with the structure of $[Ru(H)_2(PPh_3)_4]$[64]. We tentatively assign the broad singlet at $\delta_H = -12.5$ ppm to $[Ru(H)_2(PPh_3)_3]$, which is corroborated by the appearance of a broad signal at $\delta_P = 58$ ppm in the $^{31}P\{^1H\}$ NMR spectrum[65]. $[Ru(H)_2(PPh_3)_3]$ would be in equilibrium with $[Ru(H)_2(PPh_3)_4]$ via association/dissociation of a PPh_3 ligand. After 2.5 h at room temperature a new triplet at $\delta_H = -9.4$ ppm appears in the hydride region, which further increases in intensity upon heating to 60 °C. Using ^1H-^{31}P HMBC NMR we could assign this hydride signal to a singlet in the $^{31}P\{^1H\}$ NMR spectrum at $\delta_P = 50.4$ ppm (see Supplementary Figures 6–13). After 1.5 h at 60 °C, it is the dominant species in the hydride region and in the $^{31}P\{^1H\}$ NMR spectrum. The triplet hydride splitting (37 Hz), which collapses to a singlet in the $^1H\{^{31}P\}$ NMR spectrum (see Supplementary Figures 6–13), indicates the presence of just two equivalent PPh_3 ligands. When the $^{31}P\{^1H\}$ NMR experiment is decoupled with reduced power (only aromatic protons are decoupled) the singlet at $\delta_P = 50.4$ ppm splits into a doublet (see Supplementary Figures 6–13)), indicating a monohydride structure. Although this species appears to have only two PPh_3 and one hydride ligand, its accumulation indicates high stability under experimental conditions, suggesting the presence of other stabilizing ligands (such as CO). Since $[Ru(H)_2(PPh_3)_3]$ is known to decarbonylate methanol[66] and due to similar spectral characteristics compared to $[RuHCl(CO)(PPh_3)_2(pyrazine)]$[67] we tentatively assign this species to the carbonyl-containing complex $[RuHCl(CO)(PPh_3)_2(Y)]$ (with Y possibly being a solvent molecule) formed via methanol decarbonylation.

An overview of the proposed transformation of $RuCl_2(PPh_3)_3$ in our model system is provided in Fig. 7: $RuCl_2(PPh_3)_3$ undergoes a stepwise reaction with H_2 to form $[RuHCl(PPh_3)_3]$ (which is also generated by the reaction with methanol) and $Ru(H)_2(PPh_3)_3$, which is in equilibrium with $Ru(H)_2(PPh_3)_4$. $Ru(H)_2(PPh_3)_3$ can further react via alcohol decarbonylation to form the carbonyl-containing complex $[RuHCl(CO)(PPh_3)_2(Y)]$. While methanol is not present under our reaction conditions for reductive amination, it is known that $RuCl_2(PPh_3)_3$ can also enable the decarbonylation of benzyl alcohols and aldehydes[65], which constitute a majority of our substrates.

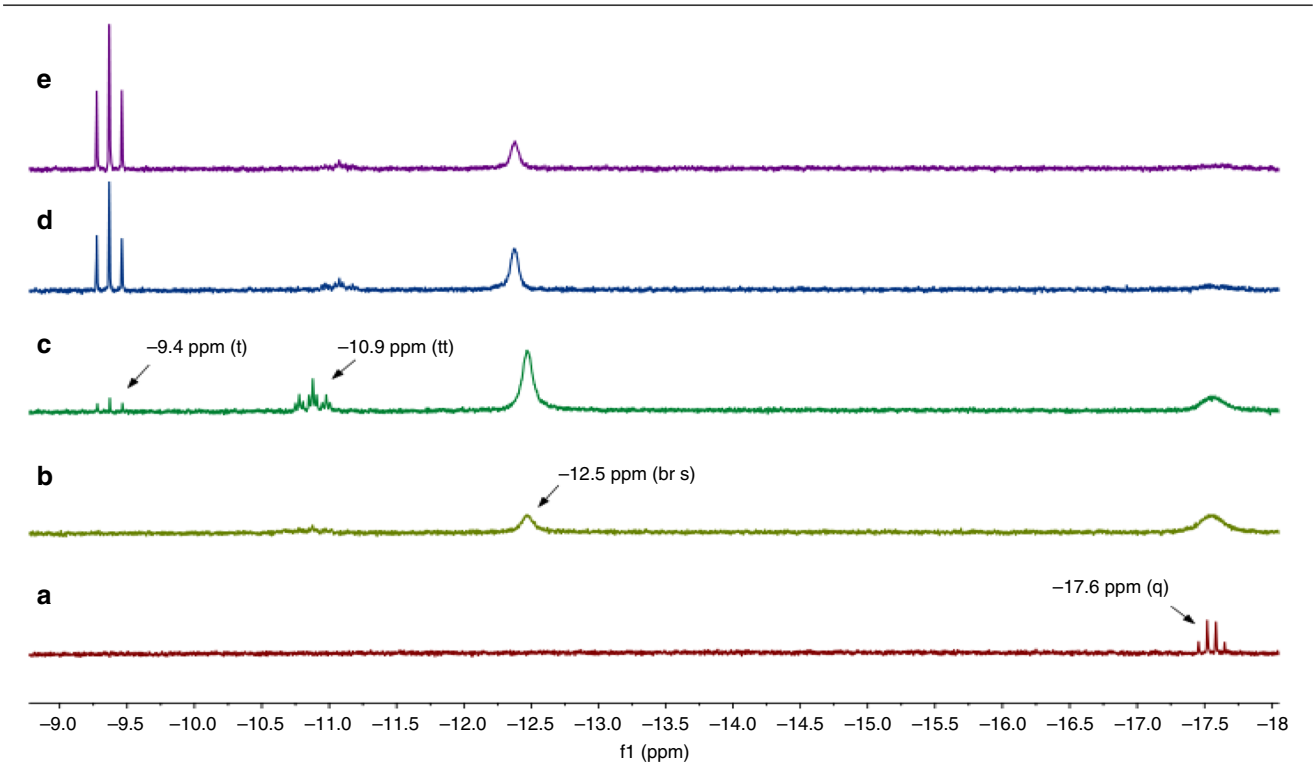

Fig. 6 Hydride region of ^{1}H NMR spectra of $RuCl_2(PPh_3)_3$ in C_6D_6/methanol. **a** RT, argon atmosphere; **b** RT, H_2 atmosphere (1.5 bar), 10 min; **c** RT, H_2 atmosphere (1.5 bar), 2.5 h; **d** 60 °C, H_2 atmosphere (1.5 bar), 30 min; **e** 60 °C, H_2 atmosphere (1.5 bar), 1.5 h

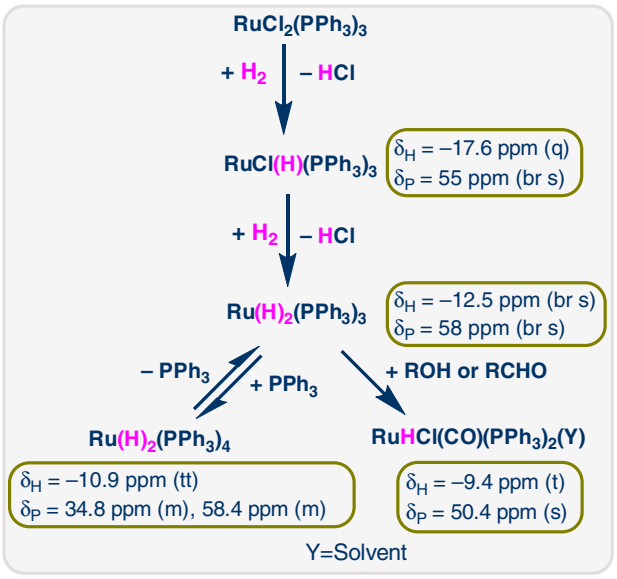

Fig. 7 Generation of different species from $RuCl_2(PPh_3)_3$ in presence of hydrogen. $RuCl_2(PPh_3)_2$ = precatalyst; $Ru(H)Cl(PPh_3)_3$ and $Ru(H)_2(PPh_3)_3$ = active catalytic species

Also, a number of previously reported ruthenium systems for reductive amination as well as alcohol amination are based on carbonyl-containing (pre-)catalysts[26,27,35–37]. Therefore, the question arises whether our active catalyst contains a carbonyl ligand or if it conforms to a previously proposed $[RuHX(PPh_3)_3]$ structure ($X = H^-$ or Cl^-)[68,69]. To answer this question, we have compared the catalytic performance of $[RuHCl(PPh_3)_3]$ and $[RuHCl(CO)(PPh_3)_3]$ for benzaldehyde amination under standard reaction conditions. Interestingly, $[RuHCl(PPh_3)_3]$ performs similarly to $RuCl_2(PPh_3)_3$ (88% benzylamine, 4% benzyl alcohol, 7% dibenzylamine; Supplementary Figure 2). This confirms that $[RuHCl(PPh_3)_3]$ is part of the transformation cascade (as observed in our model system) which also includes the active catalyst. However, $[RuHCl(CO)(PPh_3)_3]$ showed poor selectivity under our reaction conditions (3% benzylamine, 5% benzyl alcohol, 90% N-benzylidenebenzylamine; Supplementary Figure 3). In addition, a reported $Ru_3(CO)_{12}$/CataCxiumPCy catalytic system, which was used in the amination of alcohols with ammonia[36], was also tested for the reductive amination of cyclohexanone (Supplementary Figure 3). Similarly, this catalyst also showed poor selectivity, yielding only 10% of cyclohexylamine. Therefore, carbonyl-containing complexes are likely not the active species under our reaction conditions. Rather, due to their decreased selectivity, they constitute a possible deactivation pathway for $RuCl_2(PPh_3)_3$ catalyzed reductive amination. This difference between our observations and previously reported carbonyl-containing ruthenium amination catalysts is attributed to the ligand: carbonyl-containing Ru(II) catalysts typically require bidentate[26] or tridentate[35] ligands. Control experiments have shown significantly decreased yield in the absence of those additional ligands[26]. In contrast, the carbonyl-free catalyst type $[RuHX(PPh_3)_3]$ appears to be sufficiently active and selective with only PPh_3-derived ligands.

After clarifying the pathway for catalyst activation we were interested to investigate the reaction cascade starting from the aldehyde/ketone and ammonia using the benzaldehyde benchmark system. The starting materials can undergo a condensation to form primary imine **A**. Intermediate **A**, however, was never detected in the reaction mixture, presumably due to its high reactivity. Instead (as can be seen in Fig. 1a), secondary imine **4** was determined to be the major intermediate. **4** is formed via condensation of the product **2** with either the starting aldehyde/ketone (releasing water) or via condensation of **2** and **A** (releasing

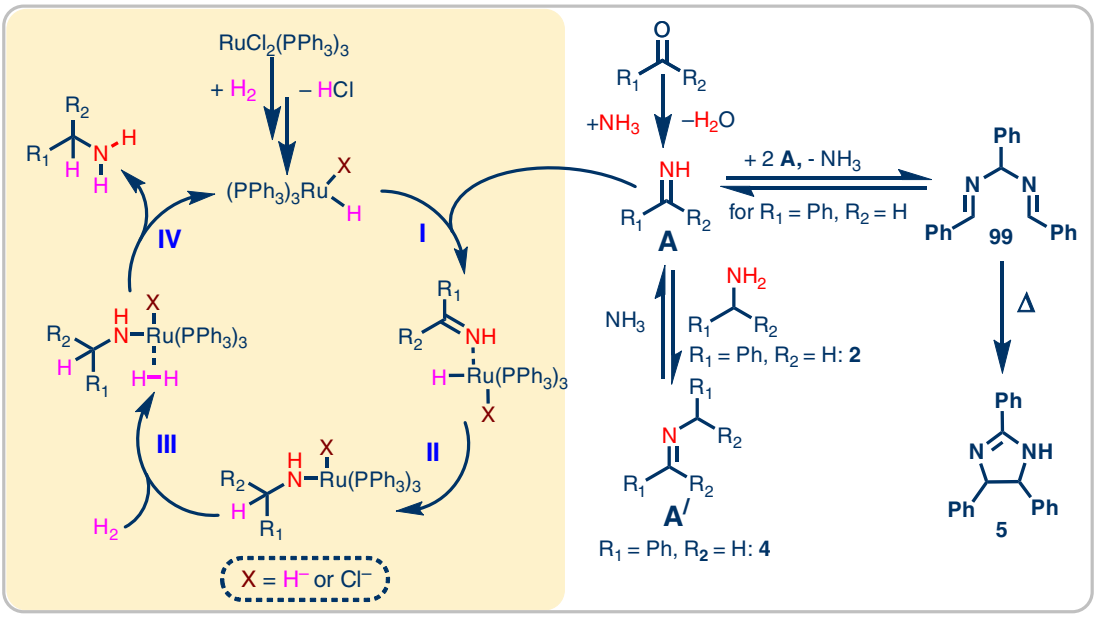

Fig. 8 Proposed reaction mechanism for the $RuCl_2(PPh_3)_3$-catalyzed reductive amination. **A** Unstable primary imine; **A**′ stable secondary imine. **5** = 2,4,5-triphenyl-2-imidazoline

NH_3). We next reacted isolated **4** under our standard reaction conditions (40 bar H_2, 5–7 bar NH_3, 24 h, $RuCl_2(PPh_3)_3$) and found almost quantitative conversion to **2** (Supplementary Figure 4). In contrast, when **4** was reacted in the absence of ammonia, 98% dibenzylamine was obtained after 24 h (Supplementary Figure 4). These results show that **4**, when exposed to NH_3, is in an equilibrium with **A** + **2**[70]. While the catalyst is able to hydrogenate both **A** and **4**, **A** is hydrogenated preferentially and is replenished by the equilibrium with **4**. If ammonia is absent or only present in low concentrations (see Fig. 1e), the formation of **A** + **2** from **4** is suppressed, leading to hydrogenation of **4** (yielding dibenzlamine). Furthermore, due to rapid hydrogenation under optimized conditions, the stationary concentration of **A** is low, precluding side reactions of this reactive intermediate. When the hydrogenation does not proceed quickly, however, accumulation and side reactions involving **A** can likely occur. Correspondingly, when a mixture of **4** and benzaldehyde was reacted under standard conditions but without H_2, 20% of the cyclic side-product **5** was obtained (the rest being unreacted starting material, see Supplementary Figure 5). Williams et al.[71] and Corey et al.[72] have reported that **A** can trimerize to form **99**, which can subsequently undergo thermal cyclization to form **5** (Fig. 8). This reaction of accumulated **A** likely explains the formation of large amounts of **5** in less active catalyst systems (see Table 1, entries 1–10; Fig. 1).

Based on these observations we propose the following mechanism (Fig. 8): Reaction of a carbonyl compound with NH_3 yields primary imine **A**, which can be in an equilibrium with secondary imine **A**′ via condensation with the product amine. The precatalyst $RuCl_2(PPh_3)_3$ is activated by H_2 to form the the active catalyst species $[RuHX(PPh_3)_3]$ (X being either H^- or Cl^-). This active catalytic species selectively reacts with the primary imine to initially form a substrate complex (**I**). Substrate coordination is followed by hydride insertion (**II**), generating a Ru-amide complex. Coordination of H_2 (**III**) followed by hydrogenolysis releases the primary amine as the final product with regeneration of the catalytic species (**IV**).

In conclusion, we demonstrated that using a simple $RuCl_2(PPh_3)_3$ catalyst, the challenging reductive amination of carbonyl compounds using ammonia and molecular hydrogen for the selective synthesis of a variety of primary amines is possible. Applying this Ru-based reductive amination, starting from inexpensive aldehydes and ketones, functionalized and structurally diverse linear and branched primary amines have been synthesized under industrially viable and scalable conditions. In general, achieving a high degree of chemoselectivity in amination/hydrogenation reactions is a challenging task. In this regard our simple Ru-based methodology represents a unique example in homogeneous catalysis for the reductive amination of functionalized and challenging molecules. We have also shown the possibility of scaling this amination protocol up to 10 g without any loss in either activity or selectivity. The application of this approach is also extended to the synthesis and amination of various drug molecules and steroid derivatives. In situ NMR investigations provided clear hints on the formation of Ru-hydride species, which have been elucidated to be the active catalytic species in this $RuCl_2(PPh_3)_3$-catalyzed reductive amination. With the help of these investigations, an appropriate reaction mechanism has been proposed.

Methods

General considerations. All carbonyl compounds (aldehydes and ketones), Ru-precursors and complexes and ligands, were obtained commercially. All catalytic experiments were carried out in 300, 100, and 500 mL autoclaves (PARR Instrument Company). In order to avoid unspecific reactions, all catalytic reactions were carried out either in glass vials, which were placed inside the autoclave, or glass/Teflon vessel fitted autoclaves. GC and GC-MS were recorded on a Agilent 6890N instrument. GC conversion and yields were determined by GC-FID, HP6890 with FID detector, column HP530 m × 250 mm × 0.25 µm. ^1H, ^{13}C NMR data were recorded on a Bruker AV 300 and Bruker AV 400 spectrometers using DMSO-d_6, CD_3OD or C_6D_6 as solvents. Ru(tris(4-methoxyphenyl)phosphine)$_3Cl_2$ and Ru(tris(4-chlorophenyl)phosphine)$_3Cl_2$ were prepared according to the reported procedure[73].

Reductive amination of carbonyl compounds with ammonia. The 8 mL dried glass vial was charged with a magnetic stirring bar and 0.5 mmol of corresponding carbonyl compound (aldehyde or ketone). Then 1.5 mL t-amyl alcohol as solvent and 2–3 mol% $RuCl_2(PPh_3)_3$ catalysts (2 mol% in case of aldehydes and 3 mol% in case of ketones) were added. The glass vial was fitted with a septum, cap and needle, and placed into a 300 mL autoclave (eight vials with different substrates at a time). The autoclave was flushed with hydrogen twice at 40 bar pressure and then it was pressurized with 5–7 bar ammonia gas and 40 bar hydrogen. The autoclave was

placed into an aluminum block preheated at 140 °C (placed inside 30 min before counting the reaction time in order to attain the reaction temperature) and the reactions were stirred for the required time. During the reaction the inside temperature of the autoclave was measured to be 130 °C and this temperature was used as the reaction temperature. After completion of the reactions, the autoclave was cooled to room temperature. The remaining ammonia and hydrogen were discharged and the vials containing reaction products were removed from the autoclave. The reaction products were analyzed by GC-MS and the corresponding primary amines were purified by column chromatography (silica; n-hexane-ethyl acetate mixture). The resulting amines were converted to their respective hydrochloride salt and characterized by NMR. For conversion into the hydrochloride salt, 1–2 mL methanolic HCl or dioxane HCl (1.5 M HCl in methanol or 4 N HCl in dioxane) was added to the ether solution of the respective amine and stirred at room temperature for 4–5 h. Then, the solvent was removed and the resulting hydrochloride salt of the amine was dried under high vacuum. For determining the yields by GC for selected amines, after completion of the reaction n-hexadecane (100 µL) as standard was added to the reaction vials and the reaction products were diluted with ethyl acetate followed by filtration using a plug of silica and then analyzed by GC.

General procedure for the gram scale reactions. The Teflon or glass fitted 300 (5–10 g) or 500 mL (20 g) (in case 5–20 g) or 100 mL (in case of 2–2.5 g) autoclave was charged with a magnetic stirring bar and the corresponding carbonyl compound (2–20 g). Then 25–150 mL t-amyl alcohol was added. Subsequently, $RuCl_2(PPh_3)_3$ (amount of catalysts equivalent to 2–3 mol%) was added. The autoclave was flushed with hydrogen twice at 40 bar pressure and then it was pressurized with 5–7 bar ammonia gas and 40 bar hydrogen. The autoclave was placed into an aluminum block preheated to 140 °C (placed 30 min before counting the reaction time in order to attain reaction temperature) and the reaction was stirred for the required time. During the reaction the inside temperature of the autoclave was measured to be 130 °C and this temperature was used as the reaction temperature. After completion of the reaction, the autoclave was cooled to room temperature. The remaining ammonia and hydrogen were discharged and the reaction products were removed from the autoclave. The reaction products were analyzed by GC-MS and the corresponding primary amines were purified by column chromatography (silica; n-hexane-ethyl acetate mixture). The resulting amines were converted to their respective hydrochloride salt and characterized by NMR.

Procedure for the in situ NMR studies. The in situ observation of the Ru-hydrides was performed under hydrogen saturation conditions in a 5 mm glass NMR tube, equipped with a PTFE gas inlet hose and a circulation unit which produces a continuous gas flow through the solution[74,75]. The brown solution of the precursor complex $RuCl_2(PPh_3)_3$ (50 mg) in 0.5 mL methanol/0.5 mL benzene-d6 was transferred to the NMR tube under Ar. After assembling the device under inert gas and characterizing the solution by its ^1H and ^{31}P NMR spectra, the system was filled with neat hydrogen (absolute pressure 1.5 bar). A gas flow of 1 mL min^{-1} was used to saturate the solution. ^1H and ^{31}P NMR spectra were taken at regular intervals to monitor the reaction progress. Changes were immediately observable as shown in Fig. 2. After three hours, the temperature was raised and kept at about 60 °C for another three hours to complete the reaction. No further changes were detected thereafter. The color of the solution was changed to brick-red at the end of the experiment. Note that maintaining a continuous gas flow till the very end was not possible, because black particles of precipitating metallic Ru were clogging the tubing.

Data availability

All data are available from the authors upon reasonable request.

Received: 4 May 2018 Accepted: 4 September 2018
Published online: 08 October 2018

References

1. Lawrence, S. A. *Amines: Synthesis, Properties and Applications*. (Cambridge University Press, Cambridge, UK, 2004).
2. Ricci, A. *Amino Group Chemistry: From Synthesis to the Life Sciences*. (Wiley-VCH, Weinheim, 2008).
3. Smith, D. T., Delost, M. D., Qureshi, H. & Njarðarson, J. T. Top 200 Pharmaceutical Products by Retail Sales in 2016. https://njardarson.lab.arizona.edu/sites/njardarson.lab.arizona.edu/files/2016Top200PharmaceuticalRetailSalesPosterLowResV3_0.pdf (2017).
4. Roughley, S. D. & Jordan, A. M. The medicinal chemist's toolbox: an analysis of reactions used in the pursuit of drug candidates. *J. Med. Chem.* **54**, 3451–3479 (2011).
5. Froidevaux, V., Negrell, C., Caillol, S., Pascault, J.-P. & Boutevin, B. Biobased amines: from synthesis to polymers; present and future. *Chem. Rev.* **116**, 14181–14224 (2016).
6. Mao, R., Frey, A., Balon, J., Hu, X. & Decarboxylative, C. (sp^3)–N cross-coupling via synergetic photoredox and copper catalysis. *Nat. Catal.* **1**, 120–126 (2018).
7. Gomez, S. A., Peters, J. A. & Maschmeyer, T. The reductive amination of aldehydes and ketones and the hydrogenation of nitriles: mechanistic aspects and selectivity control. *Adv. Synth. Catal.* **344**, 1037–1057 (2002).
8. Alinezhad, H., Yavari, H. & Salehian, F. Recent advances in reductive amination catalysis and its applications. *Curr. Org. Chem.* **19**, 1021–1049 (2015).
9. Nugenta, T. C. & El-Shazlya, M. Chiral amine synthesis-recent developments and trends for enamide reduction, reductive amination, and imine reduction. *Adv. Synth. Catal.* **352**, 753–819 (2010).
10. Wakchaure, V. N., Zhou, J., Hoffmann, S. & List, B. Catalytic asymmetric reductive amination of α-branched ketones. *Angew. Chem. Int. Ed.* **49**, 4612–4614 (2010).
11. Chusov, D. & B. List, B. Reductive amination without an external hydrogen source. *Angew. Chem. Int. Ed.* **53**, 5199–5201 (2014).
12. Natte, K., H. Neumann, H., Jagadeesh, R. V. & Beller, M. Convenient iron-catalyzed reductive aminations without hydrogen for selective synthesis of N-methylamines. *Nat. Commun.* **8**, 1344 (2017).
13. Jagadeesh, R. V. et al. Hydrogenation using iron oxide–based nanocatalysts for the synthesis of amines. *Nat. Protoc.* **10**, 548–557 (2015).
14. Reductive amination. https://www.reagentguides.com/reagent-guides/reductive-amination (2015).
15. Gusak, K. N., Ignatovich, Z. V. & Koroleva, E. V. New potential of the reductive alkylation of amines. *Russ. Chem. Rev.* **84**, 288–309 (2015).
16. Senthamarai, T. et al. Expedient synthesis of N-methyl- and N-alkylamines by reductive amination using reusable cobalt oxide nanoparticles. *ChemCatChem* **10**, 1235–1240 (2018).
17. Jagadeesh, R. V. et al. MOF-derived cobalt nanoparticles catalyze a general synthesis of amines. *Science* **358**, 326–332 (2017).
18. Komanoya, T., Kinemura, T., Kita, Y., Kamata, Y. K. & Hara, M. Electronic effect of ruthenium nanoparticles on efficient reductive amination of carbonyl compounds. *J. Am. Chem. Soc.* **139**, 11493–11499 (2017).
19. Nakamura, Y., Kon, K., Touchy, A. S., Shimizu, K.-i. & Ueda, W. Selective synthesis of primary amines by reductive amination of ketones with ammonia over supported Pt catalysts. *ChemCatChem* **7**, 921–924 (2015).
20. Liang, G. et al. Production of primary amines by reductive amination of biomass-derived aldehydes/ketones. *Angew. Chem. Int. Ed.* **56**, 3050–3054 (2017).
21. Wang, Z. Mignonac reaction. In *Comprehensive organic name reactions and reagents*. (John Wiley & Sons, New Jersey, 2010).
22. Chatterjee, M., Takayuki Ishizakaa, T. & Kawanami, H. Reductive amination of furfural to furfurylamine using aqueous ammonia solution and molecular hydrogen: an environmentally friendly approach. *Green. Chem.* **18**, 487–496 (2016).
23. Reductive amination review. https://erowid.org/archive/rhodium/chemistry/reductive.amination.html (2004).
24. Gross, T., Seayad, A. M., Ahmad, M. & Beller, M. Synthesis of primary amines: first homogeneously catalyzed reductive amination with ammonia. *Org. Lett.* **4**, 2055–2058 (2002).
25. Riermeier, T. et al. Method for producing amines by homogeneously catalyzed reductive amination of carbonyl compounds. *US* **6**, 884–887 B1 (2005).
26. Gallardo-Donaire, J., Ernst, M., Trapp, O. & Schaub, T. Direct synthesis of primary amines via ruthenium-catalysed amination of ketones with ammonia and hydrogen. *Adv. Synth. Catal.* **358**, 358–363 (2016).
27. Gallardo-Donaire, J. et al. Direct asymmetric ruthenium-catalyzed reductive amination of alkyl-aryl ketones with ammonia and hydrogen. *J. Am. Chm. Soc.* **140**, 355–361 (2018).
28. Ogo, S., Uehara, K., Abura, T. & Fukuzumi, S. pH-Dependent chemoselective synthesis of α-amino acids. Reductive amination of α-keto acids with ammonia catalyzed by acid-stable iridium hydride complexes in water. *J. Am. Chm. Soc.* **126**, 3020–3021 (2004).
29. Kadyrov, R. & Riermeier, T. H. Highly enantioselective hydrogen-transfer reductive amination: catalytic asymmetric synthesis of primary amines. *Angew. Chem. Int. Ed.* **42**, 5472–5474 (2003).
30. Tan, X. et al. Asymmetric synthesis of chiral primary amines by ruthenium-catalyzed direct reductive amination of alkyl aryl ketones with ammonium salts and molecular H_2. *J. Am. Chem. Soc.* **140**, 2024–2027 (2018).
31. Yan, T., Feringa, B. L. & Barta, K. Iron catalysed direct alkylation of amines with alcohols. *Nat. Commun.* **5**, 5602 (2014).
32. Meindl, W. R., Angerer, E. V., Schoenenberger, H. & Ruckdeschel, G. Benzylamines: synthesis and evaluation of antimycobacterial properties. *J. Med. Chem.* **27**, 1111–1118 (1984).
33. Yan, T., Feringa, B. L. & Barta, K. Direct N-alkylation of unprotected amino acids with alcohols. *Sci. Adv.* **3**, eaao6494 (2017).
34. Goldacre, R. J. Mode of action of benzylamine sulphonamide ('Marfanil'). *Nature* **154**, 796–797 (1944).

35. Gunanathan, C. & Milstein, D. Selective synthesis of primary amines directly from alcohols and ammonia. *Angew. Chem. Int. Ed.* **47**, 8661–8664 (2008).
36. Imm, S., Bähn, S., Neubert, L., Neumann, H. & Beller, M. An efficient and general synthesis of primary amines by ruthenium-catalyzed amination of secondary alcohols with ammonia. *Angew. Chem Int. Ed.* **49**, 8126–8129 (2010).
37. Pingen, D., Müller, C. & Vogt, D. Direct amination of secondary alcohols using ammonia. *Angew. Chem. Int. Ed.* **49**, 8130–8133 (2010).
38. Bähn, S. et al. The catalytic amination of alcohols. *ChemCatChem* **3**, 1853–1864 (2011).
39. Leuckart, R. Ueber eine neue bildungsweise von tribenzylamin. *Ber* **18**, 2341–2344 (1885).
40. Moore, M. L. *Organic Reactions* (Wiley, Hoboken, NJ, 2011).
41. Crossley, F. S. & Moore, M. L. Studies on Leuckart reaction. *J. Org. Chem.* **9**, 529–536 (1944).
42. Feuer, H. & Braunstein, D. M. Reduction of oximes, oxime ethers, and oxime esters with diborane. *Nov. Synth. Amines J. Org. Chem.* **34**, 1817–1821 (1969).
43. Huang, X. et al. Asymmetric synthesis of primary amines via the spiroborate-catalyzed borane reduction of oxime ethers. *Org. Lett.* **9**, 1793–1795 (2007).
44. Mirjafary, Z., Abdoli, M., Saeidian, H., Boroon, S. & Kakanejadifard, A. Oxime ethers as versatile precursors in organic synthesis: a review. *RSC Adv.* **5**, 79361–79384 (2015).
45. Ammonia. https://pubchem.ncbi.nlm.nih.gov/compound/ammonia (2016).
46. Appl, M. in *Ullmann's Encyclopedia of Industrial Chemistry*, 7th edn. (ed. Wiley-VCH) (Wiley, New York, 2011).
47. van Gysel, A. B. & Musin, W. in *Ullmann's Encyclopedia of Industrial Chemistry*, 7th edn. (ed. Wiley-VCH) (Wiley, New York, 2011).
48. Schirmann, P. & Bourdauducq, J.-P. in *Ullmann's Encyclopedia of Industrial Chemistry*, 7th edn. (ed. Wiley-VCH) (Wiley, New York, 2011).
49. Klinkenberg, J. L. & Hartwig, J. F. Catalytic organometallic reactions of ammonia. *Angew. Chem. Int. Ed.* **50**, 86–95 (2011).
50. Schranck, J. & Tlili, A. Transition-metal-catalyzed monoarylation of ammonia. *ACS Catal.* **8**, 405–418 (2018).
51. Cobb, J. E. et al. In *Encyclopedia of Reagents for Organic Synthesis* (eds. Paquette, L. A. et al.) (John Wiley & Sons, New York, 2004).
52. Burke, S. D. & Danheiser, R. L. *Triphenylphosphine, Handbook of Reagents for Organic synthesis, Oxidizing and Reducing Agents* (Wiley, Hoboken, NJ, 1999).
53. Pignolet, L. M. *Homogeneous Catalysis with Metal Phosphine Complexes* (Springer US, 2013).
54. Wilkinson's catalyst, *Comprehensive Organic Name Reactions and Reagents* (2010).
55. Müller, C. & Vogt, D. Phosphinines as ligands in homogeneous catalysis: Recent developments, concepts and perspectives. *Dalton. Trans.* 5505–5523 (2007).
56. Plummer, J. S., Shun-Ichi, M. & Changjia, Z. Dichlorotris (triphenylphosphine)ruthenium(II), *e-EROS Encyclopedia of Reagents for Organic Synthesis* (John Wiley, 2010).
57. Crabtree, R. H. Homogeneous transition metal catalysis of acceptorless dehydrogenative alcohol oxidation: applications in hydrogen storage and to heterocycle synthesis. *Chem. Rev.* **117**, 9228–9246 (2017).
58. Guillena, G., Ramon, D. J. & Yus, M. Hydrogen autotransfer in the N-alkylation of amines and related compounds using alcohols and amines as electrophiles. *Chem. Rev.* **110**, 1611–1641 (2010).
59. Sameca, J. S. M., Bäckvall, J.-E., Andersson, P. G. & Brandt, P. Mechanistic aspects of transition metal-catalyzed hydrogen transfer reactions. *Chem. Soc. Rev.* **35**, 237–248 (2006).
60. Pingen, D., Lutz, M. & Vogt, D. Mechanistic study on the ruthenium-catalyzed direct amination of alcohols. *Organometallics* **33**, 1623–1629 (2014).
61. Evans, D., Osborn, J. A., Jardine, F. H. & Wilkinson, G. Homogeneous hydrogenation and hydroformylation using ruthenium complexes. *Nature* **208**, 1203–1204 (1965).
62. Wang, G.-Z. & Bäckvall, J. E. Ruthenium-catalysed transfer hydrogenation of imines by propan-2-ol. *Chem. Commun.* 980–982 (1992).
63. Kirss, R. U., Eisenschmid, T. C. & Eisenberg, R. Para hydrogen induced polarization in hydrogenation reactions catalyzed by ruthenium phosphine complexes. *J. Am. Chem. Soc.* **110**, 8564–8566 (1988).
64. Samouei, H., Miloserdov, F. M., Escudero-Adán, E. C. & Grushin, V. V. Solid-state structure and solution reactivity of $[(Ph_3P)_4Ru(H)_2]$ and related Ru(II) complexes used in catalysis: a reinvestigation. *Organometallics* **33**, 7279–7283 (2014).
65. Mazziotta, A. & Madsen, R. Ruthenium-catalyzed dehydrogenative decarbonylation of primary alcohols. *Eur. J. Org. Chem.* **36**, 5417–5420 (2017).
66. Van der Sluys, L. S., Kubas, G. J. & Caulton, K. G. Reactivity of (dihydrogen) dihydridotris(triphenylphosphine)ruthenium. Dimerization to form $(PPh_3)_2(H)Ru(.mu.-H)_3Ru(PPh_3)_3$ and decarbonylation of ethanol under mild conditions. *Organometallics* **10**, 1033–1038 (1991).
67. Małecki, J. G. & Kruszynski, R. Synthesis, crystal and spectroscopic characterization of $[RuHCl(CO)(PPh_3)_2(pyrazine)]$. *J. Coord. Chem.* **60**, 2085–2095 (2007).
68. Aranyos, A., Csjernyik, G., Szabo, K. S. & Bäckvall, J. E. Evidence for a ruthenium dihydride species as the active catalyst in the $RuCl_2(PPh_3)$-catalyzed hydrogen transfer reaction in the presence of base. *Chem. Commun.* 351–352 (1999).
69. Masters, C. Homogeneous Transition-Metal Catalysis: A Gentle Art. 51–55 (Chapman & Hall, 1981).
70. Krupka, J., Dluhoš, L. & Mrózek, L. Evaluation of benzylamine production via reductive amination of benzaldehyde in a slurry reactor. *Chem. Eng. Technol.* **40**, 870–877 (2017).
71. Williams, O. F. & Bailar, J. C. The stereochemistry of complex inorganic compounds. XXIV. Cobalt stibenediamine complexes. *J. Am. Chem. Soc.* **81**, 4464–4469 (1959).
72. Corey, E. J. & Kühnle, F. N. M. A simplified synthesis of (±)−1,2-diphenyl-1,2-diaminoethane (1) from benzaldehyde and ammonia. Revision of the structures of the long-known intermediates "hydrobenzamide" and "amarine. *Tetrahedron Lett.* **38**, 8631–8634 (1997).
73. Samouei, H., Vladimir, V. & Grushin, V. V. New, highly efficient, simple, safe, and scalable synthesis of $[(Ph_3P)_3Ru(CO)(H)_2]$. *Organometallics* **32**, 4440–4443 (2013).
74. Baumann, W., Mansel, S., Heller, D. & Borns, S. Gas bubbles in the NMR tube: an easy way to investigate reactions with gases in the liquid phase. *Magn. Reson. Chem.* **35**, 701–706 (1997).
75. Baumann, W., Börner, A., Selent, D. Gas injection and circulation device for tracking of reactions in the liquid phase involving gaseous reactants under normal and high pressure by means of nuclear magnetic resonance spectroscopy (NMR spectroscopy pressure) under steady state conditions. *DE10333143B4*, 2008.

Acknowledgements

We gratefully acknowledge the European Research Council (EU project 670986-NoNa-Cat) and the State of Mecklenburg-Vorpommern for financial and general support. Financial support by Fonds der Chemischen Industrie (Kekulé-Stipendium n. 102151) for J.S. is also acknowledged. We thank the analytical staff of the Leibniz-Institute for Catalysis, Rostock for their excellent service.

Author contributions

R.V.J., T.S., K.M., M.B., and N.V.K. planned and developed the project. T.S., K.M., R.V.J., J.S., N.V.K., H.N., and P.C.J.K. designed the experiments. T.S. and K.M. performed catalytic experiments. W.B. and J.S. performed in situ NMR experiments. R.V.J., J.S., N.V.K., T.S., K.M., P.C.J.K., and M.B. wrote the paper. R.V.J. and M.B. supervised the project.

Additional information

Supplementary Information accompanies this paper at https://doi.org/10.1038/s41467-018-06416-6.

Competing interests: The authors declare no competing interests.

Reprints and permission information is available online at http://npg.nature.com/reprintsandpermissions/

Publisher's note: Springer Nature remains neutral with regard to jurisdictional claims in published maps and institutional affiliations.

6.5 Mechanistic Understanding of the Heterogeneous, Rhodium-Cyclic(Alkyl)(Amino)Carbene-Catalyzed (Fluoro-)Arene Hydrogenation

D. Moock, M. P. Wiesenfeldt, M. Freitag, S. Muratsugu, S. Ikemoto, R. Knitsch, J. Schneidewind, W. Baumann, A. H. Schäfer, A. Timmer, M. Tada, M. R. Hansen, F. Glorius*, *ACS Catalysis* **2020**, *10, 11,* 6309-6317

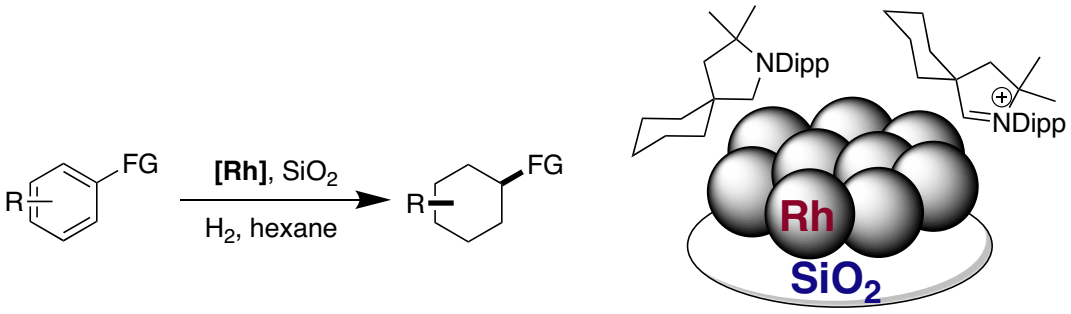

Contributions: Together with W.B., I planned and performed *in situ* NMR experiments. I analyzed the resulting data, curated information for the supporting information and revised the manuscript. Overall, my contribution amounts to ca. 5%.

Abstract: Recently, chemoselective methods for the hydro-genation of fluorinated, silylated, and borylated arenes have been developed providing direct access to previously unattainable, valuable products. Herein, a comprehensive study on the employed rhodium-cyclic(alkyl)(amino)carbene (CAAC) catalyst precursor is disclosed. Mechanistic experiments, kinetic studies, and surface-spectroscopic methods revealed supported rhodium(0) nano- particles (NP) as the active catalytic species. Further studies suggest that CAAC-derived modifiers play a key role in determining the chemoselectivity of the hydrogenation of fluorinated arenes, thus offering an avenue for further tuning of the catalytic properties.

ACS Catalysis

pubs.acs.org/acscatalysis

Research Article

Mechanistic Understanding of the Heterogeneous, Rhodium-Cyclic (Alkyl)(Amino)Carbene-Catalyzed (Fluoro-)Arene Hydrogenation

Daniel Moock, Mario P. Wiesenfeldt,[×] Matthias Freitag,[×] Satoshi Muratsugu, Satoru Ikemoto, Robert Knitsch, Jacob Schneidewind, Wolfgang Baumann, Andreas H. Schäfer, Alexander Timmer, Mizuki Tada, Michael Ryan Hansen, and Frank Glorius*

Cite This: *ACS Catal.* 2020, 10, 6309–6317

Read Online

ACCESS | Metrics & More | Article Recommendations | Supporting Information

ABSTRACT: Recently, chemoselective methods for the hydrogenation of fluorinated, silylated, and borylated arenes have been developed providing direct access to previously unattainable, valuable products. Herein, a comprehensive study on the employed rhodium-cyclic (alkyl)(amino)carbene (CAAC) catalyst precursor is disclosed. Mechanistic experiments, kinetic studies, and surface-spectroscopic methods revealed supported rhodium(0) nanoparticles (NP) as the active catalytic species. Further studies suggest that CAAC-derived modifiers play a key role in determining the chemoselectivity of the hydrogenation of fluorinated arenes, thus offering an avenue for further tuning of the catalytic properties.

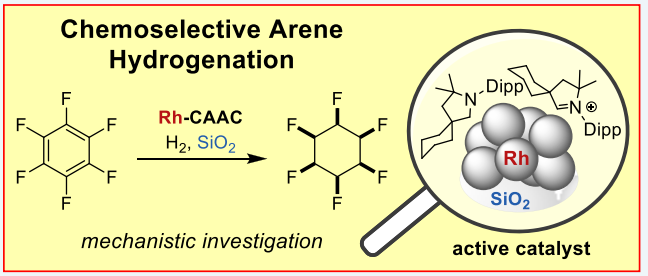

KEYWORDS: *heterogeneous catalysis, rhodium, arene hydrogenation, fluoroarenes, CAAC, nanoparticles, on-surface*

Arene hydrogenation is a powerful tool to transform readily available, planar starting materials into complex, three-dimensional building blocks.[1] These are of interest, e.g., in pharmaceutical research, and can often not be synthesized efficiently with other methods.[2] The control of the chemoselectivity, vital for the synthesis of functionalized cyclic saturated building blocks, is difficult, since very few catalysts are able to overcome the aromatic stabilization energy in absence of harsh conditions. Especially functional groups directly attached to the aromatic ring constitute a daunting challenge due to the generally prevalent hydrodefunctionalization side reaction. The bench-stable rhodium cyclic (alkyl)(amino)carbene (CAAC) precatalyst **1** in combination with a suitable additive (e.g., molecular sieves or silica gel) was essential in our recent studies on the hydrogenation of arenes bearing directly attached fluorine,[3a,b] silyl[3c] and boryl substituents,[3d] and the consecutive dearomatization-hydrogenation of fluorinated pyridines.[4] Building on research by the Bertrand group on the synthesis of CAACs[5] and their rhodium complexes,[6] this catalyst was first used by Zeng and co-workers in the preferential hydrogenation of arenes in the presence of carbonyl groups, showing a good tolerance of functional groups.[7] Although some other catalysts have proven competent in our studies, the active catalyst derived from Rh-CAAC **1** has shown a superior functional group preservation, especially for difficult substrates with fluoro, silyl, and boryl moieties.[3] Given the high synthetic utility of this precatalyst, we became interested in elucidating the catalytically active species. A general challenge in arene hydrogenation is the distinction between active homogeneous and heterogeneous species.[8] In fact, many active catalysts that were initially described as homogeneous, as they are derived from homogeneous precursors, have since been shown to actually be heterogeneous in nature.[9] The Zeng group originally assumed that the active catalyst derived from **1** is of homogeneous nature due to a mercury droplet test.[7] However, during the course of our mechanistic investigation, two studies by the Bullock group appeared providing experimental evidence for rhodium nanoparticles (NP) as active catalysts.[10] In their system, $AgBF_4$ was used to abstract chloride from **1** and initiate NP formation in the absence of another additive. Based on rhodium K-edge X-ray absorption fine structure (XAFS) analysis and IR spectroscopy (among other experiments), the authors determined that rhodium(0) NPs, which are stabilized by pyrrolidinium cation **2** (derived from the CAAC **1a** in the precursor), are the active catalyst in their case.[10a] Although Bullock and co-workers provided a thorough investigation of the active catalytic species derived from activation with $AgBF_4$, the studied conditions differ significantly from the ones found optimal in our hydrogenation methods. Most importantly, no

Received: March 4, 2020
Revised: May 4, 2020
Published: May 5, 2020

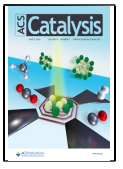

https://dx.doi.org/10.1021/acscatal.0c01074
ACS Catal. 2020, 10, 6309–6317

hydrogenation of fluorinated arenes was attempted and a silver salt was used to activate the precatalyst via a cationic pathway as opposed to molecular sieves or silica gel in our case. The resulting species derived from activation with $AgBF_4$ was evaluated by us for the hydrogenation of fluorinated arenes and proved inefficient. In fact, multifluorinated substrates such as hexafluorobenzene failed to provide any product when using an $AgBF_4$-activated precatalyst (see page S17).

Hence, a complementary study on the identity and understanding of the active catalyst system obtained in the presence of an additive like silica gel was needed. Ideally, such a study would provide a more detailed view on the chemoselective arene hydrogenation and allow for rational modifications of the catalyst in the future.

DIFFERENTIATION BETWEEN A HOMOGENEOUS AND A HETEROGENEOUS ACTIVE CATALYST

Inspired by the extensive work of the Finke group on the differentiation between heterogeneous and homogeneous active catalysts in arene hydrogenation,[8a,b,9] we began our studies with mechanistic experiments that aimed to distinguish an active heterogeneous from an active homogeneous catalyst (Figure 1). Our initial assumption of a heterogeneous reaction pathway was driven by various "telltale" signs observed during our previous studies, including the need of a stabilizing additive such as molecular sieves or silica gel, formation of a dark precipitate, and an observed induction period. In contrast to Zeng et al., we have observed a loss of catalytic activity in the presence of mercury, albeit under different reaction conditions. For the droplet test, see page S20. The conditions of the two droplet tests are adapted from the standard reaction conditions of either method, respectively, which are considerably different from one another, although both methods start with precatalyst **1**. However, the challenging reproducibility and strong dependence on reaction conditions is a known, inherent problem for mercury droplet tests and thus neither of the two possible outcomes can be used to unequivocally differentiate hetero- from homogeneous catalysis pathways and should be complemented with further experiments.[8a,b,11] Substoichiometric poisoning with tetrahydrothiophene showed the loss of catalytic activity in the reaction (see Table S3).[12] This points towards a heterogeneous active catalyst, since reactive sites would be buried inside the particles in such a system, thus requiring less than one equivalent for complete poisoning of reactivity. Furthermore, the dark gray to black solid residue obtained after hydrogenation (denoted as the residue **4**) was isolated by filtration and washed extensively with the reaction solvent. The colorless supernatant was concentrated in vacuo, and no remaining residue could be detected. The residue **4** was used as catalyst in a new reaction (Maitlis' test,[13] see Table S4) and showed fully preserved yield and selectivity, suggesting that this solid residue contained the active catalyst. Furthermore, a 3-phase-test (Collman's test)[14] was performed, in which methyl 4-hydroxybenzoate was attached to a Wang-resin and submitted to hydrogenation conditions (see page S26). No hydrogenation of the phenyl groups in the solid resin phase occurred. This is the expected outcome for a heterogeneous catalysis pathway, since a reaction is highly unlikely to occur between three phases.

We proceeded to investigate the kinetic behavior of the in situ prepared active catalyst derived from **1** and the preformed catalyst **4a** by monitoring characteristic signals of the standard substrate **5** and of the corresponding product **6** as a function of

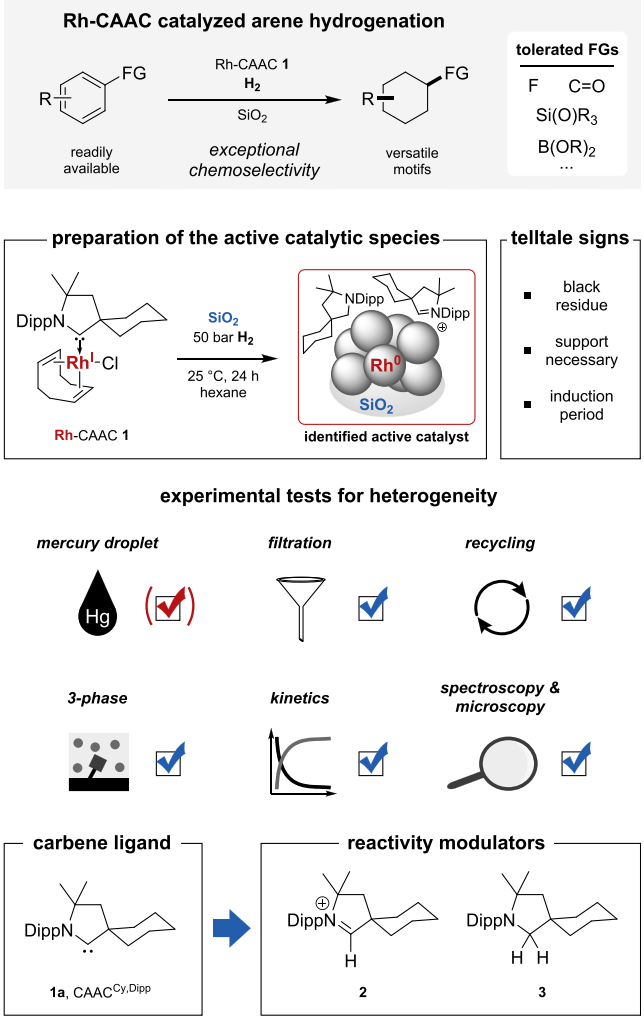

Figure 1. Overview of the established Rh-CAAC catalyzed arene hydrogenation and the studies performed in this work in order to elucidate its active catalyst species. Dipp: di*iso*propylphenyl. FG: functional group.

the reaction time using kinetic ^{1}H NMR measurements under hydrogen pressure (Figure 2). When using **1** as precatalyst in presence of silica gel, an induction period of 120−180 min was observed, which was absent when using preformed catalyst **4a**[15] (Figure 2), thus indicating that the insoluble black residue obtained after hydrogenation contains the active catalyst. In agreement with all other performed experiments, this result strongly indicates that the active catalyst is heterogeneous in nature.[16]

OBSERVATION AND CHARACTERIZATION OF NANOPARTICLES IN CATALYTIC RESIDUE 4A

The preformed catalyst **4a** was further analyzed to deeply investigate the actual structure. High-resolution transmission electron microscopy (TEM) and scanning transmission electron microscopy (STEM) with energy dispersive spectroscopy (EDS) analysis of **4a** showed the presence of rhodium NPs (Figure 3a−d). The observed lattice distances of 0.19 and 0.22 nm in the particles were attributed to a Rh(200) and Rh(111) plane, respectively. This shows that the rhodium is in metallic form (Figure 3b and page S57). The average particle size of **4a** was estimated to be 6.3 ± 2.1 nm from TEM particle

https://dx.doi.org/10.1021/acscatal.0c01074
ACS Catal. 2020, 10, 6309−6317

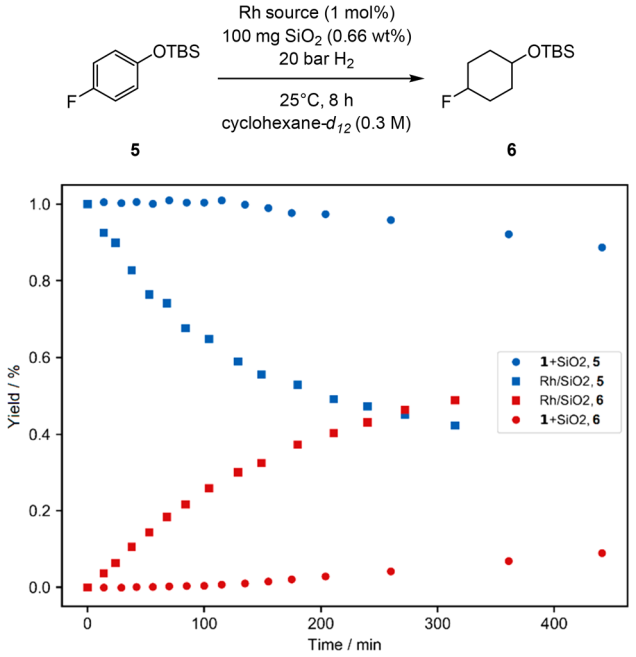

Figure 2. Yields of substrate **5** and product **6** using either precatalyst **1** + SiO_2 or preformed catalyst **4a** as a function of the reaction time. The reactions were performed in pressurized NMR tubes under hydrogen pressure and the yields were determined from the characteristic signals of **5** (proton signal at 6.77 ppm, 2H) and **6** (3.71 ppm, 1H, see pages S50–S52).

size distribution histograms (Figure 3c). X-ray diffraction (XRD) of **4a** (Figure S8) also exhibited two diffraction peaks at 41.0° and 47.4°, which were attributed to Rh(111) and Rh(200) planes of rhodium nanoparticles, respectively. The size of the rhodium NPs was also calculated by the Debye–Scherrer equation for the Rh(111) peak. The obtained value of 4.9 nm is in agreement with the TEM analysis. Rhodium K-edge X-ray absorption near edge structure (XANES, Figure 3e) indicated that the oxidation state of rhodium was close to zero. The Rh–Rh bond distance analyzed by rhodium K-edge extended X-ray fine structure (EXAFS, Figure 3f, Figure S7) was estimated to be 0.269 ± 0.003 nm (coordination number of rhodium being 8.7 ± 0.7). This is in accordance with that of rhodium metal (0.269 ± 0.001 nm), also supporting its metallic state. The Brunauer–Emmet–Teller (BET) surface area of **4a** was measured to be 398 $m^2\ g^{-1}$, which was comparable to that of the used silica gel (422 $m^2\ g^{-1}$), implying that no severe aggregation of support occurred after the formation of rhodium NPs.

PROCESS OF NANOPARTICLE FORMATION FROM RHODIUM–CAAC COMPLEX 1

In order to study the influence of the reaction time on the catalytic properties of the resulting rhodium NPs, preformed catalysts were prepared using reaction times of 3 h (**4b**) and 24 h (**4c**), respectively (Figure 4). In addition to chloride abstraction, the support is likely needed to stabilize and suppress the aggregation of growing NPs after the Rh(I) species are reduced to Rh(0).[8b] A comparison of the sizes of the formed particles with usual parameters such as the mean diameter was not possible, because the obtained size distributions were not uniform (Figure 4c). To extract information from the gathered data, we instead determined

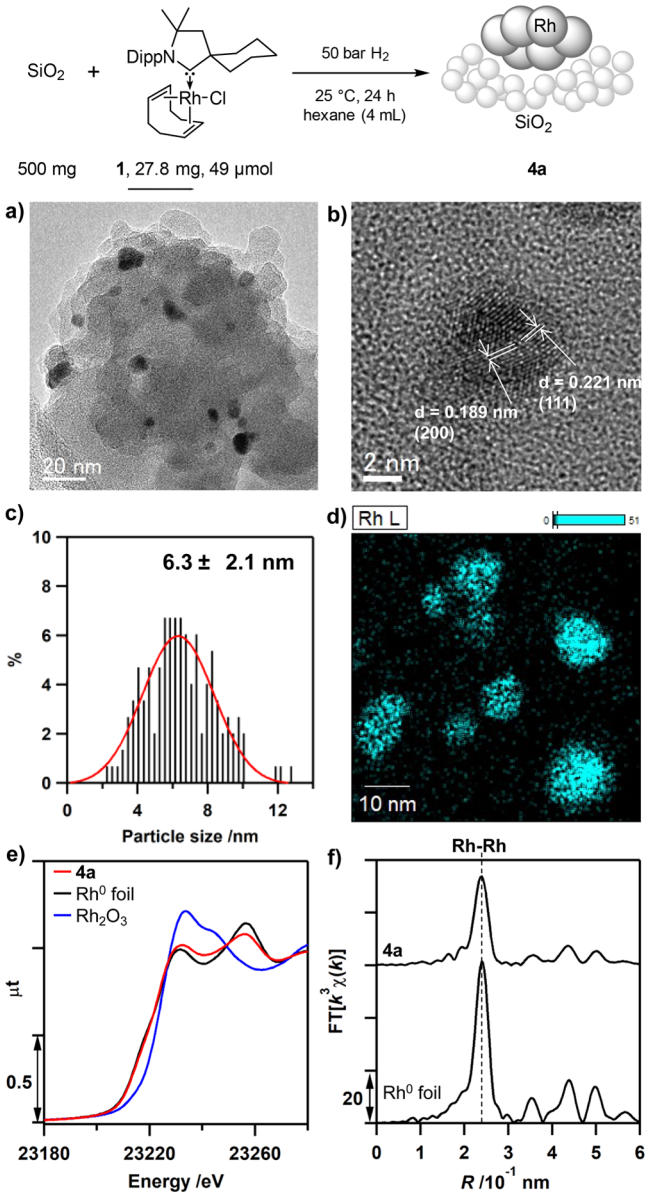

Figure 3. (a,b) TEM images of **4a** with visible lattice structure (0.19 nm Rh(200), 0.22 nm Rh(111)). (c) Histogram showing the particle size distribution of **4a**. (d) STEM-EDS image of **4a** (blue, Rh L_α characteristic X-rays). (e) Rh K-edge XANES spectra of **4a** (red), Rh(0) foil (black), and Rh_2O_3 (blue). (f) Rh K-edge EXAFS Fourier transforms of **4a** and Rh(0) foil.

the fraction of small nanoparticles, which would be the most reactive catalytic species (blue-highlighted area in Figure 4c), by defining the following parameter: $N_{s/all}$ = (number of counted particles with sizes below 3 nm)/(number of all counted particles). The fraction of the most reactive small particles was considerably larger after 3 h (**4b**, $N_{s/all}$ = 32%, Figure 4c, left) than after 24 h reaction time (**4c**, $N_{s/all}$ = 12%, Figure 4c, center). This fresh preparation of small reactive particles may explain the excellent reproducibility of our catalyst system in comparison with some commercial heterogeneous catalysts, which often show batch-dependent results for difficult reactions due to a varying particle size distribution. We also tested the influence of the amount of silica gel on the size of the rhodium NPs. Catalyst **4d**, prepared with a 3-fold excess of silica gel compared to **4b** and **4c**, and

https://dx.doi.org/10.1021/acscatal.0c01074
ACS Catal. 2020, 10, 6309–6317

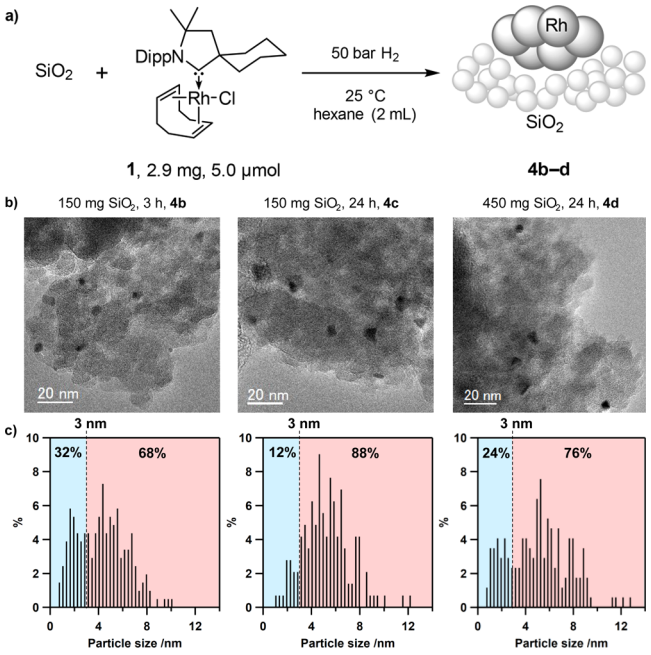

Figure 4. (a) Preparation of silica-supported NPs using different reaction times (catalysts **4b**, **4c**) or amounts of silica (catalyst **4d**). (b) Representative TEM images of **4b**–**4d**. Black dots represent areas of higher density and correspond to Rh, gray background is the silica support. (c) Histograms showing the particle size distribution of the prepared systems. Particle size distributions for all synthesized catalyst systems in this study are given in the Supporting Information.

24 h reaction time, showed a considerably increased fraction of small NPs ($N_{s/all}$ = 24%) compared to catalyst **4c** ($N_{s/all}$ = 12%). The larger number of small NPs when using more silica gel could offer one possible explanation for the observed and previously reported positive effect of increased amounts of silica gel for the hydrogenation of especially challenging highly fluorinated arenes such as hexafluorobenzene.[3d] In this previous study, increased amounts of silica led to lower amounts of defluorination and, thus, higher product yields (for a comparison see also Table S12). BET results of **4b** (395 m^2g^{-1}), **4c** (373 m^2g^{-1}), and **4d** (379 m^2g^{-1}) are very similar to those of catalytic residue **4a**. As a result, it is highly unlikely that the observed effect is caused by a surface area difference after rhodium NP formation.

LIGAND EFFECT ON CATALYSIS

We wondered if the observed high selectivity toward preservation of C–F bonds is introduced by the active ligand species derived from **1a** or if a similar selectivity could be achieved with rhodium nanoparticles of similar size and loading within the identical support material. To test this, rhodium NPs **4e**–**4g** on silica gel were prepared by impregnation of $Rh(NO_3)_3{\cdot}H_2O$ on silica gel, followed by H_2 reduction (synthesis page S6, characterization page S68; rhodium loadings were 0.87 wt % for **4e**, 5.1 wt % for **4f**, and 9.9 wt % for **4g**, respectively). No organic ligand species were attached to these rhodium NPs. When using this method, the fractions of small NPs (<3 nm) ($N_{s/all}$(**4e**) = 58%, $N_{s/all}$(**4f**) = 41%, and $N_{s/all}$(**4g**) = 27%) were somewhat higher than those obtained when using catalysts derived from Rh–CAAC **1** as precursor (e.g., **4a**–**d**). It is worth noting that we observed that an increased fraction of small NPs affects higher yields and that the fraction of small NPs decreases with an increased amount of rhodium down to 27%, which is less than that observed for catalyst **4b**. The average particle size of **4e** was estimated to be 2.8 ± 0.7 nm determined from particle size distribution histograms (Figure S12), which is slightly smaller than that of **4a** with similar Rh loading. When the rhodium loading was increased, average particle sizes were slightly increased (3.2 ± 0.8 nm for **4f** and 3.5 ± 1.0 nm for **4g**, respectively).

Catalytic reaction results for the hydrogenation of the model substrate **5** are summarized in Table 1 (see also Table S11).

Table 1. Comparison of Catalytic Performance of Different Rh/SiO_2 Systems for the Hydrogenation of 5[a]

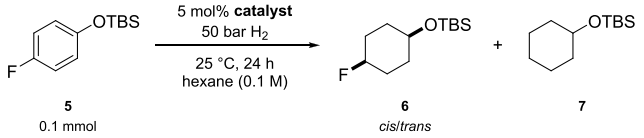

catalyst	Rh amount [wt %]	yield of **6** [%] (d. r.)	yield of **7** [%]
Rh–CAAC **1**/SiO_2	1.0	90 (94:6)	3
Rh–CAAC **1**/SiO_2	5.1	86 (94:6)	4
Rh/SiO_2 **4a**	1.0	89 (94:6)	3
Rh/SiO_2 **4e**	0.87	66 (87:13)	18
Rh/SiO_2 **4f**	5.1	59 (89:11)	23
Rh/SiO_2 **4g**	9.9	68 (88:12)	23

[a]Yields were determined via GC-FID against mesitylene as internal standard. Numbers do not add up to unity, because cyclohexane and cyclohexanol are formed as byproducts, which coelute with the solvent and thus cannot be detected.

4e–**4g** all showed a significantly increased amount of defluorination when compared to the standard system (precursor **1** used, in situ generation of **4**). In addition, the *cis*-selectivity of the NP systems is decreased. Therefore, the selectivity of the investigated system cannot be solely dependent on the NP size or rhodium loading.

OBSERVATION AND IDENTITY OF LIGAND SPECIES ON THE CATALYST SURFACE

The comparison of the catalytic results obtained using **4a** and **4e**–**4g** suggested that catalyst performance is influenced by a ligand species. Therefore, we proceeded to characterize catalyst **4a** and investigate if ligand species were present on the surface of the NPs. X-ray photoelectron spectroscopy (XPS) of catalyst **4a** revealed a broad nitrogen signal at 400–402 eV (Figure 5). The best fitting to the given data is obtained with two signals in a 1:1 ratio, separated by more than 2 eV. While the intensity of the nitrogen signal (as well as that of the rhodium signal) is low due to the sparse dispersion within the silica, the significant distance between the fitted signals strongly suggests the existence of two different nitrogen species. Given that the CAAC ligand **1a** is the sole nitrogen containing species in the precursor, two different nitrogen-containing species must have formed from that ligand under the reaction conditions. To elucidate the identity of the two unknown nitrogen-containing species in the sample, we turned to solid-state NMR spectroscopy. To overcome the problem of the sparse density of possible residues, complex **1** was prepared with a ^{13}C-enriched CAAC precursor. The synthesis of the labeled CAAC precursor was conducted starting from commercially available isotope-labeled benzoic acid, using

https://dx.doi.org/10.1021/acscatal.0c01074
ACS Catal. 2020, 10, 6309–6317

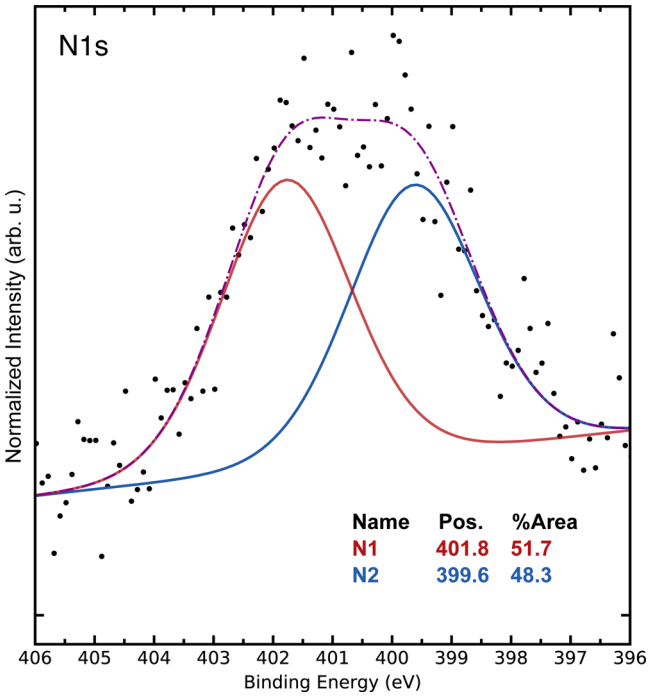

Figure 5. Plotted signal and fitting of the nitrogen-containing species, determined by XPS.

our own protocol for arene hydrogenation (see page S9 for the full synthetic route).[3e,17]

Samples for $^{13}C\{^{1}H\}$ CP/MAS NMR spectroscopy were prepared by stirring the labeled complex with silica gel under hydrogen atmosphere (cf. Figure 4a).[18] The obtained $^{13}C\{^{1}H\}$ CP/MAS NMR spectrum shows two intense ^{13}C signals at ~186 and ~65 ppm (Figure 6). Comparison with the spectrum of the labeled complex **1** confirmed that the signal at 186 ppm cannot be assigned to a ligated carbene species. Given our extensive experience in the field of carbenes on surfaces and given the high strength of carbene−metal bonds, this result was unexpected at first.[19] However, the excellent overlap with the labeled signal of the ^{13}C-enriched pyrrolidinium salt **2** suggested that this iminium cation is likely one of the two nitrogen-containing species.

That cation is likely generated by a reductive elimination of carbene and hydrogen from an intermediate carbene metal−hydride complex, as previously proposed by the Ananikov group.[20] An alternative pathway could be the dissociation of the carbene ligand and subsequent protonation by acidic silanol groups present within the silica gel. However, a dissociation of a free carbene is unlikely regarding the strength of carbene−metal bonds. Chloride is most likely the counteranion, although deprotonated silanol groups are also imaginable. Given that the iminium moiety present in **2** is reducible under hydrogenation conditions, we assumed that the remaining species corresponding to the ^{13}C signal at ~65 ppm might be the amine **3**. Hence, pyrrolidine **3** was synthesized from pyrrolidinium **2** (with chloride as a counteranion) by reduction with $LiAlH_4$. In agreement with our assumption, pyrrolidine **3** showed a distinct signal at 64.9 ppm in deuterated chloroform. It is worth noting that amines are known ligands for nanoparticles.[21] Comparison of spectra of labeled and unlabeled pyrrolidinium **2** further suggests that the smaller signals between 5 and 0 ppm are

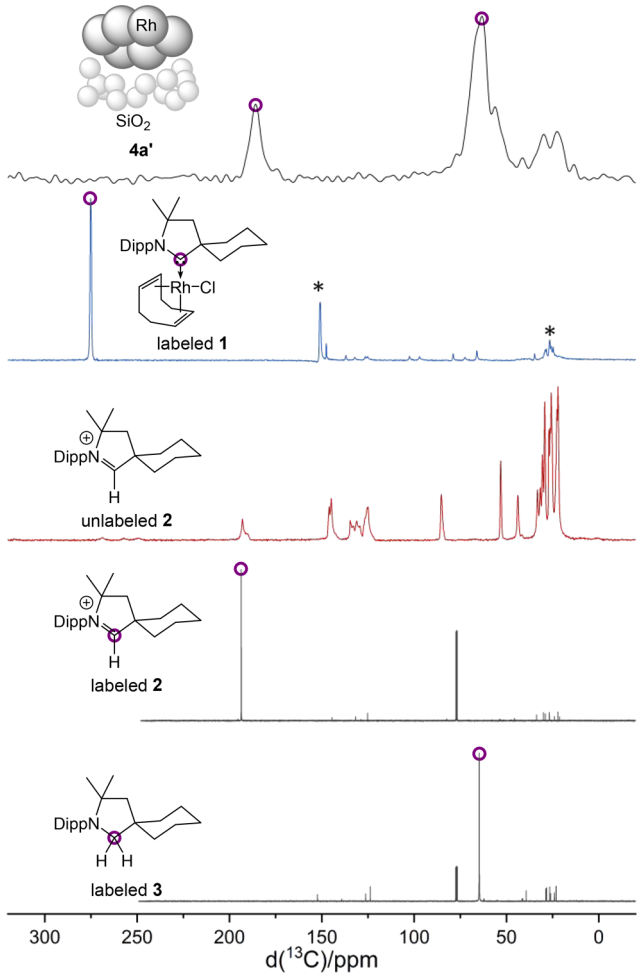

Figure 6. $^{13}C\{^{1}H\}$ CP/MAS NMR spectra of **4a′** prepared from the ^{13}C-labeled complex **1** (black), labeled complex **1** (blue), and unlabeled **2** (red). Peaks corresponding to the labeled carbon are highlighted. The two bottom spectra allow for a comparison with to the pure, ^{13}C-labeled compounds **2** and **3** in solution. *Spinning side bands of the main signal.

derived from the backbone of the pyrrolidinium cation and the pyrrolidine.

BOTTOM-UP SYNTHESIS OF A RELATED SELECTIVE HYDROGENATION CATALYST

Given the previous finding that the observed high chemoselectivity of the hydrogenation of fluorinated arenes is not solely determined by the particle size of the used rhodium catalyst, we wondered if the species **2** and **3** may have an influence on the catalytic activity and selectivity. In previous studies on the influence of ligands such as phosphines and phosphites on reactions catalyzed by Rh NPs, significant effects on the reactivity and selectivity of hydrogenation reactions were observed.[22a−c]

Furthermore, imidazolium based ionic liquids, which were covalently anchored to the Al_2O_3-support, were shown to influence the catalytic hydrogenation of benzene with dispersed Ru NPs.[22d] Driven by these reports, we set out to prepare a catalyst system similar to **4a** by adding **2** and **3** to synthesized rhodium NPs on silica (**4e−4g**) and to commercial rhodium on alumina (Table S9). These were tested for the hydrogenation of model substrate **5** using a

https://dx.doi.org/10.1021/acscatal.0c01074
ACS Catal. 2020, 10, 6309−6317

catalyst loading of 1 mol %. We started by investigating the optimal ratio of both additives at a combined loading of 1.0 equivalents relative to the used rhodium but no clear trend emerged (see Table S11). The use of one equivalent of a single species only led to high amounts of defluorination (for pyrrolidine **3**) or incomplete conversion (for pyrrolidinium **2**). These results strongly suggest that both species **2** and **3** seem to play an important role in modifying the catalytic activity. For further experiments, we therefore kept a 1:1-ratio of these species, as suggested by the XPS studies. Next, varying equivalents of that 1:1 mixture with regard to rhodium were investigated (Figure 7). The studies showed an increase in

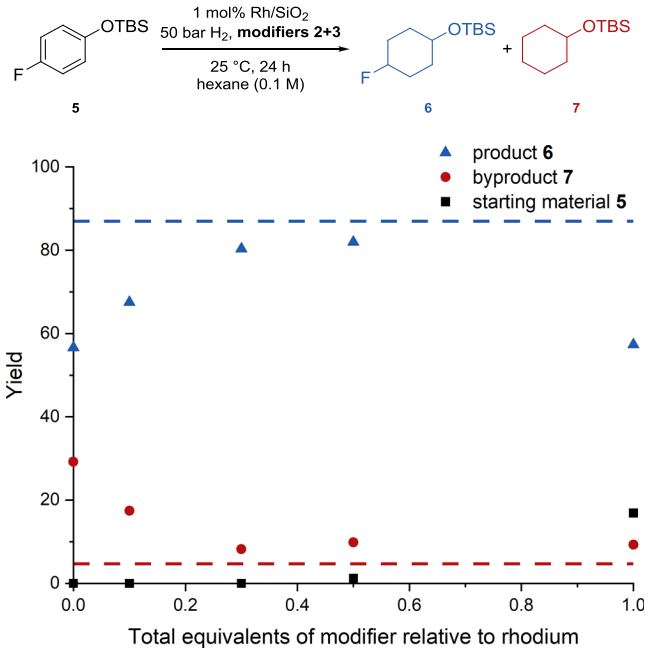

Figure 7. Yields of product **6** and byproduct **7** obtained by the hydrogenation of substrate **5** with Rh NPs on silica gel **4e** as a function of the total equivalents of a 1:1 mixture of pyrroldinium **2** and pyrrolidine **3**, which were added to the Rh NPs. Yields were determined by GC-FID analysis vs mesitylene.

conversion with decreased amounts of the modifiers. Full conversion was still achieved with as little as 0.3 equiv of the modifier mixture. Further decreasing the amount of the modifiers resulted in a significant increase in defluorination. The amount of defluorination and the obtained yield with 0.3 equivalents of a 1:1 modifier mixture was almost identical to the values observed when using the precursor **1** with silica gel and in situ generation of the active catalytic system (**4**).

As additional control experiments, preformed rhodium particles, obtained by submitting Rh(COD)Cl and silica gel to hydrogenation conditions, were tested untreated and treated with the modifiers **2** and **3**. While reactivity was observed for the former case, a complete loss of activity was noted with one equivalent of the modifier mixture, irrespective of their ratio (see Table S10). We wondered whether the identity of the rhodium ligand, in this case CAAC **1a**, may also influence the NP formation. To investigate this, different CAAC ligands **8** and **9** were used during the preparation of rhodium particles **4h** and **4i**, respectively (Figure 8). As expected, the size distribution of those rhodium particles differed from that of the active catalyst **4a** derived from ligand **1a** in the precursor

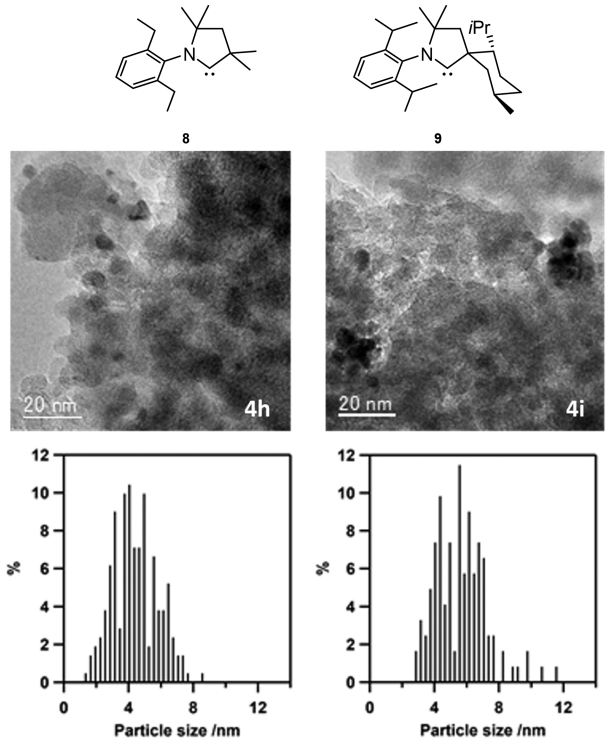

Figure 8. Structures of alternative CAAC ligands **8** and **9** with representative TEM images of corresponding rhodium particles obtained from complex precursors and the size distribution.

complex. More importantly, the catalytic results differed significantly as well (see Figure S1, Table S6) with the residues **4h** and **4i** showing either strongly reduced or no activity at all (see page S29 for a more detailed discussion).

The preformed catalyst **4e** (with and without modifiers) was also investigated for the hydrogenation of hexafluorobenzene **10**, since for this substrate the difference in chemoselectivity compared to other catalysts was especially pronounced. When applying the determined optimized amounts of modifiers to the preformed NPs the yield for hexafluorocyclohexane **11** could be increased from 4% (no modifiers) to 29% with modifiers. This constitutes 74% of the yield obtained with the established precursor Rh−CAAC **1** under otherwise identical conditions (Table 2).

In conclusion, we have elucidated the active catalyst derived from a molecular Rh−CAAC precursor, which has previously

Table 2. Comparing the Performance of Synthesized and Modified NPs with the Standard Catalyst System[23,a]

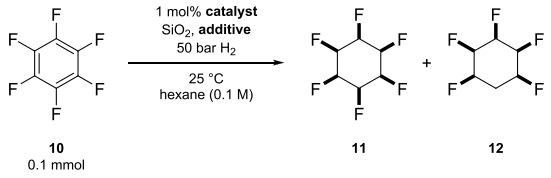

catalyst	yield **11** [%]	yield **12** [%]
Rh−CAAC **1**/44 mg SiO_2	39	22
Rh/SiO_2 (**4e**, 0.87 wt %) with 0.3 equiv of **2** and **3** (1:1)	29	8
Rh/SiO_2 (**4e**, 0.87 wt %)	4	57

[a]Isolated yields are given.

https://dx.doi.org/10.1021/acscatal.0c01074
ACS Catal. 2020, 10, 6309−6317

been shown to enable a highly chemoselective hydrogenation of a broad scope of (fluorinated) arenes and heteroarenes. By combining mechanistic and kinetic studies, we confirmed that the active catalyst is heterogeneous in nature. Various imaging, spectroscopic, and surface analysis techniques revealed silica gel-supported rhodium(0) NPs as active catalytic species. After excluding the presence of a metal-bound carbene species on the NPs, we further determined that CAAC-derived pyrrolidinium **2** and pyrrolidine **3** act as modifiers that are key in controlling the chemoselectivity of the hydrogenation of fluorinated arenes. Furthermore, the chemical identity of these modifiers and the amount of the silica gel support influence the size distribution of the NPs and thereby the catalytic properties. Finally, we were able to synthesize an active catalyst in a bottom-up approach that has a very similar reactivity compared to the established catalyst. We believe that this approach will enable much more facile means of tuning the catalytic activity of that catalyst system. Hence, the development of next-generation catalysts derived from the studied system is the subject of ongoing research in our laboratories.

■ ASSOCIATED CONTENT

Supporting Information

The Supporting Information is available free of charge at https://pubs.acs.org/doi/10.1021/acscatal.0c01074.

Experimental procedures and spectroscopic and microscopic data (PDF)

■ AUTHOR INFORMATION

Corresponding Author

Frank Glorius − *Organisch-Chemisches Institut, Westfälische Wilhelms-Universität Münster, 48149 Münster, Germany;* orcid.org/0000-0002-0648-956X; Email: glorius@uni-muenster.de

Authors

Daniel Moock − *Organisch-Chemisches Institut, Westfälische Wilhelms-Universität Münster, 48149 Münster, Germany*

Mario P. Wiesenfeldt − *Organisch-Chemisches Institut, Westfälische Wilhelms-Universität Münster, 48149 Münster, Germany;* orcid.org/0000-0002-7142-9336

Matthias Freitag − *Organisch-Chemisches Institut, Westfälische Wilhelms-Universität Münster, 48149 Münster, Germany*

Satoshi Muratsugu − *Department of Chemistry, Graduate School of Science, Nagoya University, Nagoya 464-8602, Aichi, Japan;* orcid.org/0000-0002-3596-7380

Satoru Ikemoto − *Department of Chemistry, Graduate School of Science, Nagoya University, Nagoya 464-8602, Aichi, Japan*

Robert Knitsch − *Institut für Physikalische Chemie, Westfälische Wilhelms-Universität Münster, 48149 Münster, Germany*

Jacob Schneidewind − *Leibniz-Institut für Katalyse e. V., 18059 Rostock, Germany;* orcid.org/0000-0002-5328-6626

Wolfgang Baumann − *Leibniz-Institut für Katalyse e. V., 18059 Rostock, Germany*

Andreas H. Schäfer − *nanoAnalytics GmbH, 48149 Münster, Germany*

Alexander Timmer − *nanoAnalytics GmbH, 48149 Münster, Germany*

Mizuki Tada − *Department of Chemistry, Graduate School of Science and Research Center for Materials Science (RCMS) and Integrated Research Consortium on Chemical Science (IRCCS), Nagoya University, Nagoya 464-8602, Aichi, Japan*

Michael Ryan Hansen − *Institut für Physikalische Chemie, Westfälische Wilhelms-Universität Münster, 48149 Münster, Germany;* orcid.org/0000-0001-7114-8051

Complete contact information is available at: https://pubs.acs.org/10.1021/acscatal.0c01074

Author Contributions

[×]M.P.W. and M.F. contributed equally.

Notes

The authors declare the following competing financial interest(s): The authors declare no conflict of interest. However, please, note that we patented the Process for Synthesizing Fluorinated Cyclic Aliphatic Compounds employing the investigated catalyst system: PCT/EP2018/054554.

■ ACKNOWLEDGMENTS

We are grateful to the European Research Council (ERC Advanced Grant Agreement No. 788558), Fonds der Chemischen Industrie (Kekulé Ph.D. scholarship for D.M. and J.S.), the Studienstiftung des deutschen Volkes (Ph.D. scholarship for M.P.W.), the JST PRESTO Program (No. JPMJPR15S7), the JSPS KAKHENI (Grant No. 18K05144), and Core-to-Core program "Elements Function for Transformative Catalysis and Materials" for generous financial support. TEM and STEM-EDS measurements were conducted at the High Voltage Electron Microscope Laboratory, Institute of Materials and Systems for Sustainability, Nagoya University, supported by "Advanced Characterization Nanotechnology Platform" of MEXT, Japan. XAFS measurements were performed with the approval of PF-PAC (Grant 2017G534) and the Aichi Synchrotron Radiation Center. We are also grateful to C. Schlepphorst, V. Siozios, M. Wollenburg, T. Wagener, A. Heusler, H. Lund, and R. Eckelt for helpful scientific discussions and experimental support.

■ REFERENCES

(1) For an overview on homo- and heterogeneous arene hydrogenation see: (a) Wiesenfeldt, M. P.; Nairoukh, Z.; Dalton, T.; Glorius, F. Selective Arene Hydrogenation for Direct Access to Saturated Carbo- and Heterocycles. *Angew. Chem., Int. Ed.* **2019**, *58*, 10460−10476. (b) *The Handbook of Homogeneous Hydrogenation*; de Vries, J. G., Elsevier, C. J., Eds.; Wiley-VCH: Weinheim, Germany, 2007. (c) *Arene Chemistry: Reaction Mechanisms and Methods for Aromatic Compounds*; Mortier, J., Ed.; John Wiley & Sons, Inc: Hoboken, NJ, 2016. (d) Gual, A.; Godard, C.; Castillón, S.; Claver, C. Soluble Transition-Metal Nanoparticles-Catalysed Hydrogenation of Arenes. *Dalton Trans.* **2010**, *39*, 11499−11512. (e) Qi, S.-C.; Wei, X.-Y.; Zong, Z.-M.; Wang, Y.-K. Application of Supported Metallic Catalysts in Catalytic Hydrogenation of Arenes. *RSC Adv.* **2013**, *3*, 14219−14232. (f) Giustra, Z. X.; Ishibashi, J. S. A.; Liu, S.-Y. Homogeneous Metal Catalysis for Conversion between Aromatic and Saturated Compounds. *Coord. Chem. Rev.* **2016**, *314*, 134−181. (g) Wang, D.-S.; Chen, Q.-A.; Lu, S.-M.; Zhou, Y.-G. Asymmetric Hydrogenation of Heteroarenes and Arenes. *Chem. Rev.* **2012**, *112*, 2557−2590. (h) Zhao, D.; Candish, L.; Paul, D.; Glorius, F. N-Heterocyclic Carbenes in Asymmetric Hydrogenation. *ACS Catal.* **2016**, *6*, 5978−5988.

(2) Lovering, F.; Bikker, J.; Humblet, C. Escape from Flatland: Increasing Saturation as an Approach to Improving Clinical Success. *J. Med. Chem.* **2009**, *52*, 6752−6756.

(3) Previous arene hydrogenation methods from our group employing Rh-CAAC **1**: (a) Wiesenfeldt, M. P.; Nairoukh, Z.; Li,

W.; Glorius, F. Hydrogenation of Fluoroarenes: Direct Access to All-Cis-(Multi)Fluorinated Cycloalkanes. *Science* **2017**, *357*, 908−912. (b) See Tables S9 and S12 for a comparison to a selection of commercial heterogeneous catalysts for the hydrogenation of fluorinated arenes. (c) Wiesenfeldt, M. P.; Knecht, T.; Schlepphorst, C.; Glorius, F. Silylarene Hydrogenation: A Strategic Approach That Enables Direct Access to Versatile Silylated Saturated Carbo- and Heterocycles. *Angew. Chem., Int. Ed.* **2018**, *57*, 8297−8300. (d) Wollenburg, M.; Moock, D.; Glorius, F. Hydrogenation of Borylated Arenes. *Angew. Chem., Int. Ed.* **2019**, *58*, 6549−6553. (e) Arene hydrogenation methods employing Rh-CAACs from other groups: Ling, L.; He, Y.; Zhang, X.; Luo, M.; Zeng, X. Hydrogenation of (Hetero)aryl Boronate Esters with a Cyclic (Alkyl)(amino)-carbene-Rhodium Complex: Direct Access to *cis*-Substituted Borylated Cycloalkanes and Saturated Heterocycles. *Angew. Chem., Int. Ed.* **2019**, *58*, 6554−6558. (f) Zhang, X.; Ling, L.; Luo, M.; Zeng, X. Accessing Difluoromethylated and Trifluoromethylated cis-Cycloalkanes and Saturated Heterocycles: Preferential Hydrogen Addition to the Substitution Sites for Dearomatization. *Angew. Chem., Int. Ed.* **2019**, *58*, 16785−16789. (g) For a lead reference on the chemo- and enantioselective hydrogenation of fluorinated olefins, see Ponra, S.; Rabten, W.; Yang, J.; Wu, H.; Kerdphon, S.; Andersson, P. G. Diastereo- and Enantioselective Synthesis of Fluorine Motifs with Two Contiguous Stereogenic Centers. *J. Am. Chem. Soc.* **2018**, *140*, 13878−13883.

(4) Nairoukh, Z.; Wollenburg, M.; Schlepphorst, C.; Bergander, K.; Glorius, F. The Formation of all-*cis*-(Multi)Fluorinated Piperidines by a Dearomatization−Hydrogenation Process. *Nat. Chem.* **2019**, *11*, 264−270.

(5) Seminal works on the synthesis of CAA(r)Cs by the Bertrand group: (a) Lavallo, V.; Canac, Y.; Präsang, C.; Donnadieu, B.; Bertrand, G. Stable Cyclic (Alkyl)(Amino)Carbenes as Rigid or Flexible, Bulky, Electron-Rich Ligands for Transition-Metal Catalysts: A Quaternary Carbon Atom Makes the Difference. *Angew. Chem., Int. Ed.* **2005**, *44*, 5705−5709. (b) Rao, B.; Tang, H.; Zeng, X.; Liu, L.; Melaimi, M.; Bertrand, G. Cyclic (Amino)(Aryl)Carbenes (CAArCs) as Strong σ-Donating and π-Accepting Ligands for Transition Metals. *Angew. Chem., Int. Ed.* **2015**, *54*, 14915−14919. (c) Reviews: Soleilhavoup, M.; Bertrand, G. Cyclic (Alkyl)(Amino)Carbenes (CAACs): Stable Carbenes on the Rise. *Acc. Chem. Res.* **2015**, *48*, 256−266. (d) Melaimi, M.; Jazzar, R.; Soleilhavoup, M.; Bertrand, G. Cyclic (Alkyl)(Amino)Carbenes (CAACs): Recent Developments. *Angew. Chem., Int. Ed.* **2017**, *56*, 10046−10068.

(6) Lavallo, V.; Canac, Y.; DeHope, A.; Donnadieu, B.; Bertrand, G. A rigid Cyclic (Alkyl)(amino)carbene Ligand Leads to Isolation of Low-Coordinate Transition Metal Complexes. *Angew. Chem., Int. Ed.* **2005**, *44*, 7236−7239.

(7) Wei, Y.; Rao, B.; Cong, X.; Zeng, X. Highly Selective Hydrogenation of Aromatic Ketones and Phenols Enabled by Cyclic (Amino)(Alkyl)Carbene Rhodium Complexes. *J. Am. Chem. Soc.* **2015**, *137*, 9250−9253.

(8) For reviews on the distinction between homo- and heterogeneous catalyst systems see (a) Widegren, J. A.; Finke, R. G. A Review of Soluble Transition-Metal Nanoclusters as Arene Hydrogenation Catalysts. *J. Mol. Catal. A: Chem.* **2003**, *191*, 187−207. (b) Widegren, J. A.; Finke, R. G. A Review of the Problem of Distinguishing True Homogeneous Catalysis from Soluble or Other Metal-Particle Heterogeneous Catalysis under Reducing Conditions. *J. Mol. Catal. A: Chem.* **2003**, *198*, 317−341. (c) Dyson, P. J. Arene Hydrogenation by Homogeneous Catalysts: Fact or Fiction? *Dalton Trans.* **2003**, *15*, 2964−2974 It can be concluded that no singular experiment can unambiguously distinguish between a homo- or heterogeneous nature of the active catalyst and a definitive elucidation requires a series of experiments.

(9) For selected examples of studies on the distinction between a homo- or heterogeneous nature of the active catalyst see (a) Lin, Y.; Finke, R. G. A More General Approach to Distinguishing "Homogeneous" from "Heterogeneous" Catalysis: Discovery of Polyoxoanion- and Bu_4N+-Stabilized, Isolable and Redissolvable, High-Reactivity $Ir_{\sim 190-450}$ Nanocluster Catalysts. *Inorg. Chem.* **1994**, *33*, 4891−4910. (b) Weddle, K. S.; Aiken, J. D.; Finke, R. G. Rh(0) Nanoclusters in Benzene Hydrogenation Catalysis: Kinetic and Mechanistic Evidence That a Putative $[(C_8H_{17})_3NCH_3]$+$[RhCl_4]$- Ion-Pair Catalyst Is Actually a Distribution of Cl- and $[(C_8H_{17})_3NCH_3]$+ Stabilized Rh(0) Nanoclusters. *J. Am. Chem. Soc.* **1998**, *120*, 5653−5666. (c) Bayram, E.; Linehan, J. C.; Fulton, J. L.; Szymczak, N. K.; Finke, R. G. Determination of the Dominant Catalyst Derived from the Classic $[RhCp^*Cl_2]_2$ Precatalyst System: Is It Single-Metal Rh(1)Cp*-Based, Subnanometer Rh_4 Cluster-Based, or $Rh(0)_n$ Nanoparticle-Based Cyclohexene Hydrogenation Catalysis at Room Temperature and Mild Pressures? *ACS Catal.* **2015**, *5*, 3876−3886.

(10) (a) Tran, B. L.; Fulton, J. L.; Linehan, J. C.; Lercher, J. A.; Bullock, R. M. Rh(CAAC)-Catalyzed Arene Hydrogenation: Evidence for Nanocatalysis and Sterically Controlled Site-Selective Hydrogenation. *ACS Catal.* **2018**, *8*, 8441−8449. (b) Tran, B. L.; Fulton, J. L.; Linehan, J. C.; Balasubramanian, M.; Lercher, J. A.; Bullock, R. M. Operando XAFS Studies on Rh(CAAC)-Catalyzed Arene Hydrogenation. *ACS Catal.* **2019**, *9*, 4106−4114.

(11) Chernyshev, V. M.; Astakhov, A. V.; Chikunov, I. E.; Tyurin, R. V.; Eremin, D. B.; Ranny, G. S.; Khrustalev, V. N.; Ananikov, V. P. Pd and Pt Catalyst Poisoning in the Study of Reaction Mechanisms: What Does the Mercury Test Mean for Catalysis? *ACS Catal.* **2019**, *9*, 2984−2995.

(12) For poisoning studies of metals with sulfur-containing compounds see the following book chapter: Bartholomew, C. H.; Agrawal, P. K.; Katzer, J. R. Sulfur Poisoning of Metals. In *Advances in Catalysis*; Eley, D. D., Pines, H., Weisz, P. B., Eds.; Academic Press, 1982; Vol. *31*, pp 135−242;. For a case study see Garbarino, G.; Romero Perez, A.; Finocchio, E.; Busca, G. A Study of the Deactivation of Low Loading Ni/Al2O3 Steam Reforming Catalyst by Tetrahydrothiophene. *Catal. Commun.* **2013**, *38*, 67−73.

(13) Hamlin, J. E.; Hirai, K.; Millan, A.; Maitlis, P. M. A Simple Practical Test for Distinguishing a Heterogeneous Component in a Homogeneously Catalyzed Reaction. *J. Mol. Catal.* **1980**, *7*, 543−544.

(14) Collman, J. P.; Kosydar, K. M.; Bressan, M.; Lamanna, W.; Garrett, T. Polymer-bound Substrates: A Method to Distinguish between Homogeneous and Heterogeneous Catalysis. *J. Am. Chem. Soc.* **1984**, *106*, 2569−2579.

(15) The catalytic system of Rh on SiO_2 can be prepared by stirring **1** with silica gel under hydrogen pressure with or without any substrate. In our studies we have found no difference in reactivity between both cases (see page S23). Different amounts of silica gel can be used, which we have found to have an impact on reactivity. Where appropriate, letters have been used in addition to number **4** in this manuscript to differentiate between catalyst systems prepared under slightly different conditions.

(16) Schwartz, J. Alkane Activation by Oxide-Bound Organorhodium Complexes. *Acc. Chem. Res.* **1985**, *18*, 302−308 Following Schwartz's definition, a heterogeneous catalyst is described by having multiple active sites, as opposed to one active site in a homogeneous catalyst. This definition includes insoluble, supported catalysts, as well as soluble nanoclusters.

(17) An alternative pathway for the amine synthesis is a direct hydrogen splitting starting from the free carbene: Frey, G. D.; Lavallo, V.; Donnadieu, B.; Schoeller, W. W.; Bertrand, G. *Science* **2007**, *316*, 439−441.

(18) For studies analyzing carbenes on surfaces with solid-state NMR techniques, see (a) Baquero, E. A.; Tricard, S.; Flores, J. C.; de Jesús, E.; Chaudret, B. Highly Stable Water-Soluble Platinum Nanoparticles Stabilized by Hydrophilic *N*-Heterocyclic Carbenes. *Angew. Chem., Int. Ed.* **2014**, *53*, 13220−13224. (b) Ernst, J. B.; Muratsugu, S.; Wang, F.; Tada, M.; Glorius, F. Tunable Heterogeneous Catalysis: N-Heterocyclic Carbenes as Ligands for Supported Heterogeneous Ru/K-Al_2O_3 Catalysts to Tune Reactivity and Selectivity. *J. Am. Chem. Soc.* **2016**, *138*, 10718−10721. (c) Ernst, J. B.; Schwermann, C.; Yokota, G.; Tada, M.; Muratsugu, S.; Doltsinis, N. L.; Glorius, F. Molecular Adsorbates Switch on Heterogeneous

https://dx.doi.org/10.1021/acscatal.0c01074
ACS Catal. 2020, 10, 6309−6317

Catalysis: Induction of Reactivity by *N*-Heterocyclic Carbenes. *J. Am. Chem. Soc.* **2017**, *139*, 9144−9147. (d) Baquero, E. A.; Tricard, S.; Coppel, Y.; Flores, J. C.; Chaudret, B.; de Jesús, E. Water-Soluble Platinum Nanoparticles Stabilized by Sulfonated *N*-Heterocyclic Carbenes: Influence of the Synthetic Approach. *Dalton Trans.* **2018**, *47*, 4093−4104.

(19) For recent reviews on the field of carbenes on surfaces, see (a) Hopkinson, M. N.; Richter, C.; Schedler, M.; Glorius, F. An overview of *N*-heterocyclic carbenes. *Nature* **2014**, *510*, 485−596. (b) Zhukhovitskiy, A. V.; MacLeod, M. J.; Johnson, J. A. Carbene Ligands in Surface Chemistry: From Stabilization of Discrete Elemental Allotropes to Modification of Nanoscale and Bulk Substrates. *Chem. Rev.* **2015**, *115*, 11503−11532. (c) Smith, C. A.; Narouz, M. R.; Lummis, P. A.; Singh, I.; Nazemi, A.; Li, C.-H.; Crudden, C. M. *N*-Heterocyclic Carbenes in Materials Chemistry. *Chem. Rev.* **2019**, *119*, 4986−5056. (d) Selected studies: MacLeod, M. J.; Goodman, A. J.; Ye, H.-Z.; Nguyen, H. V.-T.; Van Voorhis, T.; Johnson, J. A. Robust gold nanorods stabilized by bidentate *N*-heterocyclic-carbene-thiolate ligands. *Nat. Chem.* **2019**, *11*, 57−63. (e) Narouz, M. R.; Osten, K. M.; Unsworth, P. J.; Man, R. W. Y.; Salorinne, K.; Takano, S.; Tomihara, R.; Kaappa, S.; Malola, S.; Dinh, C.-T.; Padmos, J. D.; Ayoo, K.; Garrett, P. J.; Nambo, M.; Horton, J. H.; Sargent, E. H.; Hakkinen, H.; Tsukuda, T.; Crudden, C. M. *N*-heterocyclic carbene functionalized magic-number gold nanoclusters. *Nat. Chem.* **2019**, *11*, 419−425.

(20) (a) Astakhov, A. V.; Khazipov, O. V.; Chernenko, A. Yu.; Pasyukov, D. V.; Kashin, A. S.; Gordeev, E. G.; Khrustalev, V. N.; Chernyshev, V. M.; Ananikov, V. P. A New Mode of Operation of Pd-NHC Systems Studied in a Catalytic Mizoroki−Heck Reaction. *Organometallics* **2017**, *36*, 1981−1992. (b) Khazipov, O. V.; Shevchenko, M. A.; Chernenko, A. Yu.; Astakhov, A. V.; Pasyukov, D. V.; Eremin, D. B.; Zubavichus, Y. V.; Khrustalev, V. N.; Chernyshev, V. M.; Ananikov, V. P. Fast and Slow Release of Catalytically Active Species in Metal/NHC Systems Induced by Aliphatic Amines. *Organometallics* **2018**, *37*, 1483−1492.

(21) Kunz, S. Supported, Ligand-Functionalized Nanoparticles: An Attempt to Rationalize the Application and Potential of Ligands in Heterogeneous Catalysis. *Top. Catal.* **2016**, *59*, 1671−1685.

(22) (a) Castelbou, J. L.; Gual, A.; Mercade, E.; Claver, C.; Godard, C. Ligand effect in the Rh-NP catalyzed partial hydrogenation of substituted arenes. *Catal. Sci. Technol.* **2013**, *3*, 2828−2833. (b) Llop Castelbou, J.; Bresó-Femenia, E.; Blondeau, P.; Chaudret, B.; Castillón, S.; Claver, C.; Godard, C. Tuning the Selectivity in the Hydrogenation of Aromatic Ketones Catalyzed by Similar Ruthenium and Rhodium Nanoparticles. *ChemCatChem* **2014**, *6*, 3160−3168. (c) Castelbou, J. L.; Blondeau, P.; Claver, C.; Godard, C. Surface Characterisation of Phosphine and Phosphite Stabilised Rh Nanoparticles: A Model Study. *RSC Adv.* **2015**, *5*, 97036−97043. (d) Foppa, L.; Luza, L.; Gual, A.; Weibel, D. E.; Eberhardt, D.; Teixeira, S. R.; Dupont, J. Sputtering-deposition of Ru nanoparticles onto Al_2O_3 modified with imidazolium ionic liquids: synthesis, characterisation and catalysis. *Dalton Trans.* **2015**, *44*, 2827−2834.

(23) The conditions for the hydrogenation of hexafluorobenzene were chosen to match the optimal conditions for the bottom-up designed system as closely as possible and differ slightly from the best conditions for this system found in our earlier reports (see Table S12 and ref 3c).

https://dx.doi.org/10.1021/acscatal.0c01074
ACS Catal. 2020, 10, 6309−6317

7 References

1. Allen, M. *et al.* Technical Summary: Global warming of 1.5° C. An IPCC Special Report on the impacts of global warming of 1.5° C above pre-industrial levels and related global greenhouse gas emission pathways, in the context of strengthening the global response to the threat of climate change, sustainable development, and efforts to eradicate poverty. (2019), Intergovernmental Panel on Climate Change, available at https://www.ipcc.ch/sr15/, accessed 2020.
2. The Federal Government. The National Hydrogen Strategy. (2020), available at https://www.bmwi.de/Redaktion/EN/Publikationen/Energie/the-national-hydrogen-strategy.html, accessed 2020.
3. Eurostat. What kind of energy do we consume in the EU? (2020), available at https://ec.europa.eu/eurostat/cache/infographs/energy/bloc-3a.html, accessed 2020.
4. Schmietendorf, K., Peinke, J. & Kamps, O. The impact of turbulent renewable energy production on power grid stability and quality. *Eur. Phys. J. B* **90**, 222 (2017).
5. Stephens, I. E. L., Rossmeisl, J. & Chorkendorff, I. Toward sustainable fuel cells. *Science* **354**, 1378–1379 (2016).
6. J. Detz, R., H. Reek, J. N. & Zwaan, B. C. C. van der. The future of solar fuels: when could they become competitive? *Energy Environ. Sci.* **11**, 1653–1669 (2018).
7. Vogt, C., Monai, M., Kramer, G. J. & Weckhuysen, B. M. The renaissance of the Sabatier reaction and its applications on Earth and in space. *Nat. Catal.* **2**, 188–197 (2019).
8. Kattel, S., Ramírez, P. J., Chen, J. G., Rodriguez, J. A. & Liu, P. Active sites for CO2 hydrogenation to methanol on Cu/ZnO catalysts. *Science* **355**, 1296–1299 (2017).
9. IRENA. Hydrogen from renewable power: Technology outlook for the energy transition. (2018), International Renewable Energy Agency, available at https://www.irena.org/-/media/Files/IRENA/Agency/Publication/2018/Sep/IRENA_Hydrogen_from_renewable_power_2018.pdf, accessed 2020.
10. Ni, M., Leung, D. Y. C., Leung, M. K. H. & Sumathy, K. An overview of hydrogen production from biomass. *Fuel Process. Technol.* **87**, 461–472 (2006).

11. Brady, M. D., Sampaio, R. N., Wang, D., Meyer, T. J. & Meyer, G. J. Dye-Sensitized Hydrobromic Acid Splitting for Hydrogen Solar Fuel Production. *J. Am. Chem. Soc.* **139**, 15612–15615 (2017).
12. Holade, Y. *et al.* Recent advances in the electrooxidation of biomass-based organic molecules for energy, chemicals and hydrogen production. *Catal. Sci. Technol.* **10**, 3071–3112 (2020).
13. Glenk, G. & Reichelstein, S. Economics of converting renewable power to hydrogen. *Nat. Energy* **4**, 216–222 (2019).
14. Götz, M. *et al.* Renewable Power-to-Gas: A technological and economic review. *Renew. Energy* **85**, 1371–1390 (2016).
15. Rockström, J. *et al.* A roadmap for rapid decarbonization. *Science* **355**, 1269–1271 (2017).
16. Jesper Jacobsson, T. Photoelectrochemical water splitting: an idea heading towards obsolescence? *Energy Environ. Sci.* **11**, 1977–1979 (2018).
17. Muhich, C. L. *et al.* A review and perspective of efficient hydrogen generation via solar thermal water splitting. *WIREs Energy Environ.* **5**, 261–287 (2016).
18. Esper, B., Badura, A. & Rögner, M. Photosynthesis as a power supply for (bio-)hydrogen production. *Trends Plant Sci.* **11**, 543–549 (2006).
19. Pinaud, B. A. *et al.* Technical and economic feasibility of centralized facilities for solar hydrogen production via photocatalysis and photoelectrochemistry. *Energy Environ. Sci.* **6**, 1983–2002 (2013).
20. Hisatomi, T. & Domen, K. Reaction systems for solar hydrogen production via water splitting with particulate semiconductor photocatalysts. *Nat. Catal.* 1 (2019) doi:10.1038/s41929-019-0242-6.
21. Kern, J. *et al.* Structures of the intermediates of Kok's photosynthetic water oxidation clock. *Nature* **563**, 421–425 (2018).
22. Kok, B., Forbush, B. & McGLOIN, M. Cooperation of charges in photosynthetic o2 evolution–i. a linear four step mechanism. *Photochem. Photobiol.* **11**, 457–475 (1970).
23. Takata, T. & Domen, K. Particulate Photocatalysts for Water Splitting: Recent Advances and Future Prospects. *ACS Energy Lett.* **4**, 542–549 (2019).

24. Wang, L.-P. & Van Voorhis, T. Direct-Coupling O2 Bond Forming a Pathway in Cobalt Oxide Water Oxidation Catalysts. *J. Phys. Chem. Lett.* **2**, 2200–2204 (2011).

25. Tang, J., Durrant, J. R. & Klug, D. R. Mechanism of Photocatalytic Water Splitting in TiO2. Reaction of Water with Photoholes, Importance of Charge Carrier Dynamics, and Evidence for Four-Hole Chemistry. *J. Am. Chem. Soc.* **130**, 13885–13891 (2008).

26. Takata, T. *et al.* Photocatalytic water splitting with a quantum efficiency of almost unity. *Nature* **581**, 411–414 (2020).

27. Jia, Q., Iwase, A. & Kudo, A. BiVO 4 –Ru/SrTiO 3 :Rh composite Z-scheme photocatalyst for solar water splitting. *Chem. Sci.* **5**, 1513–1519 (2014).

28. Wang, Z. *et al.* Overall water splitting by Ta 3 N 5 nanorod single crystals grown on the edges of KTaO 3 particles. *Nat. Catal.* **1**, 756 (2018).

29. Chen, S., Takata, T. & Domen, K. Particulate photocatalysts for overall water splitting. *Nat. Rev. Mater.* **2**, 1–17 (2017).

30. Youngblood, W. J., Lee, S.-H. A., Maeda, K. & Mallouk, T. E. Visible Light Water Splitting Using Dye-Sensitized Oxide Semiconductors. *Acc. Chem. Res.* **42**, 1966–1973 (2009).

31. Hunter, B. M., Gray, H. B. & Müller, A. M. Earth-Abundant Heterogeneous Water Oxidation Catalysts. *Chem. Rev.* **116**, 14120–14136 (2016).

32. Blakemore, J. D., Crabtree, R. H. & Brudvig, G. W. Molecular Catalysts for Water Oxidation. *Chem. Rev.* (2015) doi:10.1021/acs.chemrev.5b00122.

33. Zou, X. & Zhang, Y. Noble metal-free hydrogen evolution catalysts for water splitting. *Chem. Soc. Rev.* **44**, 5148–5180 (2015).

34. Concepcion, J. J., Tsai, M.-K., Muckerman, J. T. & Meyer, T. J. Mechanism of Water Oxidation by Single-Site Ruthenium Complex Catalysts. *J. Am. Chem. Soc.* **132**, 1545–1557 (2010).

35. Inoue, H. *et al.* The Water Oxidation Bottleneck in Artificial Photosynthesis: How Can We Get Through It? An Alternative Route Involving a Two-Electron Process. *ChemSusChem* **4**, 173–179 (2011).

36. Wang, Y. *et al.* Mimicking Natural Photosynthesis: Solar to Renewable H2 Fuel Synthesis by Z-Scheme Water Splitting Systems. *Chem. Rev.* **118**, 5201–5241 (2018).

37. Wang, Q. *et al.* Oxysulfide photocatalyst for visible-light-driven overall water splitting. *Nat. Mater.* **18**, 827–832 (2019).

38. Maeda, K. Z-Scheme Water Splitting Using Two Different Semiconductor Photocatalysts. *ACS Catal.* **3**, 1486–1503 (2013).

39. Wang, Q. & Domen, K. Particulate Photocatalysts for Light-Driven Water Splitting: Mechanisms, Challenges, and Design Strategies. *Chem. Rev.* **120**, 919–985 (2020).

40. Yu, T. *et al.* Triplet–Triplet Annihilation Upconversion for Photocatalytic Hydrogen Evolution. *Chem. – Eur. J.* **25**, 16270–16276 (2019).

41. Zhang, M. *et al.* Improving Hematite's Solar Water Splitting Efficiency by Incorporating Rare-Earth Upconversion Nanomaterials. *J. Phys. Chem. Lett.* **3**, 3188–3192 (2012).

42. Einzinger, M. *et al.* Sensitization of silicon by singlet exciton fission in tetracene. *Nature* **571**, 90–94 (2019).

43. Martinez, M. S., Nozik, A. J. & Beard, M. C. Theoretical limits of multiple exciton generation and singlet fission tandem devices for solar water splitting. *J. Chem. Phys.* **151**, 114111 (2019).

44. Liu, J. *et al.* Metal-free efficient photocatalyst for stable visible water splitting via a two-electron pathway. *Science* **347**, 970–974 (2015).

45. Godemann, C. *et al.* A Model of a Closed Cycle of Water Splitting Using ansa-Titanocene(III/IV) Triflate Complexes. *J. Am. Chem. Soc.* **137**, 16187–16195 (2015).

46. Hollmann, D. *et al.* Hydrogen Generation by Water Reduction with [Cp*2Ti(OTf)]: Identifying Elemental Mechanistic Steps by Combined In Situ FTIR and In Situ EPR Spectroscopy Supported by DFT Calculations. *Chem. – Eur. J.* **19**, 13705–13713 (2013).

47. Goez, M., Schiewek, M. & Musa, M. H. O. Near-UV Photoionization of [Ru(bpy)3]2+: A Catalytic Cycle with an Excited Species as Catalyst. *Angew. Chem. Int. Ed.* **41**, 1535–1538 (2002).

48. Goez, M., von Ramin-Marro, D., Othman Musa, M. H. & Schiewek, M. Photoionization of [Ru(bpy)3]2+: A Catalytic Cycle with Water as Sacrificial Donor. *J. Phys. Chem. A* **108**, 1090–1100 (2004).

49. McGrail, B. T., Pianowski, L. S. & Burns, P. C. Photochemical Water Oxidation and Origin of Nonaqueous Uranyl Peroxide Complexes. *J. Am. Chem. Soc.* **136**, 4797–4800 (2014).

50. Kee, J. W., Tan, Y. Y., Swennenhuis, B. H. G., Bengali, A. A. & Fan, W. Y. Hydrogen Generation from Water upon CpMn(CO)3 Irradiation in a Hexane/Water Biphasic System. *Organometallics* **30**, 2154–2159 (2011).

51. Vogler, A. & Kunkely, H. Splitting of alkyl carbonates photocatalyzed by copper complexes as a model for an artificial photosynthesis. *Inorg. Chem. Commun.* **14**, 96–98 (2011).

52. Kunkely, H. & Vogler, A. Water Splitting by Light with Osmocene as Photocatalyst. *Angew. Chem. Int. Ed.* **48**, 1685–1687 (2009).

53. Ge, P. *et al.* Biphasic water splitting by osmocene. *Proc. Natl. Acad. Sci.* **109**, 11558–11563 (2012).

54. Katakis, D. F., Mitsopoulou, C., Konstantatos, J., Vrachnou, E. & Falaras, P. Photocatalytic splitting of water. *J. Photochem. Photobiol. Chem.* **68**, 375–388 (1992).

55. Zarkadoulas, A., Koutsouri, E. & Mitsopoulou, C. A. A perspective on solar energy conversion and water photosplitting by dithiolene complexes. *Coord. Chem. Rev.* **256**, 2424–2434 (2012).

56. Kohl, S. W. *et al.* Consecutive Thermal H2 and Light-Induced O2 Evolution from Water Promoted by a Metal Complex. *Science* **324**, 74–77 (2009).

57. Yang, X. & Hall, M. B. Mechanism of Water Splitting and Oxygen−Oxygen Bond Formation by a Mononuclear Ruthenium Complex. *J. Am. Chem. Soc.* **132**, 120–130 (2010).

58. Sandhya, K. S. & Suresh, C. H. Water Splitting Promoted by a Ruthenium(II) PNN Complex: An Alternate Pathway through a Dihydrogen Complex for Hydrogen Production. *Organometallics* **30**, 3888–3891 (2011).

59. Ma, C., Piccinin, S. & Fabris, S. Reaction Mechanisms of Water Splitting and H_2 Evolution by a Ru(II)-Pincer Complex Identified with Ab Initio Metadynamics Simulations. *ACS Catal.* **2**, 1500–1506 (2012).

60. Li, H. & Hall, M. B. Computational Mechanistic Studies on Reactions of Transition Metal Complexes with Noninnocent Pincer Ligands: Aromatization–Dearomatization or Not. *ACS Catal.* **5**, 1895–1913 (2015).

61. Alberico, E. *et al.* Unravelling the Mechanism of Basic Aqueous Methanol Dehydrogenation Catalyzed by Ru–PNP Pincer Complexes. *J. Am. Chem. Soc.* **138**, 14890–14904 (2016).

62. Chen, Y. & Fang, W.-H. Mechanism for the Light-Induced O2 Evolution from H2O Promoted by Ru(II) PNN Complex: A DFT Study. *J. Phys. Chem. A* **114**, 10334–10338 (2010).

63. Shehzad, N., Tahir, M., Johari, K., Murugesan, T. & Hussain, M. A critical review on TiO2 based photocatalytic CO2 reduction system: Strategies to improve efficiency. *J. CO2 Util.* **26**, 98–122 (2018).

64. Afanasyev, O. I., Kuchuk, E., Usanov, D. L. & Chusov, D. Reductive Amination in the Synthesis of Pharmaceuticals. *Chem. Rev.* **119**, 11857–11911 (2019).

65. Wiesenfeldt, M. P., Nairoukh, Z., Dalton, T. & Glorius, F. Selective Arene Hydrogenation for Direct Access to Saturated Carbo- and Heterocycles. *Angew. Chem. Int. Ed.* **58**, 10460–10476 (2019).

66. Wiesenfeldt, M. P., Nairoukh, Z., Li, W. & Glorius, F. Hydrogenation of fluoroarenes: Direct access to all-cis-(multi)fluorinated cycloalkanes. *Science* **357**, 908–912 (2017).

67. Luque-Urrutia, J. A. & Poater, A. The Fundamental Noninnocent Role of Water for the Hydrogenation of Nitrous Oxide by PNP Pincer Ru-based Catalysts. *Inorg. Chem.* **56**, 14383–14387 (2017).

68. Yao, L. *et al.* A DFT study on the mechanisms of hydrogenation and hydrosilylation of nitrous oxide catalyzed by a ruthenium PNP pincer complex. *Comput. Theor. Chem.* **1128**, 48–55 (2018).

69. Mutoh, K., Nakagawa, Y., Sakamoto, A., Kobayashi, Y. & Abe, J. Stepwise Two-Photon-Gated Photochemical Reaction in Photochromic [2.2]Paracyclophane-Bridged Bis(imidazole dimer). *J. Am. Chem. Soc.* **137**, 5674–5677 (2015).

70. Ghosh, I., Ghosh, T., Bardagi, J. I. & König, B. Reduction of aryl halides by consecutive visible light-induced electron transfer processes. *Science* **346**, 725–728 (2014).

71. Khalil, M., Gunlazuardi, J., Ivandini, T. A. & Umar, A. Photocatalytic conversion of CO2 using earth-abundant catalysts: A review on mechanism and catalytic performance. *Renew. Sustain. Energy Rev.* **113**, 109246 (2019).

72. Liu, L. & Li, Y. Understanding the Reaction Mechanism of Photocatalytic Reduction of CO2 with H2O on TiO2-Based Photocatalysts: A Review. *Aerosol Air Qual. Res.* **14**, 453–469 (2014).

73. Kreft, S. *et al.* Improving Selectivity and Activity of CO2 Reduction Photocatalysts with Oxygen. *Chem* **5**, 1818–1833 (2019).

74. Liu, L., Gao, F., Zhao, H. & Li, Y. Tailoring Cu valence and oxygen vacancy in Cu/TiO2 catalysts for enhanced CO2 photoreduction efficiency. *Appl. Catal. B Environ.* **134–135**, 349–358 (2013).

75. Slamet, H. W. N., Purnama, E., Riyani, K. & Gunlazuardi, J. Effect of copper species in a photocatalytic synthesis of methanol from carbon dioxide over copper-doped titania catalysts. *World Appl. Sci. J.* **6**, 112–122 (2009).

76. Munuera, G., González-Elipe, A. R., Soria, J. & Sanz, J. Photo-adsorption and photo-desorption of oxygen on highly hydroxylated TiO2 surfaces. Part 3.—Role of H2O2 in photo-desorption of O2. *J. Chem. Soc. Faraday Trans. 1 Phys. Chem. Condens. Phases* **76**, 1535–1546 (1980).

77. Boonstra, A. H. & Mutsaers, C. A. H. A. Relation between the photoadsorption of oxygen and the number of hydroxyl groups on a titanium dioxide surface. *J. Phys. Chem.* **79**, 1694–1698 (1975).

78. Kiwi, J. & Graetzel, M. Specific analysis of surface-bound peroxides formed during photoinduced water cleavage in titanium dioxide-based microheterogeneous systems. *J. Mol. Catal.* **39**, 63–70 (1987).

79. Ardenkjær-Larsen, J. H. *et al.* Increase in signal-to-noise ratio of > 10,000 times in liquid-state NMR. *Proc. Natl. Acad. Sci.* **100**, 10158–10163 (2003).

80. Liland, K. H., Almøy, T. & Mevik, B.-H. Optimal Choice of Baseline Correction for Multivariate Calibration of Spectra. *Appl. Spectrosc.* **64**, 1007–1016 (2010).

81. Zhao, J., Lui, H., McLean, D. I. & Zeng, H. Automated Autofluorescence Background Subtraction Algorithm for Biomedical Raman Spectroscopy. *Appl. Spectrosc.* **61**, 1225–1232 (2007).

82. Xu, Z., Sun, X. & Harrington, P. de B. Baseline Correction Method Using an Orthogonal Basis for Gas Chromatography/Mass Spectrometry Data. *Anal. Chem.* **83**, 7464–7471 (2011).

83. Shin, H., Sampat, M. P., Koomen, J. M. & Markey, M. K. Wavelet-Based Adaptive Denoising and Baseline Correction for MALDI TOF MS. *OMICS J. Integr. Biol.* **14**, 283–295 (2010).

84. Svoboda, R. Tangential area-proportional baseline interpolation for complex-process DSC data – Yes or no? *Thermochim. Acta* **658**, 55–62 (2017).

85. Ruijter, J. M. *et al.* Evaluation of qPCR curve analysis methods for reliable biomarker discovery: Bias, resolution, precision, and implications. *Methods* **59**, 32–46 (2013).

86. Klementev, K. V. Extraction of the fine structure from x-ray absorption spectra. *J. Phys. Appl. Phys.* **34**, 209–217 (2000).

87. Beweries, T. *et al.* Catalytic and Kinetic Studies of the Dehydrogenation of Dimethylamine Borane with an iPr Substituted Titanocene Catalyst. *ChemCatChem* **3**, 1865–1868 (2011).

88. Wang, Y., Kang, H., Liu, X. & Tong, Z. Combination of RT-qPCR Testing and Clinical Features For Diagnosis of COVID-19 facilitates management of SARS-CoV-2 Outbreak. *J. Med. Virol.* **n/a**,.

89. Gross, T., Seayad, A. M., Ahmad, M. & Beller, M. Synthesis of Primary Amines: First Homogeneously Catalyzed Reductive Amination with Ammonia. *Org. Lett.* **4**, 2055–2058 (2002).

90. Gallardo-Donaire, J. *et al.* Direct Asymmetric Ruthenium-Catalyzed Reductive Amination of Alkyl–Aryl Ketones with Ammonia and Hydrogen. *J. Am. Chem. Soc.* **140**, 355–361 (2018).

91. Corey, E. J. & Kühnle, F. N. M. A simplified synthesis of (±)-1,2-diphenyl-1,2-diaminoethane (1) from benzaldehyde and ammonia. Revision of the structures of the long-known intermediates “hydrobenzamide” and “amarine”. *Tetrahedron Lett.* **38**, 8631–8634 (1997).

92. Baumann, W., Börner, A. & Selent, D. Gas injection and circulation device for tracking of reactions in the liquid phase involving gaseous reactants under normal and high pressure by means of nuclear magnetic resonance spectroscopy (NMR spectroscopy pressure) under steady state conditions. (2008), DE10333143B4.

8 Appendix

8.1 Supporting Information for “Two-photon water splitting at a molecular ruthenium complex”

Supporting Information for

Two-photon water splitting at a molecular ruthenium complex

Jacob Schneidewind*, Miguel A. Argüello Cordero, Henrik Junge, Stefan Lochbrunner, Matthias Beller

*Corresponding author, **e-mail:** Jacob.Schneidewind@catalysis.de

Other supplementary materials for this manuscript:

Original data and analysis code are publicly available at:
https://github.com/jschneidewind/Water-Splitting

1 Table of Contents

1.1 Table of Figures

1.2 Table of Tables

2 Methods and Materials

All experiments involving ruthenium complexes (unless stated otherwise) were carried out under argon using either standard Schlenk technique or in an argon filled glovebox (MBRAUN). Organic solvents were purified using a solvent purification system (Innovative Technology) and stored under argon. Water was purified using a Merck Milli-Q system, followed by degassing using argon sparging and storage under argon. Organic deuterated solvents were degassed using three freeze-pump-thaw cycles and stored over 3 Å molecular sieves. D_2O was distilled under argon.

Carbonylchlorohydridotris(triphenylphosphine)ruthenium(II) ($(PPh_3)_3RuCl(CO)H$) was purchased from Strem Chemicals, 2-((Di-tert-butylphosphinomethyl)-6-diethylaminomethyl)pyridine (in the following abbreviated as PNN) was purchased from Sigma Aldrich. Potassium *tert*-butoxide was purchased from TCI, nitrous oxide was purchased from Linde and all other chemicals were purchased from Sigma Aldrich. Chemicals were used as received.

(PNN)RuCl(CO)H was prepared as previously described.[1]

Nuclear magnetic resonance (NMR) spectra were recorded on a Bruker AV-300 (300 MHz), AV-400 (400 MHz) or f300 (300 MHz) spectrometer and analyzed using MestreNova. ^{1}H and ^{13}C chemical shifts are reported relative to the respective solvent peak as parts per million. ^{31}P chemical shifts are reported relative to 0.3M H_3PO_4 in D_2O (set to $\partial(^{31}P) = -0.425$ ppm) as parts per million. Multiplicities are indicated using the following abbreviations: s (singlet), d (doublet), t (triplet), q (quartet), m (multiplet), b (broad).

Infrared spectroscopy was performed using a Bruker-ALPHA FT-IR spectrometer in attenuated total reflectance measurement mode. The following abbreviations are used: br (broad), s (singlet), vs (very strong singlet), m (multiplet).

Electron paramagnetic resonance (EPR) spectroscopy was performed using a X-band Bruker EMX CW-micro EPR spectrometer equipped with an ER4119HS high-sensitivity resonator using a microwave power of ca. 6.9 mW, modulation frequency of 100 kHz and modulation amplitude up to 5 G.

UV/Vis spectroscopy was performed using an Analytik Jena SPECORD S 600 diode array UV/Vis spectrometer (40 ms integration time, 100 accumulations). Fluorescence spectroscopy was performed using a Cary Eclipse fluorescence spectrometer (Agilent), with 20 nm slit widths for excitation and emission (excitation wavelength: 370 nm).

Elemental analysis was performed using a Leco TruSpec Micro CHNS analyzer.

Oxygen measurements were performed using a FireStingO2 optical oxygen meter (PyroScience GmbH) along with trace range robust probes (PyroScience GmbH, for liquid phase measurements) or trace range oxygen sensor spots (PyroScience GmbH, for gas phase measurements). Temperature compensation was done using a Pt100 temperature sensor (Therma Thermofühler GmbH).

Irradiation was performed using two different light sources:
(a) A Lumatec SUPERLITE S 04 with a liquid light guide (Lumatec, light guide diameter: 1 cm). This is a mercury vapor light source with an integrated filter wheel to select different wavelength regions (for the spectral power distribution of the selected filter configurations, see Figure 6.1-1). This light source is referred to as the “Hg light source” in the following.
(b) A 250 W quartz tungsten halogen (abbreviated as QTH) Research Light Source with a F/1, 1.5 inch, two element, plano convex condenser (Newport). The light source was equipped with a 6 cm quartz distilled water filter (Quantum Design), which filters out all wavelengths below 280 nm and above 1000 nm, and a manual light source shutter (Newport). Furthermore, the light source was combined with different colored class alternative longpass filters (Newport) to further control the irradiation wavelengths. This light source is referred to as the “QTH light source” in the following.

3 Synthesis Procedures and Characterization

3.1 Synthesis of Complex 1

3.1.1 Synthesis using N_2O

Complex 1 was synthesized following a modified version of the previously reported procedure.[2]

(PNN)RuCl(CO)H (302.5 mg, 0.62 mmol) and KO*t*Bu (69.5 mg, 0.62 mmol) were placed in a Schlenk flask, followed by addition of 30 ml Et_2O, yielding a dark red suspension. The suspension was stirred at room temperature for one hour, yielding a dark red solution with a small amount of solid (KCl). The solution was filtered into a separate Schlenk flask to remove the formed KCl and then the solvent was removed under vacuum, yielding a black-red solid of (PNN*)Ru(CO)H (PNN* indicates dearomatization of the PNN ligand). (PNN*)Ru(CO)H was directly used for the next reaction step without further purification and assuming quantitative conversion.

To the Schlenk flask containing (PNN*)Ru(CO)H, 16 ml THF were added, yielding a dark red solution (see Figure 3.1-1). To this solution, 9 equivalents of H_2O (100 µl, 5.6 mmol) were added, resulting in an immediate color change from dark red to dark yellow/orange (see Figure 3.1-1) due to formation of complex **2-trans**. It is important at this stage to add no more than 9 equivalents of H_2O, as the presence of more water leads to a different reaction product (see Figure 7.7-1) when **2-trans** is exposed to N_2O.

The THF solution of **2-trans** containing 9 equivalents of H_2O was transferred to a separate reaction assembly (see Figure 3.1-2), where it was sparged with N_2O for 10 – 20 min. Afterwards, the Schlenk flask containing the solution of **2-trans** was closed under a N_2O atmosphere and was stirred at room temperature in the dark for 22 h. After the reaction time, a dark green solution was formed (see Figure 3.1-1). If more than 9 equivalents of water were present in the reaction solution, a dark red solution was formed instead, containing the different reaction product shown in Figure 7.7-1.

The dark green solution was concentrated in volume by roughly half, followed by addition of 100 ml Et_2O, leading to precipitation of a solid. The solid was filtered off, washed three times with 1 ml Et_2O each and dried under vacuum, yielding **1** as a yellow solid (70 mg, 23% yield with respect to (PNN)Ru(CO)ClH, see Figure 3.1-3). The final product typically contains up to 3% of unreacted **2-trans**, which could not be removed. Unfortunately, repeated attempts to crystallize **1** were unsuccessful.

We would like to note at this point that complex **1** is in fact a yellow solid, yielding a yellow solution in H_2O (see Figure 3.1-3), and not a green solid yielding a green aqueous solution as described before.[2] The green color of the solution after reaction with N_2O can be attributed to Ru(III) species, which are formed as side products during the reaction (see Figure 8.2-1 for an EPR spectrum of the green raw product after reaction with N_2O). Complex **1**, however is an EPR inactive Ru(II) species. The green color of the final product, which was previously described, might therefore be attributed to some residual Ru(III) species. These residual Ru(III) species might also explain the additional absorption features in the originally reported UV/Vis spectrum[2] compared to our UV/Vis spectrum. Furthermore, we found that in chlorinated solvents (such as dichloromethane, DCM), **1** can be converted to chloride complexes (possibly due to reaction with trace amounts of HCl present in the solvent). We therefore avoided the use of chlorinated solvents with **1**.

Spectroscopic data for **1**:

^{1}H NMR (400 MHz, H_2O, r.t.) δ 7.37 (t, *J* = 7.9 Hz, 1H, py-*H*^{4}), 7.10 (d, *J* = 7.9 Hz, 1H, py-*H*^{3}), 7.00 (d, *J* = 7.8 Hz, 1H, py-*H*^{5}), 3.87 (dd, *J* = 15.3, 3.2 Hz, 1H, py-NC*H*$_2$), 3.75 (d, *J* = 15.2 Hz, 1H, py-NC*H*$_2$), 3.48 (dd, *J* = 17.5, 10.9 Hz, 1H, py-PC*H*$_2$), 3.04 (dd, *J* = 17.4, 7.4 Hz, 1H, py-PC*H*$_2$), 2.79 (dq, *J* = 13.9, 6.9 Hz, 1H, C*H*$_2$CH$_3$), 2.50 (dq, *J* = 14.4, 7.2 Hz, 1H, C*H*$_2$CH$_3$), 2.45 – 2.29 (m, 2H,

C*H*$_2$CH$_3$), 1.02 (d, *J* = 14.5 Hz, 9H, P(C(C*H*$_3$)$_3$)$_2$), 0.76 (t, *J* = 7.0 Hz, 3H, CH$_2$C*H*$_3$), 0.71 (t, *J* = 7.1 Hz, 3H, CH$_2$C*H*$_3$), 0.68 (d, *J* = 13.0 Hz, 9H, P(C(C*H*$_3$)$_3$)$_2$) ppm. (see Figure 7.1-1)

^{1}H NMR data is provided in H_2O since it avoids disappearance of methylene protons (which occurs for D_2O). In the ^{1}H NMR spectrum of **1** in DMSO-d_6, a broadened singlet can be observed at $\partial(^1H)$ = 4.22 ppm, integrating to 2H (see Figure 7.1-3). This signal might be attributed to the two hydroxo protons,[3] being shifted significantly downfield compared to the previously described value of $\partial(^1H)$ = -7.4 due to interaction with DMSO-d_6.

^{13}C NMR (101 MHz, DMSO-d_6, r.t.) δ 207.92 (d, *J* = 15.1 Hz, *C*O), 164.41 (s, py-*C*^{3}), 160.55 (s, py-*C*^{5}), 138.51 (s, py-*C*^{4}), 122.22 (d, *J* = 8.1 Hz, py-*C*^{6}), 120.97 (s, py-*C*^{2}), 62.10 (s, py-N*C*H$_2$) , 51.00 (s, *C*H$_2$CH$_3$), 44.17 (s, *C*H$_2$CH$_3$), 37.78 (d, *J* = 12.9 Hz, P(*C*(CH$_3$)$_3$)$_2$), 37.60 (d, *J* = 24.8 Hz, py-P*C*H$_2$), 36.51 (d, *J* = 15.0 Hz, P(*C*(CH$_3$)$_3$)$_2$), 30.48 (d, *J* = 3.6 Hz, P(C(*C*H$_3$)$_3$)$_2$), 28.97 (d, *J* = 2.6 Hz, P(C(*C*H$_3$)$_3$)$_2$), 9.28 (s, CH$_2$*C*H$_3$), 8.87 (s, CH$_2$*C*H$_3$) ppm. (see Figure 7.1-4)

^{31}P{^{1}H} NMR (162 MHz, DMSO-d_6, r.t.) δ 92.56 (s, *P*^{t}Bu$_2$) ppm. (see Figure 7.1-5)

^{31}P{^{1}H} NMR (162 MHz, H_2O, r.t.) δ 88.24 (s, *P*^{t}Bu$_2$) ppm. (see Figure 7.1-2)

IR (ATR): $\tilde{\nu}$ = 3393br (OH), 2948m, 1917vs (CO), 1568s cm^{-1}. (see Figure 8.1-1)

UV/Vis (H_2O): λ_{abs} (ε / cm^{-1} M^{-1}) = 370 (1630), 305 (3510).

Elemental analysis: anal. calc. for $C_{20}H_{37}N_2O_3PRu$ • 3 H_2O: C, 44.52; H, 8.03; N, 5.19. Found: C, 44.25; H, 8.078; N, 5.002.

3.1.2 Photographs Showing Synthesis and Product

Figure 3.1-1 Photographs of synthesis stages during preparation of complex 1
Left: Solution of [Ru(PNN*)(CO)H] in THF (dark red solution).
Middle: Solution on the left after addition of 9 equivalents of H_2O, forming complex **2-trans** (dark yellow/orange solution).
Right: Solution in the middle after reaction with N_2O for 22h (dark green solution).

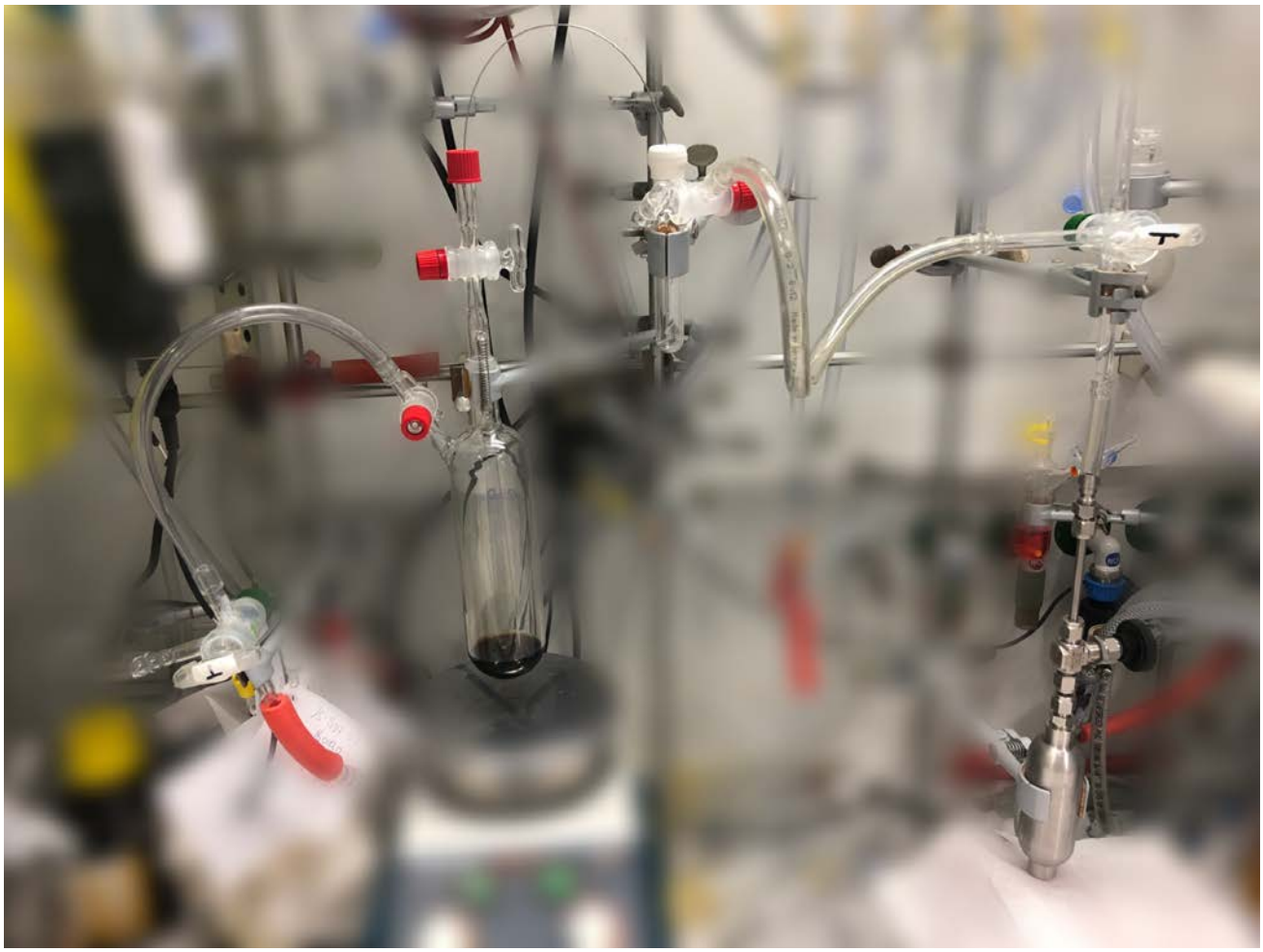

Figure 3.1-2 Reaction set-up for reaction of 2-trans with N_2O
From right to left: N_2O gas tank (right bottom) is connected to a T-piece (right), which leads to the Schlenk line (top connection) and to a Schlenk flask (top middle). This Schlenk flask is topped with a rubber septum containing a cannula (top), which leads into the main reaction flask (containing **2-trans**) through a septum (red cap) and a valve. The main reaction flask is connected to a second T-piece valve (left), which leads to the Schlenk line (bottom) and to a separate bubble counter (left). Background is blurred to highlight the reaction assembly.

Figure 3.1-3 Complex 1 as a solid (left) and in aqueous solution (right)

3.1.3 Synthesis using Ag_2O

(PNN)$RuCl_2$(CO) (66 mg, 0.126 mmol, mixture of cis and trans isomers) and Ag_2O (179 mg, 0.772 mmol) were placed in a Schlenk flask along with 4.5 ml of acetone and 0.6 ml of H_2O, yielding a dark yellow suspension. The suspension was stirred for 2 h in the dark, after which it was filtered into a separate Schlenk flask, yielding a dark yellow solution. Subsequently, all volatiles were removed under vacuum and the dark yellow residue was redissolved in 2.1 ml THF, yielding a dark yellow solution with some insoluble material. The insoluble materials were removed via filtration, and 18 ml Et_2O were added to the dark yellow THF solution to precipitate the product. The solid was filtered off, washed three times with 1 ml Et_2O each and dried under vacuum, yielding a yellow solid.

While this synthesis procedure does yield complex **1** (see Figure 7.1-6 and Figure 7.1-7 for NMR spectra of the product), the obtained product is less pure than the one obtained via the N_2O synthesis route. The main impurity can be observed at $\partial(^{31}P)$ = 55.12 ppm, which might be attributed to an alkyl phosphinic acid resulting from ligand oxidation by Ag_2O. Due to the less pure nature of the product, the N_2O synthesis route was the preferred one. However, further improvements to this silver based synthesis route might offer a more simple and general access to ruthenium dihydroxo complexes.

3.1.4 Synthesis via Reflux of 2-trans

This is a modified version of the previously described procedure for the synthesis of **1** via reflux of **2-trans**.[2]

(PNN*)Ru(CO)H was synthesized as described in 3.1.1, using 53 mg (0.109 mmol) of (PNN)RuCl(CO)H. To the Schlenk flask containing solid (PNN*)Ru(CO)H, 2.5 ml of H_2O were added, yielding a clear, light yellow solution of **2-trans**.
The solution was then refluxed for three days, during which time the color of the solution changed to dark red/orange and a small amount of black, insoluble material formed.

At the end of the reaction time, the solution was cooled to room temperature and analyzed using NMR spectroscopy (see Figure 7.1-8 and Figure 7.1-9), showing formation of **1** along with unreacted **2-trans** and other, unidentified reaction products. The obtained product was not isolated.

3.2 Synthesis of Complex 2-trans

3.2.1 Synthesis in H_2O

Complex **2-trans** was synthesized in H_2O as described in 3.1.4, yielding a clear, light yellow solution. The obtained product was analyzed using NMR spectroscopy (see Figure 7.2-1 and Figure 7.2-2) and was not isolated. Obtained NMR data was consistent with the previously described.[2]

3.2.2 Crystallization of 2-trans

(PNN*)Ru(CO)H (31 mg, 0.069 mmol, synthesized as described in 3.1.1) was dissolved in 1.1 ml toluene, yielding a dark red solution. To this solution, 9 equivalents of H_2O (11 µl, 0.61 mmol) were added, leading to a rapid color change to form a clear orange solution with a small aqueous phase at the bottom. The organic phase was transferred to a separate Schlenk flask and stored at -32 °C overnight, yielding colorless/light yellow crystals. In an ice bath, the liquid phase was removed using a syringe and the crystals were washed twice with 0.4 ml ice-cold heptane.

The thus obtained crystals were used in both the N_2O and reflux synthesis route for complex **1**, yielding the same results as in situ prepared **2-trans** (as described above).

When the aqueous phase of this synthesis (still containing some of the toluene phase as well) was stored at room temperature for one day, colorless, plate-shaped crystals of **2-trans** suitable for X-ray crystallography were formed.

3.3 Synthesis of (p-cymene)$RuCl_2$(CO)

(p-cymene)$RuCl_2$(CO) was prepared using a previously described procedure.[4]

In a 50 ml Schlenk flask (internal volume ca. 65 ml), a orange/red solution of [(p-cymene)$RuCl_2$]$_2$ (200 mg, 0.33 mmol) in 4 ml DCM was placed under vacuum using freeze-pump-thaw and warmed back to room temperature. Subsequently, 16 ml of CO gas (ca. 0.66 mmol, 2 equivalents) were injected into the Schlenk flask through a septum using a gas-tight syringe. The solution was then stirred at room temperature for 45 min, during which the color changed to deep red. Subsequently, the solvent was removed, yielding a salmon pink solid (187 mg, 85% yield). Characterization by NMR spectroscopy (see Figure 7.3-1) was consistent with the previously reported data.[4]

3.4 Synthesis of (PNN)$RuCl_2$(CO)

(p-cymene)$RuCl_2$(CO) (375 mg, 1.12 mmol) was suspended in THF (10 ml) and a solution of PNN (376 mg, 1.17 mmol in 15 ml THF) was added, yielding a red suspension. It was then refluxed for 15 h, yielding an orange solution with a yellow solid. The reaction solution was cooled to room temperature and stored at -32 °C overnight, leading to precipitation of more yellow solid. After warming back to room temperature, the volume of the reaction solution was reduced by ca. 70% under vacuum, followed by addition of 80 ml of heptane. The solid was filtered off from the yellow suspension and washed three times with 4 ml of heptane, followed by drying under vacuum. This yielded a yellow solid (457 mg, 78% yield with respect to (p-cymene)$RuCl_2$(CO)). Characterization by NMR spectroscopy showed the presence of a mixture of the cis and trans isomers (see Figure 7.4-1 and Figure 7.4-2, ca. 3% of impurity are visible at $\partial(^{31}P)$ = 74.57 ppm) and the obtained data was consistent with the previsouly reported.[5]

4 Procedures for Irradiation and Subsequent Data Analysis

4.1 NMR Scale Irradiation

4.1.1 Irradiation Procedure

550 µl of a 0.01M solution of **1** (prepared via the N_2O synthesis route) in H_2O was placed inside a J. Young NMR tube along with a flame sealed capillary containing a 0.3M H_3PO_4 solution in D_2O. ^1H and quantitative $^{31}P\{^1H\}$ NMR spectra were then recorded before irradiation. Subsequently, the NMR tube was irradiated with either the QTH or Hg light source (or both) while being cooled with a 20 W fan (for the irradiation set-up see Figure 4.5-1).

For the concentration-time profile experiments, only the QTH light source was used for irradiation, being equipped with the distilled water filter. The total irradiation time was 46.5 h. For dual irradiation experiments, either or both light sources were used, the Hg light source being filtered to 320 – 400 nm (see Figure 6.1-1, fixed intensity setting) and the QTH light source being equipped with a > 495 nm longpass filter in addition to the distilled water filter. For each dual irradiation experiment, the irradiation time was 17 h. In all cases care was taken not to alter the positioning of either the NMR tube or light sources between experiments, so as not to change the photon flux received by the NMR tube. QTH and Hg light sources were arranged at a 90° angle.

After irradiation with the QTH light source (no longpass filter) or Hg light source, the color of the solution changed to yellow/orange. In case of irradiation with the QTH light source equipped with a > 495 nm longpass filter, no color change occurred. Immediately after irradiation, ^1H and quantitative $^{31}P\{^1H\}$ NMR spectra were recorded.

Irradiation experiments could also be performed in the same way using complex **1** prepared via the Ag_2O synthesis route. In this case, however, **1** had to be dissolved in a 52 mM aqueous KOH solution instead of pure H_2O. This was likely necessary to compensate for the weakly acidic nature of **1** obtained via the Ag_2O route (likely due to the phosphinic acid impurity). When irradiation of **1** (Ag_2O route) was performed in 52 mM KOH aq., the results were effectively identical to those obtained using the above described procedure. For simplicity, however, all reported experiments (except noted otherwise) were performed using **1** obtained via the N_2O synthesis route in pure H_2O.

4.1.2 Interpretation of NMR Results

Irradiation with either the QTH light source (no longpass filter) or Hg light source resulted in the same qualitative changes as observed by NMR spectroscopy. Figure 7.5-1 and Figure 7.5-2 show representative examples of ^1H and $^{31}P\{^1H\}$ spectra recorded after irradiation, respectively. In the ^1H spectrum, appearance of a new hydride signal at $\partial(^1H)$ = -5.24 ppm can be observed. In the $^{31}P\{^1H\}$ spectrum, the major changes are a significant reduction in signal intensity for $\partial(^{31}P)$ = 88.22 ppm (complex **1**), and the appearance of two new signals at $\partial(^{31}P)$ = 104.36 ppm and $\partial(^{31}P)$ = 95.12 ppm (along with some smaller signals).

Through ^1H-^{31}P HMBC (see Figure 7.5-3) it could be established that the hydride at $\partial(^1H)$ = -5.24 ppm and the $\partial(^{31}P)$ = 104.36 ppm signal are coupled, showing that this is a species distinct from **2-trans** ($\partial(^1H)$ = -18.9 ppm, $\partial(^{31}P)$ = 104.2 ppm, see Figure 7.5-3). However, it can be observed that in the dark (over the course of hours and days), the $\partial(^{31}P)$ = 104.36 ppm species converts to **2-trans** (see Figure 7.6-1 and Figure 7.6-2). Furthermore, when **2-trans** is irradiated (Hg light source, 320 – 500 nm) in the presence of O_2, it converts to the $\partial(^{31}P)$ = 104.36 ppm species (see Figure 7.5-5 and Figure 7.5-6). The interconversion of these two species indicates that they are isomers. When comparing their NMR characteristics, the biggest difference is the significantly downfield shifted hydride signal at $\partial(^1H)$ = -5.24 ppm for the $\partial(^{31}P)$ = 104.36 ppm species. Such a chemical shift is consistent with the hydride being trans to a CO ligand.[6,7] This is corroborated by DFT calculations for different isomers of **2**, which predict a change of ca. 10 ppm for the hydride signal when the hydride ligand is trans to the CO ligand (see Table 11.2-8), as compared to being trans to

the OH ligand (as is the case for **2-trans**). Furthermore, DFT calculations predict **2-cis** (where the hydride ligand is trans to CO and the OH ligand is in the equatorial position) to be less stable than **2-trans** by more than 10 kcal/mol. This difference in stability would explain the spontaneous conversion of the $\partial(^{31}P)$ = 104.36 ppm species to **2-trans**. Based on the characteristic hydride shift and these DFT results, we therefore assign the $\partial(^{31}P)$ = 104.36 ppm species to **2-cis**.

The second major product of irradiation can be observed at $\partial(^{31}P)$ = 95.12 ppm. For this species, the phosphorous signal couples to two different tert-butyl groups (see ^{1}H-^{31}P HMBC of aliphatic region in Figure 7.5-4). This indicates that, just like complex **1**, this complex has no symmetry, resulting in two chemically distinct tert-butyl groups. This observation rules out that this species is the trans isomer of **1**. In the dark, the species slowly converts back to **1** (see Figure 7.6-3, in this case the experiment was performed using **1** prepared via the Ag_2O route in 52 mM KOH aq., but the same is observed using the standard reaction conditions). We tentatively assign this species to **Oxo Dimer**, an oxo-bridged dimer formed via formal dehydration of **1** (see Figure 11.5-32 for the computed structure). DFT calculations predict **Oxo Dimer** to be slightly less stable than **1**, explaining why slow hydrolysis back to **1** might occur in the dark. Furthermore, a reasonable pathway for photochemical **Oxo Dimer** formation can proposed based on Ru-O bond formation in intermediate [**B-Trans**]T_0 (see 9.2).

Due to these isomerization reactions, NMR spectra for quantitative analysis were recorded immediately after irradiation.

4.1.3 Data Analysis for Concentration-Time Profile

For the concentration-time profile, quantitative $^{31}P\{^{1}H\}$ NMR spectra were recorded before (t = 0 h) and after 0.75, 2.97, 21.07, 24.44, 42.54 and 46.45 h of irradiation (irradiation of the sample was stopped after the indicated time, NMR spectra were recorded and irradiation was then resumed). For each time point, the relative concentrations of **1**, **2-cis** and **Oxo Dimer** were determined via integration of the corresponding $^{31}P\{^{1}H\}$ NMR signals. For t = 0 h, a small amount of **2-trans** could be observed, which was treated as **2-cis** in the following (since **2-trans** can photochemically convert to **2-cis**, see above). Therefore, the amount of **2-cis** at t = 0 h is not equal to zero. For all subsequent time points, no **2-trans** was observed.

For data analysis, the concentrations of **1**, **2-cis** and **Oxo Dimer** were normalized, so that for each time point the sum of the concentrations for these three compounds would be equal to one. This normalization ignores the formation of other products. However, since the amount of side products observable by $^{31}P\{^{1}H\}$ spectroscopy amounts to only around 7% after 46.45 h of irradiation this was deemed acceptable.

The resulting, normalized concentrations of **1**, **2-cis** and **Oxo Dimer** are shown in Figure 4.1-1 as dots. These datapoints were then fitted with a kinetic model based on the reaction network shown in Table 4.1-1, with k_1, k_2 and k_3 being the optimization parameters. Fitting was performed via the following steps:

1. Converting the reaction network to the corresponding rate laws describing the time-dependent concentration changes of **1**, **2-cis** and **Oxo Dimer**;
2. At each optimization step, numerically solving the resulting system of differential equations with an updated guess for k_1, k_2 and k_3 (generated using the L-BFGS-B algorithm), until convergence was reached. The optimized parameters for k_1, k_2 and k_3 are shown in Table 4.1-1.

From the data shown in Figure 4.1-1 it can be seen that **Oxo Dimer** is not an intermediate formed en route to **2-cis**, as the rate of **2-cis** formation does not increase with increasing **Oxo Dimer** concentration.

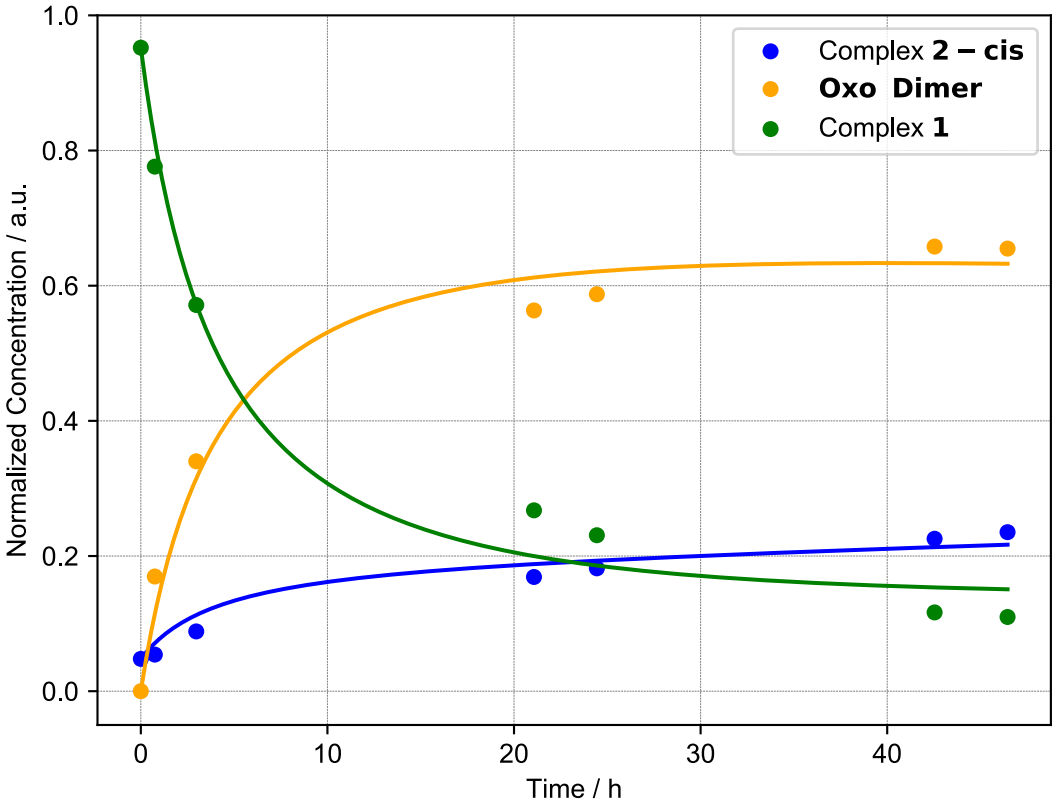

Figure 4.1-1 Concentration-time profile for irradiation of complex 1 with QTH light source
Dots show normalized concentrations obtained via integration of NMR spectra measured after indicated irradiation times. Straight lines are kinetic fit obtained using the kinetic model: **1** + **1** → **Oxo Dimer** (k_1), **1** + **1** → 2 **2-cis** (k_2), and **Oxo Dimer** → **1** + **1** (k_3).

Table 4.1-1 Optimized parameters for kinetic model

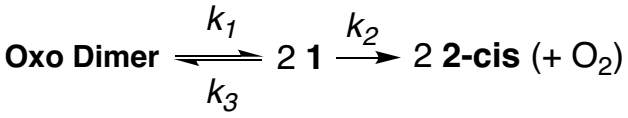

k_1 / h^{-1}	k_2 / h^{-1}	k_3 / h^{-1}
0.197	0.04	0.0076

4.1.4 Data Analysis for Dual Irradiation

For the dual irradiation data set, two irradiation experiments using only the Hg light source (320 – 400 nm), two experiments using both the Hg light source (320 – 400 nm) and the QTH light source (> 495 nm) as well as one experiment using only the QTH light source (> 495 nm) were performed.

For each experiment, quantitative $^{31}P\{^1H\}$ NMR spectra were recorded before and after irradiation. Relative concentrations of **1**, **2-trans** (before irradiation), **2-cis** (after irradiation), **Oxo Dimer** and an unidentified byproduct at $\partial(^{31}P)$ = ~ 97 ppm were determined via integration. For each experiment, concentrations were normalized so that the sum of the concentrations of all components would be the same before and after irradiation. When comparing the different experiments, the sum of all normalized concentrations differed at most 4% between them.

For each experiment, the yield of **2-cis** was determined by subtracting the normalized concentration of **2-trans** before irradiation from the normalized concentration of **2-cis** after irradiation. This was done to correct for any **2-cis** that was formed via photochemical isomerization of **2-trans**. The thus

obtained corrected concentration of **2-cis** was divided by the sum of all concentrations for the experiment to give the yield of **2-cis**. Reported yields for irradiation with either the Hg light source (320 – 400 nm) or both light sources are the averages of two separate irradiation experiments.

4.2 Liquid Phase O_2 Measurement

4.2.1 Irradiation Procedure

A 5 ml Schlenk flask with a GL14-threaded neck was equipped with a 5 mm PTFE stirring bar and a trace range robust O_2 probe, positioned so that it would later be immersed in the liquid phase (see Figure 4.5-3). The O_2 probe was connected to the Schlenk flask in a gas tight manner via the GL14-threaded neck with a 3 mm BOLA laboratory screw joint.
The Schlenk flask was then connected to the Schlenk line using a T-piece adapter, with one connection to the Schlenk line, one to the Schlenk flask and one connection being closed with a septum. Subsequently, ca. 500 - 550 µl of an aqueous solution of **1** (prepared via the N_2O synthesis route, 0.01 or 0.005 M concentration, it was confirmed that both concentrations gave the same results, see 4.2.6) was transferred into the Schlenk flask. The transfer was done via cannula transfer through the septum inlet of the T-piece adapter and through the valve of the Schlenk flask, taking care not to introduce any external O_2 into the flask.
Once the transfer was complete, the Schlenk flask was closed and placed into a double-walled beaker filled with water (see Figure 4.5-2 and Figure 4.5-3), which was thermostatted to 16.5 °C (unless stated otherwise). A PT100 temperature sensor (for temperature compensation of the O_2 measurement) was placed next to the Schlenk flask into the same water bath and the whole assembly was allowed to equilibrate for 15 – 20 min while being stirred at 1400 rpm.

After equilibration, the baseline O_2 concentration was typically measured for 15 – 30 min. Afterwards the flask was irradiated for 240 – 400 s. In case of the intensity dataset, irradiation was performed using the Hg light source (320 – 500 nm) with variable intensity settings. The same light source was used to measure the kinetic isotope effect and temperature dependence of the reaction. For the dual irradiation dataset, irradiation was performed using the Hg light source (320 – 400 nm), the QTH light source (different longpass filters), or both. When both light sources were used, the shutters of both were opened simultaneously. See Figure 4.5-2 and Figure 4.5-3 for the irradiation set-ups. In all cases, care was taken not to alter the position of the light sources or the reactor between experiments, so as not to change the photon flux received by the reactor. Hg and QTH light source were arranged at a 90° angle.

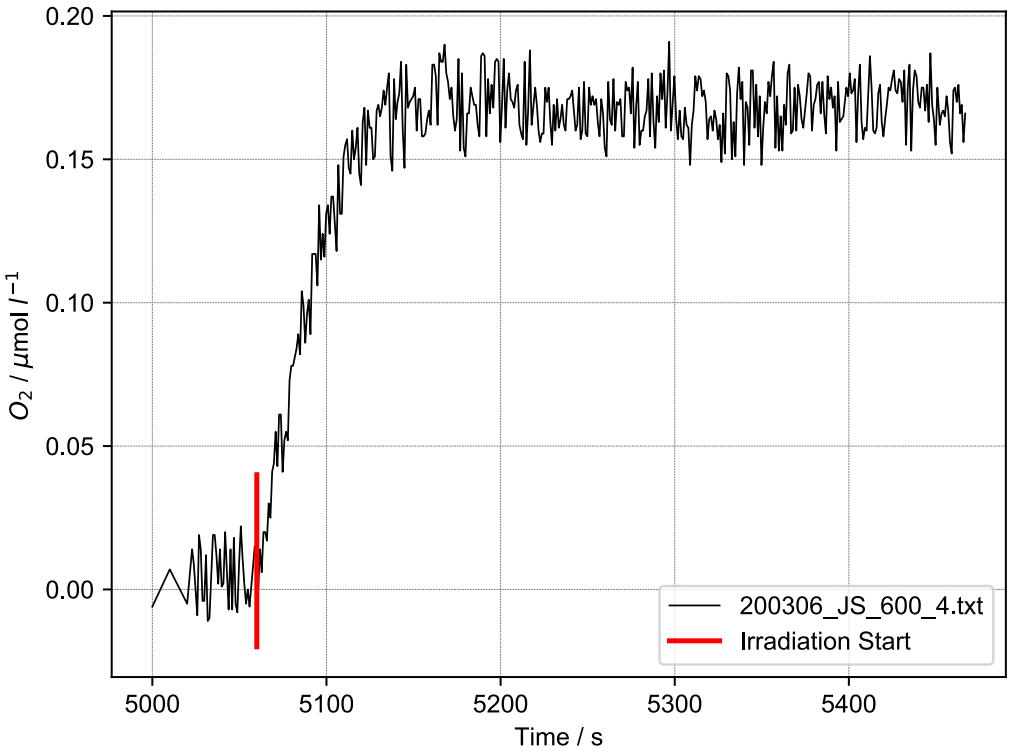

Figure 4.2-1 Exemplary liquid phase O_2 raw data (320 – 500 nm, 1 W intensity setting)

4.2.2 General Remarks on Data Analysis

For data analysis, the irradiation start point was set to t = 0 s. Furthermore, the baseline O_2 concentration was calculated using the average of all datapoints recorded before irradiation start and subtracted from the datapoints, so that $[O_2](t = 0\ s) = 0$ µmol/l.

To determine reaction rates, the following rate law was used:

$$\frac{d[O_2]}{dt} = k_0 - k_1[O_2] \qquad \text{Equation (1)}$$

For this rate law, O_2 is assumed to be formed in a zero-order reaction with rate constant k_0 and to be consumed in a first-order reaction with rate constant k_1. The assumption that O_2 is formed in a zero-order reaction stems from the fact that O_2 concentrations are only measured in the initial reaction phase, where the concentration change of **1** is negligible. The first order reaction consuming O_2 can be seen as an overall description of O_2 loss in the liquid phase due to diffusion into the gas phase and due to consumption by side reactions (see 4.3.2), both of which can be assumed to be first order in O_2 in the initial reaction phase.

When integrated, Equation (1) gives the following function:

$$[O_2](t) = [O_2]_0\, e^{-k_1 t} - k_0\, e^{-k_1 t}\, \frac{1}{k_1} + \frac{k_0}{k_1} \qquad \text{Equation (2)}$$

With $[O_2]_0$ being the O_2 concentration at t = 0 s (which is equal to zero given our preprocessing). Equation (2) was fitted to all datapoints from t = 0 s until the end of irradiation, optimizing the parameters k_0 and k_1. k_0 is not only the zero-order rate constant for O_2 formation but also the initial rate of O_2 formation (since $[O_2]_0$ = 0 µmol/l, unit of initial rate is µmol l^{-1} s^{-1}). k_1 is the overall observed rate constant for the disappearance of O_2 (due to diffusion and side reactions).

To obtain k_0 with higher precision (for kinetic isotope effect, temperature dependence and dual irradiation data sets), a second analysis procedure was also used ("average k_1 procedure"): for this

procedure, Equation (2) was first fitted to the data optimizing both k_0 and k_1. Within one group of experiments (e.g. all experiments with the same intensity and temperature), the average k_1 value was determined. Afterwards, Equation (2) was fitted to the data of each experiment in the group again, this time fixing k_1 to be the group's average value. Therefore, only k_0 has to be optimized and it is obtained with higher precision.

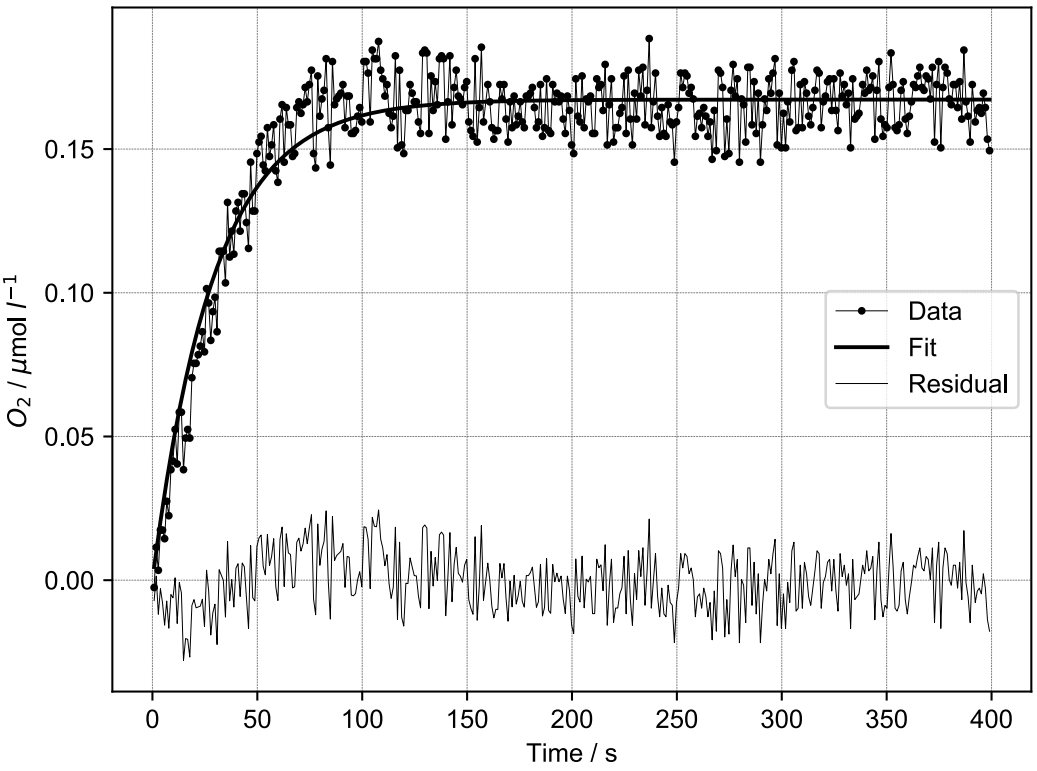

Figure 4.2-2 Exemplary liquid phase O_2 data analyzed as described in 4.2.2 (320 – 500 nm, 1 W intensity setting

4.2.3 Data Analysis for Intensity Experiments

For the intensity dataset, irradiation was performed with five different intensity settings for the Hg light source (320 – 500 nm): 0.25, 0.375, 0.5, 0.75 and 1 W (the power values are not identical to the power received by the reactor, but they are proportional, see Chemical Actinometry section). For each intensity setting, at least two experiments were performed. Initial rates were calculated as described in 4.2.2 and for each intensity setting, the average of the corresponding experiments is reported (maximum deviation between experiments: 0.0005 µmol l^{-1} s^{-1}). In case of the intensity dataset, no difference was observed whether the average k_1 procedure was used or not. Temperature changes during irradiation were negligible (typically below 0.6 °C on the highest intensity setting).

The obtained initial rates were then fitted with a square function ($f(x) = ax^2$), optimizing only a. This showed that the dependence of initial O_2 formation rate on intensity can be described well using a square relationship.

4.2.4 Data Analysis for Kinetic Isotope Effect and Temperature Dependence

To determine a possible H/D kinetic isotope effect (KIE), the standard irradiation procedure was used, but instead of H_2O, **1** was dissolved in D_2O (due to rapid exchange of hydroxo protons, the deuterated derivative of **1** is quickly formed). Irradiation was performed using the Hg light source

(320 – 500 nm) with the 1 W intensity setting. Two separate experiments in D_2O were performed and initial rates were calculated as described in 4.2.2, using the average k_1 procedure, and then averaged. As a reference, 1 W experiments from the intensity dataset were used, which were also analyzed using the average k_1 procedure and averaged. The obtained H/D KIE is 1.18.

To determine a possible temperature dependence of the reaction, the standard irradiation procedure was used, but instead of setting the thermostat temperature to 16.5 °C, it was set to 26.5 °C. Irradiation was performed using the Hg light source (320 – 500 nm) with the 1 W intensity setting. Two separate experiment at 26.5 °C were performed and initial rates were calculated as described in 4.2.2, using the average k_1 procedure, and then averaged. As a reference, 1 W experiments from the intensity dataset were used, which were also analyzed using the average k_1 procedure and averaged. The obtained ratio of initial rates at 16.5 °C and 26.5 °C is 0.78. The fact that the observed initial rate is in fact slightly slower at higher temperature might be attributed to accelerated, thermal side reactions consuming O_2.

Table 4.2-1 H/D kinetic isotope effect and temperature dependence of O_2 formation

$\frac{k_0(H)}{k_0(D)}$	$\frac{k_0(26.5\,°C)}{k_0(16.5\,°C)}$
1.18	0.78

4.2.5 Data Analysis for Dual Irradiation Experiments

For the dual irradiation dataset, there are three distinct groups of experiments:

1. Irradiation using the Hg light source (320 – 400 nm, 0.3 W intensity setting)
2. Irradiation using the QTH light source (different longpass filters)
3. Irradiation using both the Hg (320 – 400 nm, 0.3 W intensity setting) and QTH (different longpass filters) light source (dual irradiation)

The QTH light source was used with five different longpass filters: 455 nm, 495 nm, 550 nm, 590 nm and 630 nm cut-on wavelength. For irradiation using the QTH light source or dual irradiation, there are thus five subgroups each, corresponding to each longpass filter.
For the dual irradiation dataset it was found that data analysis could be improved (lower spread of initial rates for reproduction experiments) by correcting the analysis start point: instead of fitting Equation (2) from the start of irradiation, the start point was shifted forward to the point minimizing the residual for the fit of Equation (2) (a correction of typically 0 – 30 s). This correction allows excluding early datapoints, which tend to underreport O_2 concentration due to a time delay caused by diffusion into the sensor matrix.
Furthermore, it should be noted that dual irradiation experiments proved to be very sensitive to the alignment of the two light sources, since the beams had to overlap properly to observe a synergistic effect. Thus, some experiments could not be used for data analysis due to improper light source alignment.

For experiments using only the Hg light source, initial rates were calculated as described in 4.2.2, using the average k_1 procedure. Thus obtained k_0 values were averaged to give the average 320 – 400 nm initial rate.

For both QTH and dual irradiation, the following procedure was used to calculate initial rates: Equation (2) was fitted to all experiments, optimizing both k_0 and k_1. Subsequently, a linear regression model was fitted to the k_1 values of all QTH or dual irradiation experiments, respectively. For each group, this linear model provides a description of the dependence of k_1 on longpass filter cut-on wavelength. Subsequently, Equation (2) was again fitted to all experiments, this time fixing k_1 to be the linear regression value of the respective linear model (QTH or dual irradiation) and wavelength. For the dual irradiation group, thus obtained k_0 values were averaged for each wavelength. For the QTH irradiation group, another linear regression model was fitted to the k_0

values, this time yielding a linear model to describe the dependence of k_0 on longpass filter cut-on wavelength.

To give the reported excess initial rate of O_2 formation, the following method was used: for each wavelength, the average 320 – 400 nm initial rate as well as the QTH linear regression k_0 value for the respective wavelength were subtracted from the average dual irradiation initial rate.

At this point we would like to note that the small apparent O_2 signals observed when only the longpass filtered QTH light source was used are likely not due to actual O_2 evolution. This is based on the observation that no **2-cis** was formed when only the QTH light source (> 495 nm) was used for irradiation. Rather, the small signals might be caused by the temperature change of ca. 2 °C caused by the QTH light source despite the reactor being submersed in a water bath. Regardless, through the above described analysis method, any contribution of the QTH light source to the observed O_2 signal during dual irradiation is accounted for by subtracting the obtained QTH linear regression k_0 values. Furthermore, subtraction of the average 320 – 400 nm initial rate accounts for the contribution of the Hg light source during dual irradiation. Reported excess initial rates are therefore the result of a synergistic effect of both light sources.

4.2.6 Note on Reaction Order/Concentration Dependence

As noted in 4.2.1, the observed reaction rates are identical for 0.01 and 0.005 M solutions of **1**. This is because in this concentration range, complete photon absorption by the sample solution occurs, leading to an apparent zero order reaction in **1**.[8] Attempts to perform measurements using solutions of significanly lower concentration, below the complete absorption regime, were unsuccesful. Hence, the actual reaction order in **1** could not be determined.

4.3 Gas Phase O_2 Measurement

4.3.1 Irradiation Procedure

A 5 ml Schlenk flask (internal volume ca. 10 ml) with a NS14 ground glass joint was topped with a hollow, flat top glass stopper, on the inside of which a contactless trace range oxygen sensor spot was glued. This allows measurement of gas phase O_2 concentration inside the reactor via contactless read out through the glass stopper. The Schlenk flask was then connected to the Schlenk line using a T-piece adapter, with one connection to the Schlenk line, one to the Schlenk flask and one connection being closed with a septum. Subsequently, 2 ml of an aqueous solution of **1** (prepared via the N_2O synthesis route, 0.01 M) was transferred into the Schlenk flask. The transfer was done via cannula transfer through the septum inlet of the T-piece adapter and through the valve of the Schlenk flask, taking care not to introduce any external O_2 into the flask.
Once the transfer was complete, the Schlenk flask was closed and stirred overnight in the dark at room temperature to equilibrate. A PT100 temperature sensor (for temperature compensation of the O_2 measurement) was placed next to the Schlenk flask.

After equilibration, an optical fiber was mounted to the outside of the flat top glass stopper to read out the oxygen sensor spot. Then, the baseline O_2 concentration was measured for ca. 4 h. Afterwards the flask was irradiated for 16 h using the Hg light source (320 – 500 nm, 0.15 W intensity setting), resulting in a color change to a yellow/orange solution. During irradiation the flask was cooled using a 20 W fan.

4.3.2 Data Analysis and O_2 Consumption Reaction

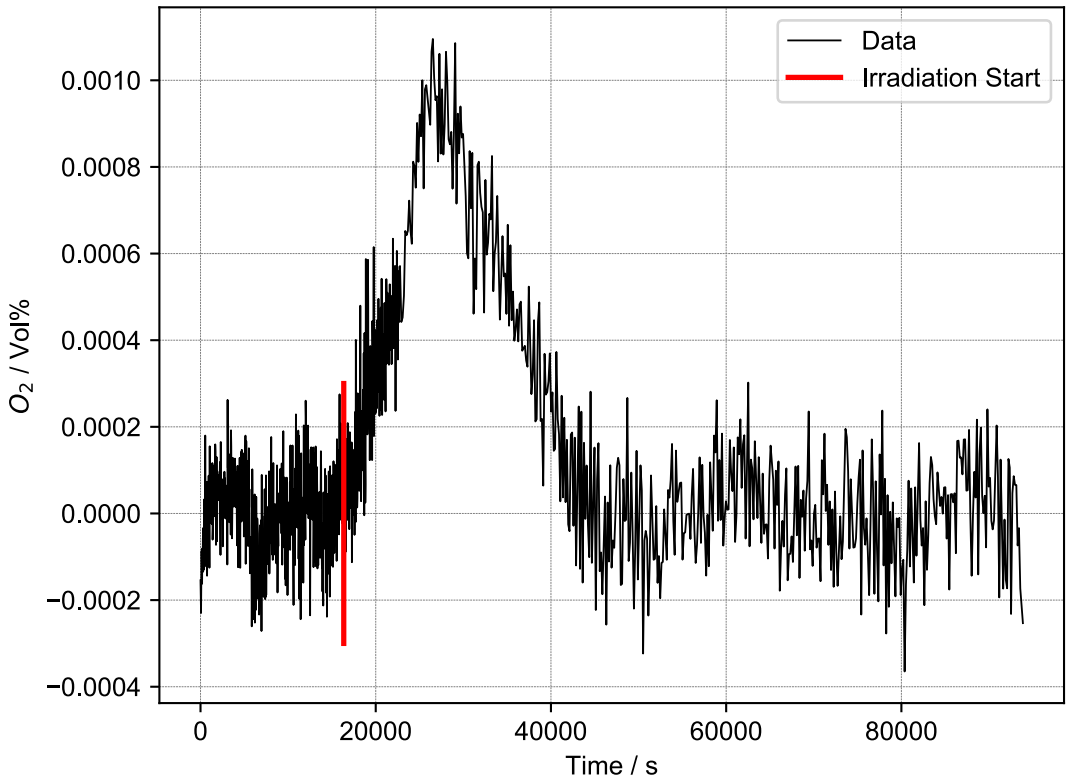

Figure 4.3-1 Gas phase O_2 detection data for irradiation of complex 1 with Hg light source (320 – 500 nm)
Data has been baseline corrected with a sixth-degree polynomial fitted to baseline intervals [0 s, 16350 s] and [46300 s, 94000 s]. Irradiation was turned on at t = 16350 and turned off at t = 76000 s.

The obtained gas phase O_2 concentration data shows a small peak shaped feature resulting from O_2 evolution superimposed on a continuously decreasing background. Therefore, a sixth-degree polynomial was fitted to baseline intervals [0 s, 16350 s] (t = 16350 s is the start time for irradiation) and [46300 s, 94000 s] and subtracted from the entire measurement to obtain a baseline corrected signal, shown in Figure 4.3-1.

As can be seen in Figure 4.3-1, once irradiated is started, an increase in the gas phase O_2 concentration can be detected due to O_2 evolution for ca. 3 h. Afterwards, the O_2 concentration drops back to baseline value again over the course of ca. 6 h. This kind of behavior is consistent with a two-reaction sequence, wherein O_2 is formed in the first reaction (O_2 evolution from **1**, decreasing reaction rate over time due to consumption of **1**) and consumed in the second reaction.

In a separate experiment, complex **1** (synthesized via Ag_2O synthesis route, in 52 mM KOH aq.) was irradiated using the QTH light source (only water filter) in air, resulting in conversion of **1** into mostly NMR inactive species (see Figure 7.5-7 - Figure 7.5-10). We hypothesized that **1**, when irradiated in the presence of O_2, oxidizes to form mostly Ru(III) species as well as phosphorous oxides. This can explain the consumption of O_2 during water splitting and the formation of NMR inactive species when **1** is irradiated in air.

4.4 Comparison of 2-cis and O_2 Formation Rates

To confirm that **2-cis** and O_2 are indeed both formed in the same reaction, their initial rates of formation were compared. If both are formed in the same reaction, their normalized rates are expected to be identical. With the available experimental data and techniques, however, only an approximate comparison can be made since **2-cis** and O_2 formation had to be studied in different experimental set-ups (NMR scale irradiation and liquid phase O_2 measurement, respectively). Therefore, multiple normalizations had to be applied to enable comparison, which will be explained in the following.

For **2-cis**, the initial rate of formation was calculated from the kinetic model shown in Figure 4.1-1. The thus obtained initial rate is 1E-05 s^{-1} in normalized units or 0.1 µmol l^{-1} s^{-1} (given a concentration of 0.01 M).

For O_2, the initial rate of formation was taken from the intensity data set for the 1 W intensity setting, being 0.0059 µmol l^{-1} s^{-1}.

The first normalization is based on the stoichiometry of the reaction (see Table 4.4-1), which shows that **2-cis** would be formed at twice the rate of O_2. Hence, stoichiometry adjusted rates are 0.05 µmol l^{-1} s^{-1} for **2-cis** and 0.0059 µmol l^{-1} s^{-1} for O_2.

The second normalization that has to be applied has to correct for the different areas, which were irradiated in each set-up. For NMR scale irradiation, the irradiated area was 0.424 × 4 cm (1.696 cm^2), while the irradiated area was 0.8 × 1 cm (0.8 cm^2) for liquid phase O_2 measurements. Since the reaction rate is proportional to irradiated area for a photochemical reaction (the light cone was bigger than the reactor in both cases), initial rates normalized to 1 cm^2 are 0.0295 µmol l^{-1} s^{-1} for **2-cis** and 0.0074 µmol l^{-1} s^{-1} for O_2.

The last normalization is based on the different flux densities used in the experiments. The initial rate of O_2 formation is based on irradiation with the Hg light source with the 1 W intensity setting, which corresponds to a photon flux of 1.32E+18 s^{-1} received by the reactor (see Chemical Actinometry). For NMR scale irradiation, the QTH light source (equipped with only the water filter) was used instead. The photon flux of the QTH light source cannot be easily determined using the applied chemical actinometry method, so it is estimated based on power meter measurements. It

should be noted that these power values are not identical to the power received by the reactor. Instead, they are only proportional.

Based on power meter measurements, ca. 27% of the QTH output power is in the useful wavelength range of 320 – 630 nm. Total power measured in the position of the NMR tube was 645 mW, giving ca. 173 mW of power in the 320 – 630 nm wavelength range, with a mean photon wavelength of 475 nm.
Using the same power meter, a power of 127 mW was measured in the position of the liquid phase O_2 reactor for the Hg light source (320 – 500 nm, 1.32E+18 s^{-1} flux, mean photon wavelength of 410 nm). Based on the mean photon wavelengths (475 nm for QTH, 410 nm for Hg) and measured power values (173 mW for QTH, 127 mW for Hg), one can estimate a photon flux of ca. 2.09E+18 being received by the NMR tube using the following equation:

$$Flux_{QTH} = \frac{E_{Hg}\, P_{QTH}}{E_{QTH}\, P_{Hg}}\, Flux_{Hg} \qquad \text{Equation (3)}$$

With E_{Hg} and E_{QTH} being the mean photon energies in eV for the QTH and Hg light sources, respectively, and P_{QTH} and P_{Hg} being the measured power values. Based on the intensity dataset, it was found that rate of O_2 formation shows a square dependence on photon flux. If we assume that the same holds true for **2-cis** (since **2-cis** has shown the same synergistic effect in dual irradiation experiments as O_2 formation), the square of the ratio between the Hg and QTH light source flux values gives a flux correction factor of 2.5. Applying this factor to the **2-cis** initial rate of formation gives a flux-normalized rate of 0.0118 µmol l^{-1} s^{-1}. Comparing this to the normalized initial rate of O_2 formation, 0.0074 µmol l^{-1} s^{-1}, shows that they differ by less than 40%. Considering that these two rates were measured using different methods (NMR and O_2 detection) and in different set-ups, we consider this to be an acceptable agreement.

Table 4.4-1 Comparison of 2-cis and O_2 initial rates of formation

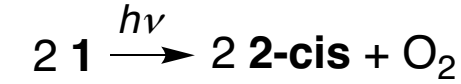

Estimated, normalized initial rate of 2-cis formation / µmol l^{-1} s^{-1}	Estimated, normalized, initial rate of O_2 formation / µmol l^{-1} s^{-1}
0.0074	0.0118

4.5 Photographs of Irradiation Set-Ups

Figure 4.5-1 Set-up for irradiation on NMR scale
Hg light source provides irradiation through the light guide in the back (320 – 400 nm filtered in this picture) and the QTH light source is visible on the right (water cooled IR filter and filter holder are visible, > 495 nm filtered in this picture).

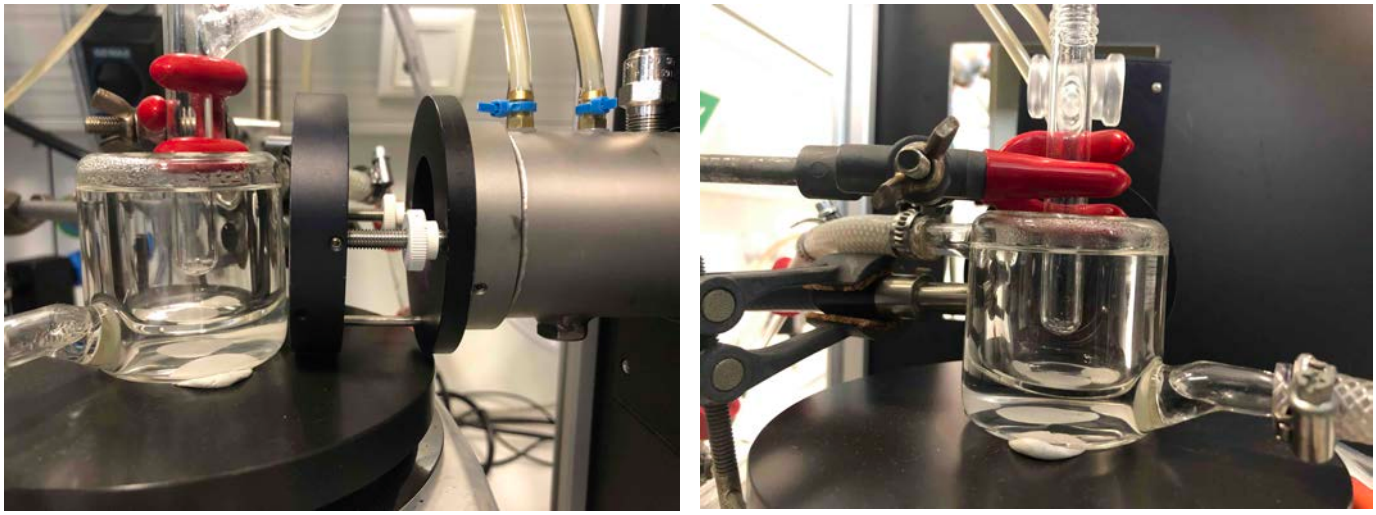

Figure 4.5-2 Set-up for irradiation with liquid phase O_2 detection
Left: Front view of set-up showing QTH light source (right) and water filled, thermostatted beaker with Schlenk flask reactor.
Right: Side view of set-up showing light guide of Hg light source (left) and side view of thermostatted reaction assembly.

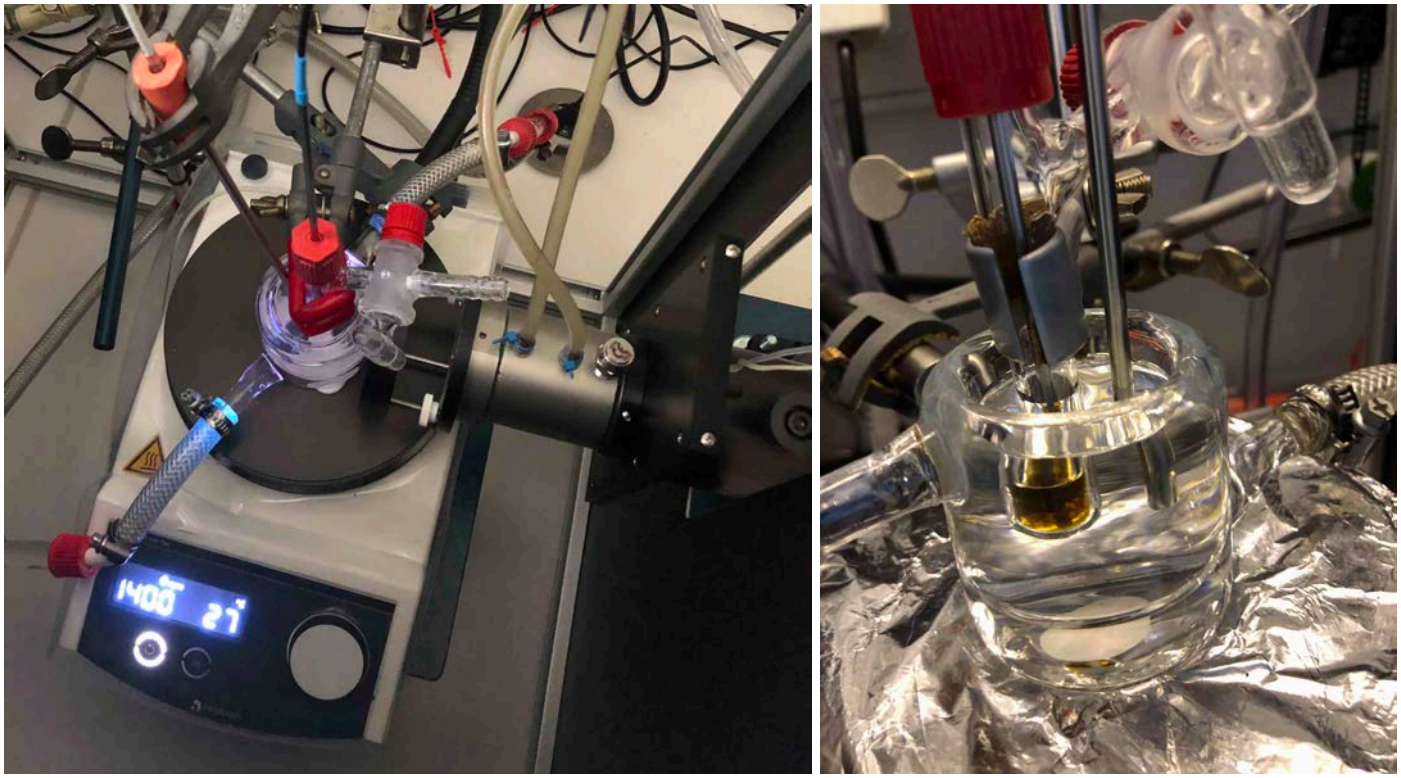

Figure 4.5-3 Irradiation set-up (liquid phase O_2 detection) in use (left) and close-up of assembled reactor

Left: Irradiation set-up in use (only Hg light source, 320 – 400 nm filtered, is turned on). QTH light source (with shutter, water cooled IR filter and filter holder) is visible on the right. Center shows the Schlenk reactor submerged in the thermostatted beaker with an O_2 sensor connected via a BOLA laboratory screw joint (red cap). Next to the reactor, a PT100 temperature sensor is submerged in the thermostatted beaker. Note that the temperature shown on the stir plate is not indicative of the actual reaction temperature.

Right: Close-up of assembled reactor with submerged PT100 temperature sensor on the right. Inside of the reactor, an aqueous solution of complex **1** can be seen, inside of which the O_2 sensor is submerged.

5 H_2O_2 Disproportionation

5.1 Experimental Procedure

Following the procedure described in 4.2.1, ca. 400 µl of degassed 5×10^{-5} M aqueous H_2O_2 were transferred into a Schlenk flask equipped for liquid phase O_2 measurement. Throughout the experiment, the flask was connected to the Schlenk line (under argon), allowing for the injection of other reagents. A PT100 temperature sensor was placed next to the flask for temperature compensation of the O_2 measurement. While being stirred and at room temperature, the baseline O_2 concentration was measured, followed by injection of 500 µl of an aqueous solution of **1** (synthesized using N_2O synthesis route, 0.005 M) through the septum of the T-piece adapter. After 50 min, 100 µl of a degassed 3 M potassium iodide (KI) solution were injected, followed by another 40 min of O_2 measurement.

5.2 Data Analysis

This H_2O_2 disproportionation experiment was performed to investigate the feasibility of a stepwise water splitting mechanism, wherein irradiation of **1** first produces H_2O_2, followed by H_2O_2 disproportionation to O_2 and H_2O catalyzed by **1**. In our view, complex **1** would be the only viable candidate for a H_2O_2 disproportionation catalyst in this scenario, since O_2 formation occurs directly at the start of irradiation (see for example Figure 4.2-1). At the start of the reaction, only **1** is present in significant quantities and it would therefore be the only compound that could catalyze H_2O_2 disproportionation at this point.

The used quantity of H_2O_2 (20 nmol) corresponds to roughly 200 times the amount of O_2 formed within the first 90 s of a liquid phase O_2 measurement experiment (Hg light source, 320 – 500 nm, 1 W setting, ~ 0.11 nmol). Furthermore, it is roughly 1% of the amount of **1** used (2.5 µmol). Therefore, this amount it is likely an overestimation of the highest H_2O_2 concentration that might occur for a H_2O_2 mechanism. Thus, the observed rate of H_2O_2 disproportionation catalyzed by **1** will be an upper bound for the H_2O_2 disproportionation rate possible under water splitting reaction conditions. If this rate is slower than the observed initial rate of O_2 formation during liquid phase O_2 measurement, a mechanism involving H_2O_2 disproportionation can be seen as unlikely.

The results of the experiment are shown in Figure 5.2-1. It can be seen that the baseline O_2 concentration of the H_2O_2 solution is elevated (1.9 µmol l^{-1}), since it proved challenging to remove all dissolved O_2 from it. Addition of the solution of **1** (having a lower O_2 concentration) at t = 150 s therefore leads to a drop in O_2 concentration. After equilibration, a linear increase in O_2 concentration with a rate of 1.2×10^{-5} µmol l^{-1} s^{-1} can be observed (see Figure 5.2-1B). We attribute this to H_2O_2 disproportionation catalyzed by **1**. At t = 3100 s, a 3 M KI solution was added to the reactor. Since KI is a known and fast-acting H_2O_2 disproportionation catalyst, this was done to confirm that H_2O_2 disproportionation can be observed under these reaction conditions. Indeed, addition of KI leads to a rapid increase in O_2 concentration, followed by return to baseline value (likely due to diffusion of O_2 into the gas phase). Importantly, after addition of KI and equilibration, no increase in O_2 concentration can be observed anymore (see Figure 5.2-1B). This suggests that all H_2O_2 has been consumed by KI catalyzed disproportionation. In turn, this supports the hypothesis that the increase in O_2 concentration before KI addition was due to catalytic H_2O_2 disproportionation and not some other process (such as leakage).

Within this interpretation, the rate of H_2O_2 disproportionation catalyzed by **1** (1.2×10^{-5} µmol l^{-1} s^{-1}) is more than an order of magnitude slower than the initial O_2 formation rate during water splitting (5.9×10^{-3} µmol l^{-1} s^{-1} for Hg light source, 320 – 500 nm, 1 W setting). Therefore, it is unlikely that a mechanism involving H_2O_2 disproportionation is responsible for O_2 evolution in this system. However, a variable not included in this experiment is irradiation. It is possible that irradiation could accelerate H_2O_2 disproportionation. This possibility could not be investigated in this experiment since irradiation would lead to a combined increase of O_2 concentration due to H_2O_2

disproportionation and O_2 evolution from **1**, which could not be distinguished. Theoretical evidence, however, also suggests that light-induced H_2O_2 formation from **1** is unlikely (see 11.2.8).

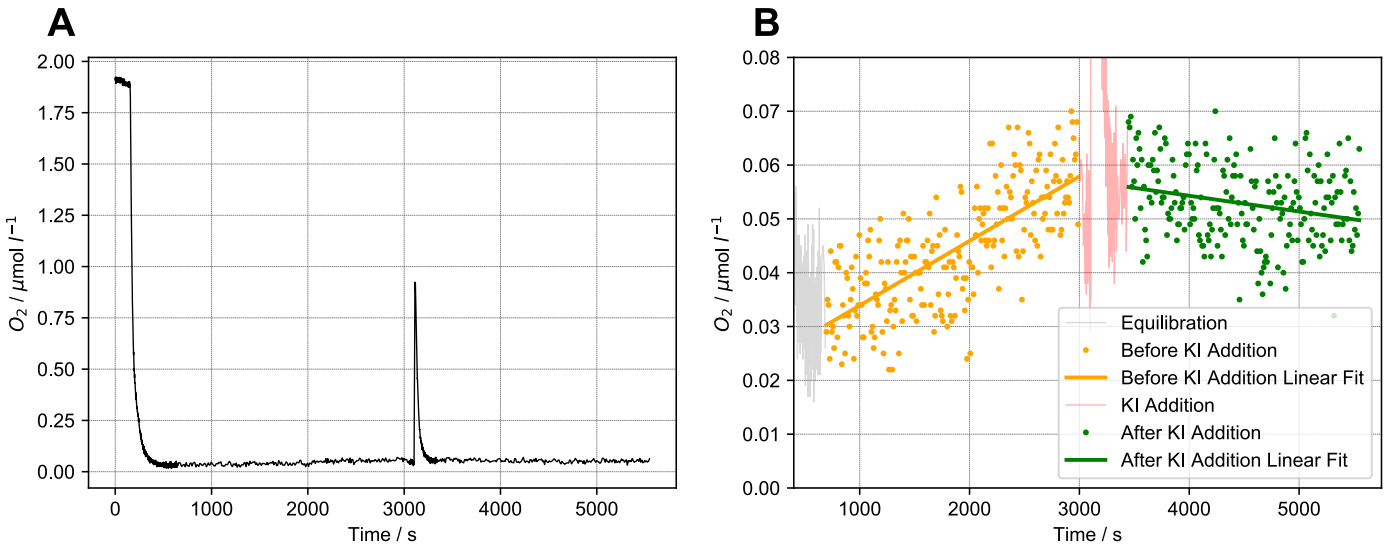

Figure 5.2-1 Liquid phase O_2 measurement for H_2O_2 disproportionation catalyzed by complex 1
A Overview of entire liquid phase O_2 measurement. At t = 0 s, only the aqueous 4×10^{-5} M H_2O_2 solution is present in the reactor. At t = 150 s, the ca. 5×10^{-3} M aqueous solution of complex **1** is injected, leading to a drop in the liquid phase O_2 concentration (since the solution of complex **1** had a lower O_2 concentration compared to the H_2O_2 solution). At t = 3100 s, 3 M aqueous KI solution was added, leading to a spike in the O_2 concentration (O_2 concentration drops again due to diffusion into the gas phase).
B Zoom-in of region before (yellow) and after (green) KI addition, with linear fits. The slope before KI addition is 1.2×10^{-5} µmol l^{-1} s^{-1}, after KI addition it is -2.9×10^{-6} µmol l^{-1} s^{-1}.

6 Chemical Actinometry

6.1 Light Source Spectra

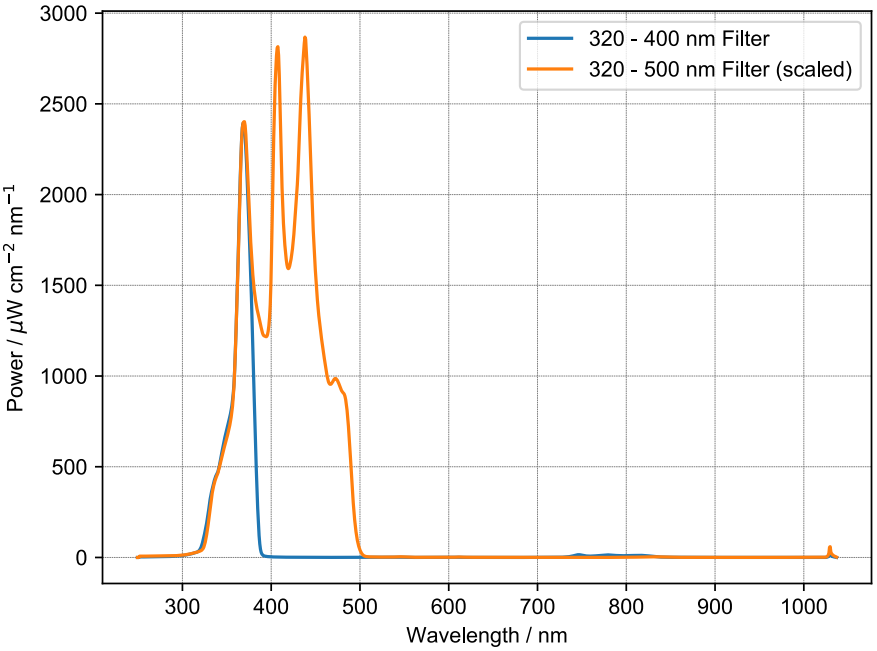

Figure 6.1-1 Spectral power distribution of Hg light source with used filter settings
Note: the actual amount of power reaching the reaction solution depends strongly on the reaction configuration, which is why chemical actinometry was performed (see below).

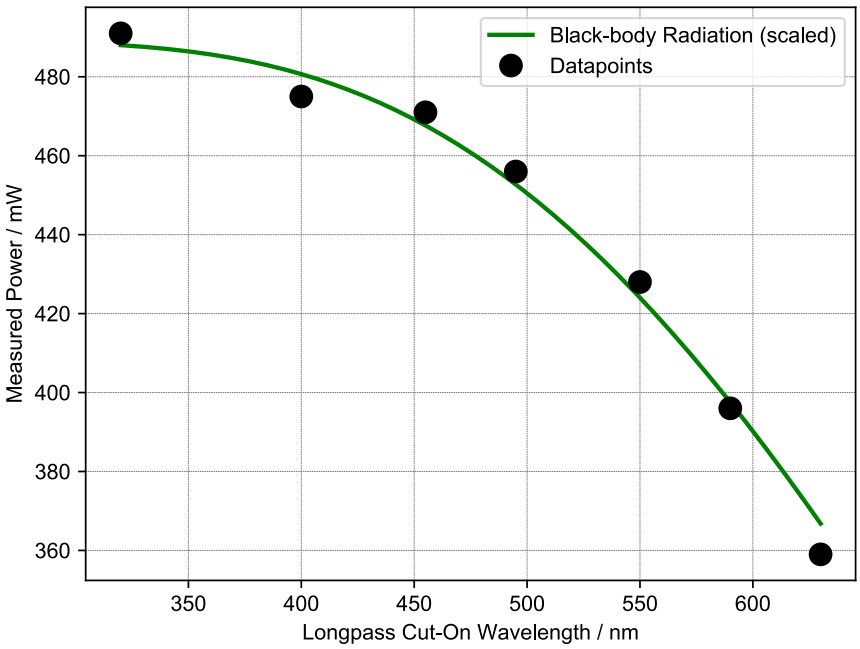

Figure 6.1-2 Measured power of QTH light source with different longpass filters
Graph shows power measured in liquid phase O_2 reactor position with different longpass filters (black dots). The scaled, predicted behavior for an ideal blackbody radiation source (3400 K) is shown in green.

6.2 Experimental Procedure

Potassium ferrioxalate actinometry was performed as described in ref. [9]. All experiments were carried out in air and in the dark. The $K_3[Fe(C_2O_4)_3]$ solution was prepared by combining an aqueous 0.2 M solution of $Fe_2(SO_4)_3$ with an aqueous 1.2 M solution of $K_2C_2O_4$. Blank experiments were performed to confirm that the absorbance of the solution was below 0.06 at 510 nm.
For each actinometry experiment, 550 µl of $K_3[Fe(C_2O_4)_3]$ solution were transferred into the liquid phase O_2 measurement reactor, which was positioned in the same way as during liquid phase O_2 measurements. It was then irradiated using the Hg light source (320 – 400 nm or 320 – 500 nm filter) for a precise amount of time (between 3 – 10 s, depending on the intensity setting). Afterwards, an aliquot of 100 µl was removed from the reactor, combined with 2 ml of a 0.2 wt% phenanthroline solution, 50 µl of buffer solution and diluted up to 10 ml in a volumetric flask. Afterwards, the absorbance of the solution at 510 nm was measured using UV/Vis spectroscopy in a 1 cm cuvette.

6.3 Chemical Actinometry Data and Analysis

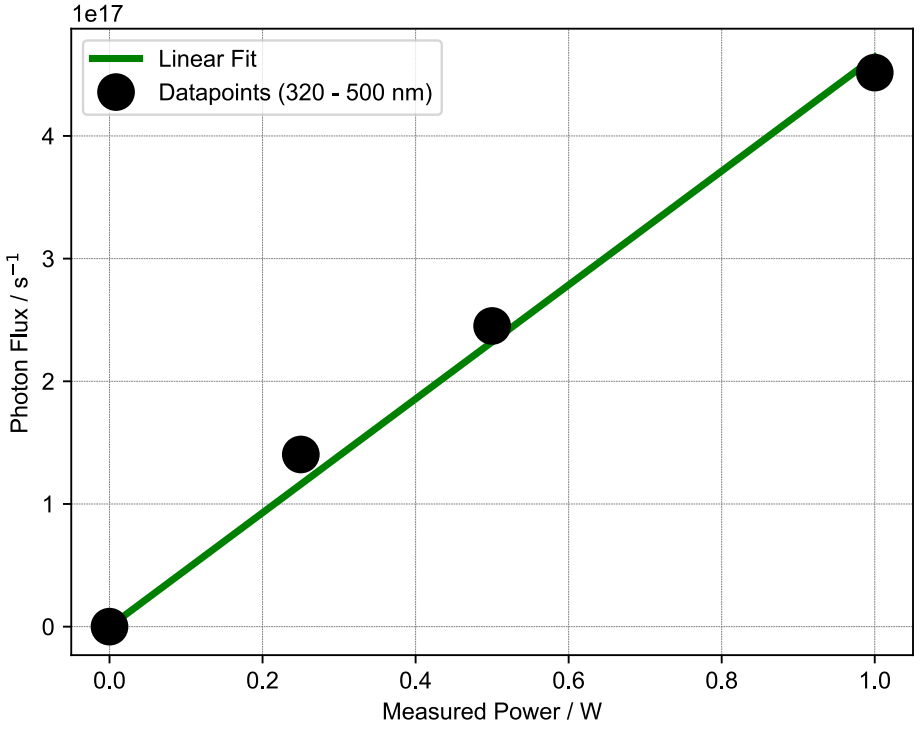

Figure 6.3-1 Chemical actinometry data for different power setting of Hg light source (320 – 500 nm)
Slope of linear fit: 4,64E+17. Note that the used ferrioxalate method does not detect all photons with wavelengths > 400 nm, which is why in the following a correction is applied to the raw photon flux values shown in this figure.

Using the obtained absorbance values, photon flux received by the reactor was calculated using the formula in ref. [9], using a quantum yield of 1.16 and the previously reported extinction coefficient of 1.11E+04 M^{-1} cm^{-1} for the iron(II) phenanthroline complex.

Figure 6.3-1 shows the obtained photon flux values for 0.25, 0.5 and 1 W intensity settings of the Hg light source (320 – 500 nm), establishing a linear correlation between intensity settings and photon flux received by the reactor.

For the 320 – 400 nm filtered Hg light source, a photon flux of 4.15E+17 s^{-1} was determined (0.3 W intensity setting).

Due to the short path length of the liquid phase O_2 measurement reactor (8 mm) and the low extinction coefficient of $K_3[Fe(C_2O_4)_3]$ for wavelengths longer than 400 nm,[9] photon flux values for the 320 – 500 nm filtered Hg light source are underestimated. In contrast, for the 320 – 400 nm filtered Hg light source, it can be assumed that quantitative photon absorption occurred. Hence, the determined photon flux value (for 320 – 400 nm) combined with the spectral power distribution of the light source (see Figure 6.1-1) can be used to calculate the correct 320 – 500 nm photon flux values:

1. The 320 – 520 nm spectral power distribution is converted to a spectral photon distribution through division of the power distribution by respective photon energies.
2. The spectral photon distribution is integrated from 320 – 500 nm and 320 – 390 nm (390 nm is the actual cut-off of the 320 – 400 nm filter, see Figure 6.1-1).
3. The 320 – 390 nm integral is used to scale the spectral photon distribution, so that the 320 – 390 nm integral is equal to the experimental photon flux of 4.15E+17 s^{-1}.
4. Integration of the scaled spectral photon distribution from 320 – 500 nm gives the corresponding photon flux for this filter setting, which is 1.56E+18 s^{-1}. It has to be considered, however, that this is the 320 – 500 nm photon flux when the light source is in the 0.3 W 320 – 400 nm intensity setting.
5. Experimentally, it was determined that the 0.3 W intensity setting (320 – 400 nm) corresponds to 1.18 W for 320 – 500 nm. Based on the linear relationship between intensity setting and photon flux (see Figure 6.3-1), it can therefore be determined that for the 1 W intensity setting (320 – 500 nm), the photon flux is 1.32E+18 s^{-1}.
6. Therefore, intensity settings for 320 – 500 nm can be converted to photon flux by multiplication by 1.32E+18 s^{-1}.

7 NMR Data

7.1 Characterization of 1

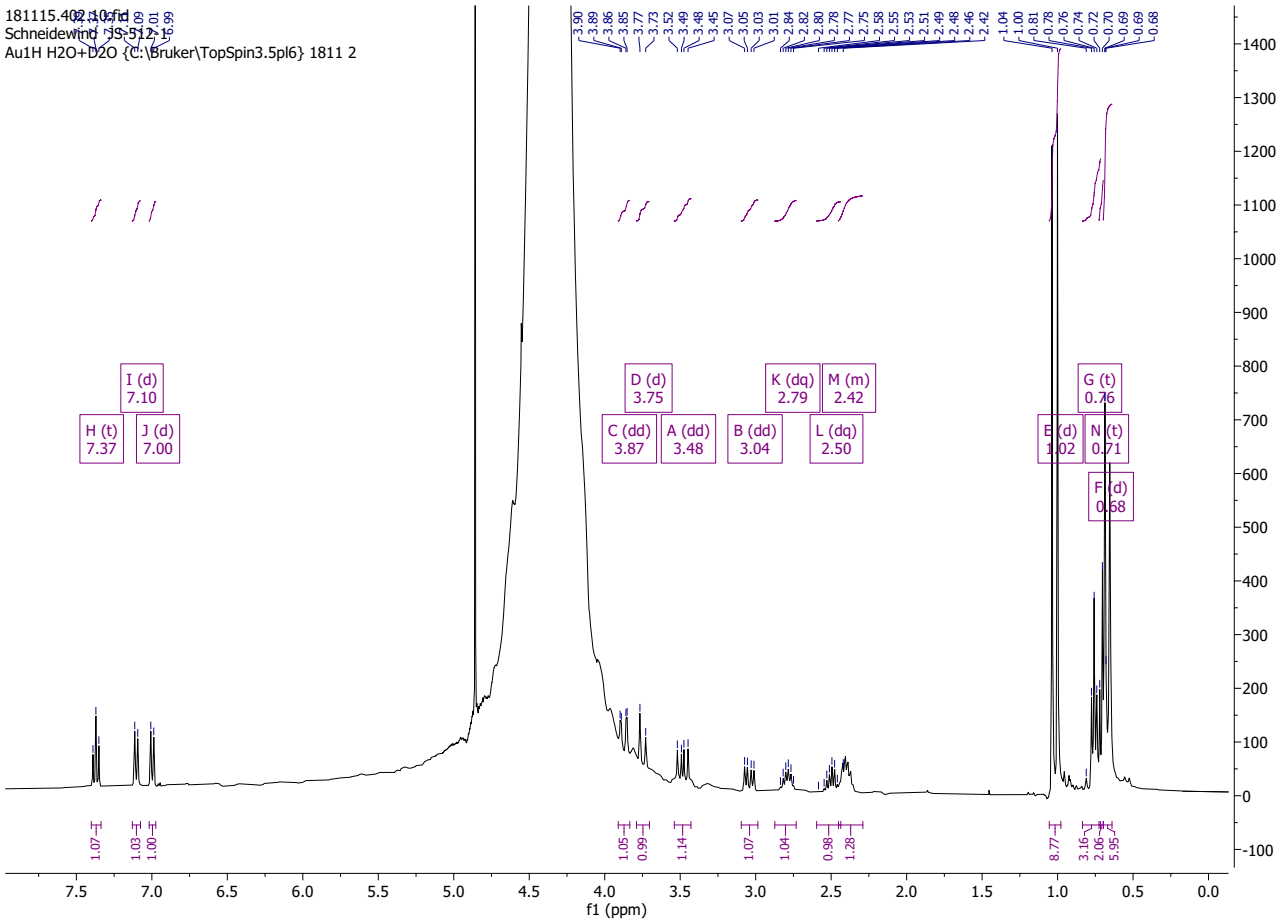

Figure 7.1-1 ^{1}H NMR spectrum of 1 in H_2O (298 K).

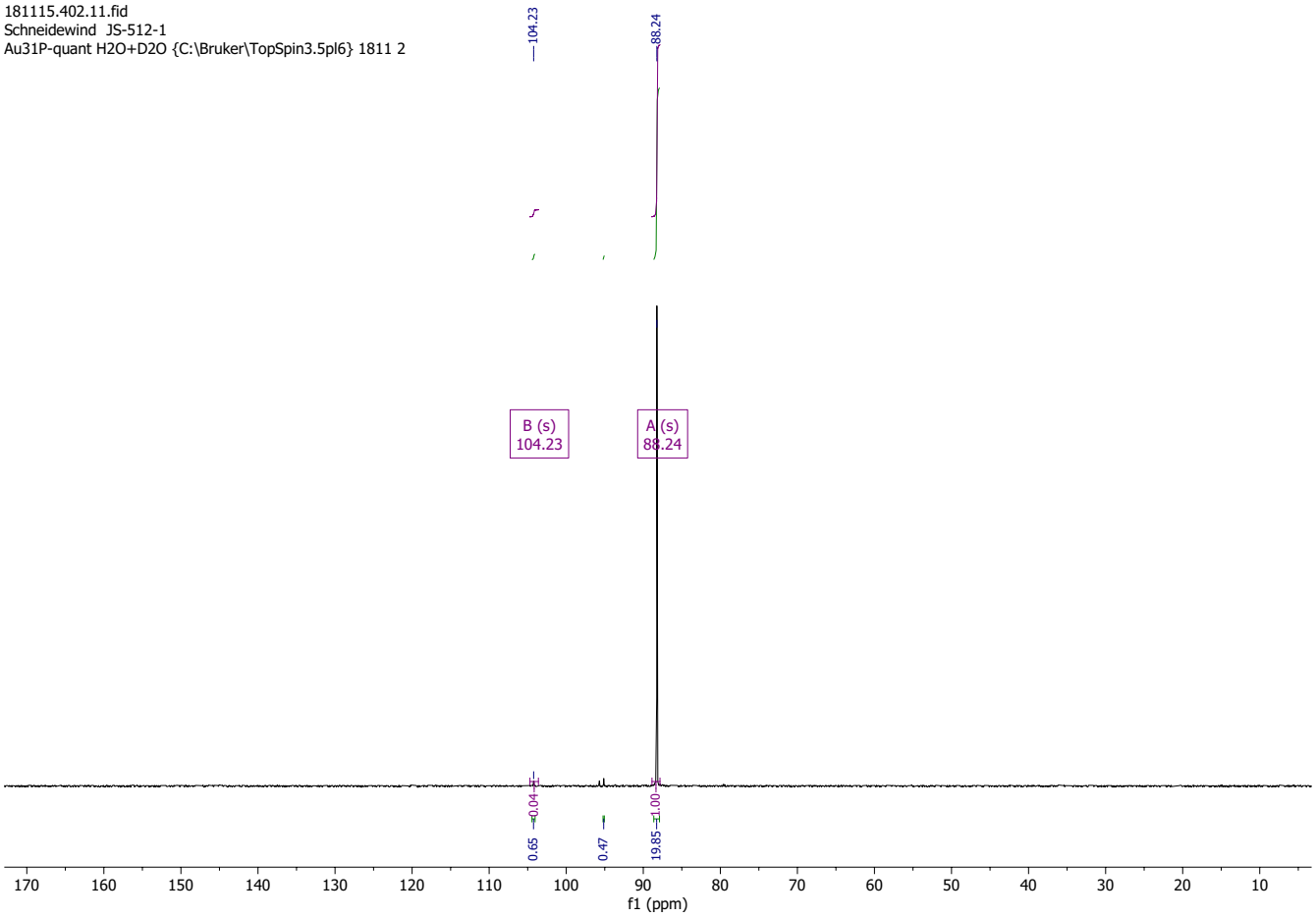

Figure 7.1-2 $^{31}P\{^{1}H\}$ NMR spectrum of 1 in H_2O (298 K)
(small amount of residual **2-trans** is visible at $\partial(^{31}P)$ = 104.23 ppm)

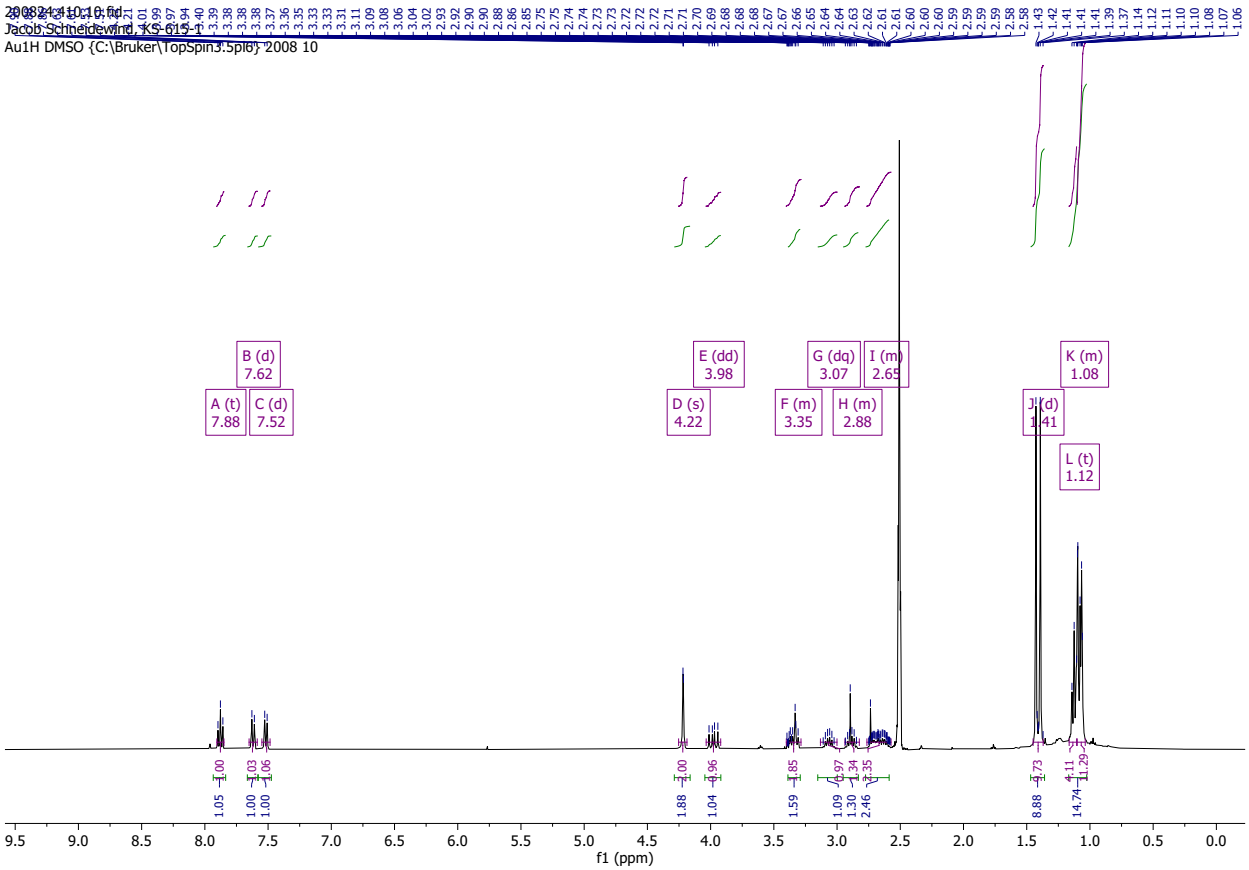

Figure 7.1-3 ^{1}H NMR spectrum of 1 in DMSO-d_6 (298 K)

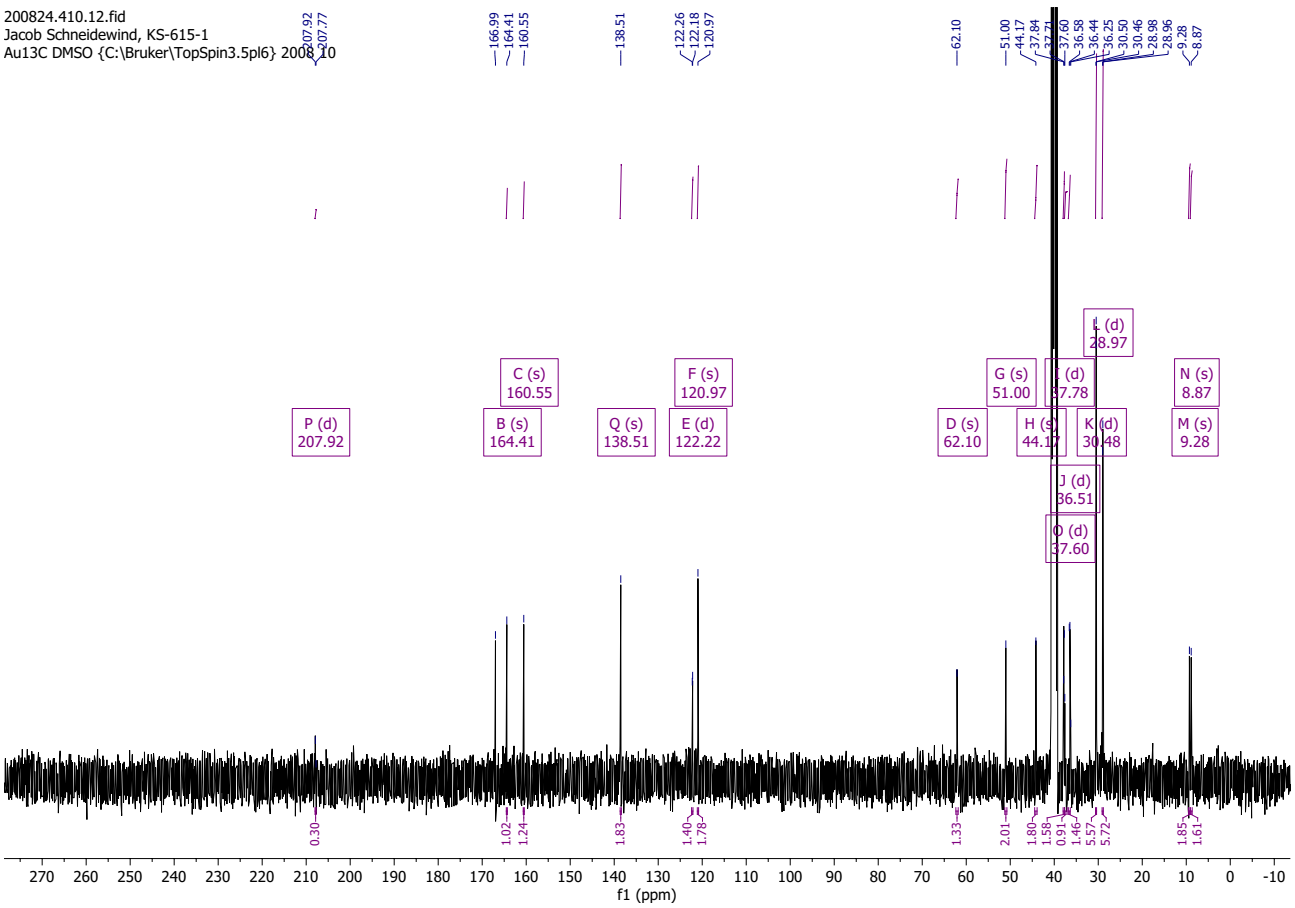

Figure 7.1-4 $^{13}C\{^{1}H\}$ NMR spectrum of 1 in DMSO-d_6 (298 K)

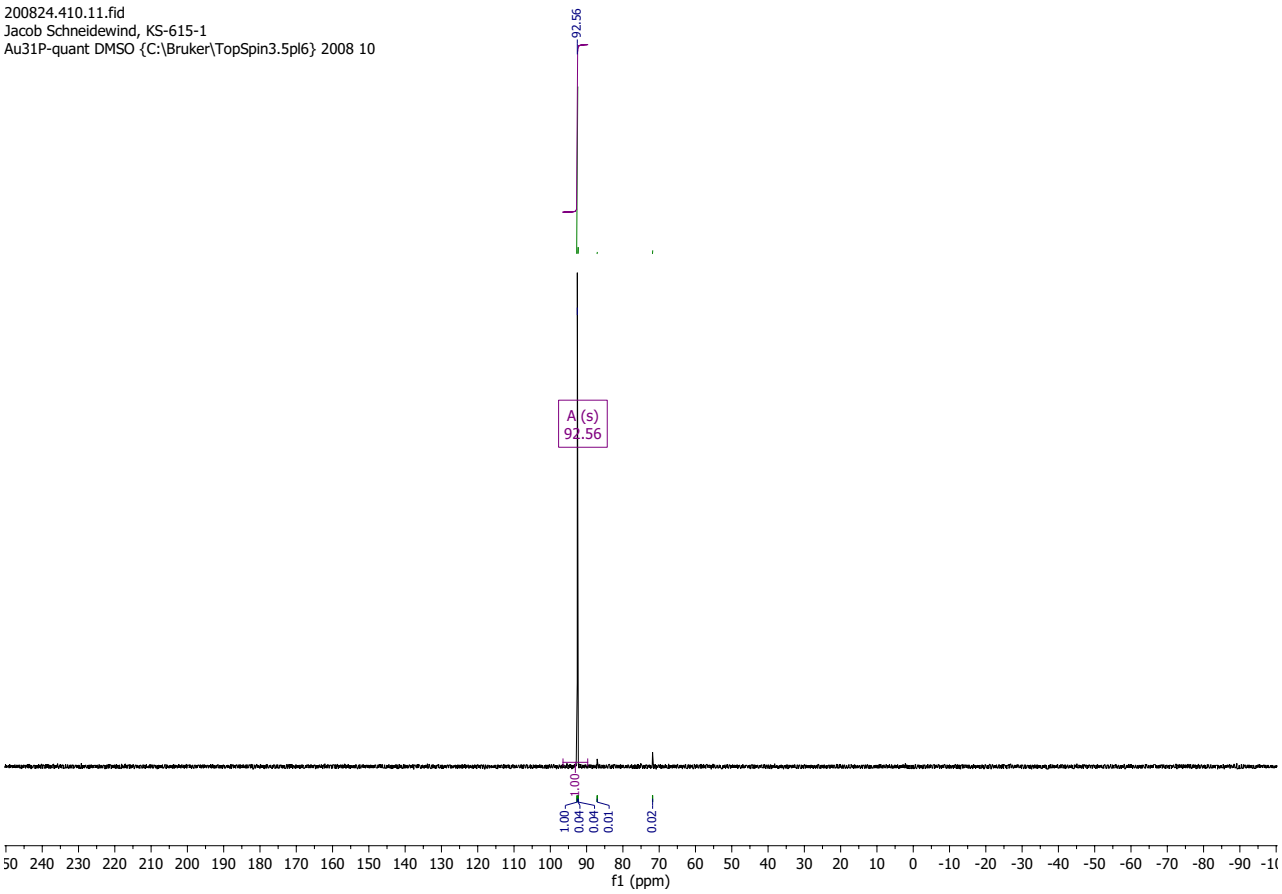

Figure 7.1-5 $^{31}P\{^{1}H\}$ NMR spectrum of 1 in DMSO-d_6 (298 K)

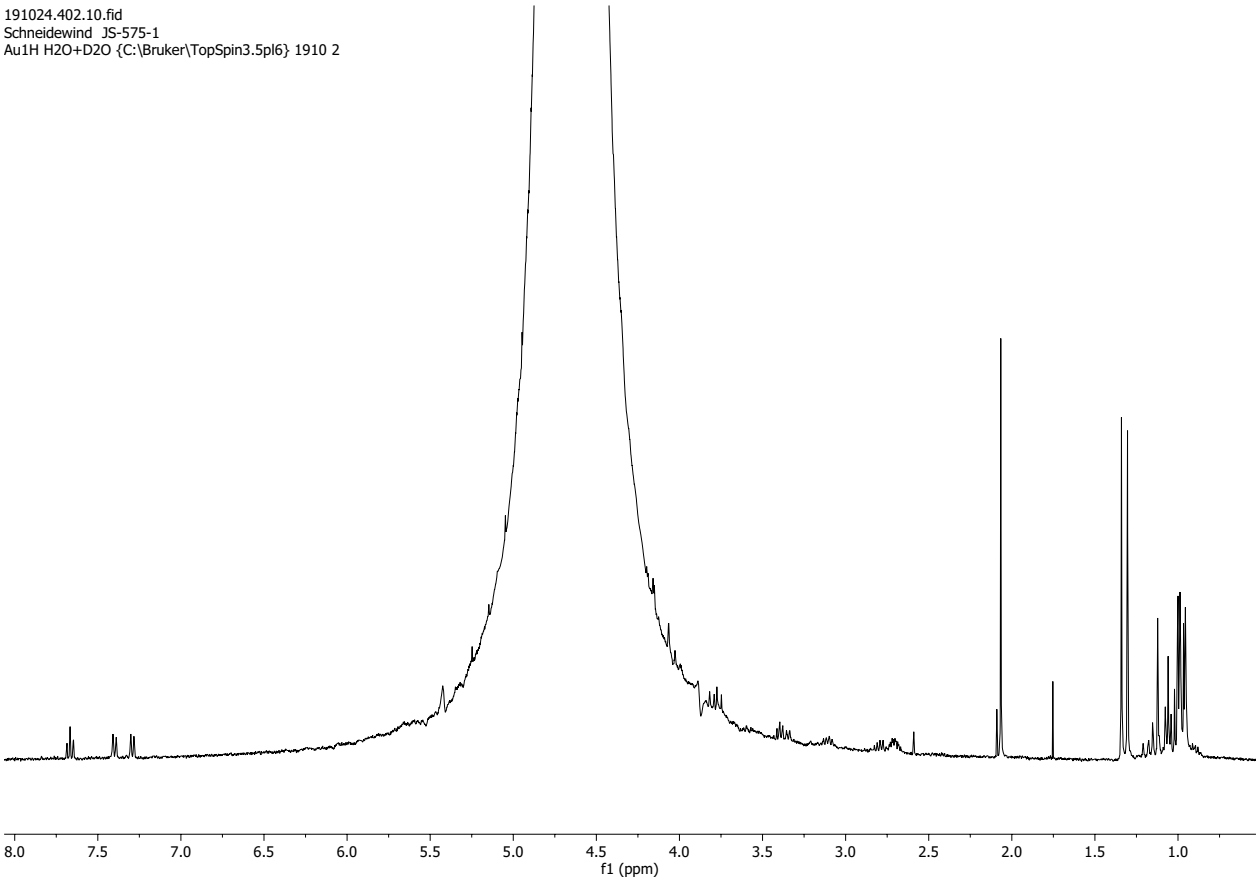

Figure 7.1-6 ^{1}H NMR spectrum of 1 in H_2O (298 K) synthesized using Ag_2O

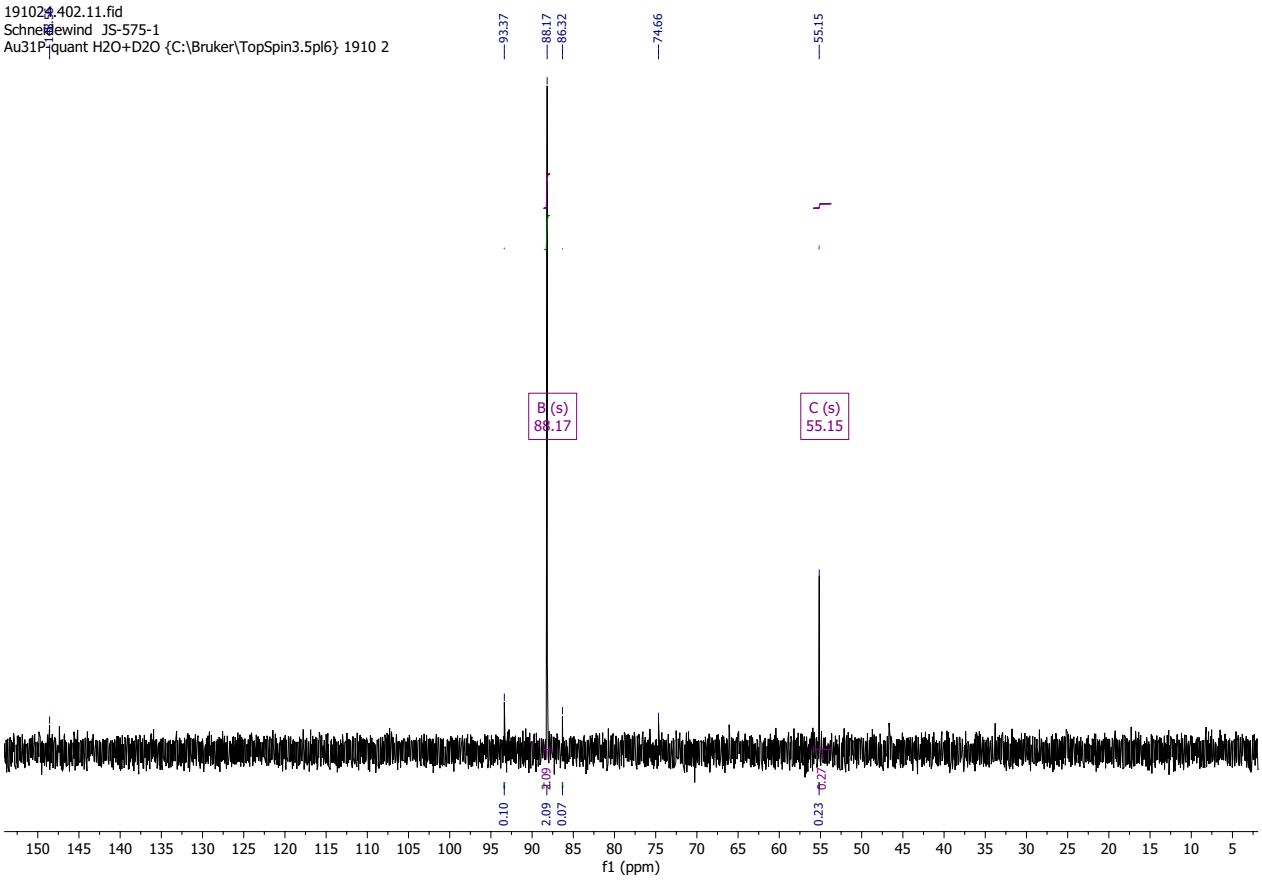

Figure 7.1-7 $^{31}P\{^{1}H\}$ NMR spectrum of 1 in H_2O (298 K) synthesized using Ag_2O

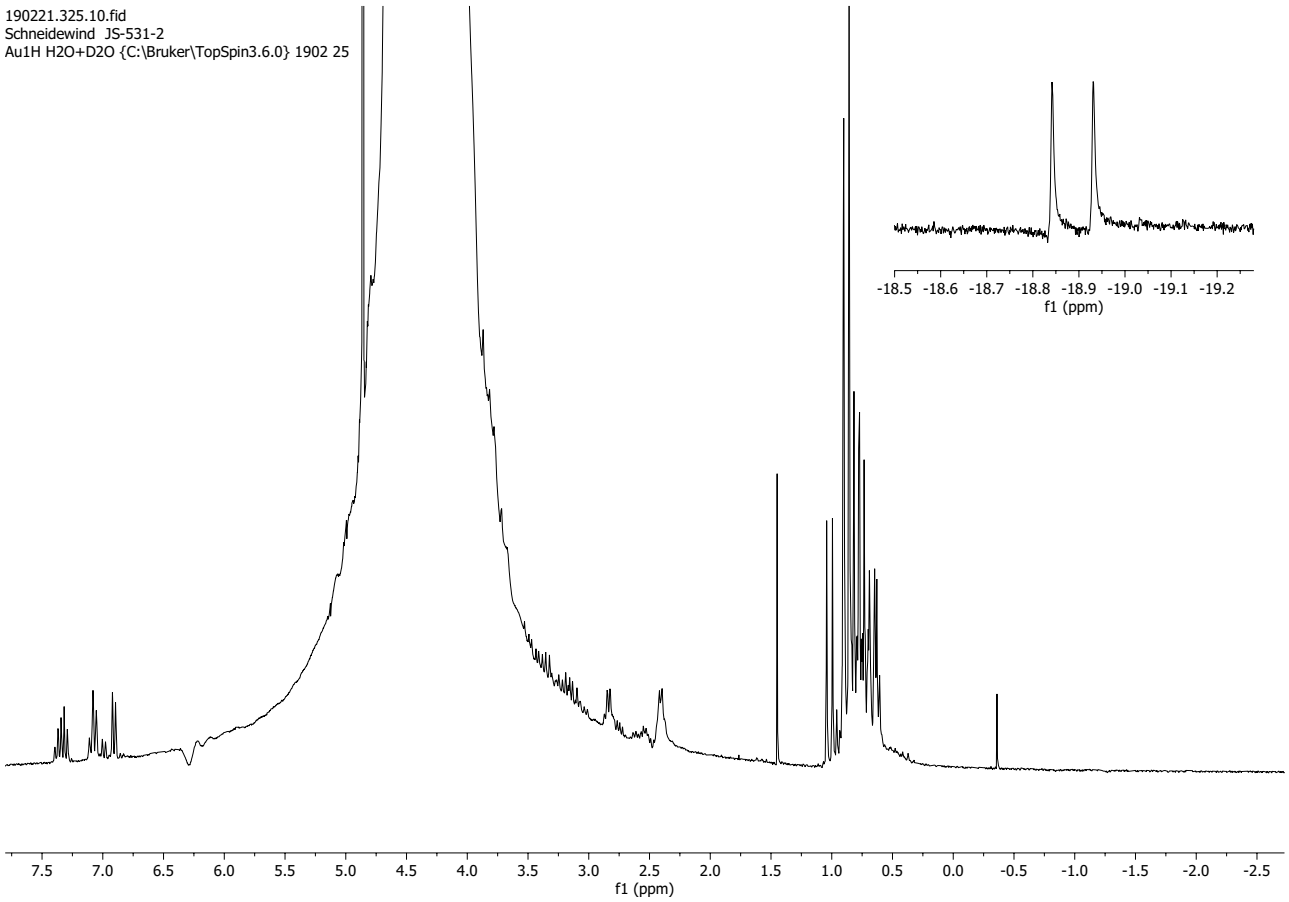

Figure 7.1-8 ^{1}H NMR of 2-trans in H_2O (298 K) after three days of reflux, displaying formation of 1
(inlet showing hydride peak of residual **2-trans**)

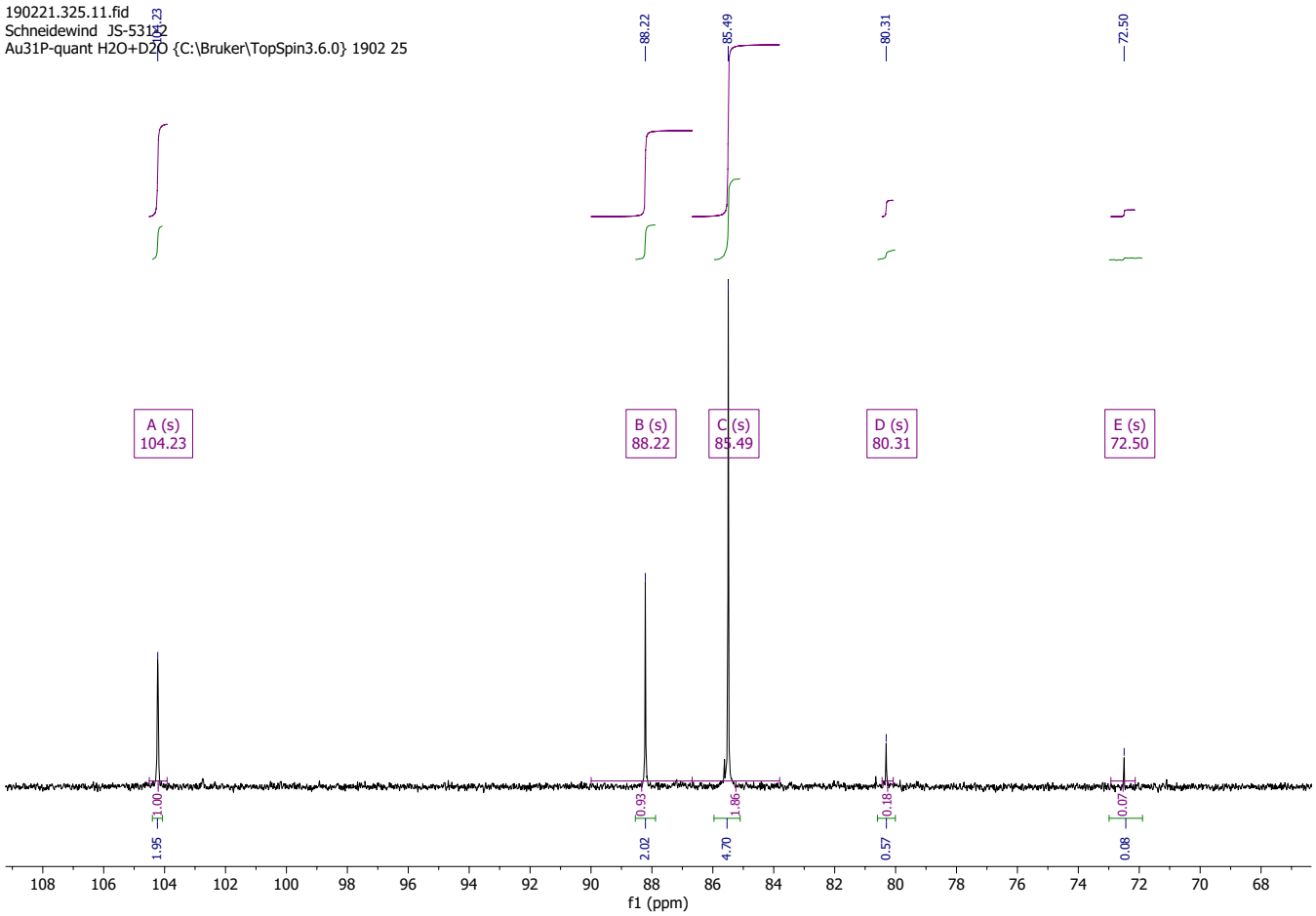

Figure 7.1-9 $^{31}P\{^{1}H\}$ NMR of 2-trans in H_2O (298 K) after three days of reflux, displaying formation of 1

7.2 Characterization of 2-trans

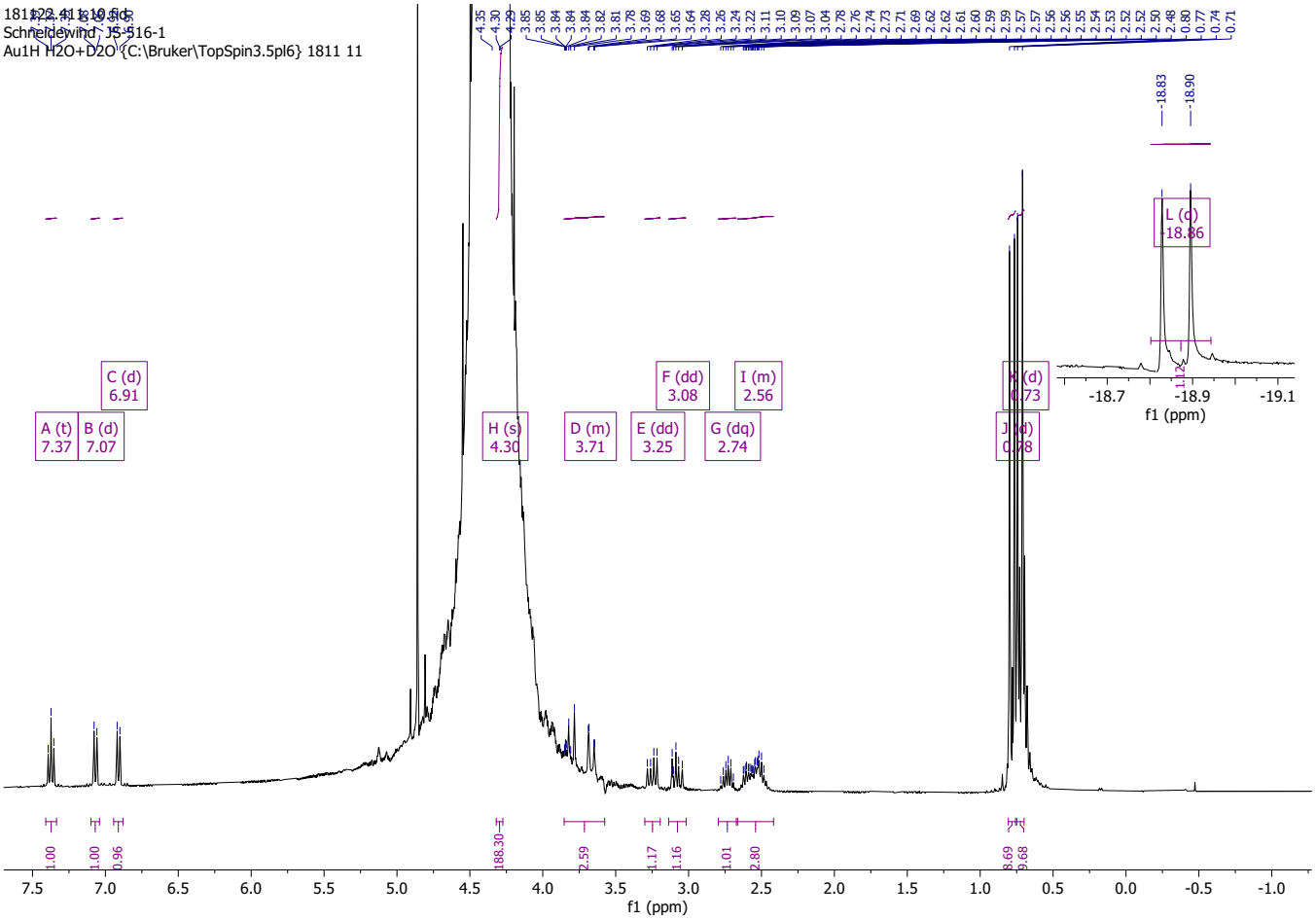

Figure 7.2-1 ^{1}H NMR spectrum of 2-trans in H_2O (298 K)
(inlet showing hydride peak)

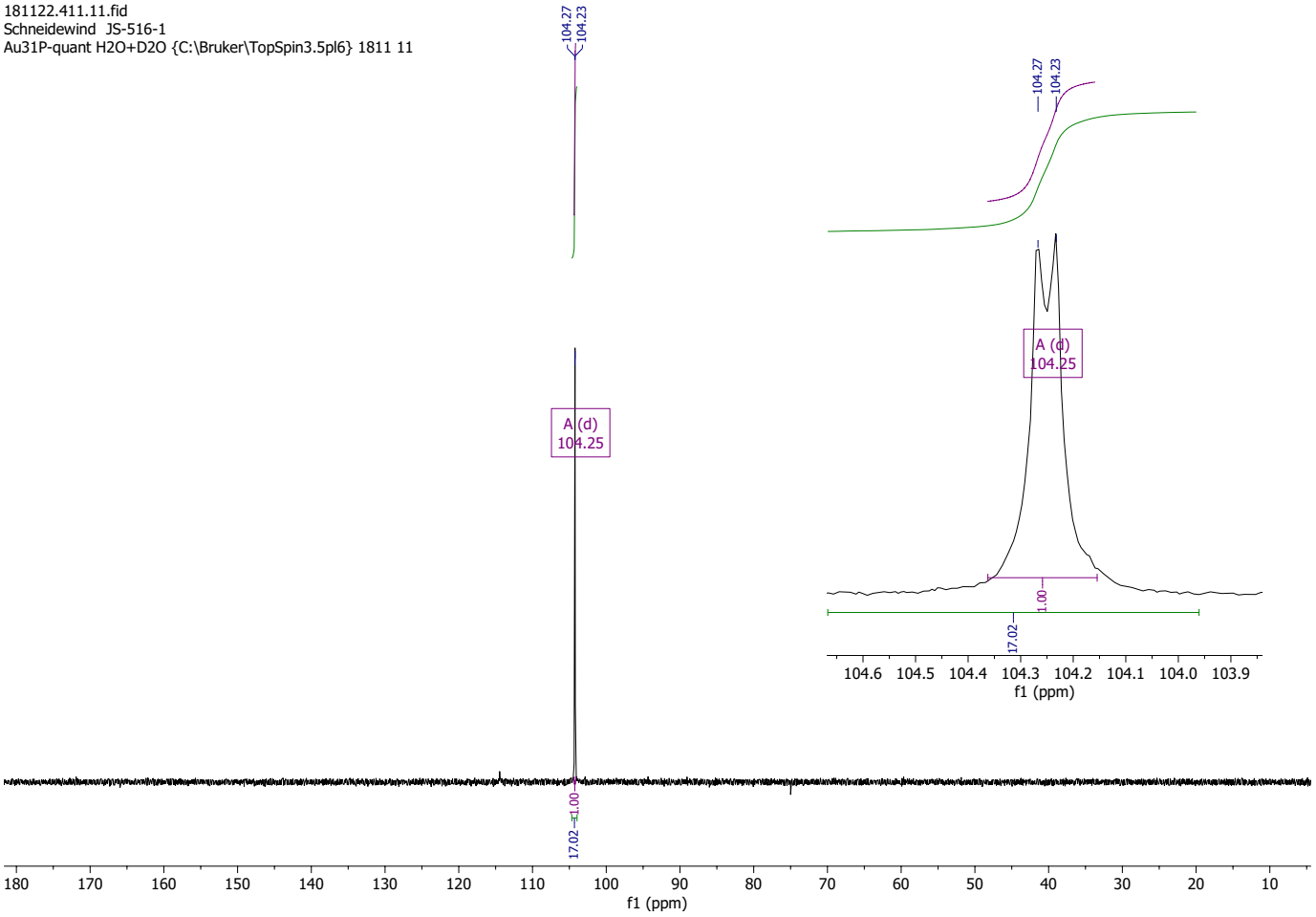

Figure 7.2-2 $^{31}P\{^{1}H\}$ NMR spectrum of 2-trans in H_2O (298 K)
(inlet shows splitting of ^{31}P signal due to coupling to hydride ligand, which is outside of decoupler range)

7.3 Characterization of (p-cymene)$RuCl_2(CO)$

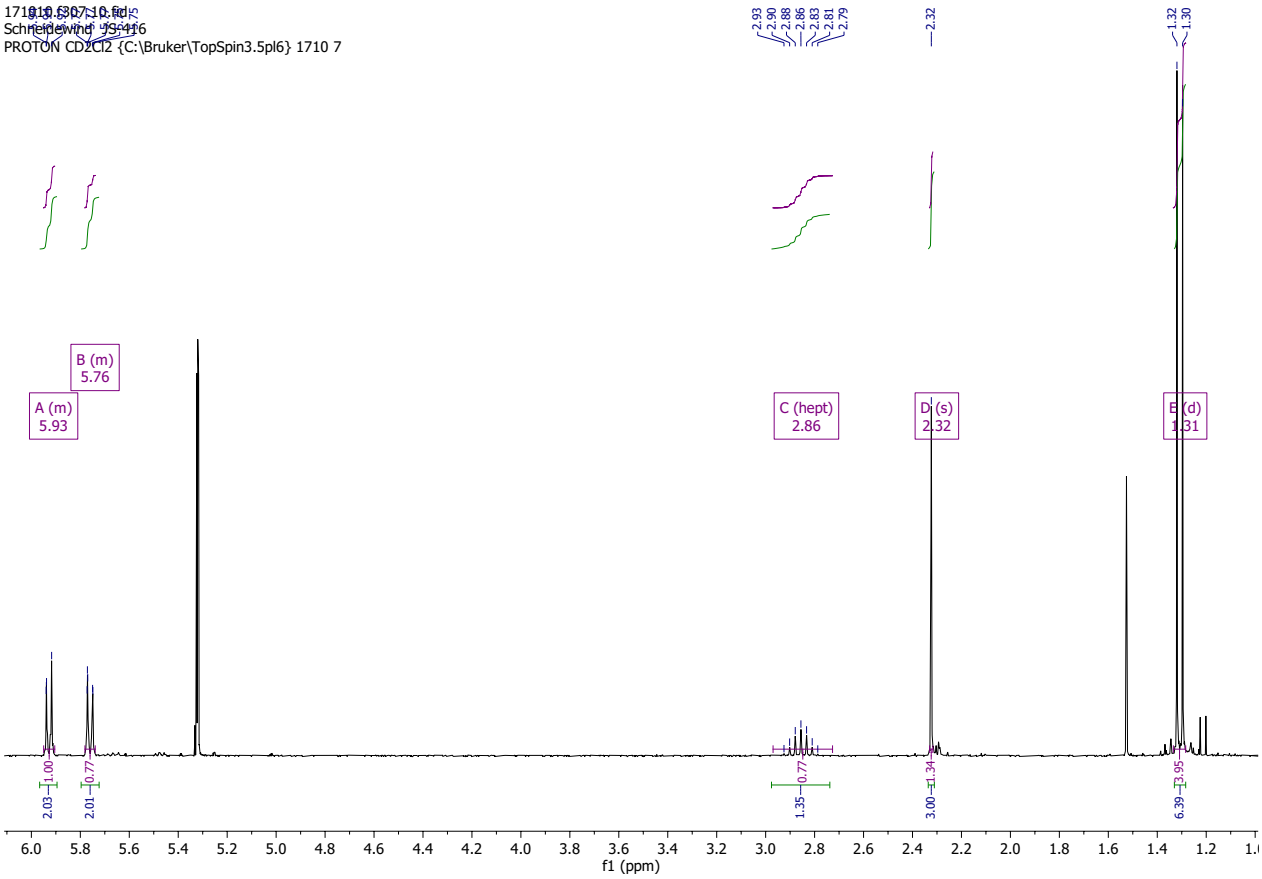

Figure 7.3-1 ^{1}H NMR spectrum of (p-cymene)$RuCl_2(CO)$ in CD_2Cl_2 (298 K)

7.4 Characterization of (PNN)RuCl$_2$(CO)

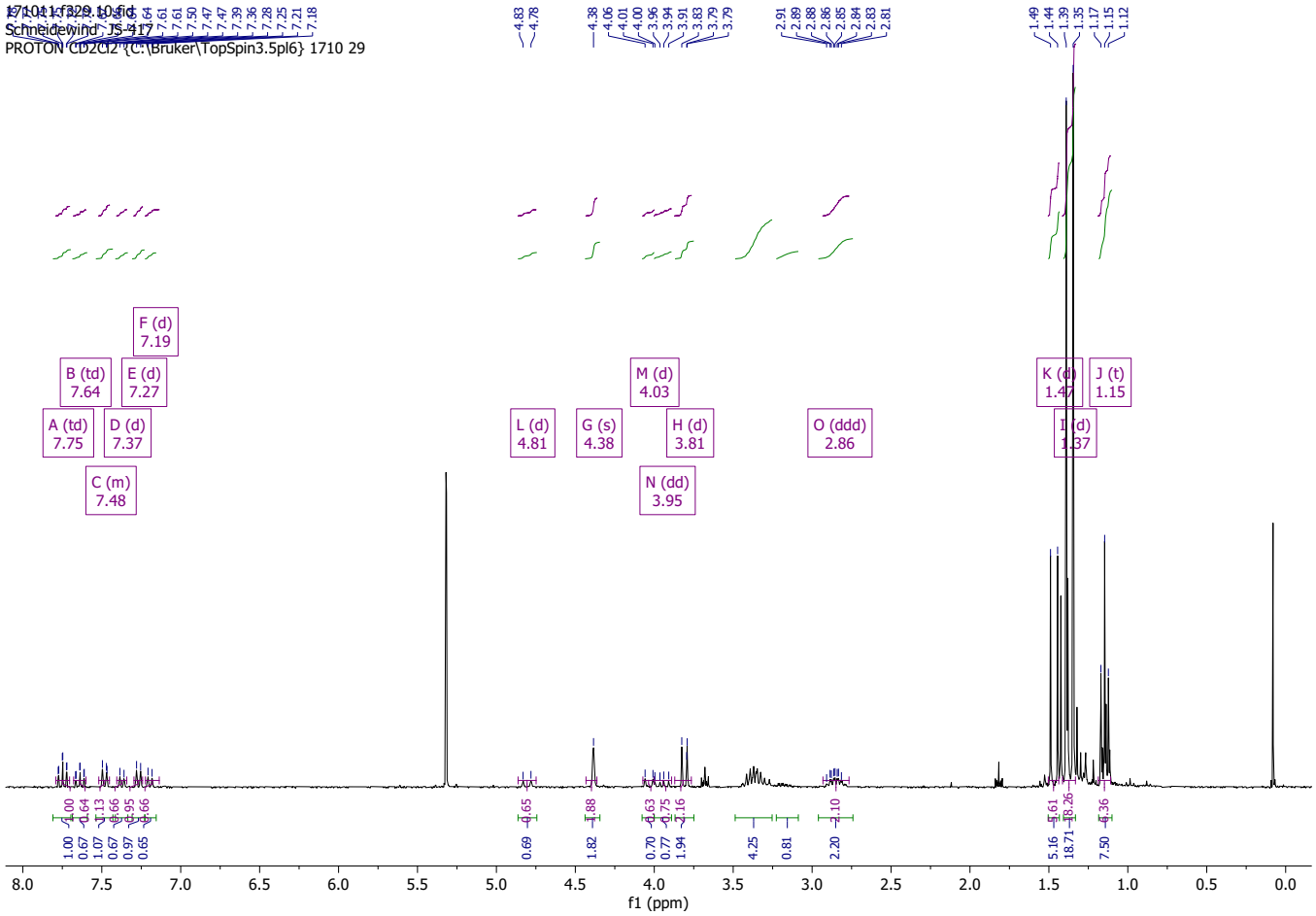

Figure 7.4-1 ^{1}H NMR spectrum of (PNN)RuCl$_2$(CO) in CD$_2$Cl$_2$ (298 K)
(mixture of cis and trans isomers)

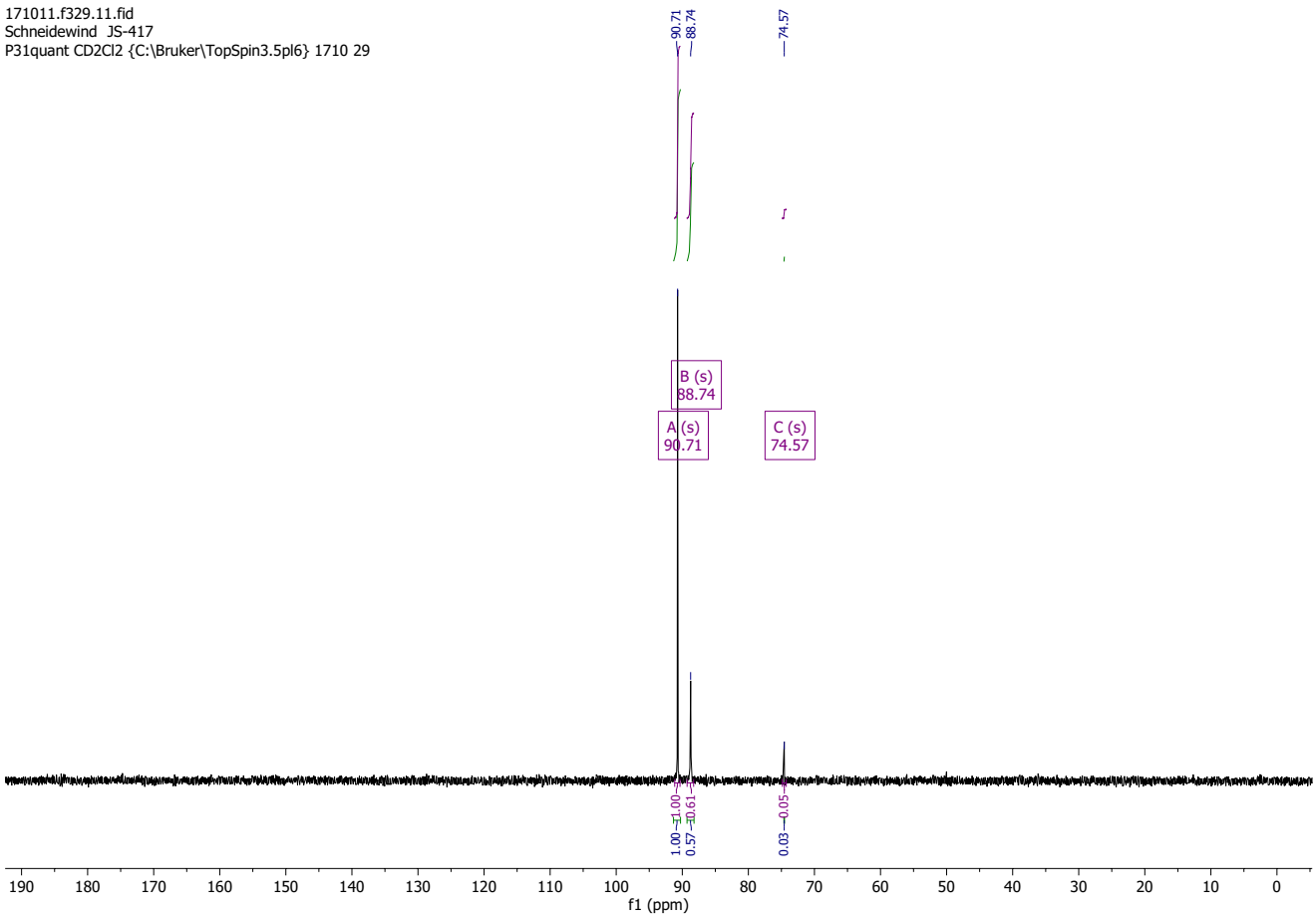

Figure 7.4-2 $^{31}P\{^{1}H\}$ NMR spectrum of (PNN)$RuCl_2$(CO) in CD_2Cl_2 (298 K)
(mixture of cis and trans isomers)

7.5 Data for Irradiated Samples

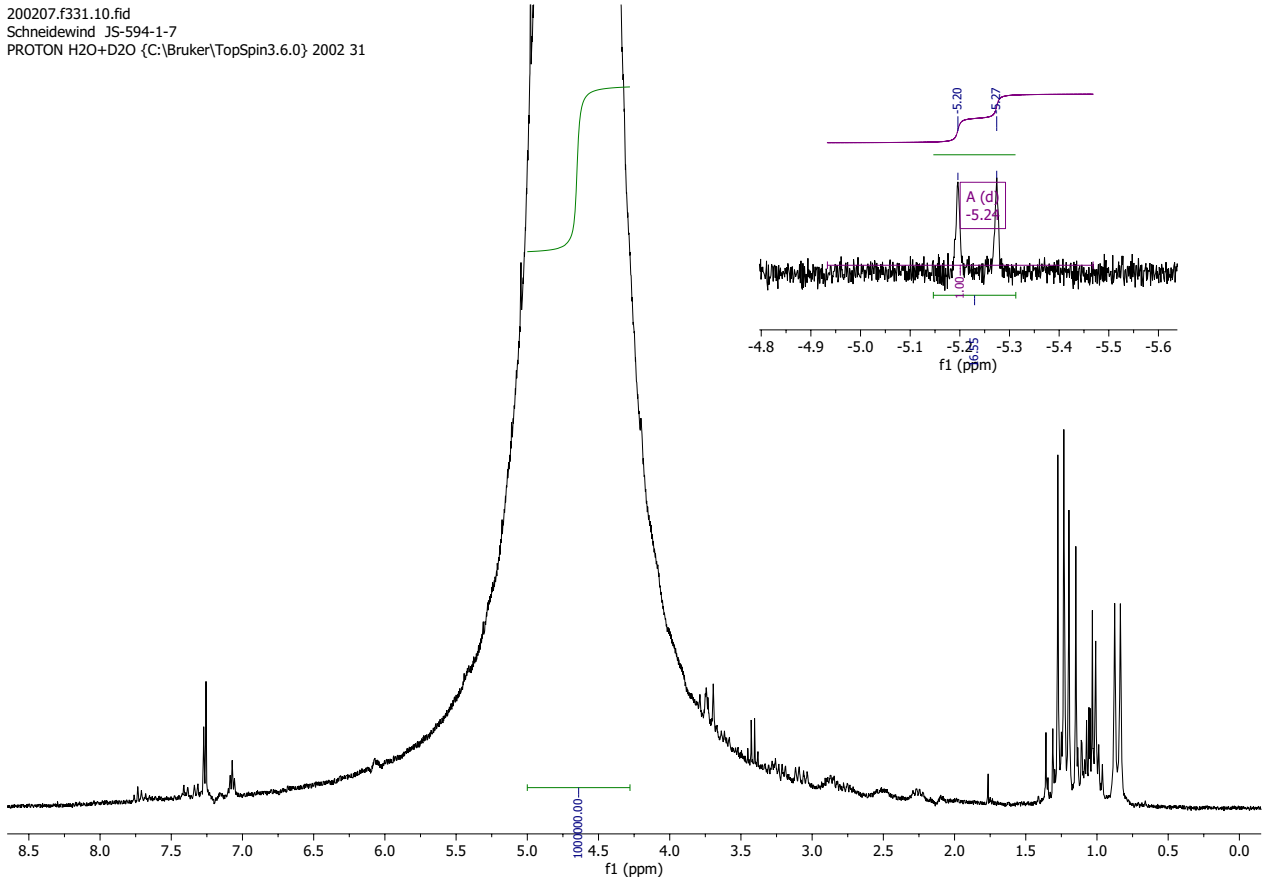

Figure 7.5-1 ^{1}H NMR spectrum of 1 (in H_2O, 298 K) after irradiation with QTH light source for 46h (irradiation without longpass filters, inlet showing hydride peak for **2-cis**)

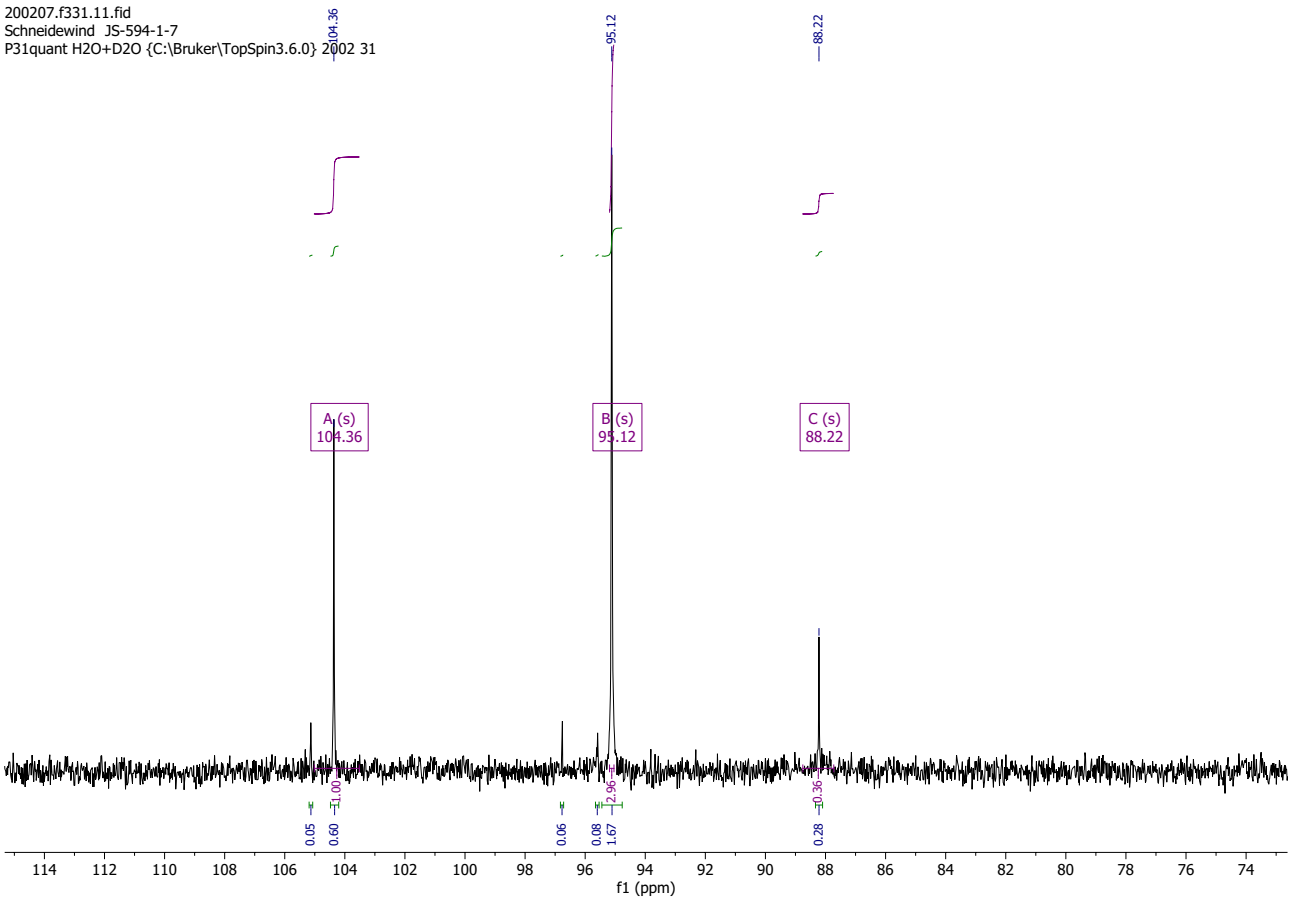

Figure 7.5-2 $^{31}P\{^{1}H\}$ NMR spectrum of 1 (in H_2O, 298 K) after irradiation with QTH light source for 46h (irradiation without longpass filters)

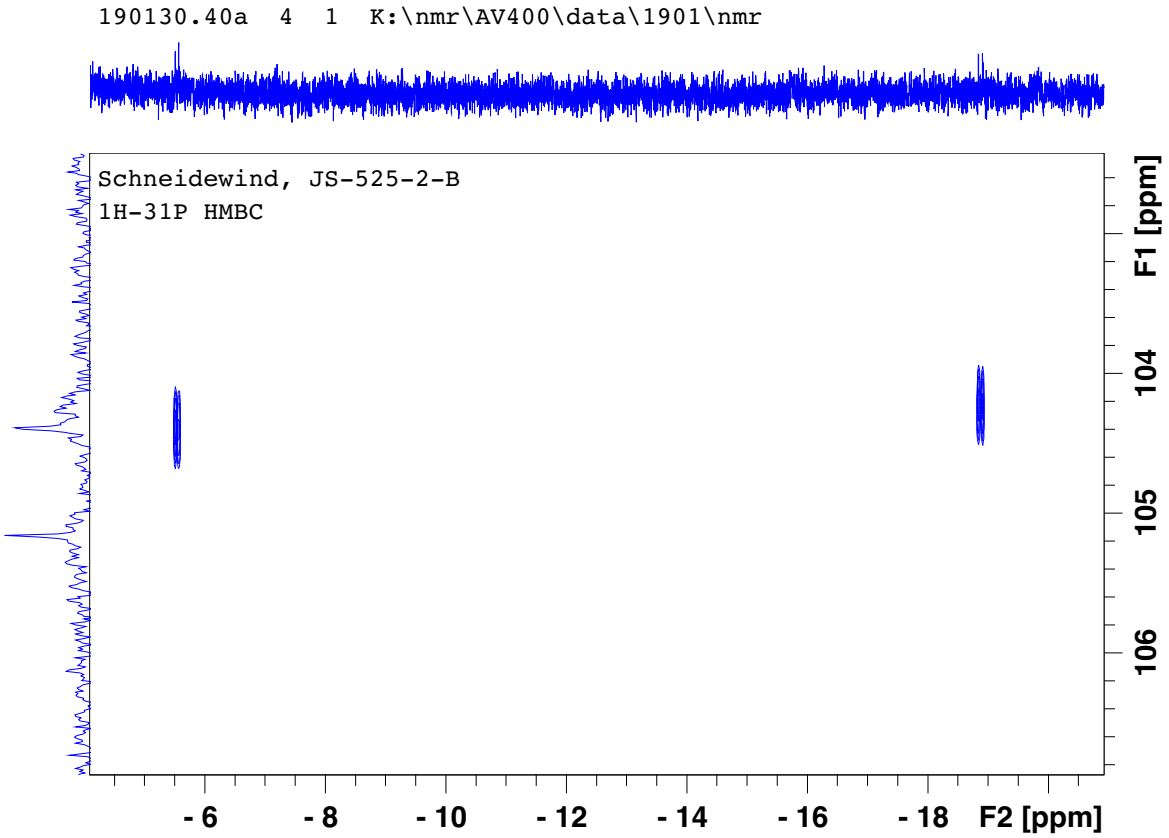
190130.40a 4 1 K:\nmr\AV400\data\1901\nmr
Schneidewind, JS-525-2-B
1H-31P HMBC
F1 [ppm]
104
105
106
- 6
- 8
- 10
- 12
- 14
- 16
- 18
F2 [ppm]

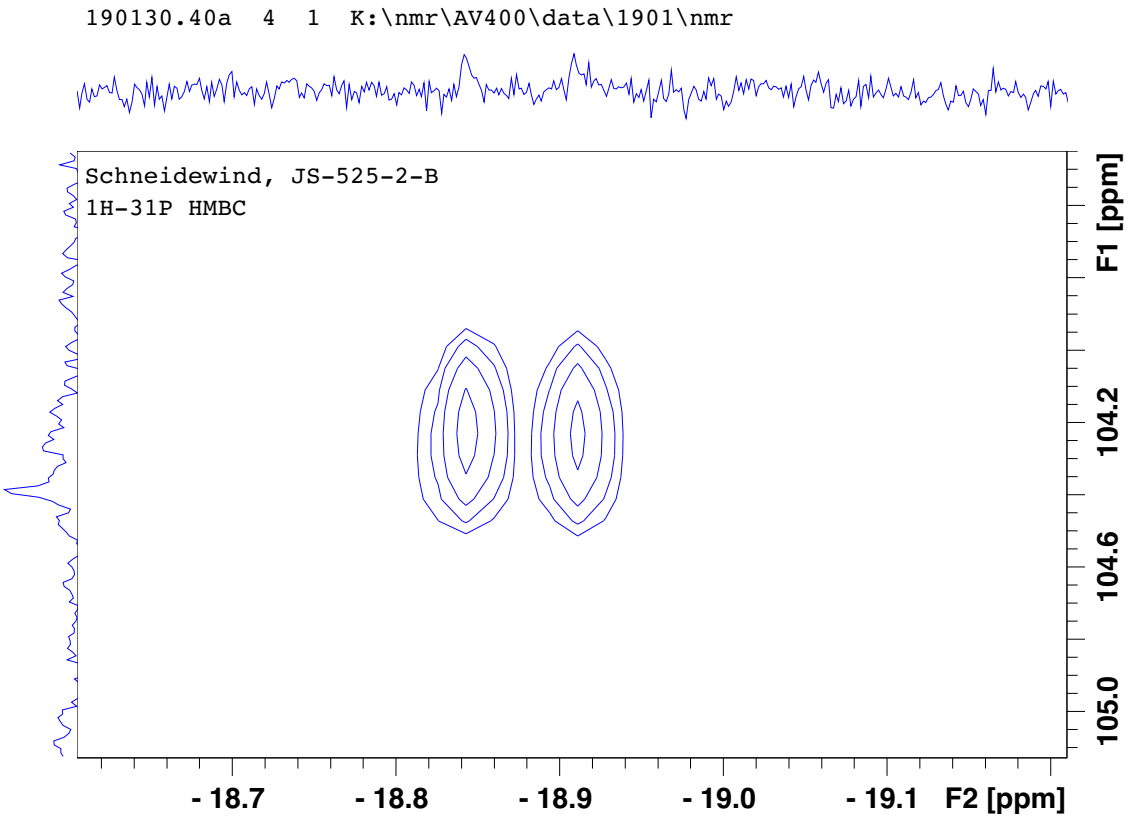
190130.40a 4 1 K:\nmr\AV400\data\1901\nmr
Schneidewind, JS-525-2-B
1H-31P HMBC
F1 [ppm]
104.2
104.6
105.0
- 18.7
- 18.8
- 18.9
- 19.0
- 19.1
F2 [ppm]

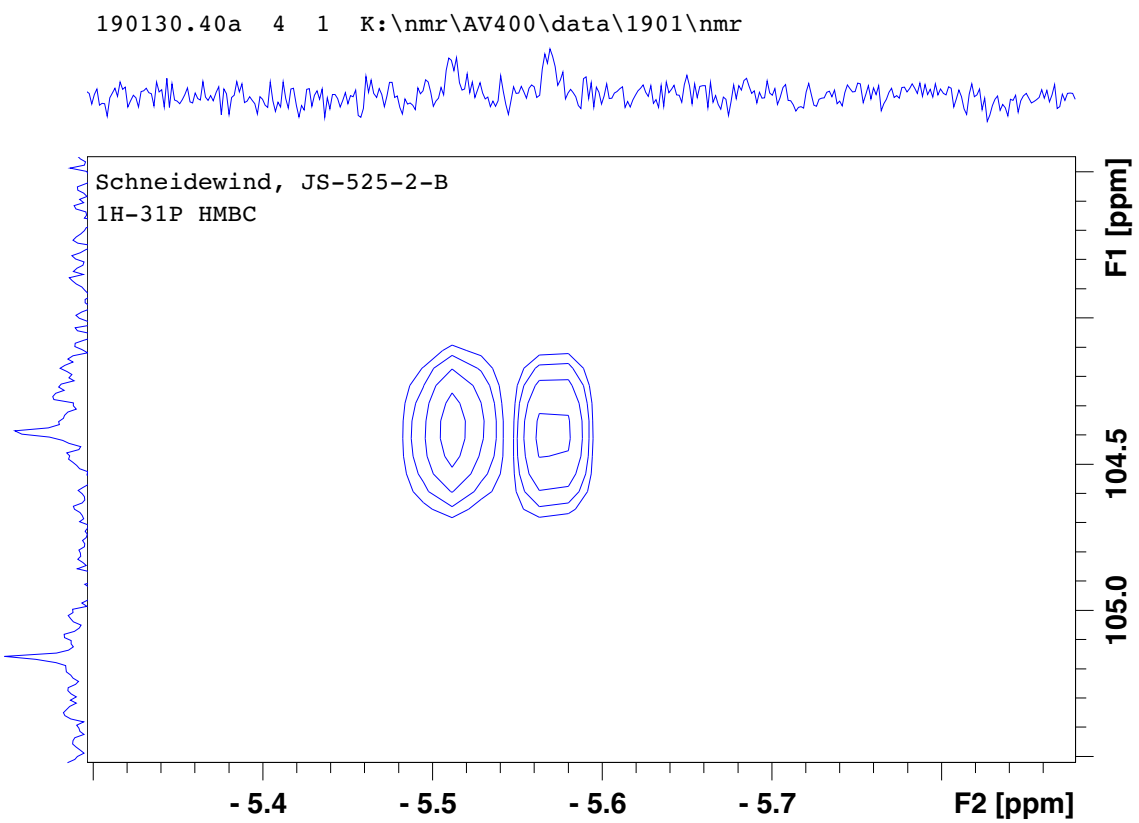

Figure 7.5-3 ^{1}H-^{31}P HMBC (hydride region) NMR spectrum of 1 (in H_2O, 298 K) after irradiation
Top: overview of entire ^{1}H-^{31}P spectrum. Middle: Zoom showing coupling of $\partial(^{31}P)$ = 104.25 ppm with $\partial(^{1}H)$ = -18.86 ppm, corresponding to **2-trans**. Bottom: Zoom showing coupling of $\partial(^{31}P)$ = 104.36 ppm with $\partial(^{1}H)$ = -5.24 ppm corresponding to **2-cis**. Note that **2-trans** is present in this sample since the HMBC measurement was performed five days after irradiation, allowing for partial isomerization of **2-cis** to **2-trans**.

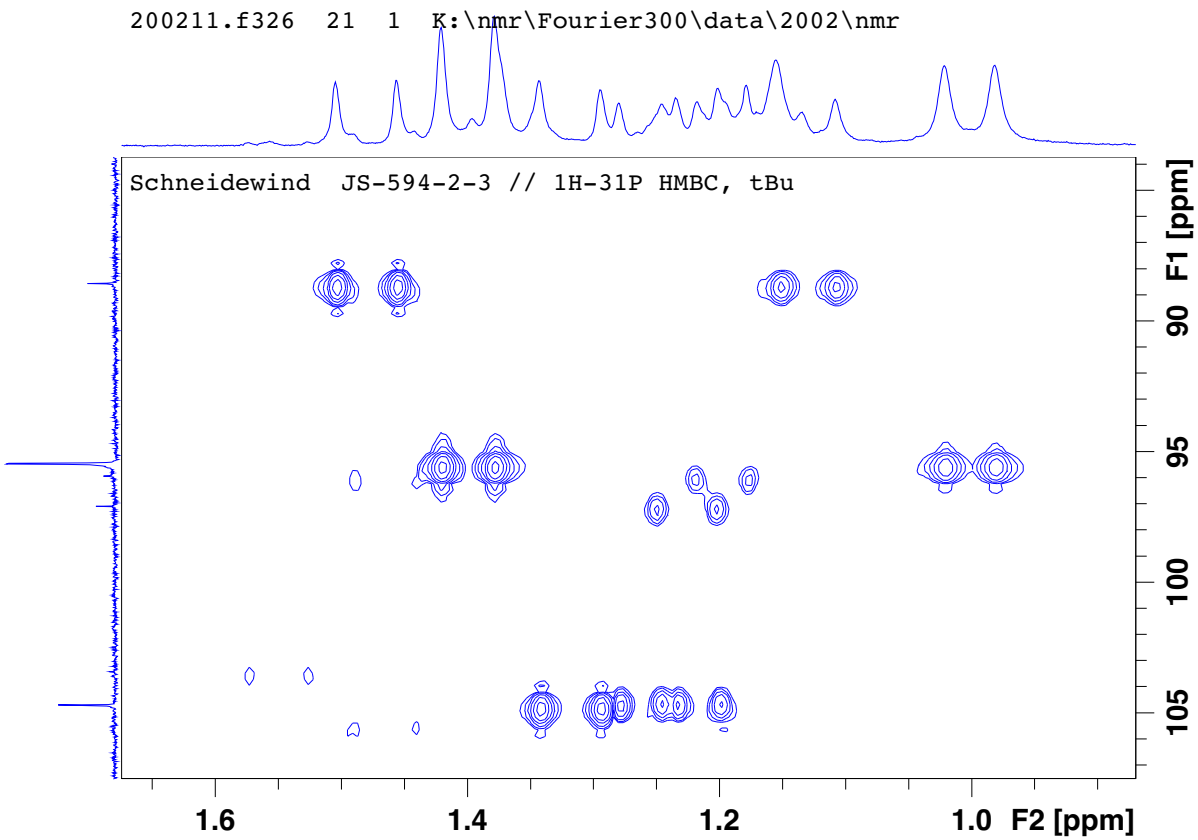

Figure 7.5-4 ^{1}H-^{31}P HMBC (aliphatic region) NMR spectrum of 1 (in H_2O, 298 K) after irradiation
Note that this spectrum was measured directly after irradiation hence no **2-trans** is present. The $\partial(^{31}P)$ = 95.12 ppm signal couples with two doublets at $\partial(^{1}H)$ = 1.4 ppm and $\partial(^{1}H)$ = 1.0, which correspond to the two tBu groups of the PNN ligand. This shows that the tBu groups in this species are not equivalent and hence this species has no symmetry.

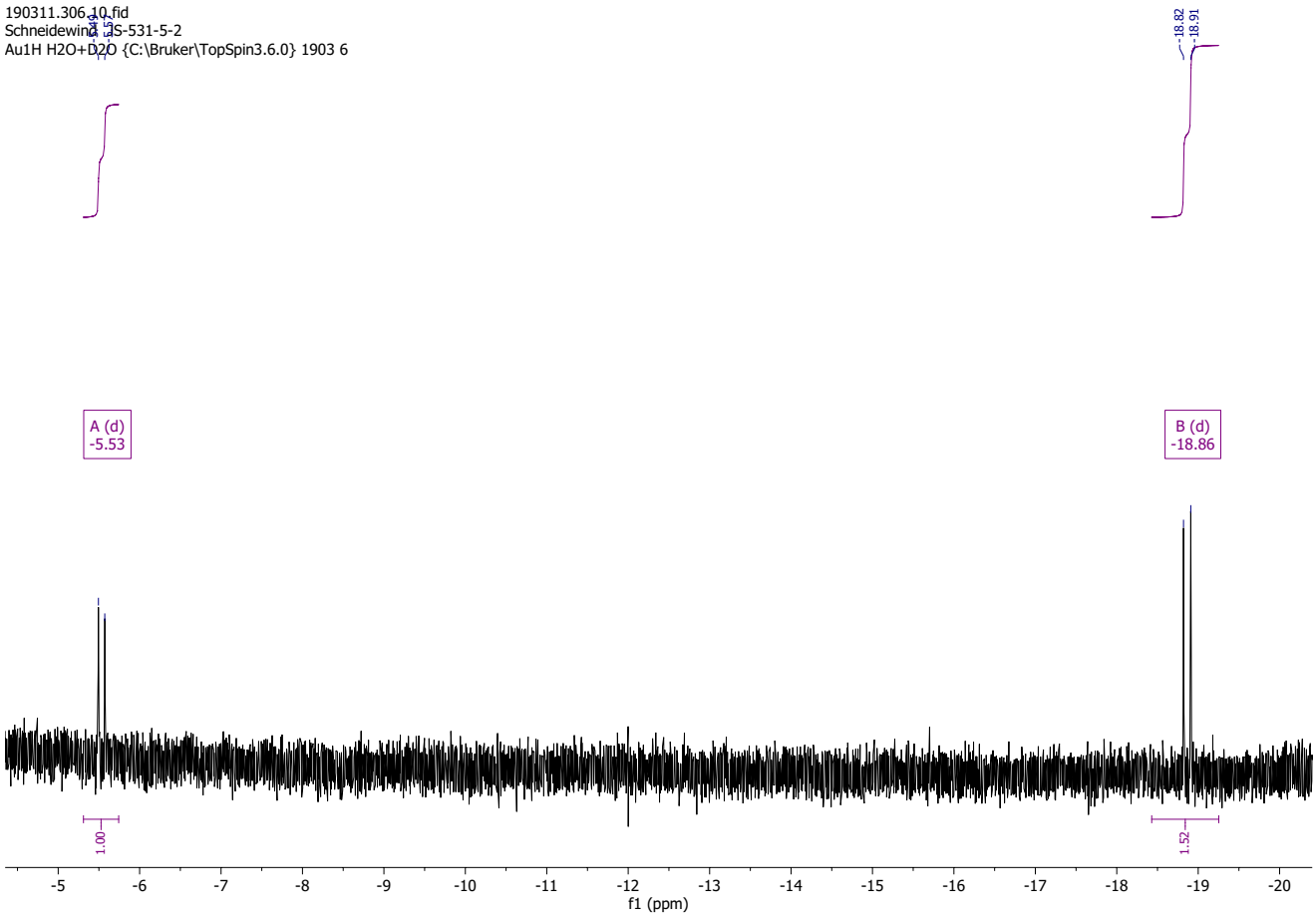

Figure 7.5-5 ^{1}H NMR spectrum of 2-trans (in H_2O, 298 K) after irradiation (320 – 500 nm, 4h) in presence of O_2

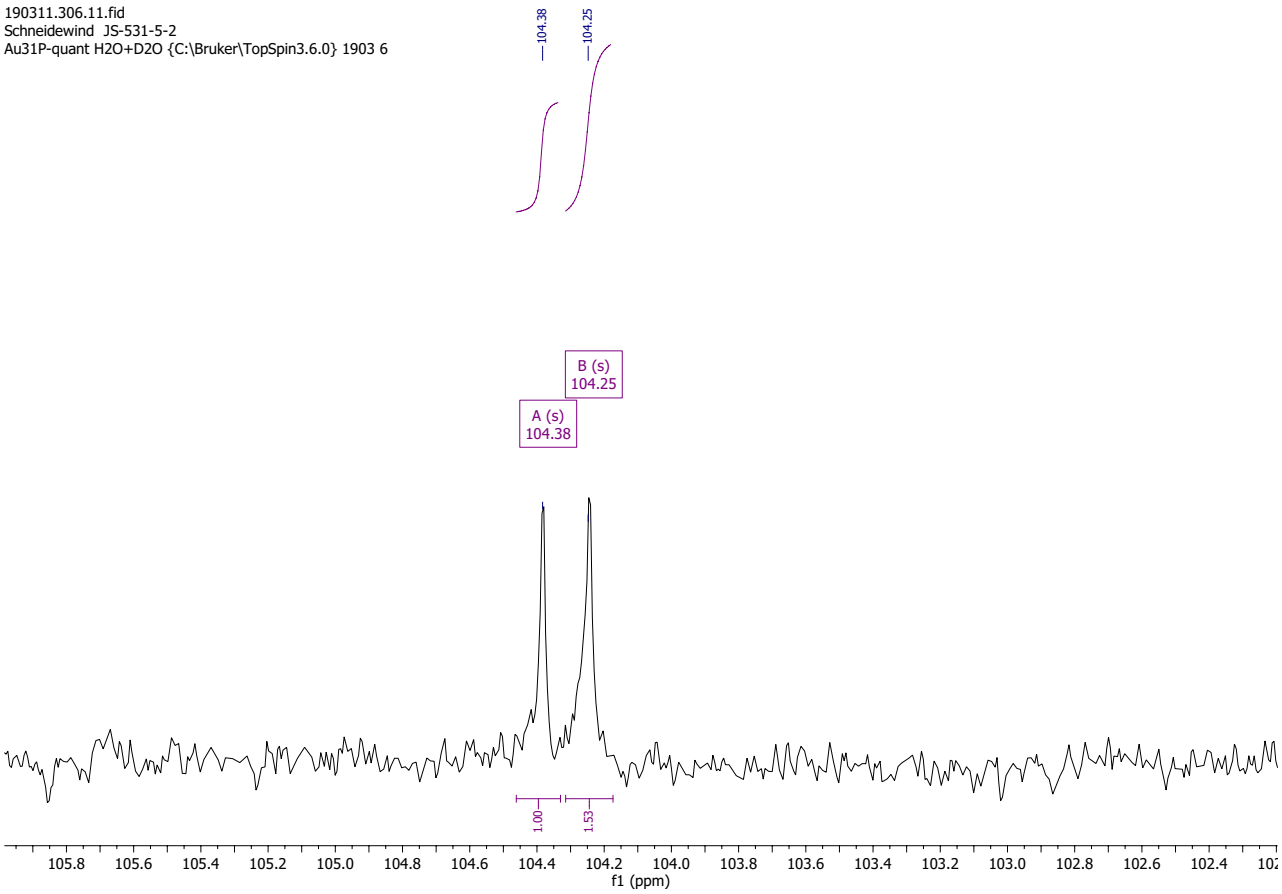

Figure 7.5-6 $^{31}P\{^{1}H\}$ NMR spectrum of 2-trans (in H_2O, 298 K) after irradiation (320 – 500 nm, 4h) in presence of O_2

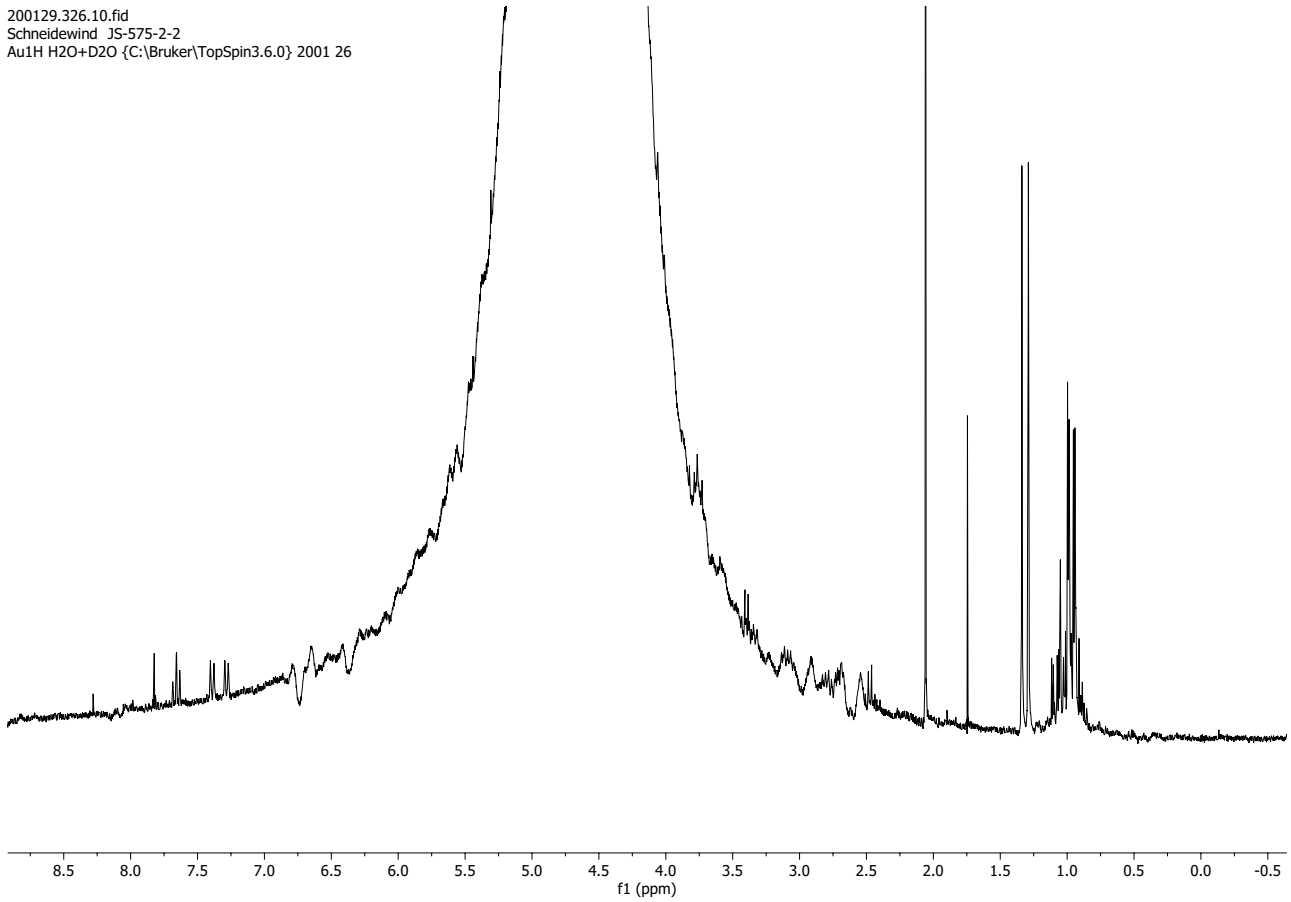

Figure 7.5-7 ^{1}H NMR spectrum of 1 (in 52 mM KOH aq., 298 K, Ag_2O synthesis route) in air before irradiation.

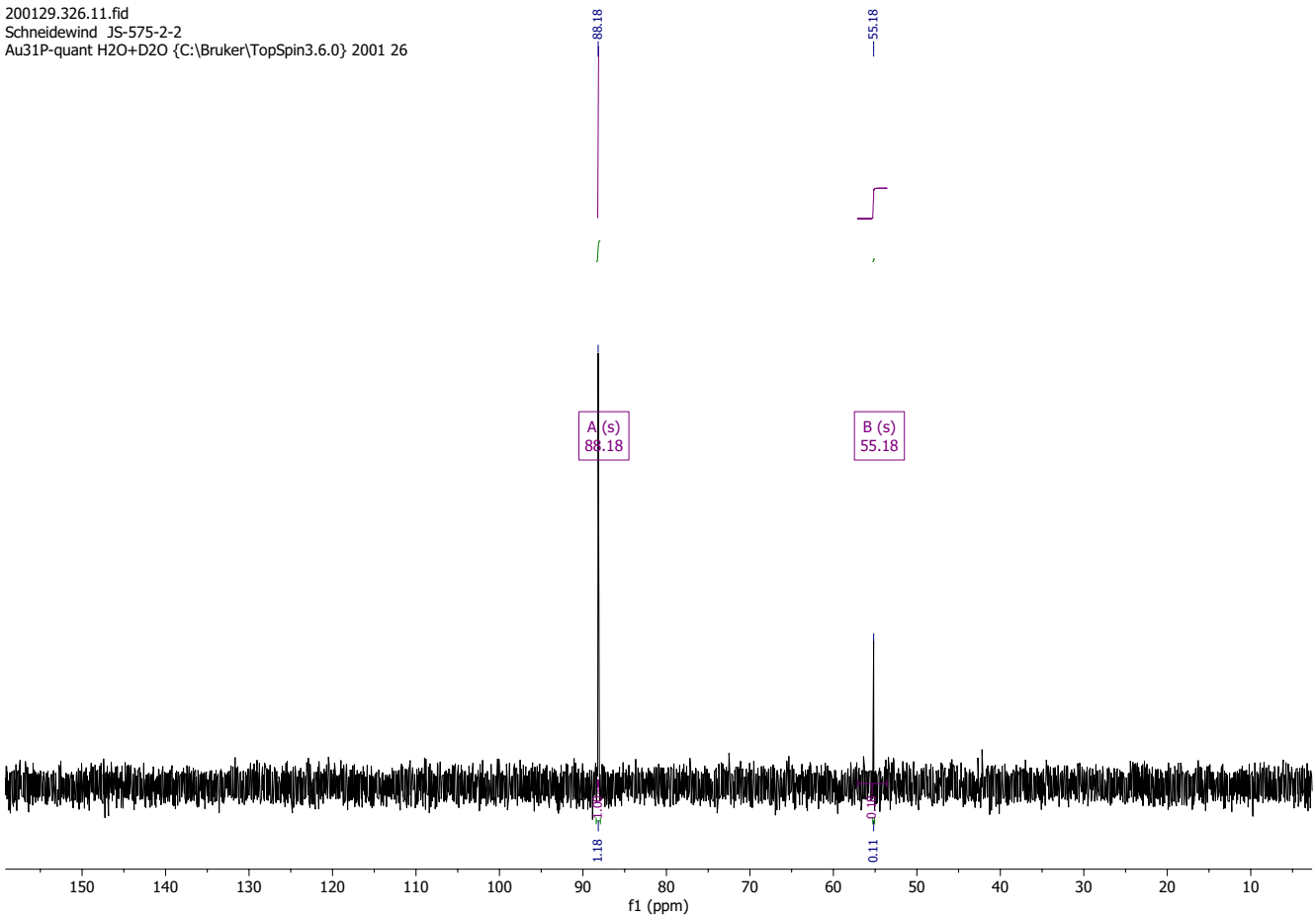

Figure 7.5-8 $^{31}P\{^{1}H\}$ NMR spectrum of 1 (in 52 mM KOH aq., 298 K, Ag_2O synthesis route) in air before irradiation.
Integrals are relative to H_3PO_4 capillary standard.

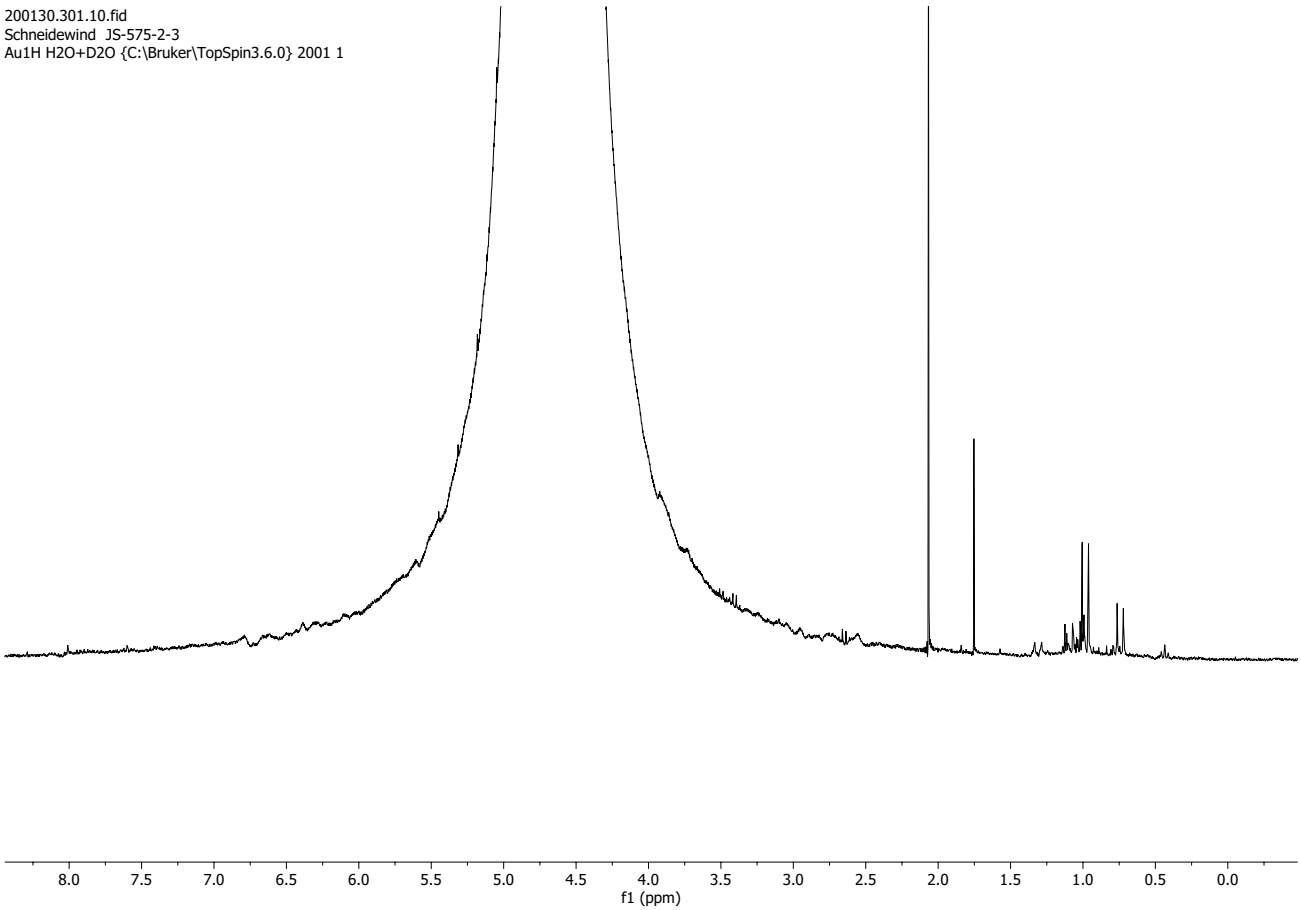

Figure 7.5-9 ^{1}H NMR spectrum of 1 (in 52 mM KOH aq., 298 K, Ag_2O synthesis route) in air after irradiation (QTH, 16h)

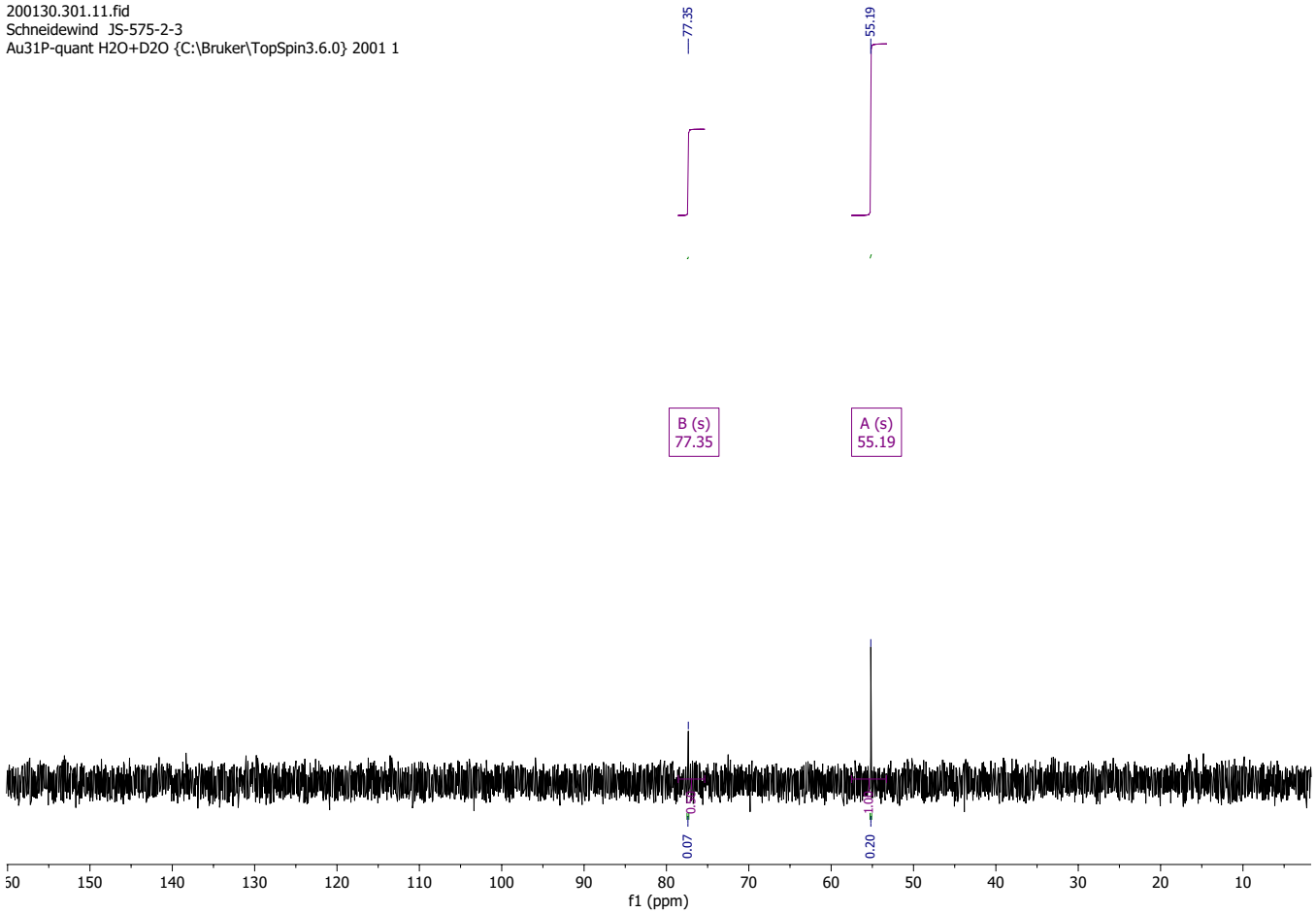

Figure 7.5-10 $^{31}P\{^{1}H\}$ NMR spectrum of 1 (in 52 mM KOH aq., 298 K, Ag_2O synthesis route) in air after irradiation (QTH, 16h)
Integrals are relative to H_3PO_4 capillary standard.

7.6 Isomerization Reactions in the Dark

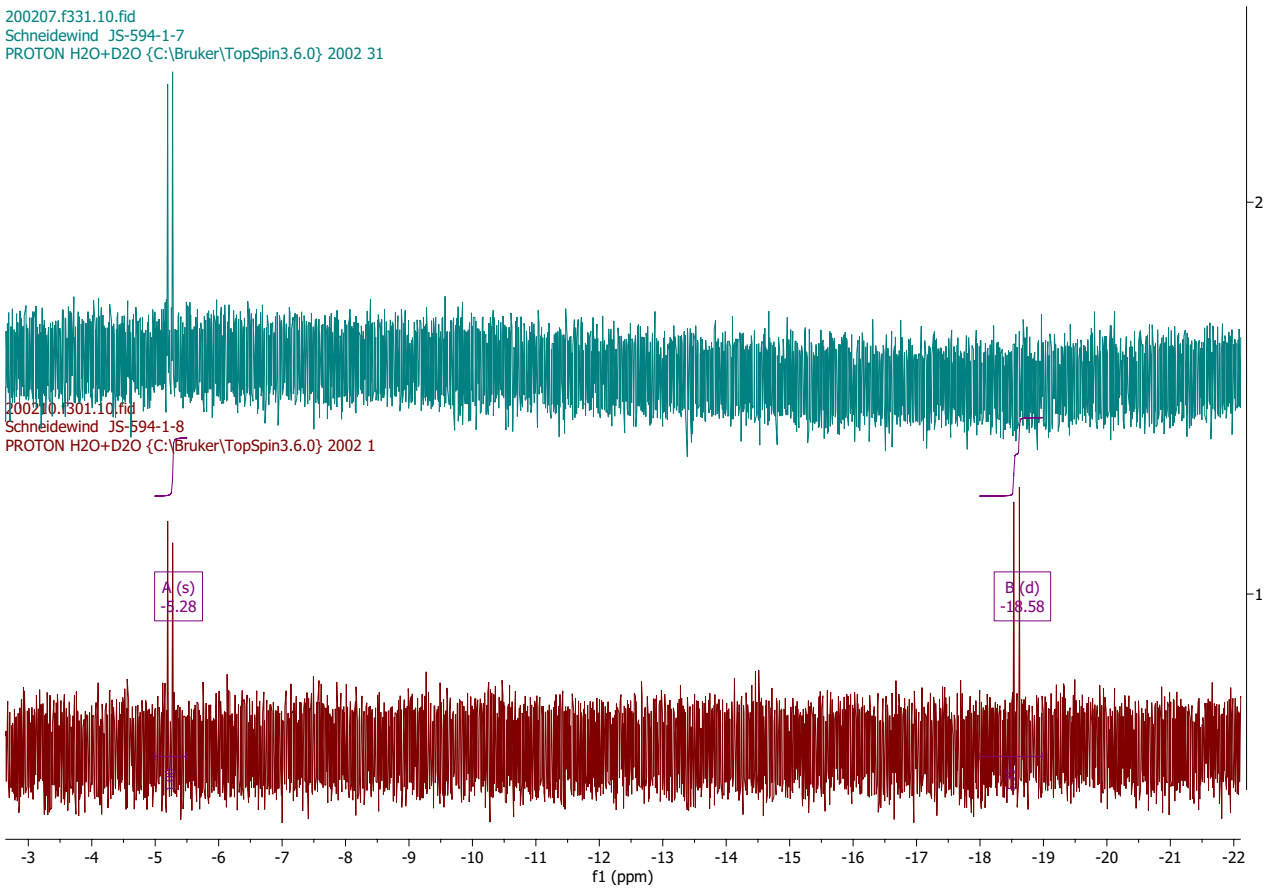

Figure 7.6-1 Stacked ^{1}H NMR spectra of 1 (in H_2O, 298 K) immediately after irradiation (top, green) and same sample after two more days in the dark (bottom, red)

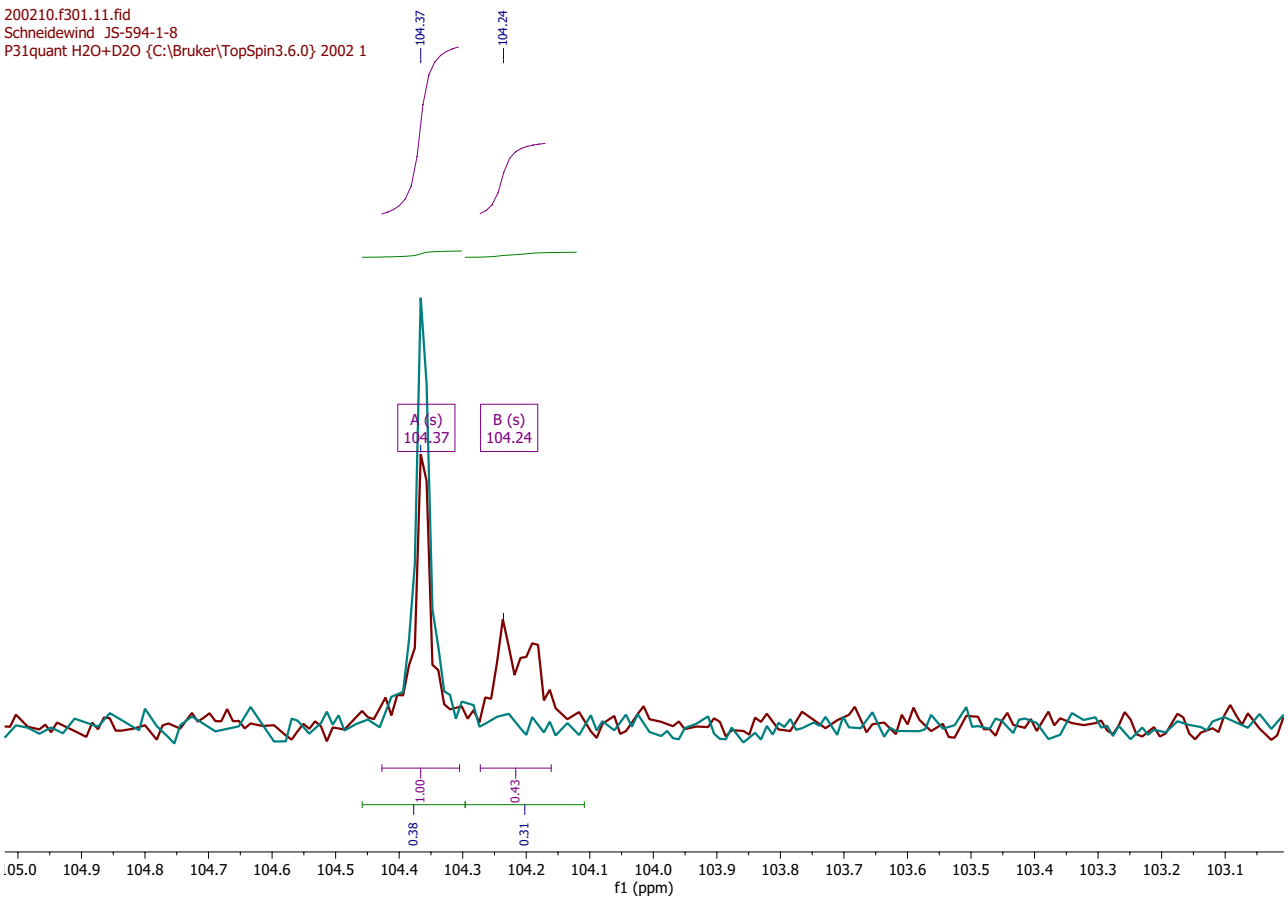

Figure 7.6-2 Superimposed $^{31}P\{^{1}H\}$ NMR spectra of 1 (in H_2O, 298 K) immediately after irradiation (green) and same sample after two more days in the dark (red)

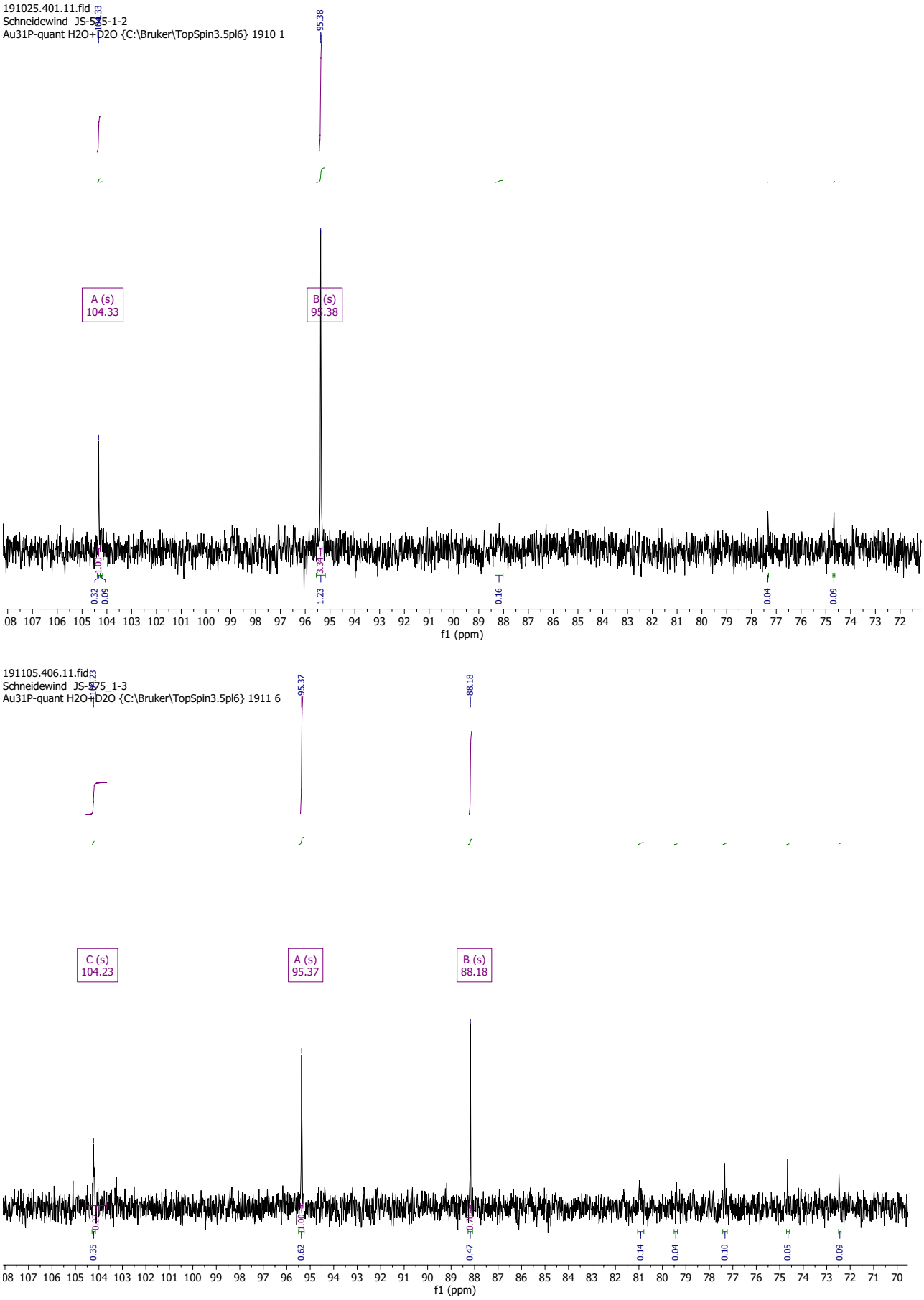

Figure 7.6-3 $^{31}P\{^{1}H\}$ NMR spectrum of 1 (in 52 mM KOH aq., 298 K, Ag_2O synthesis route) immediately after irradiation (top) and the same sample after twelve more days in the dark

7.7 Data for $\partial(^{31}P)$ = 86 ppm Product

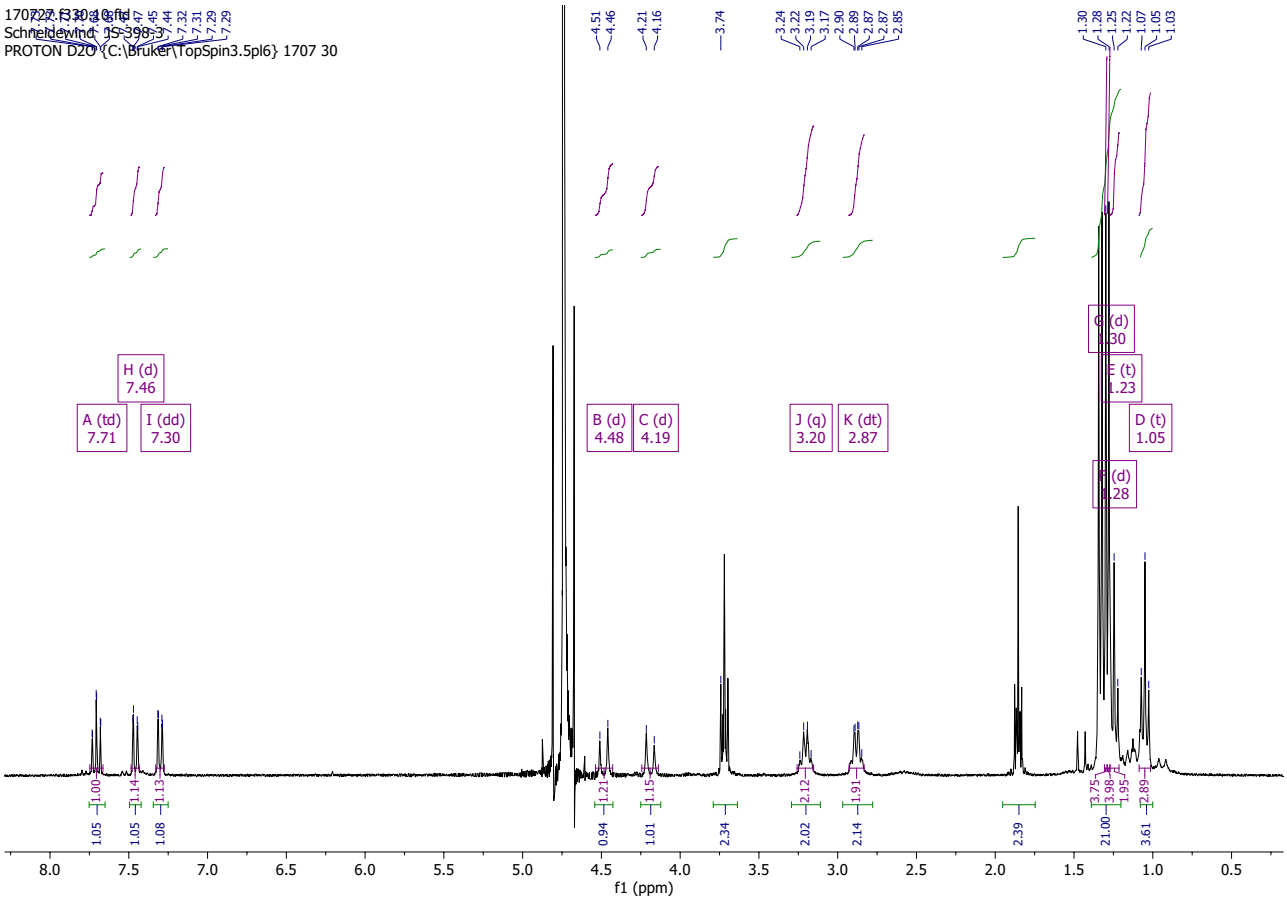

Figure 7.7-1 ^{1}H NMR spectrum of raw product (in D_2O, 298 K) after reaction of 2-trans with N_2O for 20h in presence of 83 equivalents of H_2O

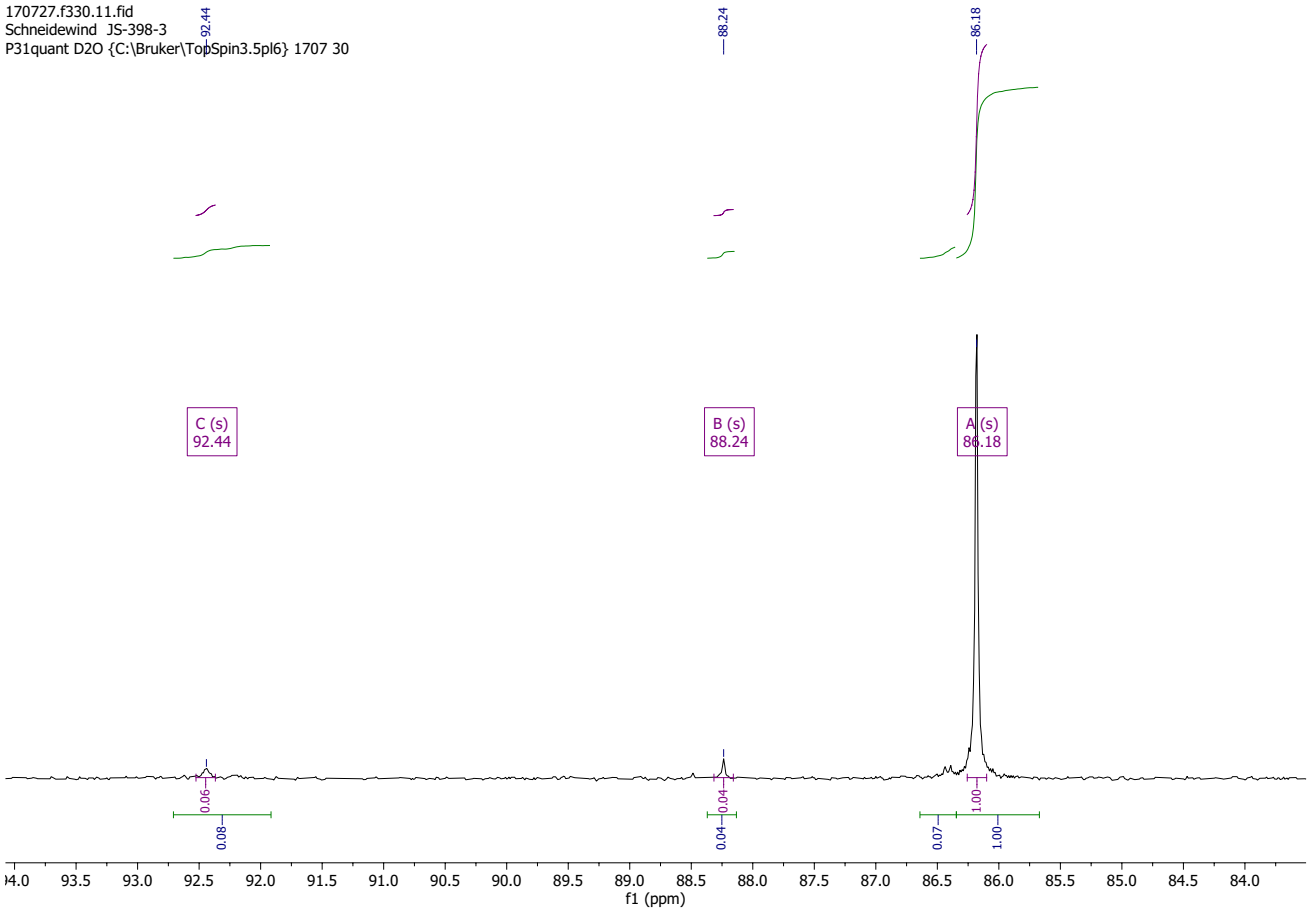

Figure 7.7-2 $^{31}P\{^{1}H\}$ NMR spectrum of raw product (in D_2O, 298 K) after reaction of 2-trans with N_2O for 20h in presence of 83 equivalents of H_2O

8 Other Analytical Data

8.1 IR Spectrum of Complex 1

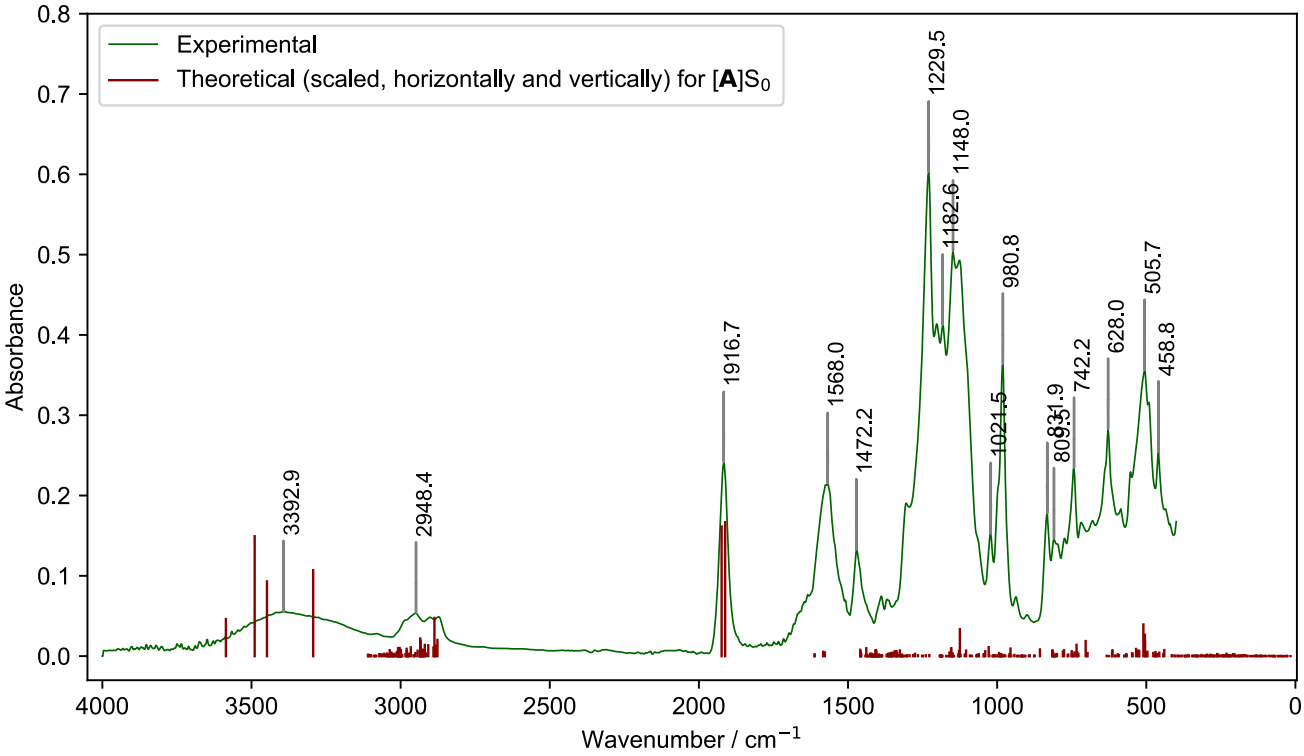

Figure 8.1-1 IR Spectrum (ATR) of complex 1 along with theoretical spectrum for $[A]S_0$
Note: theoretical spectrum is shown as vertical lines for each transition. The theoretical spectrum has been scaled horizontally by a factor of 0.96 and has been scaled vertically.

8.2 EPR Spectrum of Complex 1 Synthesis Raw Product

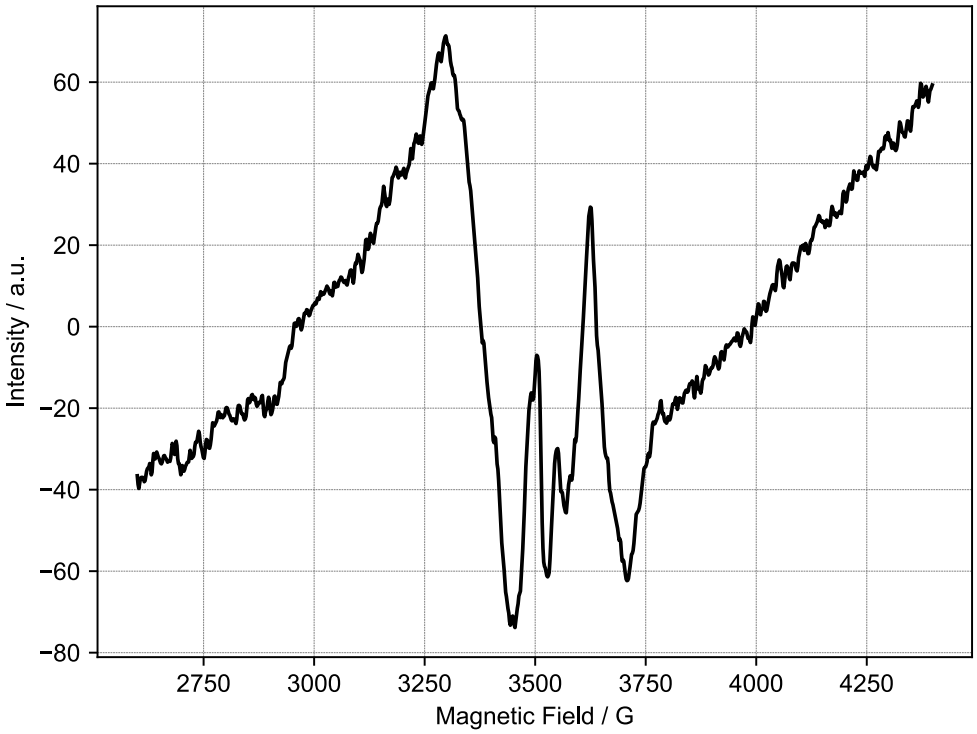

Figure 8.2-1 EPR spectrum of green raw product obtained via reaction of 2-trans with N_2O
N_2O reaction of **2-trans** was carried out as described in 3.1.1, but after the reaction, the solvent was completely removed under vacuum and the dark green solid residue was washed with Et_2O and pentane. The residue was then dissolved in DCM, yielding a green solution, which was transferred to a capillary and measured.

9 Ultrafast Pump-Probe Spectroscopy

9.1 Experimental Procedure and Analysis

Transient absorption spectra were recorded with a time resolution of ca. 200 fs by means of a pump-probe setup based on a Ti:sapphire laser system (Spectra-Physics, Spitfire Pro) operating at a centre wavelength of 800 nm and a repetition rate of 1 kHz . Pump pulses at a centre wavelength of 400 nm were generated by frequency doubling a part of the output of the Ti:sapphire system using a BBO-crystal. The energy of the pump pulses was between 0.8 and 1 µJ. A white light continuum for probing was obtained by focussing a small fraction of the Ti:sapphire output into a CaF_2-crystal. Pump and probe beam were focussed into the sample so that their overlapping spots had an effective diameter of 360 µm for the pump and 210 µm for the probe. Measurements were performed with the polarizations of the pump and probe beam set to parallel, perpendicular, and in magic-angle (54.7°). After passing through the sample, the probe beam was dispersed by a prism and transient absorption changes were recorded by an array detector in a spectrally resolved fashion.
Complex **1** was dissolved in oxygen-free water and the sample solution was transferred into a 1 mm fused silica cuvette under inert conditions. The optical density at 400 nm was ca. 0.7 to obtain transient spectra with a good signal to noise ratio (concentration ≈ 0.007 M). The cuvette was mounted and measured on a rotation stage. A rotation frequency of about 1 Hz resulted in a sufficiently fast refreshing of the sample in the interaction region to avoid degeneration of the signal during the measurements. Transient absorption data was analyzed by global fitting of a sum of exponential decays revealing time constants and the corresponding decay associated spectra (DAS). To describe the ultrafast dynamics with sufficient accuracy, two exponential decay components are necessary and a long lived one with an “infinite” lifetime (>> 2 ns) much longer than the time range of 2 ns covered by our setup.

9.2 Results and Interpretation

Decay associated spectra for the two detected species (τ = 6 ps and τ = 150 ps) are shown in Figure 9.2-1. The τ = 6 ps species can likely be attributed to an emissive S_n state of **1**, since the positive mΔOD between 450 and 650 nm agrees well with the measured fluorescence of **1**, suggesting that this feature is due to stimulated emission. The short lifetime of only 6 ps can also explain the weak nature of **1**’s fluorescence.

The experimental DAS for the τ = 150 ps species agrees well with the computed DAS for [**B-Trans**]T_0 (see 11.4.2 for details on computed DAS spectra). The lifetime of this species, however, is too short to explain the observed reaction rates based on the kinetic model (see 10.3), which predicts a minimum lifetime of $\tau \approx 10$ ns for the second-photon absorbing intermediate. We propose that [**B-Trans**]T_0 might partially isomerize to [**B**]T_0 or [**B**]T_0 might be formed directly from [**A**]S_n, but in amounts which are below the detection limit of the used experimental set-up (TD-DFT calculations predict that [**B**]T_0 absorbs 400 – 700 nm light more weakly compared to [**B-Trans**]T_0, see Figure 11.2-1, further complicating direct detection). [**B**]T_0 and [**B-Trans**]T_0 might have different relaxation channels, especially because Ru-O bond formation can lead to **Oxo Dimer** formation for [**B-Trans**]T_0 but not for [**B**]T_0. The lifetime of [**B**]T_0 might therefore be longer than the lifetime of [**B-Trans**]T_0, explaining why [**B**]T_0 can act as the second-photon absorbing intermediate.

As can be seen in Figure 9.2-2, [**A**]T_0 yields a theoretical DAS which is inconsistent with experimental data, suggesting that it is not the species corresponding to τ = 150 ps.

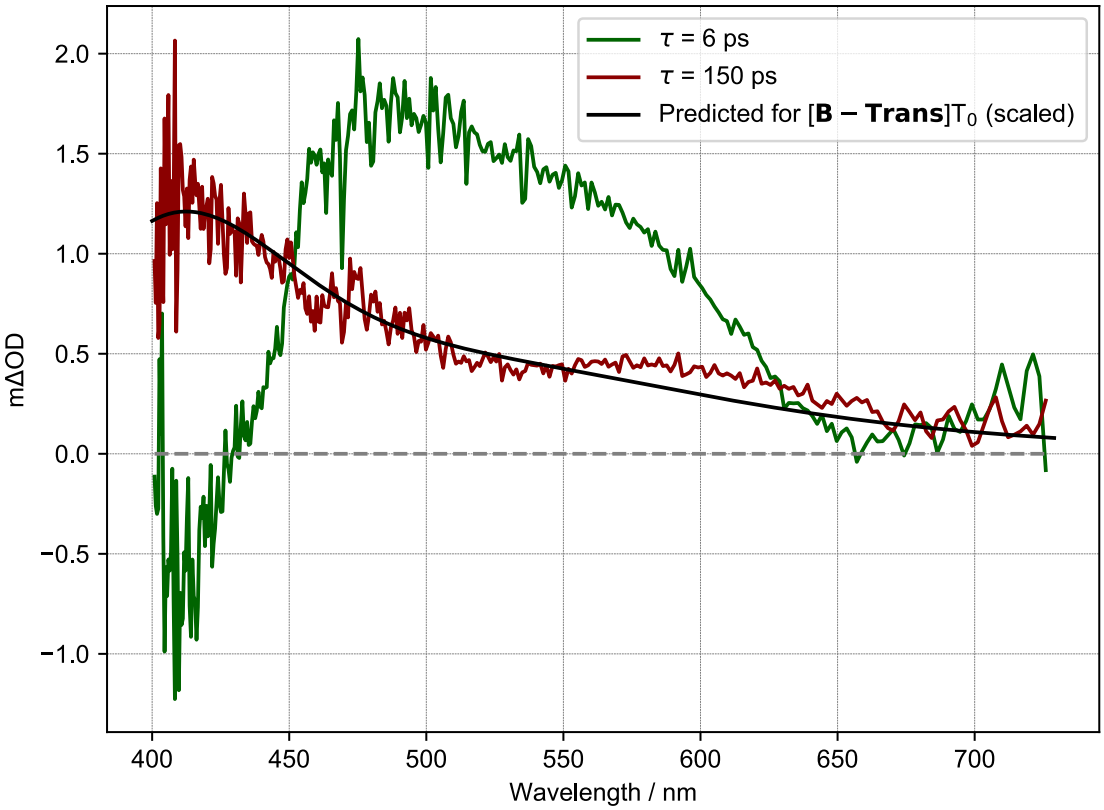

Figure 9.2-1 Decay associated spectra (magic angle polarization) and predicted DAS for [B-Trans]T_0
Predicted DAS for [**B-Trans**]T_0 was computed as the difference spectrum between [**A-Mono**]S_0 and [**B-Trans**]T_0. For the structure of [**B-Trans**]T_0 see Figure 11.5-11).

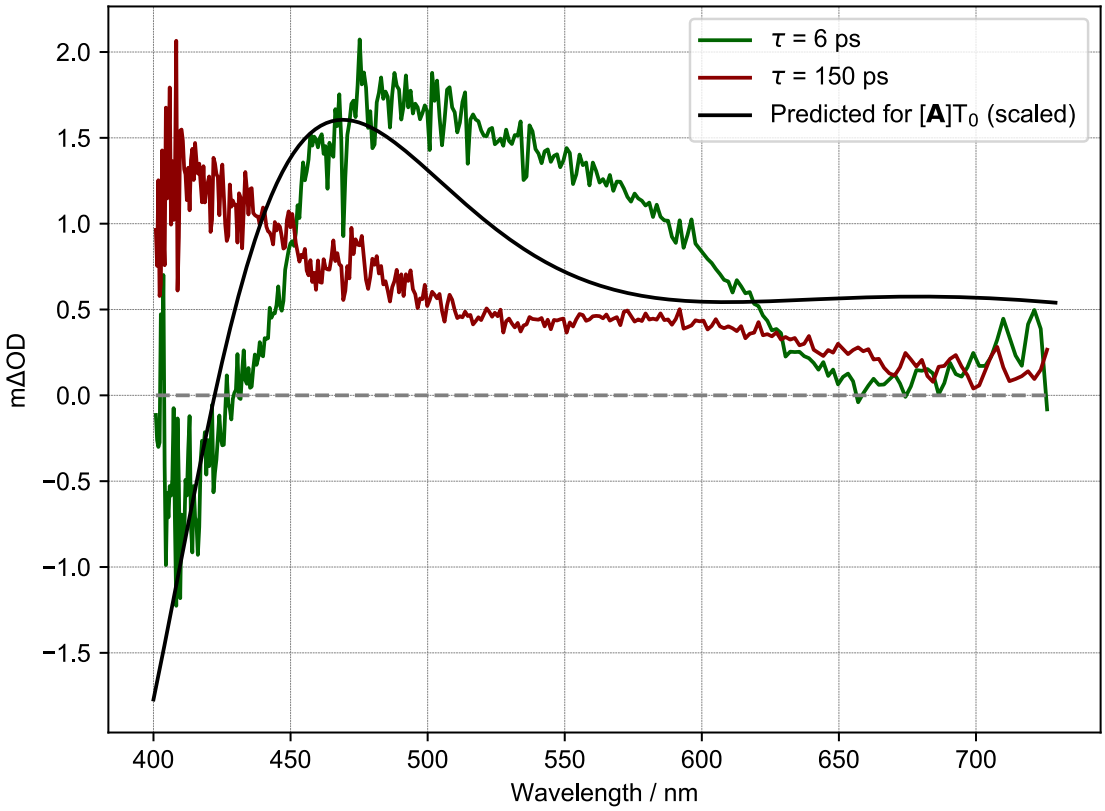

Figure 9.2-2 Decay associated spectra (magic angle polarization) and predicted DAS for [A]T_0
Predicted DAS for [**A**]T_0 was computed as the difference spectrum between [**A-Mono**]S_0 and [**A**]T_0.

10 Photochemical Kinetic Model

10.1 Description of Kinetic Model

A simple kinetic model to describe the two-photon water splitting reaction was developed using the reaction sequence shown in Table 10.3-1. In this reaction sequence, starting complex **A** absorbs a photon to form transient intermediate **B**. **B** decays back to **A** with a lifetime of τ. Furthermore, **B** can absorb a second photon to form O_2 (+ corresponding complex, which is not part of this kinetic model). O_2 can then be consumed by a third reaction (forming **X**), which also requires photon absorption (see 4.3.2). This reaction sequence is therefore a simplified version of the water splitting mechanism determined using DFT and CASSCF calculations, combined with the experimentally observed, O_2 consuming reaction.

The reaction sequence can be described using the following system of differential equations:

$$\frac{d[\boldsymbol{A}]}{dt} = \frac{1}{\tau}[\boldsymbol{B}] - q_1 c_{abs} Flux\,[\boldsymbol{A}] \qquad \text{Equation (4)}$$

$$\frac{d[\boldsymbol{B}]}{dt} = -\frac{1}{\tau}[\boldsymbol{B}] + q_1 c_{abs} Flux\,[\boldsymbol{A}] - q_2 c_{abs} Flux\,[\boldsymbol{B}] \qquad \text{Equation (5)}$$

$$\frac{d[\boldsymbol{C}]}{dt} = q_2 c_{abs} Flux\,[\boldsymbol{B}] - q_3 c_{abs} Flux\,[\boldsymbol{C}] \qquad \text{Equation (6)}$$

$$\frac{d[\boldsymbol{D}]}{dt} = q_3 c_{abs} Flux\,[\boldsymbol{C}] \qquad \text{Equation (7)}$$

Wherein q_n are the respective quantum efficiencies for each reaction step, *Flux* is the photon flux and c_{abs} is the absorption cross-section. For simplicity, it was assumed that absorption cross sections are the same for each step (1.15E-17 cm^2, which corresponds to an extinction coefficient of 3000 M^{-1} cm^{-1}). Furthermore, it was assumed that *Flux* is the same for each reaction step.

The kinetic model was fitted to experimental data from the intensity dataset. For this, all experiments with the same photon flux were averaged. Afterwards, the data was normalized to express the amount of O_2 as a fraction of the initial amount of **1** (based on 0.005 M concentration of **1**). This gave the averaged and normalized experimental data shown in Figure 10.3-1A. For the photon flux = 3.3e+17 data, Gaussian noise with the same standard deviation as the experimental data was appended from 240 s, since the experimental data was only available up to this time.
Fitting was performed by numerically solving the system of differential equations with an updated guess for τ, q_1, q_2 and q_3 at each optimization step, with *Flux* being the corresponding photon flux for each data series. Updated guesses were generated using the Nelder-Mead algorithm. This was done until convergence was reached. It should be noted that only one set of optimization parameters (τ, q_1, q_2 and q_3) describes all experiments with different photon flux values. The resulting fit is shown in Figure 10.3-1A. Optimized parameters are shown in Table 10.3-1.

10.2 Relationship between Initial Rate and Photon Flux

The described kinetic model was also used to explore the relationship between initial rate of O_2 formation and photon flux. For this, the optimized parameters shown in Table 10.3-1 were used, unless noted otherwise. With these parameters and within the photon flux range of the intensity dataset, a square relationship between initial rate of O_2 formation and photon flux is obtained (just like it was observed experimentally). In other words, fitting a function of the form $f(x) = ax^b$ (optimizing *a* and *b*) to the initial rate/photon flux data gives a value of 2 for power *b*.

We were interested to see how the relationship between initial rate and photon flux would change for increasing lifetimes τ of **B**. Thus, keeping q_1, q_2 and q_3 constant, τ was changed over several orders of magnitude, and for each τ value, power *b* was determined within the intensity dataset photon flux range. Corresponding results are shown in Figure 10.3-1. It can be seen that starting at

τ = 10^{-2} s, the relationship of initial and photon flux starts to transition to linear one, meaning that power *b* changes gradually from 2 to 1.

10.3 Interpretation of Results

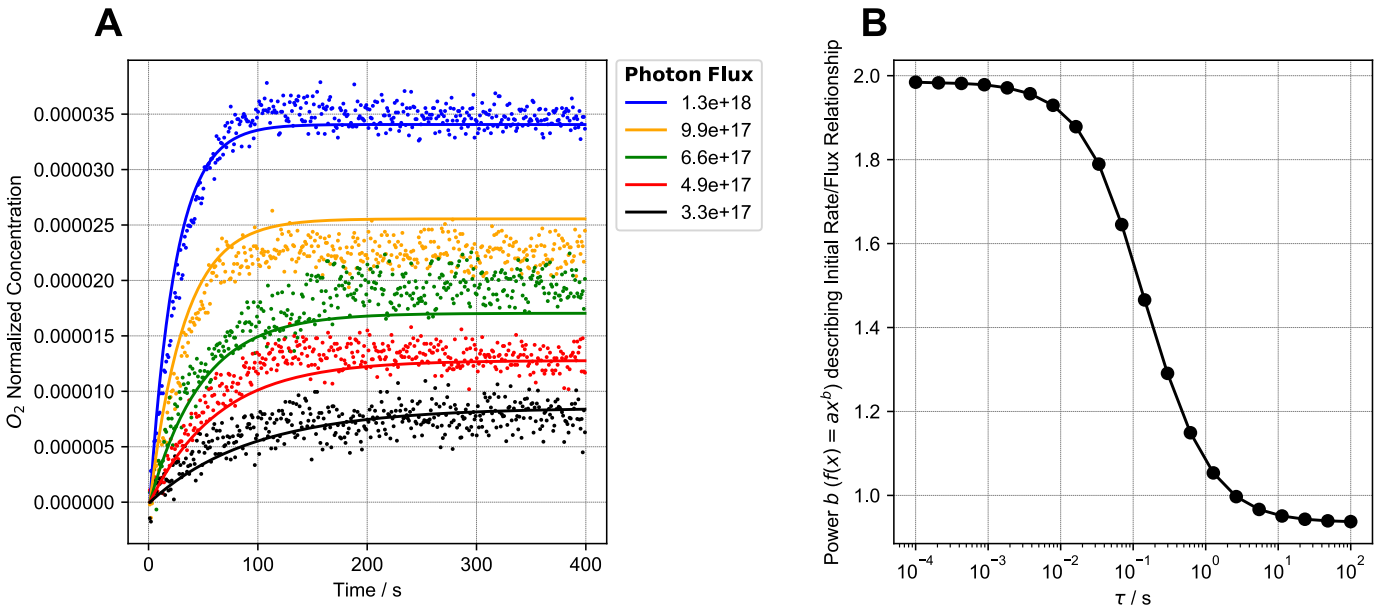

Figure 10.3-1 Photochemical kinetic model used to describe the two-photon water splitting reaction
A Fit of photochemical kinetic model to experimental data. Experimental data is for irradiation with different photon fluxes (intensity dataset) and for each flux value, all measurements with this flux were averaged and converted to normalized O_2 concentration, yielding the shown data. For the photon flux = 3.3e+17 data, Gaussian noise with the same standard deviation as the experimental data was appended from 240 s, since the experimental data was only available up to this time. Fit of the kinetic model is shown as solid lines.
B Dependence of power *b* on the lifetime of the intermediate in the two-photon mechanism. Power *b* describes the relationship between initial rate and photon flux. A value of 2 for *b* indicates a square dependence of the initial rate on photon flux (as observed experimentally), while a value of 1 indicates a linear relationship. It can be seen that for increasing lifetimes, the relationship of initial rate and photon flux transitions from a square to a linear one. For this modeling, the optimized parameters from **A** were used, changing only τ. The flux level range of the intensity dataset was used to determine *b*.

Table 10.3-1 Optimized parameters for photochemical kinetic model[a]

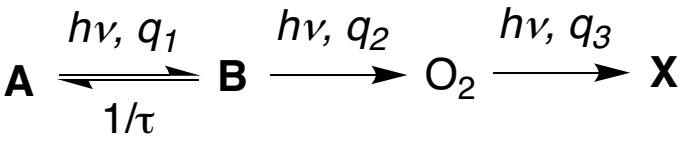

Lifetime τ / ns	Quantum Efficiency q_1	Quantum Efficiency q_2	Quantum Efficiency q_3
65	0,661	0,145	0,0028

[a] Note that there are multiple solutions giving identical fits and only one solution is shown here.

When interpreting the optimized parameters obtained via fitting of the kinetic model to experimental data it should be noted that there is no unique solution. For example, keeping q_1 and q_3 the same, τ = 6.5 µs and q_2 = 0.00145 would give the same result as the paramters shown in Table 10.3-1. This model therefore only provides a rough idea for the underlying lifetime and quantum efficiencies operative in the system. However, through examination of the initial rate/photon flux relationship (Figure 10.3-1), we can see that the lifetime of intermediate **B** must be below $\tau = 10^{-1}$ s to explain the experimentally observed square relationship between initial rate and photon flux. In turn, this provides us with lower bound for q_2, although the lifetime of **B** is probably significantly shorter than $\tau = 10^{-1}$ s (given its high energy, see DFT results), with q_2 thus being significantly higher than its lower bound. The lower bound for τ is $\tau \approx 10$ ns, which would correspond to $q_2 \approx 1$.

10.4 Comparison of Experimental Dual Irradiation Rates with Kinetic Model

To further assess the validity of the kinetic model, an approximate comparison between the excess initial rate observed in dual irradiation experiments and the prediction by the kinetic model was made.

For this comparison it is necessary to know the 455 – 630 nm photon flux used during dual irradiation experiments. Since chemical actinometry cannot be used in this wavelength region (see 6.3), the flux has to be approximated using power meter measurements.
For the Hg light source (320 – 400 nm), a power of 76 mW was measured in place of the liquid phase O_2 reactor (photon flux of 4.15E+17 s^{-1} in this position). Based on the mean photon wavelength (360 nm) and the measured flux, the theoretical power is 229 mW. Therefore, measurements using this power meter have to be corrected by a factor of 3.01 to reflect the power received by the reactor.
Using the same power meter, powers of 471 mW and 359 mW were measured for the QTH light source using 455 nm and 630 nm longpass filters, respectively (in place of the liquid phase O_2 reactor). The power in the wavelength range 455 – 630 nm is therefore 112 mW. Using the correction factor of 3.01, one obtains a corrected power of 337 mW. Based on a mean photon wavelength of 542.5 nm, the 455 – 630 nm photon flux is therefore roughly 9.23E+17 s^{-1}.

In dual irradiation experiments, an excess initial rate of ca. 0.001 µmol l^{-1} s^{-1} was observed when the 455 nm longpass filter was used. Based on a reaction volume of ca. 550 µl, this corresponds to ca. 3.3E+11 O_2 forming reactions per second. Given a 455 – 630 nm photon flux of ca. 9.23E+17 s^{-1}, this means that the probability of inducing an O_2 forming reaction is ca. 3.59E-07 per 455 – 630 nm photon.

To calculate the theoretical reaction probability we will assume the same absorbance for the second-photon absorbing intermediate as used in the kinetic model (3000 M^{-1} cm^{-1}). Based on this absorbance, an intermediate lifetime of 65 ns (see Table 10.3-1) and a 455 – 630 nm photon flux of 9.23E+17 s^{-1}, we can calculate that there is a probability of 6.93E-07 for the intermediate to absorb a photon in its lifetime. Multiplying this absorption probability by a quantum yield for the second absorption of 0.145 (see Table 10.3-1) gives us a predicted reaction probability of 1.01E-07 per 450 – 630 nm photon.

Table 10.4-1 Comparison of experimental and predicted reaction probabilities

Experimental reaction probability per 455 – 630 nm photon	Predicted reaction probability per 455 – 630 nm photon
3.59E-07	1.01E-07

Experimental and predicted reaction probabilities are in the same order of magnitude, which we consider to be a rather good agreement, given the simplicity of the kinetic model. Through this comparison it can also be seen that the rather low experimental reaction probability per 455 – 630 nm photon is likely due to a short life time of the absorbing intermediate, making second photon absorption less probable. Increasing the lifetime could therefore significantly increase both reaction rate and overall quantum yield.

11 Computational Section

11.1 Computational Methods

11.1.1 DFT Methods

All DFT calculations were performed using the PBE0 (PBE1PBE) hybrid functional, along with Grimme D3 dispersion with Becke-Johnson damping (GD3BJ). For all calculations, the SDD basis set and effective core potential was used for ruthenium, while all other atoms were described using the indicated basis set. Closed shell calculations (singlet) were performed as restricted (RHF), while open shell (doublet and triplet) calculations were performed as unrestricted (UHF) calculations. Calculations were performed using three different model chemistries:

1. Dimeric model of two ruthenium complexes interacting via non-covalent bonds. This model was used for [**A**], [**B**], [**C**], TS-[**CD**] and [**D**] [**F**] (dimer model).
2. Monomeric model, in which only the ruthenium complex on which O-O bond formation takes place (or [**F**]) is modeled. This model was used for [**A-Mono**], [**B-Mono**], [**C-Mono**], [**D**], [**E**] and [**F**].
3. In some cases, a simplified version of the monomeric model was used, in which the ligand *t*Bu and Et groups were replaced by methyl. Use of this model is indicated by “Me model”.

Use of the “-Up” designation indicates opposite (relative to the normal models) PNN ligand conformation. Geometry optimizations and frequency calculations (298 K, 1 atm) were performed in the gas phase using the cc-pVDZ basis set. Structures were confirmed to be minima or first-order saddle points by having either zero (minima) or one (first-order saddle points) imaginary frequencies. Reported gas phase Gibbs free energies are based on Gibbs free energies obtained using frequency calculations.
Single point energy calculations were performed using the cc-pVTZ basis set and SMD solvation (the solvent being water). Reported solution phase Gibbs free energies are based on singlet point energy calculations, corrected by using the thermal correction to Gibbs free energy obtained using frequency calculations.

Electronic excitations and theoretical UV/Vis spectra were calculated using TD-DFT, using the cc-pVDZ basis set and SMD solvation (in water). Typically, the 25 lowest energy transitions were computed. Theoretical UV/Vis spectra were constructed using the calculated transition wavelengths and oscillator strengths. Furthermore, transitions were broadened using Gaussian curves with a half-width at half-height of 0.333 eV. To visualize excitations, natural transition orbitals were computed, and the resulting hole-particle pairs with the highest contribution (typically > 1.7) are shown.

Scans were performed as relaxed potential energy surface scans using the cc-pVDZ basis set in the gas phase. For Scan-[**DE**]T_0, single point energy calculations using cc-pVTZ and SMD solvation (water) were performed for all optimized geometries along the scan. Since frequency calculations are not meaningful for scan geometries, only relative energies instead of Gibbs free energies (either gas phase or solution phase) are reported.

NMR calculations were performed using the cc-pVTZ basis set and SMD solvation (water). Reported chemical shifts are relative to tetramethylsilane (^{1}H) or H_3PO_4 (^{31}P).

All calculations were performed using Gaussian 16, Revision A.03.[10] Structures were prepared and visualized using Avogadro.[11] Furthermore, surfaces for closed shell molecules were also visualized using Avogadro. Surfaces for open shell molecules were visualized using Gabedit.[12] Simplified structures were visualized using PyMOL.[13] Visualizations were rendered using POV Ray.[14] In all visualizations, ruthenium is shown in turquoise, phosphorous in orange, oxygen in red, nitrogen in blue, carbon in grey and hydrogen in white. For surfaces: orbitals are shown in yellow/magenta and spin densities are shown in green.

11.1.2 CASSCF Methods

All CASSCF calculations were performed as state averaged (SA)-CASSCF calculations, using the five lowest energy states weighed equally. An active space consisting of 13 electrons in 11 orbitals, CAS(13,11), was used (see Figure 11.3-2). The active space consists of two Ru-OH σ and σ*, four pyridine π and π*, two Ru-CO π and π* (combining with oxygen lone pair orbitals), two OH and O lone pair and the singly occupied O lone pair orbitals.
The ANO-RCC-VDZ all-electron basis set was used for all atoms (which includes relativistic effects). To improve computational performance, the resolution of identity Cholesky decomposition (RICD) method was used.[15,16] For computational tractability, the simplified monomeric model using methyl groups instead of *t*Bu and ethyl on the ligand (Me model) was used for all CASSCF calculations.

For [**B-Mono**] and [**C-Mono**], geometries obtained using DFT geometry optimization were used. The geometries of conical intersections ([**BC**] D_2/D_1 MECI and [**BC**] D_1/D_0 MECI) were optimized using CASSCF with analytical gradients in the gas phase.[17] Gas phase energies are reported relative to the energy of [**B-Mono**]D_0 root 1.

Solvation was taken into account by performing single point calculations for all intermediates with the PCM conductor version and water as the solvent. For [**B-Mono**], equilibration solvation based on root 1 was used for root 1, while non-equilibrium solvation based on root 3 was used for all other roots (modeling vertical excitation from root 1 to root 3). For [**BC**] D_2/D_1 MECI, equilibrium solvation based on root 3 was used for all roots. For [**BC**] D_1/D_0 MECI, equilibrium solvation based on root 2 was used for all roots. For [**C-Mono**], equilibrium solvation based on root 1 was used. Solution phase energies are reported relative to the energy of [**B-Mono**]D_0 root 1.

All calculations were performed using OpenMolcas version 19.11.[18,19] Visualizations were performed using Pegamoid. In all visualizations, ruthenium is shown in turquoise, phosphorous in orange, oxygen in red, nitrogen in blue, carbon in grey and hydrogen in white. For surfaces: orbitals are shown in yellow/magenta, spin densities are shown in green and transition difference densities are shown in red/blue.

11.2 DFT Results

11.2.1 Relative Energies of [A] and [B] Isomers, Oxo Dimer, [F]S_0 → [A-Mono]S_0

Table 11.2-1 Relative energies of [A]S_0 and [A-Mono]S_0

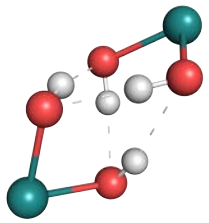

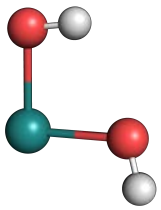

	[**A**]S_0	[**A-Mono**]S_0
ΔG°(SMD) / kcal/mol	8.05	**0.00**
ΔG°(Gas Phase) / kcal/mol	**0.00**	2.5

In Table 11.2-1 it can be seen that while dimeric [**A**]S_0 is predicted to be more stable in the gas phase compared to monomeric [**A-Mono**]S_0, it is predicted to be less stable in solution. However, the lower stability in solution might be attributed to the challenging description of hydrogen bonding energies using DFT.[20]

Table 11.2-2 Relative energies of [A] isomers

	[**A**]S_0	[**A-RR**]S_0	[**A-RS-1**]S_0	[**A-RS-2**]S_0	[**A**]T_0
ΔG°(SMD) / kcal/mol	**0.00**	0.49	1.05	1.88	21.91

Different isomers of [**A**]S_0 were computed, varying in their configuration ([**A-Mono**]S_0 is chiral, therefore either a homo- or heterochiral dimer can be formed) and conformation of the ligand. Among the computed isomers, [**A**]S_0 was found to be the most stable, although the energy differences are small. [**A**]T_0 was found to be relatively low in energy, being only ca. 22 kcal/mol less stable than [**A**]S_0.

Table 11.2-3 Relative energies of [B]T_0 isomers

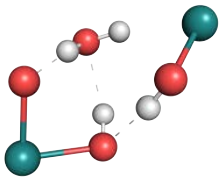

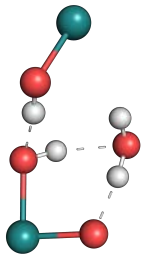

	[**B**]T_0	[**B-Trans**]T_0
ΔG°(SMD) / kcal/mol	8.56	**0.00**

Table 11.2-4 Relative energies of [B-Mono]D_0 isomers

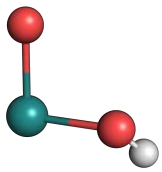

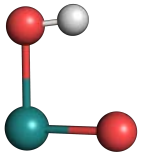

	[**B-Mono**]D_0	[**B-Mono-Up**]D_0	[**B-Mono-Trans**]D_0	[**B-Mono-Trans-Up**]D_0
ΔG°(SMD) / kcal/mol	6.86	8.68	1.53	**0.00**

When comparing [**B**] and [**B-Trans**] in both the dimeric and monomeric model, [**B-Trans**] was found to be slightly more stable.

Table 11.2-5 Relative energy of [B-Alt]T_0

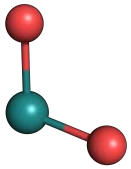

	[**B-Alt**]T_0
ΔG°(SMD) / kcal/mol	7.96 ([**B-Alt**]T_0 + H_2O + [**F**]S_0 relative to [**B**]T_0) 16.5 ([**B-Alt**]T_0 + H_2O + [**F**]S_0 relative to [**B-Trans**]T_0)
ΔG°(Gas Phase) / kcal/mol	39.1 ([**B-Alt**]T_0 + H_2O + [**F**]S_0 relative to [**B-Trans**]T_0)

[**B-Alt**]T_0 would be an alternative reaction intermediate, obtained via two consecutive proton-coupled electron transfers from [**A**] (forming one equivalent of [**F**]S_0 in the process). It is, however, less stable than either [**B**]T_0 or [**B-Trans**]T_0.

Table 11.2-6 Relative energy of Oxo Dimer

	[**Oxo Dimer**]S_0
ΔG°(SMD) / kcal/mol	12.2 (relative to [**A-Mono**]S_0) 4.2 (relative to [**A**]S_0)

Table 11.2-7 Reaction Energy for [F]S_0 + H_2O → [A-Mono]S_0 + H_2

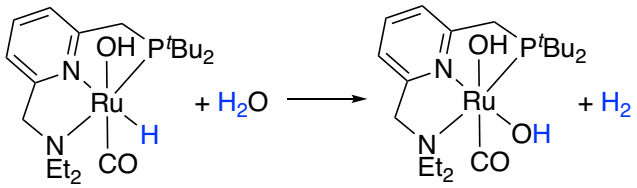

[**F**]S_0 [**A-Mono**]S_0

	[**F**]S_0 + H_2O → [**A-Mono**]S_0 + H_2
ΔG°(SMD) / kcal/mol	13.18

Considering the energy change for [**F**]S_0 + H_2O → [**A-Mono**]S_0 + H_2 (13.18 kcal/mol) and [**A**]S_0 → 2 [**F**]S_0 + O_2 (82.73 kcal/mol), as well as the relative stability of [**A**]S_0 vs. [**A-Mono**]S_0 (8.05 kcal/mol), one arrives at an energy change of 117.11 kcal/mol. This value is identical with the energy change of 2 H_2O → O_2 + 2 H_2 when using our DFT methodology, which is in good agreement with the thermodynamical value (4-electron 1.23 V, 113.46 kcal/mol).

11.2.2 TD-DFT Computed UV-Vis Spectra

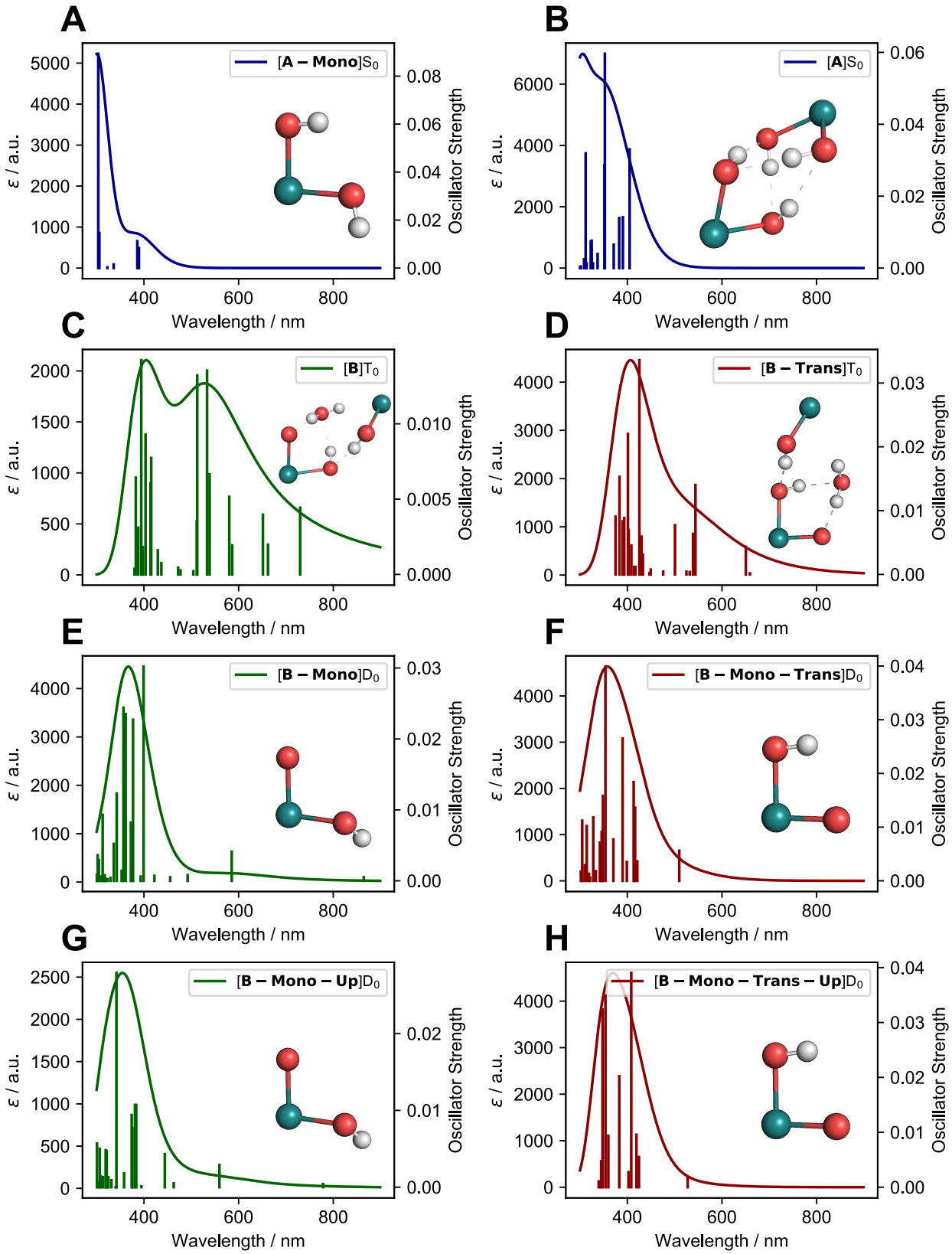

Figure 11.2-1 UV-Vis spectra computed for $[A]S_0$ and $[B]T_0$ along with isomers/monomers
Spectra for [**A**] are shown in blue, [**B**] in green and [**B-Trans**] in red. Vertical lines indicate individual transitions (oscillator strength for these transitions are shown on the right). Smooth curves show the UV-Vis spectrum, which was computed using the sum of Gaussian curves with a half-width half-maximum of 0.333 eV. Inlets show the simplified, corresponding molecular structures. "-Up" indicates opposite PNN ligand conformation. Up to 25 transitions between 300 nm and 900 nm are shown.

11.2.3 Natural Transition Orbitals for [A]S_0

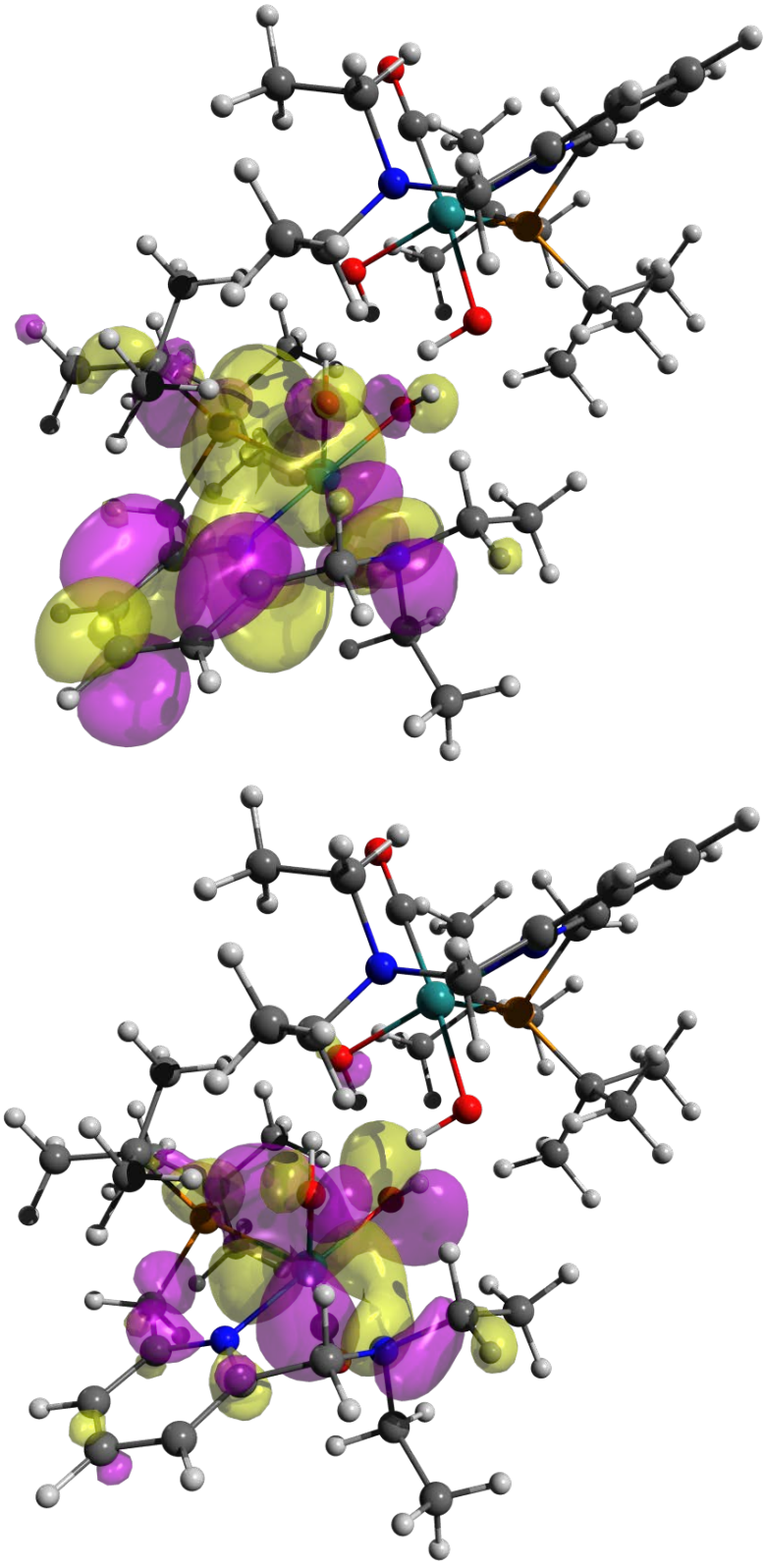

Figure 11.2-2 Transition 1 (405 nm, f = 0.033) for [A]S_0, particle (top) and hole (bottom), isovalue = 0.02

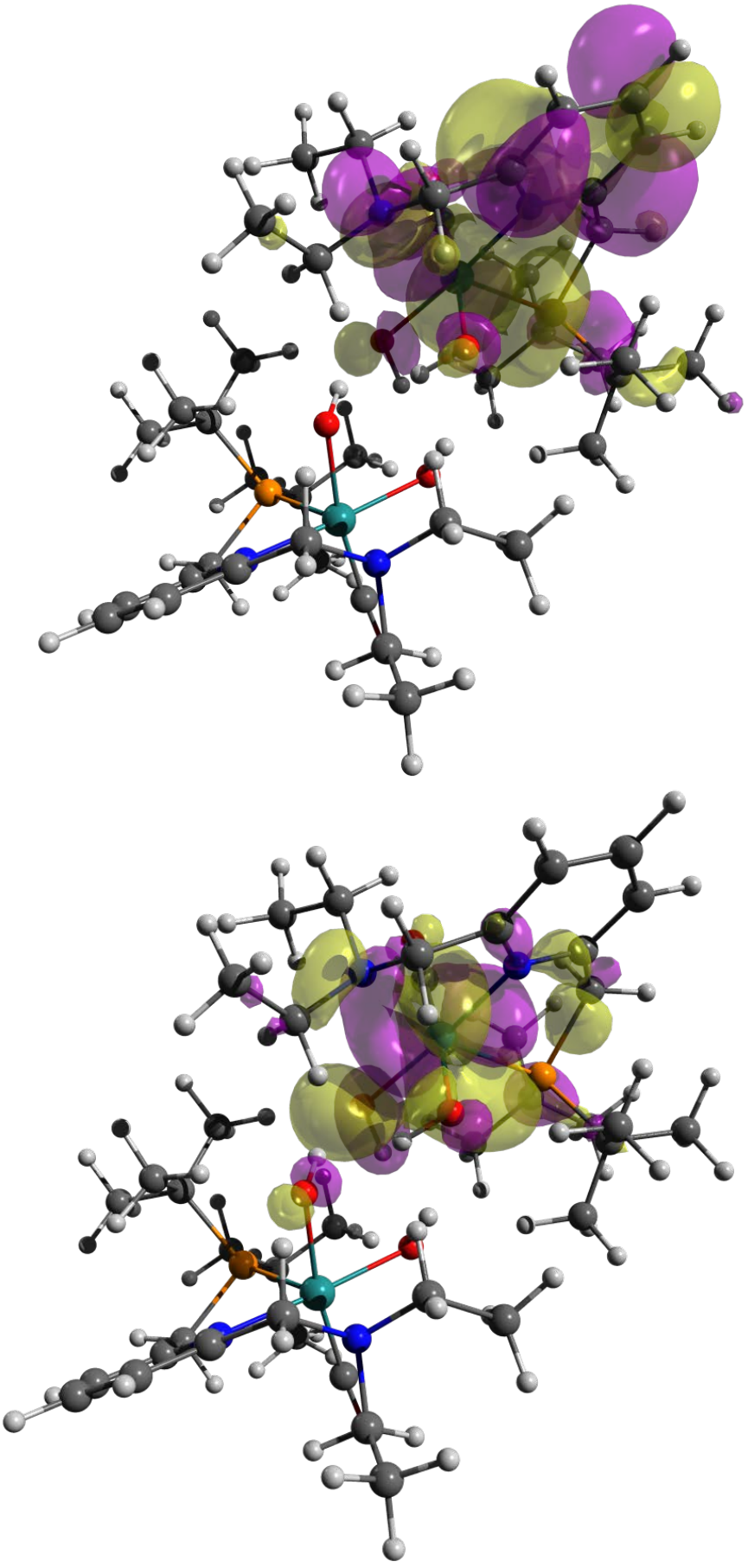

Figure 11.2-3 Transition 2 (391 nm, f = 0.0141) for [A]$S_{0,}$ particle (top) and hole (bottom), isovalue = 0.02

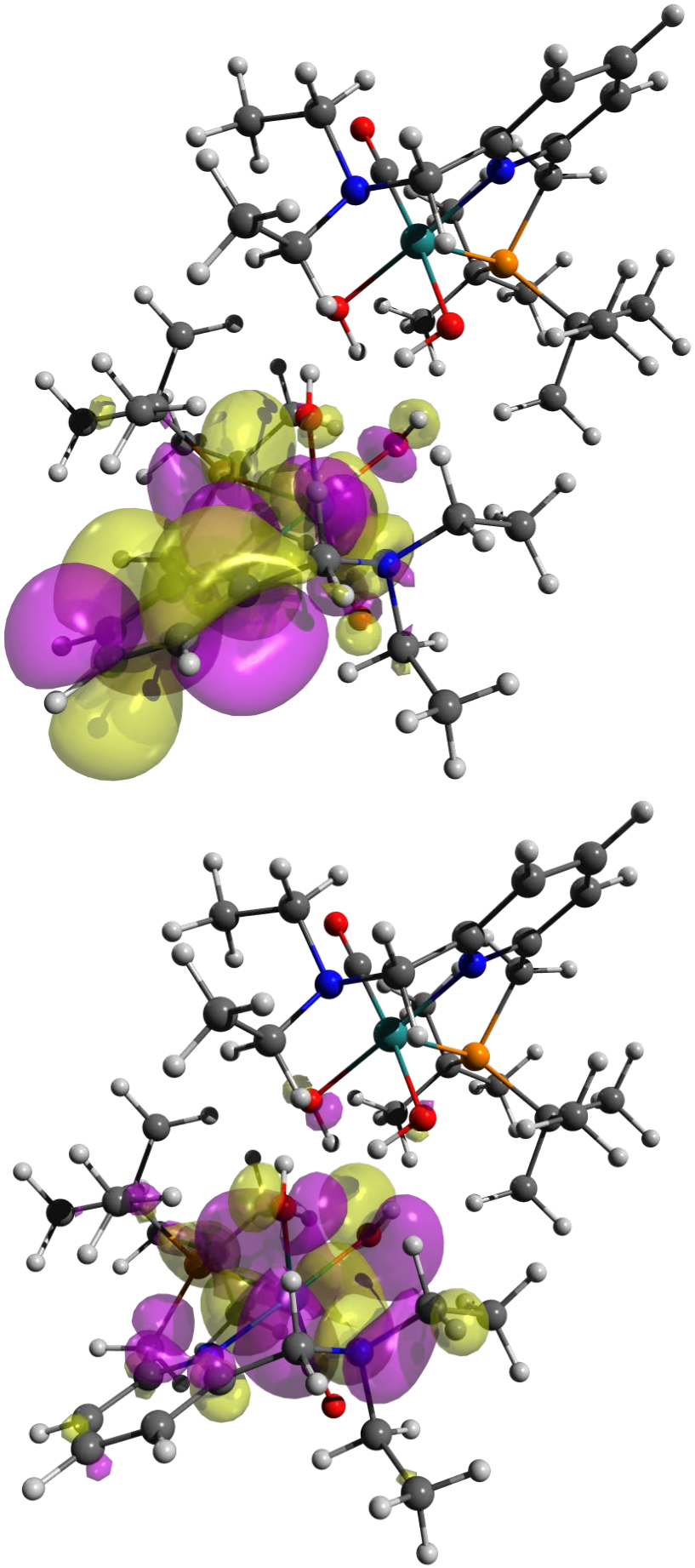

Figure 11.2-4 Transition 3 (383 nm, f = 0.014) for [A]$S_{0,}$ particle (top) and hole (bottom), isovalue = 0.02

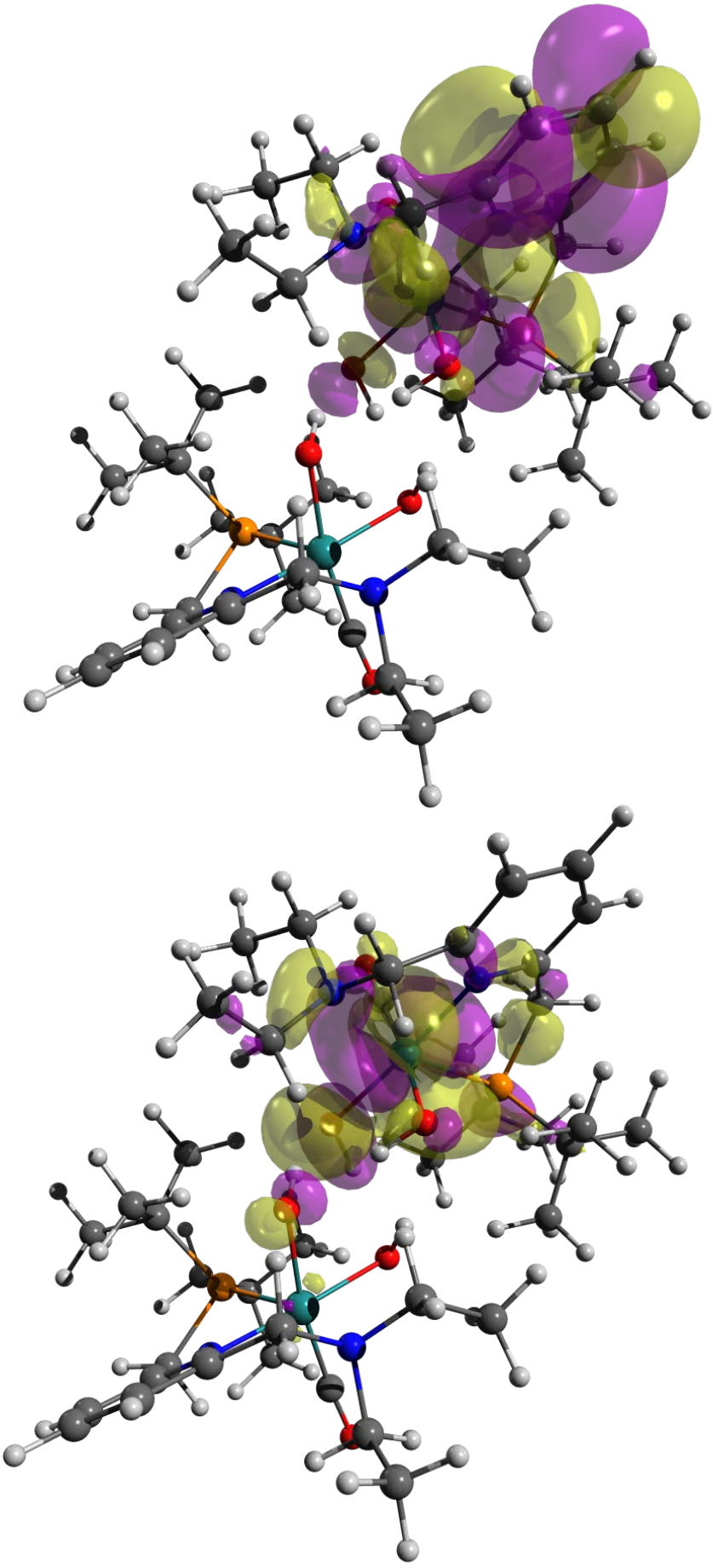

Figure 11.2-5 Transition 4 (371 nm, f = 0.0065) for [A]$S_{0,}$ particle (top) and hole (bottom), isovalue = 0.02

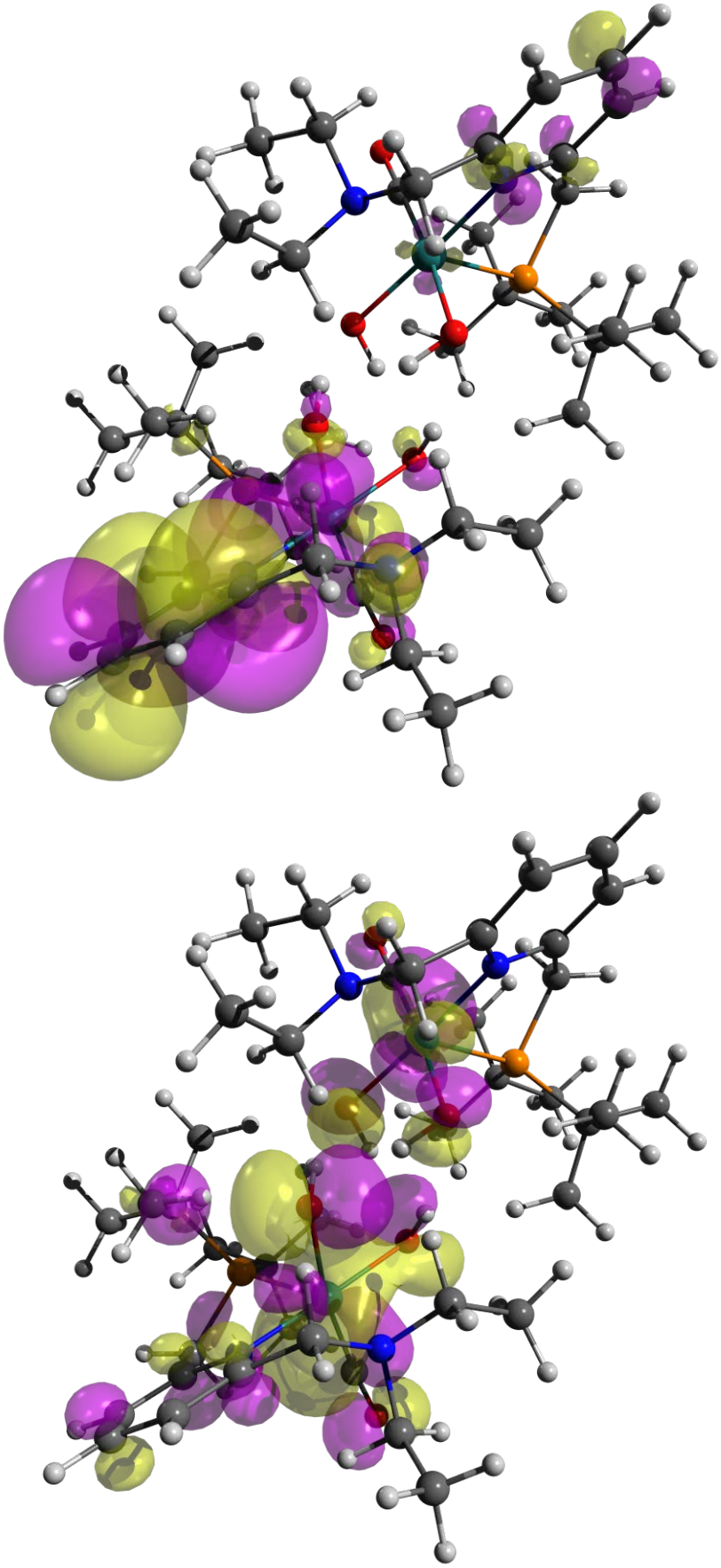

Figure 11.2-6 Transition 5 (353 nm, f = 0.0596) for [A]$S_{0,}$ particle (top) and hole (bottom), isovalue = 0.02

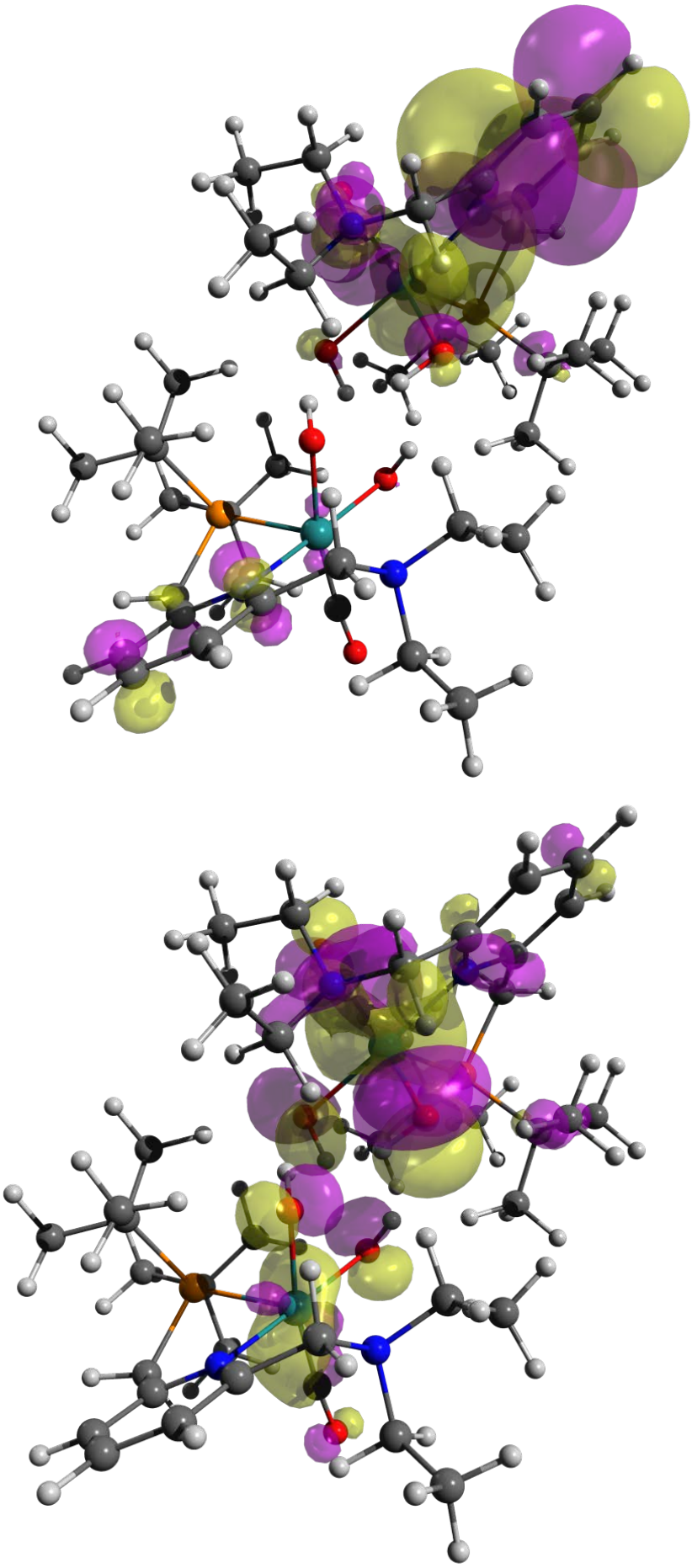

Figure 11.2-7 Transition 6 (352 nm, f = 0.0287) for [A]$S_{0,}$ particle (top) and hole (bottom), isovalue = 0.02

11.2.4 Natural Transition Orbitals for $[B]T_0$

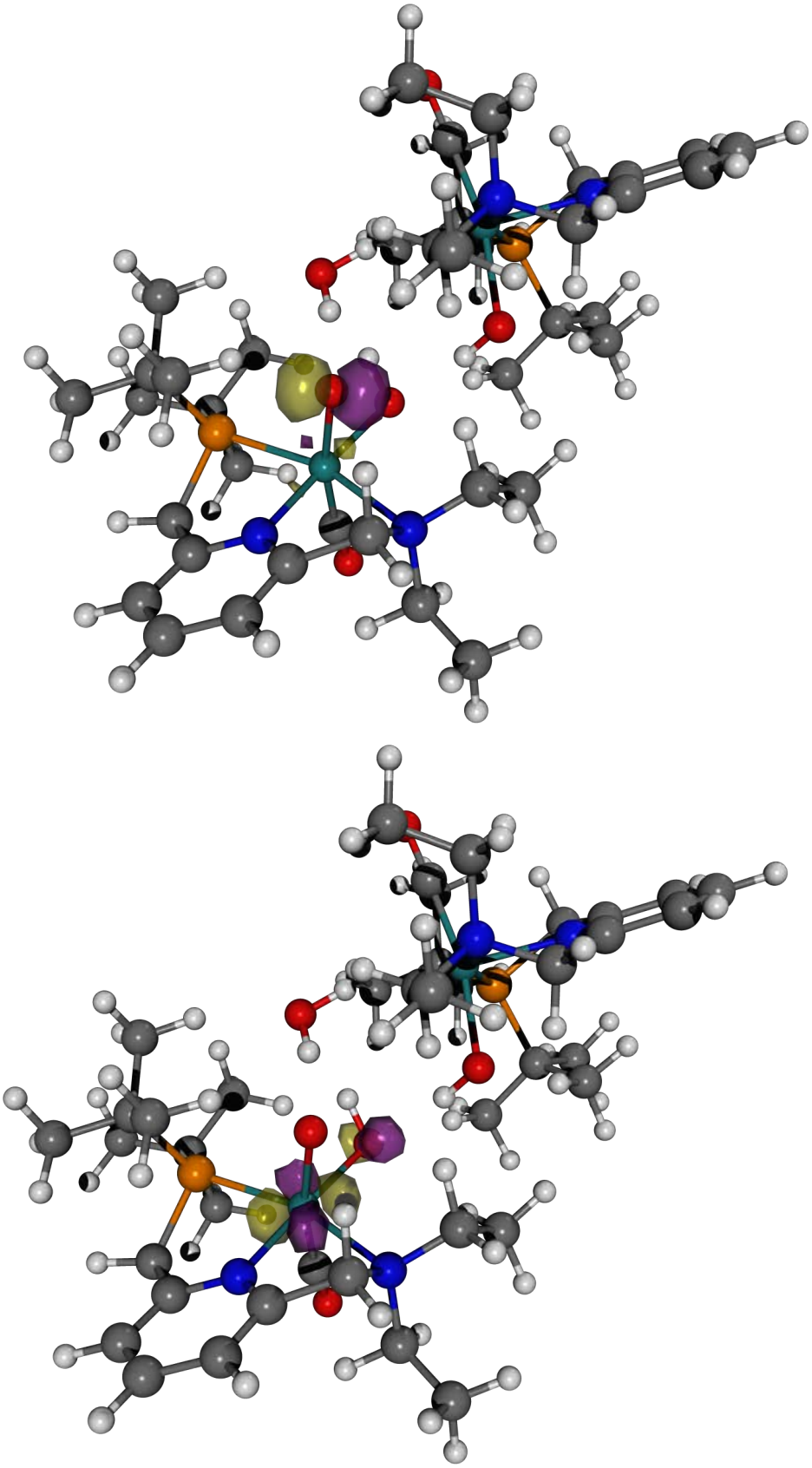

Figure 11.2-8 Transition 2 (933 nm, f = 0.0029) for $[B]T_0$, particle (top) and hole (bottom), isovalue = 0.1

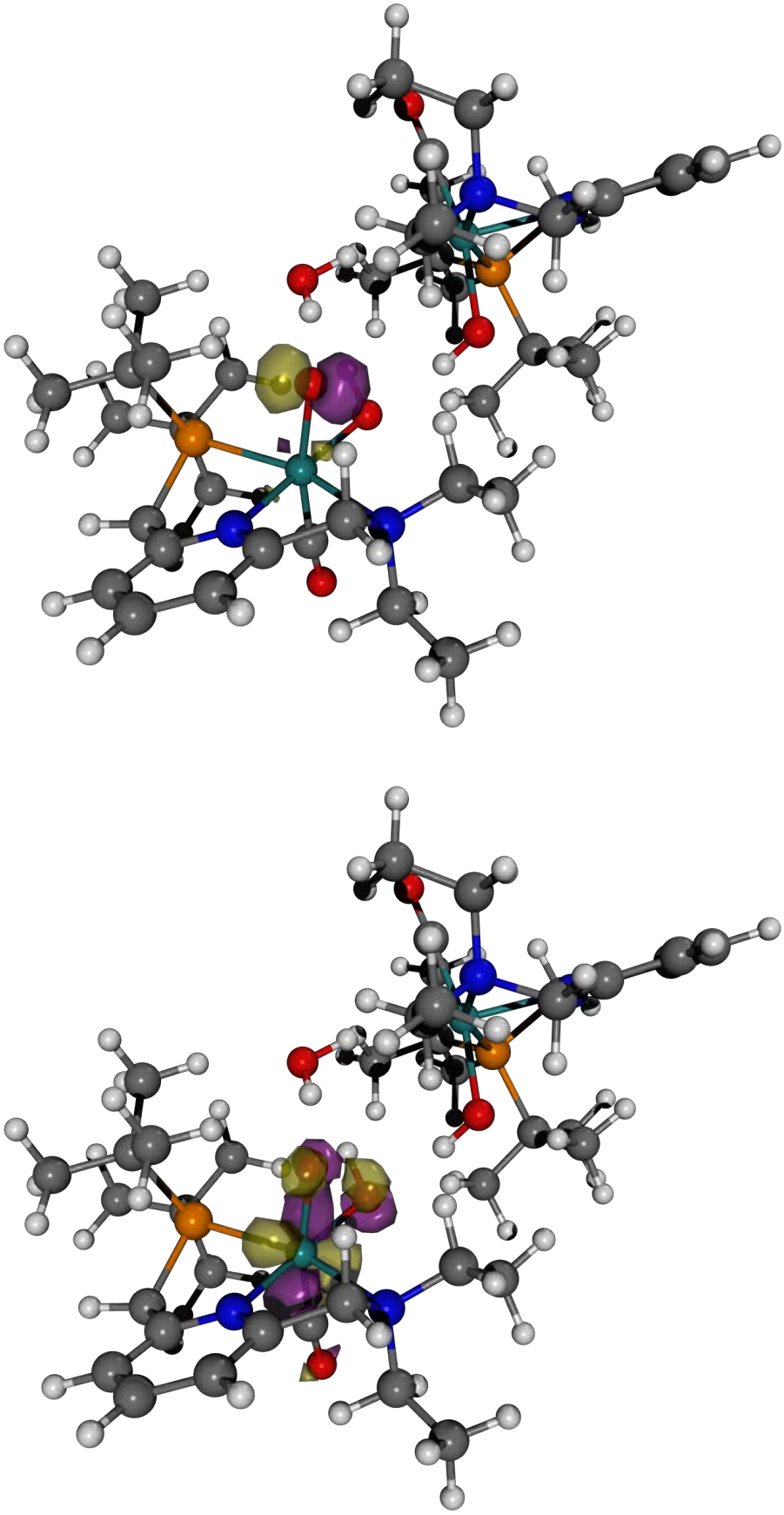

Figure 11.2-9 Transition 8 (539 nm, f = 0.0066) for [B]T_0, particle (top) and hole (bottom), isovalue = 0.1

11.2.5 Natural Transition Orbitals for [B-Mono]D_0 (Me Model)

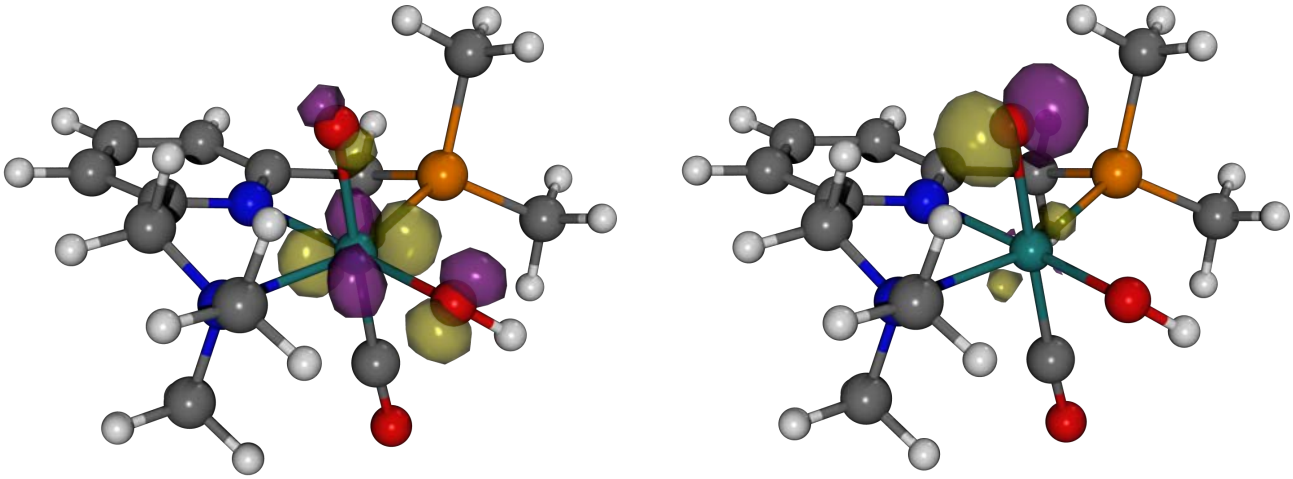

Figure 11.2-10 Transition 2 (804 nm, f = 0.0004) for [B-Mono]D_0 (Me model), hole (left) and particle (right), isovalue = 0.1

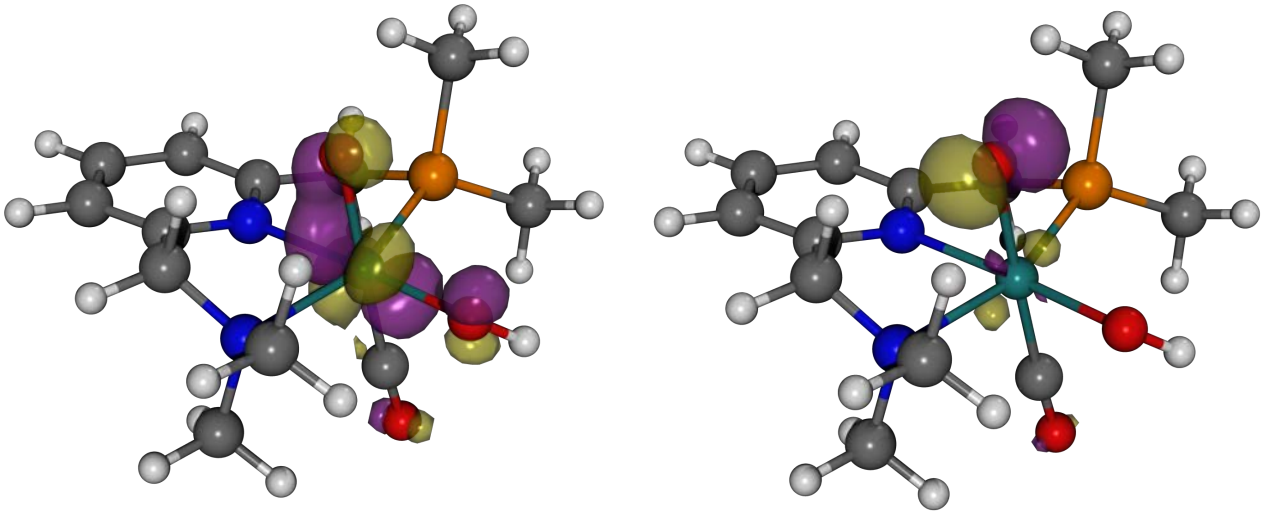

Figure 11.2-11 Transition 4 (495 nm, f = 0.0027) for [B-Mono]D_0 (Me model), hole (left) and particle (right), isovalue = 0.1

11.2.6 Spin Density Plots

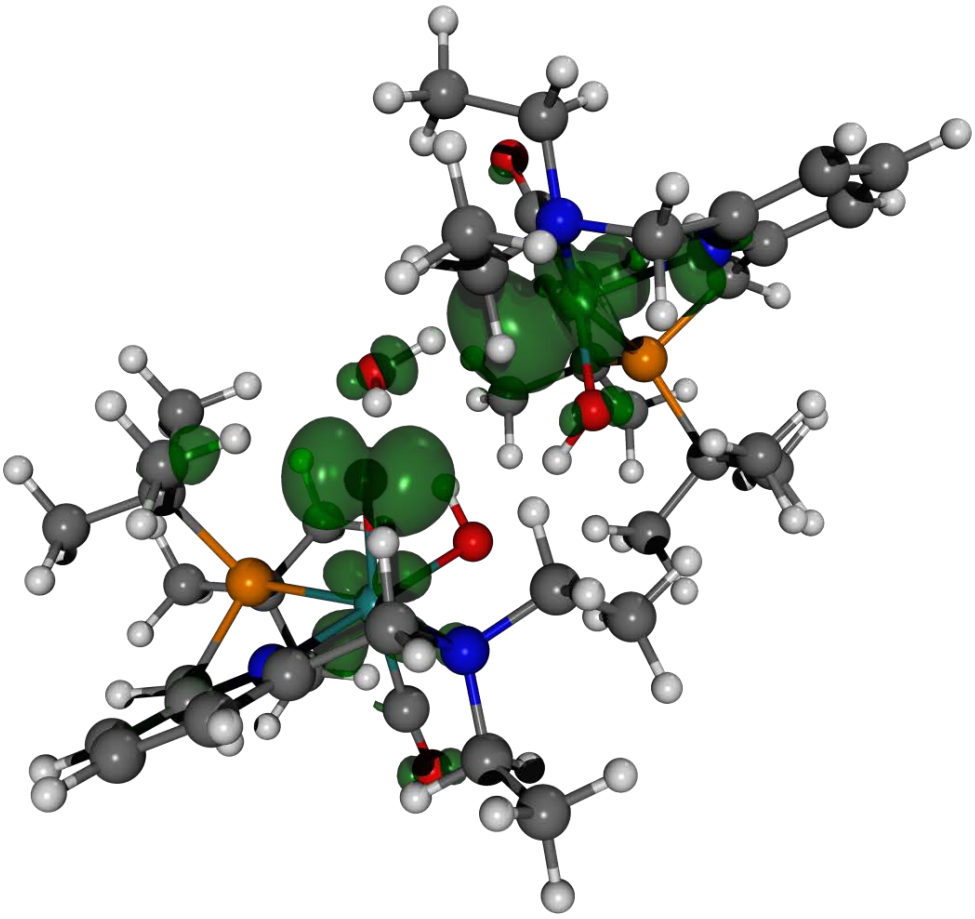

Figure 11.2-12 Spin density (isovalue = 0.004) for [B]T_0

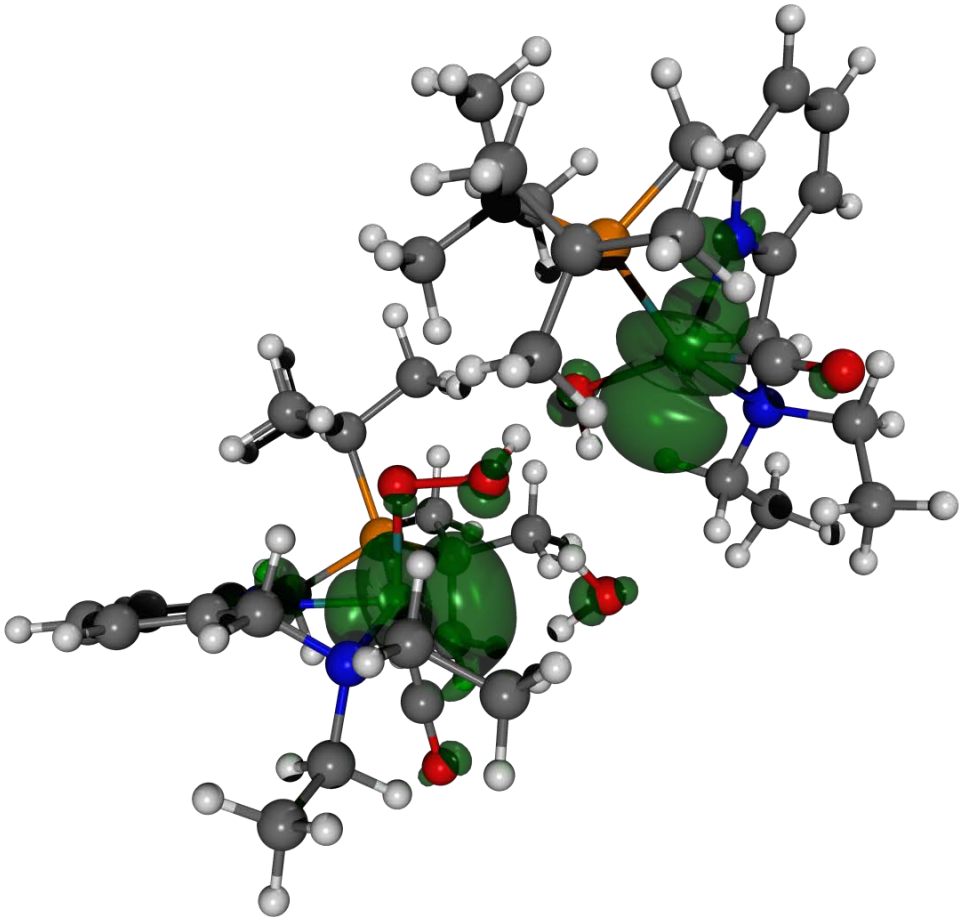

Figure 11.2-13 Spin density (isovalue = 0.004) for [C]T_0

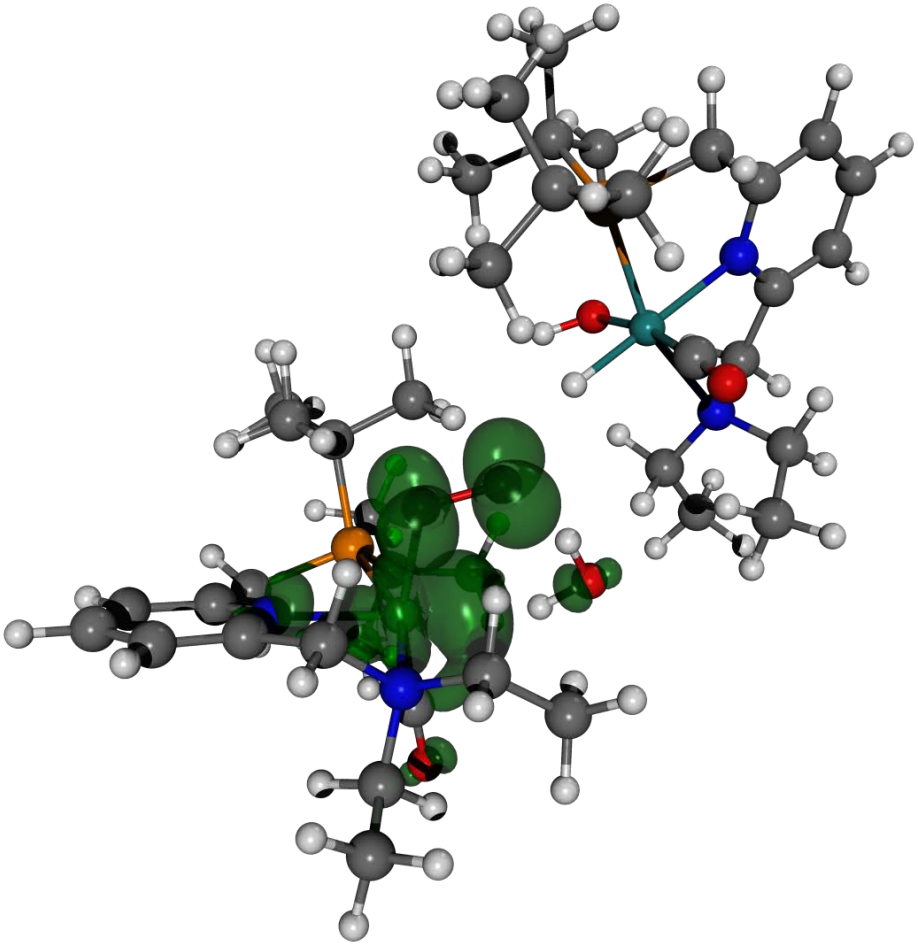

Figure 11.2-14 Spin density (isovalue = 0.004) for $[D]T_0\,[F]S_0$ (Dimer Model)

11.2.7 Scan-[DE]T_0

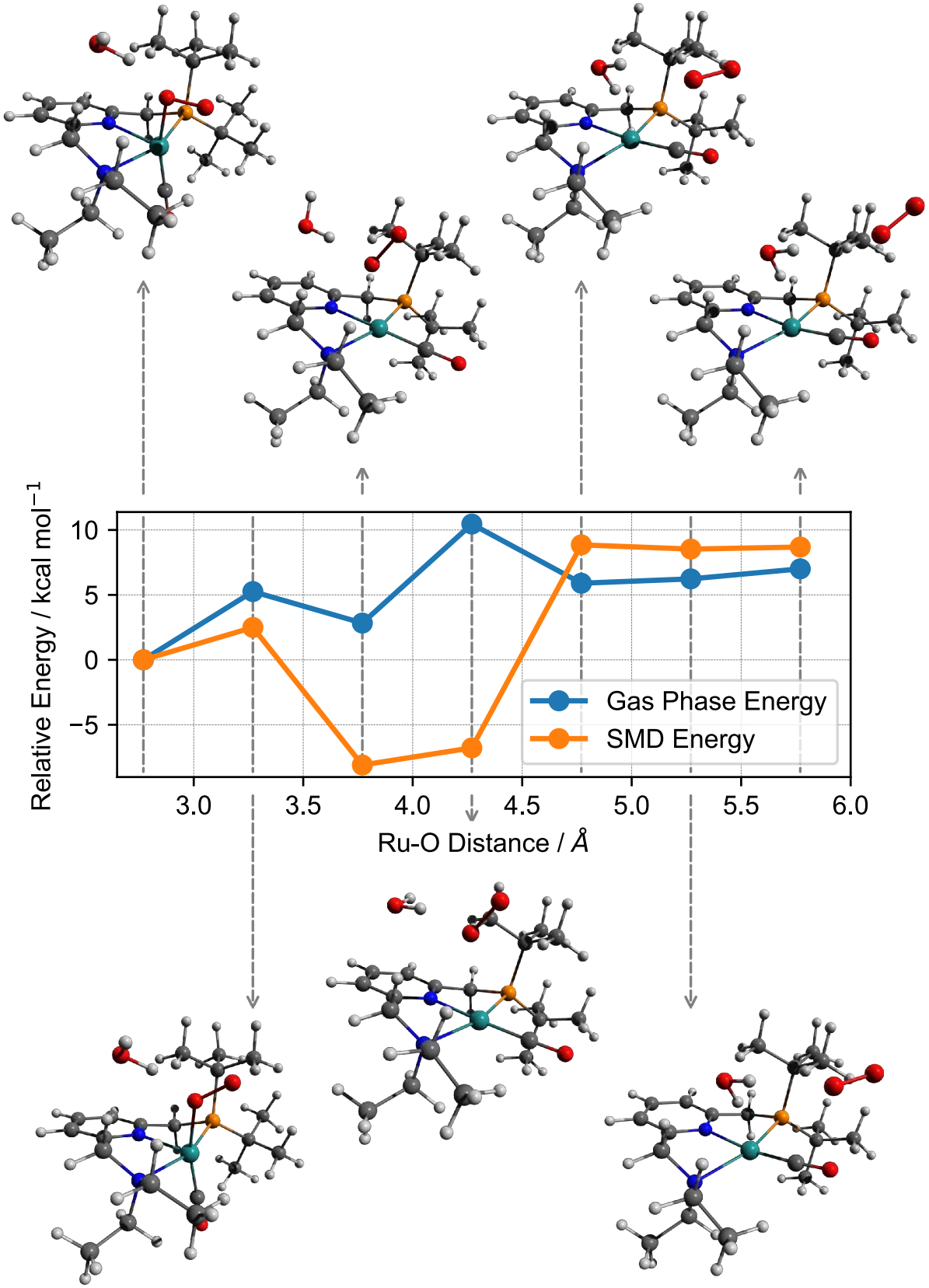

Figure 11.2-15 Energy profile for relaxed PES Scan-[DE]T_0 (gas phase and SMD energies)
Ru-O distance refers to the distance between the ruthenium center and the most distant oxygen atom of the superoxo ligand. Structures corresponding to the different points along the scan are shown outside of the plot. The decrease in energy for the third scan geometry can be attributed to movement of the CO ligand from an axial to an equatorial position.

11.2.8 O-O Bond Formation Scans

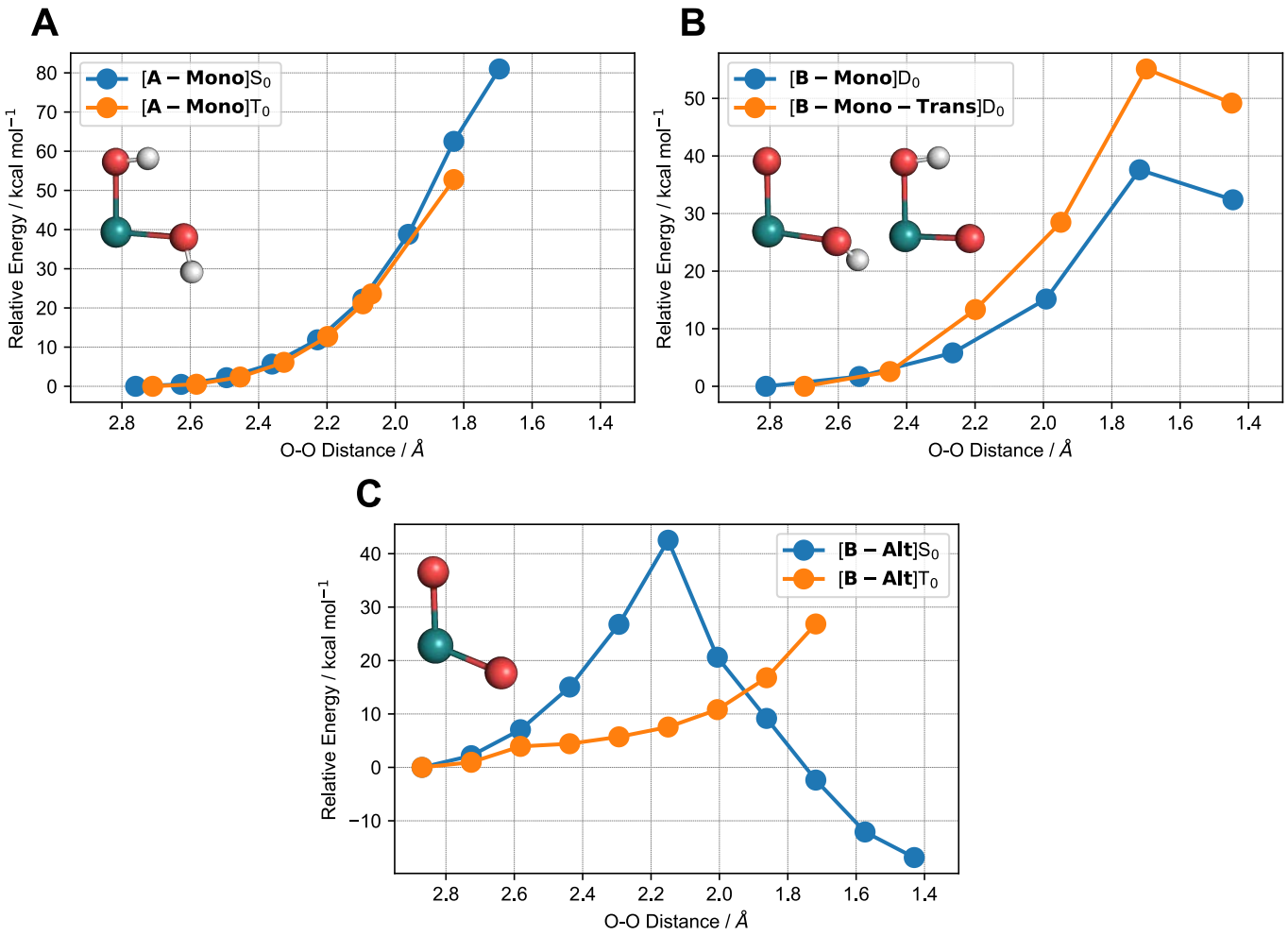

Figure 11.2-16 Energy profiles for relaxed PES scans of O-O bond formation
A Scan of O-O distance for [**A-Mono**] in singlet and triplet state. Inlet shows [**A-Mono**]S_0
B Scan of O-O distance for [**B-Mono**]D_0 (Me model) as well as [**B-Mono-Trans**]D_0 (Me model). Note that for these scans, the same methyl substituted models were used that were also used for CASSCF calculations. Inlets show [**B-Mono**]D_0 (left) and [**B-Mono-Trans**]D_0 (right).
C Scan of O-O distance for [**B-Alt**] in singlet and triplet state ([**B-Alt**] would be the hypothetical result of a second PCET preceding O-O bond formation). Inlet shows [**B-Alt**]T_0.
Energy of starting point for each scan is set to 0 kcal/mol.

Relaxed potential energy surface scans were performed to investigate potential O-O bond formation for six different reaction intermediates. These intermediates span the various possibilities of intramolecular O-O bond formation (fully protonated, singly deprotonated and doubly deprotonated). For [**A**] and [**B-Alt**], calculations were performed in the singlet or triplet ground state, while calculations for [**B-Mono**] and [**B-Mono-Trans**] were performed in the duplet ground state. These scans therefore provide an estimate for the lower bound of O-O bond formation for each intermediate.

For [**A-Mono**] in both the singlet and triplet state, no O-O bond formation could be observed (see Figure 11.2-16A). For [**A-Mono**]T_0, constrained geometry optimizations for O-O distances smaller than 1.83 Å were unsuccessful. These results are consistent with previous findings on the lack of O-O bond formation starting from [**A**].[21,22]
When comparing [**B-Mono**]D_0 and [**B-Mono-Trans**]D_0, it can be seen that the barrier for O-O bond formation is significantly lower for [**B-Mono**]D_0 (by more than 15 kcal/mol, see Figure 11.2-16B).
For [**B-Alt**], potential O-O bond formation was studied in both the singlet and triplet state. For [**B-Alt**]S_0, O-O bond formation can be observed, although with a barrier of over 40 kcal/mol (in comparison, the barrier for O-O bond formation in [**B-Mono**]D_0 is 37.6 kcal/mol). Furthermore, it is

questionable whether [**B-Alt**]S_0 is even a feasible intermediate. This is based on the observation that [**B**]S_0 was found to be unstable during geometry optimizations, reverting back to [**A**]S_0. Such instability can be attributed to the fact that in the S_0 state, there is no charge separation between the two ruthenium centers (as is the case in the T_0 state, see Figure 11.2-12). Therefore, proton transfer from one complex to another is less favorable, explaining why [**B**]S_0 reverts back to [**A**]S_0. The same reasoning can be applied to [**B-Alt**]S_0, which would likely not be formed.
Hence, [**B-Alt**]T_0 was also investigated, but no O-O bond formation was found in this case (constrained geometry optimizations failed for short O-O bond lengths).

11.2.9 Theoretical NMR Data for [F]S_0 Isomers

Table 11.2-8 Relative energies and theoretical NMR data for [F]S_0 isomers

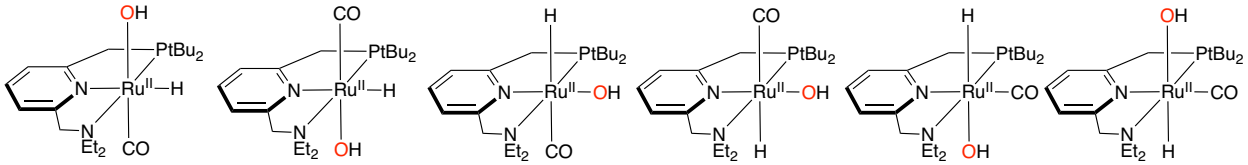

	[**F**]S_0	[**F-Up**]S_0	[**F-Cis**]S_0	[**F-Cis-Up**]S_0	[**F-Trans**]S_0	[**F-Trans-Up**]S_0
ΔG°(SMD) / kcal/mol	4.62	3.17	13.27	13.93	2.46	**0.00**
∂(^{1}H, hydride) / ppm	-9.28	-7.98	0.13	0.08	-10.02	-10.22
∂(^{31}P) / ppm	125.28	108.47	112.55	106.05	110.59	109.14
Experimental	/		∂(^{1}H) = -5.5 ppm ∂(^{31}P) = 104.3 ppm		∂(^{1}H) = -18.9 ppm ∂(^{31}P) = 104.2 ppm	

It can be seen that [**F-Trans-Up**]S_0 is the most stable isomer of [**F**], with the cis isomers being significantly less stable. While theoretical hydride chemical shifts are somewhat overestimated, the relative experimental difference between cis and trans isomers of 13.4 ppm is well reproduced (10.2 ppm). [**F**]S_0 is only slightly less stable than the trans isomers.

11.3 CASSCF Results

11.3.1 Comparison of DFT and CASSCF Energies and Absorption Wavelengths

Table 11.3-1 Comparison of DFT and CASSCF reaction energies for [B] → [C] and absorption wavelengths for [B-Mono]D_0

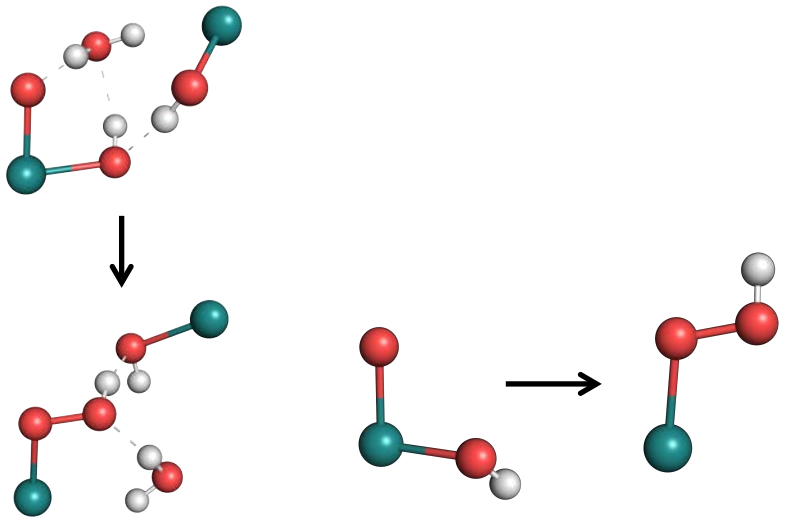

Method	Parameter	[**B**]T_0 → [**C**]T_0	[**B-Mono**]D_0 → [**C-Mono**]D_0	[**B-Mono**]D_0 → [**C-Mono**]D_0 (Me model)
DFT	ΔG° / kcal/mol[a]	35.0 (35.9)	33.5	31.9
	Transition Wavelength / nm[b]	539 (Trans. 8)	/	495 (Trans. 4)
CASSCF	ΔE / kcal/mol[c]	/	/	29.8 (36.3)
	Transition Wavelength / nm[d]	/	/	482

[a] Gas phase ΔG° (SMD ΔG° in parentheses). [b] Transition corresponding to second lowest energy transition of CASSCF model of [**B-Mono**]D_0, calculated using SMD solvation. [c] Gas phase ΔE (PCM ΔE in parentheses). [d] Second lowest energy transition of [**B-Mono**]D_0, calculated in gas phase.

Table 11.3-1 assesses the agreement between different model chemistries as well as between DFT and CASSCF for O-O bond formation from [**B**] to [**C**] as well excitation of [**B**].

For DFT, it can be seen that there is good agreement for reaction Gibbs free energies between the different model chemistries, with all of them being within 3 kcal/mol. This validates the use of either [**B-Mono**]D_0 or [**B-Mono**]D_0 (Me model) to describe O-O bond formation in [**B**]T_0. Also, relative energies of [**B-Mono**]D_0 to [**C-Mono**]D_0 (Me model) calculated using CASSCF reproduces the DFT results well.

Furthermore, excitation of [**B**] was compared between the different model chemistries/methods. In all cases, the lowest energy transition (< 0.4 eV) is an excitation of an electron from the fully occupied to the singly occupied oxo ligand lone pair. Due to its low excitation energy, this transition is likely not photochemically active.
Given the selected active space, CASSCF predicts the second lowest transition to be an excitation from a Ru d_{xz}/OH lone pair orbital to the singly occupied oxygen lone pair (see Figure 11.3-4), with a transition wavelength of 482 nm.
Corresponding transitions can be found in the TD-DFT results for [**B**]T_0 (transition 8, see Figure 11.2-9) and [**B-Mono**]D_0 (Me model, transition 4, see Figure 11.2-11), with similar transition wavelengths (see Table 11.3-1). It should be noted that the corresponding transition wavelength for [**B**]T_0 is red-shifted by ca. 45 nm. TD-DFT also predicts other, lower energy transitions: in case of [**B-Mono**]D_0 (Me model), the second lowest energy transition involves a Ru-d_{xy}/OH lone pair orbital

(see Figure 11.2-10), while the third lowest energy transition involves an oxo p_z orbital. For [**B**]T_0, in addition to these, transitions involving the second ruthenium complex can be found. The reason that these lower energy transitions predicted using TD-DFT for [**B-Mono**]D_0 are not found using CASSCF is due to the selection of the active space, which does not include orbitals which would be necessary to describe them. This limitation has to be accepted, as inclusion of more electrons and orbitals in the active space would make calculations computationally infeasible. However, as can be seen below, it was found that the second lowest energy transition in CASSCF does indeed lead to O-O bond formation.

Overall, good agreement between DFT and CASSCF results for reaction energies and excitation of [**B**] was found, justifying the applied CASSCF methodology.

11.3.2 Energy Profile including PCM Solvation

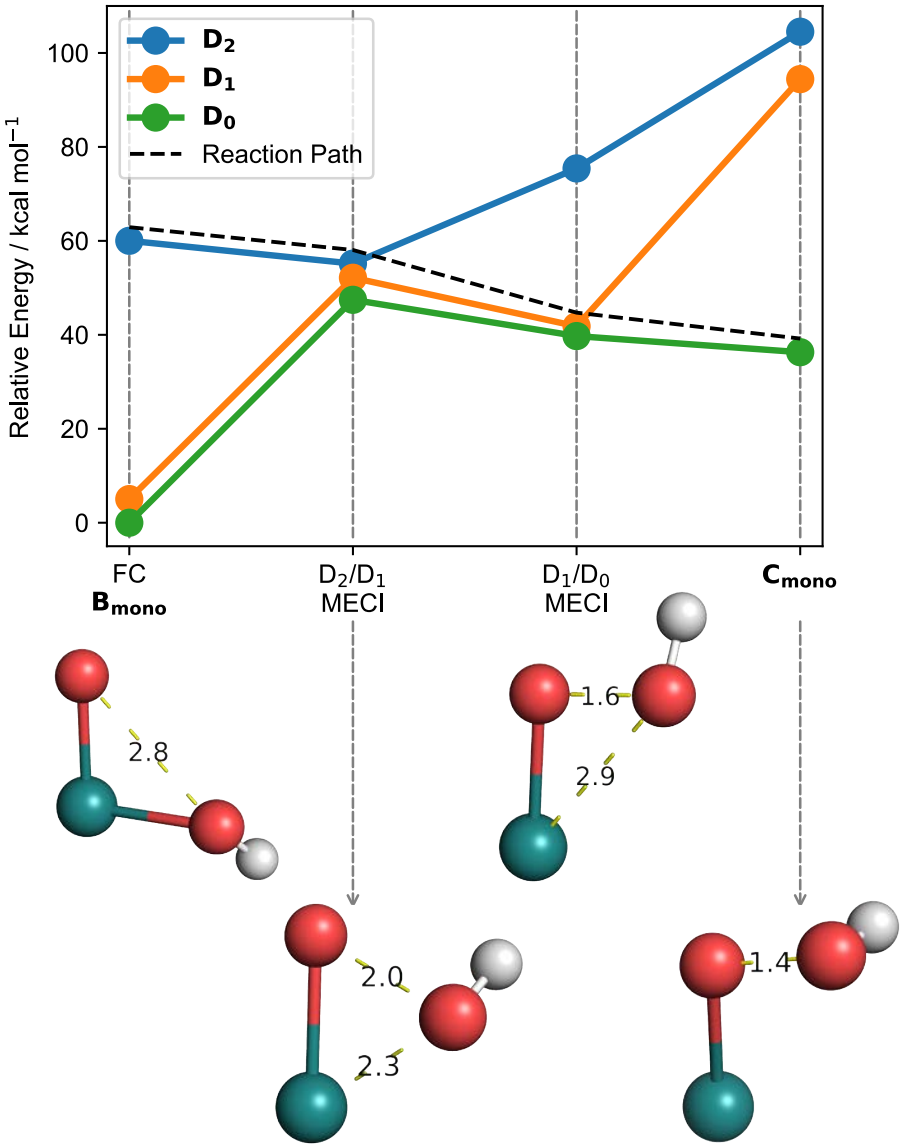

Figure 11.3-1 CASSCF energy profile including PCM solvation
Corresponding structures are shown below the plot, with bond lengths shown in Ångström. Note that degeneracy for conical intersections is slightly lost, since geometries were optimized in the gas phase.

11.3.3 Active Space Orbitals

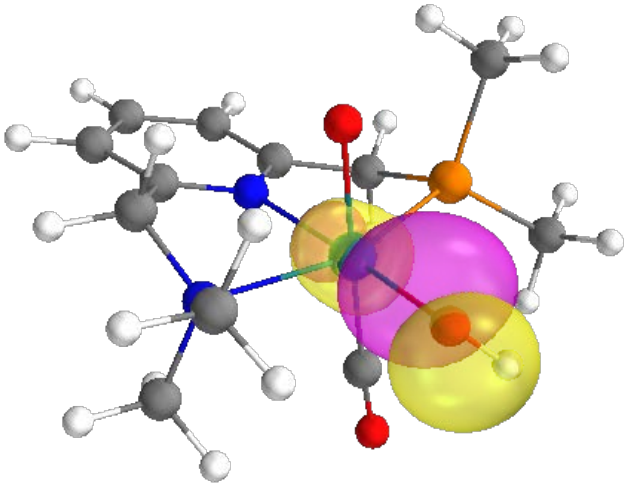

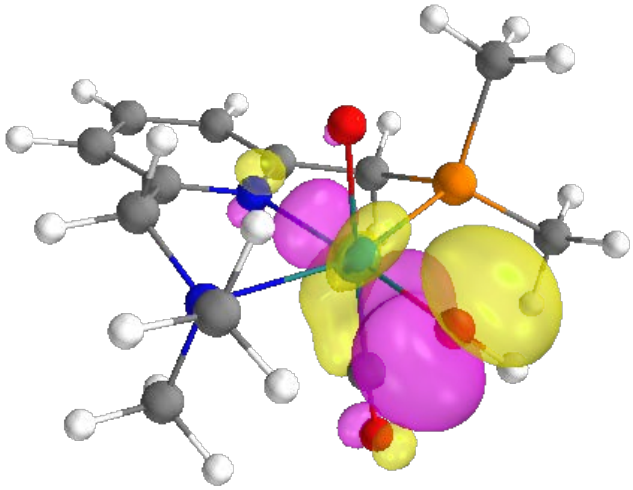

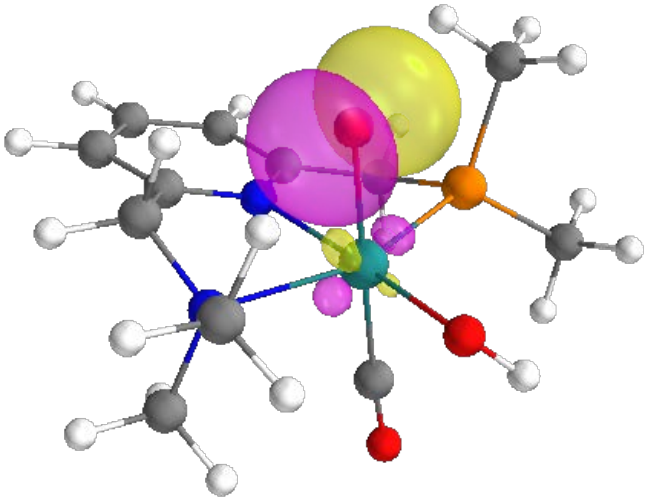

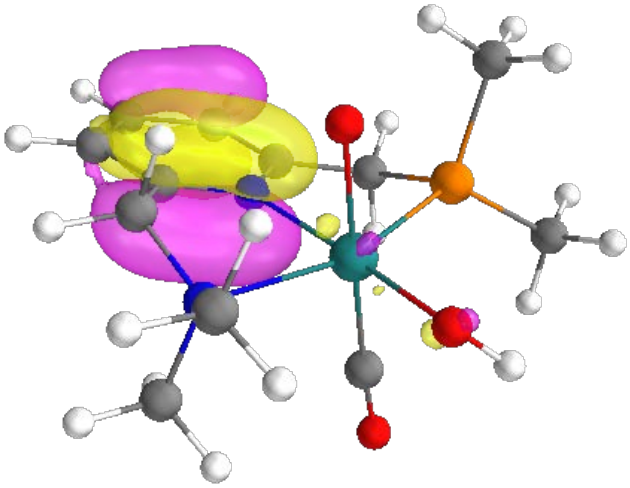

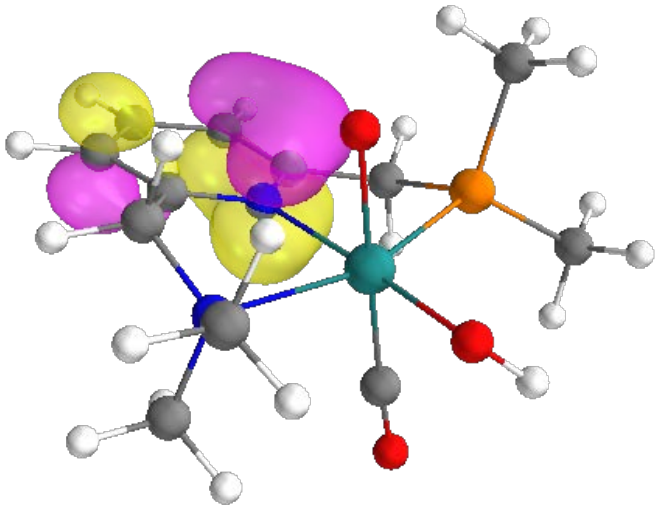

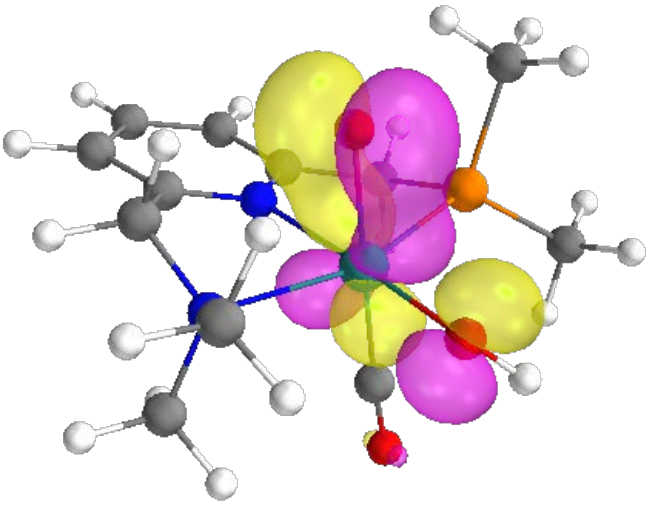

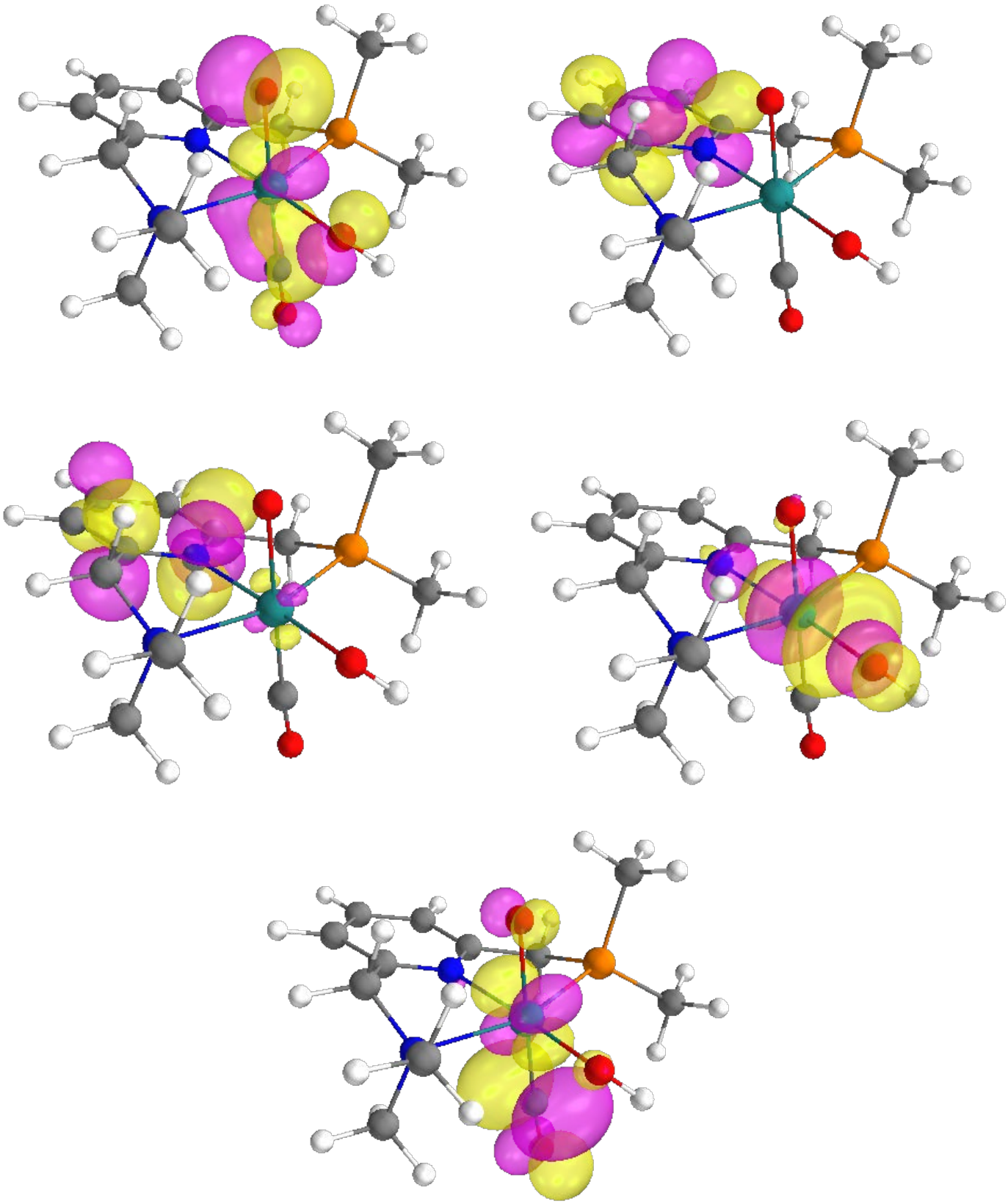

Figure 11.3-2 Active space orbitals of [B-Mono]D_0 used for CASSCF(13,11) calculations (isovalue = 0.05)
(average orbitals from SA-CASSCF(13,11) calculation for five lowest energy states are shown)

11.3.4 Surfaces for [B-Mono]D_n

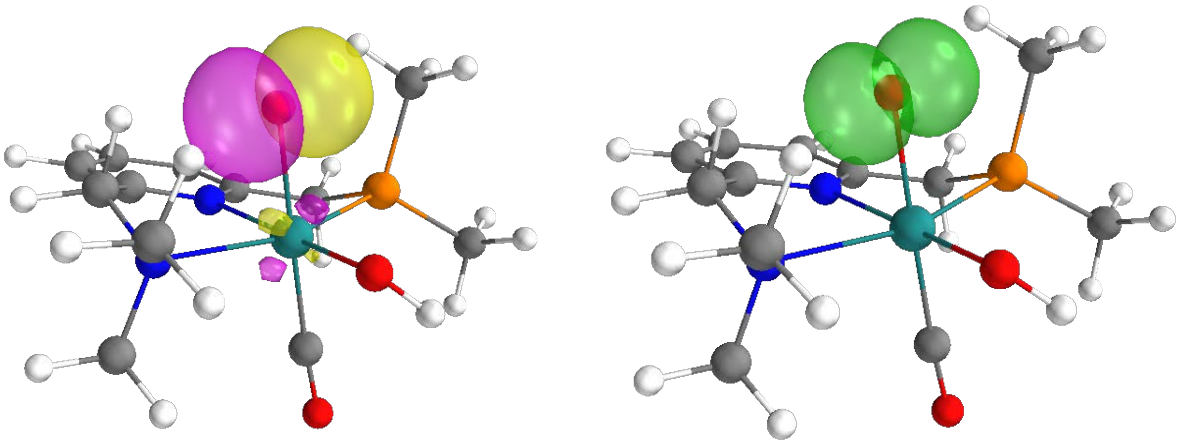

Figure 11.3-3 Singly occupied MO (left, isovalue = 0.05) and spin density (right, isovalue = 0.006) for [B-Mono]D_0

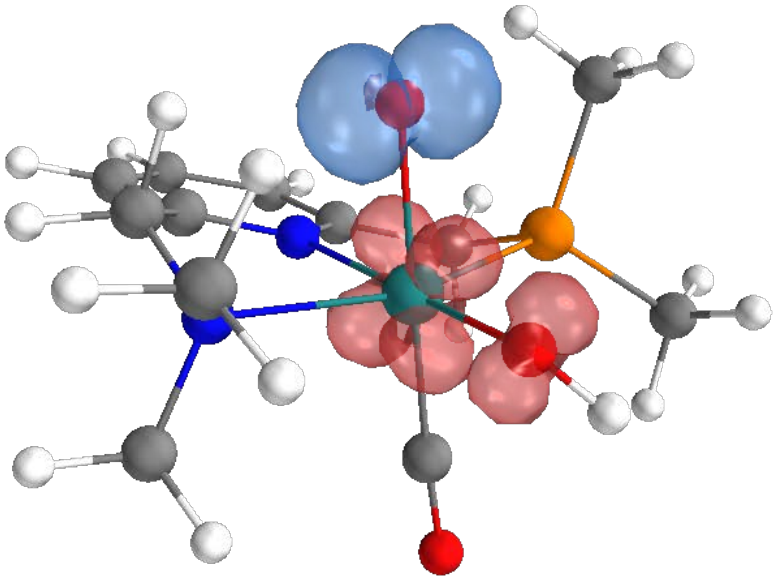

Figure 11.3-4 Unrelaxed transition difference density for [B-Mono]D_0 → [B-Mono]D_2
(detachment density in red, attachment density in blue, isovalue = 0.0005)

11.3.5 Difference Orbitals for Conical Intersections

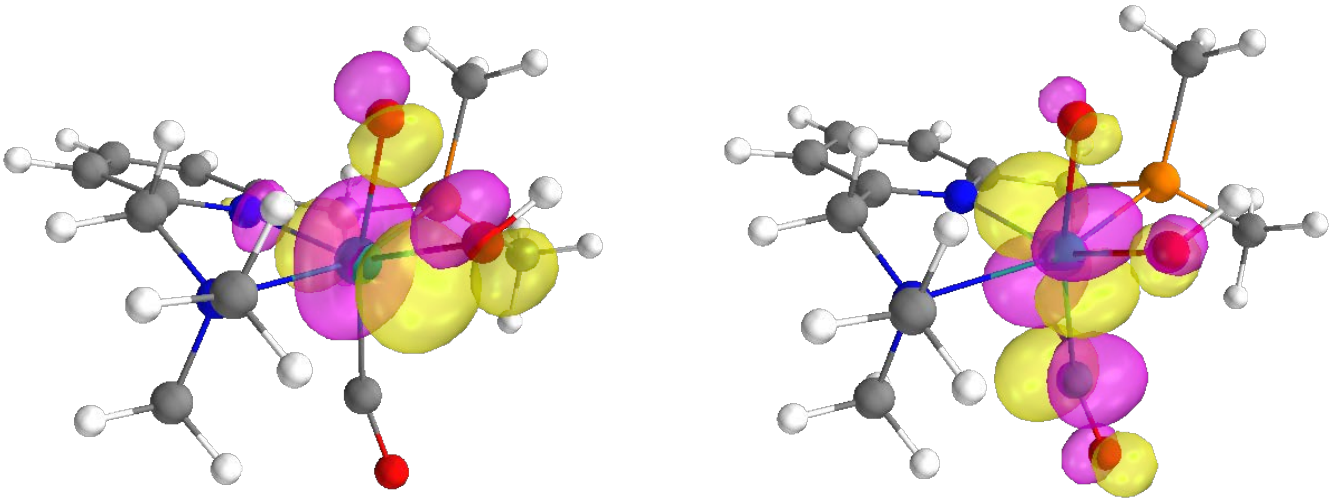

Figure 11.3-5 Difference orbitals for [BC] D_2/D_1 MECI with largest population changes (isovalue = 0.05)
(population change left: -0.8269, population change right: 0.9811)

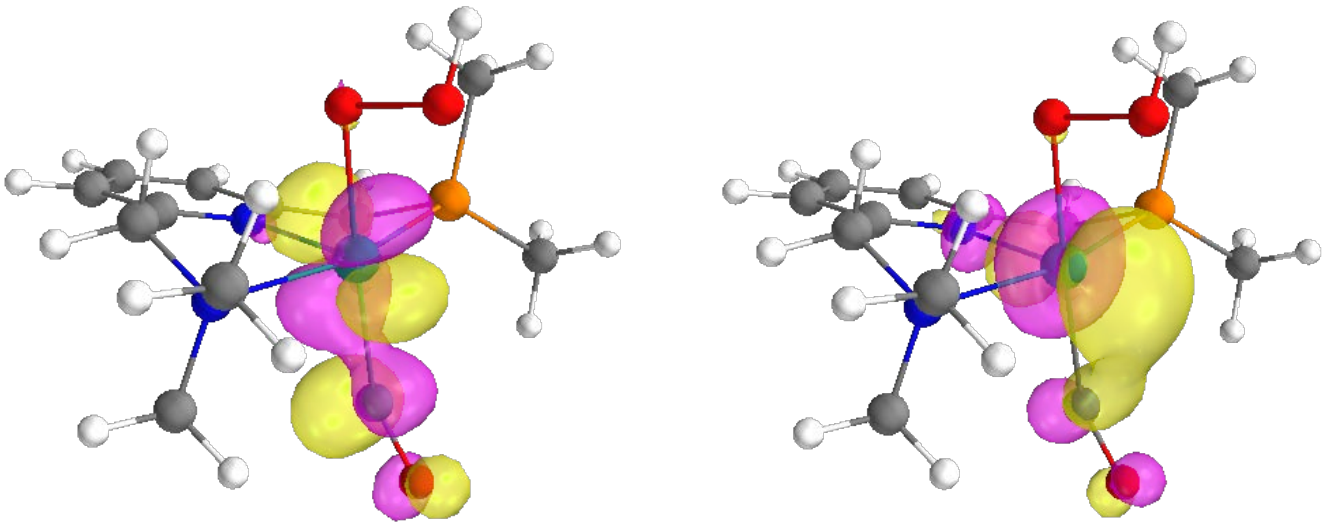

Figure 11.3-6 Difference orbitals for [BC] D_1/D_0 MECI with largest population changes (isovalue = 0.05)
(population change left: -0.8193, population change right: 0.7764)

11.3.6 Surfaces for [C-Mono]D_0

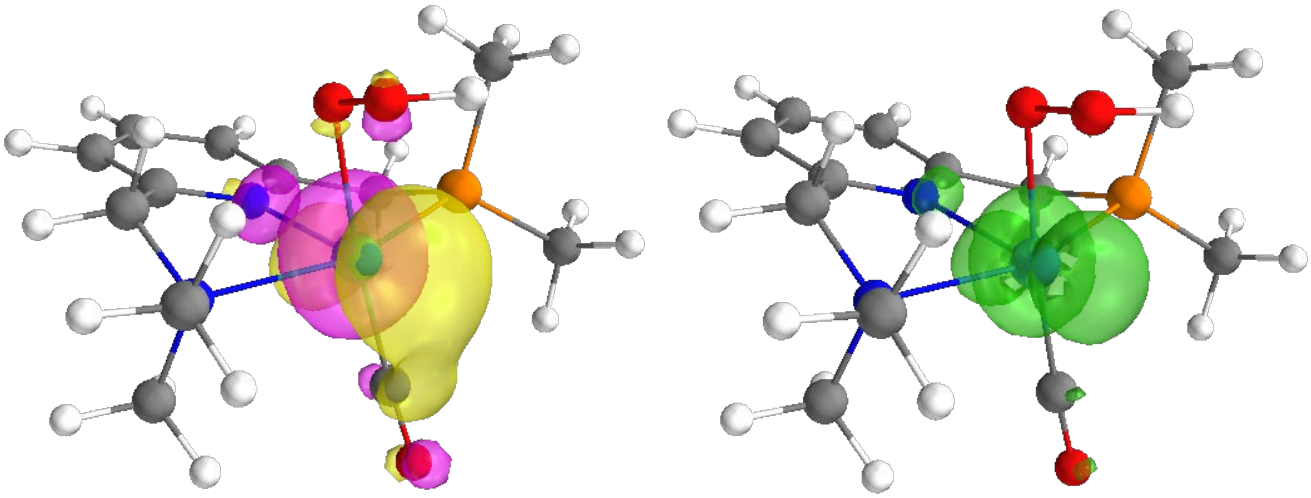

Figure 11.3-7 Singly occupied MO (left, isovalue = 0.05) and spin density (right, isovalue = 0.006) for [C-Mono]D_0

11.4 Integration of Computational and Experimental Results

11.4.1 Dual Irradiation Experiments

The liquid phase O_2 dual irradiation experiments can be seen as a way to probe the absorption characteristics of the second-photon absorbing intermediate. We developed a model convert to theoretical UV/Vis spectra into predicted dual irradiation behavior. This allows for the comparison of experimental dual irradiation data with predicted behavior of various computed intermediates.

Conversion of theoretical UV/Vis spectra to predicted dual irradiation behavior takes place in the following steps:

1. The QTH light source spectrum is described as an ideal blackbody (see Figure 6.1-2) using Planck's law with a blackbody temperature of 3400 K. The spectral power distribution is converted to a spectral photon distribution through division of the power distribution by respective photon energies.
2. For a given longpass filter wavelength (e.g. 630 nm) the corresponding intervals of the theoretical UV/Vis spectrum and spectral photon distribution are selected. Interval end is determined by the cut-off wavelength of the water filter (1000 nm for these calculations), resulting e.g. in [630 nm, 1000 nm] intervals.
3. To calculate the excess reaction rate corresponding to this longpass filter wavelength, the overlap of spectral photon distribution and theoretical UV/Vis spectrum is calculated by multiplying the corresponding intervals and then taking the sum of the resulting vector.
4. This procedure was repeated for each desired longpass filter wavelength. To obtain smooth curves, calculations were performed in 1 nm steps.
5. Resulting curves were scaled vertically through multiplication with a scaling factor to give the best possible fit to experimental data (since it is not trivial to perform this calculation to obtain accurate absolute reaction rates).

In the following, dual irradiation plots with experimental data (black dots) and thus calculated predicted behavior for different potential intermediate are shown.

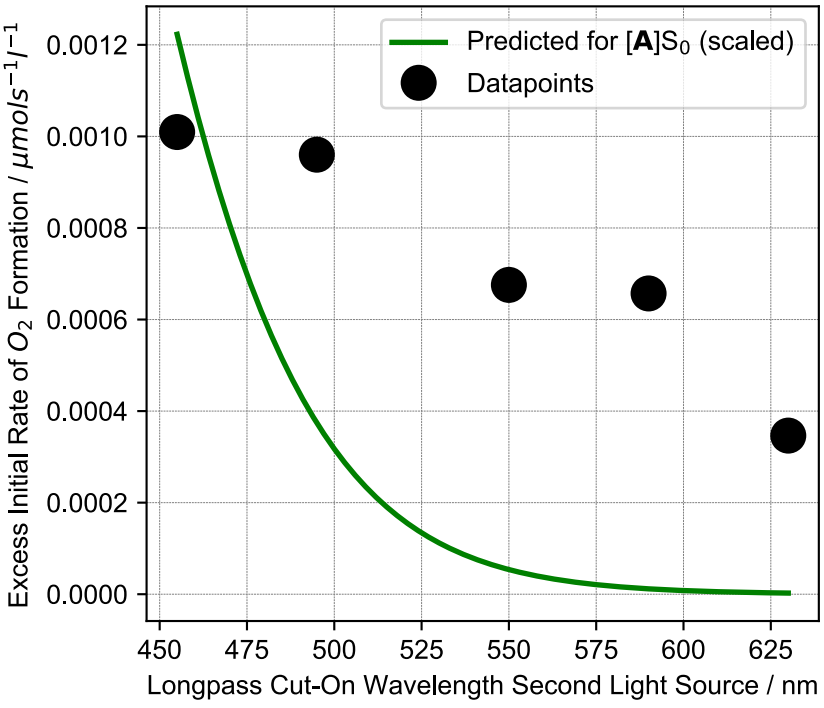

Figure 11.4-1 Dual irradiation data and predicted behavior of [A]S_0 (scaled)

As can be seen in Figure 11.4-1, predicted behavior for [**A**]S_0 is not consistent with experimental data. This is because [**A**]S_0 does not significantly absorb any wavelengths longer than 500 nm, although experimental data shows that these wavelengths already contribute to O_2 formation. Therefore, it can be ruled out that both photons involved in water splitting are absorbed by [**A**]S_0

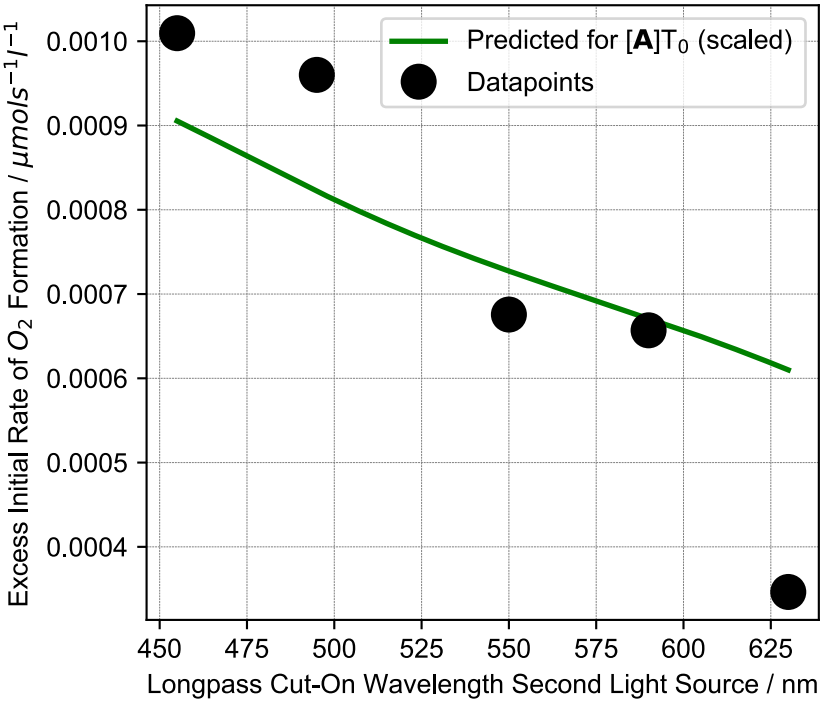

Figure 11.4-2 Dual irradiation data and predicted behavior of [A]T_0 (scaled)

The triplet state of [**A**], [**A**]T_0, could be considered another candidate for the second-photon absorbing intermediate. However, in this case poor agreement is obtained as well. This is due to the fact that [**A**]T_0 absorbs longer wavelengths only very weakly, giving a slope for longpass filter wavelength/reaction rate which is smaller than the one observed experimentally. These results showing that [**A**]T_0 is likely not the second-photon absorbing intermediate are also consistent with DFT calculations showing that O-O bond formation at [**A**]T_0 is unlikely.

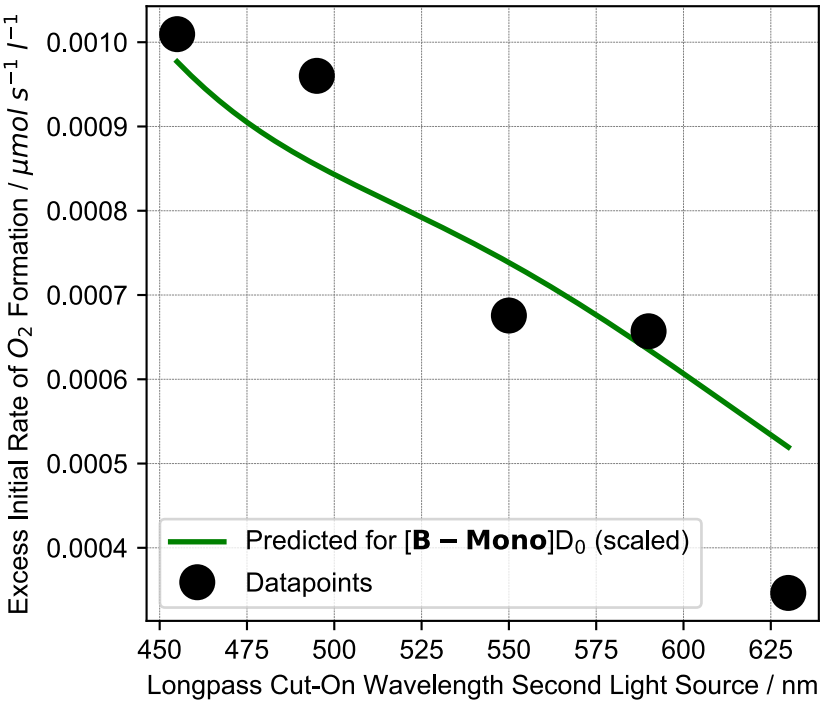

Figure 11.4-3 Dual irradiation data and predicted behavior of [B-Mono]D_0 (scaled)

As can be seen in Figure 11.4-3, [**B-Mono**]D_0 gives an acceptable fit for the dual irradiation data, although it is slightly inferior compared to the fit of [**B-Mono-Up**]D_0. As the ligand conformation does not have a significant effect on the obtained energies (see 11.2.1), the choice of ligand conformation does not have a major impact on computations. Calculations studying O-O bond formation were performed using [**B-Mono**]D_0.

11.4.2 Decay Associated Spectra

Theoretical decay associated spectra (DAS) were computed using theoretical UV/Vis spectra for a reference and an intermediate of interest. Theoretical UV/Vis spectra were used as reference (instead of experimental UV/Vis spectra) so as to allow for error cancellation between theoretical UV/Vis spectra.
DAS were computed using the following formula:

$$DAS = \left(p_{pop}\ Abs_{int} + \left(1 - p_{pop}\right)Abs_{ref}\right) - Abs_{ref} \qquad \text{Equation (8)}$$

Wherein Abs_{int} is the absorption spectrum of the intermediate of interest, Abs_{ref} is the absorption spectrum of the reference and p_{pop} is the population of the intermediate of interest after excitation. p_{pop} was assumed to be 0.1, although p_{pop} only effects the DAS magnitude and not its shape.

Thus calculated DAS were scaled vertically by multiplication with a scaling factor to yield the best fit to experimental data.

11.5 Structures and Coordinates for Computed Species

Figure 11.5-1 [A]S_0 Structure and Coordinates

128

Energy: -1951573.6088386

H	0.45669	-1.41554	-3.91019
C	-0.60849	-1.19121	-3.76131
H	-1.11536	-1.29884	-4.73276
H	-0.68914	-0.14799	-3.42124
H	-0.74297	0.90882	2.57857
O	-0.73313	0.99069	-1.30811
H	-0.86407	3.10316	1.53230
O	-1.30655	-1.17052	0.32709
H	-0.11798	0.23950	-1.31847
C	-1.15605	-2.12135	-2.70053
H	-1.34189	0.63234	4.24389
H	-1.19394	-3.16363	-3.07447
C	-1.54956	1.15446	3.29347
H	-1.17142	2.92058	-0.19928
H	-1.50205	2.23286	3.50526
H	-0.49457	-2.11224	-1.82445
C	-1.48683	3.46582	0.70359
H	-1.28687	4.54268	0.57069
H	-2.17348	-2.85488	-0.51445
Ru	-2.51776	0.09058	-0.76873
H	-2.32615	-1.22677	2.00794
N	-2.49410	-1.72633	-2.21407
C	-2.97419	-2.74821	-1.26400
C	-2.93493	0.72547	2.80365
H	-2.70322	-1.17497	3.77243
H	-2.82644	3.73565	3.11401
C	-2.99864	-0.80829	2.77427
C	-2.98156	3.26345	0.97162
P	-3.21371	1.37824	1.02207
H	-3.15290	-3.72018	-1.75468
C	-3.41191	4.01555	2.22952
H	-3.11689	-0.67633	-3.90443
H	-2.77234	-3.04850	-4.74444
H	-3.24914	5.09319	2.05928
C	-3.46221	-1.53612	-3.31726
H	-3.76709	0.77330	4.77624
C	-3.39499	1.14602	-1.98472
C	-4.00916	1.20050	3.78848
H	-3.48450	3.39830	-1.16373
C	-3.76998	3.84199	-0.20428
H	-4.05874	2.28811	3.90782
H	-3.54789	4.92029	-0.26501
C	-4.20392	-2.27738	-0.54802
N	-4.18814	-0.97126	-0.21953
C	-3.69183	-2.73052	-4.23152
H	-4.02129	-1.17123	2.58909
H	-4.41501	-1.23043	-2.86054
H	-4.48087	3.87829	2.45436
H	-4.10485	-3.60071	-3.69946
C	-5.04785	1.04374	0.77758
H	-4.42084	-2.44844	-5.00597
H	-5.01097	0.83045	3.52344
C	-5.21189	-0.41068	0.46124
C	-5.27900	-3.08726	-0.20149
H	-4.85906	3.74404	-0.07432
H	-5.27592	-4.14092	-0.48292
H	-5.32999	1.63204	-0.11068
H	-5.69471	1.35408	1.60901
C	-6.31091	-1.17896	0.83734
C	-6.34379	-2.53021	0.50361
H	-7.12815	-0.71577	1.39103
H	-7.19795	-3.14636	0.78976
O	-3.88678	1.76908	-2.83721
C	0.53409	-3.71739	2.88972
H	1.03191	1.20848	-2.61109
O	0.65050	0.63916	1.17066
H	1.12549	3.11974	-1.16533
O	1.44261	-1.31103	-0.69485
H	0.26065	1.02485	0.36109
C	0.80054	-2.40419	2.17077
H	1.68202	1.04433	-4.26091
C	1.88201	1.46254	-3.26027
H	1.45188	2.85330	0.54886
H	1.90016	2.55632	-3.36662
C	1.77392	3.42698	-0.33278
H	1.60977	4.50161	-0.14530
H	2.21320	-3.13261	0.23384
Ru	2.48771	-0.14715	0.67409
H	2.42528	-1.08233	-2.29685
N	2.22014	-2.03548	1.98131
C	2.88466	-3.01696	1.10162
C	3.21523	0.90739	-2.75460
H	3.06562	-0.85253	-3.97218
H	3.14665	3.90086	-2.70611
C	3.21891	-0.61872	-2.90429
C	3.25842	3.18593	-0.62318
P	3.39313	1.30222	-0.89528
H	3.03776	-3.98536	1.60832
C	3.72369	4.05980	-1.78770
H	3.93789	-1.53805	3.05434
H	1.86008	-0.15924	3.86531
H	3.58701	5.11498	-1.49687
C	2.93991	-1.94811	3.26960
H	4.16382	1.16053	-4.65719
C	3.31771	0.77390	2.01601
C	4.36497	1.44823	-3.61143
H	3.80161	3.07199	1.51083
C	4.07551	3.61023	0.59852
H	4.47194	2.53769	-3.58867
H	3.87932	4.67993	0.78110
C	4.18485	-2.51032	0.55399
N	4.19730	-1.20307	0.23710
C	2.23139	-1.09489	4.30517
H	4.19048	-1.05275	-2.61958
H	3.09882	-2.96832	3.67033
H	4.79216	3.92069	-2.01152
H	1.37686	-1.62062	4.75467
C	5.18533	0.84532	-0.56671
H	2.93276	-0.83914	5.11222
H	5.33086	0.99479	-3.34259
C	5.28552	-0.62889	-0.31867
C	5.29319	-3.31376	0.30802
H	5.15955	3.50693	0.43450
H	5.26682	-4.37010	0.57750
H	5.44504	1.36569	0.36985
H	5.89468	1.17571	-1.33728
C	6.41479	-1.39237	-0.60461
C	6.41695	-2.74787	-0.28829
H	7.28349	-0.91982	-1.06390
H	7.29594	-3.35964	-0.49892
H	0.51938	-1.28667	-0.38188
O	3.84337	1.29469	2.91844
H	-0.55554	-3.85917	2.95147
H	0.92613	-3.74051	3.91838
H	0.94292	-4.58591	2.35026
H	0.33909	-2.42001	1.17789
H	0.32431	-1.56825	2.69632
H	-0.67343	-0.57507	0.79032

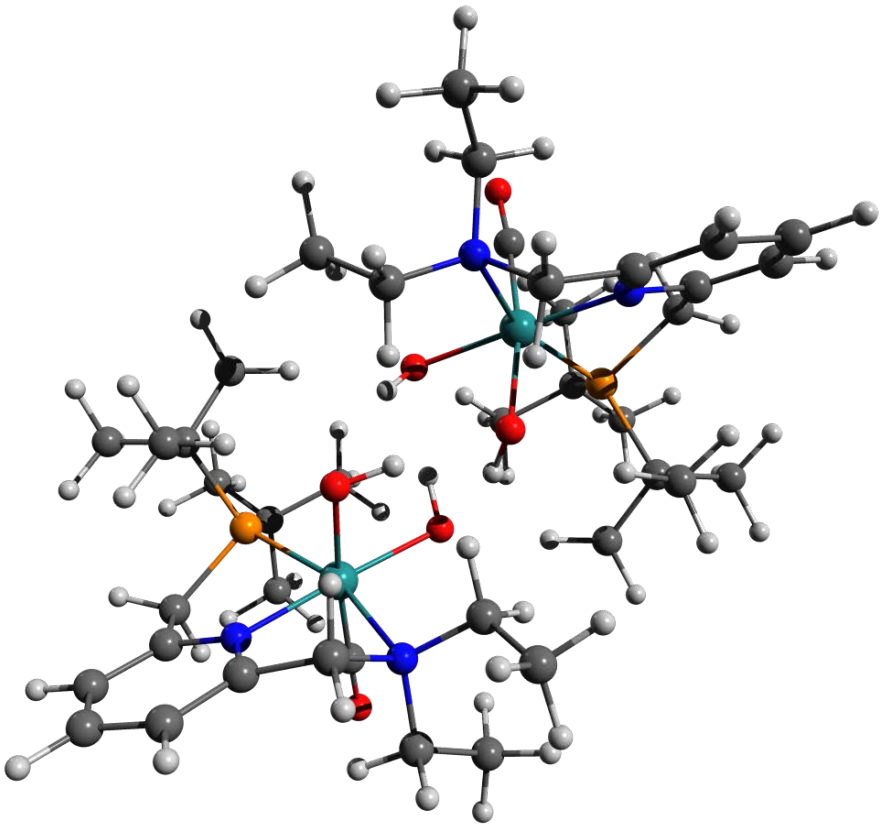

Figure 11.5-2 [A-RR]S_0 Structure and Coordinates

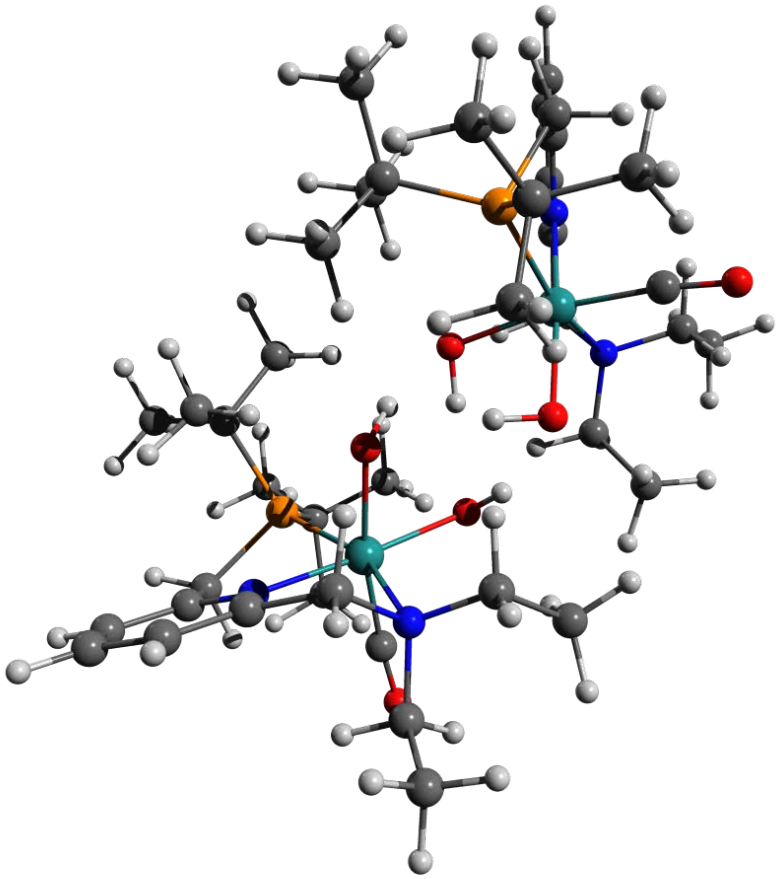

128

Energy: -1951572.9167082

C	-1.33476	1.62962	3.69683
H	-0.26977	-1.45456	-1.99998
O	-1.00000	-0.94847	1.55613
H	-0.69418	-3.51808	-0.61782
O	-1.16182	0.99921	-0.43577
C	-1.63792	2.42574	2.44563
H	-0.43706	-1.55601	-3.77219
C	-0.88137	-1.87525	-2.81475
H	-1.36512	-2.97340	0.92589
H	-0.80142	-2.97152	-2.77187
C	-1.50682	-3.69045	0.10226
H	-1.41068	-4.72148	0.48355
H	-2.11655	2.78328	-0.01923
Ru	-2.60257	-0.08485	0.60240
H	-1.90018	0.68204	-2.25402
N	-2.83716	1.95014	1.72806
C	-3.06271	2.80387	0.54647
C	-2.33492	-1.40393	-2.76955
H	-1.86051	0.28270	-4.00954
H	-2.24788	-4.41338	-2.45745
C	-2.38522	0.10267	-3.05592
C	-2.88702	-3.52920	-0.54760
P	-3.00905	-1.68496	-1.00600
H	-3.30496	3.84415	0.82365
C	-3.04458	-4.50892	-1.70925
H	-3.85094	1.17903	3.37948
H	-3.64271	3.64614	3.90445
H	-2.98825	-5.53336	-1.30402
C	-4.03307	1.92951	2.60067
H	-2.70959	-1.81161	-4.83771
C	-3.71958	-0.90744	1.79395
C	-3.14948	-2.09636	-3.86696
H	-3.90230	-3.25753	1.38718
C	-3.96162	-3.87414	0.48495
H	-3.13803	-3.18967	-3.81289
H	-3.81069	-4.92111	0.79619
C	-4.13209	2.22311	-0.32930
N	-4.09753	0.88019	-0.42939
C	-4.42734	3.25143	3.24266
H	-3.41925	0.45653	-3.18656
H	-4.86904	1.54718	1.99683
H	-4.01792	-4.41009	-2.21348
H	-4.67408	4.02796	2.50298
C	-4.83154	-1.27709	-1.21853
H	-5.32631	3.09131	3.85669
H	-4.19637	-1.75785	-3.88610
C	-4.98710	0.21414	-1.19742
C	-5.08534	2.96481	-1.01727
H	-4.97961	-3.80540	0.07074
H	-5.10111	4.05079	-0.91839
H	-5.32519	-1.69300	-0.32500
H	-5.30741	-1.72040	-2.10386
C	-5.95975	0.90972	-1.91117
C	-6.00672	2.29855	-1.82227
H	-6.66897	0.36131	-2.53192
H	-6.76286	2.85910	-2.37469
H	-0.42438	0.37664	-0.58526
O	-4.37127	-1.37026	2.64145
C	1.30359	-1.37352	3.78803
H	0.29481	1.58800	-1.99894
O	1.03826	1.02511	1.61441
H	0.88996	3.59972	-0.60082
O	1.09120	-0.88920	-0.40805
C	1.55019	-2.25204	2.58013
H	0.43562	1.60929	-3.77068
C	0.91906	1.93554	-2.83465
H	1.62411	3.10560	0.93434
H	0.91009	3.03531	-2.83283
C	1.74815	3.77187	0.06532
H	1.71600	4.82376	0.39669
H	1.98309	-2.72548	0.11055
Ru	2.60225	0.12276	0.61552
H	1.74851	-0.65907	-2.22066
N	2.75934	-1.86762	1.82092
C	2.92848	-2.78423	0.67748
C	2.33958	1.37024	-2.79326
H	1.76399	-0.31890	-3.98372
H	2.40859	4.37481	-2.55388
C	2.28703	-0.14409	-3.02839
C	3.08265	3.51160	-0.64424
P	3.06784	1.64973	-1.05231
H	3.11897	-3.82273	0.99687
C	3.23871	4.44917	-1.84065
H	3.84335	-1.07408	3.41866
H	3.51821	-3.49458	4.06914
H	3.25147	5.48578	-1.46371
C	3.97091	-1.86838	2.67360
H	2.69610	1.69491	-4.87946
C	3.76844	0.93623	1.76348
C	3.17664	1.97283	-3.92616
H	4.19024	3.22897	1.23990
C	4.22682	3.82382	0.32206
H	3.24462	3.06520	-3.90259
H	4.14280	4.88270	0.61809
C	4.00795	-2.29506	-0.23921
N	4.03247	-0.95918	-0.40353
C	4.30793	-3.17694	3.37295
H	3.29447	-0.57481	-3.13282
H	4.81461	-1.55973	2.03898
H	4.18438	4.28658	-2.37953
H	4.49584	-4.00159	2.66892
C	4.85699	1.12496	-1.29099
H	5.22779	-3.03581	3.96020
H	4.19586	1.55927	-3.95705
C	4.93388	-0.37027	-1.21712
C	4.90832	-3.11179	-0.91452
H	5.21535	3.69907	-0.14678
H	4.87646	-4.19174	-0.76656
H	5.39407	1.54156	-0.42312
H	5.33725	1.51112	-2.20034
C	5.85550	-1.14217	-1.92095
C	5.83838	-2.52595	-1.76976
H	6.57610	-0.65667	-2.57971
H	6.55364	-3.14599	-2.31319
H	0.38008	-1.02765	0.25693
O	4.44257	1.39800	2.59466
H	-1.75243	3.50226	2.68089
H	-0.80012	2.33087	1.74631
H	-2.02715	1.84874	4.52480
H	-0.31432	1.86984	4.02428
H	-1.36384	0.55228	3.47461
H	1.62589	-3.31834	2.87075
H	0.69051	-2.14886	1.90309
H	2.03483	-1.52819	4.59704
H	0.30462	-1.60278	4.18461
H	1.30428	-0.31685	3.48018
H	-0.38513	-0.22179	1.78772
H	0.41886	1.21775	0.88892

Figure 11.5-3 [A-RS-1]S_0 Structure and Coordinates

128

Energy: -1951573.3041640

C	0.44944	1.22488	-3.77639
H	0.85001	-1.78901	2.23509
O	0.88713	-1.26790	-1.44493
H	1.57788	-3.69098	0.87899
O	0.98095	0.88491	0.39954
C	0.79921	2.22961	-2.69815
H	1.26570	-1.62533	3.95664
H	0.64403	3.26790	-3.05872
C	1.65776	-1.92898	2.97132
H	1.93112	-3.16606	-0.77294
H	1.88358	-3.00310	3.03292
H	0.12105	2.06733	-1.84896
C	2.32505	-3.74865	0.07538
H	2.42815	-4.80718	-0.21773
H	1.57306	2.83785	-0.37216
Ru	2.44962	-0.09044	-0.75468
H	1.79048	0.71994	2.13147
N	2.16494	2.06545	-2.18577
C	2.41038	2.98380	-1.07523
C	2.90298	-1.09150	2.67002
H	2.20094	0.53729	3.87486
H	3.52988	-4.02953	2.56215
C	2.56397	0.39387	2.84285
C	3.69327	-3.21981	0.52014
P	3.42989	-1.36334	0.85447
H	2.44494	4.04258	-1.39333
C	4.21952	-4.02271	1.70965
H	3.05995	1.30047	-3.90411
H	2.34497	3.63209	-4.57434
H	4.34614	-5.06930	1.38574
C	3.20642	2.14589	-3.21895
H	3.61586	-1.23656	4.68387
C	3.53938	-0.75838	-2.05805
C	4.01472	-1.42166	3.67240
H	4.38662	-2.90712	-1.54788
C	4.69148	-3.40826	-0.62397
H	4.35525	-2.46207	3.64201
H	4.75187	-4.48669	-0.84501
C	3.66012	2.63839	-0.31581
N	3.87226	1.32886	-0.07270
C	3.27034	3.44640	-4.00884
H	3.45363	1.03171	2.72334
H	4.17171	1.96408	-2.72147
H	5.20328	-3.66674	2.05212
H	3.45657	4.32098	-3.36660
C	5.12282	-0.55440	0.79579
H	4.09598	3.39154	-4.73430
H	4.88796	-0.76266	3.55393
C	4.95773	0.92694	0.62682
C	4.54049	3.60455	0.16296
H	5.70742	-3.07897	-0.35564
H	4.34930	4.65660	-0.05122
H	5.59454	-0.95183	-0.11779
H	5.77818	-0.79507	1.64343
C	5.86173	1.85499	1.13857
C	5.64754	3.20948	0.90675
H	6.72471	1.50940	1.70833
H	6.34577	3.95253	1.29638
H	0.16102	0.80024	-0.13289
O	4.15621	-1.09821	-2.98708
C	-1.19301	-3.84473	-1.18152
H	-0.26419	2.42261	1.01026
O	-0.73798	-1.41373	0.85327
H	-0.39436	1.23053	3.13584
O	-1.36411	0.39954	-1.19688
H	-0.16417	-0.63117	0.95056
C	-1.71073	-2.77480	-2.11892
H	-0.62877	4.16044	0.81622
C	-0.94210	3.23229	1.32537
H	-1.01484	-0.42043	2.99262
H	-0.79963	3.39421	2.40359
C	-1.12835	0.52400	3.54629
H	-0.88319	0.35518	4.60876
H	-2.46759	-0.43411	-2.77867
Ru	-2.53285	-0.62460	0.18044
H	-2.00588	2.17779	-1.04332
N	-2.90366	-2.07190	-1.59740
C	-3.34620	-1.07479	-2.59111
C	-2.40466	2.95723	0.96836
H	-2.18292	3.96727	-0.91269
H	-2.01998	3.12487	3.94360
C	-2.56224	2.99352	-0.55736
C	-2.56286	1.05027	3.43758
P	-2.88694	1.20278	1.56571
H	-3.68593	-1.54294	-3.53017
C	-2.72345	2.33878	4.24338
H	-3.66771	-3.63450	-0.44206
H	-3.69938	-4.57063	-2.78946
H	-2.52085	2.10771	5.30280
C	-4.00430	-3.01267	-1.28002
H	-2.94425	5.02381	1.12511
C	-3.41776	-1.74699	1.32201
C	-3.29761	4.06429	1.53923
H	-3.44520	-0.96318	3.57207
C	-3.51212	0.01888	4.05009
H	-3.26800	4.14975	2.63062
H	-3.23066	-0.11510	5.10783
C	-4.40472	-0.18363	-2.01841
N	-4.21751	0.14522	-0.72650
C	-4.48818	-3.90161	-2.41606
H	-3.61973	2.93371	-0.85771
H	-4.84222	-2.41181	-0.89722
H	-3.74677	2.74021	4.18807
H	-4.88329	-3.32890	-3.26859
C	-4.75401	1.22729	1.35488
H	-5.30745	-4.53433	-2.04271
H	-4.34603	3.95500	1.22413
C	-5.07513	0.96578	-0.08390
C	-5.48543	0.32174	-2.73305
H	-4.56123	0.35307	4.03718
H	-5.62270	0.04053	-3.77768
H	-5.11703	0.37291	1.94924
H	-5.25229	2.13269	1.72618
C	-6.16943	1.50670	-0.75472
C	-6.37327	1.18280	-2.09319
H	-6.85123	2.17357	-0.22620
H	-7.22639	1.59603	-2.63427
H	-0.61046	-0.19239	-1.42034
O	-3.91652	-2.56087	1.99078
H	-0.62551	1.30058	-3.99399
H	0.64812	0.20444	-3.41292
H	0.99685	1.39251	-4.71719
H	-1.00677	-3.40740	-0.18877
H	-0.23452	-4.21439	-1.57202
H	-1.87164	-4.70722	-1.08997
H	-0.92118	-2.02245	-2.25956
H	-1.94765	-3.19941	-3.11412
H	0.39291	-1.52961	-0.63555

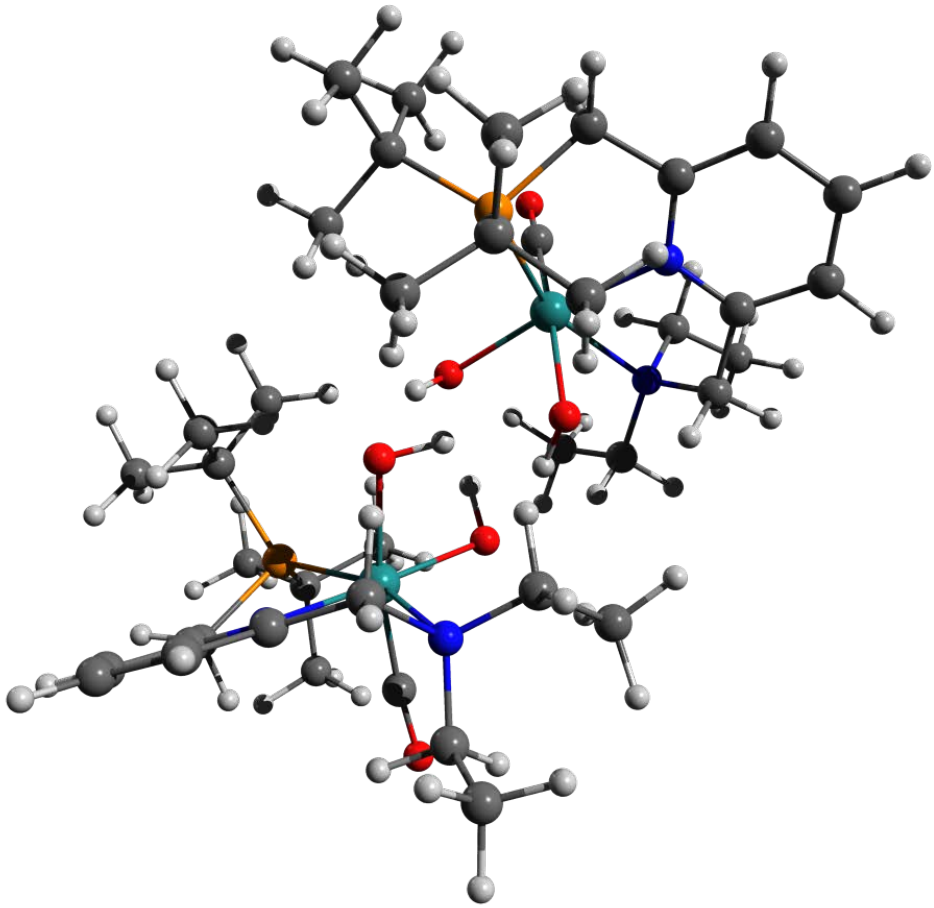

Figure 11.5-4 [A-RS-2]S_0 Structure and Coordinates

128

Energy: -1951572.5055138

C	-1.15194	-3.96254	0.55818
H	-0.28547	2.55688	-0.56699
O	-0.71663	-1.22947	-1.04323
H	-0.41574	1.72518	-2.90022
O	-1.37163	0.22431	1.25960
H	-0.14262	-0.44333	-0.99728
C	-1.67727	-3.05991	1.65360
H	-0.64876	4.24417	-0.11099
C	-0.95882	3.40685	-0.76038
H	-1.04447	0.07567	-3.01956
H	-0.80424	3.73235	-1.79927
C	-1.15597	1.09668	-3.41404
H	-0.91646	1.09973	-4.49107
H	-2.46097	-0.86938	2.68486
Ru	-2.52248	-0.57308	-0.26885
H	-2.04005	1.99190	1.39806
N	-2.87838	-2.29591	1.25096
C	-3.33258	-1.47943	2.39246
C	-2.42515	3.08378	-0.46455
H	-2.22018	3.77888	1.55552
H	-2.02347	3.73102	-3.37496
C	-2.59537	2.87446	1.04586
C	-2.58569	1.60700	-3.21317
P	-2.89982	1.44899	-1.33940
H	-3.66860	-2.09820	3.24145
C	-2.73620	3.01159	-3.79611
H	-3.62358	-3.65750	-0.14564
H	-3.64930	-4.96047	2.02194
H	-2.53836	2.95472	-4.87985
C	-3.96814	-3.18351	0.78104
H	-2.97044	5.14641	-0.27862
C	-3.38552	-1.50789	-1.58371
C	-3.31123	4.27088	-0.85685
H	-3.49938	-0.34703	-3.66603
C	-3.54712	0.69940	-3.98296
H	-3.26008	4.54057	-1.91680
H	-3.26225	0.72878	-5.04784
C	-4.39988	-0.51775	1.97028
N	-4.21716	0.01904	0.74920
C	-4.44520	-4.24977	1.75605
H	-3.65521	2.76763	1.32441
H	-4.81111	-2.53646	0.49757
H	-3.75507	3.40879	-3.67224
H	-4.85141	-3.82674	2.68713
C	-4.76609	1.42433	-1.12500
H	-5.25455	-4.82416	1.28070
H	-4.36541	4.10888	-0.58674
C	-5.08332	0.92583	0.25017
C	-5.48466	-0.14662	2.75743
H	-4.59044	1.04577	-3.92042
H	-5.61757	-0.59610	3.74205
H	-5.12379	0.67768	-1.85267
H	-5.27147	2.37505	-1.34127
C	-6.18240	1.33887	0.99957
C	-6.38195	0.79836	2.26671
H	-6.87085	2.07685	0.58688
H	-7.23854	1.10900	2.86765
H	-0.60569	-0.38424	1.38092
O	-3.86464	-2.21004	-2.38127
H	-0.53829	0.45268	4.17835
C	0.52979	0.40722	3.92102
H	1.10249	0.42570	4.86139
H	0.70910	-0.54051	3.39085
H	0.79305	-1.31344	-2.52605
O	0.91435	-1.37723	1.29448
H	1.46971	-3.38523	-1.45868
O	1.03384	0.96896	-0.20626
C	0.84882	1.56908	3.00435
H	1.21054	-0.84276	-4.19128
H	0.72851	2.53646	3.53091
C	1.59831	-1.32480	-3.27797
H	1.90942	-3.21844	0.24600
H	1.80927	-2.37257	-3.53444
H	0.13824	1.55339	2.16730
C	2.24561	-3.62799	-0.71930
H	2.31753	-4.72653	-0.64710
H	1.58278	2.70824	0.86890
Ru	2.48862	-0.13997	0.78538
H	1.77452	1.12681	-1.96506
N	2.20456	1.49639	2.42021
C	2.42865	2.68434	1.57538
C	2.85422	-0.57168	-2.83232
H	2.16359	1.25552	-3.72049
H	3.38851	-3.48871	-3.25647
C	2.53404	0.92498	-2.73502
C	3.61447	-3.05813	-1.10613
P	3.37383	-1.16762	-1.09234
H	2.45643	3.61660	2.16440
C	4.09113	-3.65269	-2.43111
H	3.12402	0.42379	3.95740
H	2.37123	2.55660	5.08958
H	4.18984	-4.74341	-2.29982
C	3.25511	1.39149	3.45879
H	3.55876	-0.36720	-4.84451
C	3.57726	-1.09645	1.89839
C	3.95888	-0.73043	-3.88287
H	4.37145	-3.13218	0.96251
C	4.63697	-3.46765	-0.04444
H	4.28934	-1.76320	-4.03702
H	4.67512	-4.56940	-0.01908
C	3.66953	2.53433	0.74934
N	3.88766	1.28977	0.28531
C	3.29696	2.50194	4.49834
H	3.43367	1.52044	-2.51419
H	4.22093	1.33668	2.93511
H	5.08006	-3.27043	-2.72699
H	3.48085	3.49358	4.05824
C	5.08766	-0.41751	-0.91673
H	4.12250	2.29925	5.19710
H	4.83902	-0.11051	-3.65529
C	4.95052	1.01411	-0.50029
C	4.52900	3.57781	0.42300
H	5.65342	-3.11756	-0.28298
H	4.33800	4.57849	0.81212
H	5.55431	-0.97211	-0.08606
H	5.73358	-0.52553	-1.79812
C	5.83620	2.02474	-0.86699
C	5.62030	3.31907	-0.40233
H	6.68607	1.79111	-1.50887
H	6.30554	4.12275	-0.67778
H	0.21141	0.79237	0.29387
O	4.18237	-1.67371	2.71045
H	-1.90771	-3.63943	2.56906
H	-0.89587	-2.33029	1.91152
H	-1.82472	-4.80355	0.32849
H	-0.19204	-4.38523	0.88638
H	-0.96821	-3.36937	-0.35049
H	0.46736	-1.56382	0.44287

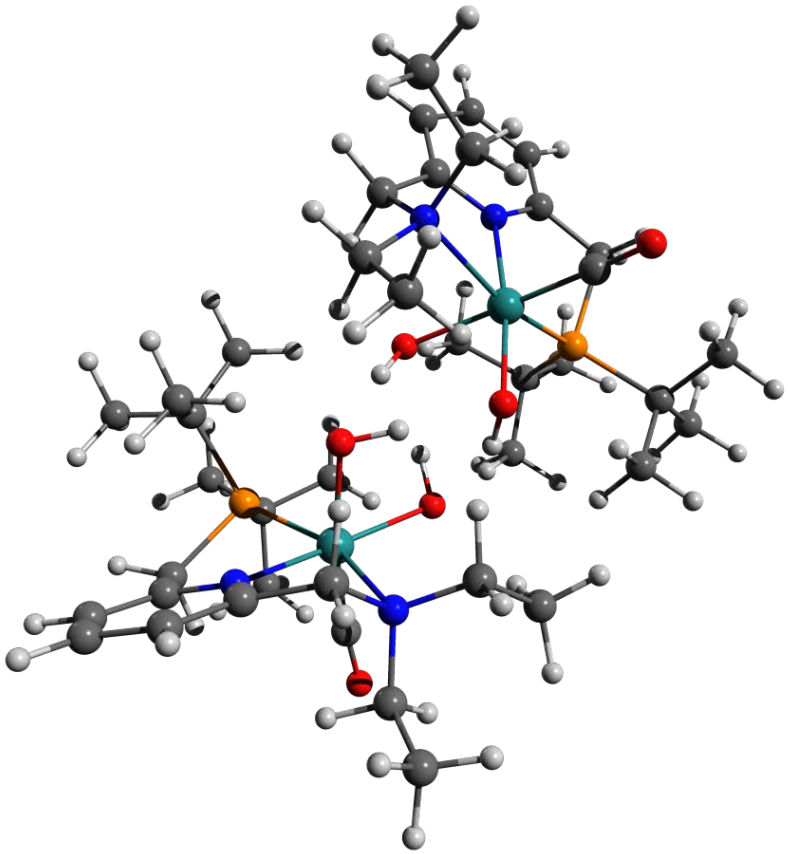

Figure 11.5-5 [A]T_0 Structure and Coordinates

128

Energy: -1951545.5657542

H	0.31863	-4.29565	-0.54368
C	-0.74782	-4.05620	-0.66007
H	-1.25666	-4.95812	-1.03476
H	-0.83424	-3.25902	-1.41383
H	-0.89863	2.85473	0.60480
O	-0.81090	-0.46520	-1.74247
H	-1.03805	3.35602	-1.86063
O	-1.24485	-0.42066	1.01348
H	-0.19731	-0.01036	-1.12069
C	-1.29305	-3.57816	0.66899
H	-1.52275	4.12018	1.69653
H	-1.26491	-4.40087	1.41479
C	-1.71674	3.57878	0.75441
H	-1.15604	1.73456	-2.60268
H	-1.68868	4.32026	-0.05772
H	-0.65852	-2.76439	1.04954
C	-1.58651	2.74850	-2.59407
H	-1.43788	3.20907	-3.58570
H	-2.24912	-1.89079	2.23744
Ru	-2.42361	-0.74411	-0.65979
H	-2.34600	1.11425	1.95336
N	-2.64389	-3.01925	0.56942
C	-3.08084	-2.50418	1.85122
C	-3.07295	2.87641	0.85781
H	-2.70549	2.56665	2.95908
H	-3.18995	4.76240	-1.58997
C	-3.03607	1.96444	2.09462
C	-3.08836	2.68472	-2.28609
P	-3.24831	1.72285	-0.65451
H	-3.31703	-3.29603	2.58922
C	-3.70208	4.08183	-2.28393
H	-3.31453	-4.05086	-1.10616
H	-2.95781	-5.85659	0.63487
H	-3.61235	4.51704	-3.29444
C	-3.62965	-3.89593	-0.06466
H	-4.02518	4.45554	1.97149
C	-3.36456	-1.34120	-2.12581
C	-4.19650	3.89629	1.03496
H	-3.37346	0.82330	-3.40463
C	-3.75014	1.85477	-3.38879
H	-4.25157	4.62811	0.21944
H	-3.51094	2.31281	-4.36297
C	-4.25781	-1.58700	1.69925
N	-4.21736	-0.72903	0.66500
C	-3.86878	-5.23942	0.61286
H	-4.03273	1.56862	2.34058
H	-4.57500	-3.33317	-0.12247
H	-4.77252	4.06406	-2.02686
H	-4.22593	-5.12822	1.64853
C	-5.03521	1.18702	-0.58544
H	-4.63688	-5.80115	0.05987
H	-5.17972	3.41023	1.13140
C	-5.19506	0.18768	0.51919
C	-5.31278	-1.58449	2.60864
H	-4.84681	1.83379	-3.30016
H	-5.31214	-2.30225	3.42990
H	-5.22278	0.68777	-1.54883
H	-5.75961	2.00674	-0.47589
C	-6.28110	0.23361	1.39299
C	-6.34423	-0.66720	2.44904
H	-7.05858	0.98311	1.24109
H	-7.18533	-0.64836	3.14469
O	-3.95239	-1.78104	-3.03127
C	0.46634	0.92944	4.49928
H	1.05119	-1.86914	-1.77387
O	0.68245	1.25187	-0.04535
H	1.17504	0.58034	-3.03899
O	1.59054	-1.20381	0.91053
H	0.68848	1.87513	-0.77795
C	0.80149	0.86999	3.01811
H	1.58372	-3.34978	-2.61470
C	1.79147	-2.27601	-2.47557
H	1.80904	2.09388	-2.35449
H	1.63051	-1.78465	-3.44595
C	1.94625	1.35647	-3.15761
H	1.77585	1.87055	-4.11806
H	2.26759	-1.13380	2.93873
Ru	2.56684	0.54429	0.42633
H	2.69920	-2.51644	0.11657
N	2.23960	0.90872	2.67109
C	2.92162	-0.28578	3.20523
C	3.22067	-2.10962	-1.96357
H	3.14970	-3.95308	-0.87315
H	2.92299	-0.73598	-4.64067
C	3.38740	-2.89712	-0.65726
C	3.37353	0.79744	-3.12893
P	3.47221	-0.27104	-1.54417
H	3.06077	-0.22542	4.29811
C	3.64980	0.06049	-4.43884
H	3.92137	2.13685	2.74600
H	1.86747	3.41929	1.76505
H	3.57127	0.79015	-5.26218
C	2.90572	2.12915	3.17040
H	4.10409	-3.77616	-2.97141
C	3.37619	2.16288	0.15103
C	4.22365	-2.68001	-2.97180
H	4.28215	2.54675	-2.13157
C	4.36805	1.95839	-3.05241
H	4.06518	-2.33910	-3.99929
H	4.16447	2.64113	-3.89428
C	4.23212	-0.55244	2.52984
N	4.26066	-0.29347	1.20812
C	2.17837	3.41271	2.81830
H	4.42733	-2.87195	-0.29351
H	3.02487	2.05829	4.26926
H	4.66297	-0.36397	-4.47338
H	1.28096	3.55834	3.43643
C	5.26488	-0.21591	-0.98745
H	2.84597	4.27026	2.98512
H	5.26986	-2.47853	-2.69355
C	5.35194	-0.57317	0.46505
C	5.33575	-1.10622	3.16925
H	5.40872	1.61545	-3.16035
H	5.29714	-1.30072	4.24147
H	5.57622	0.83481	-1.10176
H	5.94760	-0.82993	-1.59141
C	6.47694	-1.14500	1.05423
C	6.46875	-1.41095	2.41990
H	7.34875	-1.37413	0.44085
H	7.34436	-1.85234	2.89915
H	0.63496	-1.05555	0.77572
O	3.87246	3.21300	0.03062
H	-0.62825	0.88816	4.60526
H	0.80880	1.85473	4.98886
H	0.87716	0.07545	5.06003
H	0.39995	-0.04647	2.56943
H	0.32600	1.69534	2.47519
H	-0.66325	0.32172	0.76362

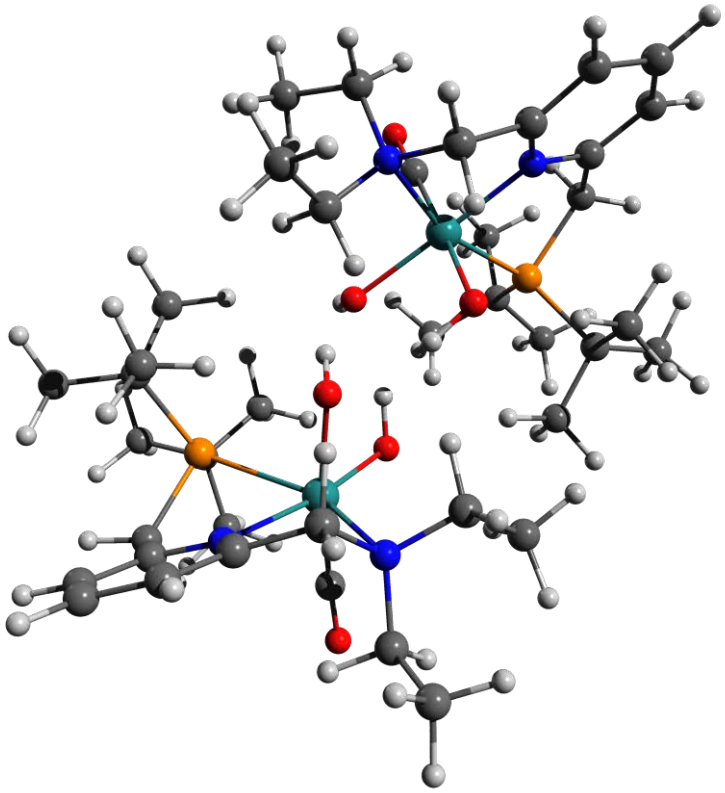

Figure 11.5-6 [A-Mono]S_0 Structure and Coordinates

64

Energy: -975781.7288466

N	-0.71461	1.41145	-0.05552
C	-1.93725	1.87355	0.26183
C	0.19459	2.20723	-0.65239
C	-2.28128	3.20266	0.05361
C	-1.33114	4.06030	-0.49717
C	-0.08773	3.55709	-0.86171
C	-2.85043	0.84429	0.85528
H	-3.27959	3.55437	0.31562
H	-1.56883	5.11248	-0.66341
H	0.66192	4.19707	-1.32817
C	1.45721	1.55183	-1.11784
N	-2.72411	-0.45534	0.16951
H	-3.89160	1.21043	0.86121
H	-2.55608	0.68653	1.90573
H	1.24304	1.16737	-2.13027
P	1.78985	-0.01998	-0.16505
H	2.29722	2.25937	-1.16090
Ru	-0.39928	-0.61383	0.08172
C	-3.28283	-0.39340	-1.19918
C	2.97324	-0.99546	-1.29362
C	-3.38475	-1.48595	1.00200
C	2.72182	0.58988	1.38220
C	2.11769	-1.74151	-2.32039
C	3.72410	-2.04167	-0.46792
C	3.96342	-0.09780	-2.03899
C	1.86381	1.68472	2.02822
C	4.09031	1.19356	1.06301
C	2.89349	-0.54913	2.39174
C	-0.39429	-0.83617	1.89956
O	-0.45848	-1.02652	3.05049
H	-2.68999	0.34812	-1.75005
C	-4.77475	-0.11819	-1.30549
H	-3.03278	-1.34793	-1.67752
H	-2.85003	-1.49718	1.96295
C	-3.35227	-2.86901	0.38750
H	-4.42405	-1.16918	1.22192
O	-0.32253	-2.62904	-0.33069
H	0.22403	-3.10148	0.30746
O	-0.53805	-0.41410	-1.96323
H	-0.51927	-1.34094	-2.23979
H	-2.32197	-3.10175	0.06512
H	-4.03521	-2.96053	-0.47067
H	-3.67404	-3.60285	1.14184
H	-5.05270	-0.10914	-2.37017
H	-5.06413	0.86089	-0.89282
H	-5.38839	-0.88876	-0.81452
H	2.78956	-2.35108	-2.94866
H	1.55854	-1.05021	-2.96420
H	1.38471	-2.39095	-1.81685
H	4.25560	-2.71733	-1.15807
H	3.03302	-2.65720	0.12777
H	4.47476	-1.60264	0.20341
H	4.59861	-0.73497	-2.67721
H	4.62793	0.47120	-1.37696
H	3.44808	0.60838	-2.70613
H	4.81061	0.44266	0.71220
H	4.50493	1.63794	1.98338
H	4.03158	1.99636	0.31245
H	3.57490	-1.32971	2.03359
H	1.93780	-1.01914	2.65161
H	3.32255	-0.13633	3.32020
H	2.33188	1.98025	2.98143
H	0.84386	1.34147	2.24529
H	1.79979	2.58622	1.40116

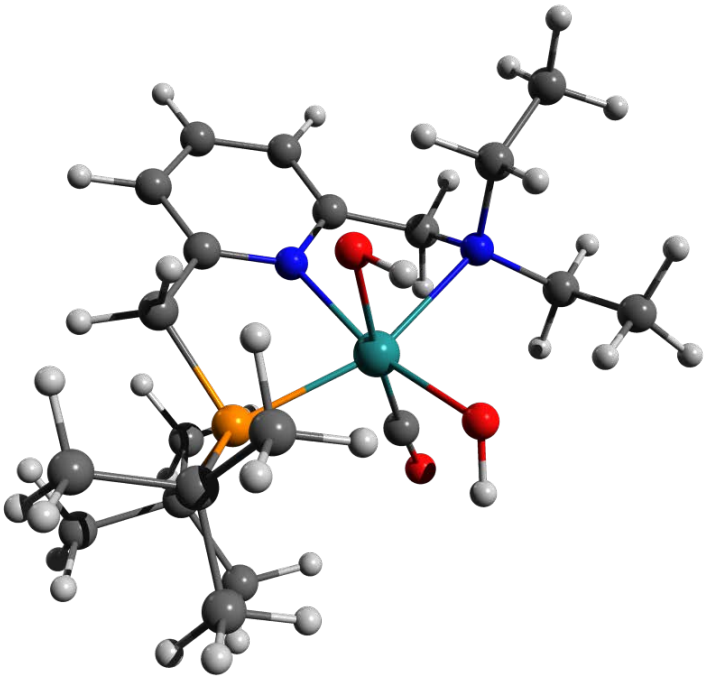

Figure 11.5-7 [B]T_0 Structure and Coordinates

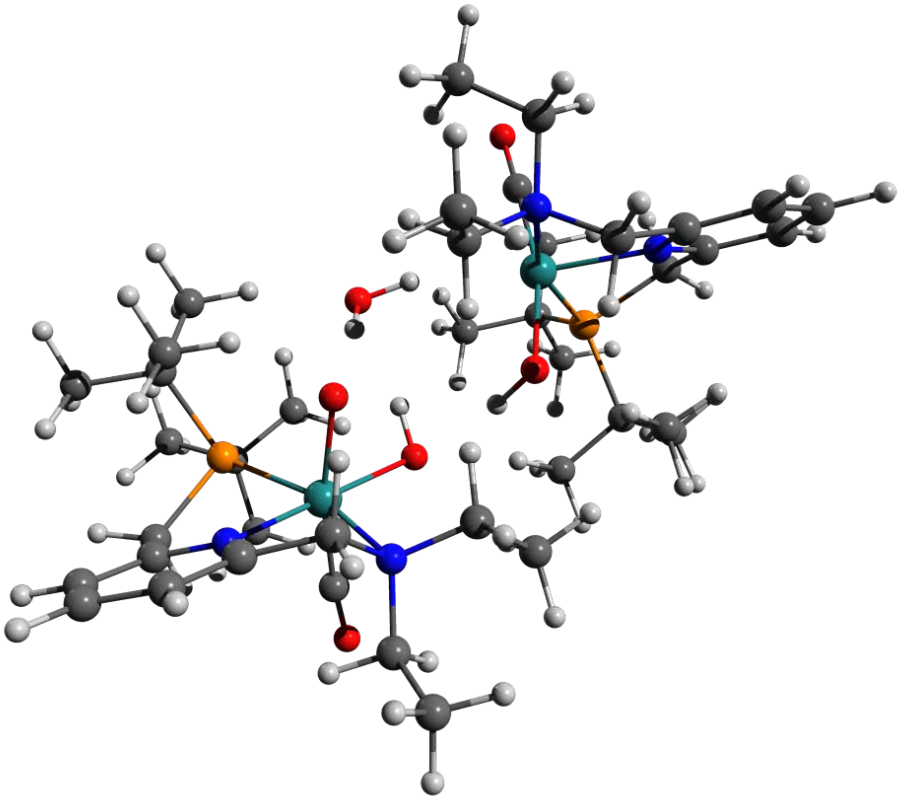

128

Energy: -1951514.6685434

H	0.84052	-2.25311	-2.78417
C	-0.23016	-2.03744	-2.88605
H	-0.57102	-2.40557	-3.86621
H	-0.34157	-0.94451	-2.83707
H	-1.64170	1.80046	2.89472
O	-0.72294	0.62491	-1.06975
H	-1.47959	3.47385	1.34965
O	-1.68143	-1.00834	0.89192
H	-0.59535	0.16002	1.52690
C	-0.95291	-2.67994	-1.72274
H	-2.72120	1.84010	4.31167
H	-0.92044	-3.78459	-1.80117
C	-2.64606	2.08586	3.23880
H	-1.25654	2.94128	-0.32533
H	-2.75935	3.17491	3.15115
H	-0.44556	-2.38791	-0.79259
C	-1.83479	3.61673	0.32271
H	-1.62574	4.65797	0.02470
H	-2.39869	-2.96096	0.34173
Ru	-2.59566	-0.16092	-0.64776
H	-2.65270	-0.58334	2.49333
N	-2.36315	-2.24342	-1.59784
C	-3.03659	-3.03916	-0.55326
C	-3.74898	1.31946	2.50435
H	-3.64812	-0.26873	3.94669
H	-3.94625	4.28929	2.05223
C	-3.60773	-0.16651	2.84936
C	-3.33511	3.34700	0.15613
P	-3.59593	1.52157	0.59701
H	-3.14219	-4.09816	-0.84126
C	-4.18056	4.31654	0.98119
H	-2.63361	-1.64826	-3.57898
H	-2.17894	-4.14639	-3.71682
H	-3.98034	5.34225	0.62908
C	-3.10242	-2.34818	-2.87765
H	-5.10777	1.73192	4.11432
C	-3.15199	0.56368	-2.27223
C	-5.11937	1.78407	3.01304
H	-3.02838	2.96955	-1.97683
C	-3.67618	3.55969	-1.31979
H	-5.36574	2.81755	2.73822
H	-3.50398	4.62220	-1.55798
C	-4.36796	-2.43769	-0.21014
N	-4.38113	-1.09200	-0.21354
C	-3.17526	-3.73298	-3.50339
H	-4.42527	-0.77276	2.43354
H	-4.11879	-1.96813	-2.69623
H	-5.25952	4.13419	0.85440
H	-3.72043	-4.45666	-2.87920
C	-5.34568	1.09320	0.04616
H	-3.71432	-3.66016	-4.45984
H	-5.93331	1.12663	2.67327
C	-5.49449	-0.39610	0.10003
C	-5.50907	-3.15651	0.12748
H	-4.72847	3.34280	-1.55912
H	-5.48528	-4.24674	0.12427
H	-5.39920	1.41082	-1.00804
H	-6.14654	1.60481	0.59464
C	-6.66267	-1.06745	0.45377
C	-6.66638	-2.45986	0.46973
H	-7.55649	-0.49909	0.71248
H	-7.57298	-3.00206	0.74405
O	-3.40404	0.96102	-3.33181
C	0.89904	-3.73171	2.71449
H	1.01359	1.04158	-2.29506
O	-0.12798	0.98651	1.82267
H	1.24131	3.20125	-0.85621
O	1.51852	-1.13690	-0.49408
H	0.82336	0.81278	1.65421
C	1.17691	-2.34510	2.15621
H	1.49211	1.02732	-4.01085
C	1.75687	1.42185	-3.01446
H	1.76771	3.00575	0.82090
H	1.64899	2.51591	-3.06415
C	1.97639	3.54475	-0.11382
H	1.81802	4.62383	0.05364
H	2.53022	-3.00441	0.15890
Ru	2.76648	-0.04139	0.73767
H	2.67561	-1.03155	-2.07911
N	2.60090	-1.98701	1.95836
C	3.23282	-2.92416	1.00403
C	3.19079	1.00164	-2.68368
H	2.99687	-0.79961	-3.83875
H	2.98925	4.01912	-2.61904
C	3.31565	-0.52190	-2.81920
C	3.41729	3.30850	-0.58173
P	3.54254	1.42138	-0.85356
H	3.38858	-3.91959	1.45565
C	3.70547	4.17978	-1.80325
H	4.35562	-1.54072	2.98214
H	2.38435	-0.23237	4.03344
H	3.62357	5.23765	-1.50059
C	3.37597	-1.98434	3.21683
H	3.94360	1.20083	-4.67999
C	3.49418	0.94625	2.09061
C	4.16731	1.62428	-3.68610
H	4.29331	3.15174	1.43832
C	4.38621	3.74278	0.52040
H	4.08475	2.71247	-3.77194
H	4.16501	4.79133	0.78193
C	4.53163	-2.40174	0.44983
N	4.51001	-1.09843	0.14339
C	2.72102	-1.22694	4.35416
H	4.35911	-0.85558	-2.70433
H	3.56550	-3.03025	3.53098
H	4.72349	4.02930	-2.19144
H	1.85839	-1.76843	4.76853
C	5.37414	0.99133	-0.69100
H	3.45166	-1.08927	5.16455
H	5.21502	1.36975	-3.46452
C	5.54851	-0.48094	-0.44195
C	5.65844	-3.17208	0.18390
H	5.43282	3.70979	0.17958
H	5.67600	-4.23157	0.44358
H	5.70147	1.52347	0.21738
H	6.00622	1.33539	-1.52244
C	6.69878	-1.20595	-0.75386
C	6.75075	-2.56054	-0.43242
H	7.54228	-0.71178	-1.23800
H	7.64639	-3.14154	-0.66061
H	0.78527	-0.56025	-0.78993
O	3.92481	1.54918	3.00268
H	-0.18949	-3.84641	2.83096
H	1.35456	-3.90128	3.70334
H	1.23928	-4.53427	2.04175
H	0.71188	-2.20240	1.17126
H	0.74400	-1.57738	2.80962
H	-0.43434	0.98733	-0.21631

Figure 11.5-8 [B-Mono]D_0 (Me Model) Structure and Coordinates

39

Energy: -778002.1873236

O	-0.55505	-2.76423	-0.44723
O	0.12508	-0.53954	-2.02669
C	2.33494	-2.33026	-0.93340
H	2.32532	0.00079	-1.74955
N	2.03471	-1.17743	-0.07897
C	2.56292	0.06056	-0.67376
C	-2.66050	0.70913	-1.96705
C	-3.68291	-0.22283	0.57254
P	-2.13697	0.26299	-0.27867
H	3.65817	0.13929	-0.54726
C	2.57390	-1.37539	1.26528
C	-0.47743	-1.05726	1.74030
C	1.86506	1.29245	-0.16828
N	0.54935	1.13551	0.08192
C	-1.69729	1.88636	0.55815
C	-0.24327	2.19517	0.34859
C	2.46033	2.54481	-0.08112
H	3.52962	2.65191	-0.26713
H	-1.87475	1.70669	1.63369
H	-2.33600	2.73055	0.25599
C	0.29836	3.47682	0.41385
C	1.66531	3.64977	0.21585
H	-0.35016	4.32785	0.62448
H	2.10798	4.64516	0.28014
O	-0.72992	-1.22961	2.86076
H	-3.43464	1.49046	-1.96458
H	-3.04101	-0.20175	-2.45134
H	-1.76103	1.01476	-2.51817
H	-3.45978	-0.44094	1.62671
H	-4.05811	-1.14273	0.10074
H	-4.45366	0.55989	0.50619
H	1.84660	-3.21136	-0.49936
H	3.42719	-2.48162	-1.02251
H	1.87627	-2.14584	-1.91327
H	2.34750	-0.50001	1.89028
H	3.67065	-1.52383	1.23530
H	2.10148	-2.25869	1.71336
Ru	-0.17204	-0.78748	-0.08391
H	-1.30296	-3.07172	0.07743

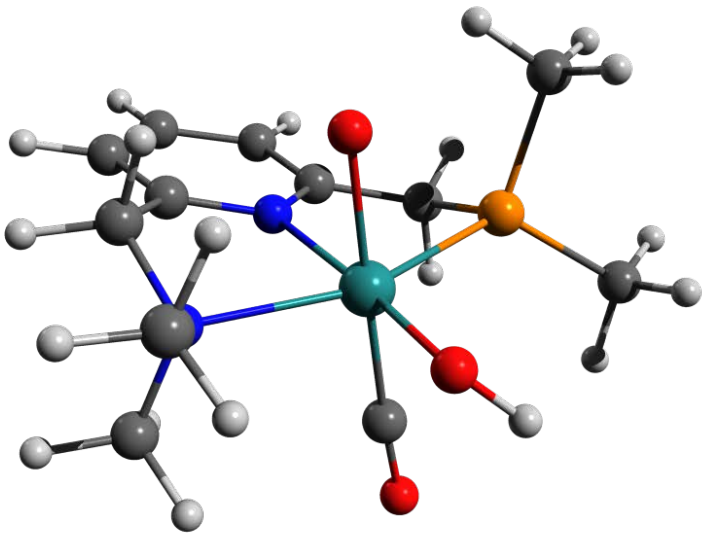

Figure 11.5-9 [B-Mono]D_0 Structure and Coordinates

63

Energy: -975165.8829902

H	-3.59713	-3.37011	1.85732
C	-3.30686	-2.75815	0.99015
H	-4.05420	-2.93520	0.20058
H	-2.30651	-3.08263	0.65924
H	1.49110	-0.73473	2.72708
O	-0.25026	-2.58975	0.68320
H	4.33842	-1.68060	0.66041
O	-0.48413	-0.19782	2.04727
C	-3.23487	-1.31048	1.42488
H	2.87147	0.05390	3.54960
H	-4.22373	-0.93932	1.76129
C	2.52841	-0.39289	2.60092
H	2.86422	-2.66213	0.46270
H	3.17429	-1.25419	2.38812
H	-2.52682	-1.20764	2.26099
C	3.65433	-2.11887	-0.07818
H	4.22969	-2.85168	-0.66789
H	-2.32081	0.92236	1.90782
Ru	-0.39555	-0.61368	0.13394
H	0.70178	1.55765	2.11987
N	-2.70573	-0.40463	0.37971
C	-2.75145	0.97496	0.89198
C	2.59529	0.67933	1.50764
H	2.14556	2.24447	2.90814
H	4.76596	0.33218	-0.95365
C	1.74084	1.87352	1.95171
C	3.06317	-1.07233	-1.02616
P	1.79654	-0.02448	-0.06751
H	-3.78161	1.36308	0.96435
C	4.17182	-0.23927	-1.67502
H	-3.20025	-1.51011	-1.31426
H	-5.43814	-1.02666	-0.23633
H	4.85933	-0.91938	-2.20537
C	-3.41984	-0.51442	-0.90804
H	4.35612	1.64830	2.25763
C	-0.57605	-1.06302	-1.67290
C	4.03188	1.16478	1.32094
H	1.56839	-2.50274	-1.74182
C	2.32624	-1.81575	-2.14048
H	4.73787	0.34781	1.11946
H	3.06007	-2.41065	-2.70890
C	-1.88057	1.90873	0.10674
N	-0.69360	1.38892	-0.26425
C	-4.92463	-0.29089	-0.87206
H	1.77858	2.70973	1.23656
H	-2.95208	0.20869	-1.59418
H	3.77213	0.46010	-2.42482
H	-5.19915	0.71495	-0.51997
C	1.54856	1.47139	-1.17724
H	-5.32498	-0.39766	-1.89143
H	4.12562	1.91569	0.52060
C	0.25002	2.15170	-0.85440
C	-2.18830	3.23851	-0.15518
H	1.83157	-1.13894	-2.85135
H	-3.15904	3.63838	0.13975
H	1.48976	1.05781	-2.19907
H	2.38389	2.18731	-1.16170
C	-0.00188	3.49525	-1.12311
C	-1.23569	4.04003	-0.77988
H	0.76850	4.10418	-1.59729
H	-1.45156	5.08839	-0.99284
O	-0.79262	-1.32801	-2.78212
H	0.34645	-3.05966	0.08963

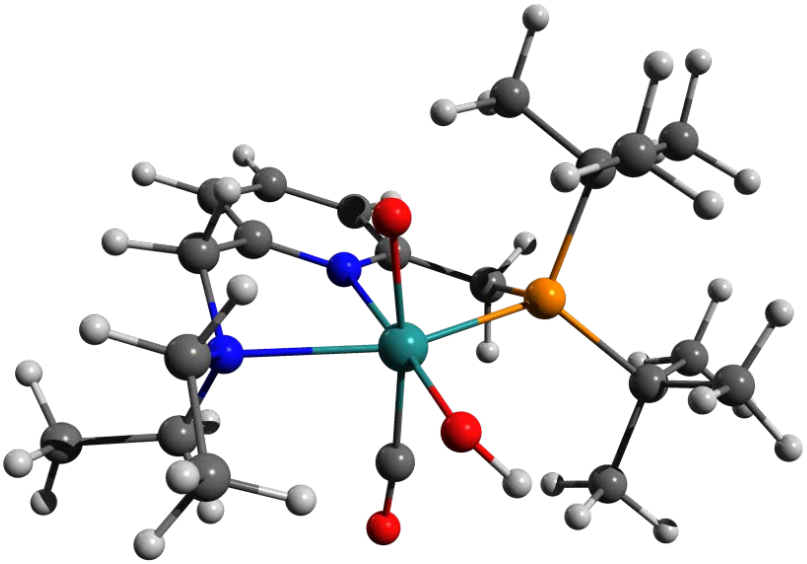

Figure 11.5-10 [B-Mono-Up]D_0 Structure and Coordinates

63

Energy: -975164.6396053

N	-0.74074	1.42138	-0.09733
C	-1.96289	1.88374	0.22032
C	0.17622	2.21737	-0.68254
C	-2.30204	3.21558	0.02029
C	-1.34598	4.07348	-0.52001
C	-0.10169	3.56952	-0.88257
C	-2.88430	0.85097	0.80217
H	-3.30015	3.56986	0.28000
H	-1.57919	5.12778	-0.67888
H	0.65212	4.21228	-1.33854
C	1.44448	1.56307	-1.13985
N	-2.70439	-0.46230	0.15473
H	-3.93071	1.19911	0.74917
H	-2.63964	0.72630	1.86984
H	1.25253	1.19198	-2.16066
P	1.78133	-0.01008	-0.18518
H	2.28303	2.27367	-1.16965
Ru	-0.39601	-0.59869	0.12102
C	-3.20909	-0.43591	-1.23905
C	2.85648	-1.04703	-1.35491
C	-3.36843	-1.49999	0.97491
C	2.78394	0.59230	1.31399
C	1.90070	-1.73018	-2.33764
C	3.55725	-2.14341	-0.55043
C	3.87599	-0.21711	-2.13684
C	1.99413	1.73965	1.95477
C	4.16940	1.11761	0.93685
C	2.92947	-0.53336	2.34160
C	-0.40004	-0.68686	1.97617
O	-0.47562	-0.77910	3.13527
H	-2.68179	0.38306	-1.74960
C	-4.71270	-0.28445	-1.40559
H	-2.83982	-1.34707	-1.72405
H	-2.87188	-1.48262	1.95655
C	-3.26382	-2.88646	0.37557
H	-4.42473	-1.21202	1.14790
O	-0.18170	-2.64843	-0.04358
H	0.14647	-3.01157	0.78796
O	-0.54564	-0.56134	-1.85533
H	-2.21126	-3.09138	0.10780
H	-3.89803	-3.00367	-0.51592
H	-3.60244	-3.62393	1.11892
H	-4.94265	-0.24441	-2.48080
H	-5.10743	0.64145	-0.95834
H	-5.27286	-1.13184	-0.98342
H	2.49969	-2.36903	-3.00935
H	1.34662	-1.00652	-2.95296
H	1.16093	-2.34476	-1.80028
H	4.02159	-2.85217	-1.25567
H	2.83394	-2.70824	0.05660
H	4.35550	-1.75779	0.09962
H	4.42435	-0.89100	-2.81628
H	4.61745	0.28340	-1.50127
H	3.38880	0.54168	-2.76701
H	4.83845	0.31922	0.58911
H	4.63419	1.56882	1.82951
H	4.12758	1.89776	0.16160
H	3.52590	-1.37251	1.96409
H	1.95694	-0.92246	2.66522
H	3.44126	-0.13502	3.23371
H	2.49440	2.03236	2.89242
H	0.96381	1.44847	2.19949
H	1.95863	2.63050	1.31020

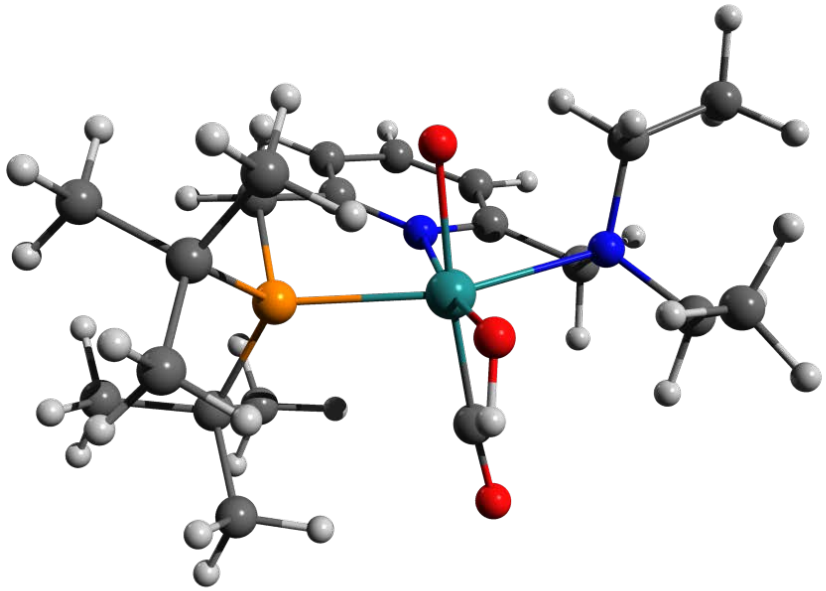

Figure 11.5-11 [B-Trans]T_0 Structure and Coordinates

128

Energy: -1951524.2043341

H	-0.03271	1.60418	4.13717
C	0.93903	1.19294	3.83039
H	1.55757	1.10677	4.73735
H	1.40931	1.90677	3.13456
H	1.46667	1.59848	-2.33918
O	1.96714	2.11966	1.02547
H	3.26370	3.58976	-1.40532
O	1.13721	-0.21512	-0.12088
H	0.67013	2.31304	-0.01713
C	0.70514	-0.13262	3.14136
H	1.65072	1.13562	-4.04736
H	0.23184	-0.85739	3.83074
C	2.20339	1.42983	-3.13929
H	3.78233	3.29263	0.25363
H	2.69252	2.39138	-3.35541
H	0.01209	-0.01986	2.29622
C	4.15143	3.47739	-0.76538
H	4.70769	4.42922	-0.78539
H	0.74442	-1.81454	1.29101
Ru	2.84345	0.41858	0.84464
H	1.84130	-0.99793	-1.75221
N	1.94541	-0.73808	2.59715
C	1.60894	-2.01774	1.94199
C	3.21917	0.33453	-2.80832
H	1.88886	-1.17928	-3.54147
H	4.74593	2.90046	-3.37196
C	2.49751	-1.00907	-2.63714
C	5.06992	2.35683	-1.26636
P	4.03937	0.75614	-1.14019
H	1.31415	-2.78482	2.67687
C	5.56579	2.70422	-2.66978
H	3.29420	0.02463	4.00180
H	1.72024	-1.32990	5.41648
H	6.15948	3.63055	-2.59746
C	2.96490	-0.96123	3.65394
H	3.65865	-0.29009	-4.80620
C	4.23993	0.99765	1.88691
C	4.20926	0.16512	-3.96646
H	6.07936	1.98017	0.66517
C	6.30687	2.25095	-0.37099
H	4.63229	1.10637	-4.32961
H	6.79448	3.23921	-0.34468
C	2.74500	-2.50792	1.09336
N	3.49427	-1.54532	0.52592
C	2.53635	-1.79930	4.84880
H	3.21037	-1.84541	-2.56623
H	3.83516	-1.42327	3.16440
H	6.22003	1.92761	-3.09094
H	2.22104	-2.81646	4.57277
C	5.23608	-0.66838	-0.89074
H	3.39534	-1.89987	5.52898
H	5.03647	-0.52011	-3.72437
C	4.50474	-1.84421	-0.31228
C	3.00870	-3.85068	0.84361
H	7.04318	1.53799	-0.77358
H	2.39588	-4.62062	1.31359
H	5.96418	-0.30988	-0.14538
H	5.79248	-0.94732	-1.79631
C	4.80936	-3.17184	-0.60228
C	4.05194	-4.18314	-0.01677
H	5.62669	-3.40435	-1.28555
H	4.27449	-5.22961	-0.23262
O	5.05375	1.38425	2.62202
C	-0.17527	-3.89764	-1.73467
H	-1.24587	1.94143	1.62104
O	0.05360	2.34163	-0.80701
H	-2.09722	3.65271	-0.87619
O	-1.42466	-0.63826	0.77242
H	-0.74161	1.85095	-0.54158
C	-0.72051	-2.48274	-1.60385
H	-1.71046	2.83297	3.09142
C	-2.00864	2.60120	2.05539
H	-2.73850	2.72199	-2.23269
H	-2.00637	3.54772	1.49496
C	-2.98459	3.51026	-1.50902
H	-3.16278	4.44821	-2.06195
H	-1.89005	-2.72701	0.59986
Ru	-2.72275	-0.16773	-0.79566
H	-2.56150	-0.09991	2.23946
N	-2.17984	-2.34650	-1.40602
C	-2.59716	-3.05718	-0.18043
C	-3.37671	1.92043	2.06136
H	-2.87080	0.75163	3.79098
H	-3.78661	4.67535	0.82229
C	-3.25875	0.56585	2.77370
C	-4.24013	3.16238	-0.70340
P	-3.83908	1.54269	0.24875
H	-2.55567	-4.15280	-0.31104
C	-4.61001	4.36190	0.16717
H	-4.00259	-2.53275	-2.38774
H	-2.33659	-1.32908	-3.95335
H	-4.83577	5.21175	-0.49896
C	-2.96552	-2.86448	-2.54726
H	-4.14001	2.67516	3.91761
C	-3.52292	0.24424	-2.37986
C	-4.38657	2.76361	2.84614
H	-5.27115	2.04492	-2.30541
C	-5.40753	2.92610	-1.66678
H	-4.35929	3.82863	2.59535
H	-5.48364	3.80019	-2.33498
C	-3.96012	-2.64603	0.30186
N	-4.22295	-1.33845	0.18289
C	-2.48161	-2.41610	-3.91157
H	-4.24057	0.07946	2.89004
H	-2.97449	-3.97228	-2.50949
H	-5.50385	4.17952	0.78007
H	-1.54096	-2.90786	-4.19977
C	-5.50898	0.68212	0.44494
H	-3.23887	-2.67937	-4.66455
H	-5.42152	2.40630	2.72913
C	-5.34408	-0.79136	0.67597
C	-4.86654	-3.49958	0.92281
H	-6.36742	2.84197	-1.13418
H	-4.65076	-4.56583	1.00540
H	-6.00520	0.80826	-0.53016
H	-6.16164	1.13571	1.20551
C	-6.28211	-1.59085	1.33036
C	-6.03973	-2.95704	1.44578
H	-7.19098	-1.14560	1.73742
H	-6.76658	-3.60086	1.94491
H	-0.51848	-0.41630	0.47013
O	-3.98373	0.48462	-3.43393
H	0.91129	-3.83865	-1.90240
H	-0.61188	-4.45486	-2.57866
H	-0.32861	-4.49142	-0.82007
H	-0.24340	-1.96131	-0.76500
H	-0.46742	-1.89627	-2.49584
H	0.80147	0.56698	-0.59067

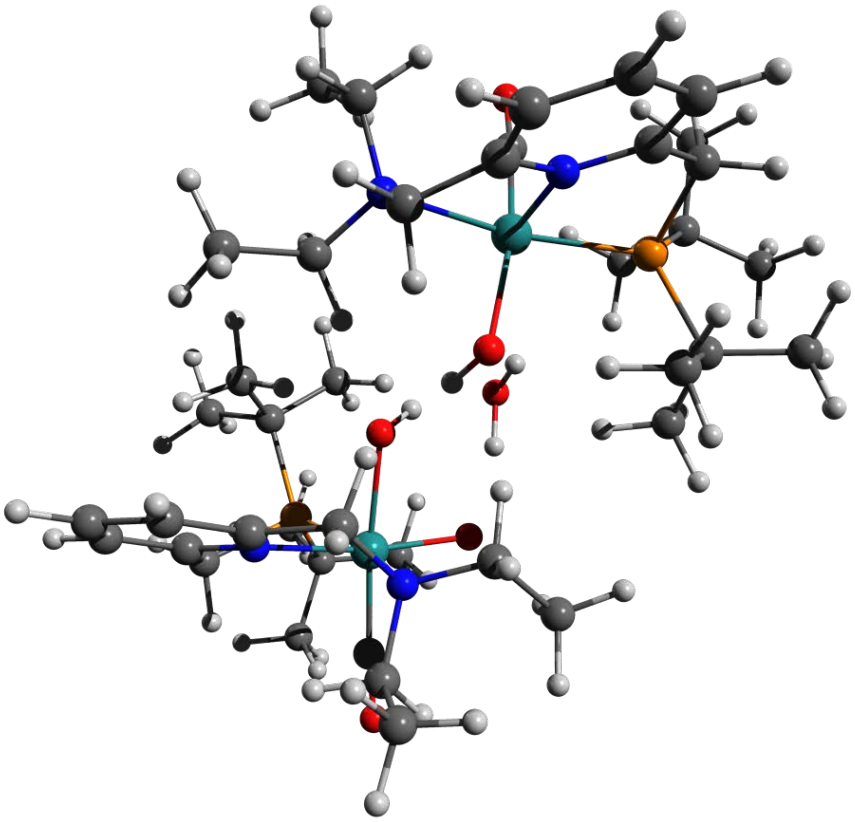

Figure 11.5-12 [B-Mono-Trans]D_0 Structure and Coordinates

63

Energy: -975172.0784791

H	-3.52147	-3.33180	1.91476
C	-3.21273	-2.73924	1.04103
H	-3.90599	-2.97992	0.22015
H	-2.19116	-3.04829	0.76397
H	1.93826	-0.69328	2.69178
O	-0.16459	-2.37754	0.90223
H	2.96531	-2.60730	0.75502
O	-0.51143	-0.09534	2.16923
C	-3.22818	-1.27357	1.41611
H	3.26996	0.29760	3.34665
H	-4.25213	-0.93762	1.66951
C	2.88237	-0.19169	2.43768
H	1.61419	-2.86521	-0.35016
H	3.61834	-0.94831	2.12774
H	-2.58714	-1.09775	2.29149
C	2.68130	-2.59912	-0.30746
H	3.27596	-3.37305	-0.82088
H	-2.30473	0.98017	1.86228
Ru	-0.40986	-0.62255	0.17304
H	0.70035	1.43941	2.15670
N	-2.67307	-0.38667	0.36774
C	-2.74464	1.00794	0.85003
C	2.64564	0.86733	1.36016
H	2.10188	2.34881	2.81099
H	4.81260	-0.98398	0.21233
C	1.66058	1.91369	1.89823
C	2.97237	-1.24134	-0.95698
P	1.80265	0.00325	-0.10829
H	-3.78248	1.37546	0.90262
C	4.46192	-0.92727	-0.82616
H	-3.12810	-1.53856	-1.31205
H	-5.39232	-1.04930	-0.30824
H	5.02152	-1.68584	-1.39840
C	-3.35946	-0.53418	-0.93590
H	4.21857	2.22703	1.87501
C	-0.54036	-1.26267	-1.54368
C	3.94788	1.59477	1.01331
H	1.59523	-1.50593	-2.66402
C	2.65159	-1.30784	-2.45228
H	4.79263	0.92558	0.82327
H	3.22919	-2.13934	-2.88826
C	-1.88127	1.92541	0.03882
N	-0.70686	1.38778	-0.33782
C	-4.86498	-0.31800	-0.93794
H	1.51175	2.74169	1.18775
H	-2.87726	0.17266	-1.62817
H	4.72653	0.05722	-1.23858
H	-5.15359	0.69064	-0.60641
C	1.50175	1.40498	-1.31722
H	-5.23715	-0.44030	-1.96609
H	3.83783	2.26939	0.14977
C	0.23022	2.12364	-0.96564
C	-2.18126	3.25278	-0.24505
H	2.95743	-0.39133	-2.98035
H	-3.14183	3.67075	0.05806
H	1.36662	0.92202	-2.29851
H	2.34420	2.10582	-1.40654
C	-0.00850	3.46423	-1.25873
C	-1.22962	4.03010	-0.90145
H	0.75780	4.05357	-1.76333
H	-1.43685	5.07689	-1.13027
O	-0.71029	-1.72257	-2.59914
H	-0.30740	-0.97807	2.52158

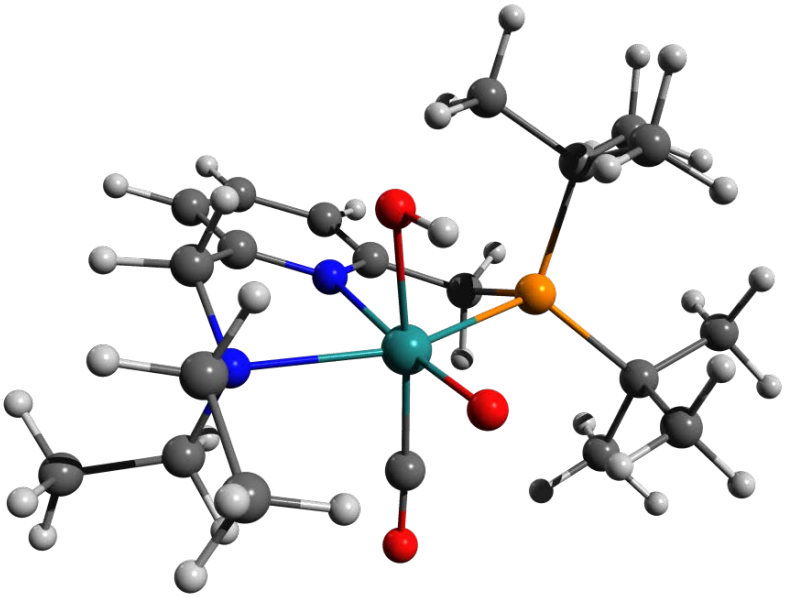

Figure 11.5-13 [B-Mono-Trans-Up]D_0 Structure and Coordinates

63

Energy: -975173.7263503

N	-0.73550	1.42125	-0.02208
C	-1.96750	1.86456	0.28053
C	0.17340	2.23170	-0.59528
C	-2.32652	3.19045	0.08017
C	-1.37539	4.06578	-0.44217
C	-0.11894	3.58115	-0.79053
C	-2.86501	0.81117	0.85662
H	-3.33302	3.52853	0.32880
H	-1.62190	5.11719	-0.59960
H	0.63046	4.23614	-1.23640
C	1.44263	1.58998	-1.06790
N	-2.69846	-0.48240	0.16027
H	-3.91549	1.14707	0.85267
H	-2.57625	0.65027	1.90818
H	1.23589	1.24028	-2.09463
P	1.78869	-0.00874	-0.17117
H	2.28334	2.29787	-1.08076
Ru	-0.41448	-0.64096	0.07272
C	-3.25948	-0.42483	-1.21093
C	2.95262	-0.96472	-1.33095
C	-3.33235	-1.54129	0.98082
C	2.72034	0.54474	1.39552
C	2.10182	-1.66971	-2.38906
C	3.68224	-2.04466	-0.52984
C	3.95300	-0.04857	-2.03970
C	1.85805	1.61627	2.07491
C	4.08721	1.16239	1.09591
C	2.89745	-0.62801	2.36501
C	-0.39102	-0.90857	1.88917
O	-0.43996	-1.10599	3.03685
H	-2.69139	0.34337	-1.75061
C	-4.75996	-0.20438	-1.31443
H	-2.97355	-1.36336	-1.70059
H	-2.84433	-1.50672	1.96523
C	-3.19827	-2.93071	0.39736
H	-4.39647	-1.28329	1.14499
O	-0.22382	-2.50500	-0.32104
O	-0.53886	-0.35007	-1.97302
H	-2.14096	-3.15136	0.17157
H	-3.79382	-3.05995	-0.51852
H	-3.56282	-3.66199	1.13397
H	-5.03187	-0.17514	-2.38023
H	-5.08940	0.75050	-0.87617
H	-5.34650	-1.01228	-0.85134
H	2.78023	-2.24866	-3.03846
H	1.53741	-0.95722	-3.00423
H	1.37671	-2.35037	-1.91752
H	4.20178	-2.71174	-1.23693
H	2.97485	-2.65965	0.04710
H	4.44129	-1.63469	0.15033
H	4.59219	-0.66907	-2.68980
H	4.61277	0.49757	-1.35440
H	3.44634	0.67926	-2.69033
H	4.80829	0.42454	0.71985
H	4.50075	1.57465	2.03148
H	4.02741	1.99115	0.37408
H	3.61500	-1.37036	1.99704
H	1.95320	-1.14306	2.57572
H	3.28477	-0.23823	3.32116
H	2.32646	1.88437	3.03586
H	0.83963	1.26333	2.28304
H	1.78947	2.53610	1.47544
H	-0.52085	-1.27160	-2.26913

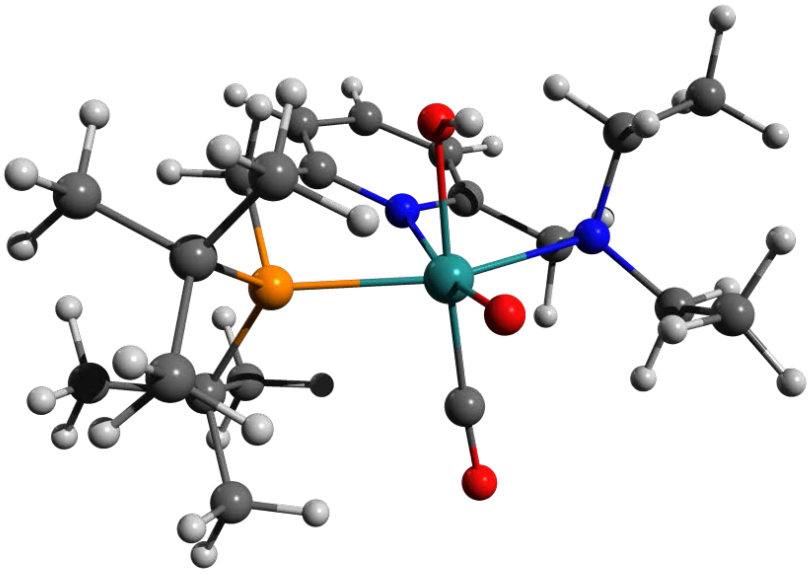

Figure 11.5-14 [B-Alt]T_0 Structure and Coordinates

62

Energy: -974727.8788646

H	-3.37170	-3.45409	1.93521
C	-3.14617	-2.83166	1.05673
H	-3.89627	-3.06852	0.28600
H	-2.14678	-3.11364	0.68908
H	1.43283	-0.73896	2.71410
O	0.00504	-2.50545	0.26301
H	4.24011	-1.78082	0.62515
O	-0.44643	-0.21944	1.93866
C	-3.15723	-1.37684	1.47382
H	2.86230	-0.05299	3.56056
H	-4.15576	-1.07734	1.84882
C	2.49277	-0.45756	2.60301
H	2.72915	-2.70038	0.34332
H	3.09225	-1.34501	2.36268
H	-2.41870	-1.21361	2.27597
C	3.55747	-2.16404	-0.14512
H	4.11907	-2.88988	-0.75579
H	-2.27115	0.85962	1.90665
Ru	-0.35462	-0.69712	0.13791
H	0.71569	1.51588	2.12337
N	-2.72905	-0.45400	0.40380
C	-2.76769	0.92147	0.91974
C	2.60744	0.64126	1.54098
H	2.14954	2.16794	2.97809
H	4.79589	0.24930	-0.92510
C	1.76287	1.83665	1.99980
C	3.02434	-1.06043	-1.06208
P	1.82004	0.00258	-0.05920
H	-3.79654	1.30265	1.03468
C	4.16657	-0.24589	-1.67315
H	-3.23597	-1.56796	-1.28232
H	-5.44523	-1.22885	-0.10792
H	4.81250	-0.92768	-2.25088
C	-3.48927	-0.59015	-0.84988
H	4.38508	1.54949	2.32069
C	-0.62707	-0.88215	-1.78209
C	4.05739	1.09118	1.37284
H	1.45359	-2.38214	-1.79420
C	2.24643	-1.73425	-2.19388
H	4.74174	0.25774	1.16261
H	2.95067	-2.35439	-2.77279
C	-1.92243	1.87476	0.12878
N	-0.71947	1.39723	-0.22866
C	-5.00080	-0.44809	-0.74224
H	1.83617	2.69550	1.31409
H	-3.09450	0.16548	-1.54675
H	3.79683	0.51719	-2.37522
H	-5.30680	0.53018	-0.34161
C	1.53853	1.52825	-1.10810
H	-5.44435	-0.54324	-1.74477
H	4.17855	1.85301	0.58630
C	0.21961	2.17956	-0.78374
C	-2.25559	3.20258	-0.12104
H	1.80126	-1.01006	-2.89205
H	-3.23994	3.57988	0.15842
H	1.51330	1.16638	-2.15038
H	2.36129	2.25550	-1.03714
C	-0.04789	3.52524	-1.03064
C	-1.30354	4.03277	-0.70786
H	0.71958	4.16173	-1.47237
H	-1.53725	5.08026	-0.90722
O	-0.88592	-0.86035	-2.90796

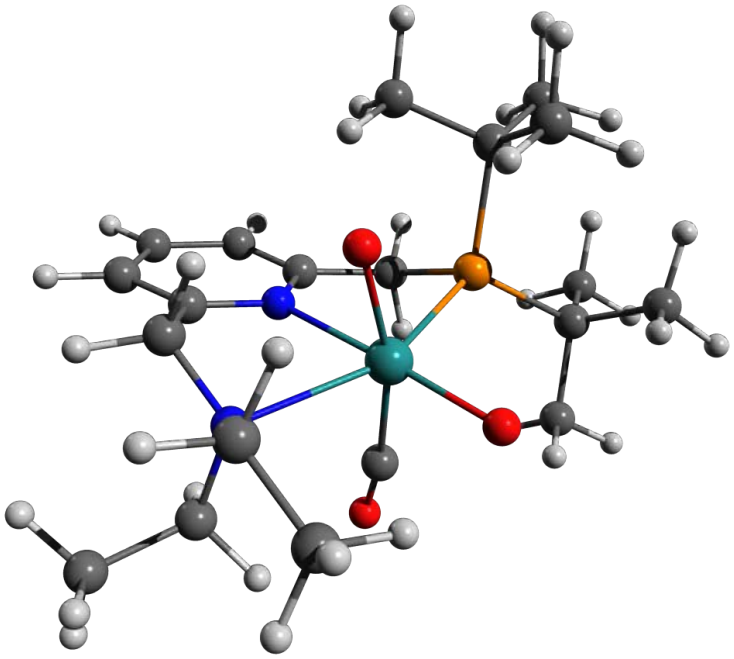

Figure 11.5-15 [BC] D_1/D_o MECI Structure and Coordinates

39
-5668.6564319599938

O	-0.34914799	-2.36258133	-2.38144151
O	0.11685657	-0.82199044	-2.03587137
C	2.45972115	-2.48770293	-0.59692125
H	2.47961778	-0.22805005	-1.63105341
N	2.10379531	-1.25231934	0.14255947
C	2.62880606	-0.06033524	-0.57055869
C	-2.95592546	0.75139328	-1.79018937
C	-3.85195267	-0.02730160	0.89974336
P	-2.30795928	0.27308186	-0.10621931
H	3.69309868	0.06167002	-0.37783977
C	2.62840602	-1.30970376	1.52619968
C	-0.41490170	-1.04519197	2.19364736
C	1.88732904	1.20543682	-0.20269598
N	0.57933910	1.07344928	0.06366621
C	-1.66417890	1.89964300	0.62849087
C	-0.20953457	2.14595474	0.30032474
C	2.47868580	2.46568668	-0.22235894
H	3.52977925	2.55859074	-0.42706967
H	-1.75784807	1.78995768	1.70762753
H	-2.26840551	2.74654963	0.32032961
C	0.34078846	3.42118238	0.26751214
C	1.70205995	3.57535527	0.01007743
H	-0.28345471	4.27631644	0.45043994
H	2.13906704	4.55889235	-0.00585560
O	-0.73061464	-1.74610669	3.13055667
H	-3.67933575	1.55973355	-1.72787910
H	-3.42495100	-0.11461877	-2.24627638
H	-2.12184913	1.04499984	-2.41770806
H	-3.57230091	-0.26896885	1.91967123
H	-4.38840515	-0.87507903	0.48484844
H	-4.50670963	0.83997556	0.89817174
H	2.07210958	-3.34198547	-0.05431959
H	3.54399273	-2.58737731	-0.68353774
H	2.00477094	-2.45857026	-1.57612531
H	2.34624449	-0.41525499	2.06620993
H	3.71628435	-1.40166085	1.51688219
H	2.20065294	-2.16034732	2.03867858
Ru	-0.11705731	-0.88144683	0.05896810
H	-0.69487285	-2.18311611	-3.27277416

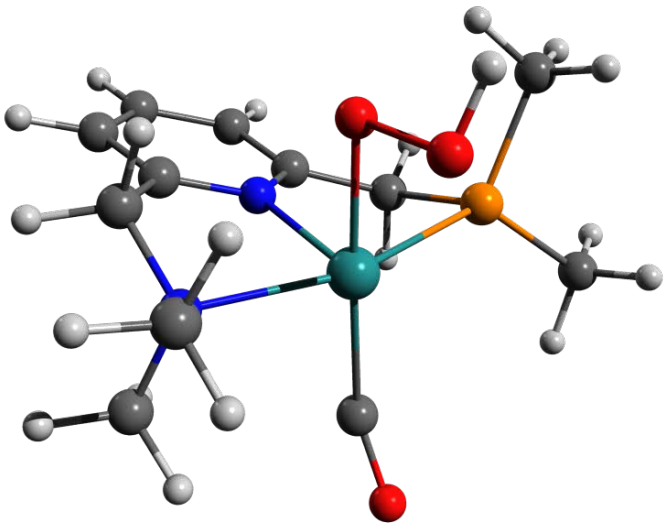

Figure 11.5-16 [BC] D_2/D_1 MECI Structure and Coordinates

39
-5668.6347902092621

O	-0.43728033	-2.88986880	-1.22059513
O	0.01072006	-1.15926324	-2.16057615
C	2.54759821	-2.43747772	-0.70919219
H	2.44612775	-0.14249022	-1.70345216
N	2.12487170	-1.23114238	0.04303850
C	2.62047055	-0.00886298	-0.64061489
C	-2.87559717	0.87962919	-1.85668339
C	-3.87797477	-0.02746943	0.75622607
P	-2.29420613	0.29809104	-0.17808649
H	3.68994019	0.11231407	-0.47556600
C	2.63446526	-1.29572540	1.43245850
C	-0.42517600	-1.11796295	2.03526966
C	1.88531427	1.24155372	-0.20809201
N	0.57880933	1.09855615	0.05344743
C	-1.66441087	1.88021247	0.65687480
C	-0.21056753	2.15434403	0.34797870
C	2.47760799	2.50106027	-0.16125789
H	3.52818477	2.60713109	-0.36260372
H	-1.76355295	1.70866859	1.72754258
H	-2.27528270	2.73776658	0.39383644
C	0.33884029	3.42996022	0.38761050
C	1.70049336	3.59590110	0.13645007
H	-0.28294042	4.27462591	0.62127536
H	2.13843195	4.57847672	0.17568621
O	-0.76941542	-1.65784233	3.06345115
H	-3.61280414	1.67336524	-1.77222999
H	-3.30868937	0.04220119	-2.39389968
H	-2.02276168	1.22893868	-2.42838256
H	-3.63710698	-0.33324758	1.76890258
H	-4.41890407	-0.83703111	0.27598941
H	-4.51302617	0.85388025	0.78345248
H	2.17775313	-3.31465047	-0.19503086
H	3.63727585	-2.48753836	-0.76820659
H	2.11698942	-2.41043829	-1.69912923
H	2.31779191	-0.42179048	1.98604882
H	3.72491453	-1.35349895	1.43491293
H	2.22794279	-2.16974797	1.92250448
Ru	-0.11712086	-0.90963409	-0.04038537
H	-1.23425376	-2.88666281	-1.78515039

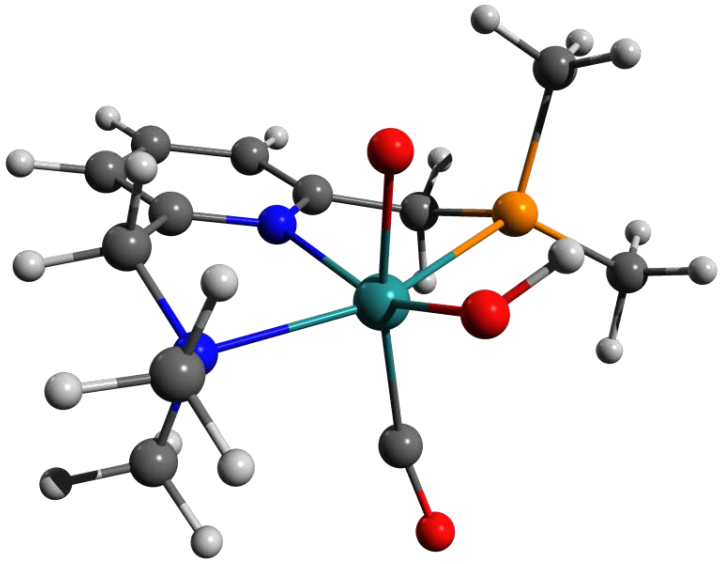

Figure 11.5-17 [C]T_0 Structure and Coordinates

128

Energy: -1951476.7711256

H	-0.89663	2.64296	3.71461
C	-1.82051	2.11644	3.43322
H	-2.52055	2.20160	4.27864
H	-1.56165	1.05757	3.29041
H	-0.28768	-1.17047	-1.92357
O	-1.54793	1.14940	-0.36805
H	-0.46505	-3.21252	-0.62748
O	-0.38495	1.09269	0.48860
H	-1.30571	-1.13414	2.37114
C	-2.35690	2.72304	2.15547
H	-0.42762	-1.22931	-3.69580
H	-2.65393	3.77688	2.32440
C	-0.84201	-1.63173	-2.75572
H	-1.18192	-2.88659	0.96029
H	-0.63509	-2.71240	-2.75244
H	-1.57419	2.71034	1.38621
C	-1.23079	-3.54977	0.08471
H	-0.97429	-4.57457	0.40376
H	-3.02154	2.81209	-0.24934
Ru	-2.93506	-0.05255	0.62261
H	-2.02696	0.77702	-2.20712
N	-3.49882	1.98143	1.57545
C	-3.93458	2.70522	0.36143
C	-2.34021	-1.32858	-2.71150
H	-2.10229	0.40060	-3.95847
H	-1.91428	-4.32214	-2.46486
C	-2.53641	0.17115	-2.96995
C	-2.63204	-3.54713	-0.53522
P	-3.01159	-1.72473	-0.96046
H	-4.32824	3.70825	0.59832
C	-2.68172	-4.52591	-1.70733
H	-4.26739	1.16253	3.33244
H	-4.46718	3.66488	3.69854
H	-2.49882	-5.54360	-1.32226
C	-4.62093	1.81899	2.52745
H	-2.60217	-1.77874	-4.79210
C	-3.82632	-1.03527	1.88254
C	-3.06671	-2.07353	-3.83578
H	-3.68005	-3.38462	1.39545
C	-3.62992	-4.03671	0.51621
H	-3.00493	-3.16488	-3.76707
H	-3.30884	-5.03384	0.86118
C	-4.92528	1.91027	-0.43937
N	-4.60825	0.61301	-0.54372
C	-5.20538	3.09470	3.11539
H	-3.60002	0.44820	-3.01407
H	-5.40405	1.25428	2.00043
H	-3.66651	-4.53633	-2.19830
H	-5.62643	3.76339	2.34944
C	-4.87492	-1.67125	-1.24538
H	-6.02607	2.82596	3.79731
H	-4.12726	-1.78721	-3.89992
C	-5.34574	-0.24586	-1.26668
C	-6.04579	2.42206	-1.08448
H	-4.64439	-4.15039	0.10438
H	-6.29998	3.47896	-0.99280
H	-5.30252	-2.14906	-0.34836
H	-5.22703	-2.22986	-2.12386
C	-6.47205	0.21034	-1.95158
C	-6.82062	1.55588	-1.85653
H	-7.06783	-0.48277	-2.54710
H	-7.70165	1.92993	-2.38145
O	-4.36685	-1.59430	2.76199
C	2.25167	-4.29309	2.27755
H	0.39583	1.33942	-1.78486
O	-0.36653	-0.90591	2.48840
H	0.73781	3.27401	-0.09012
O	1.22609	-0.75221	-0.35429
H	-0.31008	-0.13011	1.88696
C	2.07281	-2.87484	1.75462
H	0.50681	1.61081	-3.53587
C	0.94319	1.88673	-2.56096
H	1.64615	2.93677	1.37694
H	0.75294	2.95908	-2.41240
C	1.58882	3.61533	0.51389
H	1.38245	4.63756	0.87464
H	3.15971	-2.92964	-0.49344
Ru	2.95689	0.02827	0.59441
H	2.12087	-0.58001	-2.18738
N	3.30918	-2.12648	1.41908
C	3.95399	-2.77327	0.25460
C	2.43551	1.55263	-2.57945
H	2.13359	-0.10388	-3.91191
H	2.01166	4.50714	-2.06629
C	2.60575	0.06800	-2.92953
C	2.90834	3.61726	-0.26354
P	3.17228	1.81394	-0.83471
H	4.37478	-3.75778	0.52349
C	2.85567	4.65771	-1.38144
H	5.09599	-1.45939	2.25320
H	3.06137	-0.67203	3.66314
H	2.72919	5.65276	-0.92212
C	4.25634	-2.10181	2.55628
H	2.66689	2.10290	-4.63927
C	3.93524	0.88083	1.86610
C	3.13950	2.35789	-3.67561
H	4.19371	3.31580	1.50469
C	4.03763	4.02757	0.68557
H	3.05890	3.44287	-3.55122
H	3.76725	4.99536	1.13992
C	5.01008	-1.92268	-0.38787
N	4.65226	-0.63829	-0.54253
C	3.63809	-1.59024	3.84198
H	3.66631	-0.21033	-3.02644
H	4.66912	-3.11774	2.71260
H	3.78625	4.68653	-1.96801
H	2.96626	-2.32853	4.30224
C	5.01901	1.67387	-1.14702
H	4.43318	-1.35802	4.56463
H	4.20379	2.09394	-3.76710
C	5.47119	0.24205	-1.14904
C	6.23062	-2.39505	-0.85291
H	4.99148	4.17700	0.15630
H	6.50582	-3.44076	-0.70779
H	5.48192	2.15371	-0.26885
H	5.37597	2.21375	-2.03570
C	6.69276	-0.17940	-1.67161
C	7.07707	-1.50981	-1.52099
H	7.34110	0.53679	-2.17869
H	8.03652	-1.85275	-1.91186
H	0.79995	-1.32491	0.29707
O	4.54114	1.39186	2.73121
H	1.25379	-4.72684	2.44173
H	2.78425	-4.33160	3.23914
H	2.77813	-4.94998	1.56809
H	1.48695	-2.91660	0.82732
H	1.48877	-2.26647	2.45624
H	0.21945	0.42705	0.02318

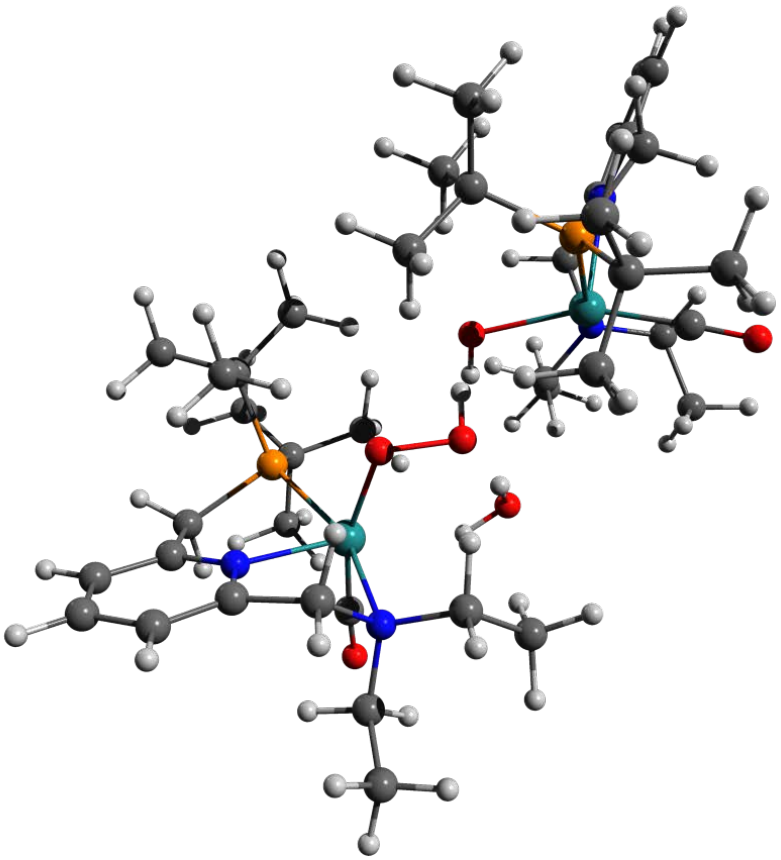

Figure 11.5-18 [C-Mono]D_0 Structure and Coordinates

63

Energy: -975022.8334593

H	-3.38754	-3.53397	1.53840
C	-3.08449	-2.85544	0.72800
H	-3.69964	-3.09181	-0.15375
H	-2.02893	-3.06009	0.48536
H	1.99577	-1.06227	2.50906
O	-0.60729	-0.32762	2.13706
H	2.91476	-2.67415	0.32376
O	-0.29406	-1.59179	2.77994
C	-3.23558	-1.42286	1.19263
H	3.29360	-0.11419	3.30022
H	-4.29666	-1.18668	1.40319
C	2.92046	-0.49241	2.33282
H	1.67766	-2.81774	-0.93524
H	3.68266	-1.17982	1.93491
H	-2.65945	-1.27479	2.11627
C	2.72113	-2.52891	-0.74944
H	3.38511	-3.20716	-1.31153
H	-2.40630	0.82036	1.83739
Ru	-0.40306	-0.64584	0.07794
H	0.71185	1.15314	2.25711
N	-2.68196	-0.44490	0.23274
C	-2.79962	0.91046	0.81070
C	2.66361	0.68570	1.39125
H	2.11002	1.99137	3.00737
H	4.82850	-0.98794	0.00830
C	1.67173	1.65167	2.05304
C	2.98786	-1.08366	-1.18558
P	1.78598	-0.00807	-0.15417
H	-3.84706	1.25313	0.85767
C	4.47434	-0.77937	-1.00993
H	-3.05069	-1.46953	-1.54924
H	-5.36112	-1.12644	-0.59265
H	5.04465	-1.43274	-1.69173
C	-3.32297	-0.50644	-1.09993
H	4.21925	1.99983	2.06831
C	-0.46669	-1.34241	-1.60788
C	3.95614	1.46644	1.13930
H	1.60134	-1.06715	-2.90517
C	2.66553	-0.93612	-2.67536
H	4.80978	0.83385	0.87683
H	3.21495	-1.71607	-3.22845
C	-1.93606	1.91036	0.09217
N	-0.72433	1.44206	-0.24299
C	-4.83357	-0.32937	-1.13733
H	1.50488	2.55053	1.43893
H	-2.83484	0.26308	-1.71691
H	4.72459	0.26002	-1.26605
H	-5.16291	0.63819	-0.72947
C	1.49998	1.54859	-1.18068
H	-5.16880	-0.37078	-2.18449
H	3.83995	2.23299	0.35738
C	0.20761	2.22244	-0.81205
C	-2.28018	3.23402	-0.15629
H	3.00074	0.03562	-3.06956
H	-3.27064	3.60548	0.11039
H	1.39644	1.18659	-2.21609
H	2.33907	2.26030	-1.16633
C	-0.06943	3.56719	-1.06201
C	-1.32544	4.07116	-0.73425
H	0.68993	4.20635	-1.51470
H	-1.56279	5.11805	-0.93256
O	-0.59256	-1.84912	-2.65857
H	0.00586	-1.27580	3.64525

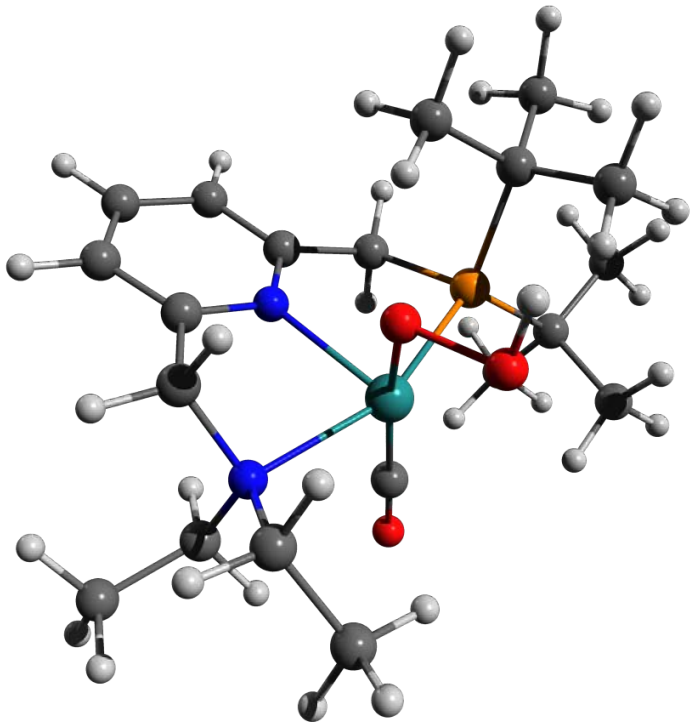

Figure 11.5-19 [C-Mono]D_0 (Me Model) Structure and Coordinates

39

O	-0.04819	-2.01605	-2.47646
O	0.05667	-0.67749	-1.94135
C	2.39625	-2.47917	-0.55239
H	2.24729	-0.24392	-1.65512
N	2.00393	-1.24720	0.14012
C	2.52464	-0.08266	-0.60105
C	-2.77035	0.64955	-1.70216
C	-3.70765	-0.11600	0.92180
P	-2.17257	0.20656	-0.02668
H	3.62423	-0.01324	-0.50776
C	2.53779	-1.24181	1.50431
C	-0.59321	-1.34333	1.86168
C	1.86066	1.20556	-0.19696
N	0.56759	1.08784	0.13363
C	-1.63830	1.86266	0.69978
C	-0.20747	2.16167	0.35840
C	2.46680	2.45591	-0.26299
H	3.52394	2.54289	-0.51795
H	-1.71414	1.71764	1.79252
H	-2.30447	2.69633	0.42805
C	0.33418	3.44392	0.27597
C	1.68706	3.58600	-0.02315
H	-0.29557	4.31699	0.45222
H	2.13311	4.58084	-0.07783
O	-0.87447	-1.61922	2.96363
H	-3.41804	1.53889	-1.69206
H	-3.33170	-0.20422	-2.11033
H	-1.88169	0.80270	-2.33215
H	-3.43984	-0.33107	1.96620
H	-4.19367	-1.00886	0.50298
H	-4.40554	0.73438	0.87989
H	2.04731	-3.33768	0.03619
H	3.49709	-2.54163	-0.66122
H	1.90799	-2.50833	-1.53414
H	2.24730	-0.31163	2.01051
H	3.64237	-1.32363	1.49550
H	2.11572	-2.08513	2.06483
Ru	-0.23290	-0.90538	0.11456
H	-1.00870	-2.14837	-2.48718

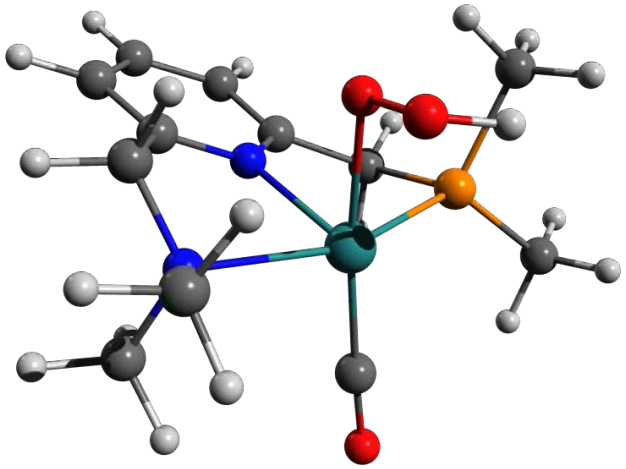

Figure 11.5-20 TS-[CD]T_0 Structure and Coordinates

128

Energy: -1951458.7937574

H	-1.35171	-0.17838	-4.75676
C	-2.22120	-0.15365	-4.08357
H	-3.12446	-0.09082	-4.70942
H	-2.13874	0.75901	-3.47388
H	-0.31864	1.26165	1.25622
O	-1.25235	-0.74231	-0.30395
H	-2.04379	3.71009	0.57254
O	-0.24646	-0.24838	-1.03991
H	-1.89038	2.23946	-1.47961
C	-2.19157	-1.38740	-3.20833
H	0.17655	1.42283	2.96913
H	-2.24584	-2.30644	-3.82265
C	-0.64075	1.60463	2.25074
H	-3.45162	3.48734	-0.48476
H	-0.79077	2.69402	2.21027
H	-1.24235	-1.41623	-2.65706
C	-3.13659	3.81978	0.51332
H	-3.37821	4.89164	0.60732
H	-2.03679	-2.65041	-1.06099
Ru	-3.10641	0.23167	-0.59524
H	-1.38113	-0.99773	1.65748
N	-3.26666	-1.41876	-2.18875
C	-3.09411	-2.63830	-1.37028
C	-1.88698	0.85737	2.72225
H	-0.74066	-0.85900	3.31285
H	-2.51385	3.83009	3.15775
C	-1.61501	-0.65250	2.67313
C	-3.86404	3.04233	1.61597
P	-3.27352	1.22443	1.46890
H	-3.29959	-3.55335	-1.95024
C	-3.58768	3.72103	2.95639
H	-4.75083	-0.40596	-3.25483
H	-4.29652	-2.41845	-4.70182
H	-4.01674	4.73650	2.92227
C	-4.62145	-1.39247	-2.79362
H	-1.44604	0.71039	4.81549
C	-4.52409	1.17809	-1.24801
C	-2.20036	1.20480	4.18122
H	-5.69123	2.59253	0.45922
C	-5.37387	3.11646	1.36930
H	-2.15025	2.27605	4.39759
H	-5.65277	4.17603	1.24528
C	-3.91805	-2.60747	-0.11301
N	-4.00636	-1.40192	0.46698
C	-4.93926	-2.47766	-3.81136
H	-2.45667	-1.23429	3.08026
H	-5.33710	-1.43361	-1.95907
H	-4.05587	3.19517	3.79998
H	-4.85941	-3.49433	-3.39810
C	-4.69944	0.19101	2.14153
H	-5.97838	-2.34659	-4.14847
H	-3.18328	0.83004	4.50675
C	-4.63802	-1.22213	1.63748
C	-4.49428	-3.72568	0.47983
H	-5.94680	2.72917	2.22569
H	-4.42361	-4.70178	-0.00194
H	-5.60672	0.65085	1.71878
H	-4.79707	0.22148	3.23677
C	-5.21829	-2.30917	2.29179
C	-5.14552	-3.56846	1.70270
H	-5.72485	-2.16529	3.24703
H	-5.60045	-4.42954	2.19587
O	-5.39774	1.77985	-1.74449
C	1.95064	4.78665	-0.60173
H	1.76965	-0.90476	2.80971
O	-1.00918	2.26865	-1.89179
H	0.60556	-2.82294	0.89836
O	2.64867	1.23333	1.58109
H	-0.64410	1.39575	-1.61062
C	1.82668	3.27959	-0.43151
H	2.44368	-1.76675	4.22068
C	2.29765	-1.81390	3.12807
H	0.76110	-2.18235	-0.73635
H	1.65697	-2.68264	2.91340
C	0.98977	-3.05220	-0.10672
H	0.44042	-3.93308	-0.48354
H	3.88465	2.90479	0.89071
Ru	2.74747	0.27612	-0.27792
H	4.03241	0.24109	2.49531
N	2.97292	2.46949	-0.91561
C	4.19078	2.85260	-0.16634
C	3.65643	-1.90891	2.43326
H	4.59850	-0.68745	3.92722
H	2.27417	-4.56489	1.74316
C	4.51053	-0.69577	2.82677
C	2.48685	-3.37191	-0.08686
P	3.34382	-1.78138	0.55157
H	4.57184	3.83524	-0.49309
C	2.71632	-4.63490	0.74062
H	3.99257	1.91376	-2.64356
H	1.46622	1.56247	-3.03246
H	2.21942	-5.47525	0.22639
C	3.22476	2.65136	-2.36265
H	4.74656	-2.97798	3.93849
C	2.63576	-0.38275	-1.96949
C	4.40805	-3.15803	2.90438
H	2.87974	-2.81597	-2.18788
C	2.95820	-3.67481	-1.51198
H	3.79705	-4.06582	2.91717
H	2.31666	-4.47217	-1.92370
C	5.28411	1.82581	-0.23900
N	4.86005	0.55630	-0.19084
C	1.99978	2.49775	-3.23958
H	5.53286	-0.77220	2.42431
H	3.67222	3.65176	-2.52665
H	3.78033	-4.89358	0.83866
H	1.28254	3.31870	-3.10775
C	5.09793	-1.84569	-0.13458
H	2.31440	2.48267	-4.29373
H	5.31141	-3.35708	2.30723
C	5.71662	-0.47646	-0.14568
C	6.64396	2.12100	-0.26229
H	3.99235	-4.05282	-1.53013
H	6.98026	3.15737	-0.31289
H	4.98049	-2.16770	-1.18174
H	5.75382	-2.57682	0.36129
C	7.09210	-0.24426	-0.14126
C	7.55456	1.06756	-0.20547
H	7.78759	-1.08325	-0.09528
H	8.62751	1.26910	-0.21384
H	1.77264	1.05510	1.93407
O	2.50241	-0.76839	-3.06688
H	1.03001	5.25530	-0.22166
H	2.05318	5.09101	-1.65505
H	2.79123	5.21755	-0.03585
H	1.73106	3.00783	0.62859
H	0.92661	2.92047	-0.94485
H	1.08400	0.09696	-0.35469

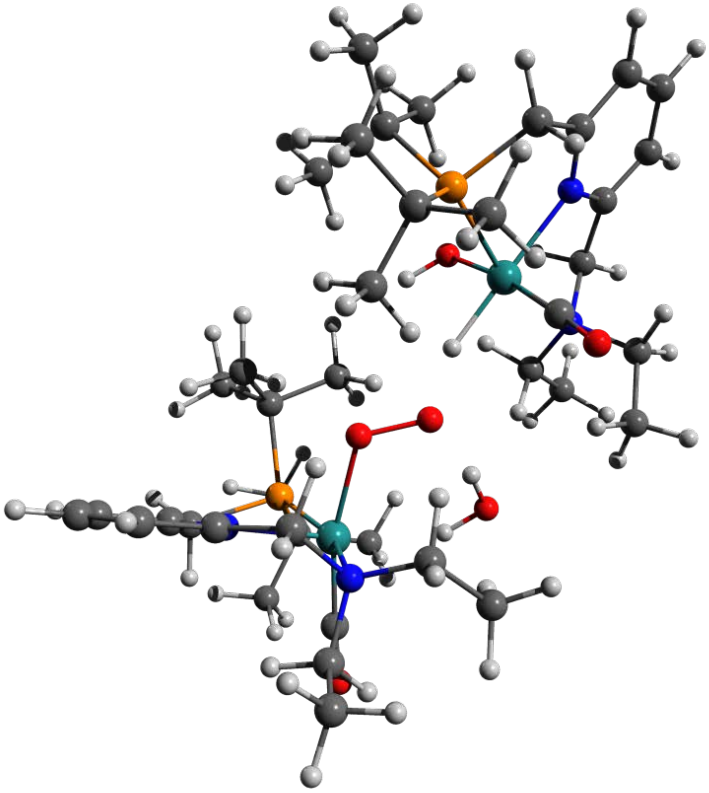

Figure 11.5-21 $[D]T_0$ $[F]S_0$ (Dimer Model) Structure and Coordinates

128

Energy: -1951474.5643316

H	2.21039	-2.23355	-4.32302
C	2.94020	-2.10065	-3.51092
H	3.78217	-2.78102	-3.70912
H	2.44399	-2.39608	-2.57405
H	0.28729	0.69700	0.93450
O	2.00197	0.89968	-1.11563
H	0.78753	-1.87017	2.19783
O	0.91009	0.32922	-1.54821
H	1.65613	-2.28902	-0.30684
C	3.35522	-0.64652	-3.46822
H	-0.28740	1.93394	2.06713
H	3.81547	-0.34125	-4.42738
C	0.39308	1.07378	1.96078
H	2.17595	-2.85811	1.70881
H	0.04202	0.28934	2.64875
H	2.46663	-0.01909	-3.31819
C	1.70714	-2.35054	2.56204
H	1.42251	-3.11900	3.30019
H	3.62475	1.64595	-2.49829
Ru	3.37129	-0.49295	-0.27560
H	2.20172	2.33336	0.26632
N	4.28549	-0.32083	-2.36027
C	4.59308	1.12622	-2.42419
C	1.82021	1.51701	2.27687
H	1.50189	3.46668	1.44084
H	1.06378	-0.50582	4.44736
C	2.22635	2.64419	1.31726
C	2.67215	-1.35764	3.21999
P	2.96471	0.03118	1.93490
H	5.18433	1.37831	-3.32006
C	2.07975	-0.90767	4.55421
H	5.27240	-2.15699	-2.21825
H	5.77660	-1.42642	-4.57931
H	2.01230	-1.78895	5.21372
C	5.53971	-1.11357	-2.42389
H	1.38104	3.07219	3.68524
C	4.29326	-2.00741	0.16757
C	1.90014	2.09943	3.69185
H	4.54301	-2.36849	2.62207
C	3.99571	-2.06566	3.52316
H	1.41175	1.48031	4.44974
H	3.77400	-2.98486	4.09033
C	5.27474	1.61909	-1.17756
N	4.80159	1.08031	-0.04426
C	6.33553	-1.03327	-3.71762
H	3.22071	3.05100	1.55899
H	6.15890	-0.78525	-1.57600
H	2.70644	-0.16287	5.06443
H	6.66552	-0.01184	-3.95952
C	4.66614	0.73279	2.33966
H	7.24174	-1.64741	-3.60772
H	2.93471	2.29472	4.01482
C	5.24957	1.46071	1.16314
C	6.26361	2.59505	-1.14450
H	4.65466	-1.44802	4.15262
H	6.64712	3.02308	-2.07160
H	5.29860	-0.14991	2.52652
H	4.69246	1.35254	3.24800
C	6.22637	2.45204	1.26262
C	6.73620	3.01873	0.09771
H	6.58475	2.76847	2.24304
H	7.50662	3.78970	0.15685
O	4.86915	-3.00676	0.36731
C	-1.97725	-4.45666	1.52802
H	-2.50178	2.18185	2.19599
O	0.83057	-2.38124	-0.81491
H	-1.09111	3.08609	-0.24809
O	-3.05347	-0.36368	1.91451
H	0.67780	-1.44550	-1.07669
C	-1.93640	-3.02562	1.01222
H	-3.38713	3.54642	2.92734
C	-3.08033	3.08788	1.97190
H	-0.98099	1.82862	-1.48757
H	-2.42915	3.80557	1.45027
C	-1.33266	2.85094	-1.29582
H	-0.75920	3.54442	-1.93434
H	-4.12042	-2.21994	1.93269
Ru	-2.98649	-0.33811	-0.18846
H	-4.60200	0.80015	2.14753
N	-3.08682	-2.59868	0.17864
C	-4.34181	-2.68580	0.95879
C	-4.32227	2.72502	1.15835
H	-5.40323	2.20156	2.93768
H	-2.90294	4.90516	-0.44755
C	-5.16594	1.73059	1.96779
C	-2.82692	3.02834	-1.58679
P	-3.73776	1.81492	-0.42011
H	-4.65609	-3.73378	1.10358
C	-3.19232	4.50319	-1.42759
H	-3.99955	-2.90770	-1.66592
H	-1.44430	-2.68958	-2.03879
H	-2.63751	5.07712	-2.18907
C	-3.24244	-3.41453	-1.04746
H	-5.65686	4.23734	1.88606
C	-2.67460	-0.47959	-1.97443
C	-5.18718	3.96793	0.92513
H	-2.91367	1.59427	-3.26355
C	-3.10729	2.65000	-3.04385
H	-4.62460	4.84203	0.58295
H	-2.43663	3.24323	-3.68784
C	-5.45941	-1.89036	0.34516
N	-5.07880	-0.71700	-0.17809
C	-1.97227	-3.62881	-1.84239
H	-6.12566	1.51303	1.47416
H	-3.67063	-4.39812	-0.76872
H	-4.26295	4.69503	-1.58765
H	-1.26561	-4.29481	-1.32963
C	-5.38276	1.41933	-1.25573
H	-2.23230	-4.08566	-2.80909
H	-6.00725	3.78417	0.21399
C	-5.96411	0.15525	-0.68740
C	-6.80155	-2.25763	0.36299
H	-4.13958	2.89557	-3.33875
H	-7.10272	-3.21866	0.78172
H	-5.12461	1.22841	-2.30996
H	-6.11529	2.23989	-1.23913
C	-7.32551	-0.14837	-0.68226
C	-7.74163	-1.36824	-0.15465
H	-8.04567	0.56188	-1.09029
H	-8.80221	-1.62728	-0.14874
H	-2.21835	0.01458	2.20818
O	-2.40941	-0.60536	-3.10682
H	-1.06114	-4.64518	2.10887
H	-2.00388	-5.20251	0.71828
H	-2.83017	-4.64733	2.19805
H	-1.92254	-2.30895	1.84537
H	-1.02934	-2.85403	0.41687
H	-1.41111	-0.09993	-0.07392

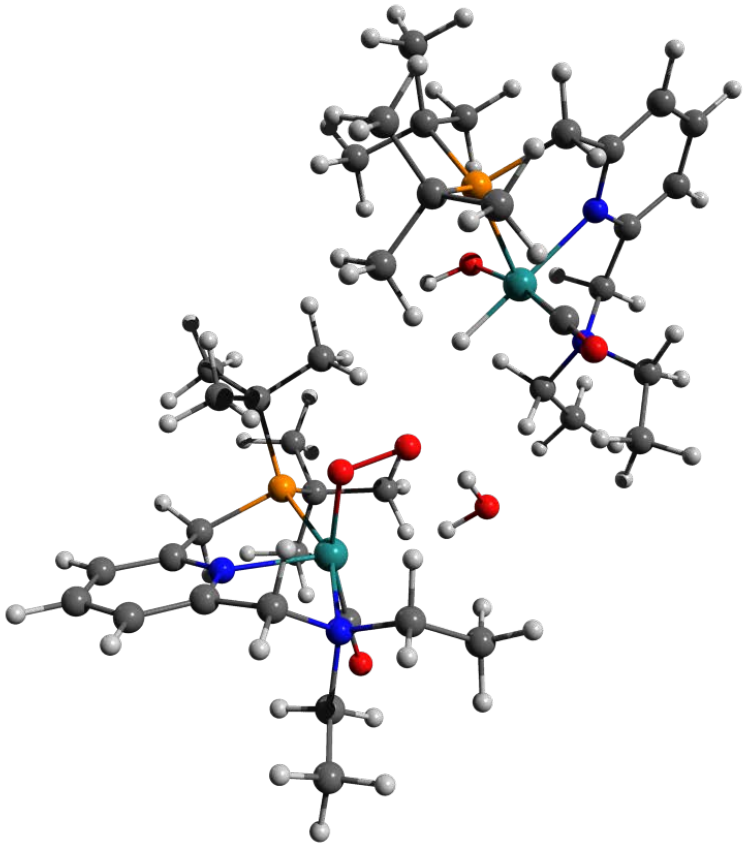

Figure 11.5-22 [D]T_0 Structure and Coordinates

65

Energy: -1022871.1899955

H	-3.38494	-3.31180	1.82737
C	-2.95512	-2.79277	0.95830
H	-3.38208	-3.24852	0.05218
H	-1.86643	-2.95916	0.96163
H	1.90861	-0.67840	2.70800
O	-0.53456	-0.35358	2.07755
H	3.01942	-2.52358	0.85085
O	-0.35394	-1.52334	2.63574
C	-3.25043	-1.31281	1.06133
H	3.09522	0.44848	3.41532
H	-4.34039	-1.12453	1.05618
C	2.80965	-0.08705	2.49421
H	1.90555	-2.89679	-0.47328
H	3.63051	-0.77775	2.24948
H	-2.86486	-0.91811	2.00937
C	2.92191	-2.54757	-0.24458
H	3.64858	-3.27877	-0.63668
H	-2.66408	1.08616	1.35598
Ru	-0.31837	-0.68828	-0.00504
H	0.53186	1.44950	2.04182
N	-2.60517	-0.51691	-0.00635
C	-2.83355	0.92076	0.27621
C	2.56533	0.92876	1.37589
H	1.84035	2.41943	2.74501
H	4.91382	-0.82138	0.45058
C	1.49019	1.92964	1.82129
C	3.19596	-1.17605	-0.87243
P	1.87279	-0.00911	-0.13540
H	-3.88007	1.20620	0.07627
C	4.65112	-0.78951	-0.61501
H	-2.77125	-1.86864	-1.59665
H	-5.17070	-1.52766	-0.94783
H	5.29862	-1.51901	-1.13009
C	-3.12403	-0.85838	-1.35592
H	4.01544	2.38917	1.98578
C	-0.23183	-1.57996	-1.59320
C	3.83591	1.74231	1.11081
H	1.97571	-1.47843	-2.68860
C	3.00900	-1.26566	-2.38964
H	4.73044	1.12740	0.97445
H	3.63245	-2.09289	-2.76752
C	-1.89906	1.81367	-0.48819
N	-0.64961	1.34073	-0.61557
C	-4.63079	-0.78598	-1.55459
H	1.33192	2.72272	1.07485
H	-2.61559	-0.18268	-2.05967
H	4.89859	0.20539	-1.01207
H	-5.05049	0.20694	-1.33435
C	1.64357	1.37017	-1.39287
H	-4.85289	-1.00424	-2.60984
H	3.73636	2.40888	0.24034
C	0.31283	2.05126	-1.22985
C	-2.24178	3.06770	-0.98206
H	3.34686	-0.34867	-2.89655
H	-3.26161	3.43938	-0.87459
H	1.62986	0.85885	-2.36903
H	2.46623	2.10001	-1.42016
C	0.03643	3.32619	-1.72152
C	-1.25326	3.83625	-1.59409
H	0.82291	3.90564	-2.20703
H	-1.49003	4.82932	-1.98022
O	-0.24541	-2.20583	-2.58353
O	-2.15763	1.34600	3.37545
H	-1.45833	0.73127	3.05377
H	-2.60547	0.82846	4.05496

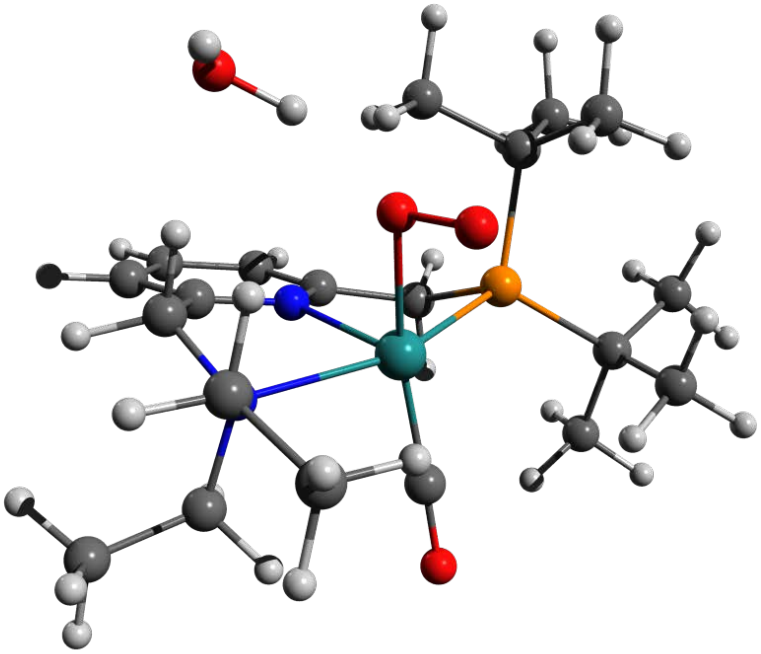

Figure 11.5-23 Scan-[DE]T_0 Geometry 5 Structure and Coordinates

65

Energy: -1022862.3366652

H	-3.52909	3.63066	0.68680
C	-3.14014	2.67577	1.07009
H	-3.70774	2.43297	1.98093
H	-2.08658	2.82131	1.34241
H	1.65759	1.62389	-1.72549
O	-0.13249	4.15116	-1.87917
H	4.21485	1.15428	0.97408
O	1.02322	4.35975	-1.65856
C	-3.28448	1.62227	-0.00542
H	3.21108	1.41790	-2.58285
H	-4.35763	1.46172	-0.23123
C	2.68412	1.24653	-1.62884
H	2.71787	1.87703	1.62409
H	3.19133	1.83450	-0.85194
H	-2.80464	1.95432	-0.93683
C	3.45799	1.07669	1.76795
H	3.96970	1.26101	2.72781
H	-2.73602	-0.06024	-1.72577
Ru	-0.40746	0.28477	0.36618
H	0.82599	-0.57996	-2.46733
N	-2.65529	0.31948	0.31333
C	-2.97713	-0.60257	-0.79572
C	2.66375	-0.25294	-1.32393
H	2.33072	-0.71345	-3.40479
H	4.61259	-1.38066	1.15940
C	1.86314	-0.94464	-2.43282
C	2.80169	-0.30485	1.80611
P	1.67304	-0.50435	0.28526
H	-4.05055	-0.86240	-0.81937
C	3.87043	-1.38738	1.96654
H	-2.68589	0.42603	2.39482
H	-5.14655	0.53499	1.74855
H	4.41231	-1.21646	2.91251
C	-3.09606	-0.23282	1.61775
H	4.51800	-0.71960	-2.31985
C	0.12668	1.97410	0.77974
C	4.08269	-0.81368	-1.31025
H	1.06471	0.39181	2.93114
C	1.86034	-0.36233	3.01447
H	4.74237	-0.26860	-0.62064
H	2.44092	-0.18706	3.93633
C	-2.13124	-1.83752	-0.76503
N	-0.88543	-1.64945	-0.28699
C	-4.59579	-0.41517	1.81058
H	1.85621	-2.04051	-2.32728
H	-2.57927	-1.19605	1.74069
H	3.43684	-2.39724	2.02516
H	-5.03675	-1.11348	1.08360
C	1.35159	-2.35785	0.29786
H	-4.77557	-0.83435	2.81187
H	4.10942	-1.88199	-1.04381
C	0.00997	-2.66200	-0.29230
C	-2.53968	-3.06661	-1.26824
H	1.37180	-1.34516	3.11201
H	-3.55523	-3.19103	-1.64581
H	1.33080	-2.64239	1.36285
H	2.14391	-2.95574	-0.17788
C	-0.33534	-3.90828	-0.80978
C	-1.62275	-4.11441	-1.29836
H	0.40247	-4.71134	-0.81812
H	-1.91004	-5.08799	-1.69942
O	0.53054	3.04880	1.03179
O	-1.02013	1.17283	-2.57593
H	-0.84821	2.12314	-2.60775
H	-0.64192	0.93092	-1.67189

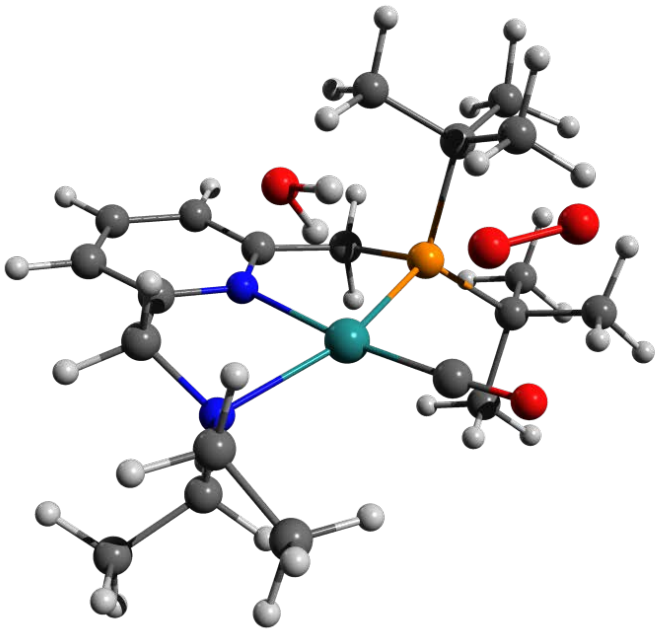

Figure 11.5-24 [E]S_0 Structure and Coordinates

63

Energy: -928588.5901943

N	-0.79133	1.42415	0.01683
C	-2.02380	1.84124	0.37017
C	0.13107	2.30928	-0.42940
C	-2.40585	3.17104	0.25270
C	-1.46998	4.09574	-0.20833
C	-0.18941	3.66159	-0.54037
C	-2.87907	0.77587	0.98864
H	-3.41494	3.47721	0.53136
H	-1.73711	5.14924	-0.30717
H	0.56365	4.36371	-0.89999
C	1.46351	1.74417	-0.81210
N	-2.65212	-0.55453	0.39254
H	-3.94471	1.06478	0.96488
H	-2.59052	0.70030	2.04990
H	1.44545	1.53749	-1.89569
P	1.70832	0.05142	-0.03024
H	2.27274	2.46679	-0.62445
Ru	-0.40599	-0.62089	0.15361
C	-3.27363	-0.64358	-0.95219
C	2.97845	-0.74783	-1.20012
C	-3.18949	-1.56064	1.33979
C	2.53410	0.45347	1.64701
C	2.19457	-1.27404	-2.40610
C	3.63932	-1.93931	-0.50368
C	4.04527	0.22764	-1.70266
C	1.63138	1.49050	2.32374
C	3.95281	1.01018	1.57578
C	2.49280	-0.81727	2.50075
H	-2.80880	0.13549	-1.57050
C	-4.79102	-0.53396	-1.01525
H	-2.93530	-1.59110	-1.39047
H	-2.55934	-1.48842	2.23915
C	-3.18632	-2.98500	0.83054
H	-4.21908	-1.27293	1.63398
C	0.03994	-2.38933	0.14073
H	-2.18198	-3.29149	0.51148
H	-3.88327	-3.13688	-0.00645
H	-3.50338	-3.65153	1.64617
H	-5.10318	-0.62787	-2.06600
H	-5.16787	0.43500	-0.65414
H	-5.29928	-1.32900	-0.44968
H	2.90715	-1.71394	-3.12478
H	1.62743	-0.48790	-2.92492
H	1.47710	-2.04963	-2.10743
H	4.23655	-2.49727	-1.24443
H	2.89196	-2.63300	-0.09153
H	4.32107	-1.63378	0.30265
H	4.74182	-0.31648	-2.36279
H	4.63926	0.67500	-0.89613
H	3.60801	1.04018	-2.30181
H	4.67507	0.27479	1.19572
H	4.28265	1.29668	2.58941
H	4.01533	1.91267	0.94747
H	3.13835	-1.61377	2.10810
H	1.46338	-1.20515	2.54493
H	2.83194	-0.58265	3.52443
H	1.98486	1.65715	3.35522
H	0.59120	1.13131	2.36546
H	1.64500	2.46423	1.80977
O	0.39658	-3.50621	0.09718
O	-0.69010	0.21173	-2.97203
H	-0.95813	1.08513	-2.66151
H	-0.52984	-0.26674	-2.11021

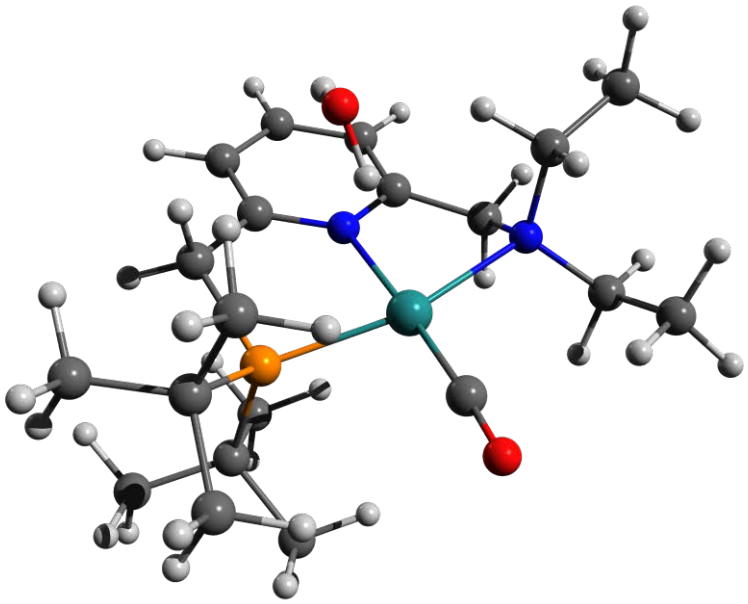

Figure 11.5-25 $^3O_2$ Coordinates

2

Energy: -94269.2503844

O	0.00000	0.00000	0.59806
O	0.00000	0.00000	-0.59806

Figure 11.5-26 [F]S_0 Structure and Coordinates

63

Energy: -928594.2432451

N	-0.74635	1.30730	-0.32033
C	-1.93878	1.84197	-0.01643
C	0.18868	2.01274	-0.97776
C	-2.25389	3.14457	-0.39308
C	-1.29825	3.89510	-1.07340
C	-0.06176	3.32937	-1.36675
C	-2.84304	0.97446	0.81471
H	-3.23108	3.56209	-0.14724
H	-1.51749	4.92094	-1.37588
H	0.70480	3.89705	-1.89553
C	1.48478	1.30907	-1.27073
N	-2.84341	-0.42575	0.38117
H	-3.85953	1.40663	0.85274
H	-2.41290	0.96630	1.83054
H	1.39796	0.81902	-2.25631
P	1.79947	-0.10207	-0.06444
H	2.31636	2.02663	-1.33554
Ru	-0.32175	-0.78130	0.27359
C	-3.46183	-0.59919	-0.94190
C	3.10916	-1.14527	-0.97707
C	-3.42210	-1.26670	1.43622
C	2.61156	0.77486	1.42559
C	2.39457	-2.02743	-2.00009
C	3.80009	-2.06975	0.02702
C	4.14004	-0.29775	-1.72864
C	1.69299	1.93832	1.81948
C	4.00605	1.33256	1.14447
C	2.66301	-0.19905	2.60550
H	0.01026	-2.25575	0.83530
H	-2.91836	0.06098	-1.63552
C	-4.95759	-0.32754	-1.02895
H	-3.24790	-1.62263	-1.27730
H	-2.81556	-1.05375	2.32917
C	-3.36080	-2.74585	1.11743
H	-4.46441	-0.95652	1.65455
C	-0.50126	-1.51406	-1.38531
O	-0.57986	-0.11284	2.25077
H	-0.37245	-0.84709	2.84019
H	-2.32717	-3.02846	0.86111
H	-4.02163	-3.03305	0.28531
H	-3.67211	-3.32484	1.99945
H	-5.29191	-0.47074	-2.06746
H	-5.21847	0.70230	-0.74089
H	-5.54132	-1.01426	-0.39748
H	3.15437	-2.60299	-2.55465
H	1.81938	-1.44712	-2.73550
H	1.71136	-2.73530	-1.51456
H	4.41226	-2.80230	-0.52475
H	3.06264	-2.62841	0.62341
H	4.46906	-1.53042	0.71081
H	4.86572	-0.97439	-2.21023
H	4.70470	0.38269	-1.08198
H	3.67478	0.29404	-2.53093
H	4.75838	0.54920	0.98004
H	4.32884	1.91247	2.02544
H	4.02144	2.01981	0.28437
H	3.31205	-1.06440	2.42213
H	1.64926	-0.54891	2.83581
H	3.05547	0.33493	3.48741
H	2.10633	2.40374	2.73046
H	0.68234	1.56615	2.04803
H	1.65255	2.72159	1.04725
O	-0.74696	-2.01597	-2.41088

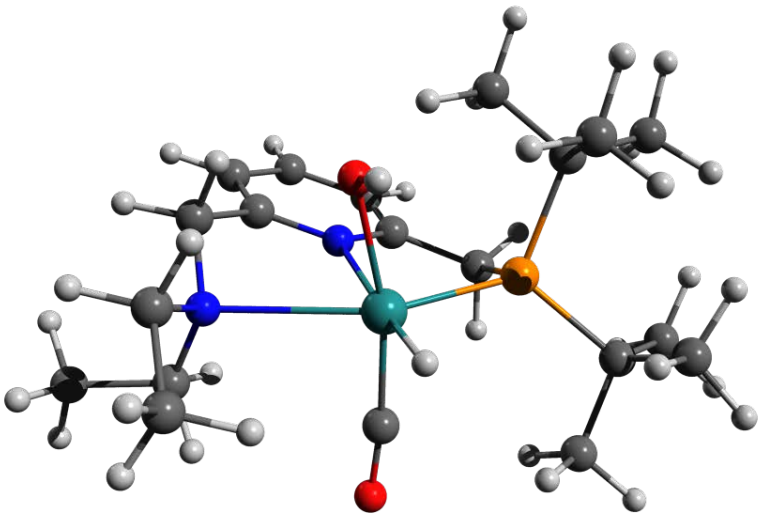

Figure 11.5-27 [F-Up]S_0

63

Energy: -928594.7107585

N	-0.76012	1.35702	0.06074
C	-1.98808	1.76019	0.41130
C	0.14561	2.21168	-0.43933
C	-2.35911	3.09652	0.32530
C	-1.41501	4.01483	-0.13317
C	-0.15550	3.57248	-0.52449
C	-2.86432	0.65143	0.91583
H	-3.36391	3.41035	0.61035
H	-1.66922	5.07414	-0.20352
H	0.58703	4.27030	-0.91343
C	1.42575	1.61295	-0.94035
N	-2.71088	-0.57889	0.10904
H	-3.91695	0.97807	0.97223
H	-2.54157	0.40295	1.94000
H	1.24037	1.35471	-1.99701
P	1.76437	-0.06514	-0.17220
H	2.26264	2.32326	-0.88030
Ru	-0.40278	-0.73311	0.00089
C	-3.28097	-0.39488	-1.24605
C	2.98529	-0.86039	-1.40368
C	-3.35596	-1.69012	0.84091
C	2.68585	0.37918	1.43916
C	2.16082	-1.50296	-2.52121
C	3.76716	-1.97521	-0.70760
C	3.94668	0.14899	-2.03561
C	1.78330	1.34786	2.21325
C	4.02979	1.07014	1.20419
C	2.90333	-0.86685	2.30296
H	-0.17741	-2.28874	-0.35044
H	-2.67991	0.38194	-1.73612
C	-4.77086	-0.09912	-1.32183
H	-3.04599	-1.30790	-1.80675
H	-2.86129	-1.74689	1.82075
C	-3.24236	-3.02668	0.14065
H	-4.41803	-1.44218	1.03317
C	-0.36341	-1.29063	1.73384
O	-0.55241	-0.24421	-2.02943
H	-0.51954	-1.07146	-2.52109
H	-2.19154	-3.21571	-0.12667
H	-3.85742	-3.08026	-0.76983
H	-3.58479	-3.82187	0.81910
H	-5.05260	-0.00593	-2.38153
H	-5.04794	0.84874	-0.83522
H	-5.39256	-0.89811	-0.88922
H	2.85351	-1.96637	-3.24406
H	1.53388	-0.76769	-3.04204
H	1.49724	-2.27858	-2.11355
H	4.30778	-2.55843	-1.47151
H	3.09396	-2.66558	-0.17658
H	4.51440	-1.59451	0.00201
H	4.62443	-0.38964	-2.71936
H	4.57013	0.67690	-1.30360
H	3.41141	0.89676	-2.63846
H	4.77741	0.39768	0.76244
H	4.42961	1.40719	2.17539
H	3.94093	1.96074	0.56358
H	3.62536	-1.56423	1.86222
H	1.96971	-1.41019	2.48923
H	3.30471	-0.55087	3.28072
H	2.24443	1.55016	3.19394
H	0.78337	0.92786	2.38544
H	1.66994	2.31323	1.69793
O	-0.39707	-1.72073	2.82230

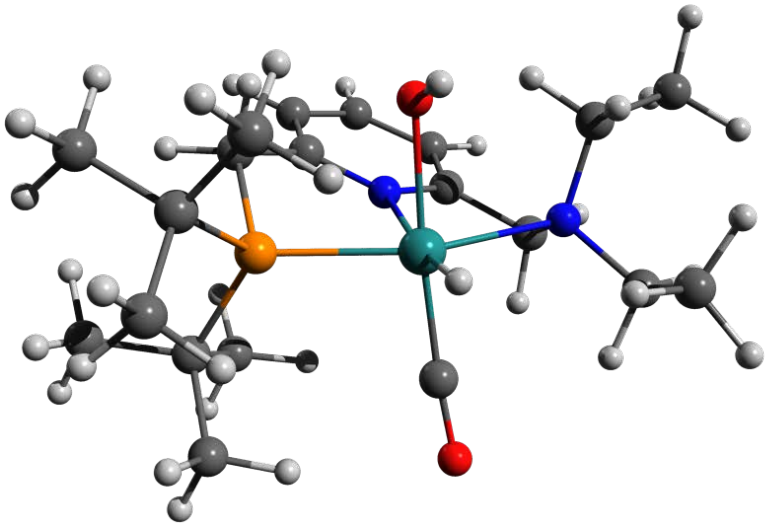

Figure 11.5-28 [F-Trans]S_0 Structure and Coordinates

63

Energy: -928595.0842646

N	-0.80008	1.42201	-0.04137
C	-2.01529	1.84205	0.33314
C	0.08710	2.25307	-0.61139
C	-2.40612	3.16389	0.15747
C	-1.49281	4.05289	-0.40659
C	-0.23606	3.59815	-0.79275
C	-2.83614	0.77931	0.99500
H	-3.40192	3.48854	0.46079
H	-1.76456	5.10007	-0.55239
H	0.48999	4.27366	-1.24616
C	1.38015	1.63724	-1.04565
N	-2.67460	-0.52971	0.33005
H	-3.89593	1.07920	1.06179
H	-2.45228	0.65674	2.02086
H	1.20532	1.24514	-2.06318
P	1.72843	0.07619	-0.07604
H	2.20011	2.36921	-1.06618
Ru	-0.40440	-0.63417	0.12216
C	-3.31677	-0.52889	-1.00610
C	2.98840	-0.83483	-1.17047
C	-3.23884	-1.55482	1.23772
C	2.56798	0.66948	1.52673
C	2.19557	-1.57220	-2.25448
C	3.75077	-1.87787	-0.35107
C	3.96721	0.12336	-1.85464
C	1.66301	1.74844	2.13123
C	3.95882	1.26826	1.32423
C	2.62271	-0.50133	2.51198
H	-0.38438	-0.55794	1.74376
H	-2.72303	0.14852	-1.63637
C	-4.80382	-0.21466	-1.04423
H	-3.12800	-1.52055	-1.43586
H	-2.59533	-1.54706	2.12912
C	-3.29428	-2.95019	0.65467
H	-4.25429	-1.24594	1.55620
C	0.02966	-2.39316	0.33554
O	-0.62223	-0.36430	-2.01252
H	-0.67378	-1.23608	-2.41991
H	-2.32106	-3.24701	0.24091
H	-4.05502	-3.04876	-0.13346
H	-3.55292	-3.66121	1.45301
H	-5.15707	-0.32368	-2.08074
H	-5.03248	0.81782	-0.73872
H	-5.40541	-0.89516	-0.42114
H	2.90435	-1.96849	-3.00088
H	1.45853	-0.92112	-2.74563
H	1.64034	-2.41699	-1.82452
H	4.33695	-2.50636	-1.04223
H	3.06523	-2.54178	0.19634
H	4.45549	-1.43199	0.36428
H	4.69269	-0.46925	-2.43693
H	4.53709	0.74184	-1.15000
H	3.45345	0.78874	-2.56369
H	4.69663	0.52824	0.98659
H	4.31802	1.67091	2.28640
H	3.95127	2.10330	0.60632
H	3.31040	-1.29420	2.19136
H	1.62198	-0.93940	2.63946
H	2.97139	-0.13229	3.49119
H	2.06319	2.03045	3.11924
H	0.63872	1.37295	2.26559
H	1.63082	2.66104	1.51687
O	0.36196	-3.49890	0.50636

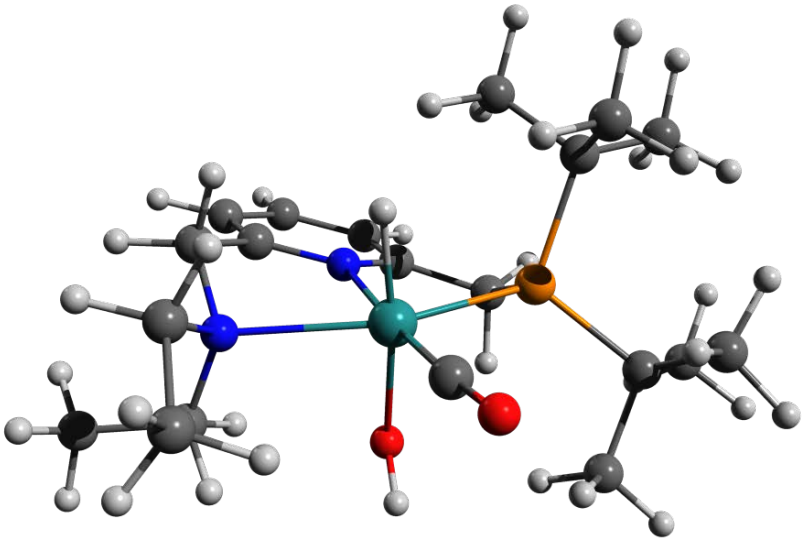

Figure 11.5-29 [F-Trans-Up]S_0 Structure and Coordinates

63

Energy: -928597.8425390

N	-0.80456	1.44495	-0.18829
C	-2.03468	1.86436	0.14891
C	0.12233	2.30384	-0.64514
C	-2.39587	3.20229	0.02647
C	-1.44432	4.11133	-0.42708
C	-0.17108	3.66150	-0.76372
C	-2.90916	0.80031	0.72946
H	-3.40264	3.52229	0.29686
H	-1.69505	5.16956	-0.52185
H	0.59223	4.35144	-1.12469
C	1.43744	1.70691	-1.03843
N	-2.68203	-0.50943	0.08359
H	-3.97137	1.09596	0.70925
H	-2.57049	0.66141	1.77189
H	1.38751	1.45664	-2.11168
P	1.72097	0.06699	-0.17905
H	2.26188	2.42278	-0.90504
Ru	-0.41200	-0.61319	0.08095
C	-3.20203	-0.52723	-1.30271
C	2.89886	-0.81317	-1.38767
C	-3.30408	-1.53096	0.95651
C	2.63956	0.54327	1.41642
C	2.06909	-1.36145	-2.55174
C	3.56812	-1.99337	-0.67902
C	3.96741	0.12012	-1.96582
C	1.76616	1.61361	2.08406
C	4.05425	1.08518	1.22953
C	2.65974	-0.68229	2.33407
H	-0.43417	-0.78203	-1.52042
H	-2.66778	0.26567	-1.84531
C	-4.70588	-0.35856	-1.46514
H	-2.86686	-1.46983	-1.75382
H	-2.72796	-1.47327	1.89224
C	-3.29003	-2.93590	0.39539
H	-4.34571	-1.23050	1.18415
C	0.02049	-2.37940	0.20529
O	-0.76410	-0.17688	2.17309
H	-0.41080	-0.88374	2.72358
H	-2.27615	-3.24304	0.10712
H	-3.94853	-3.05374	-0.47837
H	-3.64559	-3.63190	1.16954
H	-4.95447	-0.40248	-2.53621
H	-5.06907	0.60960	-1.08879
H	-5.27648	-1.15404	-0.96304
H	2.75551	-1.82586	-3.27975
H	1.50507	-0.57340	-3.07289
H	1.34279	-2.11174	-2.21769
H	4.12018	-2.59036	-1.42402
H	2.83098	-2.65636	-0.20339
H	4.29185	-1.66865	0.08138
H	4.61776	-0.46331	-2.63891
H	4.60846	0.57207	-1.20033
H	3.52795	0.92880	-2.56855
H	4.75887	0.32382	0.86597
H	4.42910	1.43550	2.20622
H	4.08739	1.94673	0.54444
H	3.28052	-1.50000	1.94507
H	1.63860	-1.05754	2.48408
H	3.06654	-0.38893	3.31631
H	2.20182	1.84961	3.07021
H	0.73977	1.22947	2.23546
H	1.74397	2.55309	1.50940
O	0.35357	-3.49676	0.25197

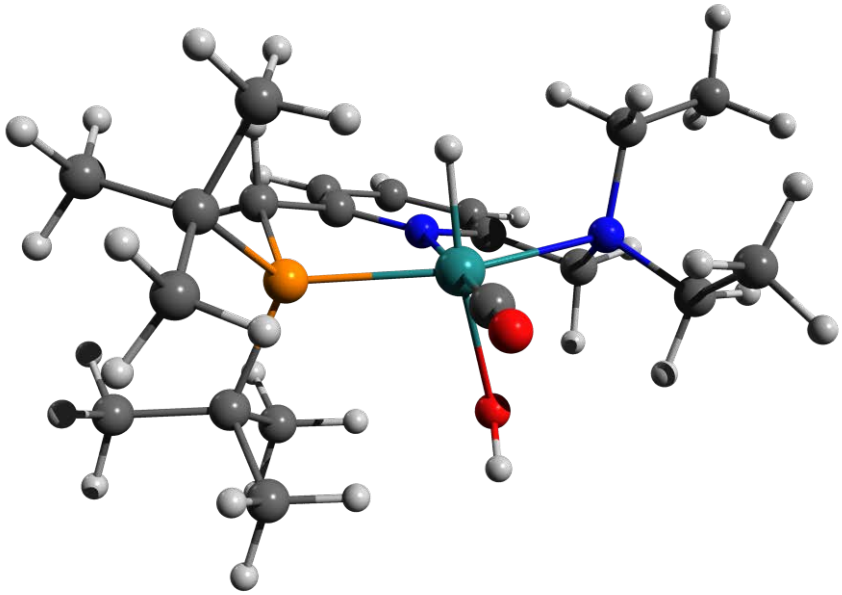

Figure 11.5-30 [F-Cis]S_0 Structure and Coordinates

63

Energy: -928584.1363893

N	0.71566	1.37102	0.24967
C	1.88601	1.90688	-0.14944
C	-0.22203	2.13284	0.85849
C	2.19685	3.23563	0.11033
C	1.25695	4.02958	0.76442
C	0.03258	3.47557	1.12784
C	2.73322	0.98067	-0.96914
H	3.15802	3.64155	-0.20754
H	1.47320	5.07710	0.98044
H	-0.73060	4.07916	1.62065
C	-1.51831	1.44743	1.18218
N	2.66800	-0.41382	-0.49369
H	3.77113	1.35162	-1.03319
H	2.30857	0.97872	-1.98663
H	-1.44297	0.99243	2.18545
P	-1.75656	-0.02385	0.03128
H	-2.35119	2.16642	1.20696
Ru	0.41346	-0.61138	-0.14255
C	3.42690	-0.55444	0.77262
C	-3.03865	-1.11267	0.91840
C	3.17947	-1.30585	-1.55970
C	-2.54199	0.74825	-1.53001
C	-2.28511	-1.92416	1.97289
C	-3.61065	-2.11050	-0.09137
C	-4.15196	-0.32493	1.61073
C	-1.68563	1.95376	-1.93209
C	-3.97745	1.23127	-1.32770
C	-2.47899	-0.26757	-2.67357
H	0.32804	-0.24845	-1.77202
H	2.99417	0.17132	1.47773
C	4.93463	-0.36535	0.69258
H	3.19723	-1.54836	1.17591
H	2.49649	-1.16511	-2.41000
C	3.19508	-2.76566	-1.16012
H	4.18443	-0.96125	-1.87714
C	0.60946	-1.12466	1.67406
O	0.15196	-2.61505	-0.66095
H	-0.04077	-2.60617	-1.60553
H	2.18267	-3.05345	-0.82169
H	3.93873	-2.98216	-0.37773
H	3.46261	-3.37173	-2.03913
H	5.35640	-0.47464	1.70297
H	5.22566	0.63128	0.32769
H	5.41672	-1.11829	0.05220
H	-3.00470	-2.58654	2.48267
H	-1.82336	-1.29010	2.74351
H	-1.50496	-2.54116	1.50536
H	-4.20342	-2.86484	0.45241
H	-2.79842	-2.63566	-0.61747
H	-4.27589	-1.63992	-0.82798
H	-4.82587	-1.03594	2.11799
H	-4.76170	0.26958	0.92036
H	-3.75465	0.34758	2.38635
H	-4.68328	0.40641	-1.16265
H	-4.30489	1.76218	-2.23745
H	-4.06683	1.93952	-0.48927
H	-3.11348	-1.14547	-2.49985
H	-1.44317	-0.60744	-2.81777
H	-2.82265	0.21757	-3.60270
H	-2.05123	2.33470	-2.90001
H	-0.63235	1.66355	-2.05282
H	-1.75400	2.77998	-1.20884
O	0.81361	-1.39650	2.78236

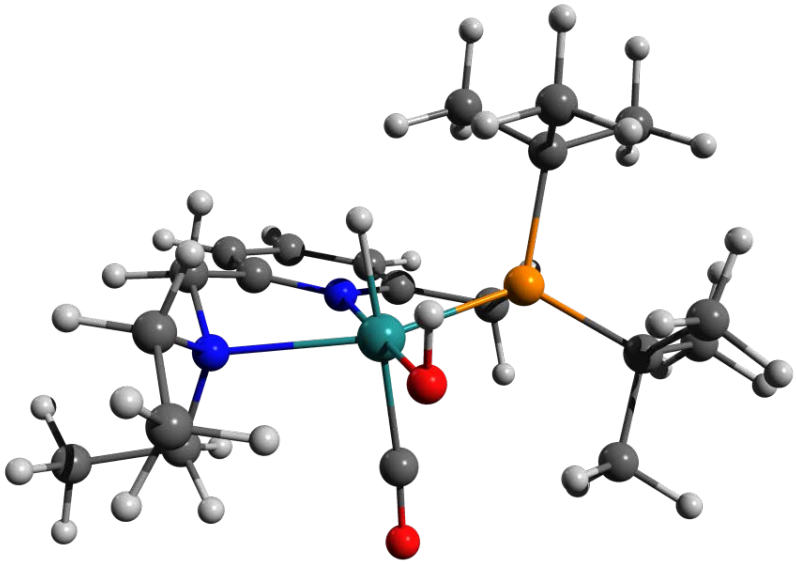

Figure 11.5-31 [F-Cis-Up]S_0

63

Energy: -928583.3465243

N	-0.76649	1.41843	-0.07154
C	-2.01036	1.85279	0.21670
C	0.14794	2.26376	-0.59987
C	-2.37124	3.18384	0.05372
C	-1.41729	4.08485	-0.41404
C	-0.15168	3.61575	-0.75320
C	-2.92299	0.78241	0.73207
H	-3.38574	3.50509	0.29284
H	-1.66577	5.14026	-0.53683
H	0.60447	4.28902	-1.15894
C	1.43193	1.64925	-1.06883
N	-2.68842	-0.50404	0.04480
H	-3.97678	1.10586	0.66433
H	-2.69735	0.61853	1.79906
H	1.29444	1.38772	-2.13247
P	1.73612	-0.00383	-0.23635
H	2.26951	2.35979	-1.00852
Ru	-0.40632	-0.58507	0.12753
C	-3.13183	-0.43630	-1.37016
C	2.76388	-0.97221	-1.51000
C	-3.38459	-1.57380	0.79678
C	2.81626	0.48715	1.25846
C	1.79173	-1.54530	-2.54607
C	3.42342	-2.15521	-0.79768
C	3.81352	-0.12407	-2.23086
C	2.06226	1.60908	1.98221
C	4.20708	1.00144	0.88987
C	2.94913	-0.70018	2.21525
H	-0.38263	-0.54300	-1.52205
H	-2.58034	0.39612	-1.82922
C	-4.62669	-0.27589	-1.60563
H	-2.75557	-1.34493	-1.85563
H	-2.93436	-1.58370	1.80041
C	-3.24221	-2.94035	0.16087
H	-4.45015	-1.29713	0.92821
C	-0.42880	-0.79162	2.01232
O	-0.17639	-2.63743	-0.18445
H	0.11822	-3.04741	0.63704
H	-2.17636	-3.12248	-0.07293
H	-3.84319	-3.03847	-0.75619
H	-3.59904	-3.70383	0.86859
H	-4.80781	-0.21749	-2.68943
H	-5.03495	0.64510	-1.16155
H	-5.20838	-1.12709	-1.22230
H	2.37599	-2.14707	-3.26386
H	1.27463	-0.75585	-3.11162
H	1.03384	-2.17538	-2.05570
H	3.86573	-2.82409	-1.55452
H	2.67531	-2.73449	-0.23591
H	4.23239	-1.84668	-0.12066
H	4.32954	-0.75890	-2.97077
H	4.57883	0.28829	-1.56235
H	3.35837	0.70854	-2.78858
H	4.85268	0.20776	0.48993
H	4.69648	1.39306	1.79777
H	4.17387	1.82343	0.15832
H	3.52252	-1.52815	1.78067
H	1.96980	-1.08747	2.52084
H	3.47731	-0.36929	3.12537
H	2.57082	1.82424	2.93635
H	1.02509	1.32521	2.20880
H	2.04757	2.54327	1.40092
O	-0.46674	-0.98768	3.15824

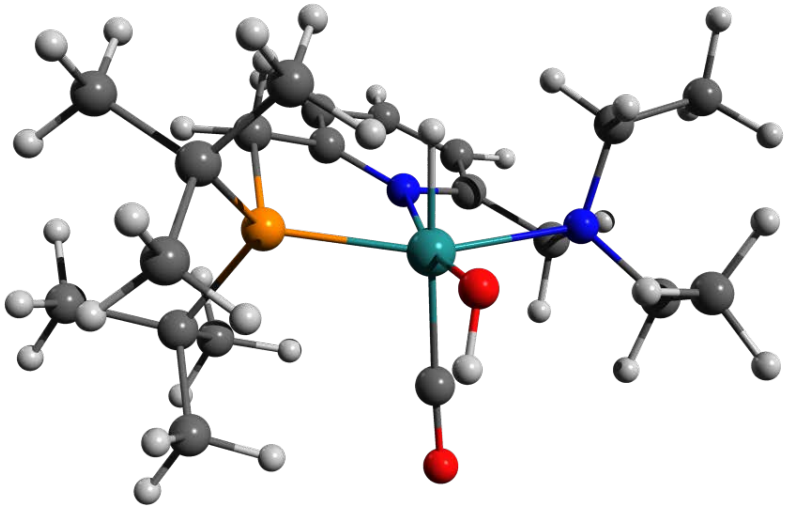

Figure 11.5-32 [Oxo Dimer]S_0 Structure and Coordinates

125

Energy: -1903622.5751306

Ru	1.95096	-0.14653	-0.32407
O	2.00832	-1.80029	0.92464
C	1.90893	1.05768	-1.69607
P	2.88599	1.33842	1.10148
N	4.01311	-0.55768	-0.70975
C	4.53060	1.60252	0.25451
H	4.32826	2.35352	-0.52810
H	5.31172	2.01152	0.91161
C	4.98001	0.33183	-0.38985
C	6.32650	0.06494	-0.62494
H	7.07516	0.80881	-0.35061
C	6.69055	-1.14695	-1.19781
H	7.73907	-1.37674	-1.39527
C	5.69184	-2.06110	-1.51010
H	5.92828	-3.02776	-1.95594
C	4.36117	-1.74588	-1.24971
C	3.26539	-2.73818	-1.48420
H	3.67502	-3.59036	-2.06069
H	2.93674	-3.07047	-0.48254
N	2.09801	-2.14698	-2.11742
C	2.29339	3.13737	1.30343
C	3.40572	4.10595	1.71752
H	4.20219	4.16830	0.96148
H	3.86246	3.86481	2.68306
H	2.96774	5.11464	1.80329
C	1.15082	3.17641	2.31683
H	0.65697	4.16110	2.27409
H	1.50238	3.02964	3.34710
H	0.39099	2.41354	2.10485
C	1.76662	3.60005	-0.05230
H	0.94948	2.96248	-0.40187
H	2.54516	3.60685	-0.82886
H	1.38789	4.63073	0.04669
C	3.33584	0.61429	2.80336
C	4.04527	1.59470	3.73568
H	3.39887	2.41977	4.06399
H	4.95979	2.01770	3.29136
H	4.35144	1.04365	4.64064
C	4.26228	-0.58364	2.56289
H	4.46589	-1.05356	3.54002
H	5.23322	-0.28524	2.13842
H	3.76716	-1.32593	1.92045
C	2.04916	0.09926	3.45054
H	2.30463	-0.40806	4.39646
H	1.57687	-0.62955	2.77817
H	1.33840	0.90239	3.68369
C	1.22294	-1.15312	-4.23495
H	0.48557	-1.92516	-4.49965
H	1.56895	-0.68709	-5.16917
H	0.71440	-0.38531	-3.63880
C	0.93641	-3.02622	-2.00061
H	0.06527	-2.47795	-2.38049
H	0.77323	-3.16167	-0.92130
C	1.03165	-4.37637	-2.69966
H	1.18407	-4.27465	-3.78584
H	0.09062	-4.92698	-2.55004
H	1.84534	-5.00091	-2.29982
C	2.40794	-1.72102	-3.48232
H	2.85344	-2.56024	-4.05949
H	3.19240	-0.95073	-3.40528
O	0.00019	-0.44384	0.00209
Ru	-1.95090	-0.14533	0.32507
C	-1.91025	1.06339	1.69316
O	-2.00709	-1.80286	-0.91908
P	-2.88584	1.33489	-1.10582
N	-2.09803	-2.13971	2.12450
N	-4.01323	-0.55597	0.71084
C	-3.26497	-2.73362	1.49287
H	-3.67443	-3.58398	2.07214
H	-2.93570	-3.06923	0.49252
C	-4.36107	-1.74256	1.25452
C	-5.69174	-2.05747	1.51527
H	-5.92807	-3.02278	1.96405
C	-6.69065	-1.14469	1.19955
H	-7.73918	-1.37425	1.39730
C	-6.32681	0.06549	0.62298
H	-7.07561	0.80824	0.34600
C	-4.98029	0.33212	0.38760
C	-4.53105	1.60091	-0.26057
H	-4.32960	2.35456	0.51970
H	-5.31194	2.00738	-0.91950
C	-3.33465	0.60529	-2.80560
C	-4.04399	1.58254	-3.74129
H	-4.34943	1.02859	-4.64473
H	-3.39782	2.40691	-4.07178
H	-4.95896	2.00646	-3.29877
C	-2.04740	0.08872	-3.45040
H	-2.30204	-0.42133	-4.39509
H	-1.57557	-0.63808	-2.77552
H	-1.33660	0.89131	-3.68528
C	-4.26076	-0.59225	-2.56192
H	-5.23202	-0.29293	-2.13882
H	-3.76567	-1.33238	-1.91697
H	-4.46372	-1.06522	-3.53771
C	-2.29407	3.13359	-1.31317
C	-3.40688	4.10043	-1.73009
H	-4.20333	4.16471	-0.97420
H	-3.86357	3.85624	-2.69489
H	-2.96935	5.10906	-1.81888
C	-1.76753	3.60044	0.04124
H	-1.38914	4.63095	-0.06073
H	-0.95022	2.96414	0.39276
H	-2.54614	3.60926	0.81771
C	-1.15158	3.17055	-2.32673
H	-0.65856	4.15578	-2.28685
H	-1.50303	3.02053	-3.35658
H	-0.39106	2.40896	-2.11267
C	-2.40857	-1.70893	3.48776
H	-2.85399	-2.54619	4.06781
H	-3.19324	-0.93918	3.40766
C	-1.22390	-1.13797	4.23864
H	-0.48672	-1.90899	4.50682
H	-1.57028	-0.66807	5.17077
H	-0.71499	-0.37267	3.63954
C	-0.93601	-3.01891	2.01126
H	-0.06533	-2.46892	2.38968
H	-0.77228	-3.15794	0.93250
C	-1.03102	-4.36670	2.71486
H	-1.18397	-4.26145	3.80063
H	-0.08966	-4.91737	2.56751
H	-1.84422	-4.99297	2.31671
O	-1.96297	1.73897	2.64636
O	1.96054	1.73006	-2.65157
H	1.03960	-1.82295	1.01395
H	-1.03823	-1.82607	-1.00680

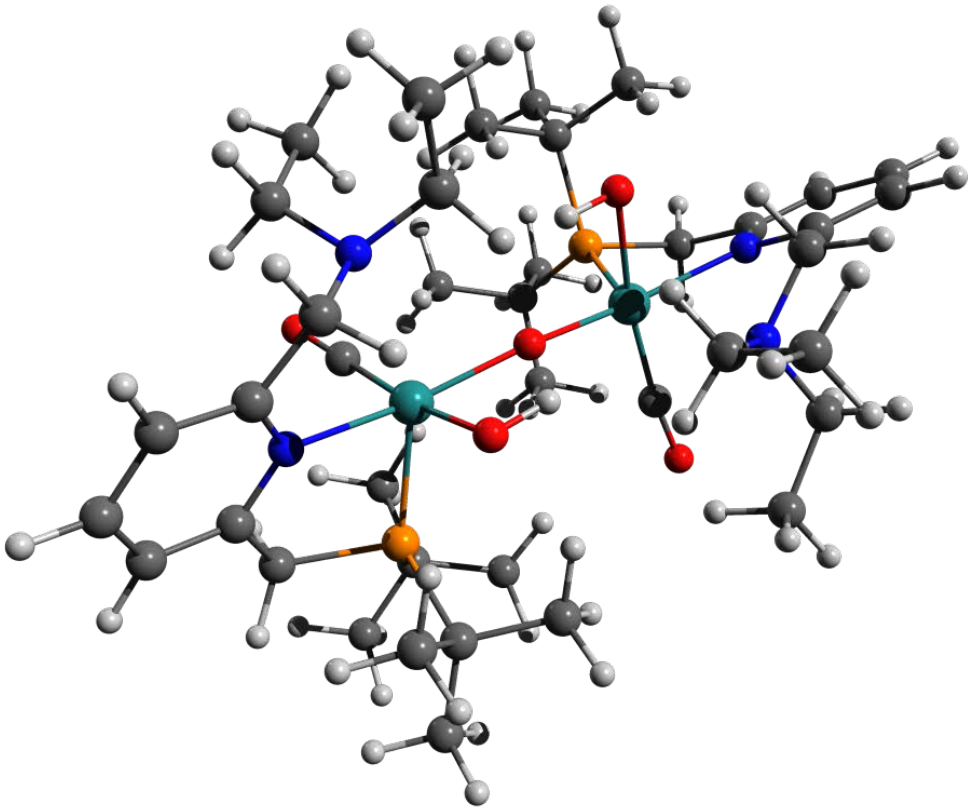

12 References

1. Zhang, J., Leitus, G., Ben-David, Y. & Milstein, D. Facile Conversion of Alcohols into Esters and Dihydrogen Catalyzed by New Ruthenium Complexes. *J. Am. Chem. Soc.* **127**, 10840–10841 (2005).
2. Kohl, S. W. *et al.* Consecutive Thermal H2 and Light-Induced O2 Evolution from Water Promoted by a Metal Complex. *Science* **324**, 74–77 (2009).
3. Dorta, R., Rozenberg, H., Shimon, L. J. W. & Milstein, D. Dimethylsulfoxide as a Ligand for RhI and IrI Complexes—Isolation, Structure, and Reactivity Towards X-H Bonds (X=H, OH, OCH3). *Chem. – Eur. J.* **9**, 5237–5249 (2003).
4. Weissman, H. PhD Thesis. (2004), Weizmann Institute of Science.
5. Zhang, J., Gandelman, M., Shimon, L. J. W. & Milstein, D. Electron-rich, bulky PNN-type ruthenium complexes: synthesis, characterization and catalysis of alcohol dehydrogenation. *Dalton Trans.* **0**, 107–113 (2006).
6. Barrios-Francisco, R. *et al.* PNN Ruthenium Pincer Complexes Based on Phosphinated 2,2′-Dipyridinemethane and 2,2′-Oxobispyridine. Metal–Ligand Cooperation in Cyclometalation and Catalysis. *Organometallics* **32**, 2973–2982 (2013).
7. Ng, C. K., Wu, J., Hor, T. S. A. & Luo, H.-K. A binary catalyst system of a cationic Ru–CNC pincer complex with an alkali metal salt for selective hydroboration of carbon dioxide. *Chem. Commun.* **52**, 11842–11845 (2016).
8. Hippler, M. Photochemical Kinetics: Reaction Orders and Analogies with Molecular Beam Scattering and Cavity Ring-Down Experiments. *J. Chem. Educ.* **80**, 1074 (2003).
9. Murov, S. L. *Handbook of Photochemistry, Section 13, pp. 299-313*. (Marcel Dekker, New York, 1993).
10. Frisch, M. J. *et al. Gaussian 16*. (Gaussian, Inc. Wallingford, CT, 2016).
11. Hanwell, M. D. *et al.* Avogadro: an advanced semantic chemical editor, visualization, and analysis platform. *J. Cheminformatics* **4**, 17 (2012).
12. Allouche, A.-R. Gabedit—A graphical user interface for computational chemistry softwares. *J. Comput. Chem.* **32**, 174–182 (2011).

13. DeLano, W. L. Pymol: An open-source molecular graphics tool. *CCP4 Newsl. Protein Crystallogr.* **40**, 82–92 (2002).

14. Plachetka, T. POV Ray: persistence of vision parallel raytracer. in *Proc. of Spring Conf. on Computer Graphics, Budmerice, Slovakia* vol. 123 (1998).

15. Delcey, M. G., Pedersen, T. B., Aquilante, F. & Lindh, R. Analytical gradients of the state-average complete active space self-consistent field method with density fitting. *J. Chem. Phys.* **143**, 044110 (2015).

16. Delcey, M. G. *et al.* Analytical gradients of complete active space self-consistent field energies using Cholesky decomposition: Geometry optimization and spin-state energetics of a ruthenium nitrosyl complex. *J. Chem. Phys.* **140**, 174103 (2014).

17. Fdez. Galván, I., Delcey, M. G., Pedersen, T. B., Aquilante, F. & Lindh, R. Analytical State-Average Complete-Active-Space Self-Consistent Field Nonadiabatic Coupling Vectors: Implementation with Density-Fitted Two-Electron Integrals and Application to Conical Intersections. *J. Chem. Theory Comput.* **12**, 3636–3653 (2016).

18. Aquilante, F. *et al.* Modern quantum chemistry with [Open]Molcas. *J. Chem. Phys.* **152**, 214117 (2020).

19. Fdez. Galván, I. *et al.* OpenMolcas: From Source Code to Insight. *J. Chem. Theory Comput.* **15**, 5925–5964 (2019).

20. Boese, A. D. Density Functional Theory and Hydrogen Bonds: Are We There Yet? *ChemPhysChem* **16**, 978–985 (2015).

21. Yang, X. & Hall, M. B. Mechanism of Water Splitting and Oxygen−Oxygen Bond Formation by a Mononuclear Ruthenium Complex. *J. Am. Chem. Soc.* **132**, 120–130 (2010).

22. Chen, Y. & Fang, W.-H. Mechanism for the Light-Induced O2 Evolution from H2O Promoted by Ru(II) PNN Complex: A DFT Study. *J. Phys. Chem. A* **114**, 10334–10338 (2010).

8.2 Supporting Information for "Improving Data Analysis in Chemistry and Biology Through Versatile Baseline Correction"

This PDF file includes:

Supplementary Text
1. Evaluation using Synthetic Data
2. Reaction Kinetics
3. Quantitative Chain Polymerase Reaction
4. X-Ray Absorption Spectroscopy
5. Supplementary Information on Combined Fitting

SI Figures 1 to 12

Other supplementary materials for this manuscript include the following:

Datasets and code for analysis found at: https://github.com/jschneidewind/LBC
Source code for web interface can be found at: https://github.com/hrishioa/lbc
Web interface can be found at: https://lbc.olickel.com

1. Evaluation using Synthetic Data

For all synthetic data experiments, data in the range x = [-2, 4] was used with a variable number of linearly spaced datapoints. Gaussian noise centered at zero with a variable standard deviation σ was added to all datapoints. As a signal, a simulated first-order chemical reaction was used, described by $y(x) = 1 - c_0 e^{-kx}$ (c_0 = 1, k = 4) and set to start at x = 0. With k = 4, the feature has essentially ended by x = 2 (99.97% of maximum value). Feature magnitude (resulting in the equal signal offset O_s) is 1. The feature was not varied in the synthetic data experiments, as its nature does not affect the baseline correction (since the feature datapoints are not considered during baseline fitting). As a baseline, a polynomial function of variable order with variable parameters was used. The pre-feature interval was defined to be x = [-2, 0) and the post-feature interval was x = [2, 4]. Baseline fitting function g*(x) was set to be a polynomial of the same order as the baseline (except when stated otherwise).

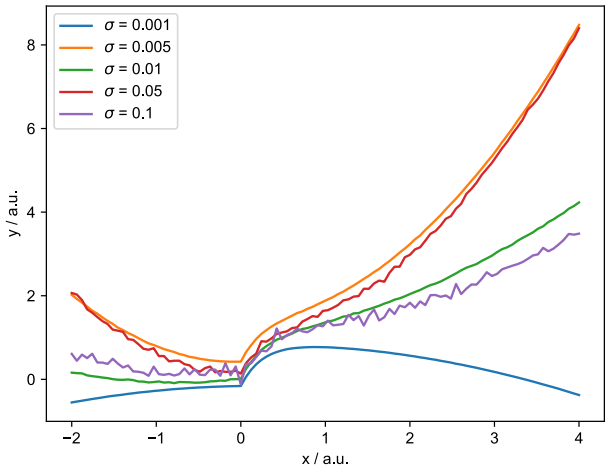

SI Figure 1. Exemplary synthetic data used for evaluation with second-order polynomial baseline, random baseline parameters (parameter range restricted to [-0.5, 0.5]) and different σ values for the Gaussian noise (total number of datapoints: 100 each).

1.1 Recovery of O_s and Baseline Parameters

SI Figure 2 shows the effect of baseline polynomial order, σ of Gaussian noise, total number of datapoints, selected baseline intervals and choice of polynomial for g*(x) on the recovery of O_s and baseline parameters using LBC. In all cases, the correct solution for c would be 1 (since O_s = 1). Root-mean square deviation of baseline parameters is defined as:

$$RMSD = \sqrt{\frac{\sum_{j=1}^{J}(a_{1,j} - a_{2,j})^2}{J}} \qquad (SI\ 1)$$

Where $a_{1,j}$ are the parameters of the actual baseline polynomial and $a_{2,j}$ are the parameters of g*(x) obtained using LBC.

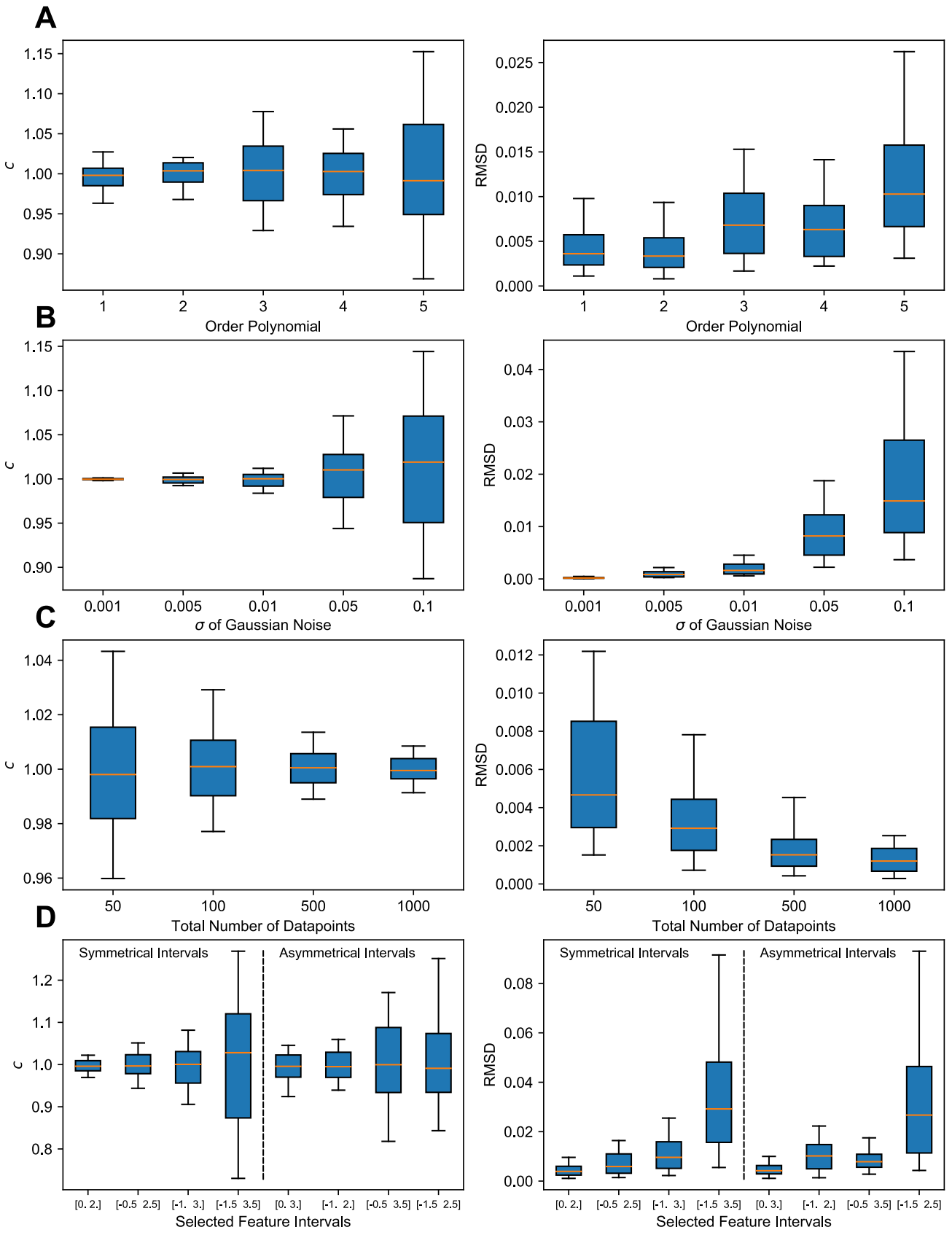
A
c
RMSD
Order Polynomial
B
σ of Gaussian Noise
C
Total Number of Datapoints
D
Symmetrical Intervals
Asymmetrical Intervals
Selected Feature Intervals
[0. 2.]
[-0.5 2.5]
[-1. 3.]
[-1.5 3.5]
[0. 3.]
[-1. 2.]
[-0.5 3.5]
[-1.5 2.5]

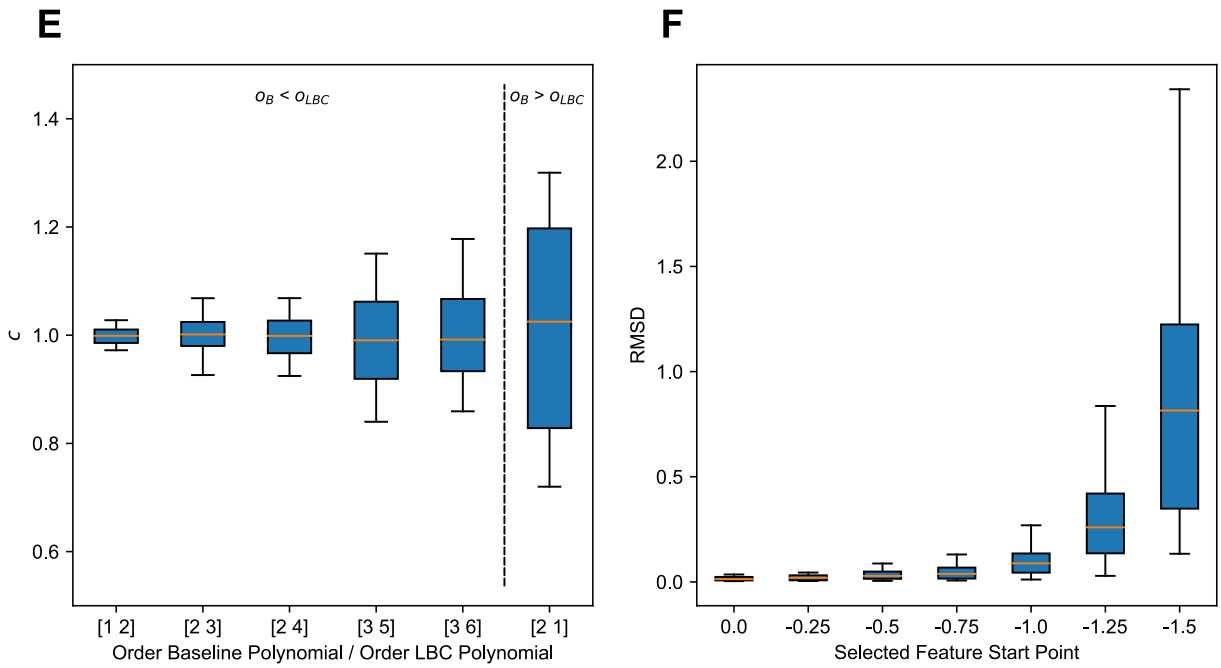

SI Figure 2. Effect of baseline polynomial order (**A**), σ of Gaussian noise (**B**), total number of datapoints (**C**), selected baseline intervals (**D**) and choice of polynomial order for g*(x) (**E**) on the accuracy and precision of recovered O_s (parameter c, left) and root-mean squared deviation (RMSD) of the recovered baseline function parameters (right) using LBC. **F** shows the effect of different feature start points on RMSD of the recovered baseline function parameters using pre-feature fitting. Boxplots show the results of 100 runs with randomly varying noise and random baseline parameters (range: [-0.5, 0.5]) for each configuration. Median is shown as orange line, boxes extend from lower to upper quartile values and whiskers show 5th and 95th percentile, respectively.
For **A**, σ is set to 0.02 and the total number of datapoints is 100.
For **B**, polynomial order is set to 2 and the total number of datapoints is 100.
For **C**, polynomial order is set to 2 and σ is set to 0.02.
For **D**, polynomial order is set to 2, total number of datapoints is 100 and σ is set to 0.02. For a given selected feature interval, the considered baseline intervals for LBC correspond to [-2, feature interval start] and [feature interval end, 4]. For example, in case of the selected feature interval [-1 3], the considered baseline intervals are [-2, -1] and [3, 4].
For **E**, σ is set to 0.02 and the total number of datapoints is 100. For a given pair of numbers on the x-axis, the first number indicates the order of the actual baseline polynomial (o_B) and the second number indicates the order of the polynomial used for g*(x) during LBC (o_{LBC}).
For **F**, polynomial order is set to 2, total number of datapoints is 100 and σ is set to 0.02. The pre-feature baseline interval used for pre-feature fitting in this case is [-2, feature start point].

Calculations with all configurations were performed 100 times with randomly varying Gaussian noise and random baseline parameters (range: [-0.5, 0.5]) to obtain distributions of c and RMSD. As it can be seen, c reliably approaches the correct signal offset O_s of 1 in all configurations. Uncertainty, however, increases with increasing polynomial order, increasing σ of the Gaussian noise, decreasing total number of datapoints and smaller baseline intervals, as expected. The same trends are also reflected for root-mean square deviations of baseline parameters but overall, low RMSD values are obtained. Using a higher order polynomial for g*(x) in LBC as compared to the actual baseline polynomial, c is still obtained with reasonable precision (SI Figure 2E, left). Using a lower order polynomial for g*(x), however, leads to a considerable loss in precision, as g*(x) does not have sufficient degrees of freedom to model the actual baseline. As can be seen in SI Figure 2F, pre-feature fitting becomes exceedingly imprecise when the

considered pre-feature interval is shortened, showing a much higher sensitivity to this change compared to LBC (SI Figure 2D right).

1.2 Comparison of LBC, Pre-Feature and Combined Fitting for Feature Analysis

To assess the effect of the baseline correction method on feature analysis, the same form of synthetic data as described above was used with the following parameters: σ of Gaussian noise: 0.02; total number of datapoints: 1000; baseline polynomial: $y(x) = -0.007x^2 + 0.05x + 0.4$. Pre-feature baseline fitting was performed using pre-feature datapoints and a polynomial of order 2 for g*(*x*), with subtraction of g*(*x*) yielding the pre-feature fitting corrected signal. LBC was performed using pre- and post-feature datapoints and also a polynomial of order 2 for g*(*x*) (subtraction of g*(*x*) yields LBC corrected signal). Thus obtained signals were analyzed by fitting integrated rate law (2) (see manuscript, *k* being the only parameter to be optimized as $[A_0]$ is set to 1) to the interval *t* = [0, 4] (here variable *t* instead of *x* is used as rate law (2) is a function of time). For comparison, rate law (2) has also been fitted as two-parameter function, optimizing both $[A_0]$ and *k* (see SI Figure 3C and D).

Robustness of the respective baseline correction method for signal analysis was assessed by using the above described synthetic data parameters but changing σ and the total number of datapoints. Following these alterations, pre-feature fitting and LBC were applied as described, followed by determination of *k*. A failed fitting (referring to unsuccessful feature analysis) is defined to be an instance where fitting rate law (2) to the baseline corrected signal yields a value for *k* which is smaller than 1. The choice of this threshold is based on the empirical observation of this failure mode (likely due to the fact that the initial guess for *k* is 1). Furthermore, a value of less than 1 for *k* can be considered unacceptably inaccurate and since the distribution of *k* is symmetrical (see Figure 2, manuscript), this threshold is also a proxy for *k* values significantly exceeding 4.

As can be seen in SI Figure 3A, pre-feature fitting is not robust to increasing levels of noise (with total number of datapoints fixed to be 1000), as the percentage of failed fittings rises rapidly as σ exceeds 0.1. LBC, on the other hand, is more robust due to the inclusion of more datapoints over a wider range, only showing few instances of failed fittings at $\sigma = 0.5$. As the total number of datapoints is reduced (with σ set to 0.2), pre-feature fitting shows a constantly increasing, high percentage of failed fittings. For LBC at this comparatively high noise level, failed fittings only arise below 100 datapoints (see SI Figure 3B). This increased robustness in the low datapoint number regime can again be explained due to the consideration of more baseline datapoints over a wider range for LBC.

Furthermore, SI Figure 3C and D show the distribution of *k* and $[A_0]$ values when equation (2) is fitted as two-parameter function (using either pre-feature fitting, LBC, combined fitting or fitting of equation (2) to data containing no baseline, control). SI Table 1 details the mean and standard deviation values for the distributions shown in SI Figure 3C and D as well as manuscript Figure 2.

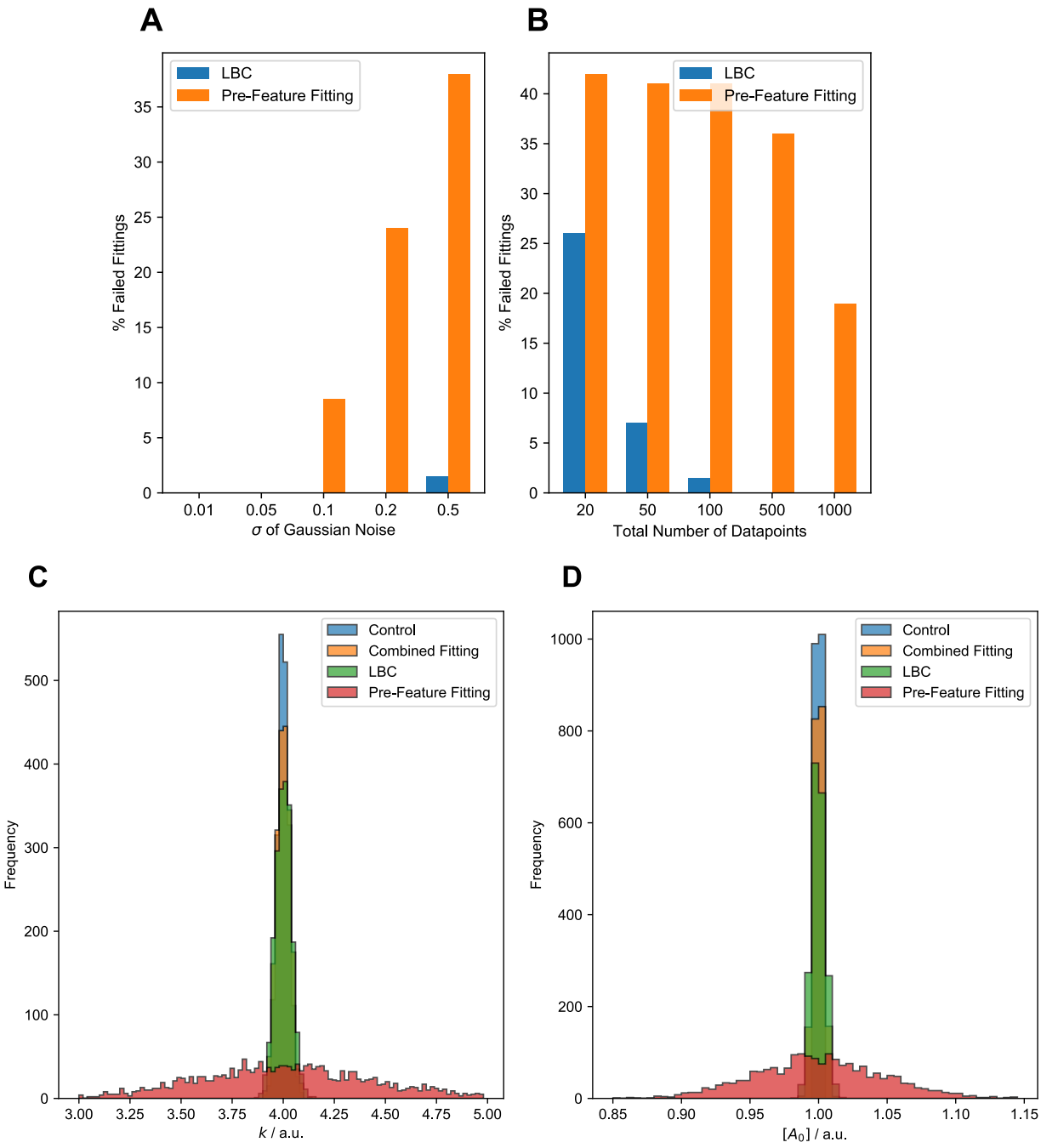

SI Figure 3. Bar plots showing failed feature fittings for different values of σ (**A**) and different total number of datapoints (**B**). Failed feature fittings for signals obtained using LBC are shown in blue, while failed feature fittings for signals obtained using pre-feature fitting baseline correction are shown in orange. Results are based on 200 runs with randomly varying Gaussian noise for each configuration. **A** Total number of datapoints: 1000; **B** σ of Gaussian noise: 0.2.

C Histogram of k obtained via fitting of integrated rate law (2) to signals obtained using different baseline correction methods as a two-parameter function (optimizing $[A_0]$ and k). Pre-feature fitting is shown in red, LBC in green and the control (fitting of (2) to signal containing noise but no baseline) in blue. Furthermore, combined fitting of baseline and feature by fitting the sum of a second-order polynomial and integrated rate law (2) is shown in orange. Analyses were performed 2000 times with randomly varying Gaussian noise in measurement.

D Distribution of $[A_0]$ values obtained during experiment described in **C**.

SI Table 1. Mean and standard deviation (in brackets) for optimized parameters shown in manuscript Figure 2B (column 1), SI Figure 3C (column 2) and SI Figure 3D (column 3).

	k (one parameter fitting)	*k* (two parameter fitting)	$[A_0]$ (two parameter fitting)
Pre-Feature Fitting	4.0 ± 0.133	4.0 ± 0.439	1.0 ± 0.0472
LBC	4.0 ± 0.049	4.0 ± 0.039	1.0 ± 0.0048
Combined Fitting	4.0 ± 0.030	4.0 ± 0.032	1.0 ± 0.0036
Control	4.0 ± 0.025	4.0 ± 0.027	1.0 ± 0.0009

From SI Table 1 (column 1) it can be seen that when equation (2) is fitted as a one-parameter function, the mean value of *k* correctly approaches 4 for all methods. The standard deviation, however, is significantly higher for pre-feature fitting compared to LBC and combined fitting. LBC and combined fitting approach the standard deviation of the control, with combined fitting performing better than LBC.
When equation (2) is fitted as a two-parameter function, the standard deviation for *k* strongly increases when pre-feature fitting is used. For combined fitting and the control, there is only a slight increase in the standard deviation. Surprisingly, for LBC the standard deviation is lower when equation (2) is fitted as a two-parameter function, although it still exceeds the standard deviation of the combined fitting approach.

2. Reaction Kinetics

2.1 Experimental Details

The reaction was performed under argon using standard Schlenk technique. A reactor equipped with a fiber-optic oxygen sensor (PyroScience, robust probe, normal) mounted in the gas phase was used, the sensor being connected to a FireStingO2 optical oxygen meter (PyroScience). Total internal volume of the reaction setup was 105 ml. At room temperature, 1 ml of an aqueous, degassed 0.52 M KI solution was placed in the reactor and stirred. Into a dropping funnel attached to the reactor, 830 µl of 9.8 mM aqueous, degassed H_2O_2 solution was placed. Afterwards, the system was completely sealed. The oxygen measurement was started, and after a defined amount of time, the valve of the dropping funnel was opened to add the H_2O_2 solution to the KI solution. After addition, the gas-phase oxygen content was measured for another 16.5h.

2.2 Analysis Details

For the first 500 s of the measurement, there was a small increase in oxygen content following a noticeably different trend compared to the subsequent baseline (see SI Figure 4B), likely the result of a more rapid equilibration after the system was sealed. Therefore, datapoints of the first 500 s were considered outliers and not used in the analysis. t = 500 s was therefore set to t = 0 s. The sampling frequency was one measurement every 10 s up to t = 3000 s, where after it was reduced to one measurement every 200 s. Furthermore, for LBC and post-feature correction (*vide infra*) all post-feature datapoints were used, although for visualization purposes, graphs are only shown up to t = 20,000 s.

H_2O_2 was added at t = 1500 s. Therefore, the pre-feature interval was set to t = [0 s, 1500 s), while the post-feature interval was defined to be t = [4000 s, 62000 s].

SI Figure 4A shows the unreasonable baseline estimate g*(*t*) obtained when performing pre-feature fitting using a second-order polynomial for g*(*t*). In Figure 4B, the entire dataset, including the discarded outlier datapoints at the beginning of the measurement and all post-feature datapoints, is shown including the LBC fit.

Due to the comparatively long post-feature phase of the measurement, post-feature fitting was also evaluated as a baseline correction method. For post-feature fitting, a second-order polynomial was fitted to the post-feature interval and then subtracted from the measurement (see SI Figure 4C and 4D). Subtraction of the post-feature baseline estimate g*(*t*) causes the post-feature phase to be zero (instead of the pre-feature phase). Therefore, the average of the first ten pre-feature datapoints was subtracted from the post-feature fitting corrected signal, obtaining the signal shown in SI Figure 4D. As can be seen in SI Figure 4D, post-feature fitting can capture the non-linear nature of the baseline and therefore yields a stationary post-feature phase. The pre-feature phase is also corrected reasonably well, although it shows a slight, monotonical increase. Furthermore, the applied correction using the average of some initial (pre-feature) values is an additional, potentially error-introducing step.

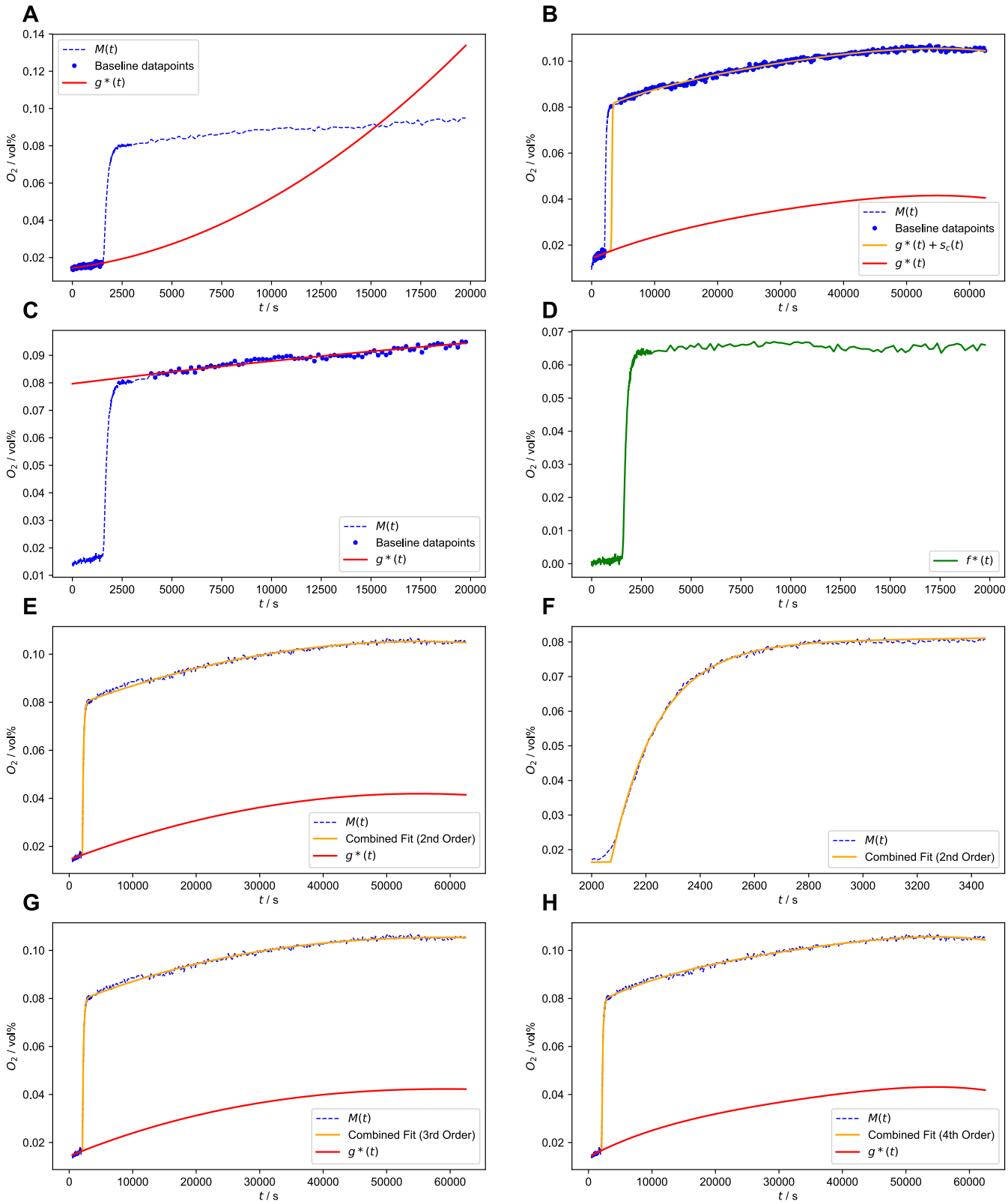
A
M(t)
Baseline datapoints
g*(t)
O2 / vol%
t / s
B
M(t)
Baseline datapoints
g*(t) + sc(t)
g*(t)
O2 / vol%
t / s
C
M(t)
Baseline datapoints
g*(t)
O2 / vol%
t / s
D
f*(t)
O2 / vol%
t / s
E
M(t)
Combined Fit (2nd Order)
g*(t)
O2 / vol%
t / s
F
M(t)
Combined Fit (2nd Order)
O2 / vol%
t / s
G
M(t)
Combined Fit (3rd Order)
g*(t)
O2 / vol%
t / s
H
M(t)
Combined Fit (4th Order)
g*(t)
O2 / vol%
t / s

SI Figure 4. Details regarding the reaction kinetics analysis.
A Unreasonable baseline estimate obtained for pre-feature fitting with a second-order polynomial for g*(*t*), displaying g*(*t*) baseline behavior contrary to the observed post-feature baseline.
B Entire dataset for KI catalyzed H_2O_2 disproportionation, including discarded outlier datapoints at the beginning of the measurement and full post-feature phase, along with LBC fit using fourth-order polynomial for g*(*t*).
C Post-feature fitting using a second-order polynomial for g*(*t*).
D Baseline corrected signal obtained by subtraction of g*(*t*) from post-feature fitting in **C**.
E Combined fitting of second-order polynomial + integrated rate law (2b) to entire measurement.
F Zoom of feature region for combined fit of second-order polynomial + integrated rate law (2b) showing modeling of feature.
G Combined fitting of third-order polynomial + integrated rate law (2b) with suitable initial guess for optimization parameters to entire measurement, showing good fit (for more information on guess dependence of combined fitting see SI section 5).
H Combined fitting of fourth-order polynomial + integrated rate (2b) with suitable initial guess for optimization parameters to entire measurement, showing good fit (for more information on guess dependence of combined fitting see SI section 5).

Signal analysis was accomplished by fitting integrated, normalized rate law (2a) to the normalized signal as a two-parameter function (*[A_0]* and *k*):

$$[B] = 1 - [A_0]e^{-kt} \qquad (2a)$$

Normalization of signals obtained with all baseline correction methods was done using the stationary value obtained by LBC (0.064 vol%). Fitting interval for the rate law was t = [1589 s, 7500 s], with the first 89 s after addition of H_2O_2 not being considered due to an apparent induction period caused by diffusion. This causes a non-first order behavior in the first 89 s after addition and would therefore distort the fit. This induction period was also the reason why the rate law was fitted as a two-parameter function (including *[A_0]* as an optimization parameter). For a normalized signal and a first-order reaction, *[A_0]* would be equal to 1. However, since not the entire signal could be used for analysis, observed *[A_0]* is smaller than one and was therefore also used as an optimization parameter. The differences in *[A_0]* for signals obtained with different baseline correction methods are small (0.8965 for LBC, 0.8910 for pre-feature fitting and 0.8949 for post-feature fitting).

Obtained *k* values are: 5.58×10^{-3} s^{-1} for LBC, 5.24×10^{-3} s^{-1} for pre-feature fitting and 5.98×10^{-3} s^{-1} for post-feature fitting. As expected, LBC yields a value between the extremes of pre- and post-feature fitting, as it is able to consider both datapoint intervals. For visualization in Figure 3 (manuscript), the rate law fit was rescaled to fit the shown, baseline corrected signal (which is not normalized).

Furthermore, combined fitting of the sum of a polynomial and integrated rate law (2b) to the entire measurement (except for initial 500 s, in the following the data was not shifted so that t = 500 s would be set to zero) was performed:

$$[B] = \begin{cases} 0 \; if \; t < t_{rs} \\ [A_0] - [A_0]e^{-k(t-t_{rs})} \; if \; t > t_{rs} \end{cases} \qquad (2b)$$

Where t_{rs} is a parameter describing the feature start time. This definition of the integrated rate law can be fitted to the entire measurement, as all function values preceding t_{rs} are set to zero and the term $t - t_{rs}$ allows for an arbitrary feature start time (rate law (2), in contrast, requires the feature to start at t = 0).

[A_0], k and t_{rs} were used as optimization parameters in addition to the polynomial parameters (with random initial guesses for *[A_0], k* and polynomial parameters and the guess for t_{rs} being 2073 s). Using this methodology, the combination of (2b) and a second-order polynomial does yield a reasonable fit over

the entire measurement range (see SI Figure 4E), which also accurately describes the feature (see SI Figure 4F). If a higher order polynomial together with random guesses for $[A_0]$, k and polynomial parameters is used, reasonable fits can be obtained (see SI Figure 4G and 4H), but convergence is not necessarily reliable (see SI section 5 for data on initial guess dependence). Likely, this is due to the additional degrees of freedom in the combined fit, which leads to interference between feature and baseline fitting. However, by using an improved strategy for guess generation, good fits can reliably be obtained using higher-order polynomials (details see SI section 5).

To compare combined fitting to baseline correction followed by feature analysis, the non-normalized signals obtained using LBC, pre- and post-feature fitting were also analyzed by fitting equation (2b) to the entire signal. In these cases, optimization parameters were $[A_0]$, k and t_{rs}. With this methodology, wherein the entire baseline corrected signal is fitted, no reasonable fit could be obtained for the pre-feature fitting corrected signal, as it is not stationary in the post-feature region.

For LBC, post-feature fitting and combined fitting the results are shown in SI Table 2.

SI Table 2. Optimized parameters $[A_0]$ and k obtained by fitting equation (2b) to baseline corrected signals obtained using either LBC or post-feature fitting and by combined fitting of equation (2b) and a fourth order polynomial.

	$[A_0]$	k / s^{-1}
LBC (fourth-order polynomial for g*(t))	6.38×10^{-2}	5.60×10^{-3}
Post-feature fitting (second-order polynomial for g*(t))	6.53×10^{-2}	5.43×10^{-3}
Combined fitting (fourth-order polynomial for g*(t), improved guess (see SI section 5)	6.25×10^{-2}	5.93×10^{-3}

Using the methodology based on equation (2b), the parameters obtained using LBC are very similar to those obtained using the normalization methodology described above. For post-feature fitting, $[A_0]$ is slightly higher than the LBC estimate and k is slightly lower than the value obtained when post-feature fitting was followed by the normalization methodology above. Combined fitting yields a value for $[A_0]$ which is slightly lower than the value obtained using LBC and it gives a higher estimate for k by roughly 6% compared to LBC.

Regarding the final amount of oxygen: based on the used quantity of H_2O_2, 4.2×10^{-6} mol of O_2 are expected to form in case of quantitative disproportionation. In the ideal gas approximation under normal conditions, this would correspond to 0.1 ml, or 0.097 vol% in the used reactor. The observed O_2 yield is therefore ~66%. As H_2O_2 disproportionation is expected to be quantitative under the employed reaction conditions, the less than quantitative yield is likely a result of not all the H_2O_2 solution reaching the bottom of the reactor (where the KI solution was placed).

3. Quantitative Polymerase Chain Reaction

3.1 Determination of Feature Start and End Points

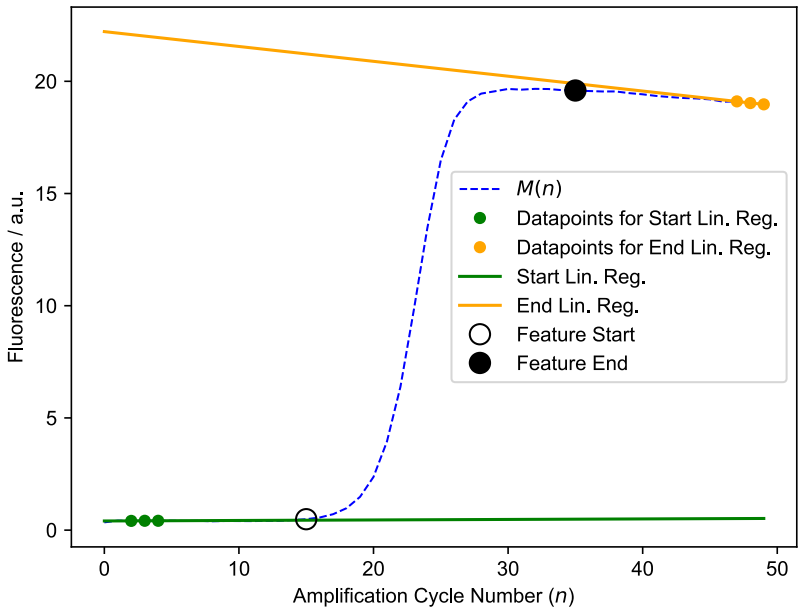

SI Figure 5. Illustration of feature start/end point determination method for m = 3 and i = 5. Pre-feature datapoints considered for linear regression are shown in green, with the resulting linear regression model shown as a green line. The feature start point is the first point exceeding the linear regression model by more than 5 standard deviations (standard deviation of the three considered pre-feature datapoints) and is only followed by datapoints also exceeding this threshold. Note that the first two datapoints are not used, since they usually display slightly inaccurate fluorescence. The feature end point is determined in a symmetrical way, being the last datapoint with fluorescence lower than the end linear regression model by more than 5 standard deviations (standard deviation of the three considered post-feature datapoints) and only being preceded by datapoints, which are also below this threshold.

3.2 qPCR Analysis

For the analysis of qPCR data using LBC, the first two datapoints of the pre-feature interval were not considered. In case of pre-feature, fitting, it was found that inclusion of the first two datapoints improves bias; therefore they were used for pre-feature baseline fitting. Since the number of considered datapoints in case of pre-feature fitting is already low, including two more datapoints (even if they display slightly inaccurate fluorescence), apparently improves this analysis approach.

For both methods, N (size of random subsample for efficiency determination) was set to 10. Pre-feature fitting used a linear baseline function for g*(n), while LBC used a second-order polynomial function. For LBC, pre-feature datapoints were weighted with a weighing factor of 8. Including a weighing factor improved robustness and accuracy since signal analysis is performed very close to the pre-feature interval. Therefore, modeling the pre-feature region more accurately by giving it a higher weight in the optimization is beneficial. The weighing factor was implemented in the residual function in the following way:

$$\overrightarrow{res} = \left(\vec{y} - s_c(\vec{n}) - g^*(\vec{n})\right)\vec{w} \qquad (SI\ 2)$$

With $\vec{w}$ being a vector of the same length as $\vec{n}$. The first *h* values of $\vec{w}$ are 8 (*h* being the number of pre-feature datapoints used for LBC), the rest being 1.

Signal analysis was accomplished by fitting PCR equation (3) to the exponential amplification phase. This phase is defined to be the interval from feature start to the point preceding the second derivative maximum (SDM). Not including the second derivative maximum point itself improved bias in the analysis for both LBC and pre-feature fitting corrected signals. Amplification efficiency E_{amp} for a gene was determined as the average of E_{amp} obtained via fitting of equation (3) as a two-parameter function to a random subsample of reactions of that gene. When calculating the average value of E_{amp} (which is usually expected to be just below 2), only values in the range E_{amp} = [1.5, 2.5] were considered. This was done because lower or higher E_{amp} values can be considered unreasonable and the result of a failed optimization. Using the thus determined, gene specific E_{amp} value, equation (3) was fitted to all reactions of the gene as a one-parameter function, obtaining F_0. All signal analysis steps were performed completely separately for LBC and pre-feature fitting corrected data.

3.3 Performance Evaluation

Analysis performance was assessed using the performance indicators developed by Ruijter et al. (*Methods,* 59, 2013, 32 – 46). Evaluation was done using 15 F_0 values per gene for all 63 genes, leading to 63 performance indicator values for each indicator. The reported indicators are bias, slope, linearity, precision, increased variation and resolution. They are visualized using boxplots showing the median value as an orange line, the box extending from lower to upper quartile and the whiskers showing the 5th and 95th percentile. For each indicator plot, the considered methods are sorted by increasing median value. For methods other than the ones developed herein, target quantities used for performance evaluation were also taken from Ruijter et al. 2013. The difference in bias between LBC and pre-feature fitting for *m* = 3 and *i* = 5 was assessed using a two-sided T-test for independent samples with assumed equal variances (as implemented in SciPy), giving a *p*-value of 0.00103 (t-statistic = -3.36). Since LBC has a mean bias of 1.032 while the mean for pre-feature fitting is 1.26, it can be concluded that LBC and pre-feature fitting show a statistically significant difference in bias, with LBC being closer to 1.

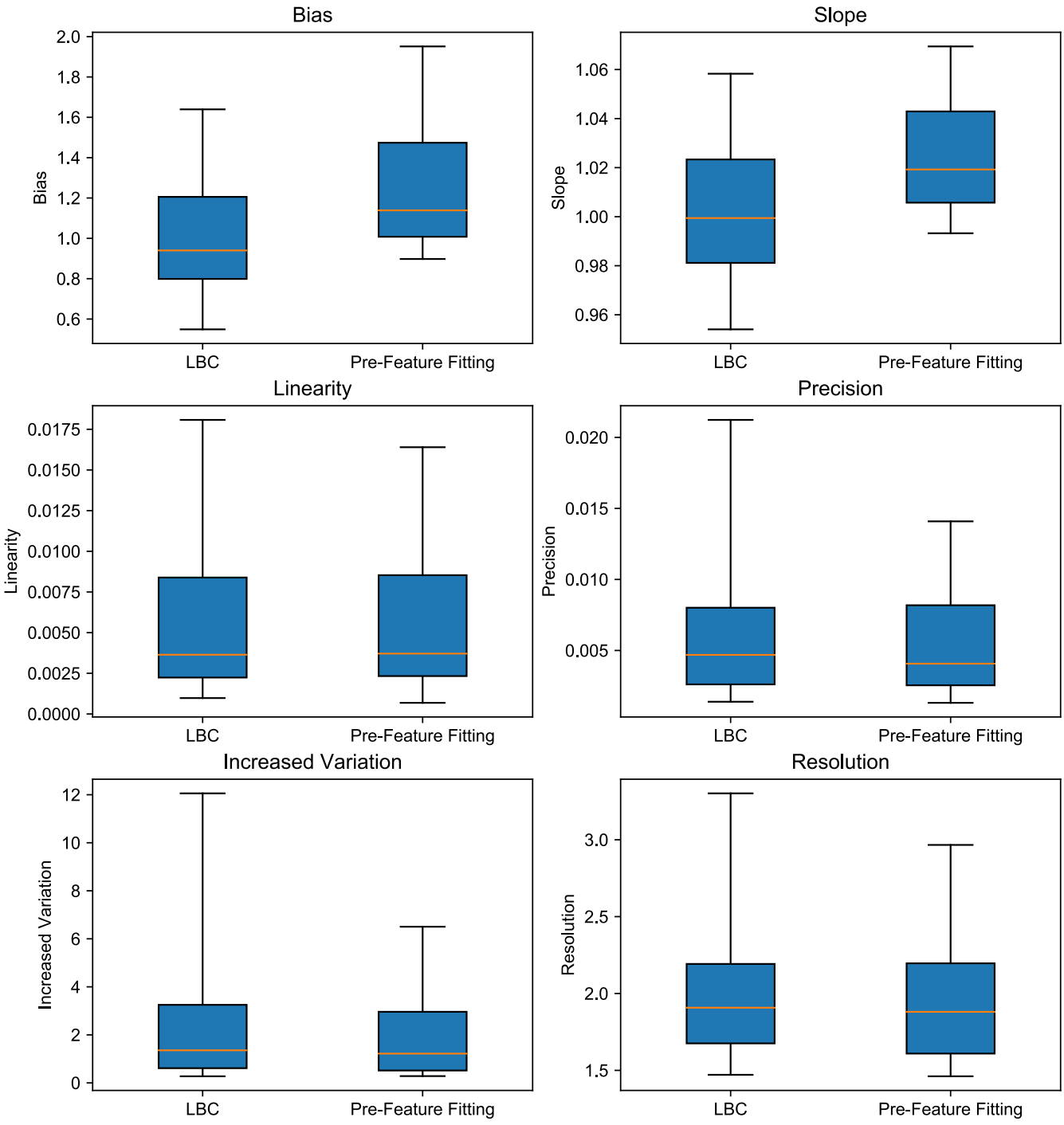

SI Figure 6. Boxplots of all performance indicators for LBC and pre-feature fitting qPCR analysis. *m* (number of datapoints considered for linear regression models) = 3, *i* (number of standard deviations for threshold) = 5.

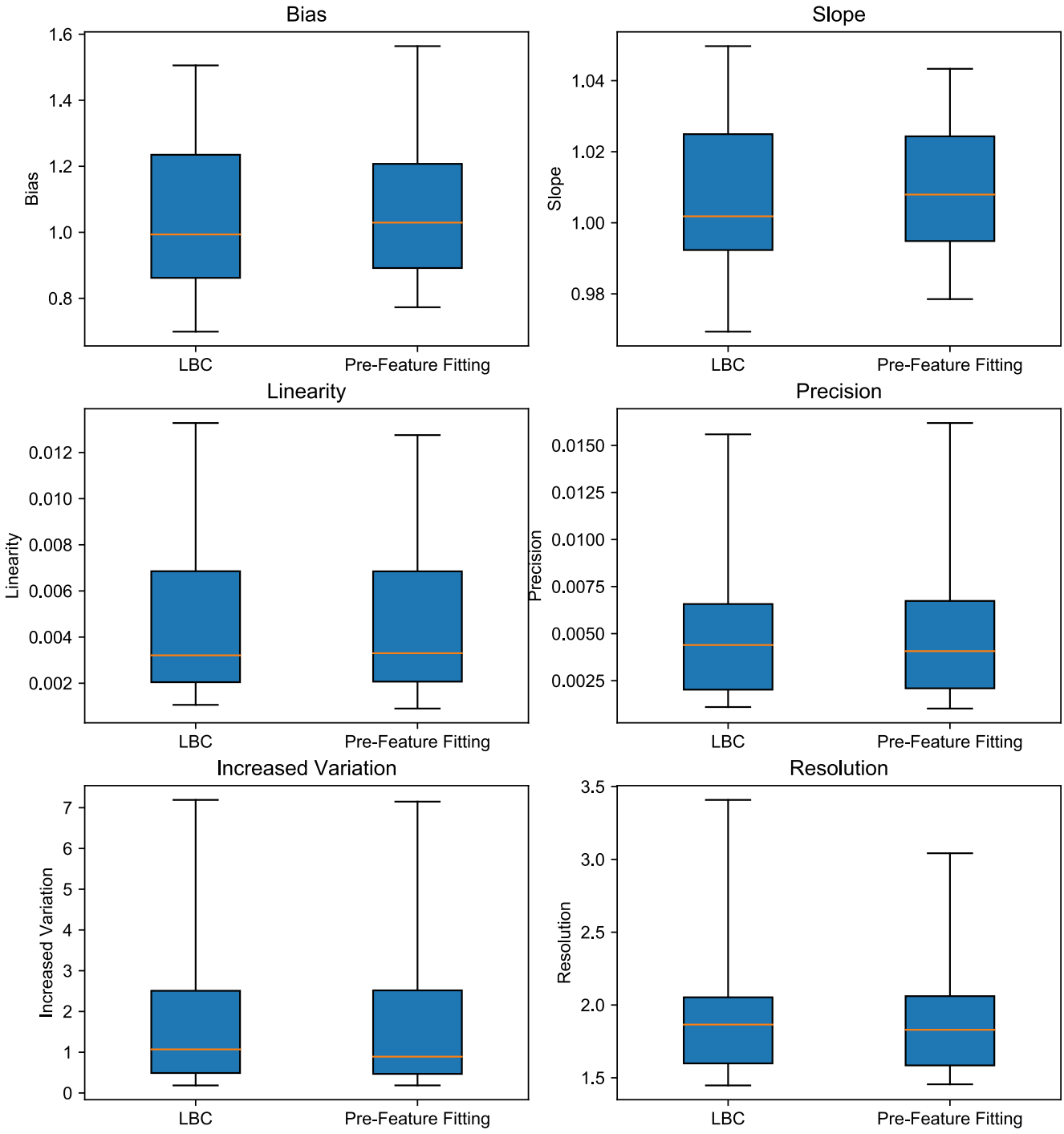

SI Figure 7. Boxplots of all performance indicators for LBC and pre-feature fitting qPCR analysis. *m* (number of datapoints considered for linear regression models) = 5, *i* (number of standard deviations for threshold) = 7.

SI

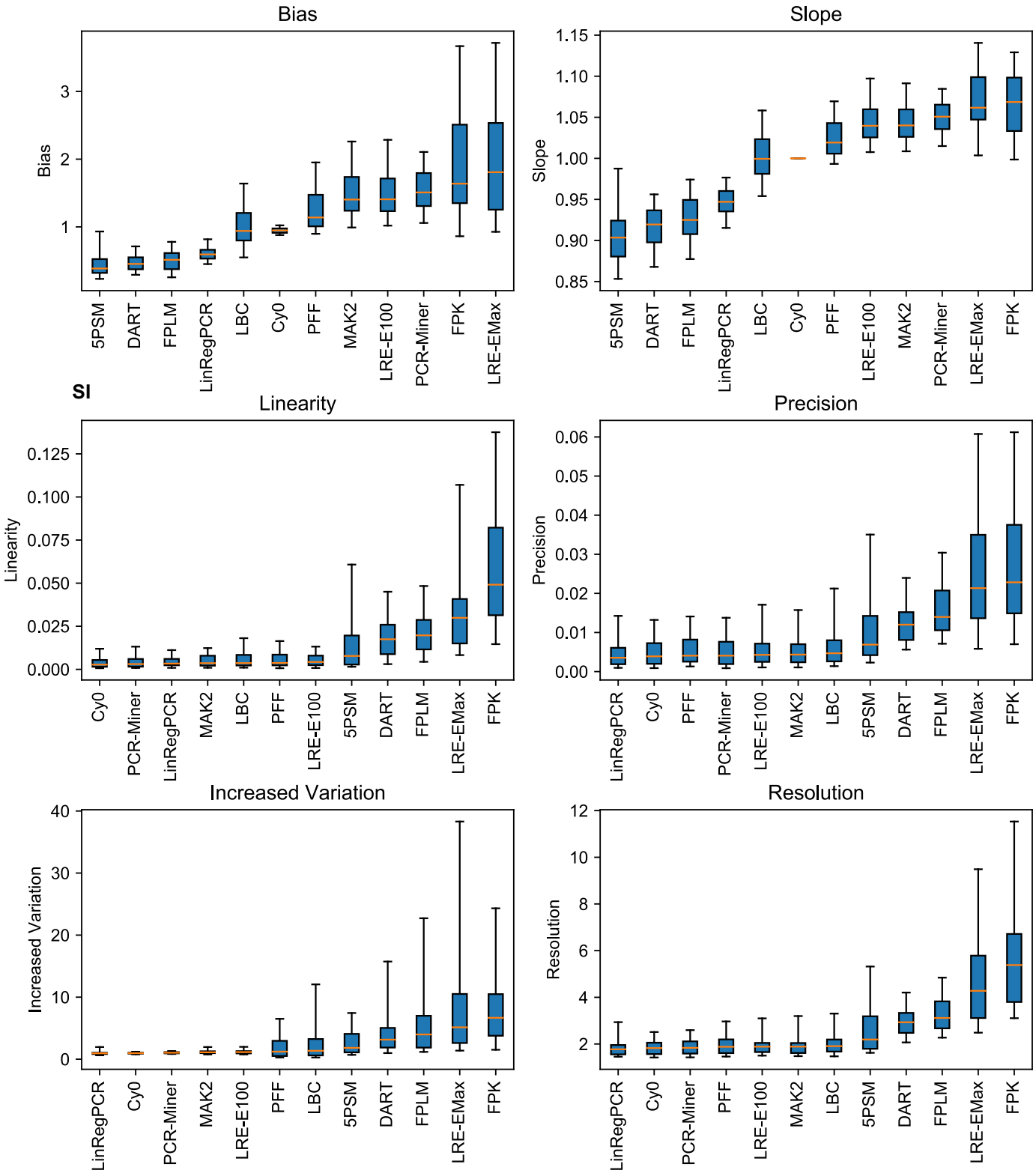
Bias
Bias
5PSM
DART
FPLM
LinRegPCR
LBC
Cy0
PFF
MAK2
LRE-E100
PCR-Miner
FPK
LRE-EMax
Slope
Slope
Linearity
Linearity
Precision
Precision
Increased Variation
Increased Variation
Resolution
Resolution

SI Figure 8. Boxplots of all performance indicators for LBC, pre-feature fitting (abbreviated as PFF) and the qPCR analysis methods reported in Ruijter et al. 2013. Parameters for LBC and pre-feature fitting: *m* (number of datapoints considered for linear regression models) = 3, *i* (number of standard deviations for threshold) = 5. As can be seen in SI Figure 6, for *m* = 3 and *i* = 5, LBC and pre-feature fitting perform similarly for linearity and resolution. In case of precision and increased variation, pre-feature fitting shows a tighter distribution and slightly lower median values. LBC, however, shows improved bias and linearity. For *m* = 5 and *i* = 7 both methods perform effectively the same (see SI Figure 7). In comparison with other qPCR analysis methods, the developed algorithm using either LBC or pre-feature fitting (*m* = 3, *i* = 5) performs on par with the best methods, showing especially good bias and linearity values (see SI Figure 8). For increased variation, however, there are numerous methods outperforming the developed algorithm.

4. X-Ray Absorption Spectroscopy

4.1 Baseline Correction for Fe_3C and $FeCl_3$ Spectra

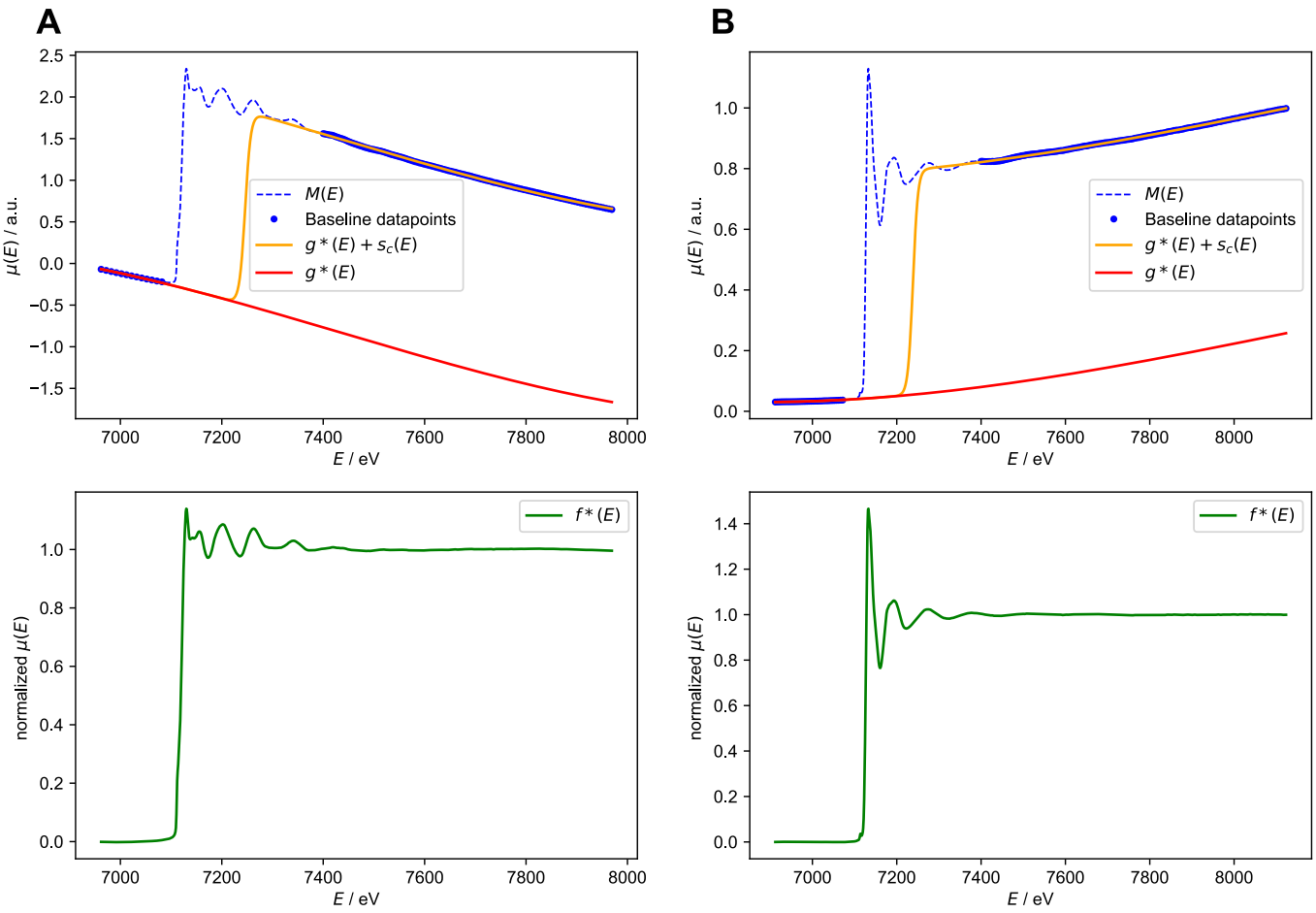

SI Figure 9. LBC applied for baseline correction and normalization of X-ray absorption *K*-edge spectra of Fe_3C (**A**) and $FeCl_3$ (**B**). **A** Feature start point set to E = 7088 eV and feature end point set to E = 7400 eV. Third-order polynomial used for g*(E). **B** Feature start point set to E = 7079 eV and feature end point to E = 7400 eV. Third order polynomial used for g*(E).

4.2 Background Estimation and White Line Analysis for Molybdenum Foil Spectrum

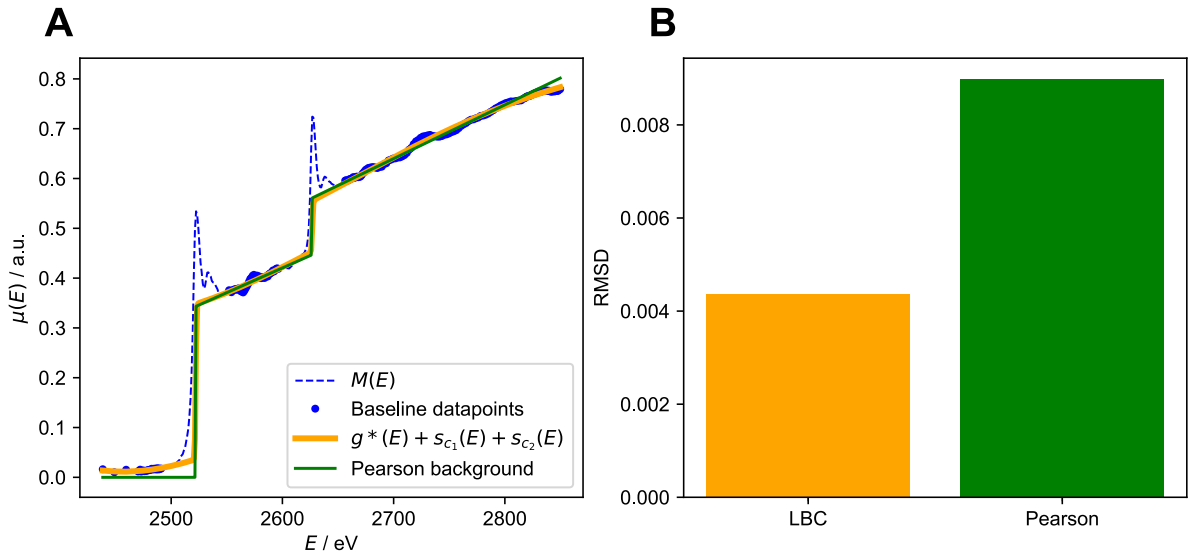

SI Figure 10. A L_{23}-edge region of molybdenum foil X-ray absorption spectrum with LBC fit ($g^*(E) + s_{c_1}(E) + s_{c_2}(E)$, fourth-order polynomial for g*(x), orange) and Pearson background (determined as described in Okamoto et al. in *Transm. Electron Energy Loss Spectrom. Mater. Sci. EELS Atlas*, John Wiley & Sons, Ltd, **2005**, pp. 317–352, green). Baseline data points considered for LBC are highlighted.
B Bar plot of RMSD calculated using equation (SI 1) between highlighted baseline data points and either LBC (orange) or Pearson background (green).

To perform LBC for the molybdenum foil spectrum, a fourth-order polynomial for g*(x) was used along with two logistic functions, $s_{c_1}(E)$ and $s_{c_2}(E)$. Feature start and end values for both edges were set at -/+ 30 eV from the absorption maximum of each edge (absorption maxima are at 2522 eV for L3 and 2626 eV for L2). This results in the following baseline intervals used for LBC: [2438 eV, 2491 eV], [2552 eV, 2596 eV], [2656 eV, 2849 eV]. For each logistic function, x_0 and r were determined from the selected baseline intervals, ensuring that $s_{c_1}(E)$ accounts for the L3 absorption edge while $s_{c_2}(E)$ accounts for the L2 absorption edge. For the determination of r, v_{75} was set to $9.99 \cdot 10^{18}$ in both cases, which results in a higher logistic growth rate, making the LBC background more comparable to the step functions used in the Pearson background. The obtained LBC fit, $g^*(E) + s_{c_1}(E) + s_{c_2}(E)$, was used as the background for white line analysis.

The Pearson background was determined as described in Okamoto et al. in *Transm. Electron Energy Loss Spectrom. Mater. Sci. EELS Atlas*, John Wiley & Sons, Ltd, **2005**, pp. 317–352. For this, linear regressions were fitted to 50 eV wide intervals starting 20 eV after each absorption maximum, giving $g^*_1(E)$ for the L3 and $g^*_2(E)$ for the L2 edge. $g^*_1(E)$ is extrapolated from the L3 edge absorption maximum to the L2 absorption maximum and it is set to zero for all energies preceding the L3 edge absorption maximum. $g^*_2(E)$ is extrapolated from the L2 absorption maximum to the end of the spectrum, providing the Pearson background for the entire spectrum.

For a given background (LBC or Pearson) white line intensities were calculated as described in Okamoto et al. in *Transm. Electron Energy Loss Spectrom. Mater. Sci. EELS Atlas*, John Wiley & Sons, Ltd, **2005**, pp. 317–352: The white line integration intervals for each white line were defined to be -/+ 20 eV from the

respective absorption maximum. The raw spectrum M(*E*) was numerically integrated in these intervals. For each integral, the corresponding integral of the background in the same interval was calculated and subtracted from it, yielding raw white line integrals. A normalization integral was then calculated by integrating the background in an interval 50 eV wide starting 50 eV past the L3 absorption maximum. Raw white line integrals were each divided by the normalization integral, yielding normalized integrals. The sum of normalized integrals for the L3 and L2 white lines is the reported white line intensity.

As can be seen in in SI Figure 10A, LBC and Pearson background differ the most for energies preceding the L3 edge. This is because the Pearson background is set to zero for these energies while LBC accurately describes the datapoints in this area. Therefore, LBC gives a lower RMSD of background and baseline datapoints (SI Figure 10B). This gives reason to believe that white line intensities, which rely on an accurate description of the background, are calculated more accurately when using the LBC background.

4.3 Baseline Correction and Pre-Edge Peak Analysis for Copper Foil Spectrum

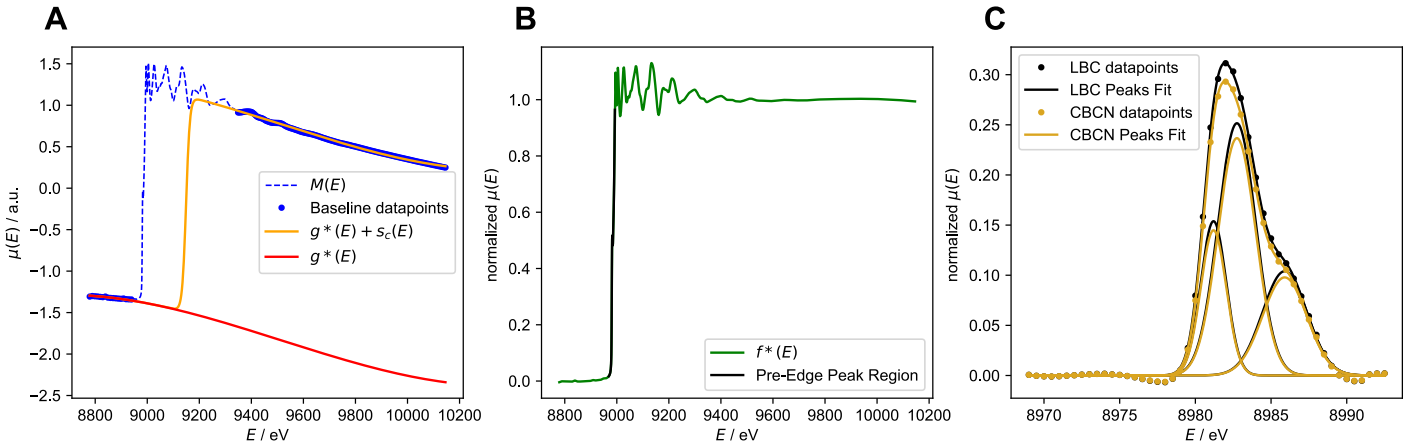

SI Figure 11. Analysis of X-ray absorption spectrum of copper foil. **A** LBC applied to copper *K*-edge region of the spectrum using a third-order polynomial for g*(*E*). **B** Baseline corrected K-edge region of spectrum obtained using LBC with pre-edge peak region highlighted in black. **C** Fitting of pre-edge peaks using multiple pseudo-Voigt functions. Analysis shows that the signal obtained via conventional baseline correction/normalization (CBCN, yellow) displays a ~6% lower pre-edge peak intensity compared to the signal obtained via LBC (black).

For LBC of the copper foil spectrum shown in SI Figure 11, the feature start point was set to *E* = 8949 eV and the feature end point to *E* = 9349 eV. A third-order polynomial was used for g*(*x*).

To analyze the pre-edge peaks, the pre-edge peak region was defined to be the interval *E* = [8969 eV, 8993 eV], with pre-edge peak features in the interval *E* = [8977 eV, 8989 eV]. With this definition, baseline corrected and normalized spectra obtained using LBC as well as using CBNC (as implemented in Larch) were each analyzed separately in the following way:

1. To remove the influence of the absorption edge in the pre-edge peak region, classical baseline correction (since pre-edge peaks are non-baseline-altering features) was performed using pre- and post-feature datapoints of the region (pre-feature interval *E* = [8969 eV, 8977 eV], post-feature interval *E* = [8989 eV, 8993 eV]). For this classical baseline correction, g*(*E*) was chosen to be the sum of an exponential function ($y(x) = ae^{bx}$) and a third-order polynomial. Fitted g*(*E*) was then subtracted from the pre-edge peak region.
2. The classically baseline corrected pre-edge peak region was fitted using the sum of three pseudo-Voigt functions with four parameters each (position, height, width and Gaussian/Lorentzian ratio, see SI Figure 11C).

As can be seen in SI Figure 11C, pre-edge peak position and multiplicity are not affected by the choice of baseline correction/normalization method. Pre-edge peak intensity, however, differs by ~6% between LBC and CBCN.

For comparison, analysis was also performed on a baseline corrected and normalized spectrum obtained using the MBACK algorithm (Weng et al., *Journal of Synchrotron Radiation,* 12(4), 506 – 510, as implemented in Larch, parameters: z = 29, edge = K, order = 4). This gives a very similar result compared to the conventional baseline correction/normalization approach, although with a slightly lower pre-edge peak intensity (~7% lower intensity for MBACK compared to LBC, while the conventional approach yields ~6% lower intensity compared to LBC).

5. Supplementary Information on Combined Fitting

Combined fitting is an approach that also utilizes pre- and post-feature datapoints (as well as feature datapoints) by fitting baseline and feature simultaneously, thus accounting for the offset introduced by the feature. It is applicable when there is a function h*(x) which can describe the whole feature.

In case of the synthetic data described above, such a function exists and combined fitting actually offers higher precision than LBC (see manuscript Figure 2B). This is likely because it utilizes even more datapoints during fitting than LBC (as it also considers feature datapoints during fitting).

However, h*(x) will usually introduce more degrees of freedom during the fitting step, which can lead to interference between baseline and feature fitting. This can make the fitting procedure more sensitive to the initial guess for the optimization parameters. To reach convergence to the optimal solution, a suitable initial guess has to be used (see SI Figure 12), which can in fact be generated using LBC.

In comparison, LBC provides a good baseline description using a fourth-order polynomial for g*(x) (see SI Figure 4B) with very stable convergence properties (see SI Figure 12A). These improved convergence properties for LBC can likely be explained by the fact that LBC only introduces one additional, highly constrained degree of freedom (parameter c, which can only describe signal offset O_s).

To evaluate the dependence of combined fitting on the initial guess for the optimization parameters, the following experiment was performed: the H_2O_2 disproportionation data was fitted as described in SI section 2 using combined fitting with equation (2b) and a fourth-order polynomial. For optimization, the Levenberg-Marquardt algorithm as implemented in SciPy (E. Jones, T. Oliphant, P. Peterson, others, *SciPy: Open Source Scientific Tools for Python*, **2001**) was used. Random initial guesses for polynomial parameters, $[A_0]$ and k were generated using the absolute values of a normal distribution with different σ values. The initial guess for t_{rs} was always 2073 s.
For each σ value, 50 fitting attempts were performed and for each attempt, the sum of the square of residuals (R_s) was calculated to judge the fit quality. In this configuration, the optimal solution has a R_s value of 2.8×10^{-4}. Thus, each attempt with a R_s value $< 3 \times 10^{-4}$ was classified as a successful fitting attempt.
For comparison, during each combined fitting attempt, LBC with a fourth-order polynomial for g*(t) (feature start = 2000 s, feature end = 4500 s) was also performed using random initial guesses (for polynomial parameters and c), generated in the same way (same σ value). For LBC, the optimal solution has a R_s value of 1.98×10^{-4}. Thus, each attempt with a R_s value $< 2 \times 10^{-4}$ was classified as a successful fitting attempt.

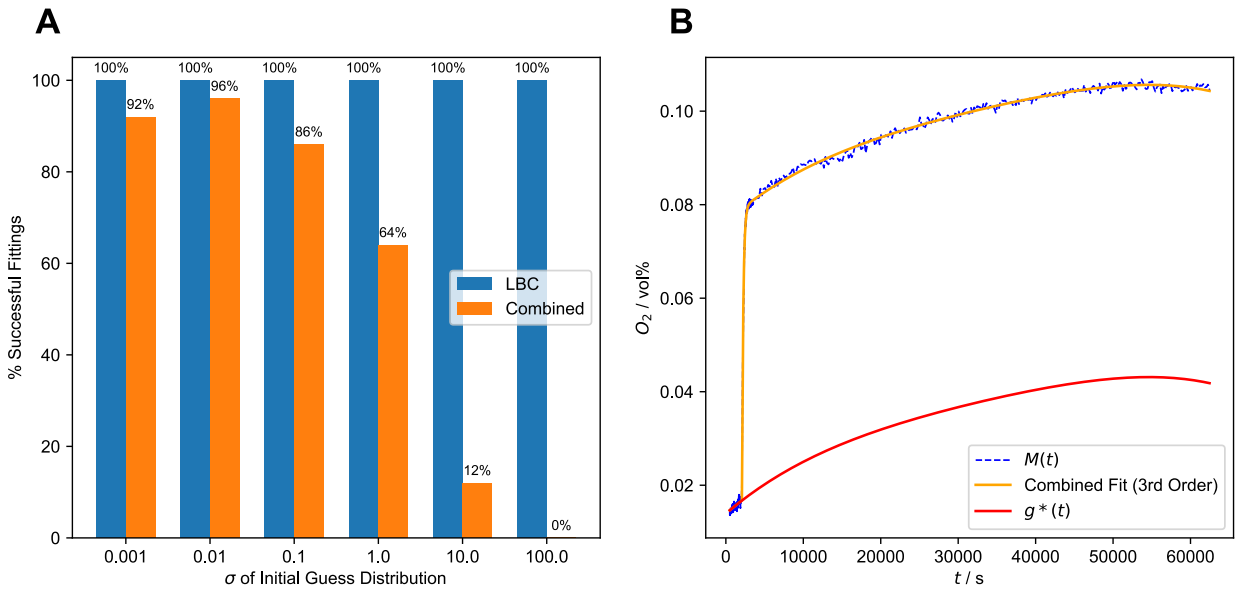

Si Figure 12. Initial guess dependence of combined fitting approach compared to LBC for H_2O_2 disproportionation data.
A Percentage of successful fitting attempts for combined fitting (fourth-order polynomial + equation (2b)) and LBC for different random initial guess distributions (absolute values of normal distribution with indicated σ value). For each σ value, 50 fitting attempts were performed.
B Optimal combined fit (fourth-order polynomial + equation (2b)) obtained using initial guess generated using LBC.

SI Figure 12A shows the percentage of successful fitting attempts for six different σ values. LBC can tolerate any guess within this random space and has a 100% fitting success rate for every σ value. For combined fitting, however, the percentage of successful fitting attempts decreases significantly for higher σ values, ultimately reaching 0% for σ = 100. This trend can likely be explained by the fact that the optimal parameters (except t_{rs}) are all smaller than 1 (optimal polynomial parameters are 1.39e-02, 1.42e-06, -3.67e-11, 6.39e-16, -4.78e-21, $[A_0]$ = 6.25e-02, k = 5.93e-03, t_{rs} = 2073). As σ increases, more values which are significantly larger than 1 are used as initial guesses, moving the initial guess further away from the optimal solution. As combined fitting has more parameters, which can interfere with one another during fitting, these poor guesses are not tolerated and no convergence to the optimal solution is achieved.

This dependence on a high-quality initial guess can be addressed using LBC. LBC can provide optimized parameters for the polynomial as well as $[A_0]$ (since for LBC, c approaches $[A_0]$ during optimization). By using these parameters as an initial guess, together with a random guess for k and t_{rs} = 2073 s, the optimal combined fitting solution is obtained (see SI Figure 12B). The high quality guess provided by LBC ensures that only k has to be significantly optimized, while the other parameters are already very close to their optimal values (since the LBC solution for the baseline and signal magnitude, $[A_0]$ in this case, are very close to those obtained using combined fitting). This reduces the problem of interference between optimization parameters and reliably yields the optimal solution.